Experimental Thermodynamics Volume IX
Advances in Transport Properties of Fluids

Experimental Thermodynamics Series

Titles in this Series:

1: **Calorimetry of Non-Reacting Systems**
Edited by J. P. McCullough and D. W. Scott
Butterworths, London, 1968.

2: **Experimental Thermodynamics of Non-Reacting Fluids**
Edited by B. Le Neindre and B. Vodar
Butterworths, London, 1975

3: **Measurement of the Transport Properties of Fluids**
Edited by W. A. Wakeham, A. Nagashima, and J. V. Sengers
Blackwell Scientific Publications, Oxford, 1991

4: **Solution Calorimetry**
Edited by K. N. Marsh and P. A. G. O'Hare
Blackwell Scientific Publications, Oxford, 1994

5: **Equations of State for Fluids and Fluid Mixtures**
Edited by J. V. Sengers, R. F. Kayser, C. J. Peters, and H. J. White, Jr.
Elsevier, Amsterdam, 2000

6: **Measurement of the Thermodynamic Properties of Single Phases**
Edited by A. R. H. Goodwin, K. N. Marsh, W. A. Wakeham
Elsevier, Amsterdam, 2003

7: **Measurement of the Thermodynamic Properties of Multiple Phases**
Edited by R. D. Weir and T. W. de Loos
Elsevier, Amsterdam, 2005

8: **Applied Thermodynamics of Fluids**
Edited by A. R. H. Goodwin, J. V. Sengers, C. J. Peters
Royal Society of Chemistry, Cambridge, 2010

9: **Experimental Thermodynamics Volume IX: Advances in Transport Properties of Fluids**
Edited by M. J. Assael, A. R. H. Goodwin, V. Vesovic and W. A. Wakeham
Royal Society of Chemistry, Cambridge, 2014

Experimental Thermodynamics Volume IX

Advances in Transport Properties of Fluids

Edited by

M. J. Assael
Faculty of Chemical Engineering, Aristotle University, Thessaloniki, Greece

A. R. H. Goodwin
Schlumberger Technology Corporation, Sugar Land TX 77478, USA

V. Vesovic
Department of Earth Science and Engineering, Imperial College London, London, UK

W. A. Wakeham
Department of Chemical Engineering, Imperial College London, London, UK

Print ISBN: 978-1-84973-677-0
PDF eISBN: 978-1-78262-525-4

A catalogue record for this book is available from the British Library

Published by The Royal Society of Chemistry,
Thomas Graham House, Science Park, Milton Road,
Cambridge CB4 0WF, UK

Registered Charity Number 207890

Visit our website at www.rsc.org/books

List of Contributors

E. H. Abramson
Department of Earth and Space Sciences, University of Washington, Seattle, WA 98195-1310, USA
evan@ess.washington.edu

J. I. D. Alexander
School of Engineering University of Alabama in Birmingham, Birmingham, AL 35294, USA
ialex@uah.edu

K. D. Antoniadis
Faculty of Chemical Engineering, Aristotle University, GR54124 Thessaloniki, GREECE
kantoniad@auth.gr

M. J. Assael
Faculty of Chemical Engineering Aristotle University, GR54124 Thessaloniki, GREECE
assael@auth.gr

R. M. Banish
Department of Chemical and Materials Engineering, University of Alabama in Huntsville, Huntsville, AL 35899, USA
banish@uah.edu

R. F. Berg
Sensor Science Division National Institute of Standards and Technology, Gaithersburg, MD 20899, USA
robert.berg@nist.gov

E. Bich
Institut für Chemie, Universität Rostock, Albert-Einstein-Straße 3a, D-18059 Rostock, GERMANY
eckard.bich@uni-rostock.de

J. F. Brennecke
Department of Chemical and Biomolecular Engineering University of Notre Dame, Notre Dame, IN 46556, USA
jfb@nd.edu

J. Brillo
Institut für Materialphysik im Weltraum, Deutsches Zentrum für Luft- und Raumfahrt (DLR), D-51170 Köln, GERMANY
Juergen.Brillo@dlr.de

H. R. Corti
INQUIMAE-CONICET
Facultad de Ciencias Exactas y Naturales,
Universidad de Buenos Aires,
Intendente Güiraldes 2160
C1428EGA, Ciudad Autónoma de Buenos Aires,
ARGENTINA
hrcorti@cnea.gov.ar

I. Egry
Institut für Materialphysik im Weltraum,
Deutsches Zentrum für Luft- und Raumfahrt (DLR),
D-51170 Köln,
GERMANY
Ivan-Egry@t-online.de

J. Fernández
Faculty of Physics, Campus Vida
University of Santiago de Compostela,
E-15782 Santiago de Compostela,
SPAIN
josefa.fernandez@usc.es

A. P. Fröba
Erlangen Graduate School in Advanced Optical Technologies (SAOT),
Friedrich-Alexander-Universität Erlangen-Nürnberg (FAU),
Paul-Gordan-Straße 6, D-91052 Erlangen, GERMANY
apf@aot.uni-erlangen.de

G. Galliero
Laboratoire des Fluides Complexes et leurs Réservoirs
Université de Pau et des Pays de l'Adour, Avenue de l'Université
BP 1155 64013 PAU Cedex,
FRANCE
guillaume.galliero@univ-pau.fr

K. A. Gillis
Sensor Science Division
National Institute of Standards and Technology, Gaithersburg, MD 20899, USA
keith.gillis@nist.gov

K. R. Harris
School of Physical, Environmental and Mathematical Sciences,
The University of New South Wales, UNSW Canberra,
PO Box 7916, Canberra BC, ACT 2610, AUSTRALIA
k.harris@adfa.edu.au

R. Hellmann
Institut für Chemie,
Universität Rostock,
D-18059 Rostock, GERMANY
robert.hellmann@uni-rostock.de

J. Hu
Institute of Modern Optical Technologies, Key Lab of Advanced Optical Manufacturing Technologies of Jiangsu Province,
Soochow University,
Suzhou, 215006,
PR China
gumuyue@163.com

W. Köhler
Physikalisches Institut
Universität Bayreuth,
D-95440 Bayreuth, GERMANY
werner.koehler@uni-bayreuth.de

A. Laesecke
Applied Chemicals and Materials Division
National Institute of Standards and Technology, Boulder, CO 80305, USA
Arno.Laesecke@boulder.NIST.gov

M. P. Longinotti
INQUIMAE-CONICET
Facultad de Ciencias Exactas y Naturales,
Universidad de Buenos Aires,
Intendente Guiraldes 2160
C1428EGA, Ciudad Autónoma de Buenos Aires, ARGENTINA
longinot@qi.fcen.uba.ar

E. R. López
Faculty of Physics, Campus Vida
University of Santiago de Compostela,
E-15782 Santiago de Compostela, SPAIN
enriqueta.lopez@usc.es

A. Mandelis
Center for Advanced Diffusion-Wave Technologies
Department of Mechanical and Industrial Engineering, University of Toronto, Toronto, Ontario M5S 3G8, CANADA
mandelis@mie.utoronto.ca

M. Massel
Department of Chemical and Biomolecular Engineering
University of Notre Dame,
Notre Dame, IN 46556, USA
mmassel@nd.edu

E. F. May
Centre for Energy
The University of Western Australia
35 Stirling Highway,
Crawley, WA 6009, AUSTRALIA
eric.may@uwa.edu.au

J. B. Mehl
University of Delaware
36 Zunuqua Trail,
PO Box 307,
Orcas, WA 98280-0307, USA
jmehl@rockisland.com

M. R. Moldover
Sensor Science Division
National Institute of Standards and Technology, Gaithersburg, MD 20899, USA
michael.moldover@nist.gov

Y. Nagasaka
Department of System Design Engineering, Keio University,
Yokohama 223-8522, JAPAN
nagasaka@sd.keio.ac.jp

A. A. H. Pádua
Institute of Chemistry of Clermont-Ferrand
Blaise Pascal University & CNRS,
63177 Aubiere, FRANCE
agilio.padua@univ-bpclermont.fr

R. A. Perkins
Applied Chemicals and Materials Division
National Institute of Standards and Technology, Boulder, CO 80305, USA
richard.perkins@nist.gov

W. S. Price
Nanoscale Organisation and Dynamics Group, University of Western Sydney,
Penrith South, NSW 2751, AUSTRALIA
w.price@uws.edu.au

S. E. Quiñones-Cisneros
Instituto de Investigaciones en Materiales
Universidad Nacional Autónoma de México
Circuito Exterior S/N, Ciudad Universitaria, México DF 04510, MEXICO
seqc@unam.mx

N. Riesco
Department of Earth Science and Engineering,
Imperial College London,
London, SW7 2AZ, UK
n.riesco@imperial.ac.uk

J. V. Sengers
University of Maryland
Institute of Physical Science & Technology
College Park, MD 20742, USA
sengers@umd.edu

C. Shi
Department of Chemical and Biomolecular Engineering
University of Notre Dame,
Notre Dame, IN 46556, USA
chaojunshi926@gmail.com

R. Tai
Institute of Modern Optical Technologies,
Key Lab of Advanced Optical Manufacturing Technologies of Jiangsu Province, Soochow University,
Suzhou, 215006, PR China
sea.terry@gmail.com

D. Tomida
Institute of Multidisciplinary Research for Advanced Materials (IMRAM),
Tohoku University, Sendai, Miyagi, 980-8577, JAPAN
tomida@tagen.tohoku.ac.jp

J. P. M. Trusler
Department of Chemical Engineering,
Imperial College London,
London, SW7 2BY, UK
m.trusler@imperial.ac.uk

V. Vesovic
Department of Earth Science and Engineering,
Imperial College London,
London, SW7 2AZ, UK
v.vesovic@imperial.ac.uk

W. A. Wakeham
Department of Chemical Engineering,
Imperial College London,
London, SW7 2BY, UK
w.wakeham@imperial.ac.uk

C. Wang
Institute of Modern Optical Technologies,
Key Lab of Advanced Optical Manufacturing Technologies of Jiangsu Province, Soochow University,
Suzhou, 215006, PR China
chinhua.wang@suda.edu.cn

S. Wiegand
ICS-3 Institute of Condensed Matter Forschungszentrum Jülich,
52425 Jülich, GERMANY
s.wiegand@fz-juelich.de

S. Will
Lehrstuhl für Technische Thermodynamik, Universität Erlangen-Nürnberg,
D-91058 Erlangen, GERMANY
stefan.will@ltt.uni-erlangen.de

J. Winkelmann
Department of Physical Chemistry,
University Halle-Wittenberg,
D-06120 Halle, GERMANY
winkelmann@chemie.uni-halle.de

J. T. Wu
Center of Thermal and Fluid Science,
Xi'an Jiaotong University,
Xi'an, Shaanxi, 710049, CHINA
jtwu@mail.xjtu.edu.cn

A. Würger
Laboratoire Ondes et Matière d'Aquitaine
Université de Bordeaux
33405 Talence Cedex, FRANCE
a.wuerger@loma.u-bordeaux1.fr

C. Yokoyama
Institute of Multidisciplinary Research for Advanced Materials (IMRAM), Tohoku University, Sendai, Miyagi, 980-8577, JAPAN
chiaki@tagen.tohoku.ac.jp

Acknowledgments

We are indebted to all the authors in this volume for their cooperation and to past and present members of the International Association for Transport Properties for their unwavering support for this project. Very special thanks are owing to Sofia Mylona of the Aristotle University of Thessaloniki whose skills and efforts during the editing process have kept the editors sane.

Some of the illustrations that appear in this volume have been published elsewhere. The present authors, editors and publishers are grateful to all those concerned in the original publications especially other Publishers and Corporations for permission to use their original illustrations again. Some of the Figures have been edited for consistency of presentation.

Experimental Thermodynamics Volume IX: Advances in Transport Properties of Fluids
Edited by M. J. Assael, A. R. H. Goodwin, V. Vesovic and W. A. Wakeham

Published by the Royal Society of Chemistry, www.rsc.org

Preface

Monographs concerned with the general field of thermophysics were initiated by Commission 1.2 of the International Union of Pure and Applied Chemistry (IUPAC) in 1956. Its former Subcommittee on Transport Properties continued and extended the coverage from 1991. The intention of the books was that they should summarize the state of knowledge with regard to experimental and theoretical methods in thermodynamics, thermochemistry and transport properties. The texts have appeared in two series, the first[1,2] reporting methods in thermochemistry. The present volume is the ninth in the second series.[3–10] Many of the texts in the second series have been concerned with topics in equilibrium thermodynamics; the first volume was concerned with the experimental calorimetry of non-reacting systems,[3] the fourth monograph was concerned with the calorimetry of reacting fluids[6] and also provided updates to the first series.[1,2] In a complementary fashion the fifth volume[7] presented the theoretical basis for equations of state of both fluids and fluid mixtures.[11] The sixth and seventh volumes[8,9] were concerned with the measurement of the thermodynamic properties of single and multiple phases, respectively, and were updates to the second volume[4] reporting measurements of a broader class of thermodynamic properties including techniques with industrial applications for chemically-non-reacting systems. The eighth volume was an update of reference 7 and included subject matter of importance to the practitioner, including equations of state for chemically-reacting and non-equilibrium fluids, and others, which have undergone significant developments. It is noteworthy that this eighth volume was the first published in conjunction with the International Association of Chemical Thermodynamics (IACT)[†]

[†]http://www.iactweb.org/

Experimental Thermodynamics Volume IX: Advances in Transport Properties of Fluids
Edited by M. J. Assael, A. R. H. Goodwin, V. Vesovic and W. A. Wakeham

Published by the Royal Society of Chemistry, www.rsc.org

which is the successor body to the former Subcommittee on Thermodynamic Tables of Commission 1.2.

The former Subcommittee on Transport Properties of Commission 1.2, now known as the International Association for Transport Properties (IATP),[‡] made its first contribution to the series with the third volume.[5] It described measurements of the transport properties of fluids characterizing the relaxation of a fluid from a non-equilibrium state, while another publication,[12] also produced under the auspices of IUPAC, discussed the correlation, prediction and estimation of transport properties. In the 20 years since the publication of reference 5, there have been significant developments in the measurement and theory of the non-equilibrium state of matter. First, several new measurement techniques have been developed and other, older techniques, have received a new lease of life because of technological developments. Secondly, the advent of high-performance computing machinery has enabled theoretical calculations that were not possible hitherto. These considerations led to the decision by IATP to initiate an update of reference 5 and reference 12. As for Volumes III and VI, the principal remit for the current volume was to serve as a source book for practitioners in the measurement and theory of the transport properties of fluids whether in academia, industry or government. In order not to duplicate work contained in volume III the editors have strictly confined their coverage to new work or to results that significantly extend or improve what was reported in 1991.

However, it was recognized by IATP that the importance of the non-equilibrium state and its areas of application have increased during the last two decades so that this single update does not encompass all that is new and useful in the field of non-equilibrium thermodynamics. This realization led to the decision to produce three separate volumes in the Experimental Thermodynamics series entitled *Advances in Transport Properties* Vol. IX; *Non-Equilibrium Thermodynamics with Applications* Vol. X; and that entitled *Applied Transport Properties* Vol. XI. Volume IX, concentrates on the experimental and theoretical developments that will, with Volume X, underpin Volume XI, and includes significant enhancements of experiment and theory that were not contained in references 5 and 12, previously. With this broad remit, the Editors have assembled an international team of distinguished experts to provide each chapter. These volumes are, as were Volumes VI and VII, also of interest to the data evaluator who needs to assess the reliability of experimental data obtained with specific techniques.

This volume compliments other recent publications associated with IUPAC that have covered a range of diverse issues reporting applications of solubility data,[13] to the topical issue of alternate sources of energy,[14] heat capacities of liquids and vapors[15] and the application of chemical thermodynamics to other matters of current industrial and scientific research including separation technology, biology, medicine and petroleum in one[16] of

[‡]http://transp.cheng.auth.gr/index.php/iatp/terms

eleven monographs of an IUPAC series entitled *Chemistry for the 21st Century*.[17]

Anthony R. H. Goodwin
Titular Member of, Physical and BioPhysical Division (I),
Interdivisional Committee on Terminology, Nomenclature and
Symbols (ICTNS) and Commission I.1 on Physicochemical Symbols,
Terminology, and Units of the International Union of Pure
and Applied Chemistry

Schlumberger Technology Corporation
150 Gillingham Lane
Sugar Land, TX 77478, U.S.A.

Professor Sir William A. Wakeham
Chairman International Association of Transport Properties
Royal Academy of Engineering
London, UK

References

1. *Experimental Thermochemistry*, ed. F. D. Rossini, for IUPAC, Interscience, New York, 1956.
2. *Experimental Thermochemistry, Volume II*, ed. H. A. Skinner, for IUPAC, Interscience, New York, 1962.
3. *Experimental Thermodynamics, Volume I, Calorimetry of Non-Reacting Systems*, ed. J. P. McCullough and D.W. Scott, for IUPAC, Butterworths, London, 1968.
4. *Experimental Thermodynamics, Volume II, Experimental Thermodynamics of Non-Reacting Fluids*, ed. B. Le Neindre and B. Vodar, for IUPAC, Butterworths, London, 1975.
5. *Experimental Thermodynamics, Volume III, Measurement of the Transport Properties of Fluids*, ed. W. A. Wakeham, A. Nagashima and J. V. Sengers, for IUPAC, Blackwell Scientific Publications, Oxford, 1991.
6. *Experimental Thermodynamics, Volume IV, Solution Calorimetry*, ed. K. N. Marsh and P. A. G. O'Hare, for IUPAC, Blackwell Scientific Publications, Oxford, 1994.
7. *Experimental Thermodynamics, Volume V, Equations of State for Fluids and Fluid Mixtures, Parts I and II*, ed. J. V. Sengers, R. F. Kayser, C. J. Peters and H. J. White, Jr, for IUPAC, Elsevier, Amsterdam, 2000.
8. *Experimental Thermodynamics, Volume VI, Measurement of the Thermodynamic Properties of Single Phases*, ed. A. R. H. Goodwin, K. N. Marsh and W. A. Wakeham, *for IUPAC*, Elsevier, Amsterdam, 2003.
9. *Experimental Thermodynamics, Volume VII, Measurement of the Thermodynamic Properties of Multiple Phases*, ed. R. D. Weir and T. W. de Loos, for IUPAC, Elsevier, Amsterdam, 2005.

10. *Experimental Thermodynamics Volume VIII: Applied Thermodynamics of Fluids*, ed. A. R. H. Goodwin, J. V. Sengers and C. J. Peters, for IUPAC, Royal Society of Chemistry, Colchester, U.K., 2010.
11. L. S. Garcia-Colin and F. J. Uribe, *J. Stat. Phys.*, 2002, **106**, 403–404; L. S. Garcia-Colin and F. J. Uribe, *J. Stat. Phys.*, 2003, **112**, 885.
12. *Transport Properties of Fluids: Their Correlation, Prediction and Estimation*, ed. J. Millat, J. H. Dymond and C. A. Nieto de Castro, for IUPAC, Cambridge University Press, Cambridge, U.K., 1996.
13. *Developments and Applications of Solubility*, ed. T. M. Letcher, for the IUPAC, Royal Society of Chemistry, Cambridge, 2007.
14. *Future Energy: Improved, Sustainable and Clean Options for our Planet*, ed. T. M. Letcher, for IUPAC, Elsevier, Amsterdam, 2008.
15. *Heat Capacities of Liquids and Vapours*, ed. E. Wilhelm and T. J. Letcher, for IUPAC, Royal Society of Chemistry, Cambridge, 2009.
16. *Chemical Thermodynamics*, ed. T. M. Letcher, for IUPAC, Blackwells Scientific Publications, Oxford, 2000.
17. C. L. Watkins, *J. Chem. Educ.*, 2000, **77**, 973.

Contents

Experimental Thermodynamics Volume IX: Advances in Transport Properties of Fluids
Edited by M. J. Assael, A. R. H. Goodwin, V. Vesovic and W. A. Wakeham

Published by the Royal Society of Chemistry, www.rsc.org

CHAPTER 1

Acoustic Techniques for Measuring Transport Properties of Gases

KEITH A. GILLIS AND MICHAEL R. MOLDOVER

1.1 Introduction: Acoustic Measurements of Gas Properties

The acoustic resonance frequencies f and the resonance half-widths g of a gas-filled cavity are functions of the cavity's size and shape, the speed of sound in the gas c, and the thermophysical properties of the gas. In a first approximation, the resonance frequencies f depend on the speed of sound; in contrast, the resonance half-widths g are sums of terms that account for energy dissipated by the gas's thermal conductivity λ, shear viscosity η, bulk (or second) viscosity ζ,[†] and the term g_{mech}, where g_{mech} accounts for energy losses from mechanical effects such as friction in joints, transducer losses, and acoustic radiation outside the cavity. Cavity resonators used for measuring the speed of sound are designed to have narrow resonance peaks so that the resonance frequencies can be determined precisely and so that the frequencies are comparatively insensitive to the transport properties λ, η, and ζ. In contrast, cavity resonators used to measure these transport properties are designed so that the energy dissipated by λ, η, and ζ is much larger than g_{mech}. Consequently, resonators that are optimized to measure transport properties have broad resonance peaks. With reasonable precautions,

[†]The IUPAC *Green Book* recommends the symbol κ for bulk viscosity, however, for the sake of consistency with previous publications concerning the topic of this chapter ζ will be used herein after.

Experimental Thermodynamics Volume IX: Advances in Transport Properties of Fluids
Edited by M. J. Assael, A. R. H. Goodwin, V. Vesovic and W. A. Wakeham

Published by the Royal Society of Chemistry, www.rsc.org

the measurements of the resonance frequencies and half-widths have very low uncertainties; the uncertainty of acoustic determinations of transport properties is dominated by imperfect modeling/understanding of cavity resonators and g_{mech}.

The sections that follow describe the design and performance of three acoustic resonators that we developed for measurements in gases: one resonator was optimized for measurements of shear viscosity, one was optimized for thermal conductivity measurements, and one was optimized for bulk viscosity measurements. The three resonators are small so that they require only small gas samples whose temperature and pressure are easily controlled over wide ranges, and they are rugged with no moving parts. Using the first resonator, we accurately measured the shear viscosity of hazardous gases at temperatures between 200 K and 400 K and pressures up to 3.4 MPa. With the third resonator, we accurately measured the critical-fluctuation-driven bulk viscosity of xenon on the critical isochore at reduced temperatures 100 times closer to the critical point (290 K and 5.8 MPa) and at frequencies 3000 times lower than ever before.

Of the three transport properties, the shear viscosity is easiest to measure at low densities. Accurate acoustic measurements of the thermal conductivity are more difficult because the dissipation from thermal conduction is usually smaller than that from viscosity by a factor on the order of $(\gamma - 1)$, and $(\gamma - 1) \ll 1$ for polyatomic molecules of interest. (Here $\gamma \equiv C_p/C_V$ is the heat-capacity ratio.) (In Section 1.3, we discuss an exception to this generalization. In a spherical cavity, the acoustic velocity of the radially-symmetric modes is perpendicular to the cavity's walls; therefore these modes are not damped by the shear viscosity.) In low-density gases,[1] the bulk viscosity $\zeta \propto \rho^2$, which vanishes as $\rho \rightarrow 0$; therefore, it is too small to measure. Near the critical point, ζ diverges more strongly than the other transport coefficients; therefore, it dominates acoustic losses and is easy to measure accurately.

1.2 Shear Viscosity Measurements: The Greenspan Viscometer

1.2.1 Description

In 1953, Greenspan and Wimenitz[2] attempted to determine the viscosity of air from measurements of f and g in a two-chambered Helmholtz resonator somewhat like the resonator shown in Figure 1.1. Their results deviated relatively from literature data by as much as 38 %. In 1996, we began a program to develop an accurate viscometer based on Greenspan's concept, which we call the Greenspan acoustic viscometer. Since then, we have improved the theory[3] and the resonator design[4–7] to achieve significantly better results; our measurements with the Greenspan viscometer deviate relatively from reference data by less than ± 0.5 %.

The Greenspan acoustic viscometer is a double Helmholtz resonator composed of two gas-filled chambers connected by a tube (or duct)

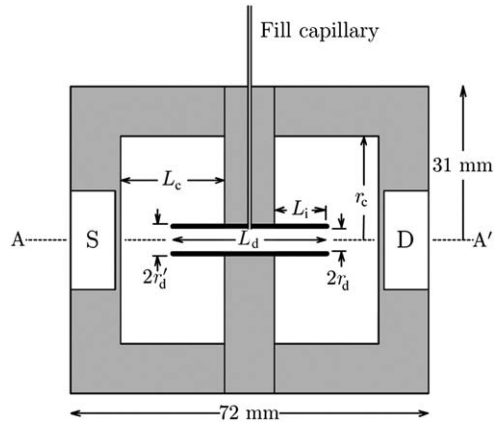

Figure 1.1 Cross section of a Greenspan viscometer.[3] The dotted line AA′ indicates the axis of circular symmetry for all parts except the fill capillary. Two cylindrical chambers fitted with source (S) and detector (D) transducers are coupled by a concentric cylindrical duct. The dimensions in millimetres for the viscometer are: $L_d = 31.17$, $r_d = 2.316$, $r_d' = 3.21$, $r_c = 21.02$, $L_c = 21.04$, and $L_i = 10.5$. The fill capillary has an inner radius $r_f = 0.1$ mm (not to scale) and a length $L_f = 80$ mm.

(see Figure 1.1). The fundamental acoustic mode is a low-frequency, low-Q mode in which the gas oscillates between the two chambers through the duct. As a characteristic of a Helmholtz acoustic mode, the wavelength of the mode is much longer than the internal dimensions of the resonator. The frequency response of the Helmholtz mode is easy to measure because the mode is non-degenerate and isolated; its frequency is far below the other acoustic modes of the enclosed gas and below the elastic modes of the resonator body. The low frequency leads to a thick boundary layer that reduces the requirement for a fine surface finish compared to the moderate-frequency resonators used for sound speed measurements. The low Q reduces the relative importance of the difficult-to-estimate contributions to the measured half-width g_{meas} and also reduces the need to maintain very high temperature stability. The only requirement is that the transducers have a smooth, well-behaved response (no peaks) in the range $f_{meas} \pm 4g_{meas}$ that can be described by a low-order polynomial. The Greenspan viscometer is rugged; it has no moving parts (aside from the minute motion of the transducers) and can be made from corrosion-resistant alloys. In our work, the acoustic transducers, and the ''dirty'' materials of which they are made, are separated from the test gas by thin metal diaphragms that are machined into the chamber's walls.

In the lowest-order approximation, neglecting dissipation, the gas in the duct and just outside the duct ends moves like a rigid plug with mass $\rho A_d (L_d + 2\delta_i)$ that oscillates back and forth between two identical springs. Here, ρ is the gas density, $A_d = \pi r_d^2$ is the cross-sectional area of the duct, r_d and L_d are the duct radius and length, and the length $\delta_i \approx 0.655\ r_d$ is an

inertial end correction that accounts for diverging flow at the end of the duct. As gas flows into a chamber, the pressure in that chamber increases and provides a restoring force, like a spring. The combined stiffness $2\rho c^2 A_d{}^2/V_c$ of the two springs is a result of the compression and rarefaction of the gas in the chambers. In this level of approximation, the resonance frequency is

$$f_0 = \frac{1}{2\pi}\sqrt{\frac{\text{stiffness}}{\text{mass}}} = c\sqrt{\frac{r_d^2}{2\pi V_c(L_d + 2\delta_i)}}, \tag{1.1}$$

where c is the speed of sound in the gas, and V_c is the volume of each chamber. The wavelength of sound (c/f_0) is determined by geometric factors and is independent of the properties of the gas. For the resonator described in ref. 3, eqn (1.1) predicts $f_0 = (0.9299\ \text{m}^{-1}) \times c$, which is a few hundred hertz for most gases near ambient temperature. However, the corresponding wavelength (approximately 1.075 m) is the same for all gases. Heat and momentum diffusion near the cavity walls decrease the measured resonance frequency f_{meas} from the estimate in eqn (1.1) by a few percent, but eqn (1.1) is sufficient as a design aid.

For the Helmholtz mode, the acoustic velocity is greatest in the duct; therefore, shear in the gas flow near the duct's wall dissipates most of the acoustic energy. If this were the only dissipation mechanism, the gas's shear viscosity η could be determined from a measurement of the resonance frequency f_{meas} and the quality factor Q_{meas} using the expression

$$\eta \approx \frac{\rho\pi r_d^2 f_{\text{meas}}}{Q_{\text{meas}}^2}\left(\frac{1 + 2\delta_i/L_d}{1 + 2\varepsilon_{r0} r_d/L_d}\right)^2. \tag{1.2}$$

The numerically-calculated parameters δ_i and ε_{r0} describe, respectively, the inertial and dissipative effects of the duct ends. However, heat transport between the oscillating gas and the metal wall of the resonator causes significant acoustic energy dissipation; therefore eqn (1.2) overestimates η. The fractional overestimate is $0.44\,(\gamma - 1)\,Pr^{-1/2}$ for the viscometer described in ref. 3, where $Pr = \eta\, C_p/\lambda$ is the Prandtl number, and λ is the thermal conductivity of the gas. This overestimate ranges from 36 %, for monatomic gases such as argon and helium, to as little as 5 % for typical polyatomic gases. Fortunately, the design of the Greenspan viscometer is such that, in most cases, the uncertainty in the thermal conductivity of the gas is a small contribution to the uncertainty of the deduced viscosity. For example, the thermal conductivities of helium and argon have such low relative uncertainties, ± 0.002 % and ± 0.02 % respectively, that their contribution to the uncertainty of the viscosity measurement is negligible, despite the rather large effect of heat conduction. For a typical polyatomic molecule with $\gamma \approx 1.1$ and $Pr \approx 0.7$, a relative uncertainty in the thermal conductivity of ± 10 % contributes only about ± 0.2 % to the relative uncertainty of the deduced viscosity.

The next level of approximation includes the most important dissipation mechanisms that contribute to the half-width g_{meas} and the resonance

line shape. In this approximation, the inverse of the resonance quality factor $Q^{-1} \equiv 2g_{\mathrm{meas}}/f_{\mathrm{meas}}$ is the sum of three terms:

$$\frac{1}{Q} = \frac{\delta_{\mathrm{v}}}{r_{\mathrm{d}}} \cdot \frac{L_{\mathrm{d}} + 2\varepsilon_{\mathrm{r}} r_{\mathrm{d}}}{L_{\mathrm{d}} + 2\delta_{\mathrm{i}}} + (\gamma - 1)\frac{\delta_{\mathrm{t}} S_{\mathrm{c}}}{2V_{\mathrm{c}}} + (\gamma - 1)\frac{C_{\mathrm{relax}}}{C_p}\frac{2\pi f_{\mathrm{meas}}\tau_{\mathrm{relax}}}{1 + (2\pi f_{\mathrm{meas}}\tau_{\mathrm{relax}})^2}. \quad (1.3)$$

The first term in eqn (1.3) is the damping that occurs in the viscous boundary layer at the wall and near the ends of the main duct. Here, $\delta_{\mathrm{v}} = [D_{\mathrm{v}}/(\pi f_{\mathrm{meas}})]^{1/2}$ is the thickness of the viscous boundary layer in oscillating flow at frequency f_{meas}, where $D_{\mathrm{v}} = \eta/\rho$ is the viscous diffusivity (also called the kinematic viscosity). The second term is the damping from heat conduction that occurs near the wall of the chambers, which have surface area S_{c}. The length $\delta_{\mathrm{t}} = [D_{\mathrm{t}}/(\pi f_{\mathrm{meas}})]^{1/2}$ is the thickness of the thermal boundary layer, where $D_{\mathrm{t}} = \lambda/(\rho C_p)$[‡] is the thermal diffusivity. Although δ_{v} and δ_{t} differ only by the factor $Pr^{-1/2}$, the second term is significantly reduced by the smaller surface area-to-volume ratio $S_{\mathrm{c}}/V_{\mathrm{c}}$ in the chamber and the factor $(\gamma - 1)$, which is small for polyatomic molecules. The third term in eqn (1.3) is important for certain gases (*e.g.* CH_4, CO_2) that have symmetries such that many intermolecular collisions are required for their internal degrees of freedom to adjust to the temperature change associated with the acoustic oscillation. In such gases, the acoustic dissipation is characterized by the product $C_{\mathrm{relax}}\tau_{\mathrm{relax}}$, where C_{relax} is the heat capacity associated with the slowly relaxing degrees of freedom and τ_{relax} is the relaxation time, which is proportional to ρ^{-1}.

The next section describes the model for acoustic response of the Greenspan viscometer and how its measurement is used to determine the gas viscosity. Ref. 3 contains more details and a derivation of the model.

1.2.2 Basic Theory

In a Greenspan viscometer, a continuous sound source located in one chamber generates an acoustic wave at frequency f that is reflected back and forth between the chambers through the duct. We assume the time dependence is $e^{i\omega t}$ with $\omega = 2\pi f$. When the frequency is such that a reflected wave arrives back at the source in phase with the wave being generated there, resonance occurs. Acoustic waves in long gas-filled ducts are governed by the equations first proposed by Kirchhoff,[8] whose classic paper includes a description of the effects of the coupled acoustic, thermal, and vorticity waves in ducts of circular cross section. The low-frequency (long-wavelength) limit of Kirchhoff's solutions is generally attributed to Crandall.[9] Below the cutoff frequency for transverse modes in a duct, only plane waves can propagate. In a duct with a circular cross section, this limit corresponds to wavelengths greater than about 1.7 times the duct diameter, *i.e.* about 8 mm for the duct

[‡]The IUPAC *Green Book* recommends the symbol a for thermal diffusivity, however, for the sake of consistency with previous publications concerning the topic of this chapter D_{t} will be used herein after.

in Figure 1.1, which is much shorter than the wavelength of the natural mode of the Greenspan viscometer.

Low-frequency sound wave propagation in a duct is described accurately by a set of differential equations for lossy transmission lines that relate the acoustic pressure p and volume velocity U. When there is an acoustic source with frequency f and volume velocity U_0 in one chamber (chamber 1), a steady-state acoustic pressure p_2 develops in the other chamber (chamber 2). Finite-length transmission lines are conveniently described by an equivalent circuit containing lumped acoustic impedances in a T-network. The complete equivalent circuit we use to model the Greenspan viscometer, shown in Figure 1.2, contains a T-network for each half of the central duct (split by the symmetrically-located fill capillary) with additional impedances that model the effects of the duct ends (Z_{end}), the chambers (Z_V), and the fill capillary (Z_c). The acoustic response of the Greenspan viscometer p_2/U_0 is a complex-valued function of frequency that contains the line shape of the Helmholtz resonance.

The acoustic response based on the equivalent circuit is

$$\frac{p_2}{U_0} = \frac{Z_b^2 Z_c Z_V^2}{D_1 D_2}, \tag{1.4a}$$

where the factors in the denominator are

$$D_1 = (Z_b + Z_a)(Z_V + Z'_a) + Z_b Z_a \tag{1.4b}$$

$$D_2 = Z_b Z_V + 2Z_c(Z_b + Z_V) + Z'_a(Z_b + 2Z_c) + Z_a(Z_b + Z_V + Z'_a). \tag{1.4c}$$

Eqn (1.4a) is the basis of the complex resonance function used in the data analysis. The Helmholtz resonance condition is defined as the complex frequency $F_H = f_H + ig$ for which $D_1 = 0$, where f_H is the measured resonance frequency and g is the resonance half width. [$2g$ is defined as the full-width at half-maximum of the energy response function. The quality factor Q is defined as $Q = f_H/(2g)$.] The acoustic pressure for the Helmholtz mode is an odd function of distance from the resonator's mid-plane, so there is a pressure node at the entrance to the capillary; therefore the resonance frequency and the line shape for the Helmholtz mode are independent of Z_c. The effect that Z_c has on the total acoustic response in eqn (1.4) in the

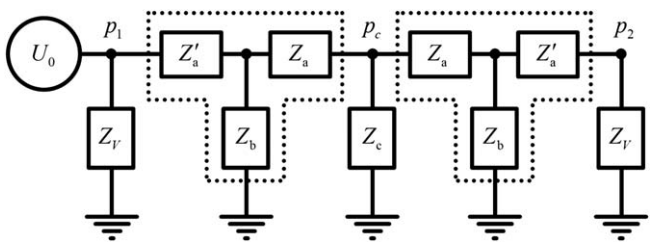

Figure 1.2 Equivalent circuit for the Greenspan viscometer shown in Figure 1.1 and described by eqn (1.4). The centrally-located fill capillary has acoustic impedance Z_c.

vicinity of the Helmholtz mode is to change the "background" due to the tails of other modes, which is weakly dependent on frequency.

Within the chambers, the gas compressibility in the long wavelength limit considered here is isothermal near the walls and adiabatic far from the walls. The acoustic impedance of each chamber calculated from the average compressibility within the chamber is given by the expression[10]

$$Z_V = \frac{\rho c^2}{\mathrm{i}\omega V_\mathrm{c}} \frac{1}{\sqrt{1 + \frac{1}{2}(1-\mathrm{i})(\gamma-1)S_\mathrm{c}\delta_\mathrm{t}/V_\mathrm{c}}}, \tag{1.5}$$

which includes the effect of heat conduction over the chamber's surface area S_c.

The T-network impedances shown in Figure 1.2 are given by the expressions

$$Z_\mathrm{a} = Z_0 \tanh(\Gamma L_\mathrm{d}/4),\ Z_\mathrm{b} = Z_0/\sinh(\Gamma L_\mathrm{d}/2), \tag{1.6a}$$

$$Z'_\mathrm{a} = Z_\mathrm{a} + Z_\mathrm{end},\ \text{and}\ Z_\mathrm{end} = \frac{\rho\omega}{A_\mathrm{d}}(\mathrm{i}\delta_\mathrm{I} + \delta_\mathrm{R}). \tag{1.6b}$$

In eqn (1.6), the characteristic impedance Z_0 and the propagation parameter Γ for waves in the duct are given by the expressions

$$Z_0 = \frac{\rho c}{A_\mathrm{d}} \frac{1}{\sqrt{[1 + (\gamma-1)F_\mathrm{t}](1 - F_\mathrm{v})}} \tag{1.7a}$$

and

$$\Gamma = \frac{\mathrm{i}\omega}{c}\sqrt{\frac{1 + (\gamma-1)F_\mathrm{t}}{1 - F_\mathrm{v}}}. \tag{1.7b}$$

The complex-valued quantity F_x is the loss function,

$$F_\mathrm{x}(\kappa_\mathrm{x}) = \frac{2J_1(\kappa_\mathrm{x})}{\kappa_\mathrm{x} J_0(\kappa_\mathrm{x})}, \tag{1.8}$$

which accounts for viscous dissipation (x = v) or thermal dissipation (x = t) near the wall of a circular duct. Here, J_0 and J_1 are Bessel functions of order 0 and 1, respectively, and $\kappa_\mathrm{x} = (1-\mathrm{i})r_\mathrm{d}/\delta_\mathrm{x}$ with $\delta_\mathrm{v} = (2D_\mathrm{v}/\omega)^{1/2}$ and $\delta_\mathrm{t} = (2D_\mathrm{t}/\omega)^{1/2}$.

The lengths δ_I and δ_R in eqn (1.6b) are the inertial and resistive end corrections, respectively, for the main duct. These lengths have been evaluated numerically.[11] To first order in δ_v the resistive length is

$$\delta_\mathrm{R} = \varepsilon_\mathrm{r}\delta_\mathrm{v} \tag{1.9}$$

When the duct ends are square, the coefficient ε_r varies weakly with $\delta_\mathrm{v}/r_\mathrm{d}$ according to

$$\varepsilon_\mathrm{r} = \varepsilon_{\mathrm{r}0} + \varepsilon_{\mathrm{r}1/3}(\delta_\mathrm{v}/r_\mathrm{d})^{1/3} + \varepsilon_{\mathrm{r}1}(\delta_\mathrm{v}/\nu_\mathrm{d}). \tag{1.10}$$

For the geometry of the viscometer described in ref. 3, the coefficients were evaluated numerically to be $\varepsilon_{r0} \approx 0.987$, $\varepsilon_{r1/3} \approx -0.348$, and $\varepsilon_{r1} \approx 1.15$. The constant term ε_{r0} is sensitive to the shape of the duct ends. Rounding the sharp edges decreases ε_{r0} and a slight burr can increase it. When the Greenspan viscometer is used for absolute measurements, the sensitivity of ε_{r0} to the geometry of the duct ends contributes to the uncertainty in the measured viscosity. In practice, we can adjust ε_{r0} to improve the agreement of the experimental values of the viscosity of helium with the accurately known theoretical values.[13] In ref. 3, we increased ε_{r0} by 4 % to 1.03. It follows from eqn (1.2) that a relative uncertainty in ε_{r0} of 4 % contributes an uncertainty of 1 % to the viscosity measurement.

The inertial end correction δ_I is, to first order in δ_v,

$$\delta_I = \delta_i + \varepsilon_i \delta_v. \tag{1.11}$$

As noted previously, $\delta_i \approx 0.655\, r_d$ for the experimental resonator discussed in ref. 3; δ_I differs from this by a viscous boundary layer correction term and hence provides a more accurate representation of the inertial end effects. Note that the numerically-calculated value $\varepsilon_i \approx 0.86$ is somewhat smaller than the calculated value of $\varepsilon_{r0} \approx 0.987$. Improved experimental agreement was obtained with a modest increase to $\varepsilon_i \approx 0.96$.

The fill capillary is a duct that is terminated with impedance Z_t. We model the capillary as an acoustic transmission line with characteristic impedance Z_{0f} and propagation parameter Γ_f given by eqn (1.7) and (1.8) with r_d replaced by r_f. In this model the impedance Z_c for the fill capillary is

$$Z_c = Z_{1f} + Z_{e1f} + \frac{Z_{2f}(Z_{1f} + Z_{e2f} + Z_t)}{Z_{2f} + Z_{1f} + Z_{e2f} + Z_t}, \tag{1.12}$$

where the T-network elements Z_{1f} and Z_{2f} have the same form as Z_a and Z_b, respectively, in eqn (1.6a) with Z_0 replaced by Z_{0f}, Γ replaced by Γ_f, and $L_d/2$ replaced by L_f. The impedances Z_{e1f} and Z_{e2f} account for the end effects at the junction with the main duct and at the termination, respectively; they have the same form as Z_{end} in eqn (1.6b) with A_d, δ_I, and δ_R replaced by A_f, δ_{If} and δ_{Rf}, respectively. The lengths δ_{If} and δ_{Rf} describe the end corrections for the fill capillary, similar to δ_I and δ_R in eqn (1.9) and (1.11), but with r_d replaced with r_f. These corrections are negligible provided that $r_f/L_f \ll 1$. The capillary end effect impedances are small compared to Z_{1f} by a factor that is proportional to r_f/L_f, which is about 0.001 for the viscometer in Figure 1.1. If the capillary is terminated by a volume, such as a closed valve, the impedance Z_t can be approximated by eqn (1.5) using suitable values for the volume and surface area. However, if the termination volume is large compared to $A_f \times$ wavelength (as is usually the case), then Z_t is small compared to Z_{0f}, and sufficient accuracy is achieved by setting $Z_t = 0$.

1.2.3 Experimental Results

The Helmholtz mode response function and the supporting quantities in eqn (1.4) to (1.12) constitute a physical model of the sound pressure that is

generated by a continuous sound source as a function of frequency in terms of the properties of the gas medium. The source transducer generates a volume displacement in one chamber that is proportional to the applied source voltage V_s, which is the amplified output of a sinusoidal function generator. A microphone in the other chamber outputs a voltage signal V_{mic} that is proportional to the acoustic pressure there. The voltages V_s and V_{mic} are measured with two dual-phase lock-in amplifiers that are referenced to the function generator. We measured the response at 21 uniformly-spaced frequencies spanning the range $\pm 2g$ about the center frequency f_H in steps of increasing and then decreasing frequency. We computed the complex ratio $V_{mic}/V_s = u + iv$ at each frequency and fit the data by adjusting the speed of sound c and the viscous diffusivity D_v using the function

$$u + iv = A' \frac{\tilde{Z}_b^2 \tilde{Z}_c \tilde{Z}_V^2}{\tilde{D}_1 \tilde{D}_2} + B' + C'(f - f'') + D'(f - f'')^2, \qquad (1.13)$$

where A', B', C', and D' are adjustable complex-valued parameters, and f'' is approximately the average frequency in the data set. (The parameter f'' is not adjusted; it is included in eqn (1.13) to increase the reliability of the data-fitting routine.) The parameter A' is an arbitrary scale factor that depends on the sensitivity of the microphone and the strength of the source. The dimensionless expression multiplying A' is the acoustic response in eqn (1.4) with each of the impedances reduced by Z_0 (indicated by the tilde) to remove the explicit dependence on ρc. The background parameters B', C', and D' account for electrical cross talk between the source and detection circuits and for the frequency response of the transducers. C' and sometimes D' were included in the fit when justified by an F-test. Figure 1.3 compares the measured response function of a Greenspan viscometer filled with argon to a least-squares fit using eqn (1.13) with 8 adjustable parameters. The response function has been normalized by the maximum value. The deviations from the fit are random and have a root-mean-square (RMS) of 0.006 %, which shows that eqn (1.13) describes the measured response function extremely well.

Researchers at NIST measured the viscosity of 16 gases, see Table 1.1, using Greenspan viscometers that are similar in size to the design in Figure 1.1.[4–7,12] In principle, the Greenspan viscometer is an absolute instrument dependent on accurate dimensional measurements and numerically-calculated parameters for the duct end corrections. In practice, the instrument must be calibrated with a reference gas such as helium or argon (due to difficult-to-measure details at the duct's ends, irregularities in the shape of the duct along its length, or crevices at the seals in the chambers).

Figure 1.4 shows the viscosity of argon, helium, xenon, nitrogen, and methane[4] measured with a Greenspan viscometer before and after calibration compared to reference values. In order to calibrate the particular resonator used in ref. 4, we adjusted the resistive end correction ε_{r0} and the surface area of the chambers to minimize the RMS deviations in Figure 1.4a. The calibration reduced ε_{r0} from the predicted value of 0.972 to 0.939 and increased the chamber surface area by the fractional amount (1.19 μm/δ_t),

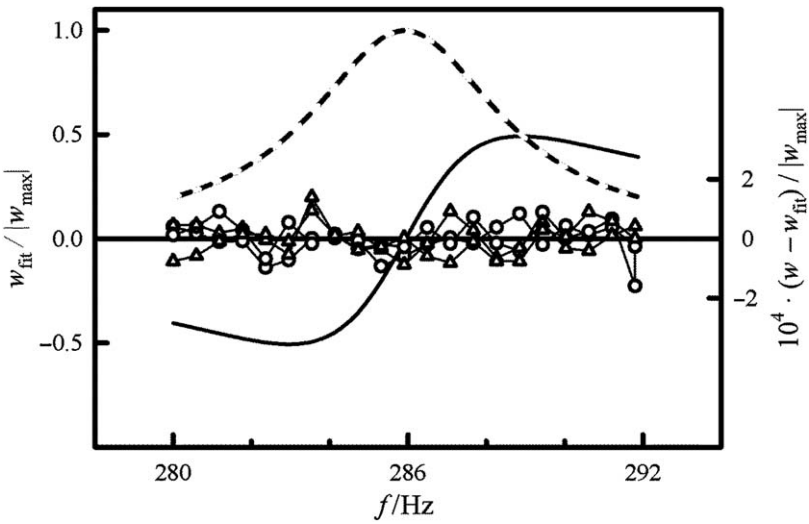

Figure 1.3 The acoustic response of a Greenspan viscometer filled with argon at 280 K and 1 MPa. The measured ratio $V_{mic}/V_s = w$ was fit using eqn (1.13) with 8 adjustable parameters, where V_{mic} is the vector signal from the microphone and V_s is the vector source excitation voltage. V_{mic} and V_s were measured using two dual-phase lock-in amplifiers with a common reference. The in-phase (—) and quadrature (– –) components of the fit, normalized by the maximum amplitude $|w_{max}|$, are plotted on the left axis as a function of frequency f. The normalized deviations from the fit $(w - w_{fit})/|w_{max}|$ for the in-phase, ○, and quadrature, △, data are plotted on the right axis with the fit as the baseline. The 84 data points were acquired at 21 equally-spaced frequencies over the range $f_{meas} \pm 2g_{meas}$, where $f_{meas} = 285.89$ Hz and $g_{meas} = 2.91$ Hz. The root-mean-square of the deviations is 6×10^{-5}.

which ranged from 1 % to 5 %. We speculate that the surface area correction was due to the roughness of the chamber surface or a crevice where the chambers and diaphragms were attached. Subsequent viscometers[5–7] with polished interior surfaces and diaphragms that were machined in place did not require a surface area calibration.

Figures 1.4c and 1.4d compare literature data with measurements of the viscosity and speed of sound made with a Greenspan viscometer[5] that was calibrated with helium using *ab initio* viscosity values.[13] The viscosity results are all within ± 0.5 % of the literature values. Most of the speed-of-sound results are within ± 0.03 % of the literature values. However, the results for C_2F_6 and SF_6 have larger deviations from literature values at the higher pressures on the 300 K isotherm where both C_2F_6 and SF_6 approach their critical points. Near critical points, all thermodynamic properties (including the speed of sound) are particularly sensitive to impurities. Therefore, the larger deviations resulted from differences in the concentrations of impurities in our gases and the gases used for the literature studies.

Table 1.1 Summary of gases studied using a Greenspan viscometer. The temperature range ΔT, maximum pressure P_{max}, and publication reference are listed for each compound. Mixture components are specified as mole fraction.

Compound	ΔT/K	P_{max} / MPa	
Helium	298 to 348	3.2	*a,b,c*
Argon	225 to 373	3.4	*a,b,c*
Xenon	298.15	1.1	*a*
0.47 Helium–0.53 Xenon	250 to 375	1.8	*a*
Hydrogen	225 to 400	3.3	*d*
Nitrogen	298.15	3.4	*a,b,c*
Carbon monoxide	225 to 375	2.5	*c*
Carbon dioxide	225 to 375	2.5	*c*
Nitrous oxide	200 to 375	3.4	*e*
Ammonia	300 to 375	3.4	*c*
Nitrogen trifluoride	225 to 375	3.4	*e*
Methane	293.15	3.3	*a,b,c*
Carbon tetrafluoride	200 to 400	3.4	*b*
Silicon tetrafluoride	215 to 375	2.5	*c*
Sulfur hexafluoride	298.15	1.7	*b,c*
Hexafluoroethane	225 to 375	3.1	*b*
Propane	293 to 373	3.4	*b,c*
Octofluorocyclobutane	300 to 375	1.6	*c*

[a]J. Wilhelm, K.A. Gillis, J. B. Mehl and M. R. Moldover, *Int. J. Thermophys.*, 2000, **21**, 983.
[b]J.J. Hurly, K.A. Gillis, J.B. Mehl and M.R. Moldover, *Int. J. Thermophys.*, 2003, **24**, 1441.
[c]A.F. Estrada-Alexanders and J.J. Hurly, *J. Chem. Thermodynamics*, 2008, **40**, 193.
[d]J.J. Hurly and M. R. Moldover, private communication.
[e]J.J. Hurly, *Int. J. Thermophys.*, 2004, **25**, 625.

Figure 1.5 compares literature data[14,15] for the zero-density limit of viscosity of hydrogen with measurements made with the Greenspan viscometer. The agreement is excellent throughout the temperature range 225 K to 400 K.

1.3 Thermal Conductivity

In principle, the thermal conductivity of dilute gases can be deduced from the widths of the radially-symmetric acoustic modes of a spherical or nearly spherical (''quasi-spherical''), gas-filled cavity of known radius a. For such modes, the half-width is a sum of three terms:

$$\frac{g}{f} = \frac{(\gamma-1)\delta_t}{2a}\left[1 - \frac{(2\gamma-1)\delta_t}{a}\right] + \left(\frac{\pi f \delta_t}{c}\right)^2\left[(\gamma-1) + \frac{4}{3}Pr\right] + \frac{g_{mech}}{f}. \quad (1.14)$$

The first term in eqn (1.14), accounts for heat exchange between the wall of the cavity and the gas; the second term accounts for attenuation of sound throughout the volume of the cavity; the third term accounts for mechanical losses, and we have assumed the bulk viscosity $\zeta \equiv 0$. At low densities (below

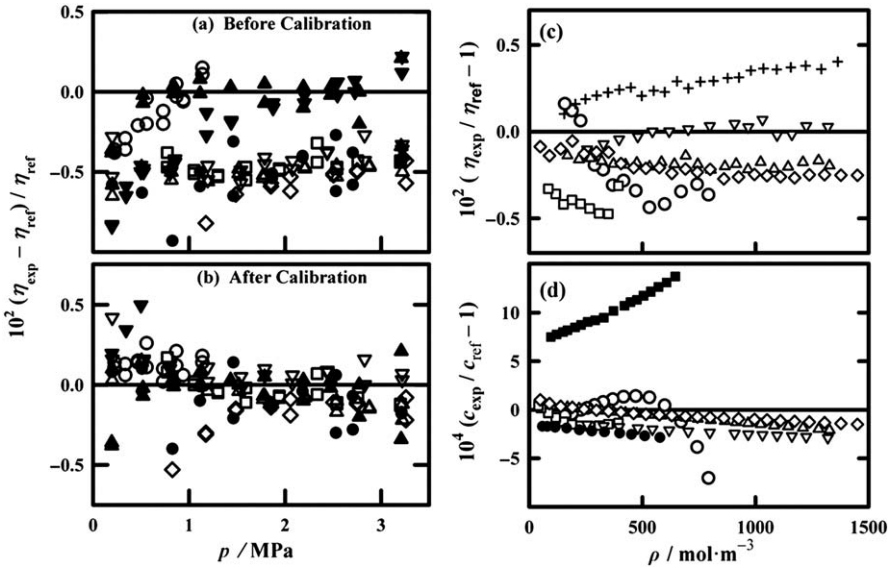

Figure 1.4 Viscosities η of several gases measured in the Greenspan viscometer compared to reference values as a function of pressure p (a and b) and amount of substance density ρ (c and d). Fractional deviations from reference values as a function of pressure (a) before calibration and (b) after calibration.[4] ▲, argon at $T = 298$ K; ▼, argon at $T = 348$ K; △, methane at $T = 298$ K; ▽, methane at $T = 348$ K; □, helium at $T = 298$ K; ◇, helium at $T = 348$ K; ●, nitrogen at $T = 298$ K; and ○, xenon at $T = 298$ K. Fractional deviations of measured (c) viscosities and (d) sound speeds near $T = 300$ K from reference values as a function of density.[5] +, argon; ▽, helium; △, nitrogen; ○, sulfur hexafluoride; ◇, methane; ●, tetrafluoromethane; ■, hexafluoroethane; and □, propane.

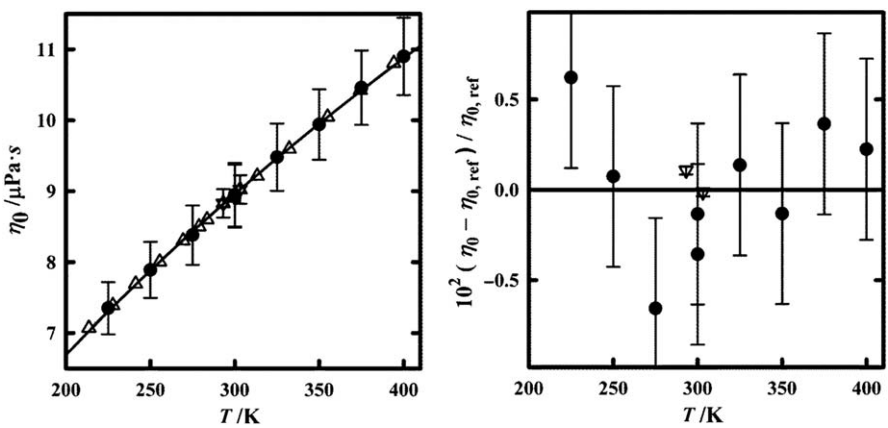

Figure 1.5 The viscosity η of hydrogen at zero density plotted as a function of temperature T. (a) ●, Hurly[12] with a Greenspan viscometer; △, May *et al.*[15]; ▽, Kestin and Yata.[14] (b) Deviations of the measured values from May *et al.*[15]

a few hundred 100 kPa at ambient temperature), the first two terms in eqn (1.14) diverge as (δ_t/a) and $(\delta_t/a)2$, while the third term g_{mech} approaches zero as a linear function of the pressure, albeit with a complicated frequency-dependence. Therefore, eqn (1.14) can be used to determine the thermal conductivity of a gas, provided that a crude estimate of the Prandtl number *Pr* is available and provided that γ is known, for example from measurements of the acoustic resonance frequencies of the same gas-filled cavity. Eqn (1.14) is consistent, within 0.002 *g*/*f*, with extraordinarily careful measurements of *g*/*f* using argon- and helium-filled quasi-spherical cavities that were made to re-determine the Boltzmann constant.[16] Despite this success, spherical cavities and eqn (1.14) cannot be used to easily determine the thermal conductivities of process gases even though such data would be useful to manufacturers and users of thermal mass flow controllers. The difficulty in applying eqn (1.14) to process gases at low densities is that $(\gamma - 1)$ for process gases is only 1/5 to 1/10 of $(\gamma - 1)$ for helium and argon, which is 0.67 at low densities. Therefore, using eqn (1.14) to determine the product $(\gamma - 1)\,(\delta_t/a)$ for process gases is subject to 5 to 10 times greater uncertainties from g_{mech} and *Pr*. As the density is increased, separating the thermal losses from the mechanical losses becomes increasingly difficult because g_{mech}/f increases as ρc^2 while δ_t/a decreases as $[\lambda/(\rho C_p c)]^{1/2}$. Therefore, using a spherical cavity and eqn (1.14) to measure thermal conductivity is not promising.

In an effort to develop an acoustic method for thermal conductivity measurements,[17] we designed a cylindrical resonator containing a metal honeycomb lattice aligned with cylinder's axis, as shown in Figure 1.6a, that increases the thermal losses for some modes relative to viscous losses and mechanical losses. For even-numbered longitudinal modes, which have a temperature antinode at the honeycomb, the effective area for heat conduction is increased by a factor of $(a/r_h)(l/\lambda_a)$ where r_h is the hydraulic radius of one honeycomb cell (which must be larger than δ_t and δ_v); a is the radius of the cylindrical cavity; λ_a is the wavelength of sound; and l is the length of the honeycomb (which must be less than $\approx \lambda_a/4$). Figure 1.6b (top) shows the measured half-widths g_{meas} for several modes and gases at constant temperature as a function of δ_t/r_h (for even-numbered modes) or δ_v/r_h (for odd-numbered modes), where r_h is the hydraulic radius of a honeycomb cell. The data span a factor of 50 in g_{meas} and a factor of 10 in δ_t for the three gases shown. The fractional deviations between the measurements and our acoustic model for all three gases are within ± 2.5 % of a single function of δ_t/r_h that underestimates g_{meas} by 10 % at high density (small δ_t/r_h) and overestimates g_{meas} by 4 % at low density (large δ_t/r_h). [See Figure 1.6b (bottom).] The results from this cavity at low densities were puzzling because the measured values of the half-widths were smaller than the calculated values. This shows that our model for the cavity containing a honeycomb is not accurate. We believe that the honeycomb concept should be explored further.

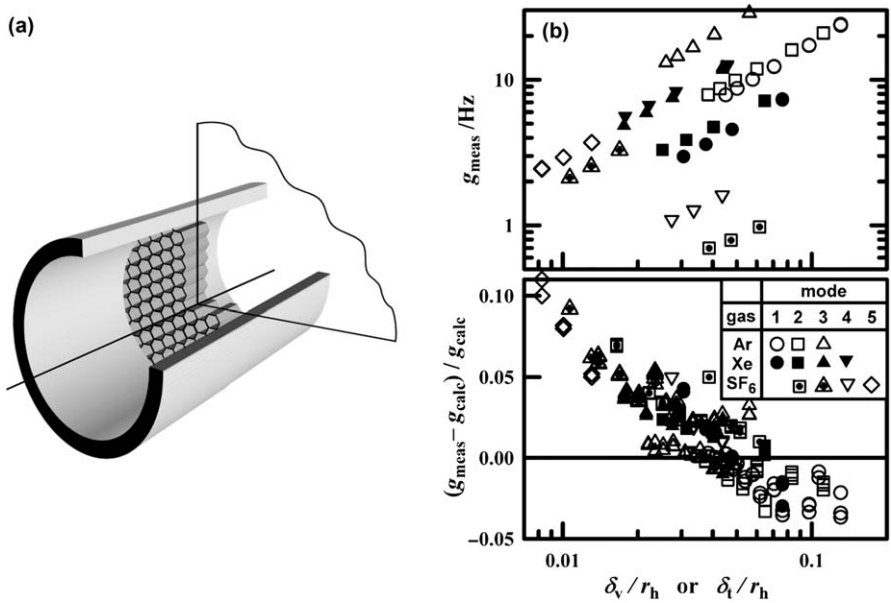

Figure 1.6 (a) A sectioned view of a cylindrical resonator containing a honeycomb lattice (the resonator's end plates are not shown). (b) Odd-numbered longitudinal modes have a velocity antinode within the honeycomb; they are more sensitive to η than corresponding modes without the honeycomb, and their half-widths are plotted as a function of δ_v/r_h, where r_h is the hydraulic radius of a honeycomb cell. Even-numbered longitudinal modes have pressure and temperature antinodes within the honeycomb; they are more sensitive to λ than corresponding modes without the honeycomb, and their half-widths are plotted as a function of δ_t/r_h.

1.4 Bulk Viscosity Measurements Near the Liquid–Vapor Critical Point

The bulk viscosity ζ is a transport coefficient that characterizes damping of volume changes of a fluid. The quantity $-\zeta\ \nabla\cdot\mathbf{u}$, which appears in the relation between the stress tensor and the rate-of-shear tensor, represents a stress, due to internal relaxation processes, that opposes the rate of change of volume. These relaxation processes govern the energy exchange between translational degrees of freedom (the acoustic mode) and other internal modes of the fluid, such as molecular vibrations, metastable intermolecular bound states, or critical fluctuations. An acoustic wave in a relaxing medium loses a fraction $\omega\zeta/(\rho c^2)$ of its energy per cycle due to bulk viscosity.

For a low-density gas of hard spheres, kinetic theory predicts $\zeta \propto \eta\rho^2$, which vanishes as $\rho \to 0$. For this reason, ζ is often ignored when considering the transport properties of noble gases such as xenon. In the liquid

state near the triple point of xenon, (ζ/η) is about 0.3; however, ζ is difficult to measure because liquids are not very compressible compared with the walls of the cavity.[18] However, ζ can become much larger than η, particularly in polyatomic gases that require many collisions to equilibrate their internal degrees of freedom with their translational degrees of freedom. For such gases, there is a peak in the sound attenuation when $\omega\tau_{\mathrm{relax}} \approx 1$, where τ_{relax} is the relaxation time that characterizes the equilibration between the internal and translational degrees of freedom.

The attenuation α_λ of a sound wave propagating in free space over a distance of one wavelength is given by

$$\alpha_\lambda = \frac{\pi\omega}{c^2}\left[(\gamma-1)\frac{\lambda}{\rho C_p} + \frac{4}{3}\frac{\eta}{\rho} + \frac{\zeta}{\rho} + (\gamma-1)\frac{c^2}{\omega}\frac{C_{\mathrm{relax}}}{C_p}\frac{\omega\tau}{1+(\omega\tau)^2}\right] \tag{1.15}$$

where the first two terms constitute the ''classical attenuation'' due to thermal conduction and viscous losses within the sound wave itself. The third term is the attenuation from bulk viscosity explicitly as a function of ζ, whereas the last term describes the bulk viscosity of a single relaxing mode. The volume processes described in eqn (1.15) also increase the half-widths of resonances in a gas-filled cavity by the amount $g_{\mathrm{b}} = f\,\alpha_\lambda/(2\pi)$.

In a fluid at its critical density ρ_{c} the characteristic size of equilibrium density fluctuations (the so-called the correlation length) diverges as the critical temperature T_{c} is approached with the universal power law $\xi \propto (\Delta T^*)^{-0.63}$, where $\Delta T^* \equiv (T - T_{\mathrm{c}})/T_{\mathrm{c}}$. The dynamic behavior of the fluid's thermophysical properties in the critical region is determined by a characteristic lifetime $\tau \propto (\Delta T^*)^{-1.93}$ for fluctuations of size ξ. The bulk viscosity arises from the dynamic response of critical fluctuations, and at zero frequency it diverges as $\zeta \propto (\Delta T^*)^{-1.93}$ as $\Delta T^* \rightarrow 0$, which is a much stronger divergence than the divergence of the thermal conductivity $[\lambda \propto (\Delta T^*)^{-0.57}]$ or of the shear viscosity $[\eta \propto (\Delta T^*)^{-0.069}]$. The bulk viscosity is a function of the product $\omega\tau$. At low frequency, such that $\omega\tau \ll 1$ in the critical region, the bulk viscosity exhibits universal power-law behavior. When $\omega\tau \sim 1$, the bulk viscosity deviates from the universal power law, an indication that the fluctuations are not in equilibrium. When $\omega\tau \gg 1$, the bulk viscosity approaches its maximum, non-universal limit. Low-frequency sound waves reach the condition $\omega\tau = 1$ closer to T_{c} and deeper into the asymptotic critical regime than do high-frequency sound waves.

Acoustic resonators have been rarely used to study liquid–vapor critical phenomena for two reasons: (1) the usual theory of acoustic resonators does not fully account for the critical behavior of the thermophysical properties, and (2) at equilibrium, near-critical fluids stratify in Earth's gravity, so the speed of sound becomes a function of height in the sample. We developed a theory of acoustic resonators that is appropriate for near-critical fluids, and we greatly reduced stratification by stirring the fluid.

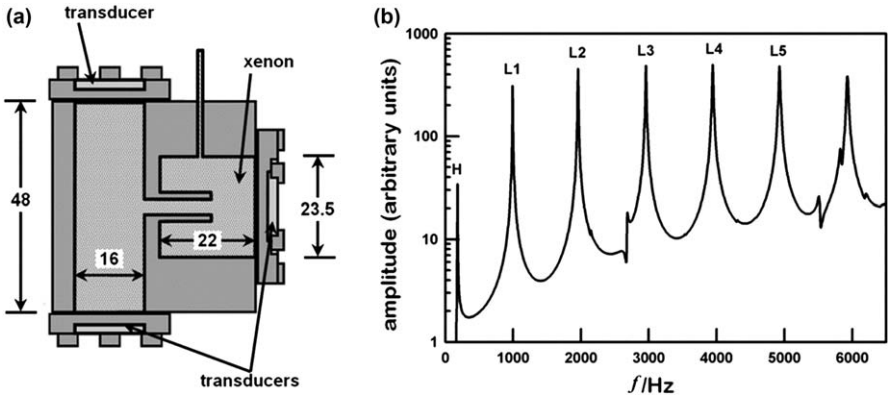

Figure 1.7 (a) Horizontal cross-section of a cavity resonator that has well-isolated acoustic modes spanning a wide frequency range. (b) Acoustic resonances when the cavity is filled with xenon near its critical density and critical temperature. In the Helmholtz (H) mode at 120 Hz, the xenon oscillates through the reentrant tube connecting two circular, cylindrical chambers (16 mm diameter, 48 mm long and 23.5 mm diameter, 22 mm long). In the longitudinal modes (L1,. . .,L5), the xenon oscillates in plane waves along the 48 mm-long cylinder.[19,20]

We developed an acoustic resonator that was optimized for measurements of bulk viscosity in xenon (BVX) near its critical point.[19–21] Figure 1.7a shows a horizontal cross section through the resonator. Ref. 19 describes the BVX resonator in more detail. The resonator had two horizontal cylindrical chambers oriented at right angles to each other and connected by a small cylindrical tube. The asymmetric design yields a spectrum with a low-frequency Helmholtz mode (H) and five longitudinal modes (L1,. . .,L5) that span a factor of 27 in frequency (see Figure 1.7b). The lowest frequency we measured, $f_H \approx 120$ Hz near T_c, was 3000 times lower than previous work.[22,23] The lower frequencies and the reduced density stratification, which we achieved by stirring the xenon, enabled our measurements to probe deeper into the asymptotic critical region than ever before. Figure 1.8a shows an example of our measured dissipation (Q^{-1}) as a function of reduced temperature $(T - T_c)/T_c$ for the lowest frequency (120 Hz) and the highest frequency (3.8 kHz) that we studied. The measured dissipation is a combination of bulk viscosity and dissipation in the thermal boundary layer. The dashed lines show the dissipation due to bulk viscosity predicted by theory. Figure 1.8b shows the bulk viscosity that is consistent with our measurements as a function of reduced temperature. The dashed line is the bulk viscosity at zero frequency, which exhibits the asymptotic power law behavior. At finite frequency, the bulk viscosity deviates from the power law when $\omega\tau \approx 1$, which occurs at successively higher reduced temperatures as the frequency increases.

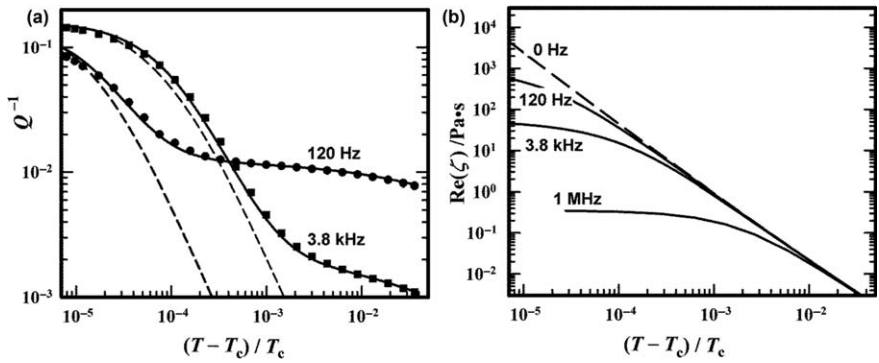

Figure 1.8 (a) For the resonator in Figure 1.7, Q^{-1} increases as the critical temperature T_c is approached. The dashed curves show the contribution to Q^{-1} from the bulk viscosity ζ at 120 Hz (H mode) and 3.8 kHz (L5 mode). The solid curves and the measurements (●, ■) are the sum of the dashed curves and surface contributions to Q^{-1}. (b) The real part of the bulk viscosity ζ of xenon at three frequencies. At zero frequency, $\zeta \propto [(T - T_c)/T_c]^{-1.93}$; at non-zero frequencies, ζ levels off when $\omega\tau \approx 1$. Near the critical point, $\zeta \gg \lambda/C_p \gg \eta$.[19–21]

References

1. J. O. Hirschfelder, C. F. Curtiss and R. B. Bird, *Molecular Theory of Gases and Liquids*, 2nd edition, Wiley & Sons, Inc., New York, 1964, 644–645.
2. M. Greenspan and F. N. Wimenitz, *NBS Report*, 1953, 2658.
3. K. A. Gillis, J. B. Mehl and M. R. Moldover, *J. Acoust. Soc. Am.*, 2003, **114**, 166.
4. J. Wilhelm, K. A. Gillis, J. B. Mehl and M. R. Moldover, *Int. J. Thermophys.*, 2000, **21**, 983.
5. J. J. Hurly, K. A. Gillis, J. B. Mehl and M. R. Moldover, *Int. J. Thermophys.*, 2003, **24**, 1441.
6. J. J. Hurly, *Int. J. Thermophys.*, 2004, **25**, 625.
7. A. F. Estrada-Alexanders and J. J. Hurly, *J. Chem. Thermodyn.*, 2008, **40**, 193.
8. G. Kirchhoff, *Ann. Phys. Chem.*, 1868, **134**, 177; English translation in *Benchmark Papers in Acoustics: Physical Acoustics*, ed. R. B. Lindsay, Dowden, Hutchinson & Ross, Stroudsburg, Pennsylvania, 1974, p. 7.
9. I. B. Crandall, *Theory of Vibrating Systems and Sound*, Van Nostrand, New York, 1927, 229–241.
10. F. B. Daniels, *J. Acoust. Soc. Am.*, 1947, **19**, 569.
11. J. B. Mehl, *J. Acoust. Soc. Am.*, 1999, **106**, 73.
12. J. J. Hurly and M. R. Moldover, private communication.
13. J. J. Hurly and M. R. Moldover, *J. Res. Natl. Inst. Stand. Technol.*, 2000, **105**, 667.
14. J. Kestin and J. Yata, *J. Chem. Phys.*, 1968, **49**, 4780.

15. E. F. May, R. F. Berg and M. R. Moldover, *Int. J. Thermophysics*, 2007, **28**, 1085.
16. K. A. Gillis, *Metrologia*, 2012, **49**, L21.
17. M. R. Moldover, K. A Gillis, J. J. Hurly, J. B. Mehl and J. Wilhelm, *Modern Acoustical Techniques for the Measurement of Mechanical Properties*, ed. Moises Levy and Henry E. Bass, Academic Press, San Diego, California, USA, 2001, ch. 10, 377–427.
18. P. Malbrunot, A. Boyer, E. Charles and H. Abachi, *Phys. Rev. A*, 1983, **27**, 1523.
19. K. A. Gillis, I. I. Shinder and M. R. Moldover, *Phys. Rev. E*, 2004, **70**, 021201.
20. K. A. Gillis, I. I. Shinder and M. R. Moldover, *Phys. Rev. E*, 2005, **72**, 051201.
21. K. A. Gillis, I. I. Shinder and M. R. Moldover, *Phys. Rev.Lett.*, 2006, **97**, 104502.
22. P. E. Mueller, D. Eden, C. W. Garland and R. C. Williamson, *Phys. Rev. A*, 1972, **6**, 2272.
23. J. Thoen and C. W. Garland, *Phys. Rev. A*, 1974, **10**, 1311.

CHAPTER 2

Optical Methods

ANDREAS PAUL FRÖBA, STEFAN WILL, YUJI NAGASAKA, JOCHEN WINKELMANN, SIMONE WIEGAND AND WERNER KÖHLER

2.1 Introduction to Optical Methods

ANDREAS PAUL FRÖBA AND STEFAN WILL

This chapter is devoted to the measurement of transport properties by optical methods, in particular by light scattering methods that are either newly developed or have significantly progressed with respect to a reduction of uncertainty or application. All these methods are based on the analysis of light scattering caused by equilibrium, non-equilibrium or induced fluctuations.

A fundamental problem, which arises with conventional methods for the determination of transport properties, is that a macroscopic gradient has to be applied that must be large enough, to give rise to a measurable effect, yet small enough to cause only little perturbation to the system under investigation.[1] This difficulty is strongly enhanced in the vicinity of the critical point, where induced gradients may make any measurement impossible. An approach to overcome these limitations is the application of light scattering techniques. These methods make use of microscopic fluctuations, which are related to diffusive processes and thus to the transport properties to be measured. The main advantages of light scattering techniques can be summarized as follows. Measurements may be performed in or close to thermodynamic equilibrium, almost without any input of energy. Experiments are conducted in a non-contact mode, allowing access to regions of thermodynamic state that can hardly be probed by other techniques. Light scattering techniques allow for the determination of a wide range of transport

Experimental Thermodynamics Volume IX: Advances in Transport Properties of Fluids
Edited by M. J. Assael, A. R. H. Goodwin, V. Vesovic and W. A. Wakeham

Published by the Royal Society of Chemistry, www.rsc.org

and other thermophysical properties. In some instances, properties can be determined even simultaneously. In most cases, light scattering techniques are based on rigorous working equations, where no calibration procedure is needed and the reliability of the measurements can be easily checked.

The most frequent application of light scattering techniques for the study of thermophysical properties of fluids is based on the analysis of microscopic statistical fluctuations originating from the random thermal movement of molecules in macroscopic thermodynamic equilibrium. Light scattering from bulk fluids and light scattering by surface waves are both routinely used to determine the thermophysical properties of fluids over a wide range of states.[2] Properties accessible by the analysis of light scattering caused by microscopic statistical fluctuations include thermal diffusivity,[3–5] mutual diffusivity,[6–9] dynamic and kinematic viscosity,[4–6,10–14] sound attenuation,[15] speed of sound,[3–5,15] and surface tension.[4,5,11] There are many research activities that use light scattering techniques to a greater or lesser extent for the analysis of the critical behavior of fluids. These research activities include ternary liquid mixtures near the critical solution point[16] and ionic fluids with liquid–liquid phase transitions.[17] Besides these classical applications of light scattering, where the systems are selected owing to their high degree of scattering that facilitates signal detection, there are also other applications. For example, Nagasaka and co-workers apply light scattering of surface waves for the measurement of viscosity and surface tension under extreme conditions, such as for high temperature melts.[18] Laser-induced capillary wave methods are used to monitor properties and provide a corresponding signal that can be used within process control.[19,20]

For fluids that are not at equilibrium, non-equilibrium Rayleigh scattering and the forced Rayleigh scattering techniques are used to determine thermophysical properties. For Rayleigh scattering experiments in a liquid mixture in the presence of a macroscopic stationary temperature gradient, non-equilibrium fluctuations arise from a coupling between local microscopic diffusive fluctuations and transverse momentum fluctuations.[21] In typical liquid mixtures, with experimentally accessible temperature gradients, three non-equilibrium modes decouple into a viscous mode, a heat mode, and a concentration mode so that for a binary mixture the decay rates of these modes are determined by the kinematic viscosity, the thermal diffusivity, and the mutual diffusivity, respectively.[22] Although non-equilibrium Rayleigh scattering is not used for routine determinations of these transport coefficients, Sengers and co-workers[22–24] showed that the technique may provide an alternative for measuring Soret coefficients of liquid mixtures, through an analysis of the amplitude of the non-equilibrium concentration fluctuations.

For forced Rayleigh scattering (FRS), an interference grating is, metaphorically, ''written'' into a slightly absorbing pure fluid or fluid mixture, giving rise to a transient temperature grating. The concept of forced Rayleigh scattering, however, involves the replacement of the statistical, weak, and random fluctuations utilized in classical Rayleigh light scattering with driven, strong, and coherent excitations.[25–27] Scattering from the induced

fluctuations is orders of magnitude greater than that from the random ones and has a well-defined phase. The data available from the two scattering processes are closely related but not identical. Classical Rayleigh scattering provides correlations for the random fluctuations, while forced Rayleigh scattering directly yields the dynamics of the induced fluctuations. Analysis of the imposed transient temperature grating in a pure fluid yields the thermal diffusivity of the fluid, but in a mixture there is a concomitant concentration distribution whose analysis can yield the thermal diffusion coefficient or the mass diffusion coefficient. These techniques were first developed and applied to transport property measurements in fluids and materials by Nagashima and co-workers,[28–31] Fiebig and co-workers,[32–34] and Köhler and co-workers.[35–38] Thus the general FRS technique can be used to determine thermal diffusivity, (Section 2.4) but with the acronym TDFRS is applied to measurements of thermal diffusion coefficients in mixtures (Sections 2.5 and 2.6).

2.2 Light Scattering by Surface Waves – Surface Light Scattering

ANDREAS PAUL FRÖBA AND STEFAN WILL

2.2.1 Introduction

Surface light scattering (SLS) probes, as the name indicates, the dynamics of thermal fluctuations on the surface of a liquid or, in a more general formulation, at phase boundaries. Nowadays, objects of investigations extend, for example, from polymer solutions,[39,40] over surfactant monolayers,[41] liquid crystals,[42,43] ionic liquids,[44,45] and ferrofluids,[46] to high-temperature melts.[18,47] Thus, the discussion of SLS presented herein cannot claim to be complete. Rather, this section aims at capturing the essence of both the theoretical and experimental developments within SLS and the application of it to the precise determination of viscosity and surface tension of fluids.

The theory of light scattering by surface waves was developed from a linearized hydrodynamic description of surface fluctuations in the 1960s. A compilation of the efforts concerned with the theory of surface light scattering can be found in the standard work of Langevin.[48] The advent of helium lasers in the 1960s permitted the first experimental investigation of the theory used to describe the method.[49–55] Although the early experiments, conducted in about 1967,[49] were able to demonstrate the feasibility of using SLS to determine viscosity and surface tension, the results obtained did not conclusively establish the method for the determination of thermophysical properties even for simple liquids.[56–59] For example, the line widths of the spectrum obtained at the free surface of water by Byrne and Earnshaw[58,59] were found to deviate systematically by up to about 20 % from the values anticipated from hydrodynamic theory with accepted values of the surface tension, viscosity, and density. This led Earnshaw[60] to state that the propagation of surface fluctuations were incompatible with the predictions obtained from the then accepted theory for a surface having no abnormal rheological properties. The apparent discrepancies could be resolved with the surface shear viscosities predicted by Goodrich.[61] In 1987 Hård and Neumann[62] showed that clean water exhibited no measurable anomalous surface properties and contradicted the previously unchallenged findings of Earnshaw.[60] A relatively high uncertainty was reported for the determination of viscosity and surface tension by light scattering by surface waves during the 1990s.[63–66]

During the past decade research has been conducted to provide low-uncertainty values of both viscosity and surface tension for liquids of relatively low viscosity and high surface tension. It is to these research activities that we now turn. The first significant research activity[67–69] was the development of procedures for the routine use of SLS to determine both

surface tension and liquid kinematic viscosity with a relatively low uncertainty for fluids with low viscosity and high surface tension. The second step, reported by Fröba *et al.*,[70–72] demonstrated that SLS could also be applied to high-viscosity fluids. These developments are described in the remainder of this section, and a compilation of viscosity and surface tension data obtained by SLS for working fluids in chemical and energy engineering and reference fluids, are given.

2.2.2 Basic Principles

In this section, a simplified overview of the SLS technique is provided. In this case, the presence of a second fluid phase is neglected, so that the SLS can be considered as capillary waves on a free liquid surface.[73] For an exact treatment of the capillary the reader is referred to ref. 74 and 75.

2.2.2.1 Dynamics of Surface Fluctuations

In macroscopic thermal equilibrium, liquid surfaces exhibit surface waves that are caused by the thermal motion of molecules. The existence of such fluctuations continuously distorts the flat equilibrium state of a surface resulting in a rough surface. This rough surface can be represented mathematically as a sum of Fourier components, that is a superposition of surface waves with different amplitudes ξ_q and wave vectors $\vec{q}$, as illustrated in Figure 2.1. Each Fourier component of the rough surface behaves optically as a weak phase grating and acts to scatter a small fraction of incident light around both the reflected and refracted beams. Surface fluctuations observable in the light scattering experiment typically cover a wavelength range from about (0.1 to 1000) μm. The total root-mean-square amplitude of the surface roughness integrated over all wavelengths is typically between (1 and 100) nm. In an SLS experiment, the dynamics of surface fluctuations are studied as a function of frequency and damping. For the temporal decay of surface fluctuations, two cases may be distinguished. For the case of relatively low viscosity and relatively large surface tension, the amplitude of the surface fluctuation decays in the form of a damped oscillation, while in the case of a relatively large viscosity and relatively small surface tension, the amplitude is damped exponentially.

The scattering geometry typically used for light scattering experiments on liquid surfaces is shown in Figure 2.1, where scattered light is observed near reflection. By choice of the angle of incidence ε and the scattering angle Θ_S, the scattering vector $\vec{q} = \vec{k}'_I - \vec{k}'_S$ is determined and, from this, the wave vector and frequency of the observed surface vibration mode. Here, $\vec{k}'_I$ and $\vec{k}'_S$ denote the projections of the wave vectors of the reflected ($\vec{k}_I$) and scattered light ($\vec{k}_S$) to the surface plane, respectively. For the observation of scattered light within the irradiation plane and

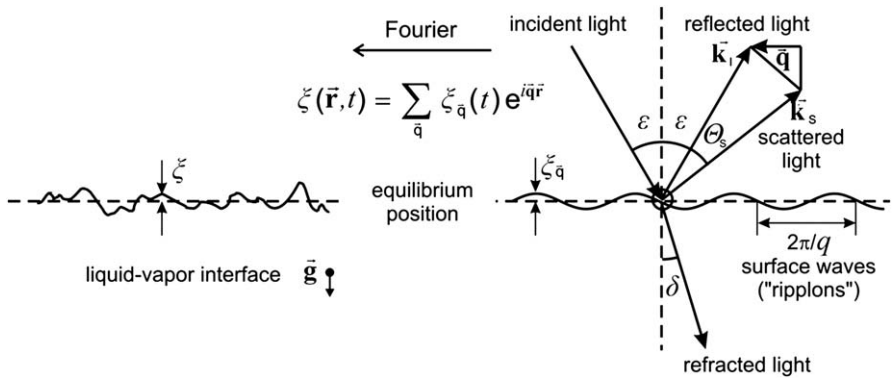

Figure 2.1 Representation of a liquid–vapor interface by a superposition of surface waves with different amplitudes and wavelength.[68]
Reprinted from A. P. Fröba and A. Leipertz, Accurate Determination of Liquid Viscosity and Surface Tension Using Surface Light Scattering (SLS): Toluene under Saturation Conditions between 260 K and 380 K, *Int. J. Thermophys.*, 2003, **24**, 898, Figure 1, Copyright 2003, with kind permission from Springer Science and Business Media.

assuming elastic scattering (*i.e.* $k_I \cong k_S$), the modulus of the scattering vector is given by

$$\begin{aligned} q &= |\vec{k}_I' - \vec{k}_S'| \cong 2k_I \sin(\Theta_S/2)\cos(\varepsilon - \Theta_S/2) \\ &= \frac{4\pi n}{\lambda_0}\sin(\Theta_S/2)\cos(\varepsilon - \Theta_S/2), \end{aligned} \tag{2.1}$$

where n is the fluid refractive index and λ_0 is the laser wavelength in vacuum.

Based on classical hydrodynamic theory, the temporal decay of a particular surface mode of the form $\exp[i\,\vec{q}\,\vec{r} + S\,t/\tau_0]$, with a wave vector $\vec{q}$ at a given point $\vec{r}$, is obtained in the limiting case of a free liquid surface from the dispersion equation

$$D(S) = Y + (1+S)^2 - \sqrt{1+2S}. \tag{2.2}$$

Eqn (2.2) results from a solution of the Navier–Stokes equations of continuity and momentum for an incompressible fluid. The reduced frequency S, $S = i\alpha\tau_0$, is related to the complex frequency α, $\alpha = \omega_q + i\Gamma$, and to the characteristic viscous time τ_0, which is given by

$$\tau_0 = \frac{\rho}{2\eta q^2}, \tag{2.3}$$

where ρ and η are the density and dynamic viscosity of the liquid, respectively. The real part of the complex frequency Re α represents the frequency

ω_q and its imaginary part the damping Γ of the surface mode observed. The reduced capillary number Y, given by

$$Y = \frac{\rho}{4\eta^2 q}\left[\gamma + \frac{g\rho}{q^2}\right], \tag{2.4}$$

also depends on surface tension γ and local acceleration of free-fall g. At relatively small wavelengths, the last term in eqn (2.4), which arises from the force of inertia, can be neglected without significant increase in uncertainty. The solution of the dispersion equation, eqn (2.2), is shown as a function of Y in Figure 2.2. In general, two physical solutions for the reduced frequency S have to be considered, which, in the case of an oscillatory decay of surface waves, represent complex conjugates. There exists a critical value for Y such that when $Y \leq 0.145$ surface fluctuations are over-damped and do not propagate. In this case, the two solutions for the reduced frequency S are real numbers ($\mathrm{Im}[S] = 0$; $\omega_q = 0$) associated with different damping rates.

The reduced frequency S can be represented to a first-order approximation by

$$S_{1,2} \approx \pm \mathrm{i}\sqrt{Y} - 1 \tag{2.5}$$

or

$$S_1 \approx -Y \quad \text{and} \quad S_2 \approx -0.45, \tag{2.6}$$

for an oscillatory or over-damped decay of surface waves, respectively. These first-order approximations, which are often used in the literature to provide a qualitative description of the dynamics of surface fluctuations, are indicated in Figure 2.2 by dashed lines. The differences between the solid and dashed lines, shown in Figure 2.2, clearly indicate the operating limits of the first-order approximations given by eqn (2.5) or (2.6), that only apply for descriptions of

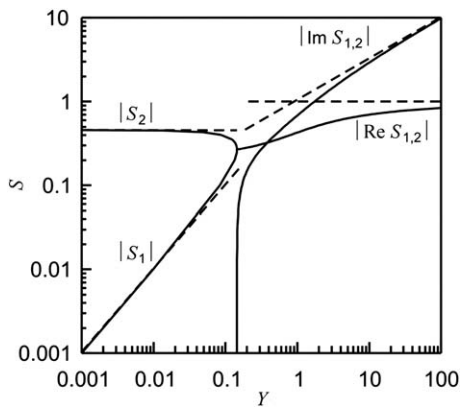

Figure 2.2 Numerical solution of the dispersion equation in its reduced form, eqn (2.2) (shown by a solid black line —), and solutions as a first approximation, eqn (2.5) and eqn (2.6) (shown with a dashed black line - - -).

the dynamics of surface waves when either $Y \gg 1$ or $Y \ll 1$. For intermediate values of Y, however, the dynamics of surface waves can no longer be described with sufficient certainty by the first-order approximation.

2.2.2.2 Correlation Function

In SLS, scattered light emerging from the interaction between incident light and the fluctuating surface structure can be analyzed with photon correlation spectroscopy (PCS). In this type of detection, the time-dependent correlation function of the scattered light intensity is measured at a point in the far field. When the scattered light is superimposed with a coherent reference light of much greater intensity, the normalized intensity correlation function is given by

$$g^{(2)}(\tau) = 1 + \frac{2I_S}{I_{LO}} g_q(\tau). \tag{2.7}$$

In eqn (2.7), g_q is the normalized time-dependent correlation function of the surface fluctuations observed for a well-specified modulus of the wave vector $\vec{q}$ given by[56]

$$g_q(\tau) = (S_2 - S_1)^{-1}[S_2 \exp(S_1|\tau|/\tau_0) - S_1 \exp(S_2|\tau|/\tau_0)]. \tag{2.8}$$

In eqn (2.7), I_S and I_{LO} denote the time average of the intensity of the scattered light caused by the surface fluctuations and the corresponding intensity of the coherent reference light, commonly known as the local oscillator.

In the case when the surface fluctuations propagate (that is for $Y > 0.145$), there are two physical solutions for the reduced frequency S, which represent complex conjugates, $S_{1,2}/\tau_0 = \pm i\omega_q - \Gamma$, and the practical normalized intensity correlation function takes the form

$$g^{(2)}(\tau) = a + b\cos\left[\omega_q\tau - c\right] \exp(-\tau/\tau_C). \tag{2.9}$$

In eqn (2.9), the phase term $c(= \text{atan}\lfloor\Gamma/\omega_q)\rfloor$ largely accounts for the deviations of the spectrum from the Lorentzian form and vanishes only in the limiting case of infinite values of the reduced capillary number ($Y \gg 1$). The reciprocal of the damping constant Γ ($= 1/\tau_C$), denoted as correlation time τ_C, and the frequency ω_q are identical to the mean life time and to the frequency of propagation of the fluctuation for a given modulus of the wave vector $\vec{q}$. The adjustable parameter a in eqn (2.9) accounts for the deviation of the baseline from the ideal value of unity, given by eqn (2.7). This deviation from the ideal case may be caused, for example, by slow fluctuations in the light source. The parameter b in eqn 2.9 is essentially determined by the ratio of scattered light to reference light and the coherence of the optical system.

In the case of over-damped surface fluctuations (that is for $Y \leq 0.145$), the two physical solutions for the reduced frequency S are, as shown in Figure 2.2, real numbers, which are associated with the two damping

constants $S_1/\tau_0 = -\Gamma_1 = -1/\tau_{C,1}$ and $S_2/\tau_0 = -\Gamma_2 = -1/\tau_{C,2}$, respectively. The correlation function, eqn (2.7), is then given by two exponentially decaying modes according to

$$g^{(2)}(\tau) = a + b_1 \exp(-\tau/\tau_{C,1}) - b_2 \exp(-\tau/\tau_{C,2}). \quad (2.10)$$

In eqn (2.10) *a,* b_1, and b_2 are adjustable parameters. In the limiting case of infinitesimal values of the reduced capillary number $Y \ll 1$, which is equivalent to $S_1 \ll S_2$, the correlation function, eqn (2.10), reduces to one exponential with correlation time $\tau_{C,1}$. The ability to resolve both modes is determined by the ratio of their signal amplitudes b_1/b_2, which is given by the ratio of the reduced frequencies S_2/S_1. Generally, it is easier to simultaneously determine both signals in the region close to critical damping ($Y = 0.145$) where, as Figure 2.2 shows, the reduced frequencies S_1 and S_2 and, thus, the amplitudes b_1 ($\propto S_2 \propto \Gamma_2 = 1/\tau_{C,2}$) and b_2 ($\propto S_1 \propto \Gamma_1 = 1/\tau_{C,1}$) of the two components have comparable values.

2.2.3 Experimental

Figure 2.3 shows a schematic of an SLS experiment for the simultaneous measurement of viscosity and surface tension of transparent fluids by observing the forward scattered light near refraction. This arrangement, which differs from the more commonly employed scattering geometry illustrated in Figure 2.1, is chosen to optimize the signal and stability. To observe the light scattered by surface waves, the optical path is aligned so that the laser beam and the direction of detection intersect on the liquid surface (or phase boundary) in the measurement cell. A frequency-doubled continuous-wave Nd:YVO_4-laser with a wavelength of $\lambda_0 = 532$ nm and power between about 2 mW and 300 mW serves as a light source. After passing through two circular stops without any lens, part of the scattered light together with the coherent reference light reach the detector system, which consists of two photo multiplier tubes (PMTs). The received signals are then amplified, discriminated and fed into a digital correlator with either a multiple-tau or a single-tau structure to compute the correlation function.

The optical arrangement of Figure 2.3 is determined to permit the analysis of scattered light at variable and relatively high wave vectors for capillary waves of an order of about 10^6 m^{-1} where instrumental broadening effects are negligible. Light scattered on the liquid surface is detected perpendicularly to the surface plane and, as Figure 2.1 shows, $\Theta_S = \delta$. In this arrangement, the modulus of the wave vector q can be deduced exactly as a function of the angle of incidence, $q = 2\pi/\lambda_0 \sin(\Theta_i)$, without knowledge of the fluid refractive index n. In this experiment, the angle of incidence Θ_i is set between 3° and 6° and is measured directly with a high precision rotation table (with an uncertainty $\Delta\Theta_i = \pm 0.005°$). More detailed information concerning the selection of the components for the SLS experiment and the sample cell design can be found in ref. 67 to 69.

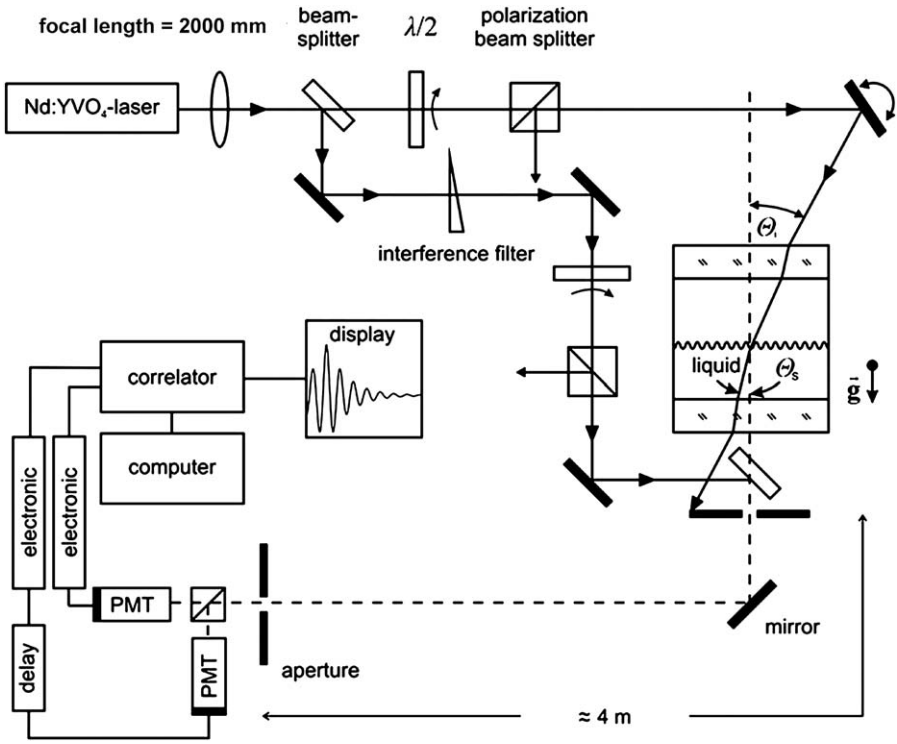

Figure 2.3 A setup for a SLS experiment.[68]
Reprinted from A. P. Fröba and A. Leipertz, Accurate Determination of Liquid Viscosity and Surface Tension Using Surface Light Scattering (SLS): Toluene under Saturation Conditions between 260 K and 380 K, *Int. J. Thermophys.*, 2003, **24**, 906, Figure 4, Copyright 2003, with kind permission from Springer Science and Business Media.

2.2.4 Measurement Examples and Data Evaluation

In the following, some typical correlation functions are shown and their evaluations for the central quantities decay rate or correlation time and frequency is discussed. Again, it should be noted that the relations in the first-order approximation given in section 2.2.2.1 between the reduced frequency S and the reduced capillary wave number Y connecting the dynamics of surface waves, *i.e.* damping $\Gamma(=1/\tau_C)$ and frequency ω_q, with the thermophysical properties viscosity, density, and surface tension or interfacial tension, never allow their determination with low uncertainty. For data evaluation, an exact description of the dynamics of surface waves in form of their dispersion relation is necessary. Reference data for density are also used as input values for a numerical solution of the dispersion relation, which takes into account the presence of a second fluid phase,[74,75] which can be neglected only for a few experimental conditions.[68,69]

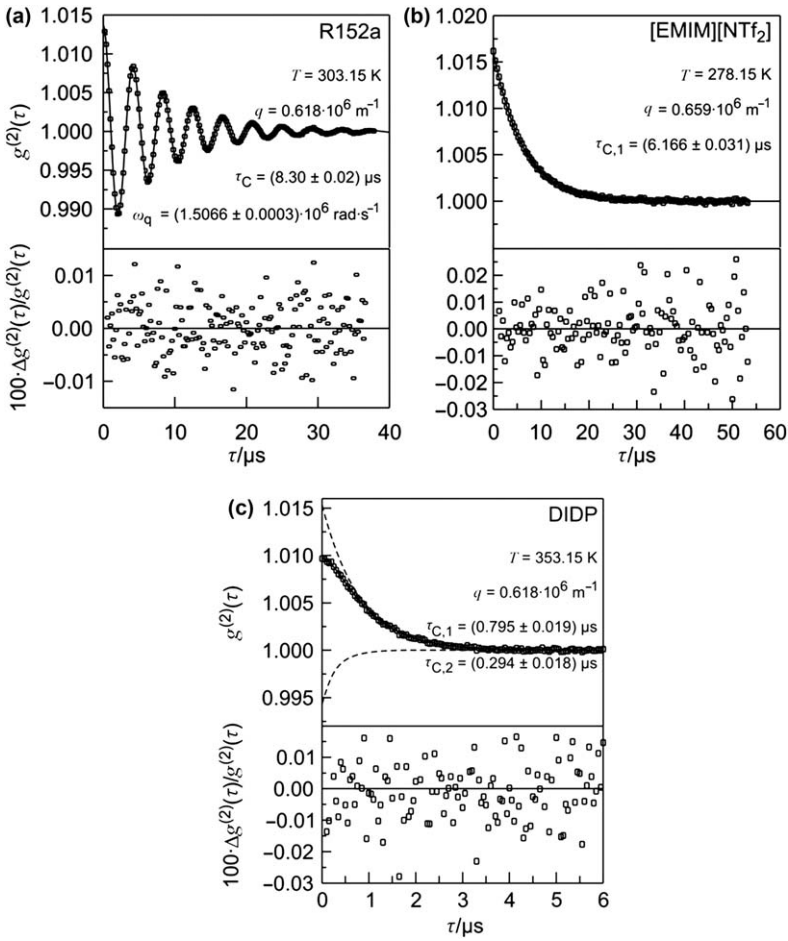

Figure 2.4 Experimental correlation functions $g^{(2)}(\tau)$ according to y-axis in the figure obtained at phase boundaries between liquid and vapor for different fluids: (a) 1,2-difluoroethane (R152a), fit to the correlation function according to eqn (2.9) for the determination of τ_C and ω_q; (b) 1-ethyl-3-methylimidazolium bis(trifluoromethylsulfonyl)imide [EMIM][NTf_2], fit to the correlation function by a simple exponential associated with $\tau_{C,1}$ in eqn (2.10); (c) diisodecyl phthalate (DIDP), fit to the correlation function by a double exponential according to eqn (2.10) demonstrating the existence of two modes with $\tau_{C,1}$ and $\tau_{C,2}$.

Figure 2.4(a) shows an example of a correlation function as it was obtained from scattering at a liquid–vapor interface of 1,2-difluoroethane (R152a) at the vapor pressure at a temperature of 303.15 K. The experimental correlation function, eqn (2.9), has to be evaluated for the quantities, ω_q and τ_C, which may be done directly by a standard nonlinear fit in which the squared sum of the residuals is minimized. The evaluation of the experimental data for viscosity and surface tension has to be performed on the basis of a full solution

of the dispersion relation, where also reference data for the density and viscosity of the vapor phase are used. Far from the critical point, the uncertainties in reference data have a comparatively small influence on the final results for the liquid viscosities, so that for this quantity an overall maximum relative uncertainty of less than $\pm 1\,\%$ can be achieved. The uncertainty in surface tension is directly influenced by the uncertainty of the density used for the evaluation. In combination with the uncertainties of the surface light scattering experiment, the total relative uncertainty in the measured surface tension is $\pm 1\,\%$. The uncertainty in liquid viscosity is clearly larger at higher temperatures, yet for temperatures not too close to the critical point ($T_R < 0.95$), and a relative uncertainty of $\pm 2\,\%$ can be obtained.

For an over-damped behavior of surface fluctuations, Figure 2.4(b) shows an example of a correlation function, as obtained from scattering on a liquid surface of 1-ethyl-3-methylimidazolium bis(trifluoromethylsulfonyl)imide, commonly given the acronym [EMIM][NTf_2], at a pressure of 0.1 MPa and a temperature of 278.15 K. For the experimental correlation function, only one exponential signal associated with the relaxation time $\tau_{C,1}$ can be resolved. The signal ratio of the two modes does not allow for their simultaneous investigation as discussed in section 2.2.2.2. The investigation of [EMIM][NTf_2] at a temperature of 278.15 K is associated with a reduced capillary number Y of about 0.004; the order of magnitude of the amplitude ratio b_1/b_2 is thus estimated to be larger than 110. In general, for a low uncertainty determination of the dynamic viscosity η for fluid of high viscosity, the dispersion relation of surface waves must be considered in its complete form. To this end, data obtained for the dynamics of surface waves, *i.e.* the damping Γ_1 at a defined wave vector q, have to be combined with reference data for surface tension γ and density ρ. By the provision of data for surface tension, the relative overall maximum relative uncertainty of values for the dynamic viscosity obtained from SLS can be found to be about $\pm 1\,\%$.[70,71]

Figure 2.4(c) shows an example for the evaluation of a correlation function recorded for an over-damped behavior of surface fluctuations at a liquid surface of diisodecyl phthalate (commonly given the acronym DIDP) at $p \approx 0.1$ MPa, where two modes could be determined simultaneously according to eqn (2.10).[72] In this case, both viscosity and surface tension were determined. The detection of two modes, however, is possible only for reduced capillary wave numbers close to unity, $Y \approx 1$, where the dynamics of the surface fluctuations change from an over-damped to an oscillatory behavior. In this case, the decay times $\tau_{C,1}$ and $\tau_{C,2}$ of the two modes, as well as their amplitudes b_1 and b_2, become similar. Furthermore, given the opposite sign of both modes, as shown in eqn (2.10), the overall contribution to the correlation function vanishes at the critical damping, where $b_1 = b_2$ and $\tau_{C,1} = \tau_{C,2}$. Thus, the uncertainty in the determination of the decay times increases approaching the critical damping. For an over-damped behavior of surface fluctuations close to the critical damping, the simultaneous determination of viscosity and surface tension can be performed only with a large uncertainty. For both properties, depending on the distance to the critical damping, uncertainties between $\pm(5$ and $20)\,\%$ can be found.[72]

2.2.5 Fields of Application

During the past decade, SLS has been increasingly applied to the determination of the thermophysical properties of fluids. This has been made possible by the continual development and improvement of the method and because of the requirement for reliable data for working fluids in both chemical and energy engineering. In the remainder of this section, we provide a compilation of thermophysical property data obtained with SLS at The Erlangen Graduate School in Advanced Optical Technologies (SAOT) and Lehrstuhl für Technische Thermodynamik (LTT), Friedrich-Alexander-Universtät Erlangen-Nürnberg, Germany.

2.2.5.1 Viscosity Standards

The SLS measurements performed with methylbenzene (toluene) were used to develop the method for routine measurements of both surface tension and liquid kinematic viscosity with a known uncertainty.[67,68] In this work, the simplified theory, which only allows a rough understanding of the SLS technique, could not be used because it does not permit the determination of viscosity and surface tension with low uncertainty. Furthermore, the analysis of the scattered light at relatively large wave vectors permits the minimization of instrumental broadening effects. In view of these stipulations, we found no measurable differences between the results obtained from SLS when compared with those obtained from conventional methods and a relative uncertainty of ± 1 % was obtained for viscosity. The use of SLS for the determination of viscosity has one significant advantage over most other viscometers in that there is no requirement for calibration. Thus, measurements of viscosity obtained from SLS[68] could contribute primary data to develop standard reference correlations for the viscosity of methylbenzene.[76] Similarly, measurements with pentane have contributed to the database for a low-viscosity standard.[77]

The viscosity of diisodecyl phthalate (DIDP) was also determined by SLS. These measurements were part of a project co-ordinated by the International Association for Transport Properties (IATP) to provide an industrial standard of moderately high viscosity (≈ 100 mPa · s).[78] For high viscosity fluids, the analysis of the SLS measurements to determine viscosity requires values of the surface tension obtained from alternate techniques. Nevertheless, most other viscometers are relative instruments and require a calibrant, whereas no calibrant is required for the SLS-technique. For temperatures between (273 and 313) K, corresponding to a viscosity range of about (650 to 40) mPa · s, respectively, the viscosity of DIDP was determined by the SLS with a total relative uncertainty of ± 1.4 %.[70]

2.2.5.2 Refrigerants

SLS has been used to determine the kinematic viscosity and surface tension for numerous pure, partially-halogenated chlorofluorocarbons (HCFCs) and

(hydrofluorocarbons) HFCs.[11,79,80] In this work, continuous improvements were made to the SLS measurement scheme and the associated data evaluation procedures, as described in ref. 67 to 69. Specifically, the refrigerants studied by SLS at the phase border are as follows: 2,2-dichloro-1,1,1-trifluoroethane (R123); trifluoromethane (R23); difluoromethane (R32); pentafluoroethane (R125); 1,1,1-trifluoroethane (R143a); 1,1,1,2-tetrafluoroethane (R134a); 1,2-difluoroethane (R152a); 1,1,1,3,3-pentafluorobutane (R365mfc); 1,1,1,2,3,3,3-heptafluoropropane (R227ea); 1,1,1,2,2,3,3-heptafluoro-3-methoxypropane (HFE-7000); $C_5H_3F_9O$ which is an azeotropic mixture (two inseparable isomers) of 1,1,1,2,2,3,3,4,4-nonafluoro-4-methoxybutane and 2-[difluoro(methoxy)methyl]-1,1,1,2,3,3,3-heptafluoropropane (HFE 7100); $C_6H_3F_9O$ which is an azeotropic mixture of 1-ethoxy-1,1,2,2,3,3,4,4,4-nonafluorobutane and 2-[difluoro(ethoxy)methyl]-1,1,1,2,3,3,3-heptafluoropropane (HFE-7200); 1,1,1,2,2,3,4,5,5,5-decafluoro-3-methoxy-4-trifluoromethyl-pentane (HFE-7300); and, 3-ethoxy-1,1,1,2,3,4,4,5,5,6,6,6-dodecafluoro-2-trifluoromethyl-hexane (HFE-7500).[69,81–83] For the sake of brevity, these compounds will be referred to with identification schema used by the refrigeration industry and shown in parentheses above.

In 2001, SLS was used to study the binary refrigerant mixture (R125 + R143a)[†] given the symbol R507A by the refrigeration industry and the ternary mixture (R125 + R134a + R143a)[‡] given the symbol R404A by the refrigeration industry.[84] Subsequently, SLS has been used to study the mixtures (R32 + R125) given the symbol R410A,[§] (R32 + R125 + R134a) given the symbol R407C,[¶] (R125 + R134a + R600) given the symbol R417A,[‖] and (R125 + R134a + R600) given the symbol R417B[**] as well as other binary and ternary refrigerant mixtures,[5,84,85] a mixture containing four HFCs,[86] and an organic Rankine cycle fluid.[4,87] The kinematic viscosity and surface tension of some of these refrigerants as determined by SLS are shown in Figure 2.5, which includes results for mixtures[4,69,85] for pure HCFCs[69] and HFCs.[69,81,82] Refrigerants from the latter group form the components of the mixtures shown in Figure 2.5.

2.2.5.3 *Ionic Liquids*

During the last five years, SLS has been used to determine the dynamic viscosity and surface tension of pure ionic liquids (ILs)[12–14,88] and their mixtures with molecular solvents.[89] The dynamic viscosity obtained for ILs

[†]R507A is {x pentafluoroethane + (1 − x) 1,1,1-trifluoroethane} where the mole fraction $x = 0.41184$.

[‡]R404A is {x_1 pentafluoroethane + x_2 1,1,1,2-tetrafluoroethane + (1 − x_1 − x_2) 1,1,1-trifluoroethane} where the mole fractions $x_1 = 0.35782$ and $x_2 = 0.038264$.

[§]R410A is {x difluoromethane + (1 − x) pentafluoroethane} where the mole fraction $x = 0.69761$.

[¶]R407C is {x_1 difluoromethane + x_2 pentafluoroethane + (1 − x_1 − x_2) 1,1,1,2-tetrafluoroethane} where the mole fractions $x_1 = 0.38111$ and $x_2 = 0.17956$.

[‖]R417A is {x_1 pentafluoroethane + x_2 1,1,1,2-tetrafluoroethane + (1 − x_1 − x_2) butane} where the mole fractions $x_1 = 0.41446$ and $x_2 = 0.5231$.

[**]R417B is {x_1 pentafluoroethane + x_2 1,1,1,2-tetrafluoroethane + (1 − x_1 − x_2) butane} where the mole fractions $x_1 = 0.74426$ and $x_2 = 0.20225$.

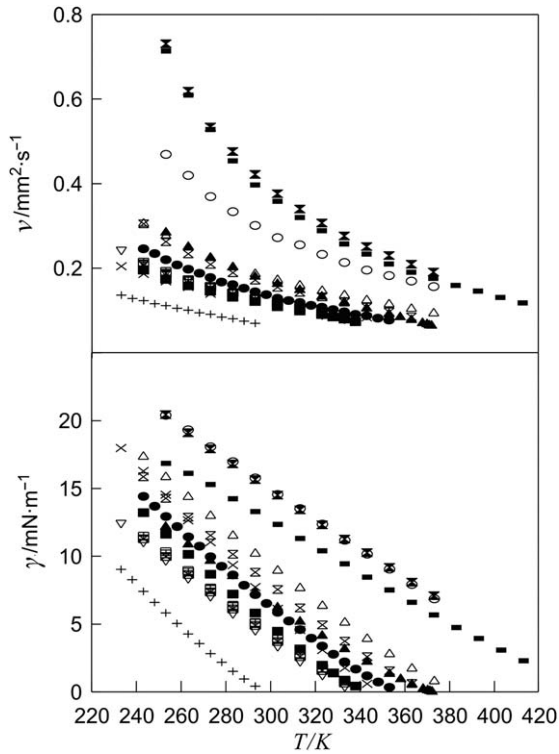

Figure 2.5 Liquid kinematic viscosity ν and surface tension γ of different refrigerants and an organic Rankine cycle fluid (SES36) under saturation conditions as a function of temperature T from SLS: +, trifluoromethane (R23); ×, difluoromethane (R32); ▽, petanfluoroethane (R125); □, 1,1,1-trifluoroethane (R143a); ⧖, 1,1,1,2-tetrafluoroethane (R134a); △, 1,1-difluoroethane (R152a); ○, 2,2-dichloro-1,1,1-trifluoroethane (R123); ▲, 1,1,1,3,3-pentafluoropropane (R227ea); ⧗, 1,1,1,3,3-pentafluorobutane (R365mfc); ▬, an azeotropic mixture of (1,1,1,3,3-pentafluorobutane + 1,1,2,3,3,3-hexafluoro-1-propene, oxidized, polymerised) (SES36); ⊠, (pentafluoroethane + 1,1,1-trifluoroethane) (R507A); ⊞, (pentafluoroethane + 1,1,1,2-tetrafluoroethane + 1,1,1-trifluoroethane) (R404a); ■, (difluoromethane + pentafluoroethane) (R410A); ●, (difluoromethane + pentafluoroethane + 1,1,1,2-tetrafluoroethane) (R407C).

are shown in Figure 2.6 as a function of temperature between 273.15 K and 333.15 K.[12,13] For these fluids, an over-damped surface fluctuation was observed. In this case, with a first order approximation, the quantity directly accessible by SLS of the ratio of dynamic viscosity to surface tension. Combining the ratio of ν/γ obtained from SLS with the density and interfacial tension from other conventional measurements, the dynamic viscosity η was obtained at temperatures from (273.15 to 333.15) K with an estimated expanded relative uncertainty of between ± (2 to 3) %.

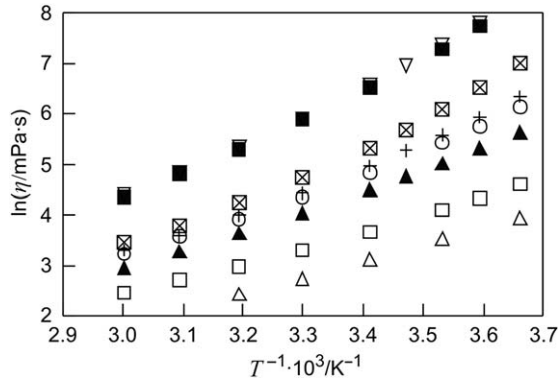

Figure 2.6 Natural log of the dynamic viscosity ln(η), for ionic liquids as a function of T^{-1}: ○, [EMIM][$EtSO_4$] (1-ethyl-3-methylimidazolium ethylsulfate); □, [EMIM][NTf_2] (1-ethyl-3-methylimidazolium bis(trifluoromethylsulfonyl)imide); △, [EMIM][$N(CN)_2$] (1-ethyl-3-methylimidazolium dicyanamide); ■, [OMA][NTf_2] (trioctylmethylammonium bis(trifluoromethylsulfonyl)imide); ⊠, [EMIM][$MeSO_3$] (1-ethyl-3-methylimidazolium methanesulfonate); +, [EMIM][$MeOHPO_2$] (1-ethyl-3-methylimidazolium methylphosphonate); ▽, [EMIM][$OcSO_4$] (1-ethyl-3-methylimidazolium octylsulfate); ▲, [BBIM][NTf_2] (1 butyl-3-butylimidazolium bis(trifluoromethylsulfonyl)imide).

2.2.5.4 Critical Behavior

Carbon dioxide has been studied with SLS to determine the applicability of the method within the critical region.[69] In general, the results obtained for both surface tension[90] and viscosity[91] of carbon dioxide from SLS[69] were in excellent agreement with those determined from conventional techniques. The SLS data were also analyzed to provide the critical exponent for surface tension. The universal exponent,[69] $n = (1.266 \pm 0.006)$, was determined for the surface tension of carbon dioxide from the surface light scattering measurements with, as shown in Figure 2.7, a van der Waals type surface tension equation. This result is in good agreement with Widom's scaling law for the interfacial tension.[92] For the latter, the universal exponent n is 2ν, where $\nu = 0.63$ is the exponent for the divergence of the correlation length.

2.2.6 Conclusion

During the past decade, SLS has matured, through research, to become a routine instrument for the determination of the thermophysical properties of fluids. In principle, the SLS is based on working equations firmly based in the principles of physics and the reliability of the measurements can be easily verified. The precise determination of both liquid viscosity and surface tension by SLS requires both an exact description of the dynamics of surface waves by hydrodynamic theory and the correct experimental design. For the

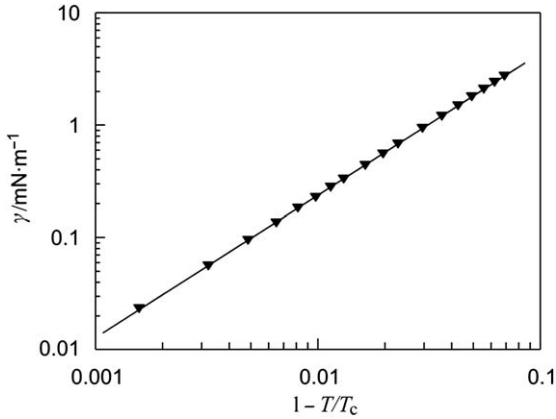

Figure 2.7 Surface tension γ of carbon dioxide close to the vapor–liquid critical point probed by surface light scattering as a function of temperature T reduced by the critical temperature T_c in the form $(1 - T/T_c)$ Representation of the experimental data by a van der Waals equation, $\gamma = \gamma_0(1 - T/T_c)^n$, where n is an universal exponent, equal to (1.266 ± 0.006). ▼, measured by SLS; ———, van der Waals equation with adjusted exponent.

latter, this requires the minimization of instrumental broadening effects and a defined heterodyne detection scheme for the analysis of the scattered light. When these elements coexist, the viscosity and surface tension obtained from SLS agree, within the assigned mutal uncertainties, with values obtained from conventional methods. The uncertainty of the results obtained has been determined by comparison with values obtained from instruments with quite different sources of systematic error.

The SLS method has provided data which have contributed significantly to the thermophysical properties for several fluids. These include fluids that can be industrial standard reference fluids for viscosity and working fluids for refrigerants, organic Rankine cycle fluids, and ionic liquids. These investigations have clearly demonstrated the applicability of the SLS technique to fluids that cover a wide range of viscosities from about 10 μPa · s to 1 Pa · s. Future challenges for SLS lie with the development of the technique for specific purposes, which include the application to high-temperature melts. Improvements in the design of the experiment including the provision of compact sensors might see SLS used for *in situ* measurements and process control.

2.3 Laser-induced Capillary Wave Technique

YUJI NAGASAKA

2.3.1 Introduction

In section 2.2 the discussion concentrated upon the use of Surface Light scattering from spontaneous capillary waves on the surface of a liquid. It was pointed out therein that when the viscosity of the liquid is relatively large and the surface tension relatively small, this technique is somewhat limited because the spontaneous capillary waves are overdamped. This is unfortunate because the physical properties of many liquid metals of technological interest fall into the category of high viscosity and low surface tension. For that reasons it has been necessary to develop different optical techniques to study such systems. For example, Rhim *et al.*[93] measured the surface tension and viscosity of molten zirconium at temperatures up to about 2200 K by detecting the characteristic oscillation frequency and the decay time of a liquid zirconium droplet, which was electrostatically levitated. The droplet oscillation was externally induced by superimposing a small sinusoidal electric field on the levitation field. A second way to overcome the difficulties with the SLS technique (section 2.2) for such systems is to replace the weak and random fluctuations by strong and coherent excitations from a laser-induced grating. The laser induced capillary wave technique (given the acronym LiCW) enables the determination of the viscosity and surface tension in a contact-free manner. The LiCW measurement has the following characteristics: (1), occurs within a very short time of between 1 μs and 1 ms; (2), has a high spatial resolution of between (10 and 100) μm; (3), a small sample volume of between 1 μL and 1 mL); and (4), operates over a wide range of viscosities from (10^{-1} to 10^{6}) mPa · s.

2.3.2 Principle of Laser-induced Capillary Wave Technique

The principle of the laser-induced capillary wave technique is shown in Figure 2.8. In this approach two pulsed laser beams of equal wavelength and equal intensity are forced to intersect on an absorbing sample surface at the crossing angle θ. The beams generate an intensity distribution within the surface-grating interference pattern with a grating period Λ of several on the order of 10 μm. The laser intensity distribution $I_h(x)$ and wave number k within the heated area can be written as

$$I_h(x) = I_{h,0}\{1 + \cos(kx)\} \tag{2.11}$$

and

$$k = \frac{2\pi}{\Lambda} = \frac{4\pi \sin(\theta/2)}{\lambda_h}, \tag{2.12}$$

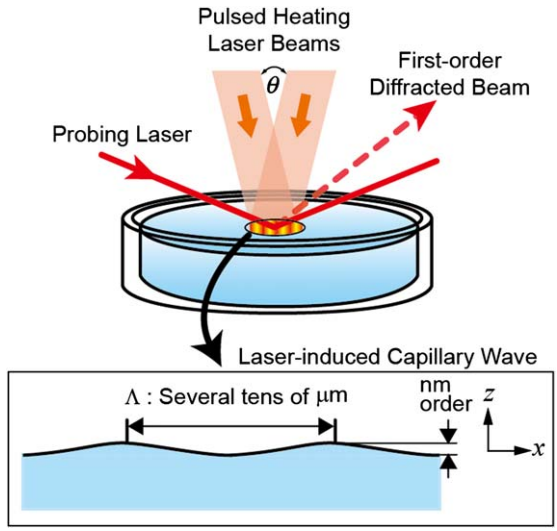

Figure 2.8 Principle of laser-induced capillary wave technique.

where $I_{h,0}$ is the heating laser beam intensity, Λ is the fringe spacing, and λ_h is the wavelength of the heating laser. At the end of heating time, which is on the order of 1 ns for the laser-heating pulse duration, the corresponding spatially sinusoidal temperature distribution induced by the grating pattern is given by

$$T(x) = T_m + \Delta T \cos(kx), \tag{2.13}$$

where T_m is the mean initial temperature rise, and ΔT is the amplitude of the spatially periodic temperature distribution.

The temperature distribution of the thermal grating creates a capillary wave on the liquid surface driven by the thermal expansion and the temperature dependence of surface tension. The displacement of the capillary wave along the z direction can be expressed by

$$u_z(t) = u_m + \Delta u(t) \cos(kx), \tag{2.14}$$

where u_m is the spatially uniform displacement and $\Delta u(t)$ is the amplitude of the laser-induced capillary wave. In the experimental apparatus, the amplitude of the created capillary wave is estimated to be less than 10 nm. When the probing laser beam is incident on the heated area, it is diffracted because the capillary wave acts like a reflection grating. The first-order diffraction efficiency is directly proportional to the square of the surface displacement as shown in the following equation:

$$I_1(t) \propto \Delta u(t)^2, \tag{2.15}$$

where $I_1(t)$ is the intensity of the first-order diffracted beam. Therefore, we obtain information regarding the behavior of the laser-induced capillary wave from measurements of the intensity of the first-order diffracted beam as a function of time. The temporal behavior of the laser-induced surface displacement $\Delta u(t)$ of a Newtonian liquid was solved by Yasumoto *et al.*[94] and can be simply expressed as

$$\Delta u(t) = f(\eta, \gamma, \partial\gamma/\partial T, \rho, \lambda, a, \alpha, u_L), \tag{2.16}$$

using the thermophysical properties of the sample liquid of viscosity η (or kinematic viscosity $\nu = \eta/\rho$), surface tension γ, temperature dependence of surface tension $\partial\gamma/\partial T$, density ρ, thermal conductivity λ, absorption coefficient a, thermal expansion coefficient α and speed of sound u_L at the experimental heating laser beam intensity $I_{h,0}$ and fringe spacing $\Lambda = 2\pi/k$. The temporal behavior of the laser induced capillary wave predominantly depends on the viscosity for damping and the surface tension for restoration, although there are eight properties involved in eqn (2.16). The sensitivity analysis of eqn (2.16) regarding all thermophysical properties was carried out numerically,[95] with the result that it is possible to determine the viscosity and surface tension by detecting the time dependence of the first-order diffracted beam $I_1(t)$ and the grating period Λ.[19,95–98]

2.3.3 Experimental Apparatus

An example of the experimental apparatus is shown in Figure 2.9.[19] A pulsed CO_2 laser (Edinburgh Instruments Ltd., MTL-3; wavelength 10.6 μm, pulse width 50 ns, maximum output energy 65 mJ) is employed as a heating source. Repetition rates from a single shot to 100 Hz can be used. The pulsed heating beam is positioned vertically over mirror 1 (M1) and divided into two

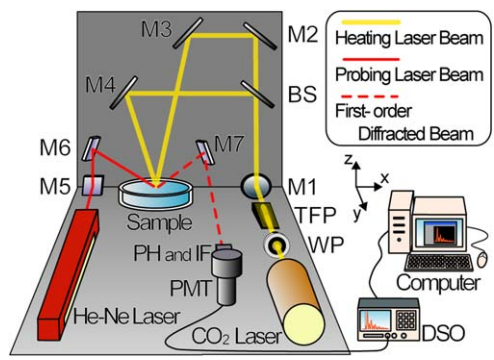

Figure 2.9 Experimental apparatus of laser-induced capillary wave technique using pulsed CO_2 laser.

beams of equal intensity by means of a beam splitter (BS). The two beams intersect on the sample surface by reflecting on M2, M3 and M4 to produce an interference pattern. These optical devices are fixed on a vertical optical bench. The radius of the heating beams is approximately 6 mm on the sample surface. Typically the range of fringe spacing of the grating is adjusted from about (20 to 200) μm. The liquid sample is filled in a petri dish (depth 1.6 mm and radius 5 cm). The probing laser is a He-Ne laser (wavelength 632.8 nm, output power 15 mW and beam radius 2 mm). The first-order diffracted beam signal as a function of time is detected by a photomultiplier tube (PMT; Hamamatsu, R928) through a pinhole (PH) and a interference filter (IF). The output signal is sent to a digital storage oscilloscope (DSO) and is transferred to a computer. The entire apparatus is arranged on an optical bench.

In order to determine the fringe spacing prior to the experiment, the CO_2 laser beams intersect on the surface of the transparent PMMA plate of 2 mm thickness, which is set at the same position as the sample surface. In this way, the grating pattern that is generated by an identical optical configuration to that used in the experiment is printed on the surface of the PMMA plate. By irradiating the He-Ne laser on the printed grating area, the diffracted beam is generated so that we are able to determine the grating period by measuring the diffraction angle.

2.3.4 Viscosity Measurement of Newtonian Liquids

To confirm the reliability of the laser-induced capillary technique, we measured the viscosity of nine Newtonian pure liquid samples at a temperature of 298 K and a pressure of about 0.1 MPa.[97] The samples were propanone, methylbenzene, water, ethanol, 1-hexanol, ethane-1,2-diol, as well as the standard liquids for calibrating a viscometer certified by the National Institute of Advanced Industrial Science and Technology (AIST) in Japan of JS100, JS1000, and JS14000. Figure 2.10(a) and (b) show the detected signals for methylbenzene $\{\eta(298\ \text{K}, 0.1\ \text{MPa}) = 0.55\ \text{mPa}\cdot\text{s}\}$ and JS14000 $\{\eta(298\ \text{K}, 0.1\ \text{MPa}) = 7080\ \text{mPa}\cdot\text{s}\}$ and their fitting curves obtained by solving the inverse problem. Wavelengths of the capillary wave were set to 52.0 μm for methylbenzene and 61.0 μm for JS14000. The detected signals are remarkably different from each other, but they agree well with their fitting curves. In this calculation, the values of thermophysical properties, such as density, were taken from the literature, and the uncertainty of the thermophysical properties contributes to the uncertainty of the calculated viscosity.[95] In the case of methylbenzene, the relative standard deviation for 10 viscosity measurements was about ±1 % in the analysis of signals after 16 times averaging. Figure 2.11 shows the measured viscosity of each of these pure liquids *versus* their reference values.[99,100] The measured values are relatively within about ±10 % of the reference values.

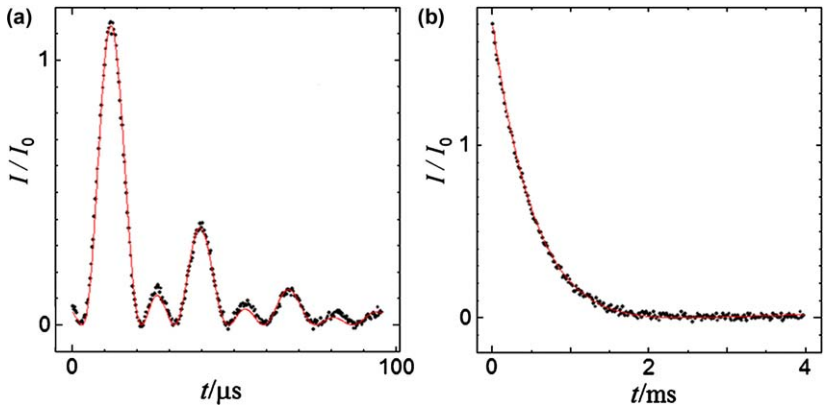

Figure 2.10 Typical examples of detected signals intensity ratio I/I_0 where I_0 is a baseline intensity for (a) methylbenzene with $\Lambda = 52.0$ μm and (b) the Japanese standard reference fluid for viscosity JS14000 ($\Lambda = 61.0$ μm). ●, measured value; ——, fit.

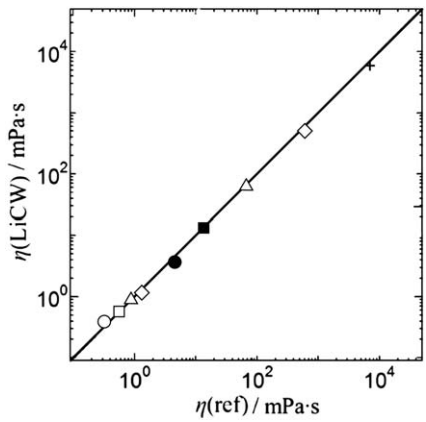

Figure 2.11 Viscosity of nine Newtonian liquids obtained with the laser-induced capillary wave technique (LiCW) η(LiCW) compared with the reference values η(ref) at $T = 298$ K. ○, propanone; □, methylbenzene; △, water; ◇, ethanol; ●, hexa-1-ol; ■, ethane-1,2-diol; ▲, Japanese certified reference fluid for viscosity JS100; ◆, Japanese certified reference fluid for viscosity JS1000; and +, Japanese certified reference fluid for viscosity JS14000.

2.3.5 Applications to Milk Fermenting to Yogurt and Whole Blood

To demonstrate the applicability of LiCW to liquid food processing, the time-varying apparent viscosity of milk fermenting to yogurt has been determined. In this case, the sample was prepared by mixing commercial milk

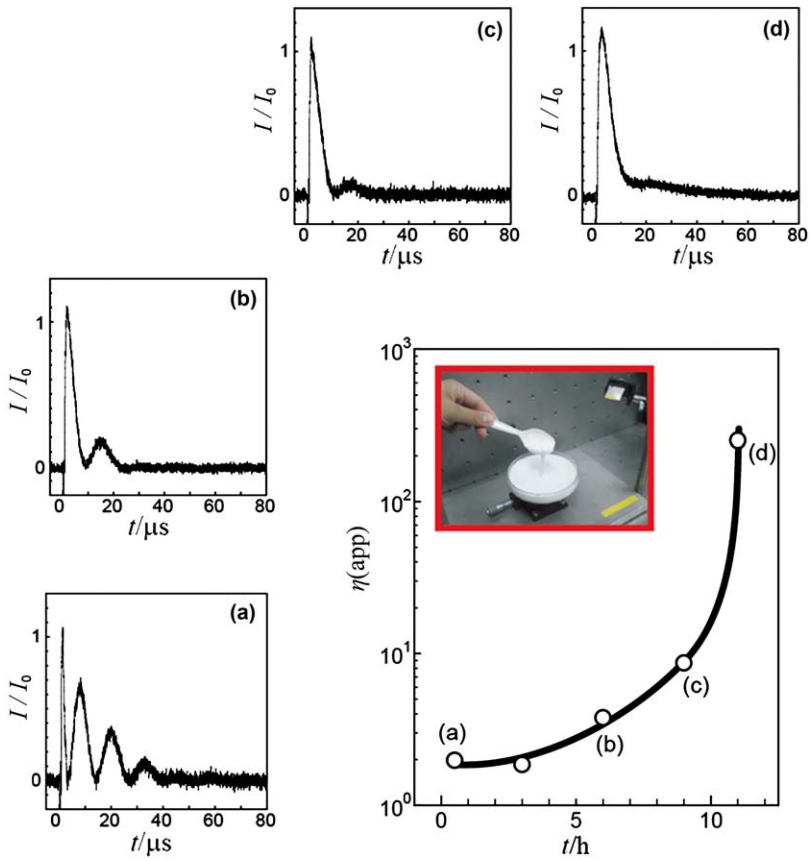

Figure 2.12 Apparent viscosity change η(app) as a function of time t for milk fermenting into yogurt. ○, measured value; ——, fit. The corresponding laser-induced capillary waveforms of intensity I/I_0, where I_0 is a baseline, are shown as a function of the measurement time for the following fermentation times: (a), 0.5 h; (b), 6 h; (c), 9 h; and (d), 11 h.

with a starter culture in a petri dish; the mixture was equivalent to the ratio of 10 cm^3 of milk combined with 1 cm^3 of culture. Fermentation was conducted at $T = 298$ K for a time of 11 h. The apparent viscosities obtained (0.5, 6, 9 and 11) h after commencement of fermentation are illustrated in panel (a) through (d), respectively of Figure 2.12. As Figure 2.12 shows, the viscosity increased more than a factor of 100 during the fermentation. In the calculation used to determine viscosity, it was assumed that the fluids were Newtonian, although yogurt is generally considered to be a non-Newtonian liquid classified as a pseudo-plastic. The shear rate of the sample in the LiCW method seems to depend on the power of the heating laser. In this particular experiment, the power was kept constant. Therefore, the measured values in this experiment are an apparent viscosity under a certain fixed shear rate. The maximum absolute value of the shear rate was estimated to

be about 10^3 s^{-1} because the capillary wave oscillates at high frequency. Our results lead to the conclusion that the laser-induced capillary wave technique can potentially be used to measure the viscosity of liquid foods during their production *in situ*.

To measure the viscosity of whole blood, we have developed a laser-induced capillary wave technique with a pulsed YAG laser as a heating source. This experiment requires a blood volume on the order of microlitres. To demonstrate the feasibility of this approach, the viscosity of human whole blood, which was taken from two healthy donors having different hematocrit, was measured with the laser-induced capillary wave viscometer. The sample volume was 90 μL at a temperature of 310 K.[101] The volume heating laser-induced capillary wave theory for this weakly absorbing wavelength laser (1064 nm) was also developed.[102]

2.4 Near-critical Light-scattering Techniques

JOCHEN WINKELMANN

2.4.1 Introduction

Dynamic light scattering (DLS) has proven to be a powerful technique for studying the transport behaviour in liquid mixtures both in the vicinity of a critical point and also far from it. When studying the transport processes in a liquid mixture caused by the motion of solute molecules we have to monitor the real-time fluctuations in terms of the intensity-time correlation function $G^{(2)}(\tau)$ of the scattered light. These measurements provide information about hydrodynamic transport properties of solutes, such as diffusion coefficients.

In DLS experiments we obtain the time-dependent intensity autocorrelation function ACF as a superposition of waves scattered from individual scattering centres. The intensity ACF, normalized to the average intensity of the signal, has the form[103]

$$G(q,t) = 1 + \beta_0 S(q,t)^2, \tag{2.17}$$

where β_0 is a constant and S denotes the dynamic structure factor. In pure fluids, contributions to the ACF may result from entropy fluctuations, whereas in liquid mixtures there are additional contributions due to concentration fluctuations. Thus, after normalization of the intensity, the ACF becomes a sum of two or even more exponential terms[103]

$$G^{(2)}(\tau) = 1 + \{I_S \exp(-\tau/\tau_T) + I_C \exp(-\tau/\tau_c) + ..\}^2 \tag{2.18}$$

where the I_S and I_C are the intensities due to scattering caused by entropy and concentration fluctuations, respectively. From eqn (2.18) we can extract both the contribution from thermal diffusivity and the mass diffusion coefficients D by extrapolation to zero wave vector **q** with the following:

$$a = \lim_{q\to 0}\left(1/q^2\tau_T\right) \quad \text{and} \quad D = \lim_{q\to 0}\left(1/q^2\tau_C\right). \tag{2.19}$$

Generally any diffusive process would result in an additional exponential term to eqn (2.18) with its own characteristic decay time and the corresponding transport coefficient. Usually in binary liquid mixtures the ACF shows a single exponential decay, corresponding to one transport mode which represents mass diffusion. Thus DLS provides a suitable tool for measuring binary inter-diffusion coefficients.[104]

In a theoretical approach Anisimov *et al.*[105] predicted the existence of a two-exponential decay function with two corresponding transport modes in a near-critical binary mixture. They show that a coupling can occur between these two transport modes associated with mass diffusion and heat diffusion, respectively. The authors[105] discuss in detail the conditions under which weak or strong coupling between the contributions of the effective

diffusivities D_1 and D_2 in DLS are to be expected. They found that the physical meaning of the two diffusivities D_1 and D_2 changes depending on the points on the critical locus that were considered. Contrary to the case of the infinite-dilution limit, they found that for a liquid–liquid consolute point the slow mode D_1 is associated with mass diffusion and the fast D_2 with heat diffusion. Fröba *et al.*[7] determined diffusion modes from DLS-measurements. For an equimolar mixture (methane + ethane) they verified the theoretical predictions of Anisimov *et al.*[105] by a simultaneous determination and separation of mass diffusion from the heat diffusion mode.

In ternary liquid mixtures all classical methods of Fick's diffusion coefficient determination, like Taylor dispersion or interferometry,[1] require macroscopic concentration gradients and the macroscopic mass transport results in a 2×2 matrix of Fick's diffusion coefficients D_{ij}. As a consequence the classical experiments in ternary systems provide us with two eigenvalues of diffusive mass transport.[1] Previous DLS studies on mixtures (phenylamine + cyclohexane + 1,4-dimethylbenzene)[106] and (dimethylformamide + methylbenzene + heptane)[107] in the near-critical region around a critical solution point revealed only one diffusive mode in the ACF. As expected, the resulting mass diffusion coefficient D showed a critical ''slowing down'' when approaching the liquid–liquid critical solution temperature.

Leaist and Hao[108] give a comparison of their Taylor dispersion and DLS measurements in a ternary sodium dodecyl sulfate salt solution. They formally extended the theory of Mountain and Deutch[109] to ternary mixtures, introducing two eigenvalues of mass diffusion. But they admit that there is no way to further resolve these expressions. In the limiting cases of a diffusing macroparticle in solution only one diffusive transport mode would result, that is, due to the large difference in size only the scatter of the micelles could be observed. To resolve these discrepancies, systematic studies, both theoretical and experimental, have to be performed in suitable ternary liquid mixtures.

2.4.2 Experimental Methods and Results

In our study on the transport behaviour in ternary mixtures with liquid–liquid phase separation we choose systems, composed of molecules of similar size, in the vicinity of their critical solution points. We want to compare results both from classical diffusion coefficient measurements using Taylor dispersion with those from DLS in order to identify the physical nature of transport modes found in DLS. DLS measurements were performed in the ternary mixtures (propane-1,2,3-triol + propanone + water) (GAW) and (cyclohexane + methanol + methylbenzene) (CMT), starting from the vicinity of the liquid–liquid critical solution point and going into the homogeneous phase as far away from critical singularity as the decreasing intensity allowed, using the same concentration path as for the classical Taylor dispersion.

All light scattering measurements are carried out in a commercial apparatus ALV/DLS-5000 with an ALV-5000/Fast correlator and modified fiber-optics detection, described in ref. 16, as shown in Figure 2.13.

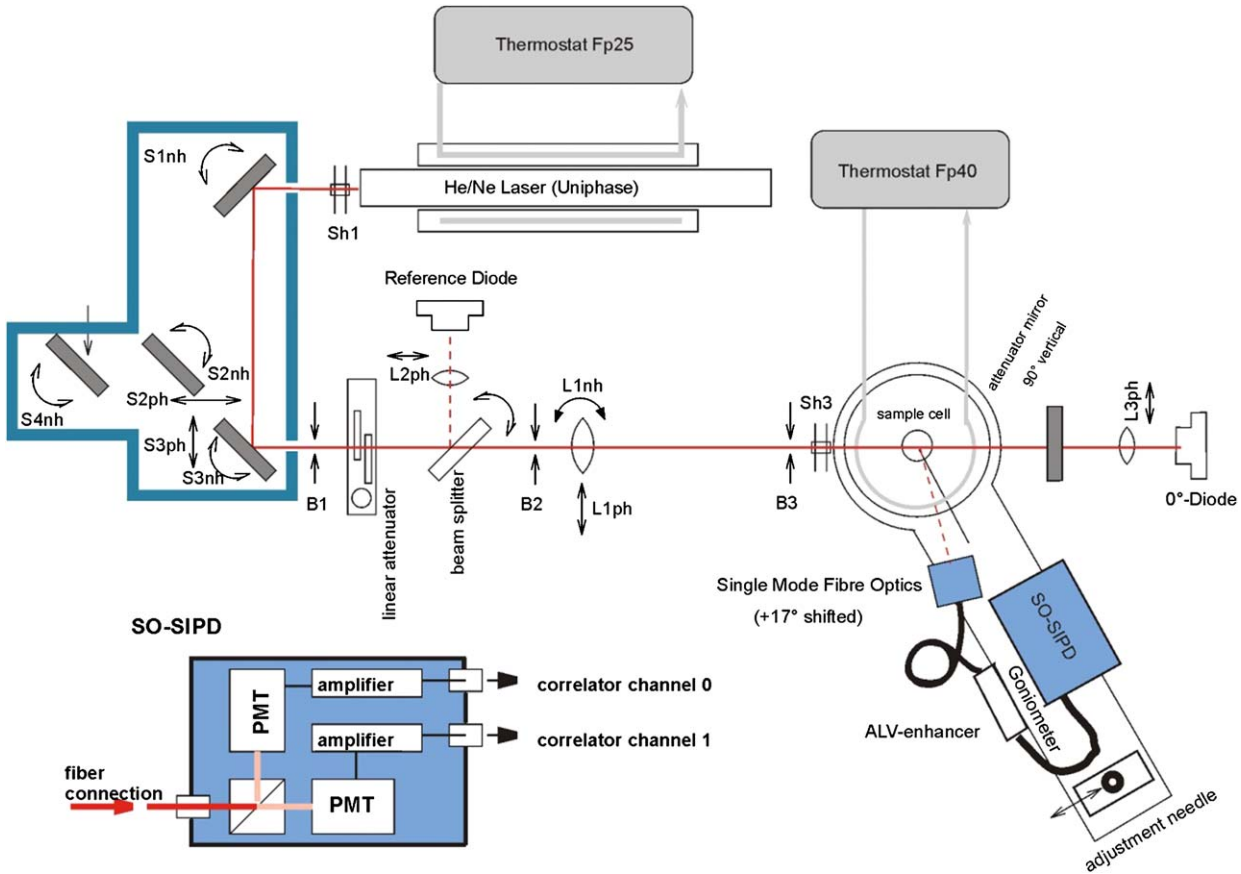

Figure 2.13 Light scattering apparatus and single-mode fiber optics recording system.

The sample cell was kept at constant temperature controlled by a PT-100 thermometer with an uncertainty of ± 0.2 mK. The room temperature was constant at 298 K during all measurements. In order to improve the quality of the signals and the signal-to-noise ratio, a special single-mode fiber optics in connection with a SO-SIPD cross-correlation detector was used. The ACF is measured with a fast photon-cross-correlator that enabled us to obtain decay times down to 12.5 ns for dynamic analysis of the scattered light.[16]

In our DLS-experiments the measured ACF's were evaluated for multiple effective relaxation times in a two-step procedure, similar to that reported by Will and Leipertz.[6,110] The corresponding transport coefficients were obtained from a linear plot of the line width as a function of q^2 and extrapolation according to eqn (2.19), as described in detail in ref. 16.

The resulting 3D plot of the ACF $G^{(2)}$-1 for the critical composition in the GAW system *versus* experimental lag time and reduced temperature $T_R = T - T_c$ is shown in Figure 2.14. It clearly reveals at least two different modes, well separated in time and with a strong temperature dependence. Far from the critical point we find double-exponential decay, while approaching T_c the slow process begins to disappear. According to Anisimov's theory[105] the slow mode corresponds to mass diffusion with critical slowing down, whereas the faster mode corresponds to thermal diffusivity. A plot of the resulting D and a *versus* reduced temperature is shown in Figure 2.15. We observe a

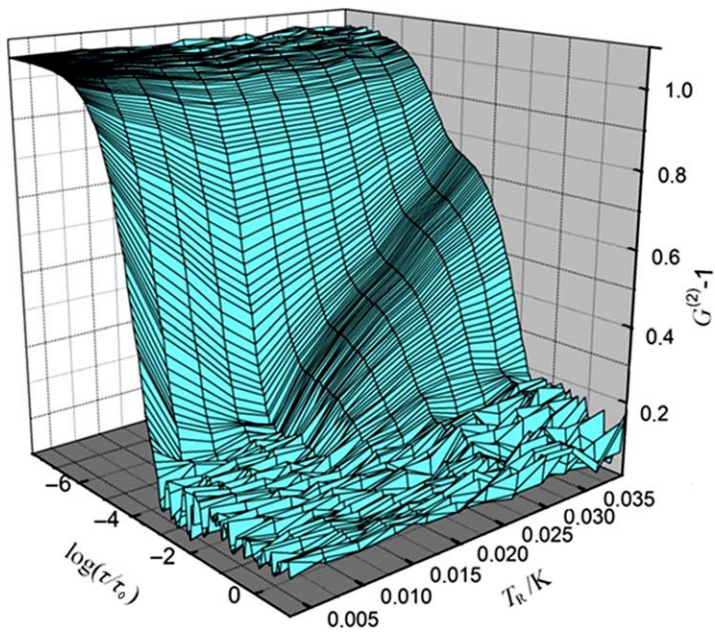

Figure 2.14 3-D plot of the ACF $G^{(2)}$-1 as a function of reduced temperature T_R and lag time ratio τ/τ_0 where $\tau_0 = 1$ μs in the near-critical region of the GAW-system.

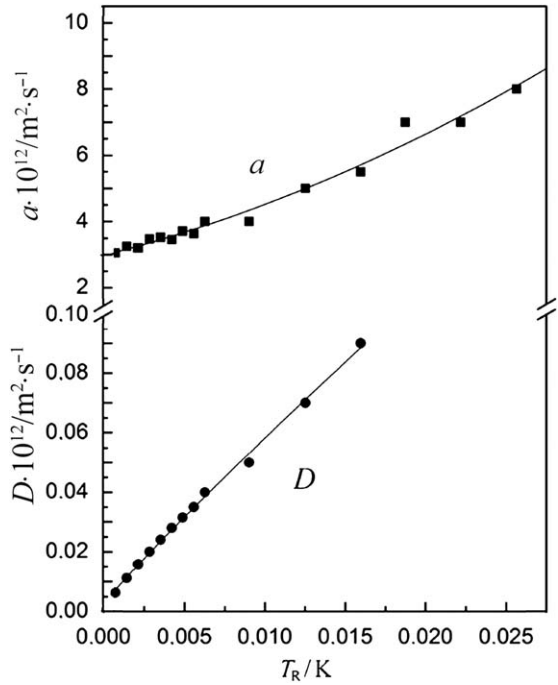

Figure 2.15 The slow mass diffusion mode D and the faster thermal diffusivity a, which are well separated and extracted from the ACF for the GAW-system, are shown as a function of the reduced temperature T_R.

completely different behaviour of both diffusivities. The D has a steep descent towards the critical temperature whereas the a slightly decreases towards a finite value at T_c. This behaviour is very similar to the results found in the binary mixture (methane + ethane).[7] It demonstrates that we did not find two modes of mass diffusion in a ternary mixture. To prove this result we performed similar measurements on a critical composition in the ternary CMT-system. A 3D-plot of the ACF *versus* reduced temperature in the range $0.8 \leq T_R \leq 2.50$ reveals a behaviour very similar to that of the GAW-system with two clearly separated transport modes, even at larger temperature differences from the critical temperature. A plot of the resulting D and a versus reduced temperature is shown in Figure 2.16.

2.4.3 Theoretical Interpretation

2.4.3.1 Systems at Concentrations Far From the Critical Range

Based on thermodynamic fluctuation theory, Bardow[111] derived expressions for the DLS-spectrum of a ternary mixture of relatively low molar mass. His approach assumed that outside the critical region the cross-coupling between mass and heat diffusion can be neglected. Thus, when calculating the

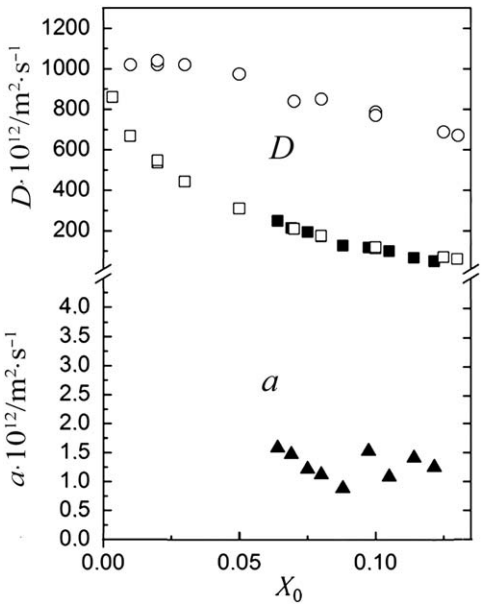

Figure 2.16 Comparison of the eigenvalues of Fick's diffusion coefficient matrix for the GAW-system *versus* mole fraction of glycerol with diffusion modes from DLS-measurements. □ and ○ represent the eigenvalues of Fick's matrix, while ■ is the slow mass diffusion mode *D* from DLS and ▲ the fast thermal diffusivity *a*.

probability distribution for fluctuations, the temperature fluctuations can be decoupled analogously to the binary case. The concentration fluctuations that are related to the **G**-matrix of concentration derivatives of the chemical potentials will be decoupled by diagonalization of **G** using the eigendecomposition **P** of Fick's diffusion matrix.[111] Finally Bardow obtained expressions for the diagonal elements $\hat{G}_1$, $\hat{G}_2$ and for the mean-square fluctuations that give the prefactors of the scattering modes. Thus the scattering intensity is proportional to $1/\hat{G}_i$. He obtained the DLS-spectrum with two Lorentzian peaks from mass diffusion modes and one peak from thermal diffusion. To analyze experimental DLS-results he calculated the prefactors $\hat{G}_1$, $\hat{G}_2$ for our experimental data of the near-critical GAW-system. The ratio G_1/G_2 is about 10^2 to 10^3, that is, the slower mode scatters much more strongly than the faster mode, which due to the square-law detector contributes less than 1 % to the spectrum and cannot be resolved. In order to obtain a ratio $G_1/G_2 \approx 1$, DLS-measurements must be performed far away from the critical region. However strong overall scattering intensities are found only close to the critical region. Thus, the DLS-signal is expected to be very weak for concentrations where both mass diffusion modes are of equal strength.[111]

2.4.3.2 Systems in the Near-critical Range

In the case of ternary liquid mixtures in the near-critical range, Ivanov and Winkelmann[112] extended the theory of Mountain and Deutch[109] and took

the coupling between temperature and concentration fluctuations into account. Considering the typical conditions of a DLS-experiment we found appropriate roots of a general solution that describe the width of the Rayleigh component of scattered light. This leads to a final expression for the dynamic structure factor[112,113]

$$S(q,t) = A_1 \exp[-z_1 t] + 2A_2 \exp\left[-z_{2,3} t\right]. \tag{2.20}$$

In their theoretical approach Anisimov *et al.*[105,114–116] show that in the asymptotic vicinity of the critical point the mass diffusion coefficients reduce to

$$D_{ii} = \frac{kT_c}{6\pi\eta_s\xi}, \tag{2.21}$$

and vanish at T_c as ξ^{-1}, where ξ is the correlation length. Mixtures near a critical liquid–liquid consolute point are weakly compressible. Therefore, the thermal diffusivity a tends towards a finite value[113]

$$a = D_0\theta_d x_{c1}x_{c2}(1 - x_{c1} - x_{c2})\, k_T^0 \tag{2.22}$$

where

$$k_T = x_{c1}x_{c2}(1 - x_{c1} - x_{c2})k_T^0\left(\frac{\xi}{\xi_0}\right).$$

In eqn 2.22, the parameter θ_d relates the diffusion coefficient D_{ij} far away from the critical point to $D_{ij,0}$, and x_c is the critical mole fraction. The thermal diffusion ratio k_T diverges as the correlation length.[105,112] We find two different modes, associated with thermal diffusion (faster mode) and mass diffusion (slower mode). These modes are defined by coefficients z_1 and $z_{2,3}$ in eqn (2.20)

$$\begin{aligned} z_1 \quad &\rightarrow \quad D_1 = a = \frac{\lambda}{\rho_i c_P} \\ z_{2,3} \quad &\rightarrow \quad D_2 = D_{11,22} = \frac{k_B T}{6\pi\eta_S\xi} \end{aligned}, \tag{2.23}$$

with $D_2 \ll D_1$ *as* $(T - T_c) \rightarrow 0$. In eqn (2.23) λ is the thermal conductivity. It follows that in the close vicinity of the critical point only the fast mode with $z_1 = a$ and A_1 survives, as found in our experiments and shown in Figure 2.14.

2.4.4 Comparison of DLS-results with Taylor Dispersion Measurements

In the framework of Fick's diffusion matrix for a ternary mixture, where there are 4 diffusion coefficients and two eigenvalues, the physical meaning of the mass diffusion mode D, obtained by DLS, is still an open question. To identify the D mode we performed Taylor-dispersion measurements in an overlapping range of concentration.[117,118] When comparing the D with the

Taylor dispersion results we found that there is a striking agreement between the eigenvalue D_1 of Fick's matrix and the D, as shown in Figure 2.16. Thus, for the GAW-system we conclude that the D mode is identical with the lower eigenvalue D_2. Since in the CMT-system[113,119] a very similar behaviour of the ACF was observed with two modes a and D we conjecture that this might be a general behaviour of ternary low-molecular-weight liquid–liquid mixtures in the near-critical range. In order to prove this assumption, more systematic experimental work is needed, both by DLS and by classical methods.

2.5 Soret Coefficients of Binary Mixtures

SIMONE WIEGAND

2.5.1 Introduction

Thermal diffusion or the Ludwig–Soret effect in a liquid mixture describes the movement of molecules due to the inhomogeneity of the temperature distribution. The origin of this effect is one of the unsolved puzzles in physical chemistry. In an isotropic binary fluid mixture with a non-uniform concentration and temperature distribution the mass flux is given by

$$\mathbf{j} = -\rho(D\nabla c + c(1-c)D_{\mathrm{T}}\nabla T). \tag{2.24}$$

In the stationary state, the mass fluxes induced by the temperature gradient and the concentration gradient cancel each other out. The ratio of the concentration gradient ∇c and temperature gradient ∇T that comply with such a stationary state is characterized by the Soret coefficient S_{T}, which is defined as $S_{\mathrm{T}} = D_{\mathrm{T}}/D$, where D_{T}[††] is the thermal diffusion coefficient and D is the mass diffusion coefficient.

2.5.2 Experimental Methods

Not long ago the optical techniques to study the thermal diffusion behavior were summarized,[120] so we will concentrate on the very recent developments and the improvement of the various techniques. We will also limit the overview to methods that are especially suitable for simple low molar mass mixtures, which excludes therefore the very sensitive fluorescent microscopy methods used in biotechnology.[121] The underlying principle of all optical methods considered here is that the refractive index in the mixture changes in the applied temperature and resulting concentration gradient. Therefore, all experimental methods are limited to binary mixtures unless two wavelengths are used, as discussed in Section 2.6. Additionally, the analysis requires the independent precise determination of the refractive index gradients with temperature and concentration,[122,123] which will not be discussed here in detail.

2.5.2.1 Thermal Gratings and Thermal Lens Methods

Since the developments of Köhler[124–126] in the nineties, thermal diffusion forced Rayleigh scattering (TDFRS) has established itself as one of the methods to investigate thermal diffusion in liquid mixtures, and also in polymer solutions[120,126,127] and colloidal suspensions.[128] Furthermore, the method has also been validated in a benchmark.[129] The basic principle of the TDFRS technique (which has some similarities to the LiCW technique discussed in Section 2.3) is

[††]The IUPAC *Green Book* recommends the symbol D_{T} for the thermal diffusion coefficient, however, for the sake of consistency with previous publications (ref. 124) concerning the topic of this chapter D_{T} will be used in this chapter.

that an interference grating due to the intersection of two laser beams (writing beams) is created in the sample cell, which is converted, owing to absorption of the laser light, into a temperature grating. In the classical TDFRS a sufficient absorption of the laser light attained is reached by adding an inert dye,[126,130] which should not show photo-bleaching. Recently an IR-TDFRS set-up has been presented using an infrared laser as the writing laser in a wavelength range where water shows a weak absorption band. With this set-up, reliable measurements of aqueous mixtures with complex phase behavior such as micellar solutions and micro emulsions are possible.[131,132] Especially in those systems, the added dye can cause changes in the phase behavior and can also lead to other artifacts in the thermal diffusion.[133] Note that the physical principle of TDFRS and IR-TDFRS is the same. In the TDFRS a dye converts the light energy into heat, while in the IR-TDFRS the naturally occurring light absorption of the sample is sufficient to produce the temperature gradient.

Figure 2.17 shows as an example of a TDFRS set-up, with an infrared writing laser ($\lambda_w = 980$ nm), as it is used for aqueous systems.[134] The writing laser beam is split into two beams of approximately equal intensity that interfere in the sample cell to create an intensity grating. The light is absorbed by the fluid mixture and this leads rapidly $\{\approx(50 \text{ to } 100)\ \mu s\}$ to a refractive index grating due to temperature modulation. The latter causes slowly $\{\approx(0.015 \text{ to } 15)\ s\}$ a concentration grating by the effect of thermal diffusion. Both temperature and concentration gratings contribute to a combined refractive index grating, which are probed by an additional readout laser, in this case by a He-Ne laser ($\lambda_r = 633$ nm) as schematically illustrated in Figure 2.17b. Note that the read-out laser beam needs to fulfill the Bragg condition in respect to the generated grating. The switching of the grating is accomplished by rotating the polarization of one of the two writing beams by means of a Pockels cell or an electrical modulator.[135] Note that in this way transient heating effects are avoided, which would occur if one beam is chopped. One of the beams is reflected by a mirror mounted on a piezo attenuator, which is used for phase shift and stabilization to obtain the heterodyne signal.[125] Figure 2.17b illustrates schematically the interference grating generated by the two writing beams and the probing of the grating by the read-out beam. The fringe spacing $d = 2\pi/q$ (Figure 2.17b) is determined by the magnitude of the scattering vector $q = 4\pi/\lambda_w \sin(\theta/2)$ and can be varied by changing the scattering angle θ between the two writing beams. In order to suppress convection, the cell thickness is typically between (100 and 200) μm. The mirror M1 (Figure 2.17a) is partially transparent so that the fringe spacing d can be directly measured with a CCD camera.

The heterodyne diffraction intensity $\zeta_{het}(t)$ for a simple step-excitation after normalization to the thermal signal is given by:

$$\zeta_{het}(t) = 1 - e^{-t/\tau_{th}} - \left(\frac{\partial n}{\partial c}\right)_{p,T}\left(\frac{\partial n}{\partial T}\right)_{p,c}^{-1} S_T c(1-c) \times \left[\tau\left(1 - e^{-t/\tau}\right) - \tau_{th}\left(1 - e^{-t/\tau_{th}}\right)\right]. \quad (2.25)$$

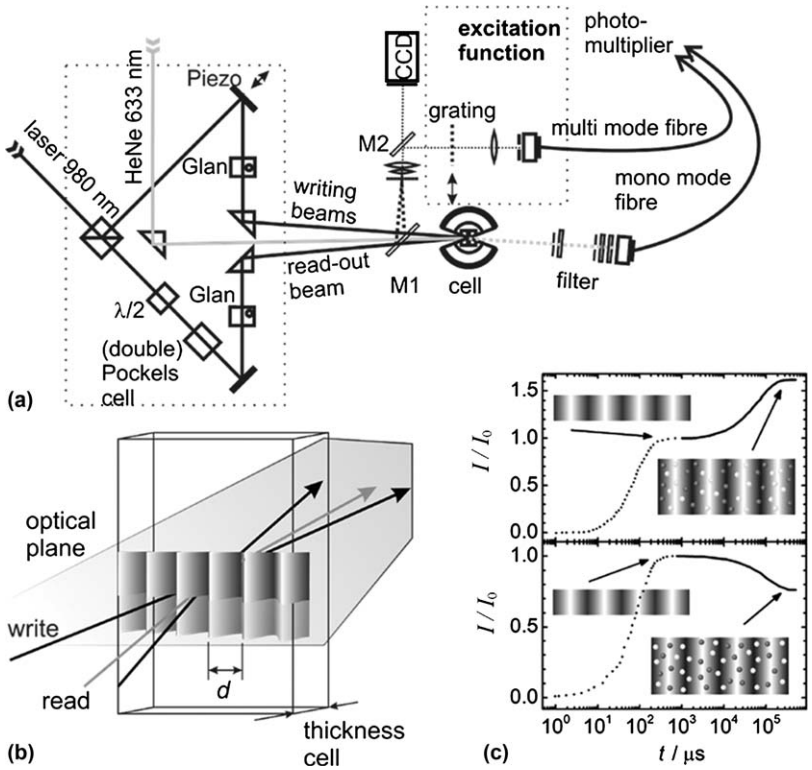

Figure 2.17 (a) Sketch of a TDFRS set-up, (b) illustration of the measurement principle and (c) two typical intensity measurements I/I_0 where I_0 is the baseline with both increasing and decreasing refractive indices due to the initiated mass diffusion caused by thermal diffusion. The images should illustrate schematically the refractive index profile in the thermal plateau and changes due to the mass diffusion in the concentration plateau.

The equilibration time for the temperature $\tau_{th} = (aq^2)^{-1}$ determines the thermal diffusivity $a = k/(\rho c_p)$ (the symbol D_{th} is also used in the literature for thermal diffusivity) expressed by the thermal heat conductivity k, the density ρ and the specific heat capacity, c_p. In the same way, the time constant $\tau = (Dq^2)^{-1}$ of the concentration signal determines the collective diffusion coefficient, D. The refractive index increments with concentration $(\partial n/\partial c)_{p,T}$ and temperature $(\partial n/\partial T)_{p,c}$ need to be determined independently using a refractometer or interferometer[122] in order to derive the Soret coefficient S_T. Note that eqn (2.25) assumes a step-excitation so that a numerical correction algorithm based on linear response theory is used to compensate for finite switching times of the grating.[122] The algorithm requires the additional measurement of the excitation function, which can be done in parallel utilizing a second partially transparent mirror M2 (Figure 2.17a). Figure 2.17c shows an example of the normalized heterodyne diffraction intensity of the

read-out laser as function of time for an aqueous solution of a non-ionic sugar surfactant octyl D-glucopyranoside[‡‡] of mass fraction 0.0069 at temperatures of (318 and 293) K. Both measurements show a fast increase of the intensity at short times, which results in the thermal plateau at a couple of hundred microseconds. At the higher temperature (top Figure 2.17c) the heterodyne diffraction intensity increases further once the thermal plateau is reached, indicating that the grating contrast increases further due to the mass diffusion of the component with the higher refractive index (here the sugar surfactant micelles) to the cold. At the lower temperature (bottom Figure 2.17c) the component with higher refractive index accumulates in the warm region so that the refractive index contrast of the grating gets weaker.

Owing to the small fringe spacing of several micrometres, the equilibration times are between (10 and 20) ms for simple binary mixtures, but even for systems with slow diffusion, such as colloidal suspensions, polymer solutions and microemulsions, the typical times are still short between (10 and 30) s. Relative concentrations of the order of $\delta c/c \approx 10^{-5}$ can be detected, which makes the TDFRS method a reliable and sensitive method to investigate the thermal diffusion behavior of binary liquid mixtures.

As schematically illustrated in Figure 2.18a, in a thermal lens (TL) experiment a focused laser beam causes local heating in a sample, which leads to the formation of a thermal lens in the mixture (local refractive index change due to temperature variations) and then to a Soret lens (local refractive index change due to concentration variations). In some of the experiments[136] a small amount of dye is added to achieve a sufficient heating by the laser beam, others use, as in the case of the IR-TDFRS, a weak absorption band of water in the infrared.[137,138] Recently, Cabrera *et al.*[139] published a TL set-up, where two lasers are used, one for writing the thermal lens and another one acting as the detector. This improves the measurement signal. Assuming a Gaussian laser beam the time dependence of the intensity in a thermal lens experiment is given by:[140,141]

$$I(t) = I(0)\left[1 + \frac{\theta_{\text{th}}}{1 + t_c/t} + \frac{\theta_{\text{Soret}}}{1 + t_c^{\text{Soret}}/t} + 0.5\left(\frac{\theta_{\text{th}}}{1 + t_c/t} + \frac{\theta_{\text{Soret}}}{1 + t_c^{\text{Soret}}/t}\right)^2\right]^{-1}, \tag{2.26}$$

with the strengths of the thermal and Soret lens given by

$$\begin{aligned} \theta_{\text{th}} &= -\frac{0.52Pbl}{k\lambda}\frac{\partial n}{\partial T}, \\ \theta_{\text{Soret}} &= -\frac{0.52Pbl\,S_T c(1-c)}{k\lambda}\frac{\partial n}{\partial T}, \end{aligned} \tag{2.27}$$

[‡‡]IUPAC systematic name is (2R,3S,4S,5R,6R)-2-(hydroxymethyl)-6-octoxyoxane-3,4,5-triol

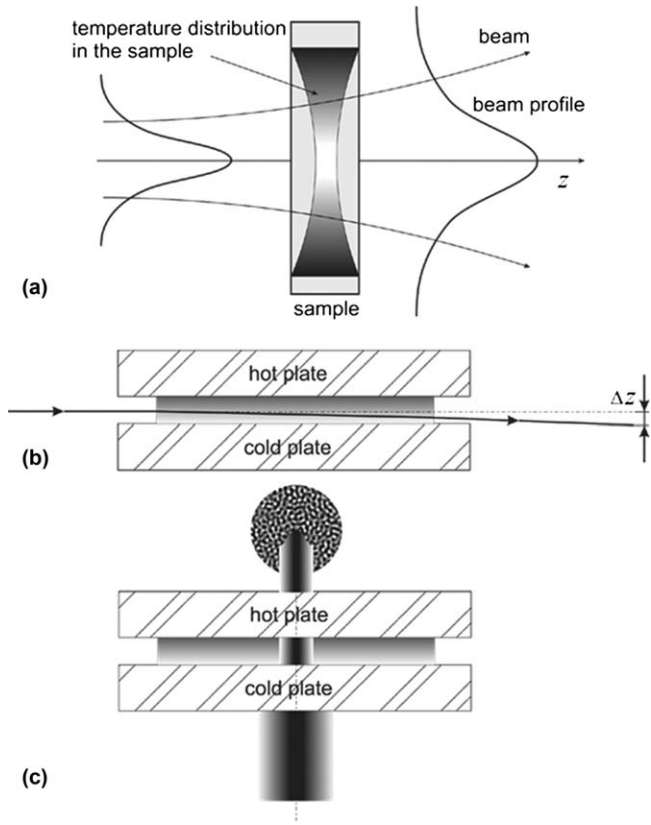

Figure 2.18 Schematic of the apparatus. (a) Principle of the thermal lens experiment in the z direction; (b) thermal diffusion cell with beam deflection and (c) with near-field scattering detection.

and the time constants $t_c = \omega^2/(4a)$ and $t_c^{\text{Soret}} = \omega^2/(4D)$. In eqn (2.27), k is the thermal conductivity and λ the wavelength. The numerical factor of 0.52 is introduced when the classical parabolic model gets extended.[141] Additional parameters are the laser power P, the absorption coefficient b, and the cell thickness l. Another way to analyze the data is by calculating the relative intensity change $(I_0 - I_\infty)/I_\infty$ at time $t = 0$ and $t = \infty$ at different positions. The final expression of this so-called z-scan method can be derived from eqn (2.26). Both approaches can be found in the literature[138,142] and they should give identical results.

The thermal lens method is a fairly fast and inexpensive method. One problem can be convection, which makes it impossible to measure very slow diffusing particles, because in those cases convection sets in before the stationary state is reached.[138] Another problem is the optical distortion of the probing beam, which is often the same as the beam to create the thermal lens. Especially in the case of a weak Soret effect, the concentration part

cannot be analyzed. Although the method has not been validated in a benchmark, the obtained data for aqueous[139,143] and non-aqueous systems agree[137] with TDFRS results.

2.5.2.2 Thermal Diffusion Cells

In conventional thermal diffusion cells, the mixture is placed between a heated top and a cooled bottom plate and the concentration changes induced by the temperature gradient can be probed by the deflection of a laser beam,[144,145] which traverses the sample parallel to the plates (as shown in Figure 2.18b). In recent years, a micrometre scale apparatus[146] has also been developed as well as a two-colour version,[147] which utilizes the dispersion of two laser beams to investigate ternary mixtures and will be discussed in detail in Section 2.6. Alternatively the dynamic of near field scattering of non-equilibrium fluctuations can be probed utilizing a transmitting beam parallel to the temperature gradient[148] (Figure 2.18c).

In the classical beam deflection experiment the time dependence of the vertical beam position $\Delta z(t)$ of the traversing beam on a detector at a distance L from the sample cell is recorded. The Soret coefficient S_T and the mass diffusion constant $\tau = h^2/\pi^2 D$ can be determined from the following working equation[145]:

$$\Delta z(t) = l \cdot L \frac{\Delta T}{h} \left[\left(\frac{\partial n}{\partial T} \right)_{p,c} - S_T c(1-c) \left(\frac{\partial n}{\partial c} \right)_{p,T} \cdot \left(1 - \frac{4}{\pi} e^{-t/\tau} \right) \right], \qquad (2.28)$$

with the liquid path l and the cell height h. Alternatively an iterative procedure can be used, as described by Königer *et al.*,[144] which includes the temperature fluctuations of the warm and the cold plate. Using the beam deflection method the benchmark values could be reproduced.[144]

Alternatively, based on theory for non-equilibrium fluctuation,[149] the scattering intensities in the thermal diffusion cell can be analyzed to determine diffusion and Soret coefficients. Note that in this case the probing beam is parallel to the temperature gradient and the intensity of the transmitted beam in the far field or near field is analyzed. The determined diffusion coefficients measured in the far as well as near field configuration agree typically well with other methods,[148,150] while the Soret coefficient deviated relatively by 25 % in the far field geometry. In the near-field experiment the scattering intensity is recorded at different times and scattering vectors. Note rather small wave vectors need to be accessed, so that the amplitude of the non-equilibrium fluctuations becomes large. By analyzing the power spectrum computed from the intensity differences at different times, the normalized intermediate scattering function can be derived. Additionally, a characteristic optical function of the used set-up needs to be determined independently.[151] The time constant $\tau(q)$ of the

normalized intermediate scattering function (often considered as a single exponential decay), is related to the diffusion coefficient as

$$\tau(q) = \frac{1}{Dq^2\left[1 + (q_c/q)^4\right]}, \tag{2.29}$$

with the critical wave vector q_c given by

$$q_c = \left[-\frac{\beta g \cdot \nabla T S_T c(1-c)}{\nu D}\right]^{1/4}. \tag{2.30}$$

In equation (2.30) $\beta = 1/\rho(\partial\rho/\partial c)$ is the expansion coefficient g the local acceleration of free fall and ν the kinematic viscosity. Note that the fluid properties are treated as constants. In a recent study, Croccolo *et al.*[148] found good agreement for the benchmark systems.

Compared to the classical beam deflection method the applied temperature differences (16 K) and the amount of data (about 24 GB) for a single experiment are substantially larger, while the experimental run times are equal, when the same cell geometry is used.

2.5.2.3 *Thermogravitational Columns with Optical Detection*

While all other methods discussed so far have to avoid convection, in the thermal gravitational column convection is needed and can enhance the concentration difference. Most thermogravitational columns work without optical detection, because the heated and cooled walls are made of non-transparent materials, *e.g.* steel or brass. Recently, a thermogravitational micro column was developed in which we used transparent sapphire windows for the walls (Figure 2.19). Sapphire has a very good thermal conductivity, so that a homogenous temperature can be achieved. Having transparent walls, we can measure the concentration difference between top and bottom interferometrically.[152] As illustrated in Figure 2.19 the upper beam is probing the top of the μ-column and the lower beam is probing the bottom of the μ-column. From the phase difference $\Delta\phi$ the thermal diffusion coefficient D_T can be determined by

$$D_T = \frac{1}{504}\frac{\alpha g}{k\nu}\frac{1}{c_0(1-c_0)}\frac{L_x^3}{L_z}\left(\frac{\partial n}{\partial c}\right)^{-1}_{p,T}\Delta\phi, \tag{2.31}$$

with the initial mass fraction concentration c_0, the kinematic viscosity ν, the thermal expansion coefficient α, the vertical distance L_z between the probing laser beams, the gap width L_x and the gravity acceleration g. Note again that the fluid properties are treated as a constant. The determined D_T values deviated relatively by about $\pm 5\,\%$ from the literature values, which is comparable with the deviations found for different methods used in the benchmark.[129] Unfortunately it was not possible to analyze the transient signal in order to obtain the diffusion coefficient. This might require a better

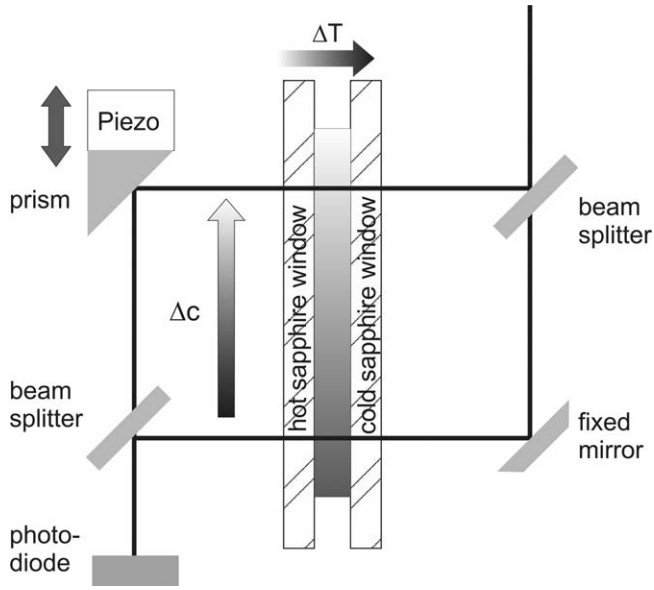

Figure 2.19 Schematic sketch of the interferometer probing the concentration difference at two different heights of the TG μ-column with a horizontal temperature gradient ΔT. The concentration difference results in a phase shift $\Delta\phi$ of the intensity signal determined by a 2π scan of the prism mounted on the piezo stack.

theoretical description incorporating the finite switching times of the gradient.

2.5.3 Conclusion

In the past years a lot of progress has been made in the development and the validation of optical methods to study the thermal diffusion behavior of liquid mixtures. Table 2.1 gives an overview on the methods discussed. It should be noted that if there are no literature values for the various auxiliary quantities indicated as necessary in the Table then additional measurements need to be made. The equilibration time refers to a low molecular mixture, such as (methylbenzene + hexane). The total measurement time might be longer due to repetitive measurements in order to reduce the signal to noise ratio as in the case of the TDFRS[153] or due to a baseline determination as in the case of the TG μ-column.[152] The sensitivity of the methods depends on the refractive index contrast and on the concentration. In the case of the TG column the effect can be enhanced due to convection. Due to the good database for non-polar and polar substances, systematic errors in the various experimental methods are easily detected. Except for the thermal lens method, which has only been successfully compared with TDFRS data, all set-ups have been validated with the benchmark systems and the relative agreement was typically in the range $\pm$(5 to 10) %.

Table 2.1 Overview of the experimental methods presented: the sample volume V covers only the volume of fluid required to fill the sample cell; the total fluid volume will depend upon the additional ancillary equipment. The operating expense covers roughly the cost of equipment and personnel, time for measurement and interpretation. The equilibration time τ_{eq} is also listed.

Method	Measured quantities	V/cm^3	τ_{eq}/s	Auxiliary quantities	Operating expense
TDFRS	S_T, D_T, D	0.06	0.03	$\left(\frac{\partial n}{\partial c}\right)_{p,T}$, $\left(\frac{\partial n}{\partial T}\right)_{p,c}$	High
Taylor dispersion beam deflection	S_T, D_T, D	0.5	1000	$\left(\frac{\partial n}{\partial c}\right)_{p,T}$, $\left(\frac{\partial n}{\partial T}\right)_{p,c}$	Low
Taylor dispersion near field scattering	S_T, D_T, D	0.7	100	$\frac{1}{\rho}\left(\frac{\partial \rho}{\partial c}\right)_{p,T}$	Moderate
Thermal lens	S_T, D_T, D	0.3	100	$\left(\frac{\partial n}{\partial c}\right)_{p,T}$, $\left(\frac{\partial n}{\partial T}\right)_{p,c}$	Low
TG μ column	D_T	0.05	1800	$\left(\frac{\partial n}{\partial c}\right)_{p,T}$	Low

2.6 Soret Coefficients of Ternary Mixtures

WERNER KÖHLER

2.6.1 Introduction

Section 2.5 has discussed the recent development of optical techniques of various kinds for the study of thermal diffusion in binary fluid systems. As well as the review of the preceding section the reader may wish to consult the detailed literature.[122,129,154–171] Since, in binary mixtures, there is only one independent concentration variable, it is sufficient to measure the change of a single concentration dependent quantity. In optical experiments it is usually the refractive index change that is sensed by a laser beam. With the exception of a few early theoretical[172] and experimental[173,174] works, the investigation of systems with more than two components has started only very recently, mainly during the last decade. This is all the more surprising since many systems where thermal diffusion is of practical importance are composed of a large number of constituents. Examples are crude oil reservoirs,[175] magmatic differentiation in the mantle of earth,[176] or scenarios for prebiotic evolution of life.[177] But also many problems that are usually treated in a binary approximation, like polymers in a mixed solvent,[178] colloids in an aqueous buffer,[179] or solutions of polydisperse polymers[180] are, strictly speaking, multicomponent systems with three or more constituents. Ternaries play a particular role when going from binary to multicomponent mixtures. They show already characteristic features of true multicomponent systems, like cross and reverse diffusion, but they are still manageable and experimentally accessible. Since there are two independent concentration variables in a ternary mixture, two ''sufficiently different'' concentration-dependent quantities must be measured in order to determine the changes of all three concentrations, as will be explained later on. In experiments with sample extraction, like thermogravitational columns, the refractive index and the density have been used,[161] whereas in optical experiments it is usually the refractive index at two different wavelengths.[147,181,182]

2.6.2 Theory

A detailed treatment of the theoretical background can be found in the textbooks of de Groot and Mazur[183] and of Haase.[184] The starting point for a phenomenological description is the linear equation for the diffusive mass flow of component i in an N-component liquid mixture of density ρ, as outlined in ref. 147:

$$\mathbf{j}_i = -\rho \left(\sum_{k=1}^{N-1} D_{ik} \nabla c_k + D'_{\mathrm{T},i} \nabla T \right) . \qquad (2.32)$$

For a ternary mixture ($N=3$, $i=1, 2$) there are two independent concentrations (mass fractions) c_i and flows $\mathbf{j}_i$. Component 3 is the dependent one:

$$c_3 = 1 - c_1 - c_2, \quad \mathbf{j}_3 = -\mathbf{j}_1 - \mathbf{j}_2. \tag{2.33}$$

The D_{ik} are the diffusion coefficients and the $D'_{T,i}$ the thermal diffusion (often also commonly named thermodiffusion) coefficients. The latter are denoted with a prime, since they are defined slightly different from the binary case, where the concentrations of the two components are usually factored out:[147,173] $D'_{T,1} = c_1 c_2 D_T$.

The Soret coefficients $S'_{T,i}$ are defined by the amplitudes of the stationary concentration gradients, where the flows vanish:

$$\nabla c_i = -S'_{T,i} \nabla T. \tag{2.34}$$

Comparison with eqn (2.32) for $\mathbf{j}_i = 0$ yields

$$S'_{T,i} = \sum_{k=1}^{N-1} (D^{-1})_{ik} D'_{T,k}. \tag{2.35}$$

$(D^{-1})_{ik}$ denotes an element of the inverse diffusion matrix. As in case of D_T, the conventional definition for binary systems, S_T, is related to $S'_{T,1}$ by $S'_{T,1} = c_1 c_2 S_T$.

The transformation to a new set of concentration variables after renumbering and/or change of the dependent concentration can be found in the appendix of ref. 147. The thermodiffusion and Soret coefficients of the dependent component are readily obtained from

$$D'_{T,3} = -D'_{T,1} - D'_{T,2} \tag{2.36}$$

and

$$S'_{T,3} = -S'_{T,1} - S'_{T,2}. \tag{2.37}$$

Combining eqn (2.32) with the mass conservation law

$$\rho \partial_t c_i = -\nabla \cdot \mathbf{j}_i, \tag{2.38}$$

eventually yields a set of coupled diffusion equations for the independent concentrations c_1 and c_2:

$$\partial_t c_i = \sum_{k=1}^{N-1} D_{ik} \nabla^2 c_k + D'_{T,i} \nabla^2 T. \tag{2.39}$$

For a description of a convection-free experiment, eqn (2.39) is augmented by the eqn

$$\partial_t T = a \nabla^2 T, \tag{2.40}$$

and the proper initial and boundary conditions for the concentrations and the temperature. a is the thermal diffusivity. The Dufour effect[185] is generally neglected in liquids and the corresponding term has been omitted in eqn (2.40).

2.6.3 Experimental Techniques

2.6.3.1 Optical Techniques – An Overview

At the present moment there are significant activities utilizing optical methods for the investigation of ternary systems. All these methods share the common principle of simultaneous detection at two wavelengths, thereby relying on the different refractive index dispersions of the constituents. Optical beam deflection (OBD) has already been equipped with two readout lasers,[147,182] and optical digital interferometry (ODI)[165,171,186] is being extended to two-color detection. It has also been suggested to equip the transient holographic grating technique TDFRS with two different readout lasers.[147] In principle, this should also be possible for thermal lensing,[138,187] but no such experiments have so far been reported in the literature.

2.6.3.2 Microgravity Experiments

Currently Soret coefficient measurements on ternary mixtures under microgravity conditions are performed aboard the International Space Station ISS within the framework of the ESA DCMIX project. These experiments are conducted with the SODI instrument and are of the ODI type with wavelengths of (670 and 935) nm.[188] The aim of the project is to provide reliable convection-free reference measurements for selected ternary systems. In the first round, DCMIX1, ternary mixtures of different compositions of the so-called Fontainebleau benchmark mixture (dodecane + isobutylbenzene[§§] + 1,2,3,4-tetrahydronaphthalene) (given the acronym nC12-IBB-THN) have been measured, but results are not yet available. The next rounds, DCMIX2 (methylbenzene + methanol + cyclohexane) and DCMIX3 (water + ethanol + 2,2′-[1,2-ethanediylbis(oxy)]diethanol), are currently under preparation and are expected to be launched in 2013 or 2014.

A few microgravity experiments have already been performed prior to DCMIX. A ternary benchmark mixture (nC12-IBB-THN) has been measured together with a quaternary system at $p = 5$ MPa aboard the FOTON-M3 spacecraft in a cell with a temperature gradient. After reaching the steady state, the two halves of the cell were separated and returned to ground for composition analysis.[160,189] The feasibility of microgravity measurements for the C12-IBB-THN system has been estimated[190] on the basis of the model of Firoozabadi.[191]

2.6.3.3 Thermogravitational Columns

Other than the optical techniques, thermogravitational columns (TG) rely on convection and can not, therefore, profit from reduced gravity. Owing to the

[§§]The IUPAC name is (2-methylprop-1yl) benzene.

decisive role of convection, the technique has limitations for systems with negative separation ratios, but there are also significant advantages. Although there are recent developments for optical *in situ* detection,[152] the traditional method is sample extraction for external composition analysis.

TGs have been used for ternary mixtures of nC12-IBB-THN,[159,161,162] nC12-IBB-THN[159] and (octane + decane + 1-methylnaphthalene) (given the acronym nC8-nC10-MN).[161] The compositions are derived from a combination of refractive index and density measurements. Density and refractive index are to a certain degree correlated, and the inversion problems are similar to the optical case, as discussed below. In principle, however, there are less restrictions and a number of alternative techniques might be envisaged for composition analysis, such as gas chromatography, mass spectrometry, optical spectroscopy, or NMR.

The TG measurements only yield the thermal diffusion coefficients $D'_{T,i}$. In order to obtain the Soret coefficients, it is necessary to measure the four values of the diffusion matrix D_{ij} separately by, *e.g.*, the sliding symmetric tube[192] or the Taylor dispersion[193] technique. In ref. 159 a good correlation with predictions from an additive rule[175] has been reported.

2.6.3.4 Optical Beam Deflection (OBD)

Two-color OBD can be regarded as a prototype technique and shall be discussed in some detail. All relevant aspects can similarly be found in the other optical methods that are based on two-color detection schemes.

Figure 2.20 shows a sketch of a two-color OBD experiment. The ternary mixture is inside a Soret cell with typical length of 10 mm, width of 5 mm and height of 1.5 mm with a vertical temperature difference of $\delta T \approx 1$ K. The experiment starts with an equilibrated sample at a constant temperature T_0 to which the temperature difference is applied. A homogeneous temperature gradient is rapidly established throughout the sample and thermal diffusion sets in. In the final steady state, thermal diffusion is balanced by Fickian diffusion.

The combined temperature and concentration gradients lead to a refractive index gradient

$$\frac{\mathrm{d}n}{\mathrm{d}z} = \left(\frac{\partial n}{\partial T}\right)_{p,c} \frac{\mathrm{d}T}{\mathrm{d}z} + \left(\frac{\partial n}{\partial c_1}\right)_{p,T,c_2} \frac{\mathrm{d}c_1}{\mathrm{d}z} + \left(\frac{\partial n}{\partial c_2}\right)_{p,T,c_1} \frac{\mathrm{d}c_2}{\mathrm{d}z}, \qquad (2.41)$$

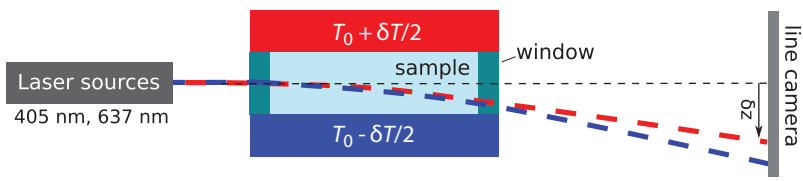

Figure 2.20 Sketch of a two-color OBD setup. A detailed description of the instrument can be found in ref. 147.

that is read out by deflection of two laser beams traversing the optical cell. The beam displacement at a distance d behind the cell, the position of the camera, is

$$\delta z = l\left\langle \frac{\mathrm{d}n}{\mathrm{d}z} \right\rangle \left(\frac{l}{2n} + \frac{l_\mathrm{w}}{n_\mathrm{w}} + \frac{l_\mathrm{d}}{n_\mathrm{air}} \right), \tag{2.42}$$

with l being the path length inside the liquid, and l_w the window thickness. n, n_w, and n_air are the refractive indices of sample, window, and air, respectively[144,147] and

$$\left\langle \frac{\mathrm{d}n}{\mathrm{d}z} \right\rangle = \int_0^d \mathrm{d}z\, I(z)\, \frac{\mathrm{d}n}{\mathrm{d}z} \left[\int_o^d \mathrm{d}z\, I(z) \right]^{-1}, \tag{2.43}$$

is the refractive index averaged over the Gaussian beam profile I(z). One set of equations is obtained for every readout wavelength, which differ by their contrast factors $(\partial n/\partial T)_{p,c}$ and $(\partial n/\partial c_k)_{p,T,c_{i\neq k}}$. The partial concentration derivatives are performed such that the independent concentration i is kept fixed while the other independent concentration k is varied at the expense of the dependent one.

The temperature and concentration fields $T(z,t)$ and $c_i(z,t)$ are obtained from eqn (2.40) and eqn (2.39). An analytic solution for the parallel plate geometry of the Soret cell with constant plate temperatures has been developed by Bierlein[194] for binary and by Leahy-Dios *et al.*[161] for ternary mixtures.

Heating and cooling of the two copper plates is accomplished either by means of circulating water[145] or Peltier elements.[144,170] In practice, perfect temperature switching without overshooting is difficult to achieve, and there are unavoidable mK fluctuations of the plate temperatures. Since these effects can hardly be taken into account in an analytic solution, the heat and diffusion equations are better integrated numerically with the measured plate temperatures as time dependent boundary conditions, as shown in Figure 2.21.

Besides a trivial amplitude factor, the fit parameters are the four diffusion coefficients D_{ik} and the two thermodiffusion coefficients $D'_{\mathrm{T},i}$, from which the Soret coefficients of the independent components can be calculated according to eqn (2.35) and the coefficients of the dependent component according to eqn (2.36) and eqn (2.37).

Two-color OBD measurements have been performed for symmetric mixtures of nC12-IBB-THN and nC8-nC10-MN.[147] The thermodiffusion coefficients have been compared to results from thermogravitational column experiments,[159,161] but there are significant deviations of unknown origin between both techniques. The problem has recently been addressed by Mialdun and Shevtsova.[195]

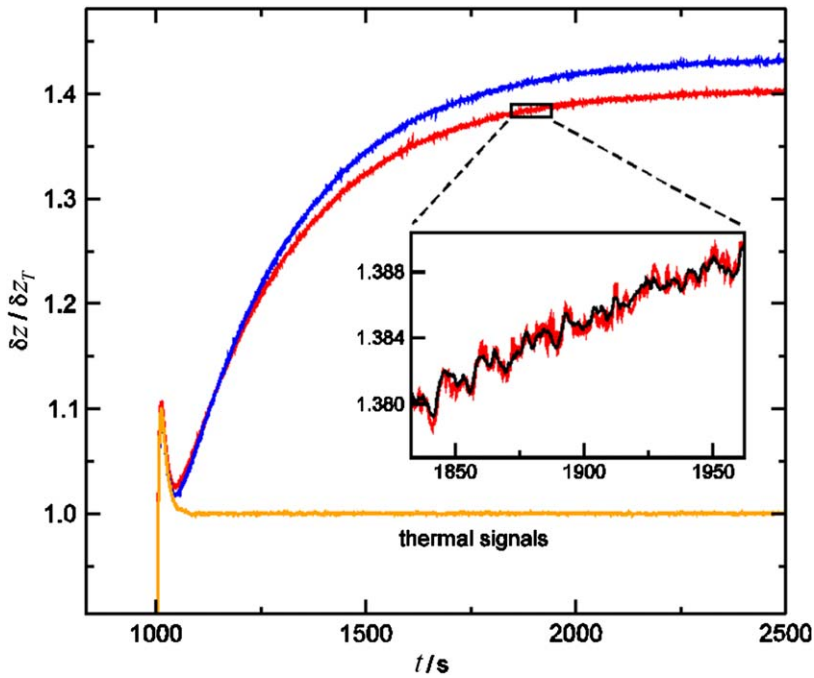

Figure 2.21 Beam deflection signals $\delta z/\delta z_T$ after normalization to the respective thermal amplitudes for a symmetric mixture of nC12-IBB-THN (nC12-IBB-THN) as a function of time t. ———, $\lambda = 405$ nm; ———, $\lambda = 637$ nm. The insert shows the measured curve (gray line) together with the fitted (black line) numerical model. The thermal signal is shown with a light gray line. The initial overshooting and even effects of tiny temperature fluctuations are perfectly reproduced.[147]
Reprinted with permission from A. Königer, H. Wunderlich and W. Köhler, *J. Chem. Phys.*, 2010, **132**, 174506. Copyright 2010, American Institute of Physics.

When compared to binary mixtures, the determination of the transport coefficients from the measured data is much more complex in the ternary case, and not all coefficients can be determined with the same accuracy from a two-color optical experiment. A complete in-depth analysis of this problem is still missing.

The Soret coefficients are encoded in the stationary amplitudes of the two signals. The rise of the signal amplitude primarily contains two time constants, which are related to the two eigenvalues of the diffusion matrix:

$$\hat{D}_{1,2} = \frac{D_{11} + D_{22} \pm \sqrt{(D_{11} - D_{22})^2 + 4D_{12}D_{21}}}{2} \tag{2.44}$$

Provided there are acceptable contrast factors, these eigenvalues and the Soret coefficients can be expected to be of reasonable accuracy. The situation is, however, less clear for the individual components of the diffusion matrix and the thermal diffusion coefficients. The latter are more directly accessible in the thermogravitational column technique. For a complete characterization, the combination of different methods will most likely be the best solution. Promising candidates for the diffusion coefficients[1] are the Taylor dispersion,[196,197] the sliding symmetric tube[192] and the open-ended capillary[161] technique.

2.6.3.5 Contrast Factors

The optical contrast factors play a decisive role, and their precise measurement is at least as important as the actual Soret experiment itself. This is best understood by recalling that the quantities of interest are the concentration changes $\boldsymbol{\delta c} = (\delta c_1, \delta c_2)$, whereas the beam deflections are caused by the refractive index changes $\boldsymbol{\delta n} = (\delta n_1, \delta n_2)$ at the two readout wavelengths λ_1 and λ_2, respectively. They are interrelated by

$$\boldsymbol{\delta n} = \mathbf{A}\,\boldsymbol{\delta c}, \tag{2.45}$$

where $\mathbf{A}$ is the 2×2 contrast factor matrix with entries

$$A_{ij} = \left(\frac{\partial n(\lambda_i)}{\partial c_j}\right)_{p,T,c_{k\neq j}}. \tag{2.46}$$

To obtain the concentration changes δc_i, the contrast matrix $\mathbf{A}$ must be inverted. Both the A_{ij} and the δn_i are measured quantities and contain errors $\varepsilon_{A_{ij}}$ and ε_{n_i}, respectively, which lead to errors ε_{c_i} of the concentrations:

$$\boldsymbol{\delta c} + \boldsymbol{\varepsilon}_{\mathbf{c}} = (\mathbf{A} + \boldsymbol{\varepsilon}_{\mathbf{A}})^{-1}(\boldsymbol{\delta n} + \boldsymbol{\varepsilon}_{\mathbf{n}}) \tag{2.47}$$

The relative error of the concentration changes can be estimated as[198,199]

$$\frac{|\boldsymbol{\varepsilon}_{\mathbf{c}}|}{|\boldsymbol{\delta c}|} \leq \mathrm{cond}(\mathbf{A}) \cdot \left[\frac{\|\boldsymbol{\varepsilon}_{\mathbf{A}}\|}{\|\mathbf{A}\|} + \frac{|\boldsymbol{\varepsilon}_{\mathbf{n}}|}{|\boldsymbol{\delta n}|}\right], \tag{2.48}$$

where $\|\mathbf{A}\|$ is the Euclidian matrix norm (largest eigenvalue of $\mathbf{A}^t\mathbf{A}$) and $\mathrm{cond}(\mathbf{A}) = \|\mathbf{A}\| \cdot \|\mathbf{A}^{-1}\|$ the condition number of matrix $\mathbf{A}$.

From eqn (2.48) it can be determined that for accurate measurements of the contrast factors and the optical signal amplitudes, the beam deflections in case of OBD, are not sufficient. Satisfactory results can only be expected for well-conditioned contrast matrices, *i.e.* $\mathrm{cond}(\mathbf{A}) \leq 100$. In practice this requirement limits the suitability of ternary mixtures for optical experiments to systems with sufficiently different refractive index dispersions. In ref. 147, wavelengths of (405 and 637) nm have been chosen to profit from the proximity of the electronic resonances of the aromatic π-electron systems in the near UV.

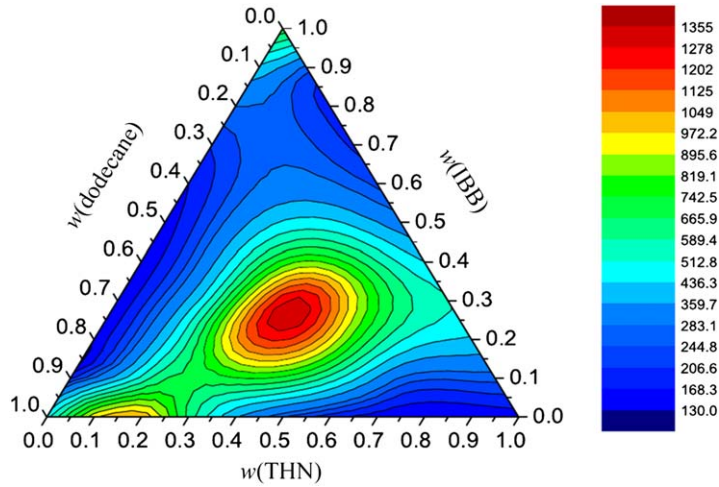

Figure 2.22 Condition number of the contrast factor matrix for nC12-IBB-THN at $\lambda_1 = 670$ nm, $\lambda_2 = 935$ nm for dodecane mass fraction c(dodecane), 2-methylprop-1-yl)benzene mass fraction c(IBB) and 1,2,3,4-tetrahydronaphthalene mass fraction c(THN).[200]
Reprinted from V. Sechenyh, J. C. Legros and V. Shevtsova, *J. Chem. Thermodyn.*, 2013, **62**, 64, with permission from Elsevier.

Figure 2.22 shows, as an example, the condition number of the contrast factor matrix of the ternary benchmark mixture THN-IBB-nC12 (with dodecane as the dependent component) for the two wavelengths of the SODI experiment aboard the ISS.[200] In particular the center near the symmetric composition is ill-conditioned and very difficult to measure.

Finally, it should be mentioned that for the thermogravitational column experiments of ref. 161, the density of the mixture instead of the refractive index at a different wavelength has been taken as the second observable. Hence, the contrast factors for these experiments are $(\partial n/\partial c_i)_{p,T,c_{k\neq i}}$ and $(\partial \rho/\partial c_i)_{p,T,c_{k\neq i}}$, with n measured at one particular wavelength.

2.6.4 Concluding Remarks

Although many fluid mixtures of practical importance contain significantly more than two components, the current state of research on ternary systems is comparable to the situation for binary mixtures a few decades ago. There are only very few investigated systems, a small number of experimental techniques, and no consistent database. Soret coefficients for mixtures with four and more components are virtually non-existent.

At present, there are two main types of experiments: thermogravitational columns and convection-free Soret cells with two-color optical detection. All these techniques have their pros and cons.

Thermogravitational columns rely on sample extraction and external composition analysis. This is more cumbersome and time consuming than *in situ* optical detection, but it also opens a route to employ sophisticated analytical tools.

The optical techniques OBD and ODI use different cell geometries and detection schemes, but the underlying concepts are, nevertheless, very similar. The ODI cell has a height of approximately ten times the one of the OBD cell and, correspondingly, hundredfold longer equilibration times and more problems to avoid the critical Rayleigh number for systems with negative separation ratios. On the other hand, digital interferometry gives access to the entire concentration profile, not merely the concentration gradient in the center.

Microgravity experiments are free of convection problems that always need careful consideration in ground based measurements. The ODI technique is presently employed for the DCMIX project aboard the ISS, but also microgravity experiments with sample taking for later analysis have already been performed.

A significant problem in all experiments on ternary and higher mixtures is the uncertainty of the chemical composition. Both for optical experiments and for thermogravitational columns the problem amounts to the inversion of a contrast or sensitivity matrix, which might be ill-conditioned. Some freedom exists for the optical techniques by choosing proper detection wavelengths, but there are clearly more choices in case of sample extraction. With the presently available *in situ* detection schemes, the extension to mixtures with more than three components appears very difficult or even impossible.

References

1. *Measurement of the Transport Properties of Fluids*, ed. W. A. Wakeham, Akira Nagashima and J. V. Sengers, Blackwell Scientific, Oxford, 1991.
2. A. P. Fröba, Dr.Sc. Thesis, Friedrich-Alexander-Universität (FAU), Erlangen-Nürnberg, 2009.
3. S. Will, A. P. Fröba and A. Leipertz, *Int. J. Thermophys.*, 1998, **19**, 403.
4. A. P. Fröba, H. Kremer, A. Leipertz, F. Flohr and C. Meurer, *Int. J. Thermophys.*, 2007, **28**, 449.
5. A. Heller, M. H. Rausch, F. Flohr, A. Leipertz and A. Fröba, P., *Int. J. Thermophys.*, 2012, **33**, 396.
6. S. Will and A. Leipertz, *Int. J. Thermophys.*, 1999, **20**, 791.
7. A. P. Fröba, S. Will and A. Leipertz, *Int. J. Thermophys.*, 2000, **21**, 603.
8. M. H. Rausch, J. Lehmann, A. Leipertz and A. P. Fröba, *Phys. Chem. Chem. Phys.*, 2011, **13**, 9525.
9. M. H. Rausch, L. Hopf, A. Heller, A. Leipertz and A. P. Fröba, *J. Phys. Chem. B*, 2013, **117**, 2429.
10. S. Will and A. Leipertz, *Int. J. Thermophys.*, 1997, **18**, 1339.
11. A. P. Fröba, S. Will and A. Leipertz, *Int. J. Thermophys.*, 2000, **21**, 1225.

12. A. P. Fröba, H. Kremer and A. Leipertz, *J. Phys. Chem. B*, 2008, **112**, 12420.
13. B. Hasse, J. Lehmann, D. Assenbaum, P. Wasserscheid, A. Leipertz and A. P. Fröba, *J. Chem. Eng. Data*, 2009, **54**, 2576.
14. T. M. Koller, M. H. Rausch, J. Ramos, P. S. Schulz, P. Wasserscheid, I. G. Economou and A. P. Fröba, *J. Phys. Chem. B*, 2013, **117**, 8512.
15. K. Kraft and A. Leipertz, *Int. J. Thermophys.*, 1995, **16**, 445.
16. D. A. Ivanov and J. Winkelmann, *Phys. Chem. Chem. Phys.*, 2004, **6**, 3490.
17. W. Schröer, S. Wiegand, M. Kleemeier and H. Weingärtner, *J. Phys.: Condens. Matter*, 1994, **6**, A157.
18. Y. Nagasaka and Y. Kobayashi, *J. Crystal Growth*, 2007, **307**, 51.
19. T. Oba, Y. Kido and Y. Nagasaka, *Int. J. Thermophys.*, 2004, **25**, 1461.
20. Y. Taguchi, A. Ebisui and Y. Nagasaka, *J. Opt. A: Pure Appl. Opt.*, 2008, **10**, 044008.
21. B. M. Law and J. C. Nieuwoudt, *Phys. Rev. A*, 1989, **40**, 3880.
22. P. N. Segrè, R. W. Gammon and J. V. Sengers, *Phys. Rev. E*, 1993, **47**, 1026.
23. W. B. Li, P. N. Segrè, R. W. Gammon and J. V. Sengers, *Physica A*, 1994, **204**, 399.
24. W. B. Li, J. V. Sengers, R. W. Gammon and P. N. Segrè, *Int. J. Thermophys.*, 1995, **16**, 23.
25. D. W. Pohl, S. E. Schwarz and V. Irniger, *Phys. Rev. Lett.*, 1973, **31**, 32.
26. H. Eichler, G. Enterlein, P. Glozbach, J. Munschau and H. Stahl, *Appl. Opt.*, 1972, **11**, 372.
27. H. Eichler, G. Salje and H. Stahl, *J. Appl. Phys.*, 1973, **44**, 5383.
28. Y. Nagasaka, T. Hatakeyama, M. Okuda and A. Nagashima, *Rev. Sci. Instrum.*, 1988, **59**, 1156.
29. Y. Nagasaka and A. Nagashima, *Int. J. Thermophys.*, 1988, **9**, 923.
30. A. Nagashima, *Int. J. Thermophys.*, 1995, **16**, 1069.
31. M. Motosuke, Y. Nagasaka and A. Nagashima, *Int. J. Thermophys.*, 2005, **26**, 969.
32. G. Wu, M. Fiebig and J. Wang, *Fluid Phase Equilib.*, 1993, **88**, 239.
33. J. Wang and M. Fiebig, *Heat and Mass Transfer*, 1995, **31**, 83.
34. J. Wang and M. Fiebig, *Int. J. Thermophys.*, 2000, **21**, 35.
35. W. Köhler and B. Müller, *J. Chem. Phys.*, 1995, **103**, 4367.
36. W. Köhler, G. Fytas, W. Steffen and L. Reinhardt, *J. Chem. Phys.*, 1996, **104**, 248.
37. J. Rauch and W. Köhler, *Phys. Rev. Lett.*, 2002, **88**, 185901.
38. D. Stadelmaier and W. Köhler, *Macromolecules*, 2008, **41**, 6205.
39. M. G. Munoz, M. Encinar, L. J. Bonales, F. Ortega, F. Monroy and R. G. Rubio, *J. Phys. Chem. B*, 2005, **109**, 4694.
40. Q. R. Huang and C. H. Wang, *J. Chem. Phys.*, 1998, **109**, 6103.
41. M. M. Velázquez, F. Ortega, F. Monroy, R. G. Rubio, S. Pegiadou, L. Pérez and M. R. Infante, *J. Colloid Interface Sci.*, 2005, **283**, 144.
42. A. Böttger and J. G. H. Joosten, *Europhys. Lett.*, 1987, **4**, 1297.
43. S. Sharma, K. Neupane, A. Adorjan, A. R. Baldwin and S. Sprunt, *Phys. Rev. Lett.*, 2005, **94**, 067801.

44. V. Halka, R. Tsekov and W. Freyland, *Phys. Chem. Chem. Phys.*, 2005, **7**, 2038.
45. V. Halka, R. Tsekov, I. Mechdiev and W. Freyland, *Z. Phys. Chem.*, 2007, **221**, 549.
46. J. Patzke, B. Rathke and S. Will, *Magnetohydrodynamics*, 2007, **43**, 429.
47. M. Ohnishi and Y. Nagasaka, *High Temp.-High Press.*, 2000, **32**, 103.
48. D. Langevin, *Light Scattering by Liquid Surfaces and Complementary Techniques*, Marcel Dekker, New York, 1992.
49. R. H. Katyl and U. Ingard, *Phys. Rev. Lett.*, 1967, **19**, 64.
50. R. H. Katyl and U. Ingard, *Phys. Rev. Lett.*, 1968, **20**, 248.
51. M.-A. Bouchiat and J. Meunier, *Phys. Rev. Lett.*, 1969, **23**, 752.
52. J. S. Huang and W. W. Webb, *Phys. Rev. Lett.*, 1969, **23**, 160.
53. J. Zollweg, G. Hawkins and G. B. Benedek, *Phys. Rev. Lett.*, 1971, **27**, 1182.
54. E. S. Wu and W. W. Webb, *Phys. Rev. A*, 1973, **8**, 2077.
55. J. C. Herpin and J. Meunier, *J. Phys. (Paris)*, 1974, **35**, 847.
56. D. Langevin, *J. Chem. Soc., Faraday Trans. I*, 1974, **70**, 95.
57. S. Hård, Y. Hamnerius and O. Nilson, *J. Appl. Phys.*, 1976, **47**, 2433.
58. D. Byrne and J. C. Earnshaw, *J. Phys. D: Appl. Phys.*, 1979, **12**, 1133.
59. D. Byrne and J. C. Earnshaw, *J. Colloid Interface Sci.*, 1980, **74**, 467.
60. J. C. Earnshaw, *Nature*, 1981, **292**, 138.
61. F. C. Goodrich, *Proc. R. Soc. Lond. A*, 1981, **374**, 341.
62. S. Hård and R. D. Neumann, *J. Colloid Interface Sci.*, 1986, **115**, 73.
63. T. M. JÆrgensen, *Meas. Sci. Technol.*, 1992, **3**, 588.
64. T. Nishio and Y. Nagasaka, *Int. J. Thermophys.*, 1995, **16**, 1087.
65. P. Tin, J. A. Mann, W. V. Meyer and T. W. Taylor, *Appl. Opt.*, 1997, **36**, 7601.
66. P. Tin, D. Frate and H. C. de Groh III, *Int. J. Thermophys.*, 2001, **22**, 557.
67. A. P. Fröba and A. Leipertz, *Int. J. Thermophys.*, 2001, **22**, 41.
68. A. P. Fröba and A. Leipertz, *Int. J. Thermophys.*, 2003, **24**, 895.
69. A. P. Fröba, Dr.-Ing. thesis, Friedrich-Alexander-Universität (FAU), Erlangen-Nürnberg, 2002.
70. A. P. Fröba and A. Leipertz, *J. Chem. Eng. Data*, 2007, **52**, 1803.
71. A. P. Fröba and A. Leipertz, *Int. J. Thermophys.*, to be submitted.
72. C. Botero and A. P. Fröba, *J. Appl. Phys.*, to be submitted.
73. V. G. Levich, *Physicochemical Hydrodynamics*, Prentice Hall, Englewood Cliffs, New Jersey, 1962.
74. P. M. Papoular, *J. de Phys. (Paris)*, 1968, **29**, 81.
75. E. H. Lucassen-Reynders and J. Lucassen, *Adv. Colloid Interface Sci.*, 1969, **2**, 347.
76. F. J. V. Santos, C. A. Nieto de Castro, J. H. Dymond, N. K. Dalaouti, M. J. Assael and A. Nagashima, *J. Phys. Chem. Ref. Data*, 2006, **35**, 1.
77. A. P. Fröba, L. P. Pellegrino and A. Leipertz, *Int. J. Thermophys.*, 2004, **25**, 1323.
78. F. J. P. Caetano, J. M. N. A. Fareleira, A. P. Fröba, K. R. Harris, A. Leipertz, C. M. B. P. Oliveira, J. P. M. Trusler and W. A. Wakeham, *J. Chem. Eng. Data*, 2008, **53**, 2003.

79. A. P. Fröba, S. Will and A. Leipertz, 20th International Congress of Refrigeration, Sydney, Australia, 1999.
80. A. P. Fröba, S. Will and A. Leipertz, *Int. J. Refrig.*, 2001, **24**, 734.
81. A. P. Fröba, K. Krzeminski and A. Leipertz, *Int. J. Thermophys.*, 2004, **25**, 987.
82. A. P. Fröba, C. Botero and A. Leipertz, *Int. J. Thermophys.*, 2006, **27**, 1609.
83. A. P. Fröba, L. Kretschmer and A. Leipertz, *J. Chem. Eng. Data*, to be submitted.
84. A. P. Fröba, S. Will and A. Leipertz, *Int. J. Thermophys.*, 2001, **22**, 1349.
85. A. P. Fröba and A. Leipertz, *Int. J. Thermophys.*, 2003, **24**, 1185.
86. A. P. Fröba, C. Botero, H. Kremer and A. Leipertz, *Int. J. Thermophys.*, 2007, **28**, 743.
87. M. Riva, F. Flohr and A. P. Fröba, *KI Luft- und Kältetechnik*, 2006, **12**, 528.
88. T. M. Koller, M. H. Rausch, P. S. Schulz, M. Berger, P. Wasserscheid, I. G. Economou, A. Leipertz and A. P. Fröba, *J. Chem. Eng. Data*, 2012, **57**, 828.
89. A. P. Fröba, P. Wasserscheid, D. Gerhard, H. Kremer and A. Leipertz, *J. Phys. Chem. B*, 2007, **111**, 12817.
90. W. Rathjen and J. Straub, in *Heat Transfer in Boiling*, ed. E. Hahne, Academic Press, New York, 1977, pp. 425–451.
91. V. Vesovic, W. A. Wakeham, G. A. Olchowy, J. V. Sengers, J. T. R. Watson and J. Millat, *J. Phys. Chem. Ref. Data*, 1990, **19**, 763.
92. B. Widom, *J. Chem. Phys.*, 1965, **43**, 3892.
93. W.-K. Rhim, K. Ohsaka, P.-F. Paradis and R. E. Spjut, *Rev. Sci. Instrum.*, 1999, **70**, 2796.
94. K. Yasumoto, N. Hirota and M. Terazima, *Phys. Rev. B.*, 1999, **60**, 9100.
95. H. Iwashima, K. Yabui and Y. Nagasaka, *Trans. JSME*, 2007, **B73**, 1892.
96. T. Oba, K. Yabui and Y. Nagasaka, *Trans. JSME*, 2006, **B72**, 428.
97. H. Iwashima and Y. Nagasaka, *High Temp. – High Pressures*, 2008, **37**, 51.
98. Y. Muramoto, N. Takahashi, N. Kamata and Y. Nagasaka, *Trans. JSME*, 2010, **B76**, 1290.
99. *Thermophysical Properties Handbook*, Yokendo, Tokyo, 2008.
100. *Standard Liquid for Calibrating Viscometer*, Tokyo, 1998.
101. Y. Muramoto and Y. Nagasaka, *J. Biorheol.*, 2011, **25**, 43.
102. H. Takiguchi and Y. Nagasaka, *Trans. JSME*, 2013, **B79**, 690.
103. B. J. Berne and R. Pecora, *Dynamic Light Scattering with Application to Chemistry, Biology, and Physics*, Malabar, 1990.
104. W. Krahn, G. Schweiger and K. Lucas, *J. Phys. Chem.*, 1983, **87**, 4515.
105. M. A. Anisimov, V. A. Agayan, A. A. Povodyrev and J. V. Sengers, *Phys. Rev. E.*, 1998, **57**, 1946.
106. O. Müller and J. Winkelmann, *Phys. Rev. E*, 1999, **59**, 2026.
107. O. Müller and J. Winkelmann, *Phys. Rev. E*, 1999, **60**, 4453.

108. D. G. Leaist and L. Hao, *J. Phys. Chem.*, 1993, **97**, 7763.
109. R. D. Mountain and J. M. Deutch, *J. Chem. Phys.*, 1969, **50**, 1103.
110. S. Will and A. Leipertz, *Int. J. Thermophys.*, 2001, **22**, 317.
111. A. Bardow, *Fluid Phase Equilib.*, 2007, **251**, 121.
112. D. A. Ivanov and J. Winkelmann, *J. Chem. Phys.*, 2006, **125**, 104507.
113. D. A. Ivanov and J. Winkelmann, *Int. J. Thermophys.*, 2008, **29**, 1921.
114. M. A. Anisimov, E. E. Gorodetskii, V. D. Kulikov, A. A. Povodyrev and J. V. Sengers, *Physica A*, 1995, **220**, 277.
115. M. A. Anisimov, E. E. Gorodetskii, V. D. Kulikov and J. V. Sengers, *Phys. Rev. E*, 1995, **51**, 1199.
116. M. A. Anisimov, E. E. Gorodetskii, V. D. Kulikov, A. A. Povodyrev and J. V. Sengers, *Physica A*, 1996, **223**, 272.
117. D. A. Ivanov, T. Grossmann and J. Winkelmann, *Fluid Phase Equilib.*, 2005, **228–229**, 283.
118. T. Grossmann and J. Winkelmann, *J. Chem. Eng. Data*, 2005, 50.
119. T. Grossmann and J. Winkelmann, *J. Chem. Eng. Data*, 2009, **54**, 485.
120. S. Wiegand, *J. Phys.: Condens. Matter*, 2004, **16**, R357.
121. S. Duhr, S. Arduini and D. Braun, *Eur. Phys. J. E*, 2004, **15**, 277.
122. G. Wittko and W. Köhler, *Philos. Mag.*, 2003, **83**, 1973.
123. A. Becker, W. Köhler and B. Müller, *Ber. Bunsen-Ges. Phys. Chem. Chem. Phys.*, 1995, **99**, 600.
124. W. Köhler, *J. Chem. Phys.*, 1993, **98**, 660.
125. W. Köhler and P. Rossmanith, *J. Phys. Chem.*, 1995, **99**, 5838.
126. W. Köhler and R. Schäfer, in *New Developments in Polymer Analytics II*, 2000, vol. 151, pp. 1–59.
127. B.-J. de Gans, R. Kita, S. Wiegand and J. Luettmer Strathmann, *Phys. Rev. Lett.*, 2003, **91**, 245501.
128. H. Ning, J. Buitenhuis, J. K. G. Dhont and S. Wiegand, *J. Chem. Phys.*, 2006, **125**, 209411.
129. J. K. Platten, M. M. Bou-Ali, P. Costeseque, J. F. Dutrieux, W. Köhler, C. Leppla, S. Wiegand and G. Wittko, *Philos. Mag.*, 2003, **83**, 1965.
130. S. Wiegand and W. Köhler, *LNP Vol. 584: Thermal Nonequilibrium Phenomena in Fluid Mixtures*, 2002, **584**, 189.
131. B. Arlt, S. Datta, T. Sottmann and S. Wiegand, *J. Phys. Chem. B*, 2010, **114**, 2118.
132. P. Naumann, N. Becker, S. Datta, T. Sottmann and S. Wiegand, *J. Phys. Chem. B*, 2013, **117**, 5614.
133. H. Ning, S. Datta, T. Sottmann and S. Wiegand, *J. Phys. Chem. B*, 2008, **112**, 10927.
134. S. Wiegand, H. Ning and H. Kriegs, *J. Phys. Chem. B*, 2007, **111**, 14169.
135. W. Köhler, A. Krekhov and W. Zimmermann, *Adv. Polym. Sci.*, 2010, **227**, 145.
136. M. P. Santos, S. L. Gomez, E. Bringuier and A. M. F. Neto, *Phys. Rev. E*, 2008, 77, 011403.
137. P. Polyakov and S. Wiegand, *Phys. Chem. Chem. Phys.*, 2009, **11**, 864.
138. R. Rusconi, L. Isa and R. Piazza, *J. Opt. Soc. Am. B*, 2004, **21**, 605.

139. H. Cabrera, L. Marti-Lopez, E. Sira, K. Rahn and M. Garcia-Sucre, *J. Chem. Phys.*, 2009, **131**, 031106.
140. S. J. Sheldon, L. V. Knight and J. M. Thorne, *Appl. Opt.*, 1982, **21**, 1663.
141. C. A. Carter and J. M. Harris, *Appl. Opt.*, 1984, **23**, 476.
142. S. Alves, A. Bourdon and A. M. F. Neto, *J. Opt. Soc. Am. B*, 2003, **20**, 713.
143. H. Ning and S. Wiegand, *J. Chem. Phys.*, 2006, **125**, 221102.
144. A. Königer, B. Meier and W. Köhler, *Philos. Mag.*, 2009, **89**, 907.
145. K. J. Zhang, M. E. Briggs, R. W. Gammon and J. V. Sengers, *J. Chem. Phys.*, 1996, **104**, 6881.
146. S. A. Putnam and D. G. Cahill, *Rev. Sci. Instrum.*, 2004, **75**, 2368.
147. A. Königer, H. Wunderlich and W. Köhler, *J. Chem. Phys.*, 2010, **132**, 174506.
148. F. Croccolo, H. Bataller and F. Scheffold, *J. Chem. Phys.*, 2012, **137**, 234202.
149. J. M. Ortiz de Zárate and J. Sengers, *Hydrodynamic Fluctuations in Fluids and Fluid Mixtures*, Elsevier, Amsterdam, 2006.
150. P. N. Segre, R. Schmitz and J. V. Sengers, *Phys. A*, 1993, **195**, 31.
151. F. Croccolo, F. Scheffold and H. Bataller, *C. R. Mecanique*, 2013, **341**, 378.
152. P. Naumann, A. Martin, H. Kriegs, M. Larrañaga, M. M. Bou-Ali and S. Wiegand, *J. Phys. Chem. B*, 2012, **116**, 2814.
153. W. Köhler and B. Müller, *J. Chem. Phys.*, 1995, **103**, 4367.
154. P. Costeseque and J.-C. Loubet, *Philos. Mag.*, 2003, **83**, 2017.
155. M. M. Bou-Ali, J. J. Valencia, J. A. Madariaga, C. Santamara, O. Ecenarro and J. F. Dutrieux, *Philos. Mag.*, 2003, **83**, 2011.
156. J. K. Platten, M. M. Bou-Ali and J. F. Dutrieux, *Philos. Mag.*, 2003, **83**, 2001.
157. C. Leppla and S. Wiegand, *Philos. Mag.*, 2003, **83**, 1989.
158. M. Gebhardt, W. Köhler, A. Mialdun, V. Yasnou and V. Shevtsova, *J. Chem. Phys.*, 2013, **138**, 114503.
159. P. Blanco, M. M. Bou-Ali, J. K. Platten, D. A. de Mezquia, J. A. Madariaga and C. Santamaria, *J. Chem. Phys.*, 2010, **132**, 114506.
160. S. VanVaerenbergh, S. Srinivasan and M. Z. Saghir, *J. Chem. Phys.*, 2009, **131**, 114505.
161. A. Leahy-Dios, M. Bou-Ali, J. K. Platten and A. Firoozabadi, *J. Chem. Phys.*, 2005, **122**, 234502.
162. M. M. Bou-Ali and J. K. Platten, *J. Non-Equilib. Thermodyn*, 2005, **30**, 385.
163. A. Königer, B. Meier and W. Köhler, *Philos. Mag.*, 2009, **89**, 907.
164. A. Königer, H. Wunderlich and W. Köhler, *J. Chem. Phys.*, 2010, **132**, 174506.
165. A. Mialdun and V. Shevtsova, *J. Chem. Phys.*, 2011, **134**, 044524.
166. F. Croccolo, H. Bataller and F. Scheffold, *J. Chem. Phys.*, 2012, **137**, 234202.
167. J. A. Madariaga, C. Santamaria, M. M. Bou-Ali, P. Urteaga and D. A. D. Mezquia, *J. Phys. Chem. B*, 2010, **114**, 6937.
168. M. E. Schimpf and J. C. Giddings, *J. Polym. Sci., Part B: Polym. Phys.*, 1989, **27**, 1317.
169. P. Kolodner, H. Williams and C. Moe, *J. Chem. Phys.*, 1988, **88**, 6512.
170. R. Piazza, S. Iacopini and B. Triulzi, *Phys. Chem. Chem. Phys.*, 2004, **6**, 1616.

171. A. Mialdun and V. Shevtsova, *C. R. Mecanique*, 2011, **339**, 362.
172. E. L. Dougherty Jr. and H. G. Drickamer, *J. Chem. Phys.*, 1955, **23**, 295.
173. J. P. Larre, J. K. Platten and G. Chavepeyer, *Int. J. Heat Mass Transfer*, 1997, **40**, 545.
174. G. Platt, T. Vongvanich, G. Fowler and R. L. Rowley, *J. Chem. Phys.*, 1982, **72**, 2121.
175. F. Montel, J. Bickert, A. Lagisquet and G. Galliero, *J. Pet. Sci. Eng.*, 2007, **58**, 391.
176. D. Walker and S. E. DeLong, *Contrib. Mineral. Petrol.*, 1982, **79**, 231.
177. D. Braun and A. Libchaber, *Phys. Rev. Lett.*, 2002, **89**, 188103.
178. R. Kita, S. Wiegand and J. Luettmer-Strathmann, *J. Chem. Phys.*, 2004, **121**, 3874.
179. R. Piazza and A. Parola, *J. Phys. Condens. Matter*, 2008, **20**, 153102.
180. P. Rossmanith and W. Köhler, *Macromolecules*, 1996, **29**, 3203.
181. V. Shevtsova, V. Sechenyh, A. Nepomnyashchy and J. C. Legros, *Philos. Mag.*, 2011, **91**, 3498.
182. K. B. Haugen and A. Firoozabadi, *J. Phys. Chem. B*, 2006, **110**, 17678.
183. S. R. de Groot and P. Mazur, *Non-equilibrium Thermodynamics*, Dover, New York, 1984.
184. R. Haase, Thermodynamics of Irreversible Processes, Dover Pub. Inc, New York, 1990.
185. R. P. Rastogi and B. L. Yadava, *J. Chem. Phys.*, 1969, **51**, 2826.
186. A. Mialdun and V. Shevtsova, *Int. J. Heat Mass Transfer*, 2008, **51**, 3164.
187. P. Martinoty, L. Hilliou, M. Mauzac, L. Benguigui and D. Collin, *Macromolecules*, 1999, **32**, 1746.
188. A. Mialdun, C. Minetti, Y. Gaponenko, V. Shevtsova and F. Dubois, *Microgravity Sci. Technol.*, 2013, **25**, 83.
189. S. Srinivasan and M. Z. Saghir, *J. Chem. Phys.*, 2009, **131**, 124508.
190. S. Srinivasan and M. Z. Saghir, *J. Non-Equilib. Thermodyn.*, 2011, **36**, 243.
191. K. Ghorayeb and A. Firoozabadi, *AIChE J.*, 2000, **46**, 883.
192. D. A. De Mezquia, M. M. Bou-Ali, M. Larraaga, J. A. Madariaga and C. Santamara, *J. Phys. Chem. B*, 2012, **116**, 2814.
193. T. Grossmann and J. Winkelmann, *J. Chem. Eng. Data*, 2009, **54**, 405.
194. J. A. Bierlein, *J. Chem. Phys.*, 1955, **23**, 20.
195. A. Mialdun and V. Shevtsova, *J. Chem. Phys.*, 2013, **138**, 161102.
196. G. Taylor, *Proc. R. Soc. A*, 1953, **219**, 186.
197. D. A. Ivanov and J. Winkelmann, *Int. J. Thermophys.*, 2009, **29**, 1921.
198. G. Hämmerlin and K.-H. Hoffmann, *Numerische Mathematik*, Springer, Berlin, 1994.
199. H. R. Schwarz and N. Köckler, Numerische Mathematik, Teubner, Wiesbaden, 2006.
200. V. Sechenyh, J. C. Legros and V. Shevtsova, *J. Chem. Thermodyn.*, 2013, **62**, 64.

CHAPTER 3

NMR Diffusion Measurements

WILLIAM S. PRICE

3.1 Introduction and Scope

This review focuses on the study of self-diffusion (intra-diffusion) by NMR, although NMR in the form of magnetic resonance imaging (MRI) can provide information on mutual-diffusion as described below. Hereinafter, however, the term 'diffusion' will signify self-diffusion. NMR provides two ways for studying diffusion and these are as follows: (i) measurement of spin relaxation; and (ii) the imposition of magnetic field gradients.[†] Although this review is almost completely concerned with the field gradient approach, for completeness a brief description of the relaxation method for the study of self-diffusion and the use of MRI to study mutual diffusion will be given. The literature pertaining to NMR diffusion measurements is vast and growing exponentially with time. Consequently, the references provided in this chapter are a mixture of seminal accounts together with more recent works, which are both accessible and span the literature. Extensive coverage of the field is given in ref. 2 to 10.

Gradient-based NMR diffusion measurements are used because of their versatility, low uncertainty and widespread availability (they can be conducted on most modern NMR spectrometers), and have thus become the preferred means of determining self-diffusion over the past few decades. Gradient-based NMR diffusion measurements are commonly referred to by a variety of names including NMR diffusometry, pulsed field gradient (PFG) NMR, pulsed gradient spin-echo (PGSE) NMR and DOSY (diffusion ordered spectroscopy). Of these, NMR diffusometry and PGSE NMR are the preferred terms.

[†]The IUPAC so called *Green Book*, Third Edition, section 2.6,[1] uses the term magnetic flux but, almost universally, in the NMR literature, this is known as the magnetic field.

Experimental Thermodynamics Volume IX: Advances in Transport Properties of Fluids
Edited by M. J. Assael, A. R. H. Goodwin, V. Vesovic and W. A. Wakeham

Published by the Royal Society of Chemistry, www.rsc.org

Until about 1990 any NMR diffusion measurement essentially involved some degree of home-built apparatus; however, now virtually every NMR spectrometer is capable of performing NMR diffusion measurements at least in low viscosity liquids. Similarly, basic diffusion NMR pulse sequences are now provided as a standard part of the commercially available software and include code to produce DOSY plots of the data. Consequently the number of papers containing the results of NMR diffusion measurements has increased exponentially. NMR confers a number of advantages over traditional techniques for the determination of diffusion coefficients and some of these are as follows: (i) effectively non-invasive; (ii) a relatively fast measurement time of less than 60 s in favourable cases; (iii) generally possible to measure the diffusion coefficients of different species in a mixture; (iv) able to measure diffusion over ten orders of magnitude from that attributed to gases[11] (of $\approx 10^{-5}$ $m^2 \cdot s^{-1}$) to very large polymers[12] (of $\approx 10^{-15}$ $m^2 \cdot s^{-1}$) with relative uncertainties of less than $\pm 1\,\%$;[13] (v) with increasingly sophisticated spectrometers, measurements can be performed on ever smaller samples; (vi) able to measure diffusion over a range of timescales thereby affording the possibility of obtaining structural information; and (vii) when combined with MRI able to provide localised diffusion information.[14]

This review focuses on diffusion in the liquid state, but some coverage is given to diffusion measurements on porous media; when the surroundings affect the motion of the diffusing nuclear spins. We note in passing that gradient based diffusion techniques are also able to measure flow,[15–17] that is closely related to electrophoretic NMR (*i.e.*, NMR-detected electrophoretic transport, which determines ion mobility in an applied electric field).[9,18–20] In the next section the salient points of studying diffusion by NMR with the relaxation approach are discussed and in subsequent sections the theory of gradient-based NMR diffusion measurements are considered. The final sections deal with details concerning the experimental aspects of NMR measurements of diffusion.

3.2 NMR Relaxation Approach

Although not commonly used, it is possible to obtain some information on the translational motion of a molecule from relaxation measurement. Specifically, if the relaxation mechanism of a molecule is well characterised a reorientation correlation time, τ_c, can be calculated from the relaxation measurement. This in turn can be used to determine the solvent viscosity η and ultimately to calculate a diffusion coefficient, D, using the Debye equation[21,22]

$$\tau_c = \frac{4\pi\eta r_S^3}{3k_B T}, \tag{3.1}$$

and the Stokes–Einstein–Sutherland equation (stick boundary condition)[23–25]

$$D = \frac{k_B T}{6\pi\eta r_S}. \tag{3.2}$$

In eqn (3.1) and (3.2) k_B is the Boltzmann constant, T is temperature and r_S is the effective hydrodynamic or Stokes radius. Nevertheless, the method is far from straightforward and to determine diffusion coefficients requires the following: (i) to obtain τ_c requires knowledge of the relaxation mechanism[26] of the probe species and can be very difficult to know with sufficient certainty and it is particularly difficult to separate *intra*-molecular relaxation from *inter*-molecular relaxation (for non-spherical molecules there will be more than one τ_c);[27,28] (ii) the probe molecule should see the solvent as a continuum; and (iii) the Stokes radius must be known and this, owing to the effects of solvation, is also far from straightforward. Furthermore, the relaxation method is unable to probe geometrical effects as it only reports on motion on the timescale of τ_c (that is typically ps to ns).

3.3 Magnetic Gradient Based Approach

3.3.1 Theory – The Ideal Case

A spatially perfectly homogeneous magnetic field is desired for ordinary NMR experiments to obtain a high resolution spectrum. However, the superposition of a well-characterised spatially-varying magnetic field gradient results in the Larmor precession frequency, ω, changing in a spatially well-defined manner in the direction of the gradient. Thus, like a piano keyboard, there is now a direct correlation between the NMR frequency and position ($\mathbf{r}$). Thus, for example, the imposition of a gradient $\mathbf{g}$ results in the Larmor precession frequency changing in the direction of the gradient as given by

$$\omega(\mathbf{r}) = \underbrace{\gamma B_0}_{\text{static field}} + \underbrace{\gamma \mathbf{g} \cdot \mathbf{r}}_{\text{gradient}}, \tag{3.3}$$

where γ is the gyromagnetic ratio of the nucleus in question. The first term of eqn (3.3), which arises from the static magnetic field $\boldsymbol{B}_0$, is of no direct consequence from the perspective of the diffusion (or MRI) experiment as it is common to all nuclear spins in the sample and instead we confine our attention to the second term of eqn (3.3). It is stressed that as the condition $|\mathbf{g} \cdot \mathbf{r}| \ll |\boldsymbol{B}_0|$ generally holds, magnetic field components perpendicular to $\mathbf{B}_0$ can be neglected and so $\boldsymbol{g}$ is defined as the gradient of the magnetic field component parallel to $\boldsymbol{B}_0$.[29] As an example, in most NMR spectrometers $\boldsymbol{B}_0$ is oriented along the z axis and so too is the gradient (*i.e.*, $\mathbf{g} = g_z$) in which case only a difference in displacement (or motion) along z will contribute to a change in the Larmor frequency according to eqn (3.3). Importantly though, with a triple axis gradient probe or measurements conducted with an MRI scanner, the gradient can be along any direction.

The theory behind MRI and magnetic gradient-based diffusion measurements is intrinsically linked,[3] the difference is that in the former case

the magnetic gradient is used to locate the nuclei in space according to the well-defined change in Larmor frequency with position, ultimately giving $\rho(\mathbf{r})$ the spin density at position $\mathbf{r}$ (and incidentally the ability to measure mutual diffusion since $\rho(\mathbf{r})$ will reflect the concentration of the nuclei in question). As depicted in Figure 3.1A the Fourier transform of a free induction decay (FID) acquired in the presence of a single gradient, for example, g_z, will give a one dimensional image $\rho(z)$ that is the projection of the spin density along the z-axis (a conventional MRI image is obtained with a sequence containing three orthogonal gradients to give $\rho(\mathbf{r})$).

It is conceptually easiest to understand how self-diffusion is measured under the ideal conditions of gradient pulses with infinitely short duration (*i.e.*, $\delta \rightarrow 0$) and in the absence of spin relaxation (Figure 3.1B and C). An

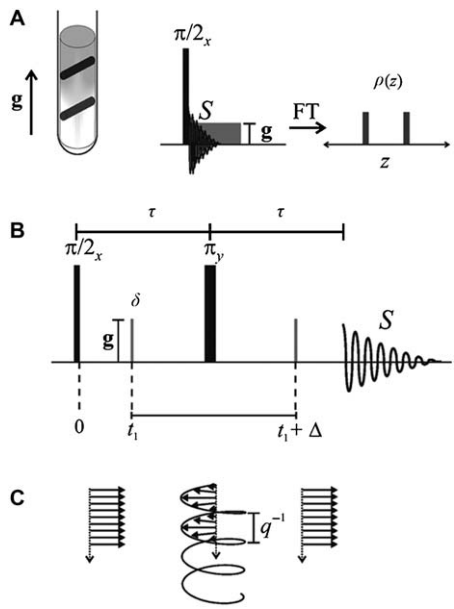

Figure 3.1 (A) Acquisition of a signal from a phantom sample consisting of an NMR tube containing two transverse cylinders of water with a read gradient directed along the long axes of the sample (*i.e.*, the z-direction). This results, upon Fourier transformation (FT), in a 1D image of the sample (*i.e.*, $\rho(z)$). (B) A Hahn spin-echo pulse sequence containing two 'infinitely' short gradient pulses of 'infinite' magnitude (the product of the duration and magnitude is finite) for measuring diffusion and (C) the effects this sequence has on transverse spin magnetisation represented by the arrows. The first gradient pulse winds the magnetisation into a helix with a pitch equal to q^{-1}, the π radio frequency (rf) pulse reflects the 'chirality' of the helix and then the second gradient pulse a time Δ later unwinds the magnetisation to reform the echo signal (*i.e.*, coherent transverse magnetisation). Diffusive motion in the direction of $\mathbf{g}$ during Δ will result in incomplete refocusing and consequently a smaller signal.

initial gradient pulse is applied to coherent transverse magnetisation to spatially encode the positions of the spins with the magnetisation being effectively wound 'instantly' into a helix. A delay sufficient to allow appreciable diffusive motion is then allowed and is followed by an equal gradient pulse but of effectively opposite polarity owing to the effects of the π rf pulse. In theory a diffusion measurement could be performed without the π pulse and with the second gradient pulse of negative polarity (*i.e.*, a gradient echo). However, in a gradient-echo only the dispersion arising from the first gradient pulse is refocussed whereas in a spin-echo the π rf pulse also removes the effect of chemical shift evolution and reduces frequency dispersion arising from residual $\mathbf{B}_0$ inhomogeneity and magnetic susceptibility effects in heterogeneous samples.

From the perspective of a single spin (nucleus) the winding effect of the first gradient pulse on the spin magnetisation is only perfectly counteracted by the second pulse if the spin has not moved along the direction of the gradient. Thus, in the absence of diffusive motion at the end of the second gradient pulse the coherent magnetisation would be recovered. Diffusion along the direction of the gradient between the two pulses degrades the encode–decode mechanism leading to a reduction in the coherence of the spin-echo and thus a smaller signal. To put this on a mathematical basis, the ability of a gradient pulse of duration δ to add phase to a nuclear spin at position $\mathbf{r}_0$ will be given by

$$\begin{aligned}\phi(\mathbf{r}) &= \gamma\delta\mathbf{g}\cdot\mathbf{r}_0 \\ &= 2\pi\mathbf{q}\cdot\mathbf{r}_0\end{aligned}, \tag{3.4}$$

and thus the residual phase after two such gradient pulses will be

$$\phi_{\mathbf{R}}(\mathbf{r}) = 2\pi\mathbf{q}\cdot(\mathbf{r}_1 - \mathbf{r}_0). \tag{3.5}$$

As defined in eqn (3.4), $\mathbf{q}$ has units of m^{-1} and plays the role of a scattering vector. $\mathbf{q}$ $[=\gamma\delta g/(2\pi)]$ can be likened to the area of the gradient pulse scaled by the gyromagnetic ratio to give the effective de-phasing power.

The NMR signal, S, is proportional to the projection of the nuclear spin magnetisation averaged over the sample (*i.e.*, $\cos(\bar{\phi}_{\mathbf{R}})$ or equivalently $e^{\mathrm{i}\cos(\bar{\phi}_{\mathbf{R}})}$). Now the chance of a spin being at $\mathbf{r}_0$ is $\rho(\mathbf{r}_0)$ and the chance of the spin moving from $\mathbf{r}_0$ to $\mathbf{r}_1$ in a time Δ will be given by the diffusion propagator $P(\mathbf{r}_0, \mathbf{r}_1, \Delta)$, and thus considering all starting and finishing positions (equivalent to averaging over the sample) the signal observed at the end of the echo sequence will be given by

$$S = E = \iint \rho(\mathbf{r}_0)P(\mathbf{r}_0, \mathbf{r}_1, \Delta)\mathrm{e}^{i2\pi\mathbf{q}\cdot(\mathbf{r}_1-\mathbf{r}_0)}\mathrm{d}\mathbf{r}_0\mathrm{d}\mathbf{r}_1. \tag{3.6}$$

In this particular case, the signal S is equivalent to the signal attenuation E $(=S/S_{q=0})$ where $S_{q=0}$ is the signal in the absence of the applied gradient. Since eqn (3.6) is, by definition, normalised {*i.e.*, we have taken the initial magnetisation M_0 to be equal to $\int\rho(\mathbf{r}_0)\mathrm{d}\mathbf{r}_0 = 1$}, what has been described is

the short gradient pulse approximation and eqn (3.6) is known as the short gradient pulse (herein after given the acronym SGP) master equation. The diffusion propagator is determined by solving the diffusion equation subject to appropriate initial and boundary conditions.[30,31] For example, for (three-dimensional) free diffusion in an isotropic and homogeneous medium the (Gaussian) propagator P is given by

$$P(\mathbf{r}_0, \mathbf{r}_1, \Delta) = \frac{1}{(4\pi Dt)^{3/2}} \exp\left[-\frac{(\mathbf{r}_1 - \mathbf{r}_0)^2}{4Dt}\right]. \tag{3.7}$$

If $\rho(\mathbf{r})$ is set to 1 and the propagator for diffusion in one dimension (*e.g.*, z)

$$P(z_0, z_1, \Delta) = \frac{1}{(4\pi Dt)^{1/2}} \exp\left[-\frac{(z_1 - z_0)^2}{4Dt}\right], \tag{3.8}$$

is substituted into eqn (3.6) then the signal attenuation E owing to diffusion is given by

$$E = \exp[-(2\pi q)^2 D\Delta]. \tag{3.9}$$

Diffusion results in a signal attenuation, however flow would result in a phase change of the signal. Thus, the two effects are separable.

Thus, by measuring E as a function of q or Δ and then regressing eqn (3.9) onto the data it is possible to obtain an estimate of D. Typically δ is of the order of 10^{-3} s whilst Δ can range from 1 ms to 1 s. It is stressed again that diffusion is measured along the direction of $\mathbf{g}$ (and thus $\mathbf{q}$).

The mean squared displacement (MSD) during Δ is defined by[32]

$$\left\langle (\mathbf{r}_1 - \mathbf{r}_0)^2 \right\rangle = \left\langle \mathbf{R}^2 \right\rangle = \int_{-\infty}^{\infty} (\mathbf{r}_1 - \mathbf{r}_0)^2 \rho(\mathbf{r}_0) P(\mathbf{r}_0, \mathbf{r}_1, \Delta) \mathrm{d}\mathbf{r}_0 \mathrm{d}\mathbf{r}_1, \tag{3.10}$$

and thus, using eqn (3.8) and (3.10), the MSD along $\mathbf{q}$ is given by

$$\left\langle R_{\mathbf{q}}^2 \right\rangle = 2D\Delta. \tag{3.11}$$

Using eqn (3.11), eqn (3.9) can be rewritten as

$$E = \exp\left[-(2\pi q)^2 \frac{\left\langle R_{\mathbf{q}}^2 \right\rangle}{2}\right], \tag{3.12}$$

which emphasises that the experiment is sensitive to the MSD during Δ. In a freely diffusing system the MSD scales linearly with Δ, and thus the measured diffusion coefficient is independent of the value of Δ used in the measurement. However, anomalous results have been observed for some ionic liquids.[33] Further, due to the directionality of the diffusion measurement it is possible to probe anisotropic systems whether anisotropic Gaussian diffusion (*e.g.*, a liquid crystal[34]) or anisotropic restricted diffusion (see below) in which case it is possible to determine true or apparent

diffusion tensors and when conducted within MRI experiments is referred to as diffusion tensor imaging.[8,14,35]

For completion, when diffusion occurs within a restricting geometry (*e.g.*, diffusion with a biological cell) the diffusion propagator and subsequent analysis becomes very much more complicated and the measured diffusion coefficient can be Δ-dependent and depend on direction if the restriction is anisotropic. For example, for diffusion between reflecting planes (planes which restrict the nuclei to be between them but do not affect the spin state) separated by a characteristic distance $2a$ with $\mathbf{g}$ directed perpendicular to the planes, the PGSE attenuation is given by[36]

$$E(\mathbf{q},\Delta) = \frac{2[1-\cos(2\pi q(2a))]}{[2\pi q(2a)]^2} + 4[2\pi q(2a)]^2 \sum_{n=1}^{\infty} \exp\left[-\frac{n^2\pi^2 D\Delta}{(2a)^2}\right] \frac{1-(-1)^n\cos[2\pi q(2a)]}{\left\{[2\pi q(2a)]^2-(n\pi)^2\right\}^2}, \quad (3.13)$$

whereas if $\mathbf{g}$ was directed parallel to the planes the measured attenuation would be described by eqn (3.9).

At very long Δ such that the measured MSD is now set by the characteristic distance of the restricting geometry, the echo attenuation profile gives direct information on the geometry itself since, starting from eqn (3.6),[8,37,38]

$$E(\mathbf{q},\Delta\rightarrow\infty) = \int \rho(\mathbf{r}_0)\exp(-\mathrm{i}2\pi\mathbf{q}\cdot\mathbf{r}_0)\mathrm{d}\mathbf{r}_0 \int \rho(\mathbf{r}_1)\exp(\mathrm{i}2\pi\mathbf{q}\cdot\mathbf{r}_1)\mathrm{d}\mathbf{r}_1 = |S(\mathbf{q})|^2, \quad (3.14)$$

where $|S(\mathbf{q})|^2$ is the Fourier transform of $\rho(\mathbf{r}_1)$. Thus $E(\mathbf{q},\Delta\rightarrow\infty)$ is the power spectrum of $\rho(\mathbf{r}_0)$ and is sensitive to average features in local structure and not motional characteristics. A direct analogy can be made between NMR diffusion measurements of restriction occurring in a restricted geometry and scattering experiments such as optical diffraction.[37,39–41] Thus, the expression diffusive diffraction is sometimes used to describe the results of NMR diffusion measurements of porous media. Since Fourier inversion of $E(\mathbf{q},\Delta\rightarrow\infty)$ returns $|S(\mathbf{q})|^2$, NMR diffusion measurements are sometimes referred to as q-space imaging (whereas conventional MRI is sometimes referred to as k-space imaging). For the case of reflecting planes, at long Δ only the (diffusion independent) first term in eqn (3.13) remains, giving

$$E(\mathbf{q},\Delta\rightarrow\infty) = |S(\mathbf{q})|^2 = \frac{2\{1-\cos[2\pi q(2a)]\}}{[2\pi q(2a)]^2}, \quad (3.15)$$

which gives diffractive minima at $q = n/(2a)$ for integer values of n.

In general, analytical solutions for cases involving restricted diffusion are not possible and even using the SGP, or other approximations,[42,43] the associated mathematics rapidly becomes intractable and numerical solutions must be used.[44,45]

NMR diffusion measurements in restricted geometries (*i.e.*, porous media) have an enormous variety of applications[46] ranging from studying emulsions,[47,48] to brain imaging[13] and petrophysical applications.[49]

3.3.2 Complications

Consideration of the assumptions in the previous section allows the sources of error and complications to be understood and perhaps obviated or a correction made. Above, we have assumed perfect pulse sequences where the only interactions with the spins were those purposely applied and that the signal from the spins of interest could be detected without interference. Some of the problems arise from machine limitations (*e.g.*, finite gradient pulses, eddy currents and not perfectly homogeneous applied magnetic fields) whilst other complications are related to the sample (spin relaxation, strong signals, *J*-evolution, radiation damping and the distant dipolar field).

3.3.2.1 Finite Gradient Pulses

Firstly, due to the inductive nature of gradient coils and limited slew rate and maximum output of amplifiers it is impossible to generate infinitely short gradient pulses. Thus, effects of diffusion must be considered during the encode and decode steps, which changes the effective time over which diffusion is measured. If the gradient pulse is considered to be a rectangle of finite duration δ and following a more complete analysis starting from the Bloch–Torrey equations,[50,51] the more commonly encountered form of the expression of signal attenuation due to free isotropic diffusion is

$$\begin{aligned} E &= \exp\left[-\gamma^2 g^2 \delta^2 D(\Delta - \delta/3)\right] \\ &= \exp\left[-(2\pi q)^2 D(\Delta - \delta/3)\right]. \end{aligned} \tag{3.16}$$

The '$-\delta/3$' term (*c.f.* eqn (3.9)) reflects the correction for the finite duration of the gradient pulse – but this correction is specific to free diffusion and does not apply to cases of restricted diffusion[52] and there is considerable interest in methods to account for it.[53,54] The correction factor also depends on the specific gradient pulse shape. For example, for half-sine shaped gradient pulses eqn (3.16) becomes[55]

$$E = \exp[-\gamma^2 g^2 \delta^2 D(4\Delta - \delta)/\pi^2]. \tag{3.17}$$

In the medical literature, the experimental parameters are typically referred to as a '*b*-value' or '*b*-factor' and so eqn (3.16) would be written as

$$E = \exp(-bD), \tag{3.18}$$

with

$$b = \gamma^2 g^2 \delta^2 (\Delta - \delta/3). \tag{3.19}$$

Clearly it is the maximum *b* value which determines the lower limit of diffusion that can be measured.

3.3.2.2 Relaxation

In the above discussion, the attenuation due to spin relaxation was conveniently neglected, but in reality it is ever present and thus in reality the signal at the end of the pulse sequence has the form

$$S = M_0 E_{\text{Relax}} E_{\text{Diff}}, \tag{3.20}$$

where, in the case of the Hahn echo sequence,

$$E_{\text{Relax}} = \exp\left(-\frac{2\tau}{T_2}\right). \tag{3.21}$$

and E_{Diff} is given by eqn (3.16). For other sequences the appropriate versions of eqn (3.16) and (3.21) must be used. Generally, because it is possible to alter $\mathbf{q}$ independently of τ, the effects of relaxation can be removed by normalisation with respect to the signal acquired with $q = 0$ according to

$$E = \frac{S}{S_{q=0}} = \frac{M_0 E_{\text{Relax}} E_{\text{Diff}}}{M_0 E_{\text{Relax}}} = E_{\text{Diff}}. \tag{3.22}$$

Thus, whilst the effects of spin relaxation are normalised out, relaxation limits the length of the sequence and thus the maximum available Δ. The last two decades have seen the maximum gradient strength of commercially available NMR diffusion probes increase from 0.5 Tm^{-1} to in excess of 30 Tm^{-1} with vastly better eddy current settling characteristics (see section below). The consequence of this is that it is possible to measure the diffusion of ever more slowly diffusing species and/or those with short relaxation times.

3.3.2.3 Gradient Behaviour

The equations provided in the previous sections assume the applied gradient is homogeneous through the sample and that it is the only magnetic gradient present. The former is never true and even on the best NMR gradient probes the applied gradient would differ relatively by at least $\pm 1\,\%$ through the sample volume. Owing to imperfections in the static field (*i.e.*, $\boldsymbol{B}_0$) and/or spatial variations in magnetic susceptibility (*e.g.*, sample edges) or even more problematically when diffusion measurements are performed in porous media, there are always 'background' gradients. Simplistically, assuming a homogeneous and static background gradient $\mathbf{g}_0$ and completing analysis as for eqn (3.16), gives the signal as[51]

$$S = M_0 \exp\left(\underbrace{-\gamma^2 g^2 D\delta^2(\Delta - \delta/3)}_{\mathbf{g}\text{ term}} \underbrace{+\gamma^2 \mathbf{g}\cdot\mathbf{g}_0 D\delta\left[t_1^2 + t_2^2 + \delta(t_1 + t_2) + \frac{2}{3}\delta^2 - 2\tau^2\right]}_{\mathbf{g}\cdot\mathbf{g}_0\text{ cross term}} \underbrace{-\gamma^2 g_0^2 D\frac{2}{3}\tau^3}_{\mathbf{g}_0\text{ term}} \right), \tag{3.23}$$

where it is assumed that $S(0) = M_0$, $t_2 = 2\tau - (t_1 + \Delta + \delta)$ and t_1 is defined in Figure 3.1. Eqn (3.23) contains three terms, the $\mathbf{g}$ term, which as before represents attenuation arising from diffusion and the applied gradient, and two additional terms, one denoted $\mathbf{g}_0$ and the other $\mathbf{g} \cdot \mathbf{g}_0$ a cross term. If instead the signal was normalised, as it was for eqn (3.22), to the signal acquired at $S(2\tau)$ in the absence of applied gradients, the attenuation of the signal would be given by,

$$E = \frac{S}{S_{q=0}}$$
$$= \exp\left(-\gamma^2 g^2 D\delta^2(\Delta - \delta/3) + \gamma^2 \mathbf{g} \cdot \mathbf{g}_0 D\delta\left[t_1^2 + t_2^2 + \delta(t_1 + t_2) + \frac{2}{3}\delta^2 - 2\tau^2\right]\right). \quad (3.24)$$

Thus, providing the length of the sequence is kept constant, the $\mathbf{g}_0$ term reflects a constant attenuation factor that can be removed by normalisation. However, if $\mathbf{g}_0$ is large, then similar to the relaxation case, it may limit the length of time for the sequence. Most problematic is the $\mathbf{g} \cdot \mathbf{g}_0$ cross term since its contribution to the signal attenuation changes as $\mathbf{g}$ is altered and its sign depends on the direction of $\mathbf{g}$ relative to $\mathbf{g}_0$.[56] Nevertheless, in the literature the presence the cross term is almost always ignored so that eqn (3.16) is used to analyse the NMR diffusion data.

The best method of improving the applied gradient homogeneity is to restrict the size of the sample volume so that it lies within the homogeneous field region either through a smaller sample tube[57] or through volume selection within the pulse sequence.[58,59] These approaches can also assist with the removal of macroscopic background gradients (*e.g.*, sample interface effects), but are unable to remove gradients arising from the effects of smaller localised susceptibility differences (*e.g.*, in porous media) and sometimes these background gradients can be very large and even time dependent (*e.g.*, with spins diffusing between regions of different gradient strength), and to remove these effects specialised sequences must be used.[60–63]

Two further complications arise directly from the gradient pulses and these are as follows: (i) that the rise and fall of the applied gradient pulses generate currents in surrounding conductors ('eddy currents') which in turn generate additional magnetic gradients; and (ii) gradient pulse mismatch. It is impossible to acquire meaningful spectra whilst these rapidly changing induced fields are active. Fortunately, gradient generation has improved enormously over the past two decades and the time needed for eddy currents to dissipate on a modern NMR probe is generally less than 1 ms. Approaches to mitigate the effects of eddy currents include the use of smoothly shaped pulses (*e.g.*, half-sine; see eqn (3.17)),[64] sequences containing bipolar gradient pulses[65] and pre-emphasis.[66] The gradient pulse pairs in the NMR sequence must be matched to the ppm level and even the smallest mismatch

results in a residual phase twist and has very deleterious effects.[64] Shaped pulses and also gradient pre-pulses[67] can help to reduce gradient pulse mismatch or the imaging-based PGSE-MASSEY sequence[68] can be used to help remove its effects.

Finally, in many cases when the B_0 field is stable it is possible to conduct an NMR diffusion measurement without field frequency locking, although locking is preferable. Nevertheless, field frequency-locking should be gated off during gradient pulses and the B_0 field should be centred prior to starting the experiment to minimise disturbances due to lock gating.[8,69] Since the gradient pulses also affect the ^{2}H lock signal the performance of the lock can be restored by adding balancing gradient pulses at the beginning and end of Δ.[70]

3.3.2.4 *J-Evolution*

Many species of interest contain homonuclear *J*-coupling spin interactions, which will result in peak phase distortions due to the creation of unwanted mixtures of in-phase and anti-phase magnetisation ('*J*-evolution' or '*J*-modulation' effects). This can have serious consequences since there can be effectively large decreases in signal-to-noise and baseline distortions that make diffusion measurements difficult if not impossible. Stimulated echo (STE; see below) sequences are less sensitive to *J*-evolution effects than Hahn-echo based sequences by virtue of the shorter transverse periods. However, it is possible to devise more sophisticated sequences to almost entirely remove the deleterious effects.[71,72]

3.3.2.5 *Intense Signals*

As NMR spectrometers are based on increasingly higher field magnets (*i.e.*, larger $\mathbf{B}_0$) and as probes become more sensitive the problems associated with large signals and, as a consequence, radiation damping and long range dipolar fields become ever more problematic.

Radiation damping is a feedback mechanism resulting from coupling between transverse magnetisation and the rf coil.[73–76] The radiation damping field acts as a torque on the spin magnetisation and tends to rotate it back to its equilibrium position. For example, at room temperature the protons in water have a T_1 of the order of 3.8 s, but radiation damping can result in the water magnetisation returning to equilibrium in a tiny fraction of this time.[77] This not only hampers the implementation of NMR diffusion sequences but can also seriously affect line shapes and intensities. There are a number of ways to minimise the effects of radiation damping including detuning the NMR probe and using a smaller sample, but it is preferable to engineer pulse sequences so that they are less vulnerable to the effects. The best and most flexible approach is to use *Q*-switching where the rf circuit is essentially disconnected during those parts of sequence where neither an rf pulse is applied nor the signal is detected.[78] Another approach, albeit not as

flexible, is to attempt to leave the spin magnetisation spatially encoded (so that the vector sum is zero) for as much of the pulse sequence as possible.[56]

The long-range (or distant) dipolar field is generated by the equilibrium magnetisation of a strong sample and is parallel to $\boldsymbol{B}_0$. If anisotropy is introduced by, for example, the application of a magnetic gradient, long range dipolar couplings might not be completely averaged. This can result in the magnetic flux density in the sample being modified during the pulse sequence which can lead to a number of enigmatic effects such as multiple spin-echoes in addition to Hahn and STE echoes.[7] Radiation damping and the long-range dipolar field can result in chaotic spin dynamics.[79,80]

Very commonly, the species of interest may be at very low concentration compared to that of a solvent. If the spectrometer's receiver gain is set to a sufficient value to digitise the solute resonance, the receiver will almost certainly be saturated by the solvent resonance resulting in a hopelessly distorted spectrum. Thus, in general it is necessary to include some form of solvent suppression[81] such as WATERGATE[82] into the NMR diffusion pulse sequence.[83,84] Some examples are given below.

3.3.2.6 *Gradient and Temperature Calibration*

Attention to the previous points will undoubtedly lead to a precise measurement of diffusion coefficient, but without excellent gradient and temperature calibration it will have a large uncertainty. There are numerous ways to calibrate magnetic gradients including calculation from the known coil dimensions,[57] one dimensional imaging, gradient mismatch and echo shape analysis.[8] However, all of these techniques have some limitations and the most common approach is to use a sample of known diffusion coefficient, D^0. In this approach, a suitable but not accurately known ('apparent') gradient, g^{app}, is used to measure the diffusion coefficient, D^{app}, of the standard sample. The true gradient strength is then determined from

$$g = g^{\mathrm{app}} \sqrt{\frac{D^{\mathrm{app}}}{D^0}}. \tag{3.25}$$

Apart from its simplicity, this approach has the advantage that it, to some extent, includes corrections for non-ideal gradient behaviour (*e.g.*, background gradients). Typically relative uncertainties of less than $\pm 1\,\%$ are achievable with this approach. However, the calibration should be performed with gradient parameters, gradient shapes, pulse sequences and sequence timings similar to those to be used for the samples of interest; the calibration should be performed for a sample volume and position in the coils similar to those intended for the measurement. A list of suitable calibrants can be found elsewhere.[8] Since some calibrants are pure liquids, complications can arise from radiation damping. The most commonly used calibrant is the residual ^{1}H signal in ^2H_2O.[85] By virtue of having two NMR sensitive nuclei at easily measurable concentrations (*i.e.*, ^{1}H and ^{2}H) ^2H_2O

has the added advantage of being able to calibrate gradients over a large range of amplitudes and verifying that the gradient output varies linearly and whether or not eddy currents are significant over the range of gradients to be used.[86]

In most probes temperature control is performed by blowing temperature regulated gas into the probe (*i.e.*, around the outside of the sample). Thus, the sample temperature may not reflect the set temperature and the discrepancy can be made even worse if, for example, the sample has a high ionic strength and the pulse sequence has either a high rf duty cycle and/or includes high power decoupling.[87] A common method of determining the in-sample temperature is to use a compound with temperature-dependent chemical shifts such as methanol or ethane-1,2-diol (ethylene glycol).[88]

3.3.2.7 *Sample Movement*

Owing to the method used to regulate the temperature of the NMR probe, there are almost certainly temperature gradients through the sample and the situation is exacerbated in samples depending on the efficiency of heat transfer and the sample viscosity. Such temperature gradients can lead to convection which, in turn, can have very serious effects on diffusion measurements.[89,90] The problem is that the standard NMR diffusion measuring pulse sequences just detect displacement and an additional source of motion (*i.e.*, convection) will lead to an apparently large diffusion coefficient.[91] Convection results in a cosine modulation of the PGSE signal,[91]

$$E = \exp[-\gamma^2 g^2 \delta^2 D(\Delta - \delta/3)]\cos(\gamma g \delta v \Delta), \tag{3.26}$$

where v is the velocity of the convective flow in the sample. Unfortunately, except in severe cases, the cosine term is not evident in the experimental data and the results will appear to be well-described by a single exponential. Analysis of the data using eqn (3.16) will result in an erroneous diffusion coefficient, which to a first approximation will be

$$D^{\mathrm{app}}(\Delta) = D + \frac{\Delta v^2}{2}. \tag{3.27}$$

Thus, a Δ-dependence of a diffusion coefficient of a pure liquid is an indication of the presence of convection. Apart from better temperature control, methods for removing the deleterious effects of convection include using a smaller and narrower sample,[89,92] and (in appropriate cases) inserting glass wool (E. von Meerwall, private communication). An alternative is to use convection compensated pulse sequences,[90,93] although these sequences will only correct for laminar flow and not turbulent flow.

We note that movement of the whole sample due to vibration or incomplete compaction in the case of a powder sample[94] results in similar complications.

3.3.3 Common Pulse Sequences

Almost all NMR diffusion sequences can be divided into spin-echo[15,51] (Figure 3.1B), which is commonly referred to as Hahn spin-echo, or stimulated echo[95,96] sequences (Figure 3.2A), with the variations upon these generally arising out of the need to remove the problems mentioned in the previous subsections including background gradients, eddy current effects or solvent suppression (see Figure 3.2B and Figure 3.3) *etc.* Carr–Purcell–Meiboom–Gill; (CPMG)-based sequences,[15,97,98] and also so-called oscillating gradient spin-echo experiments,[99,100] which are sensitive to frequency-dependent diffusion coefficient information, also exist but have not been so widely used. This chapter has been primarily concerned with methods based on B_0 gradients, however, other methods, such as B_1 (*i.e.*, rf) gradient-based methods are also possible although they have, to date, received limited use.[7,101]

The earliest NMR diffusion measurements were conducted with so-called 'steady' gradients. That is, if the gradient in the Hahn echo sequence is continuous (*i.e.*, $\delta = \tau$) then eqn (3.16) reduces to the steady gradient solution

$$E = \exp\left(-\frac{2}{3}\gamma^2 g^2 D\tau^3\right). \tag{3.28}$$

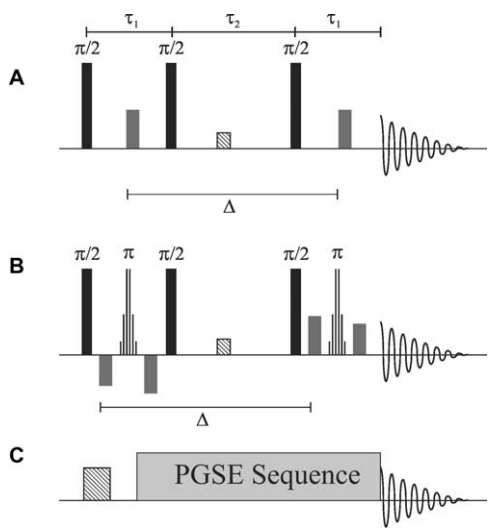

Figure 3.2 (A) The stimulated echo-based PGSE (or PGSTE) sequence. The hashed gradient pulse during τ_2 is a purge gradient to reduce the phase cycle. (B) The PGSTE-WATERGATE sequence[83] with asymmetric bipolar gradient pulses. The π pulses composed of thin vertical lines represent selective binomial-like rf pulses with an excitation null on the solvent resonance. (C) Inclusion of a purge gradient pulse in the recycle delay may allow significantly shorter recycle delays.

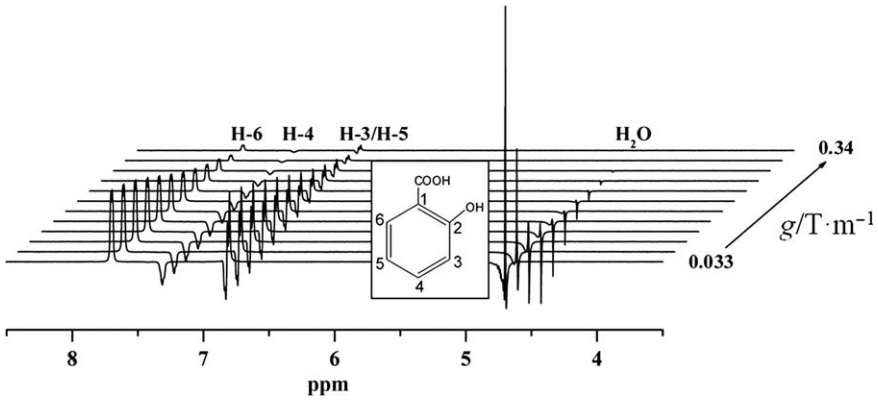

Figure 3.3 A series of PGSE–WATERGATE[83] spectra of a sample containing 80 mmol · dm^{-3} salicylate and 0.5 mmol · dm^{-3} bovine serum albumin in water (0.1 $^2H_2O + 0.9$ ^1H_2O) at a temperature of 298 K. The water resonance has been suppressed by more than four orders of magnitude. The residual water resonance gives rise to the peak at 4.7 ppm and the three peaks to the left originate from 2-hydroxybenzenecarboxylate (salicylate) (from left to right: H-6, H-4, H-3/H-5). The effects of *J*-modulation are evident on the H-4 and H-3/H-5 resonances. Reproduced with permission from W. S. Price, F. Elwinger, C. Vigouroux and P. Stilbs, *Magn. Reson. Chem.*, 2002, **40**, 391.

However, steady gradient sequences are now rarely used because of the following: (i) having the gradient on during signal acquisition removes chemical shift information (although this is not a problem if the sample only contains a single measurable component); (ii) the effective spectral width of the rf pulse is reduced in the presence of an applied gradient; and (iii) the duration of the gradient 'pulse' is now directly tied to the length of the sequence so it is impossible to alter Δ independently of τ. Consequently there can be limitations in separating relaxation from diffusion effects.

In the stimulated echo-based PGSE sequence the spin magnetisation is longitudinal during the τ_1 delay, which comprises most of Δ, so the sequence can be preferable when the longitudinal relaxation time T_1 is greater than the spin–spin relaxation time T_2. However, as the equation for the STE pulse sequence analogous to equation (3.23) contains an initial factor of $M_0/2$ (instead of the Hahn echo case of M_0), T_1 must be substantially larger than T_2 for the PGSTE sequence to be preferable. An additional issue with STE-based sequences is that an extensive phase cycle is required to remove unwanted coherences. The inclusion of a purge gradient pulse in the middle τ period greatly reduces the phase cycling requirements, as shown in Figure 3.2A. A more sophisticated approach involves the use of asymmetric bipolar gradient pulses which effectively perform phase cycling in a single scan of the sequence.[70] Further, this approach can be combined with selective π rf pulses, as shown in Figure 3.2B, to give solvent suppression.[84]

Since NMR diffusion measurements are a quantitative technique, to reliably be able to accurately measure the signal intensity (or integral) of the

resonance of interest it has generally been considered necessary to leave a delay of 5 times T_1 between scans and with unfavourable samples this can lead to long experimental times. Numerous approaches have been presented for faster diffusion measuring sequences yet most have very serious limitations (*e.g.*, loss of chemical shift information or Δ not being accurately defined). As noted above asymmetric gradient pulsed based sequences can be advantageous if the signal is strong and the time limiting factor is merely to complete the phase cycle. However, a more general approach is merely to include a purge gradient pulse during the recycle delay (Figure 3.2C) which can significantly reduce the time required for the diffusion measurements whilst retaining the accuracy and full chemical shift information.[102,103]

3.3.4 Data Analysis

It is imperative that the initial PGSE attenuation data is as distortion free as possible (*i.e.*, flat baselines), especially if there are multiple resonances, and is of the best possible resolution. Sometimes data are presented in absolute value mode as this may hide some imperfections (*e.g.*, phase disturbances from eddy currents or other gradient generation imperfections) or *J*-evolution effects, but the improvement is of cosmetic value only and it has the deleterious effect of making all of the noise positive – which further complicates the analysis. It is far better to analyse the data in phase sensitive mode and perhaps apply reference deconvolution.[104]

A common approach when analysing the data of a freely diffusing sample is to plot $\ln(E)$ *versus* b [*i.e.*, $\gamma^2 g^2 \delta^2 (\Delta - \delta/3)$; *c.f.* eqn (3.16)] and then determine the diffusion coefficient from the slope. However, this technique unequally weights the errors in the data and it is preferable to regress eqn (3.16) directly onto the data using non-linear least square regression.

In samples containing mixtures of species, analysis becomes much more complicated when there is spectral overlap, and the more prior knowledge (*e.g.*, number of diffusing species (N_D), relative concentrations, relaxation behaviour *etc.*) the better. In the case of a polydisperse system containing N_D types of freely diffusing species, where the various oligomeric species overlap, the PGSE NMR signal would be described by,

$$S = \sum_{i}^{N_D} M_{0,i} \exp\left(\frac{-2\tau}{T_{2i}}\right) \exp\left[-\gamma^2 g^2 D_i \delta^2 (\Delta - \delta/3)\right], \tag{3.29}$$

where $M_{0,i}$ ($\propto Mw_i n_i$ and n_i is the number of molecules of the i-th species present) and T_{2i} denote the equilibrium magnetisation and spin–spin relaxation time for the i-th species, respectively.

If each species contributes a 1D NMR spectrum, $S_D(\nu)_i$, where ν is the frequency, the final spectrum, $S(\nu,q)$ would be given by

$$S(\nu, q) = \sum_{i}^{N_D} \exp\left[-\gamma^2 g^2 D_i \delta^2 (\Delta - \delta/3)\right] S_D(\nu)_i, \tag{3.30}$$

or in the case of a continuum of diffusion coefficients, this becomes

$$S(\nu, q) = \int_0^\infty \exp\left[-\gamma^2 g^2 D_i \delta^2 (\Delta - \delta/3)\right] S_D(\nu, D) \mathrm{d}D. \qquad (3.31)$$

Whilst traditional NMR experiments typically involve measuring a single species or a single species dissolved in a solute, the ability to measure diffusion coupled with the realisation that a single diffusion coefficient is linked to one entire molecule opens up the possibility of spectrally separating mixtures of species on the basis of the respective diffusion coefficients[105] with some terming it 'NMR chromatography'.

As shown by eqn (3.31), $S(\nu,q)$ is the Laplace transform of the Laplace spectrum of diffusion coefficients $S_D(\nu,D)$. In theory it is possible to retrieve a spectrum of diffusion coefficients, by performing an inverse Laplace transform of equation (3.31). A 2D spectrum in which the chemical shift is given on one axis with the diffusion coefficient on the other has become known as a DOSY plot (see Figure 3.4).[4] Despite the apparent simplicity of this

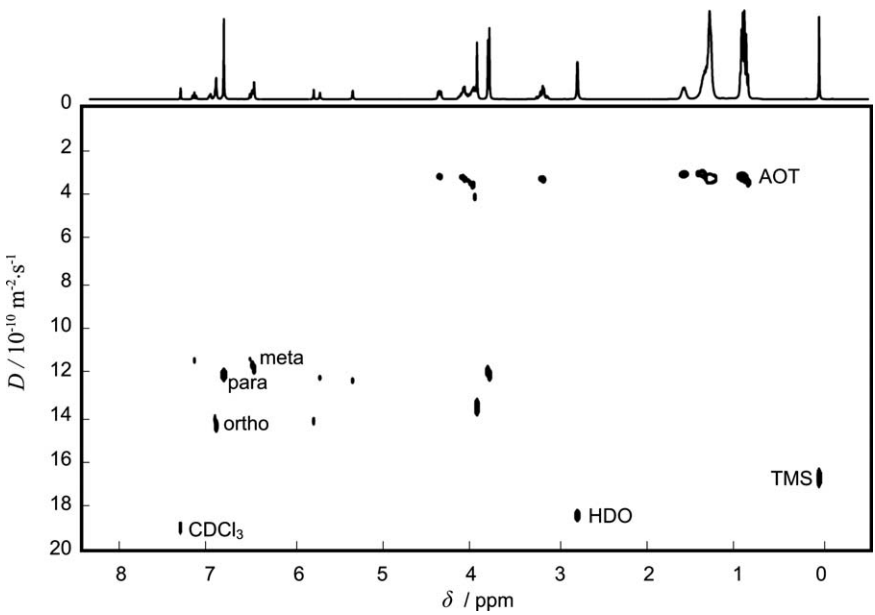

Figure 3.4 400 MHz ^{1}H DOSY plot of a sample containing 20 mmol · dm^{-3} of each of the methoxyphenol isomers and 52 mmol · dm^{-3} disodium 5,12-diethyl-7,10-dioxo-8-sulfo-hexadecane-7,10-diolate {sodium 1,4-bis(2-ethylhexyl)sulfosuccinate given the acronym {AOT}} in $CDCl_3$, with tetramethylsilane (TMS) as reference. The signals for the 1,2-methoxyphenol, 1,3-methoxyphenol and 1,4-methoxyphenol are labelled ortho, meta and para, respectively.[108]
Reproduced with permission from C. F. Tormena, R. Evans, S. Haiber, M. Nilsson and G. A. Morris, *Magn. Reson. Chem.*, 2012, **50**, 458.

approach, it is a mathematically ill-conditioned problem and, unless there are distinct resonances or vastly different diffusion coefficients, prior knowledge is required to obtain meaningful results, and numerous approaches are available.[106–108]

References

1. E. R. Cohen, T. Cvitas, J. G. Frey, B. Holmström, K. Kuchitsu, R. Marquardt, I. Mills, F. Pavese, M. Quack, J. Stohner, H. L. Strauss, M. Takami and A. J. Thor, *Quantities, Units and Symbols in Physical Chemistry, IUPAC Green Book*, 3rd edn, second printing, IUPAC & RSC Publishing, Cambridge, 2008.
2. J. Kärger, H. Pfeifer and W. Heink, *Adv. Magn. Reson.*, 1988, **12**, 1.
3. P. T. Callaghan, *Principles of Nuclear Magnetic Resonance Microscopy*, Clarendon Press, Oxford, 1991.
4. R. Kimmich, *NMR: Tomography, Diffusometry, Relaxometry*, Springer Verlag, Berlin, 1997.
5. C. S. Johnson, Jr., *Prog. NMR Spectrosc.*, 1999, **34**, 203.
6. G. A. Morris, in *Encyclopedia of Nuclear Magnetic Resonance*, ed. D. M. Grant and R. K. Harris, Wiley, New York, 2002, vol. 9, pp. 35–44.
7. I. Ardelean and R. Kimmich, in *Annual Reports on NMR Spectroscopy*, ed. G. A. Webb, Academic Press, London, 2003, vol. 49, pp. 43–115.
8. W. S. Price, *NMR Studies of Translational Motion: Principles and Applications*, Cambridge University Press, Cambridge, 2009.
9. P. Stilbs, in *Encyclopedia of Analytical Chemistry* ed. R. A. Meyers, Wiley, New York, 2009, vol. S1–S3, pp. 1439–1461.
10. P. T. Callaghan, *Translational Dynamics & Magnetic Resonance*, Oxford University Press, Oxford, 2011.
11. R. W. Mair, D. G. Cory, S. Peled, C.-H. Tseng, S. Patz and R. L. Walsworth, *J. Magn. Reson.*, 1998, **135**, 478.
12. K. Ulrich, P. Galvosas, J. Kärger and F. Grinberg, *Phys. Rev. Lett.*, 2009, **102**, 037801.
13. I. Furó and H. Jóhannesson, *J. Magn. Reson. A*, 1996, **119**, 15.
14. *Diffusion MRI: Theory, Methods, and Applications*, ed. D. K. Jones, Oxford University Press, Oxford, 2011.
15. H. Y. Carr and E. M. Purcell, *Phys. Rev.*, 1954, **94**, 630.
16. E. Fukushima, *Annu. Rev. Fluid Mech.*, 1999, **31**, 95.
17. B. Newling, *Prog. NMR Spectrosc.*, 2008, **52**, 31.
18. K. J. Packer, *Mol. Phys.*, 1969, **17**, 355.
19. M. Holz and C. Müler, *Ber. Bunsenges. Phys. Chem.*, 1982, **86**, 141.
20. P. Stilbs and I. Furó, *Curr. Opin. Colloid Interface Sci.*, 2006, **11**, 3.
21. P. Debye, *Polar Molecules*, Dover Publications, New York, 1945.
22. N. Bloembergen, E. M. Purcell and R. V. Pound, *Phys. Rev.*, 1948, **73**, 679.
23. W. Sutherland, *Philos. Mag.*, 1905, **S.6, 9**, 781.
24. A. Einstein, *Investigations on the Theory of Brownian Movement*, Dover Publications, New York, 1956.

25. G. A. Truskey, F. Yuan and D. F. Katz, *Transport Phenomena in Biological Systems*, Prentice Hall, New York, 2003.
26. J. Kowalewski and L. Mäler, *Nuclear Spin Relaxation in Liquids: Theory, Experiments, and Applications*, Taylor & Francis, New York, 2006.
27. W. S. Price, P. W. Kuchel and B. A. Cornell, *Biophys. Chem.*, 1989, **33**, 205.
28. W. S. Price, B. C. Perng, C. L. Tsai and L. P. Hwang, *Biophys. J.*, 1992, **61**, 621.
29. O. R. Mercier, M. W. Hunter and P. T. Callaghan, *Cold Regions Science and Technology*, 2005, **42**, 96.
30. J. Crank, *The Mathematics of Diffusion*, Oxford University Press, Oxford, 1975.
31. H. S. Carslaw and J. C. Jaeger, *Conduction of Heat in Solids*, Oxford University Press, Oxford, 1959.
32. K. A. Dill and S. Bromberg, *Molecular Driving Forces: Statistical Thermodynamics in Biology, Chemistry, Physics, and Nanoscience*, Garland Science, New York, 2011.
33. K. Hayamizu, S. Tsuzuki, S. Seki and Y. Umebayashi, *J. Chem. Phys.*, 2011, **135**, 084505.
34. S. V. Dvinskikh and I. Furó, *Russ. Chem. Rev.*, 2006, **75**, 497.
35. P. J. Basser and D. K. Jones, *NMR Biomed.*, 2002, **15**, 456.
36. J. E. Tanner and E. O. Stejskal, *J. Chem. Phys.*, 1968, **49**, 1768.
37. P. T. Callaghan, D. MacGowan, K. J. Packer and F. O. Zelaya, *J. Magn. Reson.*, 1990, **90**, 177.
38. P. T. Callaghan, A. Coy, D. MacGowan, K. J. Packer and F. O. Zelaya, *Nature*, 1991, **351**, 467.
39. D. G. Cory and A. N. Garroway, *Magn. Reson. Med.*, 1990, **14**, 435.
40. H. G. Hertz, in *Molecular Motions in Liquids*, ed. J. Lascombe, Reidel, Dordrecht, 1974, pp. 337–357.
41. B. Ghadirian, A. M. Torres, N. N. Yadav and W. S. Price, *J. Chem. Phys.*, 2013, **138**, 094202.
42. C. H. Neuman, *J. Chem. Phys.*, 1974, **60**, 4508.
43. D. S. Grebenkov, *Rev. Mod. Phys.*, 2007, **79**, 1077.
44. M. Nordin, M. Nilsson-Jacobi and M. Nydén, *J. Magn. Reson.*, 2011, **212**, 274.
45. B. F. Moroney, T. Stait-Gardner, B. Ghadirian, N. N. Yadav and W. S. Price, *J. Magn. Reson.*, 2013, **234**, 165.
46. F. Stallmach and P. Galvosas, in *Annual Reports on NMR Spectroscopy*, ed. G. A. Webb, Elsevier, London, 2007, vol. 61, pp. 51–131.
47. M. L. Johns and K. G. Hollingsworth, *Prog. NMR Spectrosc.*, 2007, **50**, 51.
48. O. Söderman, P. Stilbs and W. S. Price, *Concepts Magn. Reson. A*, 2004, **23**, 121.
49. K. J. Dunn, D. J. Bergman and G. A. Latorraca, *Nuclear Magnetic Resonance: Petrophysical and Logging Applications*, Elsevier, New York, 2002.
50. H. C. Torrey, *Phys. Rev.*, 1956, **104**, 563.
51. E. O. Stejskal and J. E. Tanner, *J. Chem. Phys.*, 1965, **42**, 288.

52. W. S. Price and O. Söderman, *Isr. J. Chem.*, 2003, **43**, 25.
53. P. T. Callaghan, *J. Magn. Reson.*, 1997, **129**, 74.
54. A. V. Barzykin, *J. Magn. Reson.*, 1999, **139**, 342.
55. W. S. Price and P. W. Kuchel, *J. Magn. Reson.*, 1991, **94**, 133.
56. W. S. Price, P. Stilbs, B. Jönsson and O. Söderman, *J. Magn. Reson.*, 2001, **150**, 49.
57. W. S. Price, *Concepts Magn. Reson.*, 1998, **10**, 197.
58. Y. Xia, *Concepts Magn. Reson.*, 1996, **8**, 205.
59. B. Antalek, *Concepts Magn. Reson.*, 2002, **14**, 225.
60. R. M. Cotts, M. J. R. Hoch, T. Sun and J. T. Markert, *J. Magn. Reson.*, 1989, **83**, 252.
61. P. Z. Sun, J. G. Seland and D. Cory, *J. Magn. Reson.*, 2003, **161**, 168.
62. G. Zheng and W. S. Price, *Concepts Magn. Reson. A*, 2007, **30**, 261.
63. G. Zheng and W. S. Price, *J. Magn. Reson.*, 2008, **195**, 40.
64. W. S. Price, K. Hayamizu, H. Ide and Y. Arata, *J. Magn. Reson.*, 1999, **139**, 205.
65. D. Wu, A. Chen and C. S. Johnson, Jr., *J. Magn. Reson. A*, 1995, **115**, 260.
66. D. J. Jensen, W. W. Brey, J. L. Delayre and P. A. Narayana, *Med. Phys.*, 1987, **14**, 859.
67. E. von Meerwall and M. Kamat, *J. Magn. Reson.*, 1989, **83**, 309.
68. P. T. Callaghan, *J. Magn. Reson.*, 1990, **88**, 493.
69. M. I. Hrovat and C. G. Wade, *J. Magn. Reson.*, 1981, **44**, 62.
70. M. D. Pelta, G. A. Morris, M. J. Stchedroff and S. J. Hammond, *Magn. Reson. Chem.*, 2002, **40**, S147.
71. A. M. Torres, G. Zheng and W. S. Price, *Magn. Reson. Chem.*, 2010, **48**, 129.
72. J. A. Aguilar, S. Faulkner, M. Nilsson and G. A. Morris, *Angew. Chem., Int. Ed.*, 2010, **49**, 3901.
73. G. Suryan, *Curr. Sci.*, 1949, **6**, 203.
74. V. V. Krishnan, *Curr. Sci.*, 1998, **74**, 1049.
75. V. V. Krishnan and N. Murali, *Prog. NMR Spectrosc.*, 2013, **68**, 41.
76. N. Bloembergen and R. V. Pound, *Phys. Rev.*, 1954, **95**, 8.
77. W. S. Price, K. Hayamizu and Y. Arata, *J. Magn. Reson.*, 1997, **126**, 256.
78. W. S. Price and M. Wälchli, *Magn. Reson. Chem.*, 2002, **40**, S128.
79. S. Y. Huang, Y. Y. Lin, N. Lisitza and W. S. Warren, *J. Chem. Phys.*, 2002, **116**, 10325.
80. Y. Y. Lin, N. Lisitza, S. Ahn and W. S. Warren, *Science*, 2000, **290**, 118.
81. G. Zheng and W. S. Price, *Prog. NMR Spectrosc.*, 2010, **56**, 267.
82. M. Piotto, V. Saudek and V. Sklenár, *J. Biomol. NMR*, 1992, **2**, 661.
83. W. S. Price, F. Elwinger, C. c. Vigouroux and P. Stilbs, *Magn. Reson. Chem.*, 2002, **40**, 391.
84. G. Zheng, T. Stait-Gardner, P. G. Anil Kumar, A. M. Torres and W. S. Price, *J. Magn. Reson.*, 2008, **191**, 159.
85. R. Mills, *J. Phys. Chem.*, 1973, **77**, 685.
86. N. N. Yadav, A. M. Torres and W. S. Price, *J. Magn. Reson.*, 2008, **194**, 25.
87. W. A. Bubb, K. Kirk and P. W. Kuchel, *J. Magn. Reson.*, 1988, **77**, 363.

88. D. S. Raiford, C. L. Fisk and E. D. Becker, *Anal. Chem.*, 1979, **51**, 2050.
89. W. J. Goux, L. A. Verkruyse and S. J. Salter, *J. Magn. Reson.*, 1990, **88**, 609.
90. A. Jerschow and C. Müler, *J. Magn. Reson.*, 1997, **125**.
91. N. Hedin, T. Y. Yu and I. Furó, *Langmuir*, 2000, **16**, 7548.
92. K. Hayamizu and W. S. Price, *J. Magn. Reson.*, 2004, **167**, 328.
93. G. Zheng and W. S. Price, *J. Biomol. NMR*, 2009, **45**, 295.
94. N. K. Bär, J. Kärger, C. Krause, W. Schmitz and G. Seiffert, *J. Magn. Reson. A*, 1995, **113**, 278.
95. E. L. Hahn, *Phys. Rev.*, 1950, **80**, 580.
96. J. E. Tanner, *J. Chem. Phys.*, 1970, **52**, 2523.
97. S. Meiboom and D. Gill, *Rev. Sci. Instrum.*, 1958, **29**, 688.
98. K. J. Packer, C. Rees and D. J. Tomlinson, *Mol. Phys.*, 1970, **18**, 421.
99. B. Gross and R. Kosfeld, *Messtechnik*, 1969, **7**, 171.
100. P. T. Callaghan and J. Stepišnik, *Adv. Magn. Opt. Reson.*, 1996, **19**, 325.
101. D. Canet, *Prog. NMR Spectrosc.*, 1997, **30**, 101.
102. T. Stait-Gardner, P. G. Anil Kumar and W. S. Price, *Chem. Phys. Lett.*, 2008, **462**, 331.
103. G. H. Sørland, H. W. Anthonsen, K. Zick, J. Sjöblom and S. Simon, *Diffusion Fundamentals*, 2011, **15**, 1.
104. G. A. Morris, H. Barjat and T. J. Horne, *Prog. NMR Spectrosc.*, 1997, **31**, 197.
105. P. Stilbs, *Anal. Chem.*, 1981, **53**, 2135.
106. P. Stilbs, *J. Magn. Reson.*, 1998, **135**, 236.
107. M. Nilsson, *J. Magn. Reson.*, 2009, **200**, 296.
108. P. Stilbs, *Eur. Biophys. J.*, 2013, **42**, 25.

CHAPTER 4

Viscometers

AGÍLIO A. H. PÁDUA, DAISUKE TOMIDA, CHIAKI YOKOYAMA, EVAN H. ABRAMSON, ROBERT F. BERG, ERIC F. MAY, MICHAEL R. MOLDOVER AND ARNO LAESECKE

4.1 Vibrating-wire Viscometer

AGÍLIO A. H. PÁDUA

Vibrating-wire sensors have been prominent in viscometry ever since the measurements in liquid He in the 1960s[1] using the attenuation of transverse oscillations in a tensioned wire; the measurement was founded on a hydrodynamic analysis by Stokes of the damping of fluids on oscillating bodies. Our understanding of the technique has since progressed considerably, driven by W.A. Wakeham and collaborators who designed viscometers for wide ranges of conditions. Vibrating-wire viscometers[2] and densimeters[3] were reviewed in previous books in this series. The field has seen significant developments over the last twenty years and is active at present, with improvements and extensions of the capabilities of the method.

Curiously, two communities work on vibrating-wire viscometers: one of low-temperature physicists studying superfluid ^{4}He and ^{3}He at temperatures below 1 mK. Recent reports in this field use vibrating-wire probes to observe hydrodynamic phenomena in quantum liquids[4] and not primarily to determine viscosity accurately. The other community, of physical chemists and chemical engineers, studies transport properties for application in devices and processes, often at high pressure (up to 1 GPa),[5] seeking to improve the quantitative determination of viscosity. About 200 scientific papers deal with

Experimental Thermodynamics Volume IX: Advances in Transport Properties of Fluids
Edited by M. J. Assael, A. R. H. Goodwin, V. Vesovic and W. A. Wakeham

Published by the Royal Society of Chemistry, www.rsc.org

vibrating-wire measurements, so a full account on the field is not possible here. The main recent developments concern:

1. Performing absolute viscosity measurements.
2. Extending the operation limits towards gases or high-viscosity liquids.
3. Characterising new viscosity reference substances.
4. Improving our understanding of the sensor (mode of operation, detection or simultaneous density measurements).
5. Designing robust and practical sensors for measurements *in situ*.

4.1.1 Principle of Operation

In a vibrating-wire viscometer the damping of transverse oscillations is related to the viscosity of the surrounding fluid. This setup benefits from a complete and accurate physical description. First, the mechanics of oscillation of a thin rod is described within the elastic limit for clamped, pinned or free end conditions. Second, the hydrodynamics associated with the motion of the wire in an incompressible, Newtonian fluid is understood.[6,7] Third, the output signal is resolved using equivalent circuits,[8] although optical detection has been reported.[9] The three pieces of the analytical model are rigorous within defined limits[6,7] that can be met in practice. The working equations are slightly different for steady-state or decay modes, and the equivalent circuit depends on the instrumentation, so the reader is referred to the literature.[6–8,10,11] The main point is that the sensor response is expressed purely in terms of physical parameters of the wire (length, radius, density, Young's modulus), and of the density and viscosity of the fluid. The theory specifies conditions: the radius of the wire must be much smaller than its length and the amplitude of vibration small, the walls of the container must be distant from the wire, the compressibility of the fluid negligible, and the flow laminar. A vibrating-wire viscometer should be able to perform absolute measurements (without calibration against a standard) provided its parameters are characterised by independent means and the fluid density is known.

The vibrating-wire viscometer is composed of a conducting wire tensioned in a support, placed inside a permanent magnetic field, both to drive the sensor and to obtain its response. The magnets can be mounted outside the enclosure or high-pressure vessel,[12–14] for a smaller volume, higher pressure range, and no compatibility issues between the magnets and the sample. The drawbacks are that the vessel has to be non-magnetic (which can limit the pressure) and the magnets bigger. In other designs the magnets, sometimes gold-plated to improve corrosion resistance, are inside the pressure vessel[11,15] forming a tightly integrated sensor suitable for *in situ* measurements.[16] It is often reported that the magnetic field should be aligned with certain directions imposed by the wire or the mounting in order to select a pure resonance, otherwise two resonant frequencies are observed, due to anisotropy of the wire material, an elliptical cross-section or to deformations produced by the clamping fixture.

The wire is driven into transverse oscillations by an alternating current, which generates a periodic force, and the velocity is detected as a voltage induced by the displacement in the magnetic field.[8,17] This electromechanical oscillator interacts with other electrical impedances of the instrumentation, which must be accounted for in order to extract the intrinsic signal of the sensor.[8,18–20] Some non-viscous damping is present, either due to inelastic loss within the wire (negligible at low amplitudes), friction at the clamped ends or magnetic damping.[8,17,21] Non-viscous damping is independent of the fluid and is evaluated by a measurement of the resonant characteristics in vacuum.[6,7] Non-viscous damping becomes more relevant for low viscosities (gases).[21]

The sensor can be operated in either forced, steady-state or in ring-down, transient decay. The decay mode was initially the choice for viscometry.[1,22,23] The wire is set into forced vibration or plucked for a few cycles and then the free damped oscillations are recorded, as shown in Figure 4.1. The typical time for one acquisition is 20 ms in liquids[23,24] and 100 ms in gases,[21] so multiple sampling can be done to reduce noise. Because of the short time, the transient mode is suitable for online, flow measurements.[24] The working theory limits the lateral displacement to a few per cent of the wire radius. In the transient mode, however, the wire is driven at relatively high amplitudes,[25] and, especially for gases where thinner wires are used, it is important to check the applicability of the theory by extrapolating to zero amplitude.[21]

In the forced mode a frequency range encompassing the resonance peak is scanned to describe amplitude and phase,[12,20] as shown in Figure 4.2.

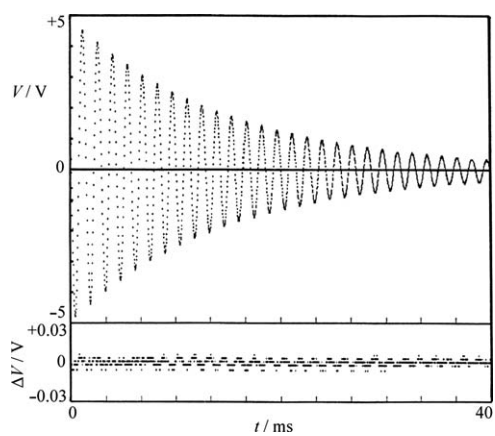

Figure 4.1 Top: Output motional electric potential difference V of the vibrating-wire viscometer immersed in methylbenzene operated in the transient mode as a function of time t.[26] Bottom: ΔV difference between the measured electric potential difference and that obtained from the working equations with the optimized viscosity at a known density.

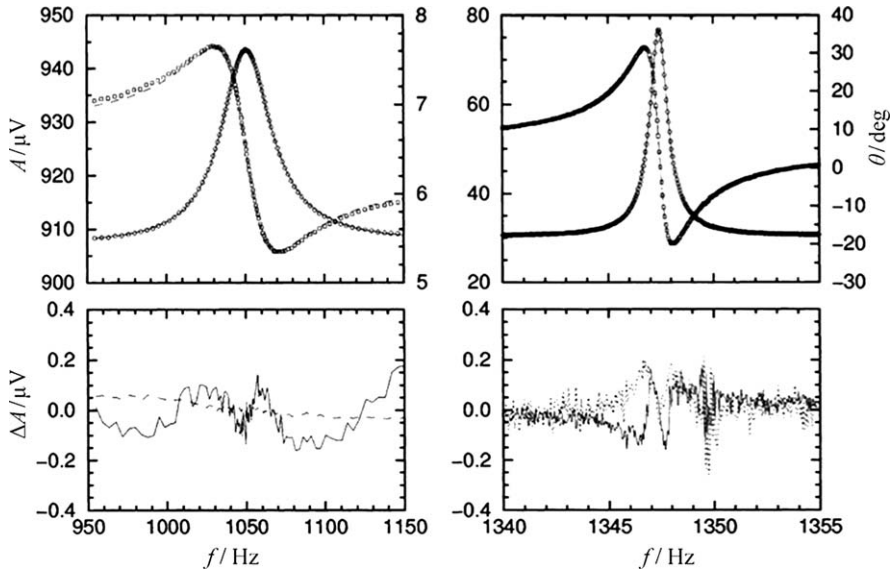

Figure 4.2 Output amplitude A and phase θ of the vibrating viscometer operated in forced oscillation. Left: vibrating wire immersed in water. Right: vibrating wire immersed in vacuum.[12] In this case, the wire was clamped at the upper end in a rigid support. A mass was suspended from the lower end so that, invoking Archimedes principle, the density was also determined simultaneously from the variation of the resonance frequency. The lines are those obtained from the working equations.

A lock-in amplifier filters out noise outside the frequency of interest and is extremely sensitive, allowing the wire to be driven at low amplitudes. The acquisition of one curve can take 600 s because the signal must stabilize after each frequency step. To have the best of both worlds, researchers devised ways of accounting for the nonlinear effects at high amplitudes[25] and use the transient mode for fast and accurate measurements.

One issue in viscometry is that the density of the fluid must be known to determine the dynamic viscosity, since the hydrodynamics of the measurement involve viscous and inertial terms. The vibrating wire is sensitive to the density through an added, hydrodynamic mass of fluid accelerated with the wire. Unfortunately, the sensitivity arising from the hydrodynamic mass is not sufficient for a precise determination of density. To circumvent this, a vibrating-wire viscometer can be coupled with a densimeter[27] and both properties measured simultaneously. An elegant alternative is to amplify the sensitivity to the density using Archimedes' principle.[10,12,18,28] In this design the vibrating wire is vertically tensioned by a suspended weight that will define the resonant frequency in vacuum. When the wire and weight are immersed in a fluid, the buoyancy on the weight lowers the resonant frequency (Figure 4.2). The measurement of density and viscosity is an enormous advantage but has some downsides. First, the instrument is delicate

because of the suspended weight. Also, the ''return'' of the signal requires a connection on the weight without altering the wire tension. Last, the volume of the weight must be known. But the vibrating-wire densimeter–viscometer is also described by rigorous theory. It was used at pressures up to 200 MPa providing relative uncertainties ($k = 2$) in density and viscosity of ± 0.2 % and ± 2 %, respectively.[10,12,18,28]

4.1.2 Absolute *versus* Relative Measurements

The distinction between absolute and relative measurements is not binary. A relative method is one without a full theory and the working equations contain empirical parameters whose values are determined using reference substances, often in the same conditions as the measurements, and even with properties similar to the sample. An absolute method is described by accurate equations containing only quantities with rigorous physical sense, accessible independently. Such a method will produce accurate results in diverse conditions. But, because of practical limitations, it may happen that a rigorous theory is available but some of the physical parameters are difficult to determine independently with the required accuracy. That method will be quasi-absolute in the sense that calibration is necessary to obtain the one or few problematic parameters, and this can be done using standard samples and conditions. From then, the accuracy should match that of a truly absolute method. The calibration step may hide deficiencies and some parameters will be ''effective'', compensating or averaging aspects that are not described well, lowering uncertainty far from the calibration point. This discussion is pertinent for measurements in general, but for viscosity it is crucial because few substances qualify as standards, and viscosity can cover many orders of magnitude according to chemical composition, temperature or pressure. Such an extent places a demanding requirement on viscometry techniques, thence the search for absolute methods.

It was demonstrated that the vibrating-wire viscometer is absolute, provided special care is taken in the manufacture and characterization of its components. The radius of the wire is the most difficult parameter to determine independently (radii range from 10 μm for gases, to 50 μm for liquids, and up to 200 μm for high viscosities). The uniformity and shape of the cross-section are important issues, as is the surface smoothness. Tungsten is chosen because of its high density, Young's modulus and tensile strength, low thermal expansion and chemical inertness. Until recently most viscometers had been built with wire of high purity but poorly characterised radius, therefore they were operated in a quasi-absolute manner, determining the radius from one calibration point. To measure the density simultaneously using the buoyancy effect, the volume of the weight should be known within ± 0.1 %. This volume can be obtained together with the wire radius from one calibration (in water[12] or methylbenzene[18]) although it can be determined independently.[10] For operation in wide ranges of conditions it is important to take into account the effects of temperature

and pressure on the wire (and weight), so it is better to select materials with well-known thermal expansion coefficients and compressibility (and the temperature-dependence of Young's modulus[10]).

Only recently, two groups[10,29] tested sensors built with carefully prepared tungsten wires, obtained through grinding to a uniform section. In one report[29] the radius of the wire was measured independently in a metrology laboratory with a relative uncertainty of 3×10^{-4}. Electron microscopy showed much smoother surfaces than those of simply drawn wires.[10] "Calibration" of the radii of the ground wires using reference fluids yielded values that coincided with the independent measurements.[10] Absolute measurements[29] of the viscosity of water at $T = 293.15\,\mathrm{K}$ and $p = 101.325\,\mathrm{kPa}$ yielded $(1.001_9 \pm 0.009_0)\,\mathrm{mPa\cdot s}$, differing from the standard value relatively by 0.03 %. The sensitivity of the vibrating-wire viscometer can still be improved by using a thinner wire. Therefore, it was demonstrated that the vibrating-wire viscometer is absolute provided all its physical parameters are characterised.

4.1.3 High-viscosity Standards

Viscosity has enormous scientific and industrial importance, and many applications concern samples of significantly higher viscosity than water, as has been discussed in section 2.2.5. Since most viscometers are relative, with limited ranges, calibration at high viscosities involves several transfers to ensure traceability to the standard substance, a costly procedure subject to error propagation. No reference substance exists at high pressure, a limitation affecting domains from lubricants to reservoir fluids. Several hydrocarbons have been recommended as high-pressure references (up to 250 MPa for toluene[30]) but these are low-viscosity liquids. Vibrating-wire viscometers are suited to produce high-pressure data because they are composed of solid bodies and the working model is rigorous. They were used to characterise candidates for high-viscosity standards[31] such as 2,6,10,15,19,23-hexamethyltetracosane (commonly known as squalane)[32] and diisodecyl phtalate (DIDP)[11,14,33] at pressures above 100 MPa, with viscosities reaching 267 mPa s.[34] Various laboratories used different methods for comparison and some deviations arise from variations in sample purity.[35,36] Recent reports[11,14] review the data showing relative uncertainties of $\pm$ 2 % for vibrating-wire measurements and agreement between different techniques within $\pm$ 5 % (except for certain discrepancies[31,33]).

In the range above 100 $\mathrm{mPa\cdot s}$, damping is high and vibrating-wire sensors are operated at low quality factors,[33] which is not a problem to the hydrodynamic model, but the amplitude becomes difficult to detect (either attenuation is too rapid or the resonance peak is too flat). So the limit for high-viscosity samples is resolution. Recommended thermophysical property data should always be obtained using different techniques to avoid systematic errors and this provides an important role for the vibrating-wire method.

4.1.4 Expanding the Limits: Complex Fluids and Online Measurements

Recently several attempts expanded the limits of vibrating-wire viscometry, towards complex fluids and towards robust and practical sensor designs. Vibrating-wire viscometers were used with industrially-relevant fluids, such as non-chlorinated refrigerants[37] or bio-sourced components of fuels.[38] Low uncertainty measurements are never simple, but today the vibrating-wire method is well understood in organic liquids. Asymmetric mixtures, of molecules with different sizes or interactions, are challenging because variations in composition lead to large viscosity changes. Vibrating-wire viscometer–densimeters have been used with gas-condensate mixtures[39] and lubricant/refrigerant mixtures.[32,40] The overall uncertainties are comparable to those in pure liquids, demonstrating that vibrating-wire sensors can be used to study complex samples.

Electrically-conducting fluids have been approached with more suspicion. Even water was used as a calibrant only in 2001[12] (after one isolated report[41]) because of eventual corrosion or conduction, but today is the reference fluid of choice.[10,29] Ionic liquids demonstrate the applicability of the method to conducting fluids.[20,42] The conductivity of these salts is not enough to shunt the sensor, and viscosities of several ionic liquids were measured at pressures up to 50 MPa[42] with values reaching 500 mPa · s[20] with an uncertainty of ± 2 %, agreeing with the literature.

The vibrating-wire viscometer has many positive qualities: compact, defined uncertainty and not involving exotic materials or procedures. It is surprising that a commercial version has not yet reached market. Vibrating-wire piezometers (for geotechnical applications) and strain gauges have been commercialized for years proving their robustness. There is no reason a robust and practical vibrating-wire viscometer cannot be produced at competitive cost. Several attempts at miniaturizing have been reported, namely one design tailored for a reservoir-fluid storage and transportation vessel,[16] and microfluidic viscometers[43] with volume under 20 μL. The uncertainty in viscosity is ± 10 %, better than expected considering the close proximity of the container walls.[43] These minute instruments to not comply with the theoretical specifications of their more accurate predecessors and, in that case, another geometry, like a cantilever[44] or tuning-fork,[4] may be easier to fabricate with micro-electro-mechanical techniques.

The main strength of the vibrating-wire viscometer is the availability of a rigorous hydrodynamic model that enables absolute or quasi-absolute measurements. The possibility of simultaneous measurement of density is another advantage. Laboratories in several European countries, in China and in the USA contributed to develop the method, in terms of sensor design, of understanding its operation and extending its applicability. The field of vibrating-wire viscometry is active and promises exciting developments for the future, in academia and in industry.

4.2 Falling Body Viscometer Developments: Small Spheres

DAISUKE TOMIDA AND CHIAKI YOKOYAMA

Falling body methods that are used to measure viscosity include the falling ball, falling sinker, and rolling ball type methods. In recent years, the development of suitable precision measurement instruments has resulted in high precision absolute viscosity measurements using the falling ball method. This chapter describes recent developments in falling body viscometers, and discusses precision viscosity measurement using the falling ball method.

4.2.1 Falling Ball Viscometer

A falling ball viscometer is an instrument used to measure the falling velocity of a ball into a fluid, which is then used to determine the fluid's viscosity using Stokes' law. The viscosity, η, is calculated using:

$$\eta = \frac{d^2(\rho_s - \rho_l)g}{18v}, \tag{4.1}$$

where d is the diameter of the ball, ρ_s is the density of the ball, ρ_l is the density of the sample fluid, g is the local acceleration of the free-fall, and v is the terminal velocity of the falling ball.

However, this equation is only valid if the terminal velocity is reached, and if the ball falls in an unbound medium without inertial effects. We must apply a number of corrections to calculate the experimental terminal velocity. For fall within a cylindrical tube with a diameter D, the correction of the wall effect is given by Faxen[45] as

$$v_{corr} = v\left[1 - 2.10444\left(\frac{d}{D}\right) + 2.08877\left(\frac{d}{D}\right)^3 - 0.94813\left(\frac{d}{D}\right)^5 + \ldots\right]^{-1}. \tag{4.2}$$

To correct for the inertial effect, Oseen's approximation[46] in the Navier–Stokes equation gives

$$v_{corr} = v\left(1 + \frac{3}{16}Re\right)^{-1}, \tag{4.3}$$

where Re is the Reynolds number. A more complete correction due to the inertial effect was derived by Goldstein[47] as

$$v_{corr} = v\left(1 + \frac{3}{16}Re - \frac{19}{1280}Re + \frac{71}{20480}Re + \ldots\right)^{-1}. \tag{4.4}$$

These last two corrections particularly imply that the Reynolds number of the flow around the ball must be kept very low and it is the satisfaction of

this condition that has eluded many earlier experimenters but has recently been achieved with very small single-crystalline silicon spheres.[48,49]

The main difficulty when using this method is measuring the velocity of the ball and so the largest contribution to measurement uncertainty comes from the velocity measurement.[49–51] For this reason we pay particular attention to the techniques associated with that measurement that have been made possible by modern technology.

Mordant and Pinton[52] developed acoustic measurement systems based on the Doppler effect, using an ultrasonic wave returned by the falling particle. Lommntzsch *et al.*[50] proposed an alternative optical method in which the ball velocity (U_∞) is determined by the sum of its velocity in the field of the camera (U_{bc}) and the camera velocity (U_c), $U_\infty = U_{bc} + U_c$.

Fujii *et al.*[48,49] developed an absolute viscosity measurement method based on the falling ball method. They measured the falling velocity of the ball by laser interference tracking using a charge coupled device (CCD) camera. This falling velocity measurement system is shown in Figure 4.3. The z-scan motion of the CCD camera on the motorized stage tracks the falling motion of the ball to keep its image within a few pixels in the captured frames. At the same time, the vertical displacement of the moving camera as a function of time is measured by the laser interferometer, which is synchronized to the shutter timing of the camera. To remove the Abbe error caused by the pitch motion of the Z stage, both the vertical and angular (pitch) displacements of the moving camera are measured simultaneously, using a dual axes laser interferometer. By combining CCD image-processing technology with laser interference tracking technology, the position of the falling ball is measured with an uncertainty of approximately 150 nm.

Brizard *et al.*[51,53] developed a method that used a line scan CCD camera, as shown in Figure 4.4. The linear camera can obtain very high measurement resolutions and acquisition frequencies, and offers the possibility of taking quasi-instantaneous velocity measurements. This technique can measure the variations in the ball velocity along the tube, and observe its trajectory. Figure 4.5 presents the image of the ball seen by the line scan camera when

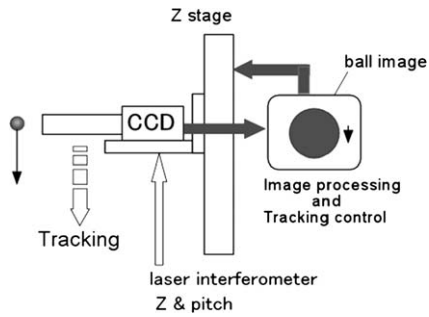

Figure 4.3 Principle of the falling ball viscometer that includes a measurement of the ball velocity.[49]

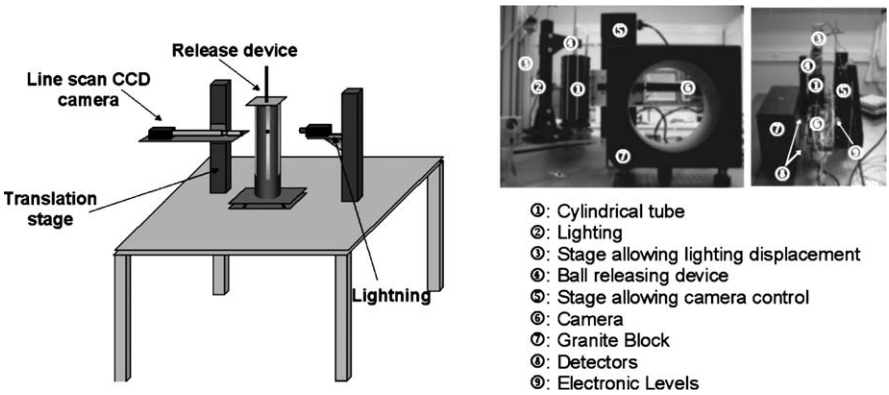

Figure 4.4 Diagram of the experimental set-up for the falling ball velocity measurement using a line scan CCD camera.[53]

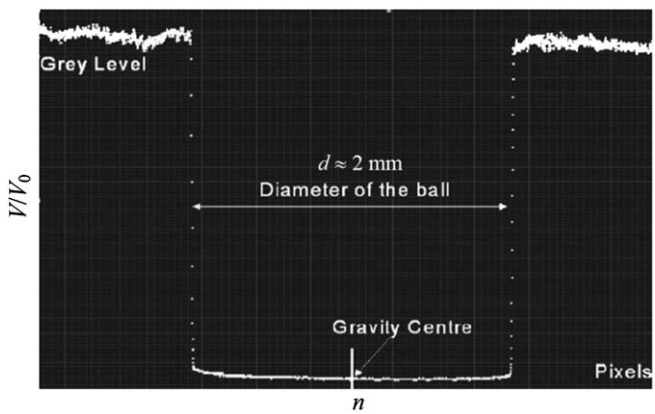

Figure 4.5 The ratio of the voltage V obtained from a charge coupled device (CCD) line-scan camera to an arbitrary reference voltage V_0 as the ball, of diameter $d \approx 2$ mm, passes in front of the lens at the time of release as a function of the number n of pixels; n can be converted to length with a calibration and, in this case, used 2000 pixels with a resolution of 1 pixel to determine the diameter d. The ball edge is determined from the gradient of response between the maximum grey level. These measurements permit the determination of the ball diameter, the barycentric position and, from knowledge of the time interval between two images obtained along a tube of length about 300 mm, the falling ball velocity.[53]

it passes in front of the lens. The ball edge is where the maximum gradient of the grey level is. This information allows one to measure the ball diameter as well as the barycentric position very accurately. By knowing the time interval between two images and the displacement of the barycenter, we can calculate the falling velocity.

The measurement of the ball's diameter is also one of the largest contributors to the uncertainty. Fujii *et al.*[48] developed technology that uses a

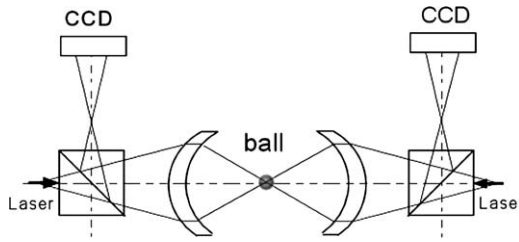

Figure 4.6 Principle of diameter measurement using phase-shifting interferometry with the spherical Fabry–Perot interferometer.[49]

single-crystal-silicon sphere as the falling ball. They used a single-crystal-silicon sphere with a diameter of 2 mm and a mass of approximately 7 mg. They measured the ball diameter using phase-shifting interferometry with the spherical Fabry–Perot interferometer as shown in Figure 4.6. A Fabry–Perot interferometer was then used to measure the diameter of a single-crystal-silicon sphere with a mass of 1 kg and a diameter of 94 mm, with an uncertainty of ± 3 nm.[54]

Feng *et al.*[55] studied falling ball viscometers in Newtonian fluids using a combination of theoretical analysis, experiments, and numerical simulations. They identified the error sources that affect the accuracy and reproducibility of these tests. They then presented the following recommendations to obtain high precision results.

- Use falling balls that are very consistent in terms of size, sphericity, and surface finish.
- Higher Anti-Friction Bearing Manufacturer's Association (AFMBA) grade balls provide more consistent results.
- Choose a falling ball and cylinder that result in a small a/D ratio ($a/D \leq 0.05$), which dramatically reduces the off-center error.
- Ensure that the apparatus is vertical and that the ball falls on the vertical axis.
- Multiple trials improve reproducibility and reduce measurement uncertainty.
- Improve the time measurement accuracy.

4.2.2 Falling Sinker-type Viscometer

The falling sinker-type viscometer is often used for precision high pressure viscosity measurements in fluids with high viscosities. Various versions of the experimental apparatus used for this method have been developed. The variations are usually in the methods that detect the passage of the body across the reference positions in the tube, or the exact shape of the falling-body. To perform accurate viscosity measurements using the falling body technique, we must consider various corrections (including the fall-tube

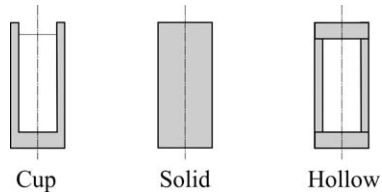

Figure 4.7 Cross-section view of sinker types for high-pressure falling body viscometer.[57]

dimensions, the effects of the fall-tube ends, the terminal velocity, the falling-body shape, and the position of the fall tube).

Daugé *et al.*[56] used a double tube to prevent any deformation of the inner tube, and measured viscosities at pressures up to 140 MPa. Both tubes contain the sample fluid, and the same pressure conditions exist inside and outside the inner tube.

Bair and Qureshi[57] used three different kinds of sinkers depending on the sample viscosity, as shown in Figure 4.7. The ''solid'' sinker has no central flow path and will fall at a velocity of 1 $mm \cdot s^{-1}$ for a viscosity of about 0.030 $Pa \cdot s$ (as shown in the center of Figure 4.7). The ''cup'' sinker has similar geometry, but its mass has been reduced by drilling so that it falls at a velocity of 1 $mm \cdot s^{-1}$ in a viscosity of 1.7 $mPa \cdot s$ (as shown in Figure 4.7). The ''hollow'' sinker has a central through-hole and falls at a velocity of 1 $mm \cdot s^{-1}$ for a viscosity of 5.5 $Pa \cdot s$.

Kumagai *et al.*[58] measured viscosity using a sinker that includes a γ-shaped stabilizer. This ensures that the sinker falls on the central axis. Kumagai *et al.* did not discuss details of the effect of this stabilizer on the viscosity measurements. They measured the viscosity of several mixtures of *n*-alkanes with squalane at temperatures between (273.15 and 333.15) K, and at pressures up to 30 MPa within relative uncertainties of $\pm 2.9\,\%$.

Sagdeev *et al.*[59] developed a falling-body viscometer that simultaneously measures the density. They confirmed the accuracy of the method using measurements of pure heptane at temperatures from (298 to 363) K and pressures up to 245 MPa. They measured the density and viscosity of pure polyethylene glycols, and their binary and ternary mixtures at temperatures from (293 to 472) K at atmospheric pressure within $\pm 2.0\,\%$ uncertainties.

4.3 Rolling Sphere Viscometry in a Diamond Anvil Cell

EVAN H. ABRAMSON

4.3.1 Introduction

Viscosities can be measured[60–63] in the high-pressure diamond-anvil cell (DAC) by dropping a sphere *through* the fluid, parallel to the two diamond faces, but results have a relative uncertainty of no better than $\pm 30\,\%$ owing to large wall effects coupled with an inability to release the sphere at precisely controlled distances from the diamonds.

King *et al.*[64] reasoned that if the sphere were instead allowed to roll down the inclined surface of one of the diamond anvils, the wall effect, although large, might be constant and therefore could be calibrated. Further, the large wall effect afforded by the near diamond would be expected to greatly lessen the relative effects of the far diamond, such that calibration would not be significantly altered by variations in the diamond-to-diamond gap as pressure was changed. Both these suppositions prove to be true.

The method has now been used to measure the shear viscosities of fluids to pressures in excess of 10 GPa and temperatures of 680 K. Viscosities have been recorded from values of 10^{-1} mPa·s up to 10^{10} mPa·s. The large compressions available in the DAC allow the use of density as an (experimentally) independent variable, in studies covering a range from the approximate hard-sphere behaviour of some supercritical fluids, to incipient glassing.

4.3.2 The Rolling Sphere

In a typical arrangement, shown in Figure 4.8, the DAC is tilted with respect to horizontal and a sphere of 30 μm to 70 μm in diameter is allowed to roll down the inner face of the lower diamond. The sphere is imaged onto a high-speed, digital camera and its position recorded as a function of time (Figure 4.9). The images are then analysed to give the terminal speed and, hence, viscosity.

For angles low enough that the sphere will roll (rather than slide) the translational speed v is given by:[66]

$$v = \left[\frac{2\gamma R^2(\rho_S - \rho_F)g}{9\eta}\right]\{\sin(\theta) - C\}, \tag{4.5}$$

where R is the sphere radius, ρ_S and ρ_F are the density of sphere and fluid, g the local gravitational acceleration of free fall, and θ the angle with respect to the horizontal. The factor γ, which relates to hydrodynamic forces, is independent of speed, angle and fluid, while C is presumed to derive from frictional forces and is observed to remain constant as the tilt angle changes.

Thus, if the experiment is repeated at several tilt angles, a plot of speed against sine of the angle yields a straight line with the viscosity inversely

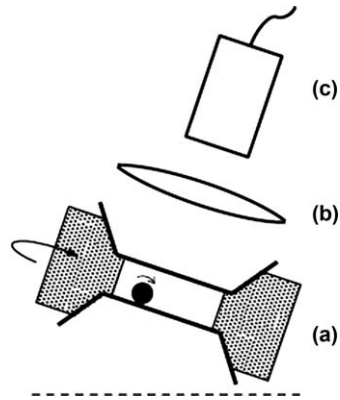

Figure 4.8 Schematic of a rolling sphere experiment. The DAC (a) is tilted, allowing a sphere to roll down the lower diamond face. The fluid is contained by the two diamonds and the steel gasket (stippled areas) into which they are impressed. The DAC can be rotated about an axis normal to the diamond faces, allowing the sphere to be brought to the top. A long-working-distance lens (b) images the contents of the DAC onto a high-speed, digital camera (c).

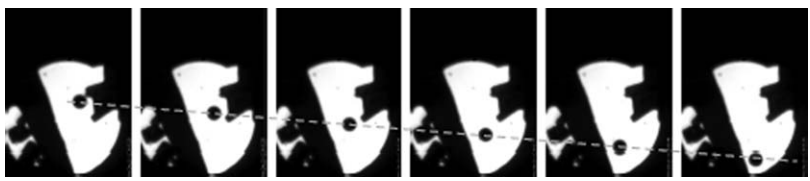

Figure 4.9 Photomicrographs of a back-lit sphere rolling in water,[65] at 30 ms intervals. The frames encompass a field of 410 μm by 547 μm and the sphere's diameter is 42 μm. The two salients machined into the gasket provide means for the sphere to detach itself from the wall. On the left side of the cell, a chamber containing water-soluble pressure markers is isolated by a gold separator. The straight, dashed line through the series of images is drawn as a (rough) indication of constant speed.

proportional to the slope as shown in Figure 4.10. No departure from inverse proportionality between η and the line's slope has been observed for Reynolds numbers, $2vR\rho_F/\eta$, ranging from 10^{-3} to 5. This result concurs with findings[67] for larger spheres (for Reynolds numbers less than 20 a fit of the data gave η proportional to $v^{-1.09}$, which is different from the inverse proportionality by less than the uncertainty of the exponent).

Within the theory of a smooth sphere rolling on a smooth plane surface[69] (see, for example, ref. 70 for a theory of a sphere with asperities), γ is a function solely of the ratio of the sphere's radius to the (presumed) small gap between sphere and surface. Measurements in our group give γ predominantly between 0.11 and 0.13, with outliers between 0.09 and 0.17. King *et al.*[64] gives $\gamma = 0.12$ to 0.14 for five out of six tests for which the sphere was

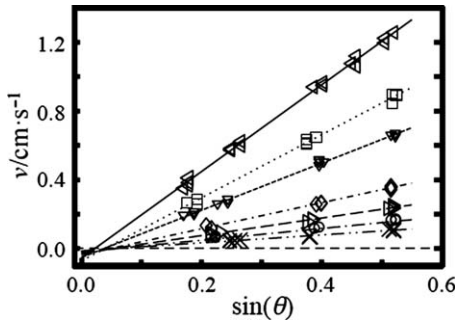

Figure 4.10 Translational speeds are plotted against the sine of the tilt angle for a sphere rolling in nitrogen[68] at $T = 294$ K. Lines are least-squares fits through the data for each pressure. ---, $p = 0.34$ GPa; · · ·, $p = 0.53$ GPa; - - -, $p = 0.69$ GPa; - · - ·, $p = 1.18$ GPa; -- -- --, $p = 1.56$ GPa; -- · -- · --, $p = 2.02$ GPa; -- · · -- · · --, $p = 2.45$ GPa. Long dashed line indicates $v = 0$. As the viscosity increases with pressure the speeds are seen to decrease correspondingly. Note that the abscissa intercept is non-zero, and that of the lowest pressure data differs significantly from the others.

likely not slipping. Similarly, macroscopic spheres with diameters (2 to 22) mm, of glass, cellulose acetate and poly(methyl 2-methylpropenoate), were found by Carty[67] to roll with $\gamma = 0.09$ to $\gamma = 0.12$.

Practically, γ is found by rolling the sphere in a fluid of known viscosity, methylbenzene and water being particularly useful as primary calibrants. This is best done with a pressure buffer consisting of an air bubble sealed into the DAC along with the fluid. In the absence of a bubble, errors in calibration develop (*e.g.*, the viscosity of methylbenzene[71] will double due to an accidental increase in pressure from 1 MPa to 100 MPa, which is less than the typical uncertainty of pressure measurement in the DAC). Raising the temperature by several hundred degrees will often result in a persistent change in γ of roughly 10 %, presumably due to modification of one or both surfaces; it is thus prudent to repeat lower temperature measurements occasionally.

Values of C are typically less than 0.10, and have often been assumed to be identically zero. However, even at the relatively large angle of $\theta = 40^\circ$, this assumption can amount to a large error in slope and thus viscosity. Beyond angles of $\approx 40^\circ$ a platinum sphere rolling on diamond has been observed to slip,[66] and speeds will increase above those given by eqn (4.5).

Viscosities recorded with this technique range from[72] (0.20 to 10^8) mPa · s;[64,73,74] modification of the technique to make use of a centrifuge has allowed measurements[73,75] to 10^{10} mPa · s. Most measurements have been of fluids which tend to glass at higher pressures,[64,73–76] but there has been at least one investigation of a dilute polymer solution[77] and several of small, non-glassing molecules,[64–66,68,78,79] some of the last set taken at pressures up to 10 GPa and temperatures up to 680 K. Such experiments

should be possible at temperatures in excess of 1000 K, limited by the materials and design of the DAC.

4.3.3 Error

Individual measurements of viscosities scatter with relative root-mean-square deviations of $\pm(2$ to $4)\%$. Comparisons with results obtained through other methods of viscometry, in an overlapping pressure range up to $\approx$ 1 GPa, usually show agreement close to, or within, stated uncertainties.[64,65,68,78,79] Measurements[64] of octamethly trisiloxane at pressures up to 1.3 GPa, extending over seven orders of magnitude in viscosity, agree with previous results within the ± 0.03 GPa uncertainty in the pressure measurement (which, however, propagates to give an uncertainty in viscosity of a factor of 3 at the highest pressures). Larger-than-expected deviations between DAC derived results and those derived from other techniques may be reasonably ascribed to inadequately modelled, pressure-induced strains in the more complex apparatus required by those techniques, particularly at higher temperatures.

For a sphere rolling in a DAC, the geometry of the sphere–surface interaction does not appear to change appreciably over the range of pressures and temperatures surveyed (the exception being the sporadic, and easily observed, change of γ with temperature noted above). For example, two different spheres used in measurements of fluid argon[79] (Figure 4.11) give the same results at temperatures from 294 K to 673 K, and pressures from 0.1 MPa (in calibrating fluids) to 5 GPa, even as the larger sphere (56 μm diameter) rolls approximately twice as fast as the smaller (38 μm) for any given viscosity and angle. Systematic errors appear to be either less than the scatter or common to all spheres.

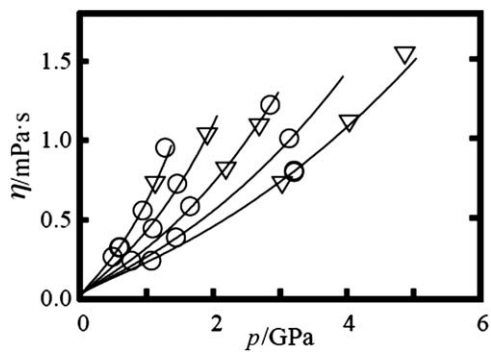

Figure 4.11 Viscosity, η, of argon[79] as a function of pressure along isotherms (from top to bottom) at temperatures of (294, 373, 473, 573 and 673) K. The curves represent a fit to a modified free-volume equation with four free parameters. ○, 38 μm diameter sphere; ▽, 56 μm diameter sphere.

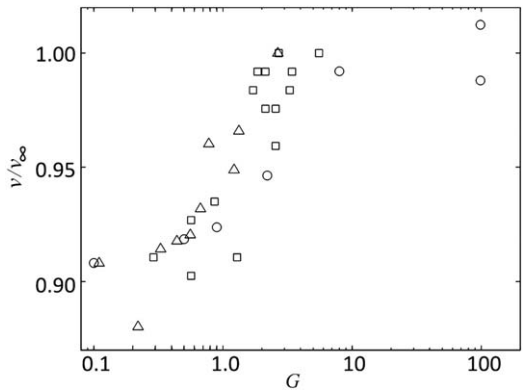

Figure 4.12 The effect on translational speed of the gap between the top of the sphere and the upper diamond surface. Speeds of three different spheres, v, normalized by their values at infinite gap, v_∞, are plotted against the ratio (G) of the gap to the sphere diameter. The spheres were rolled in methanol at an angle of $\theta = 30^\circ$. The sphere diameters were as follows: □, 70 μm; △, 90 μm; ○, 100 μm.

The gap between the top of the sphere and the upper diamond surface will vary with pressure and can be expected to influence the speed of roll. The effect of this parameter,[66] as Figure 4.12 shows, is small for ratios of gap to sphere diameter, G, between 0.1 and 1.0, more than the normal range of variation required for pressure changes in an experiment.

4.3.4 Experimental Details

In work described in the literature[65,68,72,78,79] the DAC is held in a temperature-controlled enclosure, itself mounted on a stage capable of rotation about an axis normal to the diamond surfaces. The cell is back-lit and imaged with a microscope (90 mm working distance, 9× working magnification, with a zoom out to 1.4× found useful for alignment) onto a CCD camera (with square pixels, 7.4 micron on a side, in a 640 by 480 array) recording 100 frames per second. The camera's electronic shutter is typically set at 200 μs, making it unnecessary to strobe the illumination (from a small, tungsten-halogen bulb, imaged into the cell). An electrolytic tilt gauge, the light source, rotation stage with mounted oven and cell, microscope, and camera are arrayed on a rigid, hinged beam adjustable from 0° to 90° with respect to the horizontal. With the beam in a horizontal position ($\theta = 90^\circ$) a laser may be focused onto a pressure marker included in the cell and the resulting fluorescence (or Raman scattering) imaged onto a monochromator.

Gasket holes in the DAC are typically between 300 μm and 500 μm in diameter although larger holes, and spheres, have been used in the analogous sapphire-anvil cell.[80,81] Terminal velocity[66] is usually achieved within about 0.01 s and decent measurements have been made with roll distances

comparable to the sphere's circumference, although longer rolls are preferred as they allow a better observation of any irregularities.

The sphere may be positioned toward the top of the cell by making use of its adhesion to the gasket edge (and then initiating the roll with a tap), by blocking its roll with another object (*e.g.*, a chip of ruby used for measuring pressure), or simply by rapid rotation of the cell. Occasionally the sphere will roll such as to maintain contact with the edge of the gasket. In such cases it is provident to machine a small projection into the gasket edge, sharp enough to cause the sphere to detach as shown in Figure 4.9.

Adhesive forces between the sphere and diamond surface vary greatly, with load, with load history and, occasionally, across the diamond surface. Sometimes the sphere will roll freely, often it will stick to the gasket edge as the cell is rotated but release with a gentle tap, and other times it cannot be dislodged even with a strong blow to the apparatus. A sphere which is stuck can usually be freed by freezing and then re-melting the fluid. Although such variable behaviour is vexing, it (surprisingly) does not appear to be associated with systematic differences in measured viscosity.

Platinum is particularly useful as a material for the spheres as it is relatively chemically inert and its high density ($21.4\ g \cdot cm^{-3}$) requires a less accurate knowledge of the fluid's equation-of-state for buoyancy correction. Within the range of pressures and temperatures for which this technique has so far been used, changes in density[82] of a Pt sphere require corrections to the calculated viscosity of relatively less than 1 %. Spheres have been made either by sprinkling flaked Pt into a flame [*e.g.*, (methane + oxygen)], or in electrical sparks created by intermittently bringing together two Pt wires at ≈ 50 V ac. In either case, the rain of spheres can be collected and graded (*e.g.*, by allowing them to roll down a microscope slide under ethanol), the best being selected for further use. Scanning electron micrographs of spheres made this way often reveal fissures which don't, however, seem to be a problem.

The tracks of the spheres can be determined easily with image processing software. For each roll, the sphere is found by eye in the first frame and its image defined, the software then searching subsequent frames for the best match. In order to compensate for any vibration of the cell with respect to the camera, the position of the sphere can be indexed with respect to an immobile object (usually a section of the gasket edge or the pressure marker), similarly located for each frame.

4.4 Gas Viscosity-ratio Measurements with Two-capillary Viscometers

ROBERT F. BERG, ERIC F. MAY, AND MICHAEL R. MOLDOVER

4.4.1 Introduction

In this section, we discuss the usefulness of gas viscosity ratios and how to obtain such ratios with single-capillary viscometers. Then, we focus on the two-capillary gas viscometer devised by May *et al.*[83,84] to measure gas viscosity ratios with very low uncertainties, and subsequently used by Zhang *et al.*[85] Further details, including a review of four-capillary viscometers and proposals to (i) extend the two-capillary viscometer technique to high pressures, and (ii) measure the water-to-helium viscosity ratio, will be published elsewhere.[86]

The Ar-to-He gas viscosity ratios measured by May *et al.* have proved useful for primary acoustic thermometry[87] and acoustic redeterminations of the Boltzmann constant.[88] These acoustic measurements require accurate values of the thermal conductivity of low density argon, which can be obtained by combining the measured Ar-to-He viscosity ratio with theoretical values of helium's viscosity and the Prandtl number for argon. The measured Ar-to-He viscosity ratio also has been used in the temperature range 200 K $< T <$ 400 K to test *ab initio* calculations of the viscosity and thermal conductivity of argon.[89,90] The relative uncertainty of the viscosity calculated from the Ar–Ar interatomic potential is estimated to be less than ± 0.1 % at temperatures as low as 80 K;[90] however, the uncertainty from the use of classical (rather than quantum-mechanical) calculation has not been quantified.[87] Thus, low uncertainty gas viscosity-ratio measurements at temperatures below 200 K would be a useful guide to theory. Similar measurements above 400 K would help resolve the current tension between measurements and the theory for the viscosity of hydrogen.[91]

The widespread practice of calibrating laminar flow meters with surrogate gases (such as helium or argon) and then using them to meter process gases requires accurate surrogate-to-process gas viscosity ratios.[92] With this application in mind, Berg and Moldover[93] reviewed two hundred viscosity measurements near the reference temperature $T_{\mathrm{ref}} = 298$ K and zero density for 11 gases, and determined the viscosity ratios among the gases with a relative uncertainty less than ± 0.04 %, which is smaller than the uncertainty of the separate absolute measurements.[84] They then anchored the measured viscosity ratios to the remarkably low uncertainty value

$$\eta^{\mathrm{He}}_{0,T_{\mathrm{ref}}} = (19.8253 \pm 0.0002)\mu\mathrm{Pa}\cdot\mathrm{s}, \tag{4.6}$$

calculated *ab initio* by Cencek *et al.*[94] (using only quantum mechanics, statistical mechanics, and fundamental constants) for helium at a temperature of 298.15 K and zero density. {In eqn (4.6) and the remainder of this section, the superscript is the gas g, the first subscript is the pressure p, and

Table 4.1 Reference viscosities,[93] obtained by fitting 235 viscosity ratios measured using 18 instruments. The first column gives the recommended value of $\eta^{g}_{0,T_{ref}}$, the viscosity at a temperature of $T_{ref} = 298.15$ K and zero density, and its standard ($k = 1$) uncertainty. The value for helium was calculated in ref. 94. The second column gives the corresponding ratios relative to helium. The third column gives the isothermal density derivative of the viscosity that was used to adjust measurements of viscosity to zero density. The fourth column gives the exponent a in the expression $\eta^{g}_{0,T} = \eta^{g}_{0,T_{ref}}(T/T_{ref})^{a}$ that was used to adjust $\eta^{g}_{0,T_{ref}}$ to T_{ref}. See ref. 93 for details and references.

B	$\frac{\eta^{g}_{0,T_{ref}}}{\mu Pa \cdot s}$	$\eta^{g}_{0,T_{ref}}/\eta^{He}_{0,T_{ref}}$	$\frac{10^4(d\eta/d\rho)\cdot\eta^{-1}}{m^3 \cdot kg^{-1}}$	a
H_2	8.8997 ± 0.0030	0.44891 ± 0.00034	19.2 ± 4.7	0.69
He	19.8253 ± 0.0002	1.00000 ± 0.00001	-1.1 ± 1.3	0.69
CH_4	11.0631 ± 0.0035	0.55803 ± 0.00031	19.2 ± 1.9	0.88
Ne	31.7088 ± 0.0100	1.59941 ± 0.00031	1.4 ± 0.1	0.68
N_2	17.7494 ± 0.0048	0.89529 ± 0.00027	6.3 ± 0.6	0.77
C_2H_6	9.2305 ± 0.0030	0.46559 ± 0.00033	8.2 ± 2.0	0.94
Ar	22.5666 ± 0.0060	1.13827 ± 0.00027	4.9 ± 0.5	0.85
C_3H_8	8.1399 ± 0.0028	0.41058 ± 0.00035	-4.9 ± 2.0	0.99
Kr	25.3062 ± 0.0080	1.27646 ± 0.00032	3.6 ± 0.5	0.92
Xe	23.0183 ± 0.0072	1.16106 ± 0.00031	2.7 ± 0.2	0.98
SF_6	15.2234 ± 0.0054	0.76788 ± 0.00036	0.6 ± 0.6	0.89

the second subscript is the temperature.}[†] Table 4.1 reproduces the viscosities recommended by Berg and Moldover.[93]

4.4.2 Single-capillary Viscometers

The molar flow rate $\dot{n}$ of a gas through a capillary with internal radius r and length L depends on temperature T and the pressures just upstream (p_1) and downstream (p_2) of the capillary as follows:[95,96]

$$\dot{n} = \frac{\pi r^4 (p_1^2 - p_2^2)}{16 L R T \eta^{g}_{0,T}} C^{g}(T, p_1, p_2). \tag{4.7}$$

In eqn (4.7), R is the universal gas constant, and $\eta^{g}_{0,T}$ is the viscosity determined for a gas g at temperature T in the limit of zero pressure. The first factor in eqn (4.7) comes from combining ideal-gas compressibility with the Hagen–Poiseuille equation for incompressible flow through a capillary,[97]

[†]Some might prefer the alternate notation illustrated by $\eta(g,p,T) = \eta(He,0,T_{ref})$.

and it estimates the flow rate to within a few percent for a gas near ambient temperature and pressure. The second factor,

$$C^g(T,p_1,p_2) \equiv \left(1+\sum_{i=1}^{5} c_i^g\right) f_{\text{cent}}(De, r/R_{\text{coil}}), \tag{4.8}$$

contains five terms c_i^g that are usually small corrections to the flow of an ideal gas through a straight capillary. They account for: (1) the density virial coefficients and the viscosity virial coefficient, (2) slip at the capillary wall, (3) the increase in the kinetic energy of the gas as it enters the capillary, (4) gas expansion along the length of the capillary, and (5) the radial temperature distribution within the gas resulting from gas expansion and viscous dissipation. The function f_{cent} accounts for the centrifugal effect that occurs when the capillary is coiled. It depends on the geometric ratio r/R_{coil}, where R_{coil} is the radius of curvature of the capillary coil, and the Dean number $De \equiv (r/R_{\text{coil}})^{1/2}Re$, where $Re \equiv 2M\dot{n}/(\pi r\bar{\eta})$ is the Reynolds number; M is the molar mass, and $\bar{\eta}$ is the viscosity at the average pressure defined by eqn (7) of ref. 95. Further details about each of the correction terms are given in ref. 95.

The most accurate gas viscosity ratios have been measured near room temperature; here we pay special attention to viscosity ratios at $T = 298.15$ K of dilute gases relative to that of helium, which we denote as $\eta^g_{0,T_{\text{ref}}}/\eta^{\text{He}}_{0,T_{\text{ref}}}$. In general, determining $\eta^g_{0,T_{\text{ref}}}/\eta^{\text{He}}_{0,T_{\text{ref}}}$ with a single-capillary viscometer requires measurements, for both gases, of the molar flow rate $\dot{n}$, the upstream and downstream pressures, and the temperature T of the capillary. One then applies eqn (4.8) twice, once for the test gas and once for helium, and forms the ratio of these two equations:

$$\frac{\eta^g_{0,T}}{\eta^{\text{He}}_{0,T}} = \frac{\left(p_1^2-p_2^2\right)_{\text{g}}}{\left(p_1^2-p_2^2\right)_{\text{He}}} \frac{\left(1+\sum_{i=1}^{5} c_i^g\right)}{\left(1+\sum_{i=1}^{5} c_i^{\text{He}}\right)} \frac{f_{\text{cent}}\left(De_{\text{g}}, r/R_{\text{coil}}\right)}{f_{\text{cent}}\left(De_{\text{He}}, r/R_{\text{coil}}\right)} \frac{\dot{n}_{\text{He}}}{\dot{n}_{\text{g}}}. \tag{4.9}$$

Eqn (4.9) is accurate when the capillary's geometry is consistent with the assumptions used to develop the hydrodynamic model. Three of the corrections in eqn (4.9) are proportional to r/L, so the radius-to-length ratio must be small. If the capillary is straight, small deviations of the capillary bore from circularity and uniformity are acceptable because the effective radius r is determined by fitting to the helium measurement. If a long capillary is wound into a coil, the coil's radius R_{coil} must be sufficiently uniform and well known to accurately calculate the correction function f_{cent}. The correction increases as $\varepsilon(De)^4$, where $\varepsilon \equiv 1 - y/x$ is a measure of the flatness of the capillary, and where x and y are the bore's (unknown) semi-radii.[84,95,96]

Eqn (4.9) includes a correction for slip flow that is proportional to the ratio of the mean free path to the capillary's radius: λ/r, where λ is the mean free path. The calculated correction assumes $\lambda/r << 1$. Helium requires special attention because, for a given temperature and pressure, its mean free path is the largest of any gas. More importantly, the momentum accommodation

coefficient for helium on smooth quartz glass deviates from unity and was observed to drift from year to year in the same capillary.[95]

Another effect sensitive to λ/r is the thermomolecular pressure gradient[98] that can occur when there is a large difference between the temperatures of the capillary and the pressure sensors. Not accounting for this effect will cause errors in p_1 and p_2 at sufficiently low pressures.

Determining $\eta^{g}_{0,T_{ref}}/\eta^{He}_{0,T_{ref}}$ with a single-capillary viscometer requires a flow meter with a nonlinearity and irreproducibility that are smaller than the desired uncertainty of the viscosity ratio. The flow meter's absolute uncertainty is less important because an incorrect calibration factor will cancel out of the factor $\dot{n}_{He}/\dot{n}_{g}$ in eqn (4.9) and affect only the corrections that are proportional to *Re* and *De*, where *De* is the Dean number.

4.4.3 Two-capillary Viscometers

A two-capillary viscometer, comprising two capillaries in series, can be used to measure the temperature dependence of viscosity ratios with small uncertainty and without the need for a flow meter. May *et al.*[83,84] developed and used such a viscometer to measure the viscosities of hydrogen, methane, argon, and xenon in the temperature range from 200 K to 400 K. They analysed their measurements with the relation,

$$\eta^{g}_{0,T} = \eta^{He}_{0,T_{ref}} \left(\frac{\eta^{He}_{0,T}}{\eta^{He}_{0,T_{ref}}}\right)_{\text{ab initio}} \left(\frac{\eta^{g}_{0,T_{ref}}}{\eta^{He}_{0,T_{ref}}}\right) R^{g,He}_{T,T_{ref}}. \tag{4.10}$$

Eqn (4.10) has four factors: (i), a reference value $\eta^{He}_{0,T_{ref}}$ for the viscosity of helium at zero density and 298.15 K, calculated *ab initio* from quantum mechanics and statistical mechanics;[94] (ii), the temperature-dependent ratio $(\eta^{He}_{0,T}/\eta^{He}_{0,T_{ref}})_{\text{ab initio}}$, also calculated *ab initio*;[94] (iii), a reference value for the viscosity ratio $\eta^{g}_{0,T_{ref}}/\eta^{He}_{0,T_{ref}}$ measured at 298.15 K;[93] and (iv), a measurement of the temperature-dependent ratio of viscosity ratios,

$$R^{g,He}_{T,T_{ref}} \equiv \left(\frac{\eta^{g}_{0,T}}{\eta^{He}_{0,T}}\right) \Big/ \left(\frac{\eta^{g}_{0,T_{ref}}}{\eta^{He}_{0,T_{ref}}}\right). \tag{4.11}$$

May *et al.*[83,84] used a single-capillary viscometer to measure $\eta^{g}_{0,T_{ref}}/\eta^{He}_{0,T_{ref}}$ and a two-capillary viscometer to measure $R^{g,He}_{T,T_{ref}}$. Such an approach is effective because the uncertainties of the theoretical quantities $\eta^{He}_{0,T}$ and $(\eta^{He}_{0,T}/\eta^{He}_{0,T_{ref}})_{\text{ab initio}}$ are less than $\pm 0.01\,\%$[94] and because the uncertainties of the measured values of the ratios $\eta^{g}_{0,T_{ref}}/\eta^{He}_{0,T_{ref}}$ and $R^{g,He}_{T,T_{ref}}$ are nearly equal to their precisions.

The reference ratio $\eta^{g}_{0,T_{ref}}/\eta^{He}_{0,T_{ref}}$ was measured by a single-capillary viscometer using the techniques and analysis described in ref. 83, 84 and 95, while $R^{g,He}_{T,T_{ref}}$ was measured over the temperature range of interest by the two-capillary viscometer shown in Figure 4.13. With the upstream capillary's temperature controlled at the reference temperature of 298.15 K, and the

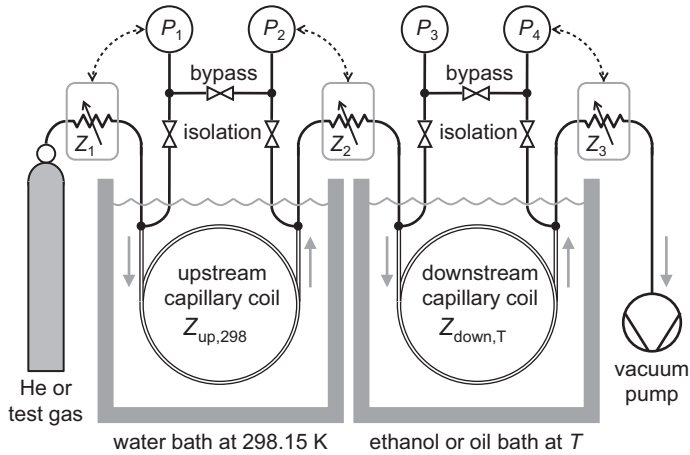

Figure 4.13 Schematic diagram of the two-capillary viscometer used by May *et al.*[83,84] The impedances Z_{up} and Z_{down} were coiled nickel capillaries with a length of 7 m and an inside diameter of 0.8 mm. The variable impedances Z_1 and Z_3 were piezoelectric gas leak valves, and Z_2 was either a leak valve or a mass flow controller.
(Reprinted from ref. 83 with permission of Springer.)

downstream capillary's temperature controlled at the measurement temperature T, helium and the test gas were flowed alternately through the two-capillary viscometer while the pressures were measured at the ends of both capillaries. Importantly, no flow rate measurements were required to determine $R^{g,He}_{T,T_{ref}}$.

Figure 4.13 indicates five flow impedances: the upstream and downstream capillaries, denoted respectively as $Z_{up,T_{ref}}$ and $Z_{down,T}$, each of which is connected to an upstream and downstream pressure gauge, and the variable impedances denoted as Z_1, Z_2 and Z_3. During a measurement p_1 and p_2 were maintained at constant, predetermined values by controlling Z_1 and Z_2. This established a stable but unknown gas flow rate $\dot{n}$ that was identical through both capillaries. If both $\dot{n}$ and $Z_{down,T}$ were known, eqn (4.7) could be used to determine the viscosity at the temperature T from accurate measurements of p_3 and p_4. However, $\dot{n}$ and $Z_{down,T}$ were unknown; therefore, eqn (4.7) was applied separately to the upstream and downstream capillaries to eliminate $\dot{n}$ and obtain an expression for the viscosity ratio $\eta^g_{0,T}/\eta^g_{0,T_{ref}}$ in terms of p_1, p_2, p_3 and p_4. Combining that expression for the test gas with a similar expression for the helium measurements yields the working equation:

$$R^{g,He}_{T,T_{ref}} = \frac{\left(p_3^2 - p_4^2\right)^g}{\left(p_1^2 - p_2^2\right)^g} \frac{\left(p_1^2 - p_2^2\right)^{He}}{\left(p_3^2 - p_4^2\right)^{He}} \frac{C^g(T,p_3,p_4)}{C^{He}(T,p_3,p_4)} \frac{C^{He}(T_{ref},p_1,p_2)}{C^g(T_{ref},p_1,p_2)}. \quad (4.12)$$

Eqn (4.12) does not contain the impedance ratio $Z_{up,T_{ref}}/Z_{down,T_{ref}}$, which depends on temperature through the thermal expansion of the downstream capillary. Instead, eqn (4.12) contains the viscosity ratio $\eta^{He}_{0,T}/\eta^{He}_{0,T_{ref}}$, which is

known from *ab initio* calculations. The dimensions of the capillaries appear only in the correction terms of eqn (4.8); therefore, approximate values of the dimensions are sufficient for eqn (4.12) . May *et al.*[83,84] used two coils of electroformed nickel tubing, each with a nominal internal diameter of 0.762 mm, a length of about 7.45 m, in a helical coil with a 0.1 m radius of curvature and a length of 0.04 m.

Stability and accurate measurements of temperature and pressure are central to the determinations of $\eta^{g}_{0,T_{ref}}/\eta^{He}_{0,T_{ref}}$ and $R^{g,He}_{T,T_{ref}}$. The nickel capillaries used by May *et al.*[83,84] were immersed in stirred liquid baths that controlled their temperatures with an uncertainty of ± 0.01 K. The flow rates and the viscometer's design ensured that the temperature of the flowing gas reached the bath's temperatures before the gas entered each capillary. The pressure transducers had full scales of 300 kPa or 150 kPa, an uncertainty of ± 0.008 % of full scale (± 24 Pa or ± 12 Pa), and a resolution of 0.16 Pa. The experimental quantities of primary importance are the difference pressures across the capillaries, $\Delta p_{12} \equiv p_1 - p_2$ and $\Delta p_{34} \equiv p_3 - p_4$. Several refinements were used to measure Δp_{12} and Δp_{34} with relative uncertainties of order $\pm 10^{-4}$. The two pairs of transducers (which measured p_1, p_2, p_3 and p_4) and the two bypass valves were housed in a temperature controlled enclosure. Before and after every measurement, the bypass valves were opened to measure the zero-offsets of Δp_{12} and Δp_{34} near the average operating pressures. The measured zero-offsets were used to tare subsequent readings of Δp_{12} and Δp_{34} made while the bypass valves were closed. The pressures p_1, p_2 and p_4 were controlled at their set points using the variable impedances Z_1, Z_2 and Z_3 and digital proportional-integral algorithms. The pressure set-points were chosen so that for both gases the flow rates and average pressures within the two capillaries were similar. The upstream capillary's upstream pressure p_1 was usually fixed near 125 kPa, and its downstream pressure p_2 was set to four values (between about 100 kPa and 120 kPa) to produce four flow rates ranging from about 4 $\mu mol \cdot s^{-1}$ to 80 $\mu mol \cdot s^{-1}$. The downstream capillary's downstream pressure p_4 was then controlled sequentially at six set points between 13 kPa and 75 kPa for each of the four flow rates. This array of 24 measurements per gas per temperature was used to estimate the dependence of the measured values of $R^{g,He}_{T,T_{ref}}$ [eqn (4.12)] on the Dean number De and the small pressure-dependence of the viscosity, as described below. Automation of the entire apparatus and experimental method, including taring of the pressure transducers was essential because the measurements of $R^{g,He}_{T,T_{ref}}$ at each temperature required a time of several hours while the apparatus stepped through two identical sets of $[p_2, p_4]$ conditions, one for helium and one for the test gas. These refinements to the apparatus and experimental method enabled the pressure differences Δp_{12} and Δp_{34} to be controlled and measured to within ± 0.01 %, with the dominant uncertainty due to the instability (≈ 2 Pa) in the uncontrolled pressure p_3.

In many cases the correction factor $C^{g}(T,p_1,p_2)$ can be determined with sufficient accuracy that eqn (4.12) can be used directly to calculate $R^{g,He}_{T,T_{ref}}$. Such cases require that (a) the Dean number and, hence, the centrifugal flow

correction be sufficiently small, and (b) that the following parameters required to evaluate the c_i^g terms for the gas are sufficiently well known: the molar mass M, the zero-density viscosity $\eta_{0,T}^g$, the density virial coefficients B and C, the thermal conductivity, the temperature derivative of the zero-density viscosity $d\eta_{0,T}^g/dT$, and the viscosity virial coefficient $B_\eta \equiv \lim_{\rho\to 0}(\partial\eta/\partial\rho)_T$. Of these, it is B_η that is least well known, but under certain circumstances the equivalent quantity $b_T^g \equiv \lim_{p\to 0}(\partial\eta/\partial p)_T/\eta = B_\eta(\partial\rho/\partial p)_T/\eta$ can be measured with a modest uncertainty by the two-capillary viscometer itself.

To determine whether the correction terms in $C^g(T,p_1,p_2)$ are sufficiently accurate, it is useful to calculate the quantity

$$\Xi^g(T) \equiv \frac{\Delta p_{34}\bar{p}_{34}}{\Delta p_{12}\bar{p}_{12}}\frac{C^g(T,p_3,p_4)}{C^g(T_{\rm ref},p_1,p_2)}, \tag{4.13}$$

and test its dependencies on the mean pressure in the downstream capillary, $\bar{p}_{34} \cong (p_3+p_4)/2$ and on the Dean number of the flow through the downstream capillary. An incorrect value of B_η will cause Ξ^g to vary with $\bar{p}_{34}$. May *et al.*[83] adjusted B_η to minimize such variation, and thereby obtained a more accurate value of B_η.

For gases that have accurately-known density and viscosity virial coefficients, the pressure-dependence of Ξ^g can be taken into account when calculating the correction terms c_i^g. However, accounting for the dependence of Ξ^g on the Dean number is more complicated. The correction for centrifugal flow in the hydrodynamic model extends to $De > 16$ only if the capillary bore is sufficiently circular and uniform. Capillaries that are robust enough to operate over a wide range of temperatures are unlikely to satisfy this criterion, and the lowest order correction to the centrifugal function $f_{\rm cent}$ in eqn (4.7) for a capillary with a slightly elliptical bore is proportional to $(De)^4$ (ref. 83,84,95,96). Under these circumstances, the value of $R_{T,T_{\rm ref}}^{g,He}$ should not be estimated directly from eqn (4.12) but rather from

$$R_{T,T_{\rm ref}}^{g,He} = \lim_{De\to 0}\Xi^g(T)\Big/\lim_{De\to 0}\Xi^{He}(T). \tag{4.14}$$

4.5 Sealed Gravitational Capillary Viscometers for Volatile Liquids

ARNO LAESECKE

4.5.1 Introduction

In 1991, Kawata *et al.*[97] reviewed the metrology with open gravitational capillary viscometers, but there has been no review of sealed instruments for volatile liquids. At that time, such instruments were increasingly used to determine the viscosity of alternative refrigerants, which might be used to replace the ozone-depleting chlorofluorocarbons.[99] Comparisons with viscosities that were measured with other types of viscometers showed systematic and unexpectedly large deviations, in one case even greater than 30 %.[100] These discrepancies were resolved in and reported by NIST.[101,102] Measurements with **sealed** gravitational capillary viscometers had been analyzed with the working equations for **open** gravitational capillary viscometers because of a gap in reference texts and standards. From its beginnings with Hagen, Poiseuille, and Hagenbach,[103] capillary viscometry had been predominantly performed with open instruments on non-volatile liquids. Applications of the technique to volatile liquids were sporadic until the new class of chlorofluorocarbon refrigerants led to the expansion of the refrigeration and air-conditioning industries in the 1950s. However, reference texts and standards for sealed instruments to recognize their distinct differences from open capillary viscometers were not developed in parallel with their more frequent use.

This section fills this gap. Section 4.5.2 gives an overview of the evolution of sealed gravitational capillary viscometers. Section 4.5.3 discusses the vapor buoyancy correction that applies to all sealed instruments. Section 4.5.4 addresses the radial acceleration correction that is needed if the capillary is curved or coiled. As with most corrections to viscosity measurements, their omission yields systematically too high results.

4.5.2 Instruments

Three types of sealed gravitational capillary viscometers were developed: (1), instruments made out of thick-walled glass; (2), open capillary viscometers enclosed in metallic pressure vessels; and (3), compact instruments made out of stainless steel. Edwards and Bonilla[104] constructed in 1944 a sealed viscometer of type 1. To achieve sufficiently high flow impedance for sufficiently long efflux times, the capillary with an inner diameter of 0.57 mm was wound in a coil with three turns. Over the next 46 years, this instrument served as an example for the studies of Mears *et al.*,[105] Phillips and Murphy[106,107] and of Shankland *et al.*[108,109] Except for the data of Edwards and Bonilla, the results of these measurements with sealed viscometers with coiled capillaries were later found to be up to 33 % higher than data that were determined with other techniques.

Sealed viscometers of type 2 were first employed by Eisele *et al.*[110] and then by Gordon *et al.*[111] The working equation of Cannon *et al.*[112] for open capillary viscometers was quoted for this sealed instrument. Kumagai and Takahashi[113] constructed type 1 sealed viscometers but with straight vertical capillaries and quoted also the working equation for open capillary viscometers. They showed that some data of Gordon *et al.*[109] deviated systematically with temperature up to ± 8 % from theirs. The results of Kumagai and Takahashi[113] were later also found to exceed literature data systematically with temperature by up to 17 %. Han *et al.*[114,115] adopted the type 2 viscometer design and used capillaries with internal diameters from 0.110 mm to 0.370 mm. Measurement results from this instrument agreed with the results of Kumagai and Takahashi[113] and with some literature data, while there were systematic deviations of more than ± 10 % from other data sets. Viscometry seemed to have a major problem.

The third type of sealed capillary viscometer was developed by Ripple at NIST.[116] The first implementation had a one-coil capillary with an internal diameter of 0.508 mm.[116] The second instrument with a straight vertical capillary is shown with its dimensions in Figure 4.14. Both instruments differed from the previously discussed sealed viscometers in that the flow

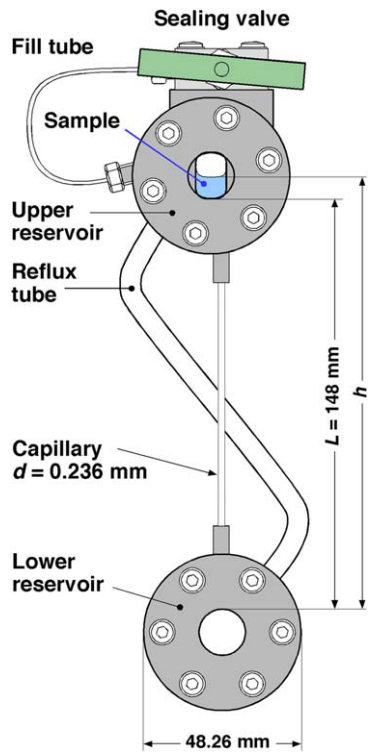

Figure 4.14 Sealed gravitational capillary viscometer with straight vertical capillary developed at NIST.[101]

rate of the sample was not determined by measuring an efflux time interval t between two marks at the upper reservoir but by observing the descent of the liquid meniscus in that part of the instrument at several levels h to obtain the rate $\dot{h} = \mathrm{d}h/\mathrm{d}t$. Using this quantity requires a modified working equation for this viscometer.[102,117] Cousins and Laesecke[118] described details of the experimental determination of $\dot{h}$ and the associated uncertainty.

Ripple and Defibaugh[101] pointed out that some of the literature data obtained in sealed gravitational capillary viscometers were analyzed without accounting for the vapor buoyancy. They detailed this contribution for the liquids they had measured and showed that correcting for this effect led to a remarkable consistency between their experimental results and the originally deviating literature data. This aspect was investigated further by Laesecke *et al.*[102] with measurements of ammonia, 1,1,1,2-tetrafluoroethane (known by the refrigeration nomenclature as R134a), and difluoromethane (R32) in the same instrument. In addition, the effect of radial acceleration on flow in coiled capillaries was quantified and demonstrated to exceed that of the vapor buoyancy at certain conditions. Accounting for the vapor buoyancy in sealed instruments and for the radial acceleration in those with coiled capillaries reconciled all originally deviating viscosity measurements in gravitational capillary viscometers with the results measured with other instruments. Even the strong deviations of the data of Phillips and Murphy,[106,107] which had been inexplicable for nearly three decades, could be reconciled. The papers of Ripple and Defibaugh[101] and Laesecke *et al.*[102] prompted Kumagai and Yokoyama[119] to publish vapor buoyancy-corrected values of the viscosity data for eleven liquids that had been published in 1991.[113]

Owing to the infrequent use of sealed instruments, published working equations for gravitational capillary viscometers had often been simplified by neglecting the influence of the gas above the liquid on the driving pressure head of the efflux. One exception is the working equation reported by Wedlake *et al.*:[120]

$$\eta = c_0(\rho_\mathrm{L} - \rho_\mathrm{V})\Delta t - b\rho_\mathrm{L}/\Delta t + c_1\gamma\Delta t. \tag{4.15}$$

The dynamic viscosity η depends on the density of the liquid ρ_L and that of the vapor or gas above the liquid, ρ_V, as well as the surface tension γ between the liquid and the gas. The measurand is the efflux time interval Δt that elapses when a known volume of liquid drains through the capillary. The constants c_0, c_1, and b are determined by calibration with viscosity standards. The first term in eqn (4.15) is the Hagen–Poiseuille term, which describes the flow of the liquid through the capillary. The second term is the correction for the kinetic energy dissipation in the liquid at the inlet and outlet of the capillary.[97] The third term is a correction for the effects of surface tension at the walls of the capillary.[102,118,120] As mentioned before, the working eqn (4.15) has to be modified for the sealed NIST viscometers

because the rate of descent of the liquid meniscus $\dot{h}$ is measured rather than an efflux time interval Δt. Then, the dynamic viscosity is obtained from

$$\eta = c_0(\rho_L - \rho_V)/\dot{h} - B\rho_L\dot{h} + C_1\gamma/\dot{h}, \quad (4.16)$$

with the revised calibration constants C_0, C_1, and B.[121] Much of the confusion about the systematic deviations of viscosity data obtained with sealed capillary viscometers arose because they had been soundly calibrated with the only available reference liquids, which were non-volatile. Viscometers that are intended for measurements of volatile liquids should be calibrated with volatile reference standards to ensure their uncertainty at the intended operating conditions. Using such reference materials would likely also reduce the difference in surface tension between the calibration liquid and the liquids to be measured, because their chemical structures might be more similar. Wedlake *et al.*[120] noted that residual surface tension errors for open gravitational capillary viscometers may be as large as ± 0.4 %. Calibration with volatile reference standards would therefore reduce the overall measurement uncertainty of sealed gravitational capillary viscometers by at least this amount. For this reason, Cousins and Laesecke[118] used pentane as calibration liquid. Unlike viscosity standards for open capillary viscometers, which are handled in ambient air, those for sealed instruments will be disseminated in pressure vessels due to their volatility and thus may be polar and hygroscopic. Laesecke *et al.*[102] proposed three fluorinated compounds as possible reference standards for sealed capillary viscometers. The characterization of such reference standards requires saturated vapor density as well as surface tension and the viscosity and density of the saturated liquid. Nevertheless, broadening viscosity reference standards to those that are volatile at ambient conditions and have lower viscosities than 0.3 mPa · s at 298 K would be valuable for lower uncertainty viscometry in general.

4.5.3 Vapor Buoyancy Correction

Sealed viscometers have to be evacuated before the sample liquid is admitted into the instrument. Depending on its volatility, the sample can be drained from a reservoir or condensed into the instrument by cooling the viscometer. When a sufficient volume of sample has been introduced, the instrument is sealed off and from this point on saturated liquid and saturated vapor are in phase equilibrium. With increasing temperature, the saturated vapor density ρ_{SV} increases and the saturated liquid density ρ_{SL} decreases. The latter reduces the driving pressure head and the former exerts buoyancy, which has to be accounted for in the first terms of eqn (4.15) and (4.16) by the density difference.

The vapor buoyancy correction may be considerable. For 1,1,1-trifluoroethane (given the acronym R143a by the refrigeration community), Kumagai and Yokoyama[119] applied this correction and obtained a 17 % lower viscosity at 323 K. Even a correction of only ± 1 % should not be

considered negligibly small. After all, this is twice that of previously mentioned surface tension effects and the uncertainty of the vapor buoyancy correction is smaller than the correction itself.[102,118] The vapor buoyancy correction has been increasingly considered in measurements with sealed gravitational capillary viscometers[122–124] but exceptions have occurred.[125]

Measurements of mixtures in sealed gravitational capillary viscometers differ significantly from measurements in open viscometers because the composition of the saturated liquid and vapor changes with temperature as more volatile components evaporate preferably. Because it is not feasible to draw liquid or vapor samples from a sealed viscometer during the measurements, the compositions of the two phases at the measurement temperatures have to be estimated by an equation of state or Helmholtz function for the sample mixture. This requires the bulk density of the mixture in the viscometer which has to be determined during mixture preparation[117] or from the internal volume of the viscometer and the sample mass by weighing the viscometer before and after filling.[126] If the composition dependence of the mixture viscosity is substantial as in systems of nonpolar and polar components, the uncertainty of the mixture viscosity measurement may be significantly higher than for pure fluids.

4.5.4 Radial Acceleration Correction

In curved or coiled tubes, the resistance to flow increases because the radial acceleration of the liquid or gas causes transverse flow. A correction for the radial acceleration is required to determine accurate viscosities. Although coiled capillaries have been used in viscometry for decades, the review of Kawata *et al.*[97] did not address radial acceleration. Often, the earliest studies of the late 1920s are quoted although these corrections have been found to be inadequate,[102,127,128] and Berger *et al.*[129] reviewed numerous later studies. The most recent and accurate correction function for flow rates in coiled capillaries was given by Berg[95] as $f_{\mathrm{cent}}(De,\ \delta)$ in terms of the Dean number $De \equiv Re\delta^{1/2}$, with the Reynolds number Re, and the ratio $\delta = (r/R_{\mathrm{coil}})$, where r is the internal radius of the capillary, and R_{coil} is the radius of the coil. This correction was discussed in section 4.4.2. When coiled capillaries are used in sealed viscometers, these correction functions have to be applied to the first two terms of the working eqn (4.15) so that

$$\eta = f_{\mathrm{cent}}[c_0(\rho_{\mathrm{SL}} - \rho_{\mathrm{SV}})\Delta t - b\rho_{\mathrm{L}}/\Delta t] + c_1\gamma\Delta t, \tag{4.17}$$

and accordingly in eqn (4.16). Berg[95] discussed the correction functions for Dean numbers up to 114 while many measurements with sealed gravitational capillary viscometers had been carried out at Dean numbers up to 35.[102] The importance of the radial acceleration correction must not be underestimated. The magnitude of the correction in sealed gravitational capillary viscometers for liquids is exemplified in Figure 4.15 which shows percent deviations of the viscosity data of Shankland *et al.*[109] and Kumagai and Takahashi[113] for R134a from the correlation of Huber *et al.*[130]

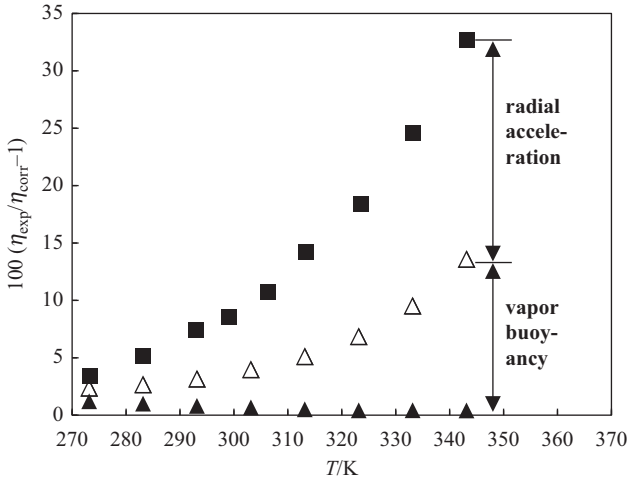

Figure 4.15 Fractional deviations of the measured viscosity, η_{exp}, for 1,1,1,2-tetrafluoroethane (R134a) from the correlation of Huber *et al.*,[130] η_{corr}, as a function of temperature *T*. ■, Shankland *et al.*[109]; △, Kumagai and Takahashi[113,119]; ▲, Kumagai and Takahashi[113,119] vapor-buoyancy corrected results.

Shankland *et al.*[109] used a sealed viscometer with a coiled capillary while Kumagai and Takahashi[113] used a sealed instrument with a straight vertical capillary. Their data require only the vapor buoyancy correction which reduces the deviation at 343 K from ± 13.6 % to ± 0.4 %. The data point of Shankland *et al.*[109] at this temperature deviates by ± 32.7 %. The difference to the deviation of the corresponding uncorrected data point of Kumagai and Takahashi is ± 19.1 % and is due to the radial acceleration.

References

1. J. T. Tough, W. D. McCormick and J. G. Dash, *Rev. Sci. Instrum.*, 1964, **35**, 1345.
2. *Experimental Thermodynamics. Vol. III. Measurement of the Transport Properties of Fluids*, ed. W. A. Wakeham, A. Nagashima and J. V. Sengers, Blackwell Scientific Publications, Oxford, 1991.
3. V. Majer and A. A. H. Padua, *Experimental Thermodynamics VI: Measurement of the Thermodynamic Properties of Single Phases*, IUPAC-Elsevier, 2003.
4. D. I. Bradley, M. Človečko, S. N. Fisher, D. Garg, A. M. Guénault, E. Guise, R. P. Haley, G. R. Pickett, M. Poole and V. Tsepelin, *J. Low Temp. Phys.*, 2012, **171**, 750.
5. P. S. van der Gulik, R. Mostert and H. R. van den Berg, *Physica A*, 1988, **151**, 153.

6. T. Retsina, S. M. Richardson and W. A. Wakeham, *Appl. Sci. Res.*, 1986, **43**, 127.
7. T. Retsina, S. M. Richardson and W. A. Wakeham, *Appl. Sci. Res.*, 1987, **43**, 325.
8. A. A. H. Padua, J. M. N. A. Fareleira, J. C. G. Calado and W. A. Wakeham, *Rev. Sci. Instrum.*, 1998, **69**, 2392.
9. F. Guillon, S. Hubert and I. L'Heureux, *Physica B*, 1994, **194–196**, 155.
10. F. Ciotta and J. P. M. Trusler, *J. Chem. Eng. Data*, 2010, **55**, 2195.
11. M. J. Assael and S. K. Mylona, *J. Chem. Eng. Data*, 2013, **58**, 993.
12. F. Audonnet and A. A. H. Padua, *Fluid Phase Equil.*, 2001, **181**, 147.
13. F. J. P. Caetano, J. M. N. A. Fareleira, C. M. B. P. Oliveira and W. A. Wakeham, *J. Chem. Eng. Data*, 2005, **50**, 1875.
14. F. Peleties and J. P. M. Trusler, *J. Chem. Eng. Data*, 2011, **56**, 2236.
15. M. E. Kandil, K. N. Marsh and A. R. H. Goodwin, *J. Chem. Eng. Data*, 2005, **50**, 647.
16. D. R. Caudwell, A. R. H. Goodwin and J. P. M. Trusler, *J. Petroleum Sci. Eng.*, 2004, **44**, 333.
17. P. L. Woodfield, A. Seagar and W. Hall, *Int. J. Thermophys.*, 2012, **33**, 259.
18. D. R. Caudwell, J. P. M. Trusler, V. Vesovic and W. A. Wakeham, *Int. J. Thermophys.*, 2004, **25**, 1339.
19. F. J. P. Caetano, J. L. C. Mata, J. M. N. A. Fareleira, C. M. B. P. Oliveira and W. A. Wakeham, *Int. J. Thermophys.*, 2004, **25**, 1.
20. J. C. F. Diogo, F. J. P. Caetano, J. M. N. A. Fareleira, W. A. Wakeham, C. A. M. Afonso and C. S. Marques, *J. Chem. Eng. Data*, 2012, **57**, 1015.
21. J. Wilhelm, E. Vogel, J. K. Lehmann and W. A. Wakeham, *Int. J. Thermophys.*, 1998, **19**, 391.
22. P. S. van der Gulik and N. J. Trappeniers, *Physica A*, 1986, **135**, 1.
23. M. J. Assael, C. M. B. P. Oliveira, M. Papadaki and W. A. Wakeham, *Int. J. Thermophys.*, 1992, **13**, 593.
24. I. Etchart, M. Sullivan, J. Jundt, C. Harrison, A. R. H. Goodwin and K. Hsu, *J. Chem. Eng. Data*, 2008, **53**, 1691.
25. M. Sullivan, C. Harrison, A. R. H. Goodwin, K. Hsu and S. Godefroy, *Fluid Phase Equil.*, 2009, **276**, 99.
26. M. J. Assael, M. Papadaki, M. Dix, S. M. Richardson and W. A. Wakeham, *Int. J. Thermophys.*, 1991, **12**, 231.
27. D. Seibt, S. Herrman, E. Vogel, E. Bich and E. Hassel, *J. Chem. Eng. Data*, 2009, **54**, 2626.
28. A. A. H. Padua, J. M. N. A. Fareleira, J. Calado and W. A. Wakeham, *Int. J. Thermophys.*, 1994, **15**, 229.
29. A. R. H. Goodwin and K. N. Marsh, *J. Chem. Eng. Data*, 2011, **56**, 167.
30. M. J. Assael, H. M. T. Avelino, N. K. Dalaouti, J. M. N. A. Fareleira and K. R. Harris, *Int. J. Thermophys.*, 2001, **22**, 789.
31. K. R. Harris, *J. Chem. Eng. Data*, 2009, **54**, 2729.
32. F. Ciotta, G. Maitland, M. Smietana, J. P. M. Trusler and V. Vesovic, *J. Chem. Eng. Data*, 2009, **54**, 2436.

33. M. M. Al Motari, M. E. Kandil, K. N. Marsh and A. R. H. Goodwin, *J. Chem. Eng. Data*, 2007, **52**.
34. F. J. P. Caetano, J. M. N. A. Fareleira, C. M. B. P. Oliveira and W. A. Wakeham, *J. Chem. Eng. Data*, 2005, **50**, 201.
35. X. Paredes, O. Fandiño, M. J. P. Comunas, A. S. Pensado and J. Fernandez, *J. Chem. Thermodyn.*, 2009, **41**, 1007.
36. K. R. Harris and S. Bair, *J. Chem. Eng. Data*, 2007, **52**, 272.
37. A. A. H. Padua, J. M. N. A. Fareleira, J. C. G. Calado and W. A. Wakeham, *J. Chem. Eng. Data*, 1996, **41**, 731.
38. X. Meng, P. Zheng, J. Wu and Z. Liu, *J Chem. Eng. Data*, 2008, **53**, 1474.
39. F. Audonnet and A. A. H. Padua, *Fluid Phase Equil.*, 2004, **216**, 235.
40. A. S. Pensado, A. A. H. Padua, M. Comuñas and J. Fernandez, *J. Supercrit. Fluids*, 2008, **44**, 172.
41. E. Charles, J. Michel, P. Majbrunot, J. Molenat and H. Abachi, *J. Phys. E: Sci. Instrum.*, 1980, **13**, 829.
42. M. E. Kandil, K. N. Marsh and A. R. H. Goodwin, *J. Chem. Eng. Data*, 2007, **52**, 2382.
43. G. Dehestru, M. Leman, J. Jundt, P. Dryden, M. Sullivan and C. Harrison, *Rev. Sci. Instrum.*, 2011, **82**, 035113.
44. W. A. Wakeham, A. D. Fitt, K. A. Ronaldson and A. R. H. Goodwin, *High Temp. – High Pressures*, 2008, **37**, 137.
45. H. Faxen, *Ark. Mathematik Astron. Fys.*, 1923, **17**, 1.
46. C. W. Oseen, *Ark. Mathematik Astron. Fys.*, 1913, **9**, 1.
47. S. Goldstein, *Proc. Soc. Rheol.*, 1929, **123**, 225.
48. K. Fujii, Y. Fujita, N. Kuramoto and Y. Kurano, *24th JSTP*, 2003.
49. Y. Fujita, N. Kuramoto, Y. Kurano and K. Fujii, in *14th ICPWS*, 2004, p. 112.
50. T. Lommatzsch, M. Megharfi, E. Mahe and E. Devin, *Metrologia*, 2001, **38**, 531.
51. M. Brizard, M. Megharfi and C. Verdier, *Metrologia*, 2005, **42**, 298.
52. N. Mordant and J. F. Pinton, *Eur. Phys. J. B*, 2000, **18**, 343.
53. M. Brizard, M. Megharfi and E. Mahe, *Rev. Sci. Instrum.*, 2005, **76**, 025109.
54. Y. Kurano, H. Kobayashi, K. Yoshida and H. Imai, *Int. J. Thermophys.*, 1992, **13**, 643.
55. S. Feng, A. L. Graham, P. T. Reardon, J. Abbott and L. Mondy, *J. Fluids. Eng.*, 2006, **128**, 157.
56. P. Dauge, A. Baylaucq, L. Marlin and C. Boned, *J. Chem. Eng. Data*, 2001, **46**, 823.
57. S. Bair and F. Qureshi, *Tribol. Trans.*, 2002, **45**, 390.
58. A. Kumagai, D. Tomida and C. Yokoyama, *Int. J. Thermophys.*, 2006, **27**, 376.
59. D. I. Sagdeev, M. G. Fomina, G. K. Mukhamedzyanov and I. M. Abdulagatov, *J. Chem. Thermodyn.*, 2011, **43**, 1824.
60. G. J. Piermarini, R. A. Forman and S. Block, *Rev. Sci. Instrum.*, 1978, **49**, 1061.

61. R. G. Munro, S. Block and G. J. Piermarini, *J. Appl. Phys.*, 1979, **50**, 6779.
62. R. G. Munro, G. J. Piermarini and S. Block, *J. Appl. Phys.*, 1979, **50**, 3180.
63. A. Audetat and H. Keppler, *Science*, **303**, 513.
64. H. E. King Jr., E. Herbolzheimer and R. L. Cook, *J. Appl. Phys.*, 1992, **71**, 2071.
65. E. H. Abramson, *Phys. Rev. E*, 2007, **76**, 051203.
66. E. H. Abramson, *J. Chem. Phys.*, 2005, **122**, 084501.
67. J. J. Carty Jr., 1957, B.S. thesis, Massachusetts Institute of Technology, Cambridge, Massachusetts, USA.
68. E. H. Abramson and H. West-Foyle, *Phys. Rev. E*, 2008, **77**, 041202.
69. J. R. Smart, S. Beimfohr and D. T. Leighton Jr., *Phys. Fluids A*, 1993, **5**, 13.
70. K. P. Galvin, Y. Zhao and R. H. Davis, *Phys. Fluids*, 2001, **13**, 3108.
71. G. Meier, R. Vavrin, J. Kohlbrecher, J. Buitenhuis, M. P. Lettinga and M. Ratajczyk, *Meas. Sci. Technol.*, 2008, **19**, 034017.
72. E. H. Abramson, *Phys. Rev. E*, 2011, **84**, 062201.
73. R. L. Cook, H. E. King Jr., C. A. Herbst and D. R. Herschbach, *J. Chem. Phys.*, 1994, **100**, 5178.
74. K. U. Schug, H. E. King and R. Bohmer, *J. Chem. Phys.*, 1998, **109**, 1472.
75. R. L. Cook, C. A. Herbst and H. E. King Jr., *J. Phys. Chem.*, 1993, **97**, 2355.
76. B. Grocholski and R. Jeanloz, *J. Chem. Phys.*, 2005, **123**, 204503.
77. R. L. Cook, H. E. King Jr. and D. G. Peiffer, *Macromolecules*, 1992, **25**, 2928.
78. E. H. Abramson, *Phys. Rev. E*, 2009, **80**, 021201.
79. E. H. Abramson, *High Pressure Res.*, 2011, **31**, 544.
80. S. Klotz, K. Takemura, T. Strassle and T. Hansen, *J. Phys: Condens. Matter*, 2012, **24**, 325103.
81. S. Pawlus, S. Klotz and M. Paluch, *Phys. Rev. Lett.*, 2013, **110**, 173004.
82. M. Matsui, E. Ito, T. Katsura, D. Yamazaki, T. Yoshino, A. Yokoyama and K.-I. Funakoshi, *J. Appl. Phys.*, 2009, **105**, 013505.
83. E. F. May, M. R. Moldover and R. F. Berg, *Int. J. Thermophys.*, 2007, **28**, 1085.
84. E. F. May, M. R. Moldover, R. F. Berg and J. J. Hurly, *Metrologia*, 2006, **43**, 247.
85. J. T. Zhang, H. Lin and J. Che, *Metrologia*, 2013, **50**, 377.
86. R. F. Berg, E. F. May and M. R. Moldover, *J. Chem. Eng. Data,* 2014, **59**, 116.
87. M. R. Moldover, R. M. Gavioso, J. B. Mehl, L. Pitre, M. de Podesta and J. T. Zhang, *Metrologia*, 2014, **51**, R1.
88. L. Pitre, F. Sparasci, D. Truong, A. Guillou, L. Risegari and M. E. Himbert, *Int. J. Thermophys.*, 2011, **32**, 1825.
89. E. Vogel, B. Jäger, R. Hellmann and E. Bich, *Mol. Phys.*, 2010, **108**, 3335.
90. J. B. Mehl, unpublished calculations, 2013.
91. J. B. Mehl, M. L. Huber and A. H. Harvey, *Int. J. Thermophys.*, 2010, **31**, 740.
92. J. D. Wright, T. Cobu, R. F. Berg and M. R. Moldover, *Flow Meas. Instrum.*, 2012, **25**, 8.

93. R. F. Berg and M. R. Moldover, *J. Phys. Chem. Ref. Data*, 2012, **41**, 43104.
94. W. Cencek, M. Przybytek, J. Komasa, J. B. Mehl, B. Jeziorski and K. Szalewicz, *J. Chem. Phys.*, 2012, **136**, 224303.
95. R. F. Berg, *Metrologia*, 2005, **16**, 11. *Erratum*, 2006, **43**, 183.
96. R. S. Srivastava, *J. Appl. Math. Phys.*, 1980, **31**, 297.
97. M. Kawata, K. Kurase, A. Nagashima and K. Yoshida, in *Measurement of the Transport Properties of Fluids*, ed. W. A. Wakeham, A. Nagashima and J. V. Sengers, Blackwell Scientific Publications, Oxford, UK, 1991, pp. 49–76.
98. M. Rojas-Cardenas, I. Graur, P. Perrier and J. G. Meolans, *Phys. Fluids*, 2013, **25**, 072001.
99. S. Solomon, *Nature*, 2004, **427**, 289.
100. R. Krauss, J. Luettmer-Strathmann, J. V. Sengers and K. Stephan, *Int. J. Thermophys.*, 1993, **14**, 951.
101. D. Ripple and D. Defibaugh, *J. Chem. Eng. Data*, 1997, **42**, 360.
102. A. Laesecke, T. O. D. Lüddecke, R. F. Hafer and D. J. Morris, *Int. J. Thermophys.*, 1999, **20**, 401.
103. L. Schiller, *Drei Klassiker der Strömungslehre: Hagen, Poiseuille, Hagenbach*, Akademische Verlagsgesellschaft, Leipzig, 1933.
104. D. A. Edwards and C. F. Bonilla, *Ind. Eng. Chem.*, 1944, **36**, 1038.
105. W. H. Mears, R. F. Stahl, S. R. Orfeo, R. C. Shair, L. F. Kells, W. Thompson and H. McCann, *Ind. Eng. Chem.*, 1955, **47**, 1449.
106. T. W. Phillips and K. P. Murphy, *J. Chem. Eng. Data*, 1970, **15**, 304.
107. T. W. Phillips and K. P. Murphy, *ASHRAE Trans.*, 1970, 77(Part II), 146.
108. I. R. Shankland, in *AIChE Spring National Meeting, Symposium on Global Climate Change and Refrigerant Properties*, Orlando, FL, 1990, p. 31.
109. I. R. Shankland, R. S. Basu and D. P. Wilson, in *Meeting of IIR Commissions B1, B2, E1, E2*, West Lafayette, IN, 1988, pp. 305–314.
110. E. H. Eisele, W. E. Fontaine and W. Leidenfrost, in *12th Int. Congr. Refrig. Prog. Refrig. Sci. Technol.*, 1969.
111. D. T. Gordon, J. F. Hamilton and W. E. Fontaine, *ASHRAE Trans.*, 1969, **75**, 40.
112. M. R. Cannon, R. E. Manning and J. D. Bell, *Anal. Chem.*, 1960, **32**, 355.
113. A. Kumagai and S. Takahashi, *Int. J. Thermophys.*, 1991, **12**, 105.
114. L.-Z. Han, M.-S. Zhu, X.-Y. Li and D. Luo, *J. Chem. Eng. Data*, 1995, **40**, 650.
115. L.-Q. Sun, M.-S. Zhu, L.-Z. Han and Z.-Z. Lin, *J. Chem. Eng. Data*, 1996, **41**, 292.
116. D. Ripple, *Rev. Sci. Instrum.*, 1992, **63**, 3153.
117. D. Ripple and O. Matar, *J. Chem. Eng. Data*, 1993, **38**, 560.
118. D. S. Cousins and A. Laesecke, *J. Res. Natl. Inst. Stand. Technol.*, 2012, **117**, 231.
119. A. Kumagai and C. Yokoyama, *Int. J. Thermophys.*, 2000, **21**, 909.
120. G. D. Wedlake, J. H. Vera and G. A. Ratcliff, *Rev. Sci. Instrum.*, 1979, **50**, 93.
121. A. Laesecke and R. F. Hafer, *J. Chem. Eng. Data*, 1998, **43**, 84.

122. Y.-Y. Duan, L. L. Shi, L.-Z. Han and M.-S. Zhu, *Fluid Phase Equilib.*, 1999, **162**, 303.
123. X.-J. Liu, L. L. Shi, L.-Z. Han and M.-S. Zhu, *J. Chem. Eng. Data*, 1999, **44**, 688.
124. J. Wu, Z. Liu, S. Bi and X. Meng, *J. Chem. Eng. Data*, 2003, **48**, 426.
125. I. M. Sivebaek, S. C. Sorenson and J. Jakobsen, 2001, SAE Technical Report.
126. A. Laesecke, R. F. Hafer and D. J. Morris, *J. Chem. Eng. Data*, 2001, **46**, 433.
127. R. A. Dawe, Ph.D. thesis, University of Oxford, 1968.
128. R. A. Dawe, *Rev. Sci. Instrum.*, 1973, **44**, 1231.
129. S. A. Berger, L. Talbot and L.-S. Yao, *Annu. Rev. Fluid Mech.*, 1983, **15**, 461.
130. M. L. Huber, A. Laesecke and R. A. Perkins, *Ind. Eng. Chem. Res.*, 2003, **42**, 3163.

CHAPTER 5

Thermal Conductivity and Diffusivity

JIANGTAO WU, MARC J. ASSAEL,
KONSTANTINOS D. ANTONIADIS, CHINHUA WANG,
ANDREAS MANDELIS, JINGPEI HU, RUI TAI,
R. MICHAEL BANISH, J. IWAN D. ALEXANDER AND
KENNETH R. HARRIS

5.1 The History of the Transient Hot-Wire Technique

JIANGTAO WU, MARC J. ASSAEL AND KONSTANTINOS D. ANTONIADIS

At the 30th International Thermal Conductivity Conference,[1] a history of the transient hot-wire technique, subsequently published in literature,[2] was presented. A summary of ref. 2 is presented here, illustrating the technique can be traced way back in time, to those first heated-wire experiments in 1780.

The transient hot-wire technique is a well-established absolute technique[3] for the measurement of the thermal conductivity of gases, fluids and solids. According to this technique, the thermal conductivity of the medium is determined by observing the rate at which the temperature of a very thin metallic wire increases with time after a step change in voltage has been applied to it, thus creating in the medium a line source of essentially constant heat flux per unit length. This has the effect of producing throughout the medium a temperature field which increases with time. The thermal conductivity is obtained from the variation with time of the temperature of the wire. We note that the wire acts with a double role; one of a line source of constant heat flux per unit length, and, when formed from a pure material

Experimental Thermodynamics Volume IX: Advances in Transport Properties of Fluids
Edited by M. J. Assael, A. R. H. Goodwin, V. Vesovic and W. A. Wakeham

Published by the Royal Society of Chemistry, www.rsc.org

such as either platinum or tantalum, one of a temperature resistance thermometer. Furthermore, to avoid end effects, two wires that are identical except for their length, are employed. Thus, if arrangements are made to measure the difference of the resistance of the two wires as a function of time, it corresponds to the resistance change of a finite section of an infinite wire (as end effects being very similar, are subtracted), from which the temperature rise can be determined. Instruments employ low uncertainty automatic bridges that permit more than 1000 measurements with times from lower than 1 ms up to 1 s (or 10 s, in the case of solids) coupled with finite elements methods to establish a very low uncertainty in thermal conductivity.

The success of this technique rests upon the fact that, by the proper choice of the design parameters, it is possible to minimize departures from this ideal model. For the remaining small corrections full analytical expressions exist. Furthermore, the effect of convective heat transfer can be rendered negligible, while for radiative heat transfer, important only at higher temperatures, an analytic correction exists.

In the following sections a typical selection of instruments is presented, in order to demonstrate the evolution of the technique, and certainly this selection does not include all investigators associated with this technique.

5.1.1 The Period from 1780 to 1970

To trace the origin of the transient hot wire one must start with Joseph Priestley in 1781, who wrote[4] ''all kinds of acid air conducted heat considerably worse than common air...'' He was probably the first one to carry out experiments in order to measure the ''power of gases to conduct heat'', *i.e.* the specific heat capacity of gases which was hitherto unknown. Similar experiments were carried out by Count Rumford (Sir Benjamin Thomson) in 1786.[5] He examined ''the conductive power of artificial airs or gases'' and while doing so he stumbled on a completely new mode of heat transfer, convection. He unfortunately concluded[5] that ''a gas was unable to conduct heat!'', and because of his reputation, this conclusion was not challenged for many years.

Sir John Leslie in *An Experimental Inquiry into the Nature and Propagation of Heat* (1804), wrote[6] about Count Rumford: ''...Were fluids absolutely incapable of conducting heat, how could they ever become heated?... How could water, for instance, be heated by the content of warm air? But the question really deserves no serious discussion''.

Nevertheless, 44 years later, the discussion about conduction on gases was still going on, when Sir William Robert Grove[7] presented an interesting communication illustrating that a platinum wire, rendered incandescent by a voltaic current, was cooled far below the point of incandescence when immersed in an atmosphere of hydrogen gas. Some years after, in 1861 Professor Gustav Magnus reported:[8] ''A platinum wire is less strongly heated by a galvanic current when surrounded by hydrogen than when it is in

atmospheric air or any other gas. It cannot be doubted that hydrogen conducts heat, and that in a higher degree than all other gases''.

Nevertheless, the debate about conduction in gases had not seen its end yet, John Tyndall in 1863 described[9] that by employing voltaic current, he raised the temperature of a platinum wire, and while it was in vacuum, until it glowed. Subsequently he let air in. This resulted in the disappearance of glow. He attributed this effect to heat carried away from the wire by convection. He then repeated the same experiment with air and then with hydrogen. The fact that he needed much more voltaic current in order to get it to glow in hydrogen, he attributed to the higher conductive power of hydrogen.

The gas conduction debate ended in essence with the wide acceptance of the work reported by James Clerk Maxwell[10,11] on the *Illustrations on the Dynamic Theory of Gases* and his calculation of a theoretical value of the thermal conductivity of a gas. Furthermore, two years later, Rudolf Julius Emanuel Clausius[12] backed up Maxwell's theories, showing that the thermal conductivity increased with temperature.

Ten years later, in 1872, Josef Stefan[13,14] with his experimental expertise measured the thermal conductivity of air with an instrument he called ''diathermometer''. His value was relatively lower than the most recent and agreed value, by 4 %.

All these discussions and experiments with heated wires in a sense prepared the ground for the work of August Schleiermacher,[15] who set out to measure the thermal conductivity of gases with a Pt hot wire (probably this is the first real hot-wire instrument). The instrument was composed of a horizontal Pt wire of diameter 0.4 mm and length 32 cm, placed in the centre of a glass cylinder and kept taut by a metallic spring. The resistance of the wire was obtained by measuring the voltage and the current through it. The temperature inside the glass was obtained from the resistance of the wire.

In 1917, Sophus Weber[16,17] published an investigation of the sources of errors involved in the determination of the thermal conductivity of gases by the method of Schleiermacher, and proposed probably for the first time, that the wire should be placed vertical, in order to reduce effects from convection.

The first ''transient'' hot-wire instrument was proposed by Bertil Stâlhane and Sven Pyk[18] in 1931, to measure the thermal conductivity of solids and powders (and some liquids). The hot wire was wound around a tube with a thermometer inside, and the whole rod was simply immersed in the powder, which was held at constant temperature. These authors also investigated the relationship between time and temperature rise, for a fine straight wire subjected to a step change in the heat input to the wire.

Eucken and Eglert[19] in 1938, improved the design of the apparatus reported by Stâlhane and Pyk, to provide an absolute transient hot-wire instrument for operation at low temperatures. Van der Held and van Drunen[20,21] contributed two items to the field, first they solved the Fourier

equation to derive the empirical expression reported by Stâlhane and Pyk, and second, they introduced the ''ideal solution'', that relates the temperature rise $\Delta\tau$ directly to the thermal conductivity λ, with the expression

$$\Delta T = \frac{q}{4\pi\lambda}\left[\ln\frac{4at}{r_o^2} - 0.5772\ \ldots\right], \tag{5.1}$$

where q is the heat per unit length, t the time, α the thermal diffusivity of the medium, and r_o the radius of the wire. Thus, absolute measurements of thermal conductivity could be performed.

De Vries[22] designed a transient hot-wire apparatus to measure the thermal conductivity of solids. Gillam *et al.*[23] in 1955 employed the ideas of Stâlhane and Pyk, and of Eucken and Englert[19] to produce an apparatus that provided the thermal conductivity with a standard ($k = 1$) relative uncertainty of ± 0.3 % for both liquids and solids. In subsequent years, additional instruments emerged and these include those reported by the following; Grassman and Straumann,[24] Haupin,[25] Turnbull,[26] Horrocks and McLaughlin,[27] Mittenbühler,[28] Burge and Robinson,[29] and Hayashi *et al.*[30]

5.1.2 From 1971 to Today

In 1971 Davis *et al.*[31] proposed a transient hot wire apparatus to determine thermal conductivity formed with a platinum wire of diameter 6.2 μm and length 1.3 cm. Measurement times of between (1 and 10) s were employed. McLaughlin and Pittman,[32] proposed a transient hot-wire instrument with a platinum wire of diameter 25 μm and length 15 cm, suspended at one end with a weight on the other. The instrument was designed to operate at temperatures between (100 to 450) K at pressures up to 10 MPa. McLaughlin and Pittman also employed a digital voltmeter to determine the change in voltage arising from the variation of the resistance of the wire. The temperature change was then calculated from the variation of the wire resistance.

However, the most significant changes to the transient hot wire method of determining thermal conductivity are attributed to Haarman[33,34] in 1971. In Haarman's experiment an automatic Wheatstone bridge was used to measure the difference between the resistance of two wires. The two wires were essentially identical except for their length so that end effects were subtracted. The bridge was capable, with the aid of high-speed electronic switches and counters, of measuring the time required for the resistance of the hot wire to reach six predetermined values. This bridge made possible a ten-fold reduction in the duration of each experiment, eliminated completely the effects arising from convection and reduced greatly other time-dependent errors.

In 1976 a full theory for the transient hot-wire experiment was presented by Healy *et al.*[35] The governing equations were solved approximately to an

"ideal" solution, and a series of corrections was proposed, in order to describe the actual experiment. These were:

(1) by proper choice of design and operating parameters, the effect of convection was eliminated,
(2) corrections rendered negligible (the wire's finite diameter, Knudsen effects, radiation, viscous heating, compression work), and
(3) corrections that were applied during the experiment (end effects, finite heat capacity of the wire, outer boundary corrections and variable fluid properties).

Thus, a combination of both the theory and advances in electronics permitted absolute measurements with a relative uncertainty of $\pm 1\,\%$. These developments saw the commencement of new series of albeit similar transient hot-wire instruments, which were developed by groups that had co-operated through research projects. Most of the transient hot-wire apparatus in the world originated from the work of J. Kestin (Brown University, U.S.A.) and W.A. Wakeham (Imperial College & Southampton University, UK).

The groups with these instruments include the following:

- C. A. Nieto de Castro (Lisbon University) and J.M.N.A. Fareleira (Instituto Superior Technico, Portugal),
- M. J. Assael (Aristotle University, Greece),
- R. Perkins (N.I.S.T., U.S.A.),
- A. Nagashima and Y. Nagasaka (Keio University, Japan), and more recently
- J. T. Wu (Jiaotong University, China), and
- E. Vogel (Rostock University, Germany).

The initial designs used included two 7 μm diameter Wollaston-process Pt wires that were fixed at both ends.[36,37] In some cases, the lower fixed end was attached to either a suspended mass or a spring.[38–40] In 1982, in order to measure the thermal conductivity of electrically conducting liquids, the material of construction was changed from platinum to tantalum because,[41] upon oxidation, Ta forms a thin layer $\{\approx$ (50 to 70) nm$\}$ of tantalum pentoxide, which is an electrical insulator. The wires, the masses and all electrical connections were fabricated from tantalum and were consequently anodized *in situ*.[42,43] Recently, the mass has been replaced by wire supports fabricated from tantalum so that they have the same linear thermal expansion as the wire;[44,45] thus permitting the wire to be maintained taut over a temperature range. In this design,[45] the wires are shorter and usually placed one over the other.

For measurements with the lowest uncertainty, the resistance of the wires are determined with electronic bridges that were developed[2] to permit more than 1000 measurements in 1 s. At the same time, the analytic "ideal solution" described previously was replaced with finite element analyses,[46] thus permitting the full representation of the geometry of the measurement device.

Lately the transient hot-wire technique has been expanded into two new regions; in the measurement of the thermal conductivity of molten metals and of solids. In the case of measurements in molten metals, the platinum wire is placed between two green alumina strips, which are consequently fired under pressure to become solid.[47] This arrangement allowed measurements of the thermal conductivity from ambient temperature up to 1200 K, and overcame problems of convection and thermal radiation. As it operated in accord with a theoretical model, its relative uncertainty was estimated to be ± 2 %. The thermal conductivity of a selection of molten metals has been measured.[48]

For measurements with solids, in order to overcome systematic errors that arise from the contact resistance between the wire and solid, the two wires were placed inside a soft silicone layer which is squeezed between the two solids.[46] The thermal contact obtained with this method effectively eliminates systematic errors arising from contact resistances. By obtaining the temperature rise from the wire's resistance measurement, at very short times the properties of the silicone layer are first obtained, and then at longer times, the properties of the solid. The absolute relative uncertainty achieved in this way is about ± 1 %.

5.2 Photoacoustic and Photothermal Methods and Tables of Thermophysical Property Measurements

CHINHUA WANG, ANDREAS MANDELIS, JINGPEI HU AND RUI TAI

Photothermal (PT) and photoacoustic (PA) techniques represent a group of high sensitivity measurement methodologies used to measure optical and thermophysical properties that include optical absorption, thermal diffusivity, thermal effusivity as well as other thermal characteristics of a sample. The basis of photothermal and photoacoustic measurements is the response of a material to absorption of optical radiation leading to change in the thermal or thermoelastic state and/or in the geometrical state of the material and/or its surrounding medium. Light absorbed and not converted radiatively, or re-emitted, results in heating (non-radiative de-excitation). The produced heat raises the temperature of the sample, thereby influencing its thermophysical and thermoelastic properties. In summary, measurements of temperature, pressure, change in thermodynamic and/or surface state, density, linear thermal expansion coefficient, speed of sound, and generally changes that occur due to optical absorption and non-radiative energy conversion are ultimately the goal of photothermal and photoacoustic measurements.

Thermal diffusivity, a, and thermal effusivity, e, are defined as:

$$a = \frac{\lambda}{\rho\, c_p} \tag{5.2}$$

and

$$e = \lambda \rho c_p, \tag{5.3}$$

where λ is the thermal conductivity, ρ the mass density, and c_p the specific heat capacity at constant pressure. The thermal diffusivity of a material is a measure of how fast the material temperature changes as a result of a thermal source in the material or its surroundings, while the thermal effusivity is a measure of a material's ability to exchange thermal energy with its surroundings.

The thermal diffusivity and effusivity are natural transport parameters involved in the photothermal and photoacoustic signal generation process. Specifically for harmonic modulation of a thermal source, such as that resulting from the absorption of modulated optical radiation, the generated thermal-wave obeys the heat conduction equation and is governed by a complex thermal wavenumber σ given by:

$$\sigma(\omega) = (1 + \mathrm{i})\sqrt{\frac{\omega}{2a}}, \tag{5.4}$$

where $\omega = 2\pi f$ is the angular modulation frequency of the incident radiation. The photothermal or low-frequency photoacoustic signal essentially depends on the thermal wavenumber which can be used to measure the thermal diffusivity of matter. Other thermophysical parameters, such as

effusivity and conductivity, can also be measured as they enter the thermal-wave field equations through suitable boundary conditions.

Based on the common physics of all photothermal and photoacoustic methodologies, several implementation methods and techniques have been introduced and used for thermophysical measurements. Each of those is characterized (and usually named) by the principal physical effect measured, and each has its special range of applications.

The photoacoustic (PA) effect is the generation of (sound) waves following the absorption of incident modulated or pulsed electromagnetic radiation in a sample[49,50] followed by thermoelastic expansion. The photoacoustic effect is measured through pressure changes using appropriate detectors such as microphones or piezoelectric sensors (transducers). These measurements are useful for determining certain properties of the studied sample. For example, in photoacoustic spectroscopy (PAS), the output signal is used to obtain the actual absorption coefficient of light in either opaque or transparent objects at a single excitation wavelength or in a range of wavelengths. Photoacoustics is not as sensitive to the scattering of light as conventional absorption measurements of transparent objects because only absorbed light can create a signal. By varying the modulation frequency and/or the wavelength of the excitation radiation one essentially varies the probed depth inside the sample, which results in the possibility of depth profiling and photoacoustic/photothermal imaging. This type of energy conversion imaging is extremely valuable as it is characterized by suppressed baseline signals even in the presence of strong scattered photon fields in the absence of optical absorbers. Therefore, PA/PT imaging can be efficiently used to monitor optical and/or thermal/thermoelastic inhomogeneities within the sample. Signal analysis includes also the possibility of determining thermophysical properties of the sample.

Thermal lens (TL)[51] is a photothermal effect resulting from laser-beam energy traversal and absorption throughout a sample, causing heating of the sample along the beam path. A radially dependent temperature distribution is created which in turn produces a refractive-index change proportional to dn/dT which is a material constant indicating the change of refractive index with temperature. This turns the medium into a lens affecting beam propagation. The lens usually has a negative focal length since most materials expand upon heating and the refractive index is proportional to the density. This negative lens causes beam divergence and the signal is detected as a time dependent decrease in power at the centre of the beam. By measuring the magnitude and time dependence of the intensity change with a small aperture photodetector placed at the beam centre beyond a cell containing the sample medium, the thermooptic properties of the sample, such as thermal diffusivity, thermal conductivity, temperature coefficient, dn/dT, and fluorescence quantum efficiencies, can be studied. Thermal lensing is typically applied for measuring trace quantities of substances in transparent materials including gases and liquid solutions.[52]

Photothermal deflection,[53] also called the mirage effect, measures the bending of a probe light beam due to optical absorption of an exciting light beam and non-radiative conversion to temperature rise in the absorbing

sample. This technique is particularly useful for measuring surface absorption and profiling thermal properties in layered materials.

Photothermal radiometry (PTR)[54] measures an increase in sample infrared radiance occurring as a consequence of absorption. Thermal photon emission from the heated sample follows the Planck (blackbody) law. This method is used to measure the thermal diffusivity and effusivity of solids and layered materials.

The photopyroelectric (PPE) technique[55] is based on the use of a pyroelectric transducer {such as poly(1,1-difluoroethene), polyvinylidene fluoride, PVDF} to detect the temperature variation of optically-induced periodic heating of a sample in intimate thermal contact with it or at a fixed and known (short) distance above or below the sample. Sample heating produces a thermal-wave field in the transducer, which is a superposition of a dc component owing to ambient temperature and continuous exposure of the sample to the heating source (optical or resistive heating), and an ac component owing to the modulation of incident energy. Two versions have been implemented based on the PPE method: the standard PPE (SPPE),[55] and the inverse PPE (IPPE).[56] The PPE technique is especially useful for measurements of thermal diffusivity and effusivity of fluids (liquids and gases) as well as solids and for performing thermophysical measurements of solids of arbitrary size with no need for confinement in a gas-microphone PA cell or use of ultrasonic transducers in contact with the sample.

A thermal-wave cavity (TWC)[57] measures the spatial resonant (standing-wave) behavior of in-cavity thermal waves which depends on the thermophysical properties of the fluid filling the cavity and on the cavity length, L. A thin metal-film wall, exposed to a modulated laser or a thin-film resistive element driven by AC current may act as surface thermal-wave sources. The other cavity wall is a thermal-to-electrical energy transducer, such as a pyroelectric thin film {poly(1,1-difluoroethene), PVDF}. It is placed parallel to the thermal-source wall and across the gap at a distance L. This transducer generates an oscillating electrical signal proportional to the amplitude and phase of the thermal wave within the cavity at the position of the transducer. Scanning of the cavity length L turns the thermal-wave cavity into a resonator, with very high sensitivity to the thermal transport property of the intra-cavity medium.

In summary, photothermal (PT) and photoacoustic (PA) techniques have been found to be powerful and advantageous for measurements of thermophysical properties such as thermal diffusivity and thermal effusivity due to the intrinsic linkage of the process of thermal-wave generation and detection to these parameters. In this chapter, the most prevalent photoacoustic and photothermal techniques are briefly reviewed with physical mechanisms and discussion on the functional range of applications. Typical measurement results including thermal diffusivity, thermal effusivity and thermal conductivity extracted from the literature over several years using PA and PT methods of various solids including semiconductors, liquids and gases are listed in Tables 5.1 to 5.4. References and specific methods employed for these results are given for further details.

Table 5.1 Thermal diffusivity, a, thermal conductivity, λ, and effusivity e for metals and dielectrics obtained by the following methods: PA, photoacoustic; PT, photothermal; PAS, photoacoustic spectroscopy; TL, lens thermal; PTD, photothermal deflection; PTR, photothermal radiometry; PPE, photopyroelectric; SPPE, standard photopyroelectric; IPPE, inverse photopyroelectric; and TWC, thermal wave cavity. The thickness h of the material is listed along with the porosity ϕ at temperature T.

Materials	Sample	Measurement $h/\mu m$ or $10^2 \cdot \phi$	a $10^{-6} \times m^2 \cdot s^{-1}$	λ $W \cdot m^{-1} \cdot K^{-1}$	e $10^4 \times W \cdot s^{1/2} \cdot m^{-2} \cdot K^{-1}$	Methods and References
AISI 304 Stainless Steel	Bulk		3.4 to 4.6			PT[58]
	Foil	940	3.2 to 3.6			PTR[59]
Co	Bulk		25.0 to 26.1			PT[60]
Mo	Film; Substrate polyimide	0.350	53.0			PT[61]
Zn	Foil	780	43.9	121		PTD[62]
AlN	Film	0.1		1.2 to 2.2		PT[63]
	Substrate silicon	1.050		4.1 to 4.9		
	Film, Substrate	0.1	4.8 to 6.4			PT[64]
	Borosilicate	0.2	6.0 to 7.2			
	Glass	0.3	8.0 to 8.8			
Al_2O_3	Foil	645	6.6 to 8.7			PT[65]
	Bulk			27.0		PT[66]
$Al_{0.97}Ti_{0.03}$	Film, Substrate polyimide	0.4	49.8			PT[61]
Bi_2Te_3	Nanowire array			1.36 to 1.54		PA[67]
CaF_2	Bulk		3.12 to 3.38	8.16 to 8.32	0.417 to 0.497	PT[68]
$CuGaO_2$	Foil	650	103.7 to 104.5			PA[69]
		500	100.6 to 101.6			
$Cu_2SO_3 \cdot CuSO_3 \cdot 2H_2O$	Foil	310	15.4	10		PAS[70]
Cr_2O_3(film on 0.997mm Fe substrate)	$T = 296$ K	229	1.283 to 1.292			PT[71]
	$T = 473$ K	229	1.084 to 1.100			
	$T = 873$ K	229	0.856 to 0.877			

Table 5.1 (*Continued*)

Materials	Sample	Measurement $h/\mu m$ or $10^2 \cdot \phi$	a / $10^{-6} \times m^2 \cdot s^{-1}$	λ / $W \cdot m^{-1} \cdot K^{-1}$	e / $10^4 \times W \cdot s^{1/2} \cdot m^{-2} \cdot K^{-1}$	Methods and References
HfO_2	Bulk			17.0		PT[66]
$LaMnO_3$	Foil	313	1.07			PTR[59]
$LaPO_4$	$\theta = 1173$ K	$\phi = 39$	32.2 to 44.2			PA[72]
θ = sintered temperature	$\theta = 1473$ K	$\phi = 10.4$	88.0 to 96.0			
$Li_xMn_2O_4$	Pellet	$x = 0.8$	74.0 to 76.0			PA[73]
PbI_2	Foil	250	2.46 to 2.54	2.62 to 2.80		PAS[74]
RuO_2	Foil		17.0	50.0		PD[75]
Ruby	Bulk		12.8			PT[60]
SiC	Foil	600	51.7 to 96.0			PT[65]
SiC(Porous)	Foil	1630	18			PTR[59]
Si_3N_4	Foil	3605	8.5			PT[65]
TiAlN (Al/Ti atomic ratio of $\sim$ 0.72)	Film Substrate AISI30	3		4.63		PT[76]
TiN	Film Substrate AISI304	3		11.9		PT[76]
TiO_2 Amorphous	Film Substrate glass	0.82		1.05	0.1730	PTR[77]

TiO_2 Crystalline: anatase	Film Substrate glass	0.98		2.79	0.2693	PTR[77]
$YBa_2Cu_3O_{7-x}$(YBCO)	3 mm long, 3 mm wide and 1 mm high	$T = 78$ K $T = 300$ K	1.4 0.9	4 4.75		PPE[78]
Fluorozirconates (ZBLAN)	Foil		0.25 to 0.26	0.69 to 0.85		TL[52]
Ge–Ga–Se glass	Foil	630	1.89 to 1.91			PA[79]
Polypropene (HDPE)	Film Substrate PVC	10	0.200			PT[80]
Poly(phenylethene) (Polystyrene)	Bulk		0.04 to 0.11			PT[60]
Pyrolytic graphite	Foil		2.0 to 2.2	5.8 to 6.0	0.397 to 0.415	PT[81]
Schott OG 590	Foil	645	0.48 to 0.54			PTR[59]
WC (0.83 WC + 0.17 Co) by mass	Film Substrate carbon steel	73.7 373.4	3.5 4.5	12.5 15.0		PTR[82]
Vitreous carbon	Foil	1340	5.7 to 6.3			PTR[59]

Table 5.2 Thermal diffusivity, a, and thermal conductivity, λ for semiconductors obtained by the following methods: PA, photoacoustic; PT, photothermal; PAS, photoacoustic spectroscopy; TL, lens thermal; PTD, photothermal deflection; PTR, photothermal radiometry; PPE, photopyroelectric; SPPE, standard photopyroelectric; IPPE, inverse photopyroelectric; and TWC, thermal wave cavity. The thickness h of the material is listed along with the porosity ϕ and temperature T.

Materials	Sample	Measurement h/μm or $10^2 \cdot \phi$	a $10^{-6} \times m^2 \cdot s^{-1}$	λ $W \cdot m^{-1} \cdot K^{-1}$	Methods and References
As_2S_3	Fresh Film	5		0.197 to 0.290	PA[83]
	Substrate Si	$T = 403$ K			
	Darkened Film	5		0.228 to 0.335	
	Substrate Si	$T = 403$ K			
Cd_2SnO_4	Film	1.03	0.1157 to 0.1163		PA[84]
		$T = 298$ K			
	Substrate glass	0.99	1.0527 to 1.0533		
		$T = 100$ K			
CdTe	Film	3.42	8.79 to 10^{-3}	0.595	PPE[85]
	Substrate glass plate	15.6	3.02 to 10^{-1}	25.5	
$CuInS_2$	Film	0.51	0.085		PTD[86]
	Substrate glass	$T = 523$ K			
GaAs	Wafer 0.635 cm	$T = 100$ K	287 to 349	304 to 370	PTD[87]
		$T = 150$ K	117 to 141	163 to 197	
		$T = 200$ K	69 to 101	106 to 158	
		$T = 305$ K	25 to 35	42 to 60	
n-GaAs(100)	Foil	568	23 to 25		PA[88]
GaP	Foil, i-type	360	43 to 46		PTD[89]
GaSb	Foil	420	23 to 25		PA[88]
Ge	Foil, n-type	400	36 to 38		PTD[89]
n-Ge(100)	Foil	786	34 to 36		PA[88]
InAs	Foil, n-type	1300	20 to 21		PTD[89]
		350	20 to 21		
InP	Foil, i-type	330	40 to 45		PTD[89]
	Foil p-type	400	39 to 43		
n-InP(100)	Foil	442	43 to 47		PA[88]
InSb	Foil, n-type	550	19 to 21		PTD[89]
		350	19 to 20		
n-$RuSe_2$	Foil;	140	0.40 to 0.48		PA[90]
Si(monocrystalline)	Foil, n-type	470	76 to 85		PTD[89]
	Foil, p-type	250	64 to 67		
Si (porous silicon)	Foil	$\phi = 12$	77.9 to 79.5	50 to 54	PA and PT[91]
		$\phi = 51$	14.7 to 15.9	3.6 to 4.9	

Table 5.3 Thermal diffusivity, a, thermal conductivity, λ, and effusivity e for liquids obtained by the following methods: PA, photoacoustic; PT, photothermal; PAS, photoacoustic spectroscopy; TL, lens thermal; PBD, photothermal beam deflection; PTR, photothermal radiometry; PPE, photopyroelectric; SPPE, standard photopyroelectric; IPPE, inverse photopyroelectric; and TWC, thermal wave cavity. The diameter of the nano-particles d are given for the material listed along with the amount concentration c, temperature T and mass fraction w.

Liquids	Liquid	Measurement d/nm	a / $10^{-8} \times m^2 \cdot s^{-1}$	λ / $W \cdot m^{-1} \cdot K^{-1}$	e / $W \cdot s^{1/2} \cdot m^{-2} \cdot K^{-1}$	Methods and References
[w 2-Propanone +	$w = 0.1$			1367 to 1437	PA[92]	
$(1 - w)$water]	$w = 0.3$			1087 to 1143		
	$w = 0.6$			837 to 917		
	$w = 0.9$			597 ~ 657		
Acetonitrile			10.5 to 10.9			TL[93]
Au nanoparticles of mass	$\gamma = 0.1$ mg $\cdot$ cm^{-3}	16	14.9 to 15.0			PA[94] TL[95]
concentration γ = Solution		63	14.6 to 14.7			
is colloidal water		99	14.5 to 14.6			
		125	14.4 to 14.5			
Castor oil			9.1 to 9.3	0.178 ~ 0.184	592 ~ 602	PPE[96]
Corn oil			8.89 to 9.07			TWRC[97]
Cyclohexane			8.4 to 8.8			PT[98]
Ethanol					550 ~ 730	PA[99]
Glycerol					871 ~ 963	PA[92]
				0.245 ~ 0.275		PT[100]
					900 ~ 960	PPE[101]
Lime oil (distilled)	(25 ± 2) K		6.33 to 6.69			PA[102]
Methanol			6.65 to 9.79	0.210		TWRC[103]
Methylene blue c is the	$c = 0.10$ mmol $\cdot$ dm^{-3}		14.2 to 16.2			PA[104]
amount concentration	$c = 10$ mmol $\cdot$ dm^{-3}		14.4 to 14.7			
	$c = 100$ mmol $\cdot$ dm^{-3}		13.7 to 14.1			
Olive oil				0.14 ~ 0.16		PT[100]
			7.58 to 8.34			TL[105]
1-propanol			7.55 to 7.85			TL[93]
				0.154	549	PA[106]
Silicon oil			8.63 to 8.68			PPE[107]
4′-(Octyloxy)–4-	$T = 298$ K (Smectic A)				530 ~ 590	PA[108]
biphenylcarbonitrile	$T = 298$ K (Nematic)				540 ~ 600	
(liquid crystal, 8OCB)	$T = 298$ K (Isotropic)				680 ~ 740	

Table 5.4 Thermal diffusivity, a, thermal conductivity, λ, and effusivity e for gases obtained by the following methods: PA, photoacoustic; PT, photothermal; PAS, photoacoustic spectroscopy; TL, lens thermal; PBD, photothermal beam deflection; PTR, photothermal radiometry; PPE, photopyroelectric; SPPE, standard photopyroelectric; IPPE, inverse photopyroelectric; and TWC, thermal wave cavity. The temperature T, pressure p of the sample along with the mole fraction of CO_2 $x(CO_2)$ are listed.

Gases	T/K	p/MPa	$x(CO_2)$	a / $10^{-5} \times m^2 \cdot s^{-1}$	λ / $W \cdot m^{-1} \cdot K^{-1}$	e / $W \cdot s^{1/2} \cdot m^{-2} \cdot K^{-1}$	Methods and References
C_2H_6		0.1		0.93 to 0.95	2.25×10^{-2}	7330 to 7350	PT[109]
C_3H_8	296			0.61 to 0.63	1.91×10^{-2}	7650 to 7670	
CO_2				1.01 to 1.08			PTD[110]
$(CO_2 + air)$		0.1	0	2.185			PA[111]
	298		0.4	1.668			
			0.8	1.272			
			1	1.094			
N_2				2.17 to 2.20			PTD[110]
N_2 in ≈ 0.0053 NO_2	298			2.17			PTD[112]
O_2				2.16 to 2.25			PTD[110]

5.3 Reduced Algorithms for Diffusivity Measurements

R. MICHAEL BANISH AND J. IWAN D. ALEXANDER

5.3.1 Introduction

This chapter gives the mathematical formulations for three algorithms for the measurement of either mass or thermal diffusivity. Concentration, or temperature, data are collected at two specific locations from the sample under test; additional locations may be included depending on the experimental arrangement. Diffusivities are obtained by the plotting the signal difference of the data from the two locations in the sample over various times. The initial theoretical derivations indicate that specific experimental geometries are required for these methodologies to be employed. However, subsequent analysis (and experimental confirmation) of the starting conditions show that considerable relaxation of the derived parameters is allowed. While the algorithms are based on a cylindrical geometry, the exact configuration of the cylinder is not central to any of these derivations and, in fact, may be either a long thin cylinder, or a flat disk. The heat or mass ''diffusing (solute) species'' can originate at one end of the cylinder, in the centre of the cylinder or at the outer edge of the cylinder. The choice of different initial conditions depends on what is convenient for experimenter and the most advantageous experimental set-up. Figure 5.1a through c shows schematically the experimental configurations that are included in this chapter. Figure 5.1a shows the initial geometry for a long-thin cylinder with either a tracer or a heat pulse applied to one end. Figure 5.1b depicts diffusion from the centre out, and Figure 1c shows tracer diffusion starting from the outer edge. Table 5.5 shows the resulting forms of the equations used to obtain diffusivity from the three different geometries. All are straight

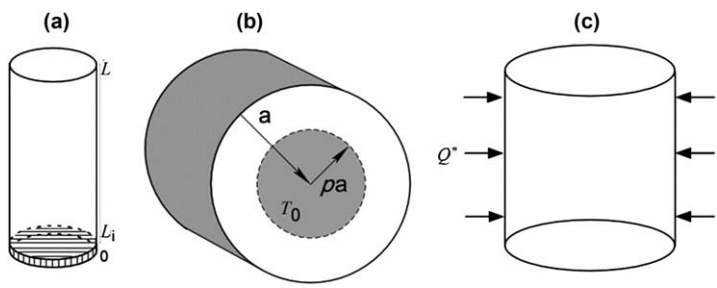

Figure 5.1 Schematic of the three cylindrical geometries considered for the reduced algorithms discussed in the text. (a) Long-thin cylinder, (b) flat-disk or cylinder with centre section heating, (c) disk (cylinder) with outside surface heating.

Table 5.5 Reduced forms of the diffusion equation for selected cylindrical geometries with constant C. D is the mass diffusivity and a is the thermal diffusivity, c is the concentration or T temperature value at a given location and time t; other terms are explained later in the text for each of the methodologies.

Cylindrical geometry	Reduced equation*
Long-thin cylinder	$\ln[c_1(t) - c_2(t)] = C - \left(\frac{\pi}{L}\right)^2 Dt$
Cylindrical disk with centre heating	$\ln[\Delta n_{ij}(t)] = C - \left(\frac{\mu}{a}\right)^2 at$
Cylindrical disk with edge heating	$\ln[\Delta n_{ij}(t)] = C - \left(\frac{\alpha}{R}\right)^2 at$

lines where the initial conditions only affect the intercept of the line and not the slope of the line, which is the diffusion coefficient itself.

The primary advantage of the three methodologies is that knowledge of the starting conditions is not necessary to determine the value of the diffusivity. Thus, these methodologies can be thought of as ''real-time'' or *in-situ* methodologies. For mass diffusivity determinations, successive measurements at different temperatures can be performed on the same sample.

What can be thought of as rather extreme deviations from the theoretical solutions will have introduced relative uncertainties less than $\pm 1\,\%$, or in some cases less than $\pm 0.01\,\%$ for diffusion coefficient determinations. This insensitivity to experimental conditions is the strength of the presented methodologies. This includes an insensitivity of the reduced algorithms to bubbles and voids along a long-thin cylindrical sample.[113,114]

Many mass diffusion methodologies are based on a segment by segment concentration analysis of a sample after freezing, *i.e.*, a shear cell.[115–117] It has been shown in ref. 118 that the error in the resulting diffusivity from this approach is larger than from the two-measurement location time-profile evolution described in this work.

The derivations of the reduced equations for the selected geometries can be performed for either mass or thermal diffusivities. The work presented in the chapter derives the equations of the various geometries for either mass or thermal diffusivity. The long-thin cylinder was derived for mass diffusivity and thus the equations are in terms of a concentration distribution. More specifically, the long-thin cylinder methodology was developed for an emitting radiotracer, thus the radiation detector count rate is the difference term in the final equation. It is relatively easy to envision either optical or X-ray absorption, or a temperature distribution, for this geometry.

5.3.2 Mathematical Formulations

5.3.2.1 Semi-infinite Cylinder (Long-thin cylinder)

The time rate of change in concentration c of a substance undergoing diffusion in one dimension z according to Fick's Law is given by:

$$\frac{\partial C}{\partial t} = D\frac{\partial^2 C}{\partial z^2}, \tag{5.5}$$

where t is the time and D the diffusion coefficient. For a semi-infinite capillary the sample is initially doped with radioactive material (a so-called tracer) of concentration c_0 over a distance L_i from the end. The continuity of the first spatial derivative of c requires this derivative vanish at each end of the sample. Eqn (5.5) is therefore to be solved for z in $[0, L]$ subject to the initial condition

$$c(z,0) = \begin{cases} c_0, & 0 < z < L_i \\ 0, & L_i < z < L \end{cases}, \tag{5.6}$$

and the boundary conditions

$$\frac{\partial c}{\partial z}(0,t) = \frac{\partial c}{\partial z}(L,t) = 0. \tag{5.7}$$

The solution is,[119]

$$C(z,t) = \frac{C_0 L_i}{L} + \sum_{m=1}^{\infty} \frac{2C_0}{m\pi} \sin\left(\frac{m\pi L_i}{L}\right) \cos\left(\frac{m\pi z}{L}\right) \exp\left[-\left(\frac{m\pi}{L}\right)^2 Dt\right]. \tag{5.8}$$

For eqn (5.8) to be valid it must be shown[120,121] that if two detectors are placed symmetrically about the midpoint of the sample (in a similar fashion as the Loschmidt cell[3]), the even terms in the series cancel when taking the difference between the concentration at the two locations. Furthermore, if detectors are placed at $L/6$ and $5L/6$ (or for that matter $L/3$ and $2L/3$) the $m = 3$ term cancel in the difference leaving only the $m = 1$ linear and the $m \geq 5$ higher order terms. The higher order terms can be neglected for $t \gg L^2/\pi^2 D$ (*e.g.* $\geq$0.5 h for the determination of a D of $\approx 10^{-4}$ cm$^2 \cdot$ s^{-1} and $L \approx 3$ cm).

The $L/6$ and $5L/6$ detector locations are good choices because of the greater concentration difference compared to the $(L/3, 2L/3)$ case. For

$$z_1 = L/6 \quad \text{and} \quad z_2 = 5L/6, \tag{5.9}$$

and considering only the $m = 1$ term in eqn (5.8) gives

$$\ln[c_1(t) - c_2(t)] = C - \left(\frac{\pi}{L}\right)^2 Dt, \tag{5.10}$$

where C is a constant and D can be determined from a least-squares fit to equation (5.10) using measurements of concentration (count-rate) difference as a function of time t.

Figure 5.2a and Figure 5.2b shows the signal received at the two detector locations *versus* time, along with the difference of the two signals, which

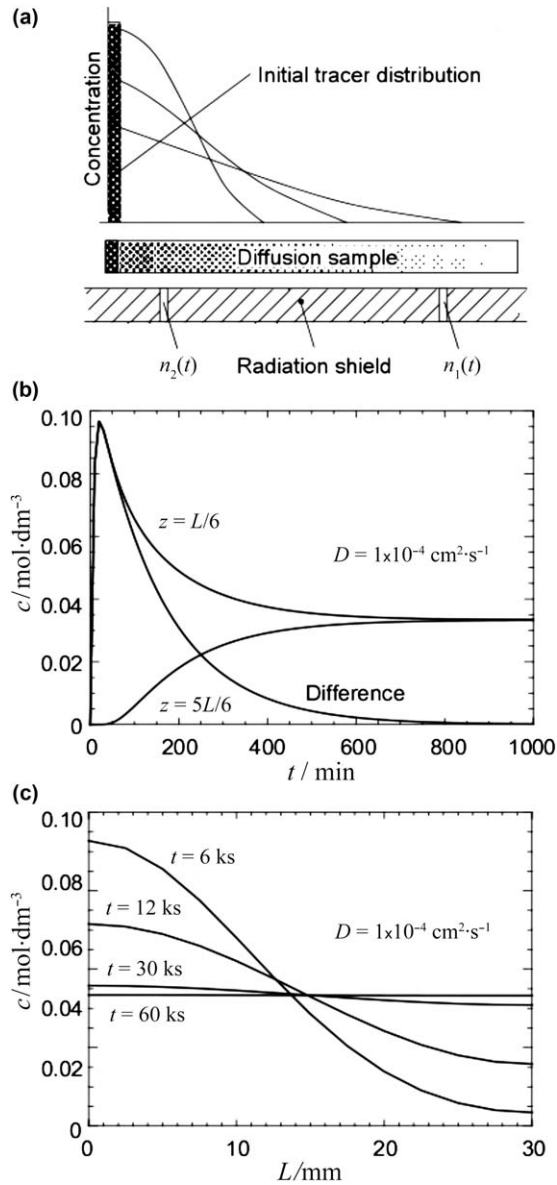

Figure 5.2 (a) Schematic presentation of the measurement locations for a diffusion couple and (radiation) shield-collimator geometry. (b) Time traces of the signals at the two measurement locations and corresponding presentation of the signal difference. (c) Diffusing species (emitter) concentration at various times for a 30 mm sample.

show, as expected from eqn (5.10), a simple exponential decay for sufficiently large times. In practice, the diffusivity can only be measured after significant signal is received at the far $5L/6$ detector (≈ 0.83 h or so with a diffusivity of order 10^{-4} $cm^2 \cdot s^{-1}$) well after the times that it is possible to neglect more and more of the higher order terms in eqn (5.10).

Figure 5.2c shows that there are considerable concentration gradients across a 1 mm or so collimator bore (or absorption beam) at both detector locations. However, as shown by Emslie and Banish[122] and confirmed by us the magnitude of this effect is rather negligible for most diffusion measurements and concentration profiles. This method has been confirmed experimentally using an ^{114m}Indium radiotracer in Indium and ^{123}Te radiotracer in Te.[123,124]

5.3.2.2 *Temperature in a Cylindrical Rod (Disk with a Central Heated Region)*

A second diffusion geometry that may be considered is one of a thin cylindrical disk where the solute diffuses out radially from the central section through the bulk solvent, Figure 5.1b.

The initial starting geometry is a perfectly insulated circular cylinder under conditions for which the temperature depends only on the cylindrical radius r. The initial temperature distribution is $T(r, 0) = f(r)$ given by

$$f(r) = \begin{cases} T_0 & \text{for } 0 < r/b < p \\ 0 & \text{for } p < r/b < 1 \end{cases} \tag{5.11}$$

where $0 < p < 1$; b is the cylinder radius, and T_0 is a constant, see Figure 5.1b. For time $t > 0$, radial heat transfer begins.

The evolution of the temperature $T(r, t)$ is then given by[125]

$$T(r,t) = \frac{2}{b^2}\left[\int_0^b rf(r)\mathrm{d}r + \sum_{n=1}^{\infty} \exp(-\kappa\alpha_n^2 t)\frac{J_0(r\alpha_n)}{J_0^2(b\alpha_n)}\int_0^b rf(r)J_0(\alpha_n r)\mathrm{d}r\right] \tag{5.12}$$

and where $\mu_n = b\alpha_n$ is the nth positive root of the Bessel function of the first kind of order 1. Using the initial conditions defined above, the integrals in eqn (5.12) become

$$\int_0^b rf(r)\mathrm{d}r = T_0\int_0^{pb} r\mathrm{d}r = \frac{1}{2}T_0(pb)^2, \tag{5.13}$$

and

$$\int_0^b rf(r)J_0(\alpha_n r)\mathrm{d}r = T_0\int_0^{pb} rJ_0(\alpha_n r)\mathrm{d}r = T_0\,(pb/\alpha_n)\,J_1(\alpha_n pb). \tag{5.14}$$

Thus we obtain

$$T(r,t) = T_0 p^2 + T_0 \sum_{n=1}^{\infty} \exp\left(\frac{-a\mu_n^2 t}{b^2}\right) \frac{2p}{\mu_n} \frac{J_0(\mu_n r/b)}{J_0^2(\mu_n)} J_1(\mu_n p). \quad (5.15)$$

The infinite sum in eqn (5.15) can be simplified by eliminating the $n=2$ and $n=3$ terms. Since the terms for $n>3$ decay rapidly with time, we will be left after a short transient with $n=1$ term, *a tractable expression that can be used to analyze experimental data*. Setting p, the ratio of the radius of the heated area to the sample radius, equal to the special value $\mu_1/\mu_2 = 0.5436$, we can eliminate the $n=2$ term, the $n=3$ term can be set to zero by choosing the temperature measurement locations r so that $\mu_3 r/b = \nu_n$ corresponds to the first three zeros of J_0, *i.e.*, $J_0(\nu_n)=0$, which are 2.4048, 5.5201 and 8.6537, respectively. With $\mu_3 = 10.17347$, this results in three special values of r given by $r_1/b = \nu_1/\mu_3 = 0.2364$, $r_2/b = \nu_2/\mu_3 = 0.5426$, and $\nu_3/\mu_3 = \nu_3/\mu_3 = 0.8506$. The next zero of J_0 is at $\nu_4 = 11.792$ and would result in a value $r_4/b>1$, outside the sample.

The geometry of the heated area and the three special values of r (temperature measurement locations for the experiments) are shown in Figure 5.3a. With the $n=2$ and $n=3$ terms set to zero by means of the choices adopted above, the temperature at each r_i is,

$$T(r_i,t) = T_0 p^2 + T_0 \frac{2p}{\mu_1} \frac{J_0(\mu_1 r_i/b)}{J_0^2(\mu_1)} J_1(\mu_1 p) \exp\left(\frac{-a\mu_1^2 t}{b^2}\right) + h.o.t. \quad (5.16)$$

where *h.o.t.* denotes higher order terms having $n>3$.

Taking the difference between two locations, for example between r_1 and r_3,

$$T(r_1,t) - T(r_3,t) = T_0 \frac{2p}{\mu_1} \frac{J_1(\mu_1 p)}{J_0^2(\mu_1)} \left(J_0\left(\mu_1 \frac{r_1}{b}\right) - J_0\left(\mu_1 \frac{r_3}{b}\right)\right) \exp\left(\frac{-a\mu_1^2 t}{b^2}\right) + \Delta(h.o.t.) \quad (5.17)$$

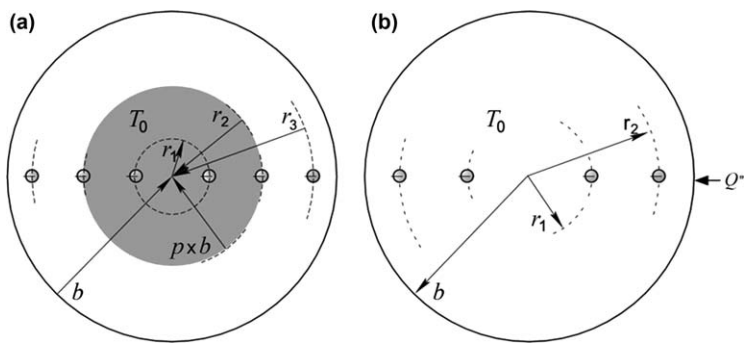

Figure 5.3 (a) Plan view of the sample showing the position of the heated region and the temperature measurement location; cylindrical disk with central region heating. (b) Plan view of the sample showing the position of the heated region and the temperature measurement location; cylindrical disk with edge heating.

It can be shown that the difference between the higher order terms in eqn (5.17) is relatively less than ±1 % of the $n=1$ term for $at/b^2>0.015$. This corresponds to a time greater than 3.7 s for $b=5$ cm and $\alpha=0.1$ cm$^2\cdot$s^{-1}. Neglecting such high order terms, and taking the natural logarithms of the differences $\Delta T_{ij}=T(r_i, t)-T(r_j, t)$, we obtain

$$\ln(\Delta T_{ij})=\ln(\beta_{ij})-\left(\frac{a\mu_1^2}{b^2}\right)t. \tag{5.18}$$

where

$$\beta_{ij}=T_0\frac{2pJ_1(\mu_1 p)}{\mu_1 J_0^2(\mu_1)}\left(J_0\left(\mu_1\frac{r_i}{b}\right)-J_0\left(\mu_1\frac{r_j}{b}\right)\right). \tag{5.19}$$

Details of all of the initial conditions, including the initial applied temperature T_0, are contained in β_{ij}. Therefore, the slope of a plot of $\ln(\Delta T_i)$ *versus* t is independent of the details of the initial conditions and is proportional to the value of a, with a known proportionality constant.

The values of thermal diffusivity are obtained from the slopes of the curves of $\ln(\Delta T_{ij})$ as a function of time, as shown in Figure 5.4. This method has

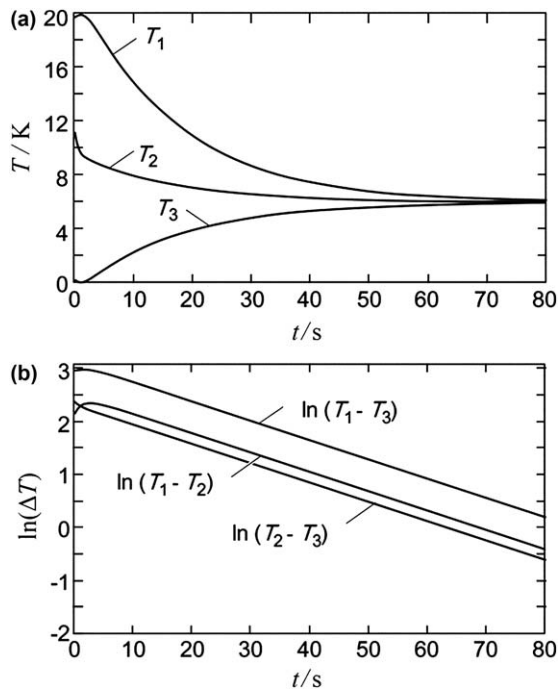

Figure 5.4 Temperature profiles and values of $\ln(\Delta T_{ij})$ as a function of time t, generated numerically by using the special heated region and measurement locations. The thermal diffusivity was 0.1 cm$^2\cdot$s^{-1}. T is the temperature at the special measurement location.

been experimentally confirmed using fine grained boron nitride and graphite.[126]

5.3.2.3 Temperature in a Cylindrical Rod (Disk with Edge Heating)

A third geometry that can be considered is a cylinder that is uniformly heated at the cylindrical surface and with perfectly insulated top and bottom faces. By neglecting the heat loss at the top and bottom faces, this problem is similar to the case of an infinite cylinder for which the temperature depends only on the cylinder's radius, r. The cylinder is considered axially symmetric so that there is no angular dependence.

The cylinder is initially at the temperature T_0, and a constant heat flux Q'' (in Watt per unit area) is applied to the surface for a time $0 \leq t \leq t_e$, schematically shown in Figure 5.1c. The rate of change of the temperature as a function of position and time $T(r,t)$ is obtained by solving the transient form of the heat equation in cylindrical coordinates

$$\frac{1}{r}\frac{\partial T}{\partial r} + \frac{\partial^2 T}{\partial r^2} = \frac{1}{a}\frac{\partial T}{\partial t}. \tag{5.20}$$

The boundary conditions for this problem are

$$T(r,0) = T_0, \tag{5.21}$$

and, at $r = R$,

$$-\lambda\frac{\partial T}{\partial r} = Q''[1 - h(t - t_e)]. \tag{5.22}$$

where h is the Unit Step function, and λ is the thermal conductivity.

Using Laplace transforms an expression for $T(r,t)$ is obtained [see ref. 116 for the complete derivation]:

$$T(r,t) = f(r,t) + h(t - t_e)f(t - t_e). \tag{5.23}$$

The inverse Laplace transform for this expression is given by Carslaw and Jaeger[125]

$$f = -\frac{Q''R}{\lambda}\left\{\frac{2at}{R^2} + \frac{r^2}{2R^2} - \frac{1}{4} - 2\sum_{s=1}^{\infty}\exp\left(-\frac{\kappa\alpha_s^2 t}{R^2}\right)\left[\frac{J_0\left(\frac{r\alpha_s}{R}\right)}{\alpha_s^2 J_0(\alpha_s)}\right]\right\}. \tag{5.24}$$

where α_s are the positive roots of $J_1(\alpha)$. It is important to note that the result from Carslaw and Jaeger has the initial condition $T_0 = 0$. For the more general case used here, the initial value T_0 of the temperature is added to their result.

The value of the Unit Step function in the solution divides the solution into two distinct pieces, since its value is zero or unity depending on whether or not heat is added to the system. These are:

(1) For $t \leq t_e$ (during the heating) the second term on the right side of eqn (5.23) is equal to zero, thus the temperature distribution is given by

$$T(r,t) = T_0 - \frac{Q''R}{\lambda}\left\{\frac{2at}{R^2} + \frac{r^2}{2R^2} - \frac{1}{4} - 2\sum_{s=1}^{\infty}\exp\left(-\frac{a\alpha_s^2 t}{R^2}\right)\left[\frac{J_0\left(\frac{r\alpha_s}{R}\right)}{\alpha_s^2 J_0(\alpha_s)}\right]\right\}, \tag{5.25}$$

and

(2) for $t \geq t_e$ (as equilibrium is reached) the temperature distribution becomes

$$T(r,t) = T_0 - \frac{Q''R}{\lambda}\left\{\frac{2at}{R^2} + \frac{r^2}{2R^2} - \frac{1}{4}\right\} + \frac{Q''R}{\lambda}2\sum_{s=1}^{\infty}\exp\left(-\frac{a\alpha_s^2 t}{R^2}\right)\left[\frac{J_0\left(\frac{r\alpha_s}{R}\right)}{\alpha_s^2 J_0(\alpha_s)}\right]$$

$$+\frac{Q''R}{\lambda}\left\{\frac{2\kappa(t-t_e)}{R^2} + \frac{r^2}{2R^2} - \frac{1}{4}\right\} - \frac{Q''R}{\lambda}2\sum_{s=1}^{\infty}\exp\left(-\frac{a\alpha_s^2(t-t_e)}{R^2}\right)\left[\frac{J_0\left(\frac{r\alpha_s}{R}\right)}{\alpha_s^2 J_0(\alpha_s)}\right]. \tag{5.26}$$

For the remaining derivation of this section, only the relaxation modelled by eqn (5.26) is studied because only the temperature profile after the end of the pulse is sought. Rearranging eqn (5.26) and factoring by $J_0(r\alpha_s/R)/(b_s^2 J_0(\alpha_s))$ yields the final expression of the temperature distribution in the cylinder *versus* time

$$T(r,t) = T_0 - \frac{Q''R}{\lambda} \times \left(\frac{2at_e}{R^2} - 2\sum_{s=1}^{\infty}\left\{\exp\left(-\frac{a\alpha_s^2 t}{R^2}\right)\left[1 - \exp\left(\frac{a\alpha_s^2 t_e}{R^2}\right)\right]\right\}\left[\frac{J_0\left(\frac{r\alpha_s}{R}\right)}{\alpha_s^2 J_0(\alpha_s)}\right]\right). \tag{5.27}$$

In contrast to the simplifications made by Pourpoint *et al.*,[123] here the infinite sum can be simplified by eliminating only the $n = 2$ term. This term can be set to zero by choosing the temperature measurement locations, r, so that $r\alpha_2/R = \nu_n$ corresponding to the first two zeros of J_0, or: $J_0(\nu_n) = 0$. The values of ν_n are: 2.4048 and 5.5201, respectively. With $\alpha_2 = 7.01559$, this results in two special values of r defined by

$$\frac{r_1}{R} = \frac{\nu_1}{\alpha_2} = 0.342779, \tag{5.28}$$

and

$$\frac{r_2}{R} = \frac{\nu_2}{\alpha_2} = 0.786833, \tag{5.29}$$

The next value of ν_3 is 8.6537, this is a measurement position physically outside the cylinder.

While it is not possible to eliminate the other terms by a similar simplification, the terms for $n \geq 3$ (higher order terms) decay rapidly with time in comparison to the first two terms and are therefore not included in the final form. The final form of the temperature *versus* time at the measurement locations is:

$$\Delta T_{ij} = \exp\left(-\frac{a\alpha_1^2 t}{R^2}\right)\frac{2Q''R}{\lambda}\left[1-\exp\left(\frac{a\alpha_1^2 t_e}{R^2}\right)\right]\left[\frac{J_0\left(\frac{r_i\alpha_1}{R}\right)-J_0\left(\frac{r_j\alpha_1}{R}\right)}{\alpha_1^2 J_0(\alpha_1)}\right]. \tag{5.30}$$

The first exponential term on the right side is the only term which is a function of time. The remainder of this equation is a constant, depending only on the measurement locations. Taking the natural logarithm of eqn (5.30) yields the final (reduced) solution

$$\ln(\Delta T_{ij}) = -\frac{a\alpha_1^2}{R^2}t + \ln(\beta_{ij}), \tag{5.31}$$

where

$$\beta_{ij} = \frac{2Q''R}{\lambda}\left[1-\exp\left(\frac{a\alpha_1^2 t_e}{R^2}\right)\right]\left[\frac{J_0\left(\frac{r_i\alpha_1}{R}\right)-J_0\left(\frac{r_j\alpha_1}{R}\right)}{\alpha_1^2 J_0(\alpha_1)}\right]. \tag{5.32}$$

Eqn (5.31) is linear in time, and therefore the thermal diffusivity can be obtained by plotting the natural logarithm of the delta temperature with respect to time. The slope of the curve involves the constants a, R and α_1 for a given geometry. Thus, using this methodology, the thermal diffusivity can be obtained knowing only the temperature versus time at selected locations. In eqn (5.31) the argument of the logarithm has the dimensions of temperature. This argument could be non-dimensionalized by dividing ΔT_{ij} by the $2Q''R/\lambda$ term in eqn (5.30) before taking the logarithm. Alternatively, eqn (5.30) could be divided by an arbitrary reference temperature. This manipulation would only shift the curve and does not lead to a different value of the thermal diffusivity. Figure 5.4b shows the experimental platform for this reduced algorithm.

The values of thermal diffusivity are obtained from the slopes of the curves of $\ln(\Delta T_{ij})$ as a function of time, as shown in Figure 5.5a and Figure 5.5b from the analytical model. The data is plotted from the end of the heat pulse time t_e, which in this case is 3 s. After the thermal diffusion time R^2/a (here approximately 6 s), the curves are parallel straight lines. This methodology has been confirmed using 304 Stainless Steel for both a thick and thin cylinder.[127]

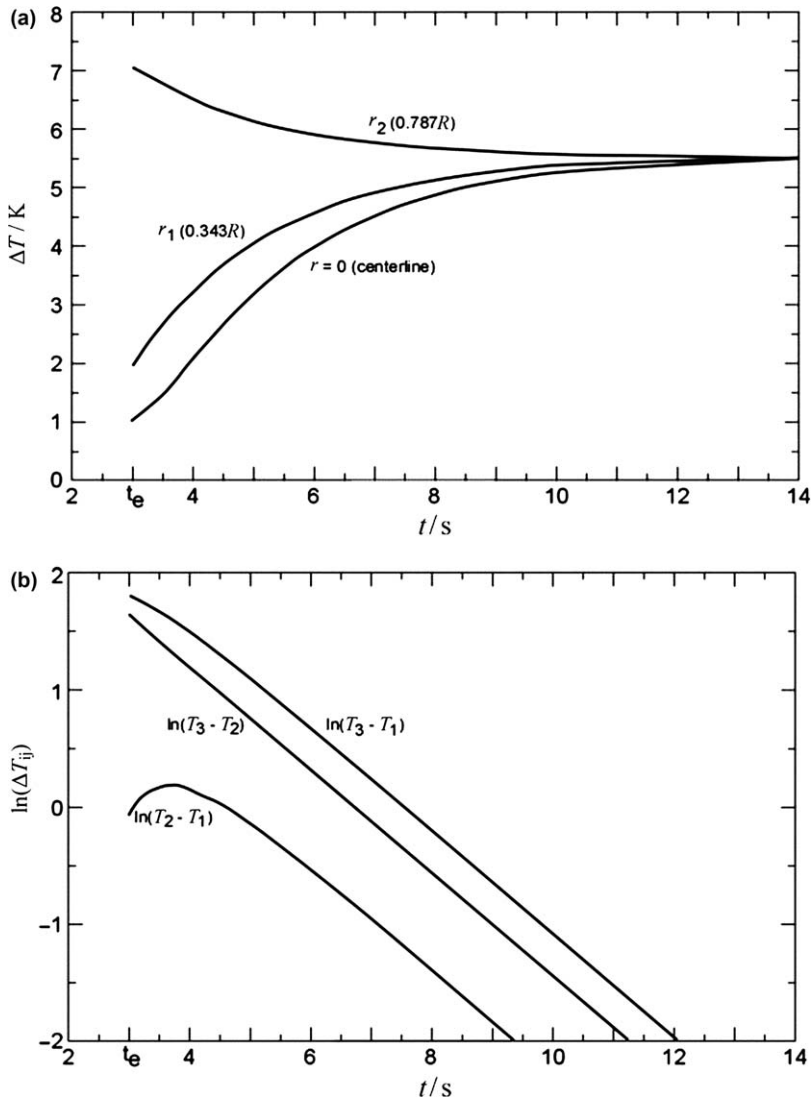

Figure 5.5 Temperature profiles (a) and values of $\ln(\Delta T_{ij})$ as a function of time t at the reduced measurement locations numerically generated using equations 26b and 28. The $a = 0.482\ \mathrm{cm^2 \cdot s^{-1}}$. $Q'' = 15\ \mathrm{W \cdot cm^{-2}}$.

Acknowledgements

This research has been supported by the National Aeronautics and Space Administration under contracts NAS8-39716, NCC8-99, NAG8-1476, and by the State of Alabama. The fruitful discussion between the various investigators is gratefully noted.

5.4 Diffusion Techniques for High Pressure and Low and High Temperatures

KENNETH R. HARRIS

5.4.1 Introduction

5.4.1.1 Scope of the Review

This section reviews recent work on the measurement of diffusion in fluids away from ambient conditions, *i.e.* high pressures, low and high temperatures and in viscous liquids. These methods are therefore specialised, but it is hoped the review will give readers an awareness of the applicability of these techniques and the potential for further application. Precise methods for use under ambient conditions are reviewed elsewhere.[3,128–131] Some of these monographs are out of print, so here references to recent applications of major techniques are included: the Loschmidt cell method[132,133] and Taylor dispersion[134] for inter-diffusion in gases; for liquids, the conductimetric method,[135] Taylor dispersion,[136,137] including the chromatographic impulse response variant,[138,139] and Rayleigh,[140] Gouy,[141] Mach–Zehnder,[142] Raman[143–146] and other[147,148] interferometric methods. For intra- or self-diffusion, modern NMR techniques are described in Chapter 3. Polymers and liquid metals are not considered.

5.4.1.2 Definitions

The term ''diffusion'' is used to describe the flow of matter due to the dissipation of concentration gradients in solution at constant pressure and temperature in the absence of convection: more generally, diffusion is the relaxation of thermodynamic chemical potential gradients due to molecular motion, but it is always changes in concentration that are observed in practice. The conventions for describing diffusion are given in ref. 3, and 128 to 131. This section deals with *mutual*[149] or *inter*-diffusion[150] coefficients, D_{12} in binary systems, *self*-diffusion[151,152] coefficients D_{Si}, determined for a *pure* substance where the species 0 and 1 have identical properties, but are distinguishable by some sort of labelling so that the concentrations are measurable, and tracer diffusion coefficients, D_{Ti}, the limiting mutual diffusion coefficient where the labelled material is different to the solvent, but present at very high dilution. Albright and Mills[153] introduced the more general concept of *intra*-diffusion for the inter-diffusion of labelled and unlabelled species in an otherwise homogeneous solution of any number of components. It is independent of the ratio of the labelled and unlabelled species, which may or may not be the case in actual tracer diffusion experiments.[154] The intra-diffusion coefficient equals the self-diffusion coefficient in a single-component system and is also the limiting value of tracer-diffusion coefficients extrapolated to remove isotope effects.[154] (Interestingly, the latter are exploited for environmental studies.[155]) Self- and tracer diffusion

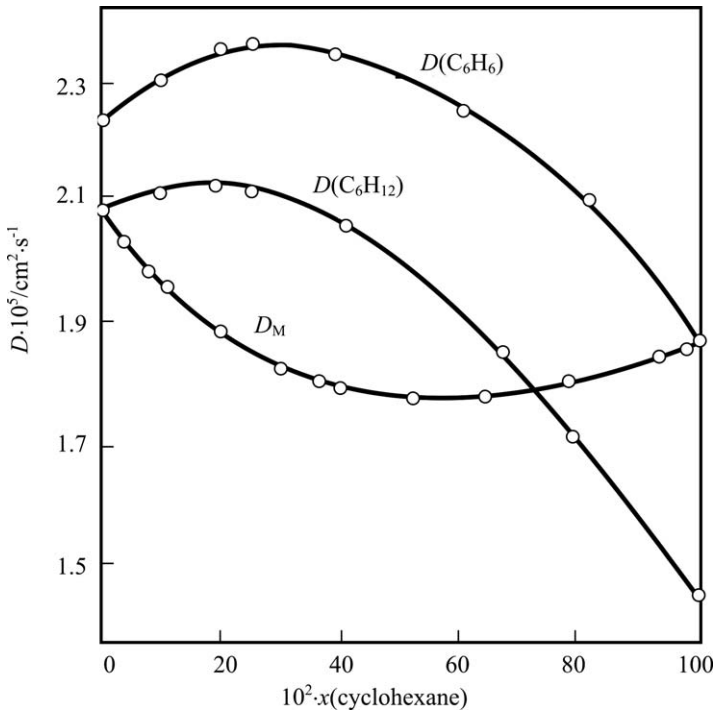

Figure 5.6 Comparison of mutual, D_M, and intra-diffusion, D, coefficients for benzene–cyclohexane.
Adapted with permission from R. Mills, *J. Phys. Chem.*, 1965, **69**, 3116. Copyright (1965) American Chemical Society.

can also be regarded as a measure of molecular motion due to fluctuations in local number density.

Figure 5.6 illustrates these definitions for the system benzene-cyclohexane.[156] Note that the two limiting intra- (or tracer) diffusion coefficients equal the two limiting mutual diffusion coefficients. The two intra-diffusion coefficients equal the self-diffusion coefficients at the opposite composition extremes and show maxima, whereas the mutual diffusion coefficient shows a minimum. Minima in the latter approach zero at consolute points[157] where phase separation occurs and inter-diffusion ceases.

5.4.2 Mutual Diffusion Techniques

5.4.2.1 Super-cooled and Viscous Liquids

The measurement of diffusion in super-cooled and viscous liquids is of great interest for a theoretical understanding of liquids and glasses,[158] and is particularly challenging.

Ediger and coworkers[159,160] have determined tracer diffusion coefficients of fluorescent probe molecules in glassy liquids with a technique based on

holographic fluorescence recovery following photobleaching or *holographic FRAP*. A proportion of trace amounts of the aromatic probe molecules are excited by crossed "writing" laser beams and undergo "photoperoxidation" in a reaction with dissolved oxygen. This sets up small concentration gradients of the unreacted probe molecules. The relaxation time for these gradients is measured from the decay of fluorescence induced by "reading" beams modulated with respect to one another. The temperature is controlled to ± 0.05 K and known to ± 2 K at temperatures in the range (235 to 515) K. The relative uncertainty in D is ± 10 %,[155] but the technique provides values over 9 orders of magnitude in D.

Matthiesen, Smith and Kay[161,162] have recently described a low temperature *film-permeation method* for the mutual diffusion of inert gases in supercooled alcohols, which varies by ≈ 5 orders of magnitude over 15 K at a temperature of about 100 K. A monolayer of gas from a molecular beam is deposited on a graphene-coated Pt(111) crystal at $T = 25$ K under very high vacuum; this layer is then covered with either pure or mixed layers of alcohol, 50 to 100 monolayers in thickness. The system is warmed above the known glass temperature and the inert gas then diffuses into the alcohol. The rate of desorption of the gas from the liquid is measured using a quadrupole mass spectrometer and the mutual diffusion coefficient determined from the time at which the desorption rate is at a maximum, t_{peak}. The temperature was determined with a stability of ± 0.01 K and an uncertainty of ± 2 K with a K-type thermocouple. The diffusion coefficient is determined from

$$D = \alpha_{peak} L^2 / t_{peak}, \tag{5.33}$$

where L is the known layer thickness and α_{peak}, a constant equal to 0.167, is the peak desorption rate on a scaled universal curve determined from a simulation of a one-dimensional permeation of a solute through a liquid membrane. An alternate film technique has been described by Eidiger *et al.*[163]

Ionic liquids pose problems for most classical diffusion measurement methods due to their high viscosity. *Laser light scattering* avoids this difficulty as the scattered radiation gives information about the relaxation of thermal concentration fluctuations and no macroscopic composition gradient is needed.[129] Rausch *et al.*[164] have described the application of this method to mutual diffusion for ionic and molecular liquid mixtures.

5.4.2.2 *Liquids at High Pressure*

Jorgenson *et al.*[165] have described a variant of the *Taylor dispersion* apparatus[3,128,129,131] for use to pressures of 350 MPa that is shown in Figure 5.7. It is uses a fused silica capillary (Polymicro Technologies, Inc., Phoenix, AZ, USA) capable of withstanding high pressure as the diffusion column, with a reservoir also at high pressure to receive the column eluent. The pressure drop is about 10 MPa. The capillary ends were fastened to the high-pressure

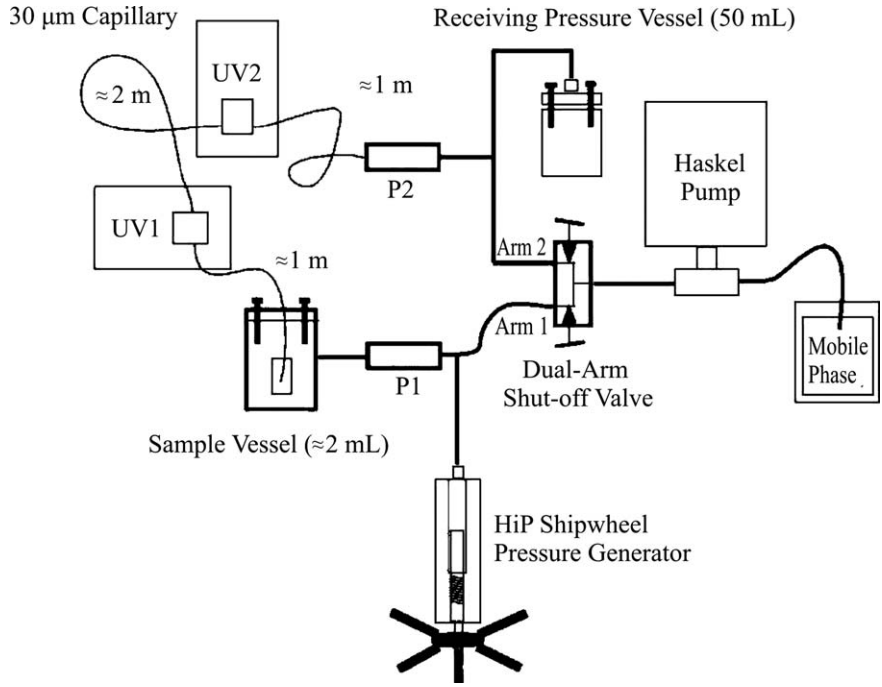

Figure 5.7 High-pressure Taylor dispersion apparatus for tracer diffusion: UV, ultra-violet absorbance detector; P, pressure sensors.
Reproduced with permission from T. J. Kaiser, J. W. Thompson, J. S. Mellos and J. W. Jorgenson, *Anal. Chem.*, 2009, **81**, 2860. Copyright (2009) American Chemical Society.

generation and measurement system with specially designed compression fittings.[166] Two Linear UVIS 200 UV-vis spectrophotometric detectors were placed at windows made by removing the polyimide coating from the capillary. This type of detector limits measurements to tracer diffusion of uv-absorbing solutes, but other types could be used. The relative uncertainty in D_T, as judged from graphical results, is about $\pm$(3 to 5)%. The solution viscosity can be measured from the flow rate with the same apparatus.

Mach–Zehnder interferometry has been used by Dysthe and Hafskjold *et al.*[167] to determine mutual diffusion coefficients for (methane + decane) over a broad composition range at pressures up to 60 MPa. The key to the apparatus is the high-pressure cell, Figure 5.8. This was initially filled with the less dense solution, equilibrated at the desired temperature. The denser solution, also thermally equilibrated, was gently injected from below until the solution boundary was in the centre of the cell. Data acquisition was then begun. As in other interferometers,[3,128,129] the phase profile $\phi(z)$ due to the refractive index gradient along the z-axis and relative to a fixed point in the cell is determined, here using a charge-coupled device video camera. The Mach–Zender system yields the second moment, $\mathscr{D}_{2m}$: the authors derive an analysis based on the assumption of ideal boundary conditions and an expansion in

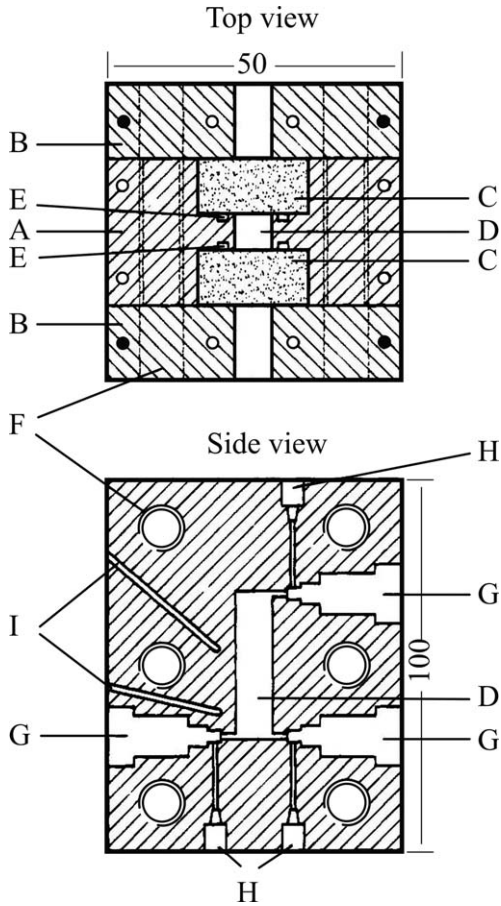

Figure 5.8 High-pressure cell for Mach–Zender interferometry mutual diffusion: ○, channels for heating wire; A, B, aluminium-bronze cell body sections; C, sapphire windows; D, cell volume; E, O-ring seals; G, valves; H, tube couplings; I, thermometer sockets.
Reproduced with permission from D. K. Dysthe, B. Hafskjold, J. Breer and D. Cejka, *J. Phys. Chem.*, 1995, **99**, 11230. Copyright (1995) American Chemical Society.

Hermite polynomials of the reduced phase of the light passing through the cell around the solution of the ideal diffusion equation. The relative uncertainty, tested against the standard reference systems ($H_2O + NaCl$) and (H_2O + 2-methyl-2-propanol) was ± (0.6 and 1.4) %, respectively.

5.4.2.3 Dense Gases and Supercritical Fluids

A large amount of work has been done on tracer diffusion of solutes in supercritical fluids, principally carbon dioxide, but also water, SF_6 and other fluids.[168,169] The method of choice is *Taylor dispersion*[3,128,129] as HPLC

pumps and detectors are readily adapted to diffusion measurements at moderate pressures. Detailed analyses have been given by several authors.[170,171] Recent improvements include methods to overcome coiling effects[172] and peak tailing, using polymer-coated columns, known as the *chromatographic impulse response* (CIR) technique,[137–139,173] split-flow methods[174] and improved data analysis.[175]

5.4.3 Self-diffusion

Spin-echo nuclear magnetic resonance (NMR) methods are the method of choice for high-temperature and high-pressure self- and intra-diffusion measurements and in high viscosity fluids. Chapter 3 describes the many pulsed magnetic field gradient spin-echo methods available in detail.

5.4.3.1 High Temperatures

Yoshida *et al.*[176] have described a high-resolution NMR probe for use to $T = 673$ K in a spectrometer with a wide-bore superconducting magnet. This is shown in Figure 5.9. The key features are the use of a high thermal conductivity ceramic (Al_2N_3) sample holder that also acts as a shield in the case of a cell explosion; dual heaters above and below the sample, moderated by air and water cooling; both low and high frequency radio-frequency coils (Au) and magnetic-field gradient coils wound on ceramic bobbins in close proximity to the sample; a sealed quartz sample cell; and a Pt–Pt/Rh thermocouple immediately below the cell for temperature measurement. The maximum magnetic-field gradient is 2700 $mT \cdot m^{-1}$. Particular care was taken to ensure homogeneity of the r.f. field over the sample by not switching the heaters on or off during signal acquisition and the minimization of temperature gradients through control of the currents in the two heaters. Half-sine-shaped gradient pulses were used to reduce phase-based and vibration artifacts.[177] The relative uncertainty in D_S varies from $\pm$(1 to 4) % at 673 K. The probe was calibrated at only the single temperature of 303 K, but the results for both ordinary and heavy water over a broad range of temperature are consistent with the results from other methods.[178]

NMR has also been applied to molten salt self-diffusion for a range of nuclei, including ^{7}Li, ^{19}F, ^{23}Na and ^{27}Al.[179–181] The probe is shown in Figure 5.9 and can be used at temperatures up to 1500 K.[182] The sample crucible is made from boron nitride, shielded with quartz and alumina tubes mounted in a mullite cradle, and heated with CO_2 lasers from above and below. Heat is removed from the system by a flow of argon gas through the cradle and a second flow of nitrogen is used to keep the r.f. and gradient coils at constant temperature. Bipolar gradients of up to 550 $mT \cdot m^{-1}$ were employed using a stimulated echo sequence[183] in the original work to reduce convection effects, later replaced by a more effective double stimulated echo sequence.[184] Checks were made that the results did not depend on the interval between the gradient pulses. The relative uncertainty, estimated

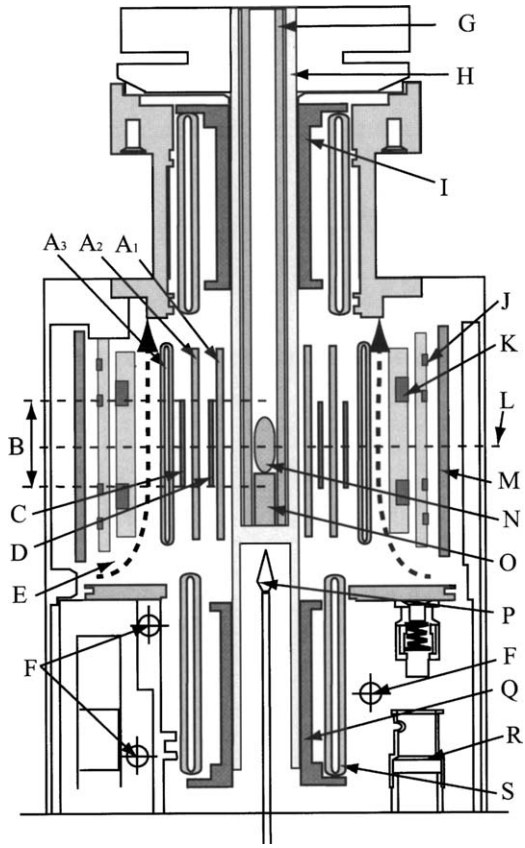

Figure 5.9 NMR probe for high temperature self-diffusion: A, mountings for low frequency (C), high frequency (D) and magnetic field gradient (K) coils; B, length of rf coil; E, air flow; F, water-cooling tubing; G, zirconia tube; H, holder for sample, N; I, Q, heaters; J, shielding coil; M, mirror; P, thermocouple; S, insulation.
Reprinted with permission from K. Yoshida, C. Wakai, N. Matubayashi and M. Nakahara, *J. Chem. Phys.*, 2005, **123**, 164506. (Fig. 1). Copyright 2005 AIP Publishing LLC.

from comparison with tracer measurements for NaF and Na_3AlF_6, was about ± 10 %.

5.4.3.2 High Pressures

There has been a decline in high pressure measurement of self-diffusion over the last two decades as its practitioners have retired. The high-pressure diaphragm cell technique was described in ref. 3. References are included here for past and current NMR systems based on steady[185–190] and pulsed field gradients.[191–195]

References

1. M. J. Assael and K. D. Antoniadis, *Proc. 30th International Thermal Conductivity Conference*, Pittsburg, USA, 2009.
2. M. J. Assael, K. D. Antoniadis and W. A. Wakeham, *Int. J. Thermophys.*, 2010, **31**, 1051.
3. *Experimental Thermodynamics. Vol. III. Measurement of the Transport Properties of Fluids*, ed. W. A. Wakeham, A. Nagashima and J. V. Sengers, Blackwell Scientific Publications, London, 1991.
4. J. Priestley, *Experiments and Observations Relating to Various Branches of Natural Philosophy; with a Continuation of the Observations on Air. Vol. II.*, Pearson and Rollason, London, 1781.
5. J. Renwick, *Life of Benjamin Thompson, Count Rumford*, Charles C. Little and James Brown, Boston, 1848.
6. J. Leslie, *An Experimental Inquiry into the Nature and Propagation of Heat*, J. Mawman, Edinburgh, 1804.
7. W. R. Grove, *Philos. Mag. Series III*, 1845, **27**, 442.
8. G. Magnus, *Philos. Mag. Series IV*, 1861, **22**, 85.
9. J. Tyndall, *Heat Considered as a Mode of Motion: Being a Course of Twelve Lectures Delivered at the Royal Institution of Great Britain in the Season of 1862*, Longman, Green, Longman, Roberts, & Green, London, 1863.
10. J. C. Maxwell, *Philos. Mag. Series IV*, 1860, **19**, 19.
11. J. C. Maxwell, *Philos. Mag. Series IV*, 1860, **20**, 21.
12. R. J. E. Clausius, *Philos. Mag. Series IV*, 1862, **23**, 417.
13. J. Stefan, *Math. Naturwiss. K1. Abt. II*, 1872, **65**, 45.
14. J. Stefan, *Sitzungsberichte der Kaiserlichen Akademie der Wissenshaft*, 1875, **72**, 69.
15. A. Schleiermacher, *Ann. Phys. Chem.*, 1888, **270**, 623.
16. S. Weber, *Ann. Phys.*, 1917, **359**, 437.
17. S. Weber, *Annalen der Physik*, 1917, **359**, 325.
18. B. Stålhane and S. Pyk, *Teknisk Tidskrift*, 1931, **61**, 389.
19. A. Eucken and Z. Englert, *Gesamte Gerichtl. Kalte-Industrie*, 1938, **45**, 109.
20. E. F. M. van der Held and F. G. van Drunen, *Physica*, 1949, **15**, 865.
21. E. F. M. van der Held, J. Hardebol and J. Kalshoven, *Physica*, 1953, **19**, 208.
22. D. A. de Vries, *Soil Science*, 1952, **78**, 83.
23. D. G. Gillam, L. Romben, H.-E. Nissen and O. Lamm, *Acta Chem. Scand.*, 1955, **9**, 1955.
24. P. Grassman and W. Straumann, *Int. J. Heat Mass Transfer*, 1960, **1**, 50.
25. W. E. Haupin, *Am. Ceram. Soc. Bull.*, 1960, **39**, 139.
26. A. G. Turnbull, *J. Chem. Eng. Data*, 1962, **7**, 79.
27. J. K. Horrocks and E. McLaughlin, *Proc. Roy. Soc. London A*, 1963, **273**, 259.
28. A. von Mittenbühler, *Ber. Dtsch. Keram. Ges.*, 1964, **41**, 15.
29. H. L. Burge and L. B. Robinson, *J. Appl. Phys.*, 1968, **39**, 51.

30. K. Hayashi, M. Fukui and I. Uei, *Mem. Fac. Ind. Arts, Kyoto Tech. Univ. Sci. Technol.*, 1971, **20**, 81.
31. P. S. Davis, F. Theeuwes, R. J. Bearman and R. P. Gordon, *J. Chem. Phys.*, 1971, **55**, 4476.
32. E. McLaughlin and J. F. T. Pittman, *Phil. Trans. R. Soc. London A*, 1971, **270**, 557.
33. J. W. Haarman, *Physica*, 1971, **52**, 605.
34. J. W. Haarman, PhD Thesis, Technische Hogeschool Delft, 1969.
35. J. J. Healy, J. J. de Groot and J. Kestin, *Physica C*, 1976, **82**, 392.
36. J. J. de Groot, J. Kestin and H. Sookiazian, *Physica*, 1974, **75**, 454.
37. C. A. Nieto de Castro, J. C. G. Calado, W. A. Wakeham and M. Dix, *J. Phys. E: Sci. Instrum.*, 1976, **9**, 1073.
38. J. Kestin, R. Paul, A. A. Clifford and W. A. Wakeham, *Physica A*, 1980, **100**, 349.
39. M. J. Assael, M. Dix, A. Lucas and W. A. Wakeham, *J. Chem. Soc. Faraday Trans I.*, 1980, **77**, 439.
40. E. N. Haran and W. A. Wakeham, *J. Phys. E: Sci. Instrum.*, 1982, **15**, 839.
41. A. Alloush, W. B. Gosney and W. A. Wakeham, *Int. J. Thermophys.*, 1982, **3**, 225.
42. W. A. Wakeham and M. Zalaf, *Physica B + C*, 1986, **139–140**, 105.
43. E. Charitidou, M. Dix, C. A. Nieto de Castro and W. A. Wakeham, *Int. J. Thermophys.*, 1987, **8**, 511.
44. S. H. Jawad, M. Dix and W. A. Wakeham, *Int. J. Thermophys.*, 1999, **20**, 45.
45. M. J. Assael, C.-F. Chen, I. N. Metaxa and W. A. Wakeham, *Int. J. Thermophys.*, 2004, **25**, 971.
46. M. J. Assael, K. D. Antoniadis and J. Wu, *Int. J. Thermophys.*, 2008, **29**, 1257.
47. M. V. Peralta-Martinez, M. J. Assael, M. Dix, L. Karagiannidis and W. A. Wakeham, *Int. J. Thermophys.*, 2006, **27**, 353.
48. M. V. Peralta-Martinez, M. J. Assael, M. Dix, L. Karagiannidis and W. A. Wakeham, *Int. J. Thermophys.*, 2006, **27**, 681.
49. A. Rosencwaig, *Photoacoustics and photoacoustic spectroscopy*, Willey, 1980.
50. A. C. Tam, *Rev. Mod. Phys.*, 1986, **58**, 381.
51. S. J. Sheldon, L. V. Knight and J. M. Thorne, *Appl. Opt.*, 1982, **21**, 1663.
52. C. Jacinto, D. N. Messias, A. A. Andrade, S. M. Lima, M. L. Baesso and T. Catunda, *J. Non-Cryst. Solids*, 2006, **352**, 3582.
53. A. C. Boccara, D. Fournier, W. B. Jackson and N. M. Amer, *Opt. Lett.*, 1980, **5**, 377.
54. A. C. Tam, *Infrared Phys.*, 1985, **25**, 305.
55. A. Mandelis, *Chem. Phys. Lett.*, 1984, **108**, 388; A. Mandelis and M. M. Zver, *J. Appl. Phys.*, 1985, **57**, 4421.
56. M. Chirtoc, D. Bicanic and V. Tosa, *Rev. Sci. Instrum.*, 1991, **62**, 2257.
57. J. Shen and A. Mandelis, *Rev. Sci. Instrum.*, 1995, **66**, 4999.

58. F. F. Cernuschi, P. G. P. G. Bison, A. A. Figari, S. S. Marinetti and E. E. Grinzato, *Int. J. Thermophys.*, 2004, **25**.
59. R. Fuente, E. Apiñaniz, A. Mendioroz and A. Salazar, *J. Appl. Phys.*, 2011, **110**, 033515.
60. A. Salazar and A. S. Lavega, *Rev. Sci. Instrum.*, 1994, **65**, 2896.
61. S. R. Choi, D. Kim and S.-H. Choa, *Int. J. Thermophys.*, 2006, **27**.
62. E. H. Lee, K. J. Lee, P. S. Jeon and J. Yoo, *J. Appl. Phys.*, 2000, **88**, 588.
63. Y. Zhao, C. Zhu, S. Wang, J. Z. Tian, D. J. Yang, C. K. Chen, H. Cheng and P. Hing, *J. Appl. Phys.*, 2004, **96**, 4563.
64. R. Kato, A. Maesono and R. P. Tye, *Int. J. Thermophys.*, 2001, **22**.
65. L. Kehoe, P. V. Kelly and G. M. Crean, *Application of the laser flash diffusivity method to thin high thermal conductivity materials, Microsystem Technologies 5*, Springer, Verlag, 1998.
66. E. Welsch, K. Ettrich, D. Ristau and U. Willamowski, *Int. J. Thermophys.*, 1999, **20**.
67. K. G. Biswas, T. D. Sands, B. A. Cola and X. Xu, *Appl. Phys. Lett.*, 2009, **94**, 223116.
68. Z. Hua, H. Ban, M. Khafizov, R. Schley, R. Kennedy, D. H. Hurley *et al.*, *J. Appl. Phys.*, 2012, **111**, 103505.
69. J. Ravi, M. K. Jayaraj, K. A. Vanaja, K. P. R. Nair1 and T. M. A. Rasheed, *Semicond. Sci. Technol.*, 2003, **18**, 693.
70. L. A. Silva, J. B. de Andrade, C. Moyses Araujo, O. Nakamura, A. F. Ferreira da Silva, M. S. O. Massunaga and H. Vargas, *Phys. Chem. Chem. Phys.*, 2001, **3**, 4800È4805.
71. B. Hay, J.-R. Filtz, J. Hameury, G. Davée, L. Rongione and O. Enouf, *Int. J. Thermophys.*, 2009, **30**, 1270.
72. D. G. Sajan, R. Komban, K. G. K. Warrier, P. Radhakrishnan, V. P. N. Nampoori and C. P. G. Vallabhan, *Int. J. Thermophys.*, 2007, **28**.
73. S. T. Lee, K. Raveendranath, M. R. Tomy, M. Paulraj, S. Jayalekshmi, K. P. R. Nair and J. Ravi, *Phys. Rev. B*, 2007, **76**, 115112.
74. T. S. Silva, A. S. Alves, I. Pepe, H. Tsuzuki, O. Nakamura, M. M. F. d'Aguiar Neto, A. Ferreira da Silva, N. Veissid and C. Y. An, *J. Appl. Phys.*, 1998, **83**, 6193.
75. D. Ferizović, L. K. Hussey, Y.-S. Huang and M. Muñoz, *Appl. Phys. Lett.*, 2009, **94**, 131913.
76. X.-Z. Ding, M. K. Samani and G. Chen, *Appl. Phys. A*, 2010, **101**, 573.
77. J. Martan, O. Hervé and V. Lang, *J. Appl. Phys.*, 2007, 064903.
78. S. B. Peralta, Z. H. Chen and A. Mandelis, *Appl. Phys. A*, 1991, **52**, 289.
79. S. Thomas, J. Isaac and J. Philip, *Rev. Sci. Instrum.*, 1995, **66**, 3907.
80. P. K. Wong, P. C. W. Fung and H. L. Tam, *J. Appl. Phys.*, 1998, **84**, 6623.
81. F. B. G. Astrath, N. G. C. Astrath, J. Shen, J. Zhou and M. L. Baesso, *J. Appl. Phys.*, 2008, **104**, 066101.
82. J. A. Garcia, A. Mandelis, B. Farahbakhsh, C. Lebowitz and I. Harris, *Int. J. Thermophys.*, 1999, **20**, 1587.
83. S. W. Kim, C. H. Kang, S. H. Hahn, S. H. Lee and J. C. Kim, *Int. J. Thermophys.*, 2004, **25**, 1871.

84. K. Jeyadheepan, P. Palanichamy, V. Swaminathan, M. Jayachandran and C. Sanjeeviraja, *Appl. Phys. A*, 2010, **98**, 919.
85. J. E. de Albuquerque, P. M. S. de Oliveira and S. O. Ferreira, *J. Appl. Phys.*, 2007, **101**, 103527.
86. A. R. Warrier, T. Sebastian, C. S. Kartha and K. P. Vijayakumar, *J. Appl. Phys.*, 2010, **107**, 073701.
87. M. Soltanolkotabi, G. L. Bennis and R. Gupta, *J. Appl. Phys.*, 1999, **85**, 794.
88. O. Pessoa, C. L. Cesar, N. A. Patel, H. Vargas, C. C. Ghizoni *et al.*, *J. Appl. Phys.*, 1986, **59**, 1316.
89. M. Bertolotti, V. Dorogan, G. Liakhou, R. L. Voti, S. Paoloni and C. Sibilia, *Rev. Sci. Instrum.*, 1997, **68**, 1521.
90. J. Bernal-Alvarado, M. Vargas-Luna, O. Solorza-Feria, R. Mondragón and N. Alonso-Vante, *J. Appl. Phys.*, 2000, **88**, 3771.
91. S. Abdalla, K. Easawi, S. Negm, G. M. Youssef, T. A. El-Brolossy and H. Talaat, *Rev. Sci. Instrum.*, 2003, **74**, 848.
92. J. A. Balderas-López, G. Gutiérrez-Juárez, M. R. Jaime-Fonseca and F. Sánchez-Sinencio, *Rev. Sci. Instrum.*, 1999, **70**, 2069.
93. D. Comeau, A. Haché and N. Melikechi, *Appl. Phys. Lett.*, 2003, **83**, 246.
94. T. Lopez-Munoz *et al.*, *Nanoscale Res. Lett.*, 2012, **7**, 423.
95. J. F. S. Ramırez, J. L. J. Perez, R. C. Valdez, C. Orea, R. G. Fuentes and J. L. Herrera-Perez, *Int. J. Thermophys.*, 2006, **27**.
96. F. A. L. Machado, E. B. Zanelato, A. O. Guimarães, E. C. da Silva and A. M. Mansanares, *Int. J. Thermophys.*, 2012, **33**, 1848.
97. J. A. Balderas-López and A. Mandelis, *Rev. Sci. Instrum.*, 2003, **74**, 700.
98. B. Jaimes, D. Pulgar, M. A. Ranaudo, J. Chirinos and M. Caetano, *Rev. Sci. Instrum.*, 2010, **81**, 024902.
99. O. Delgado-Vasallo and E. Marin, *J. Phys. D: Appl. Phys.*, 1999, **32**, 593.
100. J. Caerels, C. Glorieux and J. Thoen, *Rev. Sci. Instrum.*, 1998, **69**, 2452.
101. R. Ivanov, E. Marin, I. Moreno and C. Araujo, *J. Phys. D: Appl. Phys.*, 2010, **43**, 225501.
102. G. A. L. Muñoz, R. F. L. González, J. A. B. López and L. Martínez-Pérez, *Int. J. Thermophys.*, 2011, **32**, 1006.
103. A. Matvienko and A. Mandelis, *Int. J. Thermophys.*, 2005, **26**.
104. J. A. Balderas-López, *Rev. Sci. Instrum.*, 2006, 77, 086104.
105. R. C. Valdez, J. L. J. Perez, A. Cruz-Orea and E. Martın-Martınez, *Int. J. Thermophys.*, 2006, **27**.
106. A. Sikorska, N. Ponikwicki, A. Koniecko and B. B. Linde, *Int. J. Thermophys.*, 2010, **31**, 131.
107. S. Delenclos, D. Dadarlat, N. Houriez, S. Longuemart, C. Kolinsky and A. Hadj Sahraoui, *Rev. Sci. Instrum.*, 2007, **78**, 024902.
108. N. A. George, C. P. G. Vallabhan, V. P. N. Nampoori, A. K. George and P. Radhakrishnan, *Appl. Phys. B*, 2001, **73**, 145.
109. A. P. L. Siqueira, I. A. Esquef, M. G. da Silva, L. C. M. Miranda and H. Vargas, *Eur. Phys. J. Special Topics*, 2008, **153**, 431.

110. J. H. Rohling, J. Shen, C. Wang, J. Zhou and C. E. Gu, *Eur. Phys. J. Special Topics*, 2008, **153**, 99.
111. B. Bonno, J. L. Laporte and R. T. D'Leon, *Rev. Sci. Instrum.*, 2005, **76**, 096104.
112. B. C. Li and R. Gupta, *J. Appl. Phys.*, 2001, **89**, 859.
113. L. B. Jalbert, F. Rosenberger and R. M. Banish, *J. Phys. Condens. Matter*, 1998, **10**, 7113.
114. R. M. Banish, J. I. D. Alexander and L. B. Jalbert, *Rev. Sci. Instrum.*, 2000, **71**, 4497.
115. T. Iida and R. I. L. Guthrie, *The Physical Properties of Liquid Metals*, Oxford Science Publications, Clarendon Press, Oxford, 1988.
116. M. Shimoji and T. Itami, *Atomic Transport in Liquid Metals*, Trans Tech Publications, Switzerland, 1986.
117. Y. Malejac and G. Frohberg, *Fluid Sciences and Materials Science in Space*, Springer-Verlag, Berlin, 1987.
118. L. B. Jalbert, *Ph.D. Dissertation*, University of Alabama in Huntsville, 1997 (unpublished).
119. J. Crank, *The Mathematics of Diffusion*, Oxford Press, Oxford, 1975 (eq. (4.58)).
120. H. S. Harned and R. L. Nuttall, *J. Am. Chem. Soc.*, 1947, **69**, 736.
121. P. Codastefano, A. Di Russo and V. Zanza, *Rev. Sci. Instrum.*, 1950, **48**, 1650.
122. A. G. Emslie and R. M. Banish, *Appl. Radiat. Isotopes*, 2001, **54**, 35.
123. L. B. Jalbert, R. M. Banish and F. Rosenberger, *Phys. Rev. E*, 1998, **57**, 1727.
124. R. M. Banish and L. B. Jalbert, *Adv. Space Res.*, 1999, **24**, 131.
125. H. S. Carslaw and J. C. Jaeger, *Conduction of Heat in Solids, Section 4.5*, Oxford Science Publications, Clarendon Press, Oxford, 2000.
126. T. Pourpoint, R. M. Banish, F. Wessling and R. F. Sekerka, *Rev. Sci. Instrum.*, 2000, **71**, 4512.
127. S. Brantschen, R. M. Banish and F. Wessling, *Rev. Sci. Instrum.*, 2004, **75**, 2869.
128. H. J. V. Tyrrell and K. R. Harris, *Diffusion in Liquids*, Butterworths, London, 1984, Chapter 5.
129. P. J. Dunlop, K. R. Harris and D. J. Young, in *Experimental Methods for Studying Diffusion in Gases, Liquids and Solids, in Physical Methods of Chemistry, Vol VI Determination of Thermodynamic Properties*, eds. B. W. Rossiter and R. C. Baetzold, John Wiley, New York, 2nd edn, 1986, ch. 3.
130. *Diffusion in Condensed Matter: Methods, Materials, Models*, eds. P. Heitjans and J. Kärger, 2nd edn, Springer Verlag, Dusseldorf, 2005.
131. E. L. Cussler, *Diffusion - Mass Transfer in Fluid Systems*, 3rd edn, Cambridge University Press, Cambridge, U.K., 2008.
132. D. Buttig, E. Vogel, E. Bich and E. Hassel, *Meas. Sci. Technol.*, 2011, **22**, 105409.

133. T. Kugler, B. Jaeger, E. Bich, M. H. Rausch and A. P. Fröba, *Int. J. Thermophys.*, 2013, **34**, 47.
134. N. Matsunaga, M. Hori and A. Nagashima, *Netsu Bussei*, 2008, **22**, 211.
135. A. C. F. Ribeiro, J. J. S. Natividade and M. A. Esteso, *J. Mol. Liq.*, 2010, **156**, 58.
136. G. B. Ray and D. G. Leaist, *J. Chem. Eng. Data*, 2010, **55**, 1814.
137. A. Lewandrowska, A. Majcher, A. Ochab-Marcinek, M. Tabaka and P. Holyst, *Anal. Chem.*, 2013, **85**, 4051.
138. C. Y. Kong, Y. Chang, T. Funazukuri and S. Kagei, *J. Chromatogr., A*, 2004, **1035**, 177.
139. C. Y. Kong, Y. Chang, T. Funazukuri, S. Kagei, G. Wang, F. Lu and T. Sako, *J. Chromatogr., A*, 2012, **1250**, 141.
140. O. Annunziata, A. Vergara, L. Paduano, R. Sartorio, D. G. Miller and J. G. Albright, *J. Phys. Chem., B*, 2003, **107**, 6590.
141. A. Vergara, F. Capuano, L. Paduano and R. Sartorio, *Macromolecules*, 2006, **39**, 4500.
142. E. E. Alanis, G. G. Romero and C. C. Martinez, *Opt. Eng.*, 2000, **39**, 744.
143. A. Bardow, V. Goke, H. J. Koss, K. Lucas and W. Marquardt, *Fluid Phase Equilib.*, 2005, **228**, 357.
144. R. W. Berg, S. B. Hansen, A. A. Shapiro and E. H. Stenby, *Appl. Spectrosc.*, 2007, **61**, 367.
145. L. L. Van Loon, H. C. Allen and B. E. Wyslouzil, *J. Phys. Chem., A*, 2008, **112**, 10758.
146. E. Kriesten, M. A. Voda, A. Bardow, V. Göke, F. Casanova, B. Blümich, H.-J. Koss and W. Marquardt, *Fluid Phase Equilib.*, 2009, **277**, 96.
147. A. Anand, V. K. Chhaniwal and C. S. Narayanamurthy, *Appl. Opt.*, 2006, **45**, 904.
148. R. Riquelme, I. Lira, C. Pérez-López, J. A. Rayas and R. Rodríguez-Vera, *J. Phys. D: Appl. Phys.*, 2007, **40**, 2769.
149. G. S. Hartley and J. Crank, *Trans. Faraday Soc.*, 1949, **45**, 801.
150. N. T. Brown, *J. Chem. Soc., Trans.*, 1918, **113**, 559.
151. J. C. S. Maxwell, *Theory of Heat*, Longmans, Green and Co, London, 1971, p. 302.
152. J. Gróh and G. von Hevesy, *Ann. Phys.*, 1920, **368**, 85.
153. J. G. Albright and R. Mills, *J. Phys. Chem.*, 1965, **69**, 3120.
154. R. Mills and K. R. Harris, *Chem. Soc. Rev.*, 1976, **5**, 215.
155. E. M. LaBolle, G. E. Fogg, J. B. Eweis, J. Gravner and D. G. Leaist, *Water Resour. Res.*, 2008, **44**, W07405.
156. R. Mills, *J. Phys. Chem.*, 1965, **69**, 3116.
157. H. J. V. Tyrrell and K. R. Harris, *Diffusion in Liquids*, Butterworths, London, 1984, Chapter 5, pp. 356–358.
158. M. D. Ediger and P. Harrowell, *J. Chem. Phys.*, 2012, **137**, 080901.
159. M. T. Cicerone and M. D. Ediger, *J. Phys. Chem.*, 1993, **97**, 10489.
160. F. R. Blackburn, C.-Y. Wang and M. D. Ediger, *J. Phys. Chem.*, 1996, **100**, 18249.

161. J. Matthiesen, R. S. Smith and B. D. Kay, *J. Chem. Phys.*, 2010, **133**, 174505.
162. J. Matthiesen, R. S. Smith and B. D. Kay, *J. Phys. Chem. Lett.*, 2011, **2**, 557.
163. S. F. Swallen, K. Traynor, R. J. McMahon, M. D. Eidiger and T. E. Mates, *J. Phys. Chem., B*, 2009, **113**, 4600.
164. M. H. Rausch, J. Lehmann, A. Leipertz and A. P. Fröba, *Phys. Chem. Chem. Phys.*, 2011, **13**, 9525.
165. T. J. Kaiser, J. W. Thompson, J. S. Mellos and J. W. Jorgenson, *Anal. Chem.*, 2009, **81**, 2860.
166. K. D. Patel, A. D. Jerkovich, J. C. Link and J. W. Jorgenson, *Anal. Chem.*, 2004, **76**, 5777.
167. D. K. Dysthe, B. Hafskjold, J. Breer and D. Cejka, *J. Phys. Chem.*, 1995, **99**, 11230.
168. T. Funazukuri, C. Y. Kong and S. Kagei, *J. Supercrit. Fluids*, 2006, **38**, 201.
169. I. Medina, *J. Chromatogr., A*, 2012, **1250**, 124.
170. A. Alizadeh, C. A. Nieto de Castro and W. A. Wakeham, *Int. J. Thermophys.*, 1980, **1**, 243.
171. J. M. H. L. Sengers, U. K. Deiters, U. Klask, P. Swidersky and G. M. Schneider, *Int. J. Thermophys.*, 1993, **14**, 893.
172. T. Funazukuri, C. Y. Kong and S. Kagei, *Chem. Eng. Sci.*, 2004, **59**, 3029.
173. C.-C. Lai and C.-S. Tan, *Ind. Eng. Chem. Res.*, 1995, **34**, 674.
174. A. Plugatyr and I. M. Svishchev, *J. Phys. Chem. B.*, 2011, **115**, 2555.
175. C. Y. Kong, T. Funazukuri and S. Kagei, *Fluid Phase Equil.*, 2004, **59**, 3029.
176. K. Yoshida, C. Wakai, N. Matubayashi and M. Nakahara, *J. Chem. Phys.*, 2005, **123**, 164506.
177. W. S. Price, K. Hayamizu, H. Ide and Y. Arata, *J. Magn. Reson.*, 1999, **139**, 205.
178. K. R. Harris, *J. Chem. Phys.*, 2010, **132**, 231103.
179. A.-L. Rollet, V. Sarou-Kanian and C. Bessada, *Inorg. Chem.*, 2009, **48**, 10972.
180. A.-L. Rollet, V. Sarou-Kanian and C. Bessada, *C. R. Chim.*, 2010, **13**, 399.
181. T. Ohkubo, M. Gobet, V. Sarou-Kanian, C. Bessada, M. Nozawa and Y. Iwadate, *Chem. Phys. Lett.*, 2012, **530**, 61.
182. M. Levesque, V. Sarou-Kanian, M. Salanne, M. Gobet, H. Groult, C. Bessada, P. A. Madden and A.-L. Rollet, *J. Chem. Phys.*, 2013, **138**, 184503.
183. R. M. Cotts, M. J. R. Hoch, T. Sun and J. T. Markert, *J. Magn. Reson.*, 1989, **83**, 252.
184. A. Jerschow and N. Müller, *J. Magn. Reson.*, 1997, **125**, 372.
185. J. Jonas, *Rev. Sci. Instrum.*, 1971, **33**, 643.
186. J. Jonas and Y. T. Lee, *J. Phys.: Condens. Matter*, 1992, **4**, 305.
187. J. Jonas, *High-resolution NMR Spectroscopy at High Pressure in High Pressure Molecular Science, NATO Advanced Science Institutes,*

Series E: Applied Sciences, Springer, Dordrecht, 1999, Vol. 358, pp. 231–259.
188. P. W. E. Peereboom, N. Luigjes, K. O. Prins and N. J. Trappeniers, *Physica B + C*, 1986, **139–140**, 134.
189. P. W. E. Peereboom, H. Luigjes and K. O. Prins, *Physica A (Amsterdam, Neth.)*, 1989, **156**, 260.
190. M. Kanakubo, K. R. Harris, N. Tsuchihashi, K. Ibuki and M. Ueno, *J. Phys. Chem., B*, 2007, **111**, 2062.
191. E. Enninghorst, F. D. Wayne and M. D. Zeidler, *Mol. Phys.*, 1996, **88**, 437.
192. A. C. Jacob and M. D. Zeidler, *Phys. Chem. Chem. Phys.*, 2003, **5**, 538.
193. U. Matenaar, J. Richter and M. D. Zeidler, *J. Magn. Reson., A*, 1996, **122**, 72.
194. G. Palmer, J. Richter and M. D. Zeidler, *Z. Naturforsch., A: Phys. Sci.*, 2004, **59**, 51.
195. W. E. Price and H.-D. Lüdemann, *High Pressure in Chemistry and Physics*, Oxford University Press, Oxford, 1997, p. 225.

CHAPTER 6

New Fluids

WILLIAM A. WAKEHAM, IVAN EGRY, JÜRGEN BRILLO, YUJI NAGASAKA, MARC J. ASSAEL, JOAN F. BRENNECKE, MARJORIE MASSEL AND CHAOJUN SHI

6.1 Introduction to New Fluids

WILLIAM A. WAKEHAM

At the time of the earlier volume in the series of texts on the Transport Properties of Fluids[1] some of the newer techniques of measurement had not been applied to fluid classes that were technologically important then and remain so now. In addition, some specific fluid types had not been recognized to have the potential for technological application that they now do. For that reason in this volume we wish to give attention to both sets of material in an illustrative, rather than definitive fashion.

First we recognize that the transport properties of the fluid state of materials that are usually solid at ambient conditions have enormous technological significance. Most obviously molten metals, whether pure or in an alloyed form, have been important industrial intermediates for the production of solid metallic objects by casting, forging, forming or welding for millennia. The fact that the transport properties of the molten state of these materials were not well known obviously did not prevent their widespread adoption or use. However, in the modern era, efficiency and environmental concerns as well as the desire to engineer the solid state of objects in casting by particular heat treatments make knowledge of the fluid properties more important. In addition, molten metals are used in high quality glass manufacture and as heat transfer fluids in a number of industries including,

Experimental Thermodynamics Volume IX: Advances in Transport Properties of Fluids
Edited by M. J. Assael, A. R. H. Goodwin, V. Vesovic and W. A. Wakeham

Published by the Royal Society of Chemistry, www.rsc.org

potentially, new nuclear power plant design where the properties are of primary significance.

Despite this increasing demand, several reviews of the thermal conductivity of molten metals,[2–4] for example, have revealed relative discrepancies as large as 50 % among the experimental data reported in the literature by various authors over a wide range of temperature. Large differences also exist for other properties. The lack of accurate data is attributable in part to the inaccuracy of the experimental techniques applied so far where the main problem is the phenomenon of natural convection, which becomes much more difficult to avoid at high temperatures, since temperature control and distribution becomes more difficult to assure. In addition, of course, the conditions under which many metals are molten are quite aggressive chemically and this complicates their containment and treatment.

During the last twenty years several techniques have emerged that seek to remedy this situation. Here we describe just three examples. The first is the use of microgravity which can be created in earth-orbiting spacecraft. Such conditions allow the avoidance of buoyancy-driven convection because the gravitational field is rendered negligible. They also allow so-called containerless processing, which makes it possible to devise experimental methods for the measurement of the transport properties of molten metals, without contact with a solid surface; with obvious advantages. Section 6.2 provides a summary of what has been achieved in this area and is now also being repeated in new facilities on earth.

Section 6.3 considers the special situation of molten silicon which is of very considerable technological importance.

During the last decade, it has been possible to adapt one of the most successful techniques for the measurement of the thermal conductivity to the study of molten materials. The transient hot-wire technique, described in detail in the earlier volume,[6] and here discussed in section 5.1, eliminates natural convection from the measurement of thermal conduction, not by eliminating gravity, but by performing the measurement so quickly that it does not have a significant effect on the heat transfer process. In section 6.4, we describe the realization of this technique for molten materials at high temperatures and consider specifically its operation with molten metals where it has been possible to achieve a relative expanded uncertainty of about ± 2 % for a number of molten metals and alloys.

Finally, in Section 6.5 we consider a new class of fluids that are, in essence, molten organic salts; they are termed ionic liquids. This class of fluids has excited considerable scientific interest in the last decade because of the novel structural features that they reveal in both observations and molecular modeling. At the same time there has been considerable technological interest in these fluids by virtue of some of the unique physiochemical properties offered for the pursuit of different and more environmentally sustainable routes to chemical products. They may also provide a novel

medium for synthetic routes to biological products. The fluids pose some of the problems for transport property measurement characteristic of metals and other salts because they are electrically conducting to a greater or lesser extent. However, they are also rather difficult to purify and maintain in a pure state so that the literature is decorated by data with greater uncertainty than expected or claimed. Section 6.5 seeks to set out the current state of measurement with these interesting fluids.

6.2 Molten Metals and Microgravity

IVAN EGRY AND JÜRGEN BRILLO

6.2.1 Introduction

In the last (10 to 20) years the importance of the liquid phase has been recognised by materials scientists. In fact, almost all industrially used materials have been molten in some processing step, specifically in casting. The physics of fluids is governed by the Navier–Stokes equation and by the ubiquitous presence of convection. The high temperatures involved with liquid metals lead to experimental difficulties, the most trivial, but also most fundamental, being the availability of suitable containers. Containerless processing using electromagnetic and electrostatic levitation, within terrestrial and microgravity conditions, solved the problem of finding a suitable container for high-temperature, highly reactive metallic melts and permitted the measurement of their thermophysical properties with reduced uncertainty.

6.2.1.1 Containerless Processing and Microgravity

There are a number of containerless processing techniques, based on different levitation fields.[5] For liquid metals, the most suitable methods are electromagnetic and electrostatic levitation. In the following, the principles of these two techniques are briefly described.

In electromagnetic levitation, positioning and heating of electrically conducting samples are achieved by placing them into an inhomogeneous high frequency electromagnetic field, produced by a coil of suitable geometry.

The electromagnetic field induces a current inside the sample which interacts with it such that a Lorentz force is generated. Electromagnetic levitation not only provides positioning, it also leads to inductive heating of the levitated sample. It is intrinsically stable, *i.e.* there is a restoring force for deviations from the equilibrium position in any direction. Nevertheless, instabilities such as rotation along any axis, accompanied with flattening or even fission of the droplet, are often encountered in practice.[6,7] Under terrestrial conditions, the joint action of the gravitational and levitation force leads to a deformation of a liquid sample: the drop is elongated along the direction of the gravity vector. In addition, electromagnetic fields induce fluid flows inside a liquid, conducting body. If these flows become turbulent, they render the measurement of viscosity impossible. This can be avoided in microgravity, where only small positioning fields are required.

In electrostatic levitation, the sample is electrically charged and placed in an electrostatic field. This field is generated by two parallel disk-like electrodes. Additional horizontal stabilization is accomplished by four or more lateral electrodes placed in a plane underneath the sample. In contrast to electromagnetic levitation, electrostatic levitation is not intrinsically stable. Therefore, the sample position must be actively controlled in order to keep

the sample stably in position. This is achieved by a feedback loop consisting of expanded He/Ne lasers and associated *x* and *y* position sensitive detectors (PSD). Heating and melting of the specimen is accomplished by IR lasers, leading to temperature gradients across the sample. Charging of the sample is performed by a UV light source causing photoemission of electrons.

The samples have typical diameters between (1.5 and 3) mm and masses from (20 to 90) mg. Recently, a setup has been developed by Holland-Moritz which can also levitate samples of up to 1.5 g with dimensions similar to those obtained on electromagnetically levitated specimen.[8] Electrostatic levitation is, in principle, not restricted to electrically conducting materials. Another advantage is the absence of turbulent flow inside the sample. However, there are also a few shortcomings. One is the high technical effort the method requires and another comes from the fact that, owing to discharging of the sample, not all materials can be levitated. In fact, electrostatic levitation works best for metals with a high thermionic emission rate, *i.e.* alloys based on refractory metals, like Ti, Zr, and others.

Evidently, containerless processing of liquid metals and alloys is best carried out under microgravity conditions. For instance, the positioning fields in electromagnetic levitation are reduced by a factor of 1000 in space and consequently, the attached side effects are reduced by the same factor.

Microgravity conditions can be achieved in drop tubes or drop towers, in parabolic flights, on-board sounding rockets, and on orbiting spacecraft's such as the International Space Station ISS. The available free-fall time in a drop tube or drop tower scales with the square root of its height. An aircraft on a parabolic trajectory can provide a reduced gravity environment for about 20 s per parabola. Usually, up to 40 consecutive parabolas are performed per flight. Sounding rockets can provide free-fall periods between (300 and 1200) s. For many experiments, these times are not sufficient and it is necessary to perform the experiments on board a spacecraft.

As of today, the only successful implementation of a microgravity levitator is based on the electromagnetic levitation principle.[9,10]

Thermophysical properties of levitated samples have been measured in microgravity during two Spacelab missions, IML-2 in 1994 and MSL-1 in 1997.[11,12] Later on, the electromagnetic levitator TEMPUS was flown regularly on parabolic flight campaigns. Its successor, MSL-EML, was launched with a sounding rocket, and will be accommodated on board the ISS in 2014.

6.2.2 Thermophysical Properties

6.2.2.1 Density

Density and thermal expansion are fundamental properties. They are strongly related to the atomic short range order and, therefore, provide a direct link between the physics on the microscopic and macroscopic scale. In addition, density is needed, in many cases, for the derivation of other themophysical properties from the experimental raw data.

In levitation, the density is determined by recording the visible cross section of the levitated sample. Assuming rotational symmetry, the volume is calculated. Since the mass of the sample is known, this yields the density. Typically, a resolution of $\Delta V/V = 10^{-4}$ is required. This can be achieved using sub-pixel algorithms for edge detection, curve fitting of the shape, and statistical averaging.[13,14]

The volume of an axisymmetric sample can be calculated from

$$V_P = \frac{2}{3}\pi \int_0^{\pi} \langle R(\varphi)\rangle^3 \sin(\varphi)\, d\varphi, \tag{6.1}$$

where $\langle R(\varphi)\rangle$ is the time-averaged, angle-dependent radius of the sample which, in the case of a sphere, reduces to r_0, yielding $V_P = 4\pi r_0^3/3$. The volume, V_P, is given in pixel units and must be converted to SI units with a calibration body.

The edge detection algorithm is sensitive to blooming effects and changes in the contrast. The latter might occur as the brightness of the sample changes with temperature. In order to eliminate this problem shadowgraph techniques are used in terrestrial experiments. A comprehensive overview on density measurements carried out in terrestrial EML experiments is given by Brillo.[15] In these measurements, data of pure elements and binary and ternary liquid alloys have been obtained as functions of temperature and composition.

The following Figure 6.1 shows example data for pure liquid iron obtained in EML under gravity conditions.[16] As visible, it is possible to achieve a deep

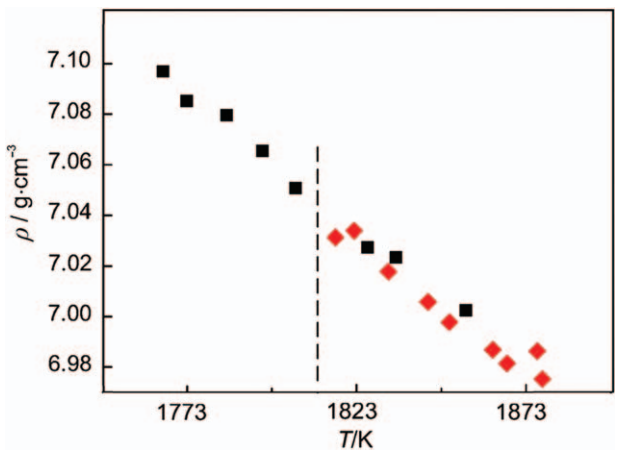

Figure 6.1 Density ρ of liquid iron measured in electromagnetic levitation under terrestrial conditions as a function of temperature T. Data can even be obtained in the undercooled regime. For comparison, values obtained with a pycnometer are also shown. ■, electromagnetic levitation for a sample of mass 1 g; ◆, value obtained from pycnometry. The vertical dashed line shows $T_L = 1811$ K.

undercooling and to measure data in this regime. For comparison, data obtained with a pycnometer are also shown.[17]

Owing to strong rotations or sample movements the condition of axial symmetry is sometimes not fulfilled. In such a case, eqn (6.1) cannot be evaluated. Mass loss owing to evaporation is another challenge.

Such difficulties can be avoided if measurements are carried out under μg-conditions. For instance, Samwer and co-workers[18] have performed measurements on glass-forming metallic alloys. More recently, the same group measured the density of liquid Si–Ge alloys during parabolic flights. They found good agreement with ground based data obtained in an electrostatic levitator, and an interesting, yet unexplained, anomaly in the thermal expansion around $\{(1-x)\mathrm{Si}+x\mathrm{Ge}\}$ where x, the mole fraction, is equal 0.25.

As an alternative to measurements under μg, densities and thermal expansions can also be measured in electrostatic levitation experiments. As the sample is almost spherical and strong movements, oscillations, or rotations, are absent, highly precise data are obtained. This is even more the case as mass loss owing to evaporation can be minimised owing to the short processing times which are in the order of a few minutes only.

In Figure 6.2, two measurements for liquid $\{(1-x)\mathrm{Zr}+x\mathrm{Ni}\}$ and $x=0.36$, carried out in different electrostatic levitators and by different groups, are shown.[19,20]

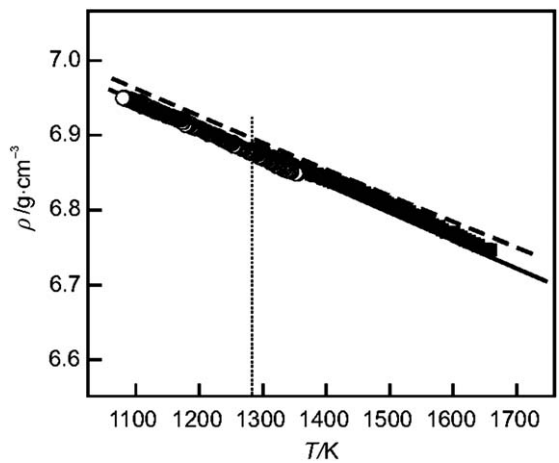

Figure 6.2 Density ρ of liquid $\{(1-x)\mathrm{Zr}+x\mathrm{Ni}\}$ with $x=0.36$ measured by electrostatic levitation as a function of temperature T.[19] The ○ and ■, respectively, correspond to two different runs with samples prepared individually for each run. ———, weighted average of the measured values ○ and ■; – – – –, measurements reported by Ohsaka.[20] The vertical dashed line shows $T_{\mathrm{L}}=1283$ K.

6.2.2.2 Surface Tension

Surface tensions of levitated samples are conveniently measured by the oscillating drop technique.[21] Liquid samples perform oscillations around their equilibrium shape. In the absence of external forces, a simple formula can be used to relate the frequency ω ($=2\pi f$) of the surface oscillations to the surface tension γ:

$$\omega^2 = \frac{32\pi}{3}\,\frac{\gamma}{m}, \tag{6.2}$$

where m is the mass of the droplet. The frequencies f used depend on the sample and its mass and typically lie in the range of (30 to 50) Hz.

Under terrestrial conditions, the liquid drop is distorted by gravity and the compensating levitation field. As a consequence, the single frequency is split into up to 5 peaks. In addition, all peaks are shifted with respect to eqn (6.2). This is due to the fact that the electromagnetic levitation field acts as an additional pressure term in the Navier–Stokes equation. It therefore leads to an apparent increase in surface tension. A correction formula to account for these effects on the frequency spectrum was developed by Cummings and Blackburn who derived a sum rule which contains only measurable frequencies.[22] It reads:

$$\begin{aligned} \frac{32\pi}{3}\,\frac{\gamma}{m} &= \frac{1}{5}\sum_m \omega_{2,m}^2 - 1.9\,\overline{\Omega_{\mathrm{tr}}^2} - 0.3\,\left(\overline{\Omega_{\mathrm{tr}}^2}\right)^{-1}\,(g/r_0)^2 \\ \overline{\Omega_{\mathrm{tr}}^2} &= \frac{1}{3}\left(\Omega_{\parallel}^2 + 2\,\Omega_{\perp}^2\right) \end{aligned} \tag{6.3}$$

In eqn (6.3) $\overline{\Omega_{\mathrm{tr}}^2}$ is the mean quadratic translational frequency of the drop, and g is the local acceleration of free fall. The integer index m runs from –2 to +2, and r_0 is the radius of the drop.

The sample oscillations are recorded with a video camera from the top, *i.e.* along the symmetry axis. The area of the cross section of the sample, its centre of mass, and two perpendicular radii are calculated for each frame. A number of frames between (256 and 4096) is taken and the corresponding time series is Fourier transformed to yield the frequencies. From the time dependence of the centre of mass the translational frequencies are derived, whereas the surface oscillation frequencies are contained in the temporal behaviour of the two perpendicular radii. Due to their different symmetries, the oscillations corresponding to different m-values can be identified using selection rules, as derived by Egry *et al.*[21] By comparing measurements in microgravity with ground-based results, the validity of the Cummings correction has been confirmed experimentally.[23]

The surface tension of alloys is dominated by the effect of surface segregation. Due to the interplay between energetic and entropic terms in the free energy, the component with the lower surface tension, the surface active

component, tends to segregate at the surface. Figure 6.3 shows isothermal surface tension values of binary liquid (Al + Cu) at a temperature of 1375 K which have been measured under gravity conditions.[24] The experimental values are shown together with a thermodynamic model calculation, as well as with data published earlier by Laty.[25]

Surface tension measurements using the oscillating drop technique are short duration experiments. Nowadays, they are routinely carried out during parabolic flight campaigns. For example, Wunderlich *et al*. have measured the surface tension of a number of industrially relevant multicomponent steels and nickel-based superalloys in the framework of ESA's ThermoLab project.[26,27] A list of the investigated alloys is given in Table 6.1.

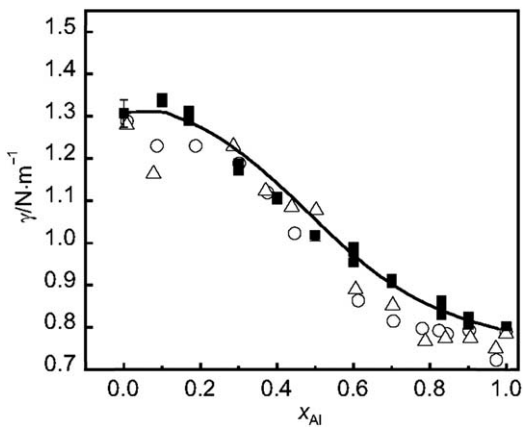

Figure 6.3 Isothermal surface tension γ of liquid (Al + Cu) alloys as function of Al mole fraction x_{Al} at a temperature of 1375 K. ■, This work, results obtained by electromagnetic levitation; ○ and △, values reported by Laty[25] from sessile drop measurements; ——, model calculation.

Table 6.1 Surface tension measurements γ of industrial alloys measured during parabolic flights at the liquidus temperature T_L in the framework of the Thermolab project.[26,27] The mole fraction x of the mixtures is listed.

Alloy	T_L/K	$\gamma(T_L)$/N · m^{-1}	Year
CMSX-4	1657	1.85	2002
IN738LC	1608	1.85	2003
MM247LC	1641	1.86	2003
C263	1641	1.74	2003
Low alloyed Steel	1753	1.61	2004
Cr alloyed Steel	1750	1.76	2004
Cu-alloy	1340	1.15	2004
Al + Ni x(Al) = 0.75	1683	1.63	2004
Ni	1728	1.71	2004
Al + Ni x(Al) = 0.315	1523	1.16	2005
Al + Ni x(Al) = 0.65	1823	1.65	2006

There have been also surface tension measurements using the oscillating drop method under microgravity conditions in Japan, notably by the group of Nogi.[28–30] This group has used either a drop tower or a short 1.5 m drop tube and measured the oscillations during free fall of the drop.

6.2.2.3 *Viscosity*

The oscillating drop technique also permits the determination of the viscosity η of liquids from measurements of the damping constant Γ of the oscillations. If r_0 is the radius of the droplet, the following law applies, which is known as Lamb's law:

$$\Gamma = \frac{20\,\pi}{3}\,\frac{r_0\,\eta}{m}. \tag{6.4}$$

Since no correction formula exists that accounts for the disturbing effects of the electromagnetic field, the application of the oscillating drop technique to viscosity measurements is not possible in terrestrial electromagnetic levitation experiments.

The viscosity is strongly temperature dependent. Its behaviour is often modelled using either an Arrhenius fit:

$$\eta = \eta_\infty \exp\left(\frac{E_a}{k_B T}\right), \tag{6.5}$$

or, in particular for glass-forming liquids, by the Vogel–Fulcher–Tamman formula:

$$\eta = \eta_\infty^{'} \exp\left(\frac{E_a^{'}}{k_B(T - T_0)}\right). \tag{6.6}$$

In equations (6.5) and (6.6), η_∞, E_a, E'_a, and T_0 are fit parameters and k_B is Boltzmann's constant. The temperature T_0 is usually identified with the ideal glass transition temperature (where the viscosity diverges), and E_a is the activation energy for viscous flow.

Egry and co-workers[31] have measured the viscosity of an electromagnetically levitated $\{(1-x_1-x_2)\mathrm{Pd} + x_1\mathrm{Cu} + x_2\mathrm{Si}\}$, where $x_1 = 0.06$ and $x_2 = 0.18$, sample during the MSL-1 Spacelab missions known by the acronyms STS-83 and STS-94. They evaluated their data according to eqn (6.4). Their result is shown in Figure 6.4 and compared to conventional terrestrial data by Lee *et al.*[32] Two different datasets are displayed: data during the STS-83 mission were taken with no crew on board Spacelab, while data during STS-94 were recorded during nominal crew operations. Both data yield the same Vogel–Fulcher fit, the higher scatter in the STS-94 data is due to g-jitter.

Electrostatic levitation allows the application of the oscillating drop technique for viscosity measurements even under terrestrial conditions. This has been demonstrated by Rhim, Paradis, Ishekawa and others for

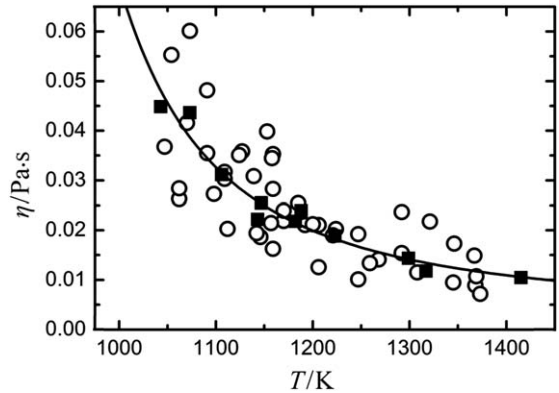

Figure 6.4 Viscosity η of $\{(1-x_1-x_2)\mathrm{Pd}+x_1\mathrm{Cu}+x_2\mathrm{Si}\}$, where $x_1=0.06$ and $x_2=0.18$, measured during two different Spacelab missions as a function of temperature T. The data were fit with a Vogel–Fulcher–Tamann (VFT) relation. ○, STS 94; ■, STS 83; and ——, Vogel–Fulcher–Tamann (VFT) eqn (6.6).

Table 6.2 Arrhenius constants η_∞ and E_a of eqn (6.5) at the liquidus temperatures T_L for the binary liquid alloy mixtures (Zr + Ni) of Ni mass fraction x(Ni) from ref. 20.

Alloy	x(Ni)	T_L/K	η_∞/mPa · s	E_a/kJ · mol^{-1}
$\{x\mathrm{Ni}+(1-x)\mathrm{Zr}\}$	0.5	1533	0.105	63.0
$\{x\mathrm{Ni}+(1-x)\mathrm{Zr}\}$	0.36	1283	0.0028	95.8
$\{x\mathrm{Ni}+(1-x)\mathrm{Zr}\}$	0.3333	1393	0.065	67.0
$\{x\mathrm{Ni}+(1+x)\mathrm{Zr}\}$	0.24	1233	0.0025	90.7

pure elements and some alloys.[20,33–35] For example, data for binary (Zr + Ni) alloys were published by Ohsaka *et al.* in 1998.[20] Their results can be represented by an Arrhenius law with activation energy for viscous flow E_a and a pre-exponential factor η_∞, and these values are listed in Table 6.2.

Recently, the viscosity of a liquid $\{(1-x)\mathrm{Zr}+x\mathrm{Ni}\}$ with $x=0.36$ sample has been measured in an electrostatic levitator.[19] In these experiments, it is important that the oscillation amplitude of the sample radius be less than 10 % of the radius at rest.[36] Thus, flow vortices leading to an additional dissipation of energy are suppressed.

Figure 6.5 shows the results for the viscosity as function of temperature. Values were obtained in the broad temperature range of (1050 to 1750) K. Large undercooling of up to 230 K was achieved. At liquidus temperature, T_L, the viscosity is 11.5 mPa · s. It reaches a value of approximately 130 mPa · s for $T \approx 1100$ K which is large compared to most non-glass forming metallic alloys.[12]

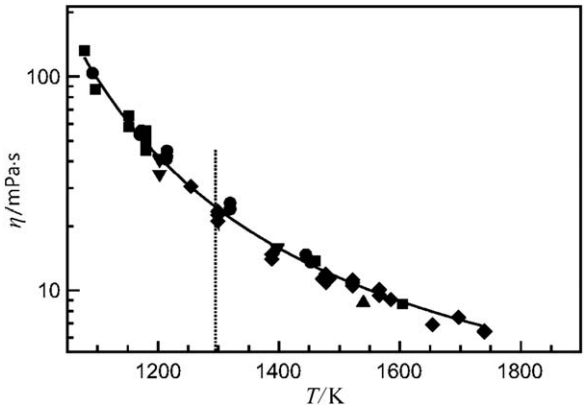

Figure 6.5 Viscosity η of liquid $\{(1-x)\mathrm{Zr}+x\mathrm{Ni}\}$ with $x=0.36$ obtained by electrostatic levitation for samples of different masses m as a function of temperature T. ●, $m(\{(1-x)\mathrm{Zr}+x\mathrm{Ni}\}$ with $x=0.36)=20.8$ mg; ▼, $m(\{(1-x)\mathrm{Zr}+x\mathrm{Ni}\}$ with $x=0.36)=27.0$ mg; ◆, $m(\{(1-x)\mathrm{Zr}+x\mathrm{Ni}\}$ with $x=0.36)=38.2$ mg; ▲, $m(\{(1-x)\mathrm{Zr}+x\mathrm{Ni}\}$ with $x=0.36)=41.0$ mg; ■, $m(\{(1-x)\mathrm{Zr}+x\mathrm{Ni}\}$ with $x=0.36)=86.2$ mg; ——, Vogel–Fulcher–Tamman eqn (6.6). The vertical dashed line shows $T_\mathrm{L}=1283$ K.

6.2.2.4 *Specific Heat*

A non-contact method developed by Fecht and Johnson[37] can be used to determine the specific heat in levitation experiments. It is a variant of non-contact modulation calorimetry, normally used in low temperature physics. The heater power is modulated according to $P_\omega(t)=\Delta P_\omega\cos(\omega t)$ resulting in a modulated temperature response $T_\omega(t)=\Delta T_\omega\cos(\omega t+\phi)$ of the sample, where ΔT_ω is the amplitude and ϕ the phase shift of the temperature response. A thermal model considering heat loss to the environment and heat conduction within the sample has been developed by Wunderlich.[38] It considers heat loss to the exterior (typically by radiation only if the experiment is carried out under vacuum), spatially inhomogeneous heating of the sample, and heat conduction within the sample. Under the condition that heat loss to the exterior can be neglected with respect to the heat conduction within the sample (adiabatic conditions), and for suitably chosen modulation frequencies, a simple relation for the specific heat, c_p, can be derived:

$$c_p=\frac{1}{\omega}\frac{\Delta P_\omega}{\Delta T_\omega}. \tag{6.7}$$

The power input into the sample, ΔP_ω, cannot be measured directly. It is related to the current flowing through the heating coil by a coupling coefficient which has to be determined separately.

Modulation calorimetry needs to be carried out under isothermal conditions, *i.e.* the sample must be allowed to thermalize at a predefined

temperature before the modulation signal can be applied. Therefore, such experiments cannot be performed during parabolic flights. Fecht and co-workers[39] applied this method during the MSL-1 Spacelab mission and during a sounding rocket experiment on a $\{(1-x_1-x_2)\mathrm{Ti}+x_1\mathrm{Al}+x_2\mathrm{Nb}\}$ with $x_1=0.08$ and $x_2=0.46$ alloy.

Fukuyama and co-workers have further developed this method and overcame the necessity of performing the experiments in microgravity.[40–43] They combined the electromagnetic levitator with a static dc magnetic field of up to 5 T. This leads to a nearly complete suppression of fluid flow. Power modulation is performed by a laser of modulated intensity shining on the top side of the sample. A pyrometer tuned at a different wavelength detects the samples' temperature response at the bottom side. In order to determine the power input ΔP_ω the normal spectral emissivity at the laser wavelength is needed. It is determined from a separate measurement using a calibrated spectrometer. The group has measured specific heats of supercooled liquid silicon[44] and liquid austenitic stainless steels.[45]

6.2.2.5 *Thermal Conductivity*

The noncontact modulated laser calorimetry method described above can also be used for the determination of thermal conductivity. To this end, the resulting phase shift between laser excitation and temperature response has to be measured as a function of modulation frequency. Fitting this response function with the thermal model yields the thermal conductivity of the sample.

Table 6.3 shows example results for the thermal conductivity measured for the pure liquid elements Si and Fe.[44,46]

6.2.2.6 *Electrical Conductivity*

It is possible to measure the electrical conductivity σ of levitated melts using a non-contact, inductive method. The impedance of a coil surrounding the sample is influenced by the sample's electrical conductivity. For spherical samples and homogeneous magnetic fields, as realised in microgravity, this relation is rather simple, whereas under terrestrial conditions, extensive mathematical and engineering effort is required to extract the required information from the measured impedance.[47,48]

Table 6.3 Thermal conductivity λ of selected liquid elements determined by the non-contact-modulation calorimetry.[44,46]

Material	$\lambda/\mathrm{W\cdot m^{-1}\cdot K^{-1}}$	Reference
Si	$(56\pm2.9)+(0.010\pm0.003)\cdot[(T/\mathrm{K})-1685)]$	44
Fe	39.1 ± 2.5	46

The complex impedance Z of the coil is a function of the oscillation frequency ω of the electromagnetic field, properties of the empty coil, and properties of the sample:

$$Z_{\text{coil}} = Z_{\text{coil}}(\omega, \delta, a_0) = R_0 + \mathrm{i}\omega L_0 + \Delta R_{\text{s}}(\delta, a_0) + \mathrm{i}\omega\, \Delta L_{\text{s}}(\delta, a_0). \tag{6.8}$$

In eqn (6.8), R_0 and L_0 are resistance and inductivity of the empty circuit and ΔR_{s}, ΔL_{s} are the changes induced by the sample. For spherical samples and a homogeneous electromagnetic field, these functions depend only on the skin depth, δ, and the radius a_0 of the sample. The skin depth is defined as

$$\delta = \sqrt{\frac{2\rho}{\mu_0 \omega}}. \tag{6.9}$$

Apart from the magnetic permeability μ_0 and the oscillation frequency ω of the electromagnetic field eqn (6.9) contains the electrical resistivity ρ of the sample, which is the reciprocal of the electrical conductivity σ ($\rho = 1/\sigma$).

The complex impedance Z_{tot} of the oscillatory circuit can be determined by measuring amplitudes of current I_0 and voltage U_0, as well as their phase shift ϕ.

For small skin depth $\delta \ll a_0$, these relations have a relatively simple form as follows:

$$\delta = \frac{r_0}{2}\left(1 - \sqrt{1 - \frac{A}{r_0^3}\left\{\frac{I_0}{U_0}\cos\phi - B\right\}}\right). \tag{6.10}$$

In eqn (6.10), A and B are instrument dependent constants, which are determined by calibration.

As is evident from eqn (6.9), the skin depth also depends on the magnetic permeability and is therefore sensitive to magnetic ordering effects. This was demonstrated experimentally on deeply undercooled $\{(1-x)\mathrm{Co} + x\mathrm{Pd}\}$ with $x = 0.8$ during the MSL-1 Spacelab mission and is shown in Figure 6.6. The Curie temperature of the solid phase is about 1250 K, and the steep rise in the apparent electrical resistivity reflects the onset of magnetic ordering. The same behaviour is found for the liquid phase, at approximately the same temperature. This supports the assertion that undercooled liquid $\{(1-x)\mathrm{Co} + x\mathrm{Pd}\}$ with $x = 0.8$ becomes a ferro-magnetic liquid.[49]

The electrical conductivity σ is of interest on its own, but it also permits the determination of the thermal conductivity λ through the Wiedemann-Franz relation,

$$\lambda = L\sigma T, \tag{6.11}$$

which is known to hold well for liquid metals.[50] In equation (6.11), L is the Lorenz-number, a universal constant, for which $L = 2.44\ \mathrm{W}\cdot\Omega\cdot\mathrm{K}^{-2}$. Thus, electrical conductivity measurements provide an alternative way, independent of convective effects, to determine the thermal conductivity.

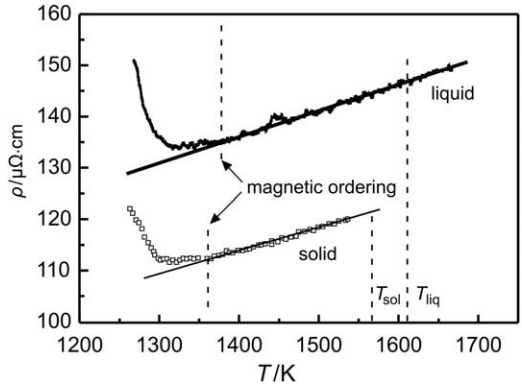

Figure 6.6 Apparent electrical resistivity ρ of solid and undercooled liquid $\{(1-x)\mathrm{Co}+x\mathrm{Pd}\}$ with $x=0.8$ as a function of temperature T. □, solid; and ■, undercooled liquid. The increase in ρ for both the liquid and solid at $T<1400$ K, which is shown by vertical dashed lines, arises from magnetic ordering effects. The solid and liquidus temperatures $T_{sol}=1560$ K and $T_{liq}=1610$ K, respectively, are shown with vertical dashed lines.

6.2.3 Summary and Outlook

In the preceding sections, we have demonstrated the potential of the combined use of the microgravity environment and containerless processing for thermophysical property measurements. Microgravity experiments provide benchmarks for terrestrial measurements owing to their inherent higher precision. However, the huge amount of data required for numerical modelling of industrial processes by far exceeds the capabilities of space borne experiments.

Whereas most thermophysical properties can be measured in a containerless environment, this is not the case for measurements of heat and mass diffusion. As of today, no containerless methods exist to measure these two quantities of fundamental importance. Apart from macroscopic, container-based methods, like shear cells or long capillaries, the most promising alternative method is based on quasi-elastic neutron scattering.[51–53] In the hydrodynamic limit, the incoherent dynamic structure factor reduces to a pure Lorentzian. Its width Γ is directly related to the self-diffusion coefficient D:

$$D=\frac{\Gamma}{\hbar Q^2}, \tag{6.12}$$

where Q is the scattering vector, $\hbar=h/(2\pi)$ and h is Planck's constant. Due to their atomistic nature, these measurements are free from any macroscopic fluid flow effects, *i.e.* convection. Unfortunately, they are restricted to metals with stable isotopes.

It remains a challenge for the future to develop new concepts, and, eventually, new hardware for the implementation of containerless measurement techniques as standard tools.

6.3 Forced Rayleigh Scattering Application to High Temperature Thermal Diffusivity of Molten Salts

YUJI NAGASAKA

6.3.1 Introduction

Molten salts and their mixtures have been widely utilized as high-temperature heat transfer fluids, latent-heat thermal energy storage materials, and electrolytes for fuel cells because of their excellent thermal and chemical characteristics under high-temperature conditions. For the reliable thermal design of these systems, it is essential to obtain accurate thermophysical properties data on molten salts. However, in the case of thermal conductivity and thermal diffusivity, there have been a very limited number of experimental studies, with discrepancies often far beyond their claimed uncertainties. It seems quite difficult to make a judgement of the reliability of available data since the experimental results differ by a factor of two to four in the worst-case. Moreover, we do not yet understand the temperature dependence of the thermal conductivity of molten salts, whether it is positive or negative.

This situation is owing to the fact that the measurement of thermal conductivity and thermal diffusivity of molten salts is very difficult and complex because of their corrosiveness and high melting temperatures. Furthermore, serious systematic errors are caused by radiative and convective heat transfer in the sample salts, which are inevitable when using the conventional steady-state techniques. In the case of molten $NaNO_3$ and KNO_3, it has been revealed by the experimental studies using the transient hot-wire method with ceramic-coated probes[3,54] that most of the previous data measured by the steady-state techniques contain significant systematic errors owing to radiation and convection. However, the coated-wire technique cannot be extended to temperatures higher than 773 K.

A potential technique to solve these problems, forced Rayleigh scattering, seems to be applicable for the measurement of thermal diffusivity of high-temperature molten salts. The distinguishing features of the forced Rayleigh scattering technique for the thermal diffusivity measurement of molten salts are summarized as follows: (1), the method has an advantage in the case when it is difficult to insert sensors in a sample (such as high-temperature corrosive melts) because of its basic feature of contact-free measurement; (2), the influence of natural convection is negligible, since the measuring time is very short (typically within 1 ms); (3), the temperature rise during measurement is very small (less than 0.1 K), thus the error owing to radiation may not be significant even at high temperatures above 1000 K; and (4), a sample volume of only a few cubic millimetres is required, which is advantageous at high temperatures.

6.3.2 Principle of Forced Rayleigh Scattering Technique and Experimental Apparatus for Molten Alkali Halides

The principle and working equations appropriate to the forced Rayleigh scattering technique are described by Nagasaka *et al.*,[55,56] we confine ourselves here to describe the experimental apparatus modified for molten salts. The heating laser is a single-mode argon-ion laser (of wavelength 514.5 nm and maximum output power of 1 W) and its continuous beam is chopped by a rotating mechanical chopper to generate a short pulse of about 1 ms. The heating laser beam is divided by means of a beam splitter into two beams of equal intensity. The beams cross in the sample to create an interference pattern. The sample is coloured by the addition of a small amount of dye so that the sample can suitably absorb the heating laser beam. Therefore, the interference pattern induces a corresponding temperature distribution which acts as an optical phase grating on a low-power probing He-Ne laser beam which is not absorbed by the sample. After the short-pulse heating, the excited temperature distribution decays exponentially through the heat conduction process in the heated area. Accordingly, the intensity of the first-order diffracted probing beam I_1 decays as

$$I_1 \propto \exp(-2t/\tau), \tag{6.13}$$

where t is the time elapsed and τ is the relaxation time constant of heat conduction. The thermal diffusivity a of the sample is expressed in terms of τ and the grating period Λ by the following equation

$$a = \frac{1}{\tau}\left(\frac{\Lambda}{2\pi}\right)^2. \tag{6.14}$$

Figure 6.7 illustrates the sample cell for molten salts, which is made of quartz glass of 1 mm in thickness. The surface of the sample cell walls is painted with a high-emissivity coating, excluding the laser beam spot area, in order to secure enough absorption of infrared light from the infrared furnace shown in Figure 6.8. The amount of sample needed for this sample cell is only (0.2 to 0.3) g. The temperature of the sample is measured with the aid of a ceramic-coated thermocouple (type R) directly immersed in the sample. The standard relative uncertainty of the temperature measured in this manner is estimated to be $\pm$ 15 K, which is not so poor if one takes into account the rather weak temperature dependence of the thermal diffusivity of molten salts.

6.3.3 Thermal Diffusivity Measurement of Molten Alkali Halides

By employing the forced Rayleigh scattering experimental apparatus, we reported the results of thermal diffusivity measurements of 13 kinds of molten alkali halides in the temperature range from (937 to 1441) K at

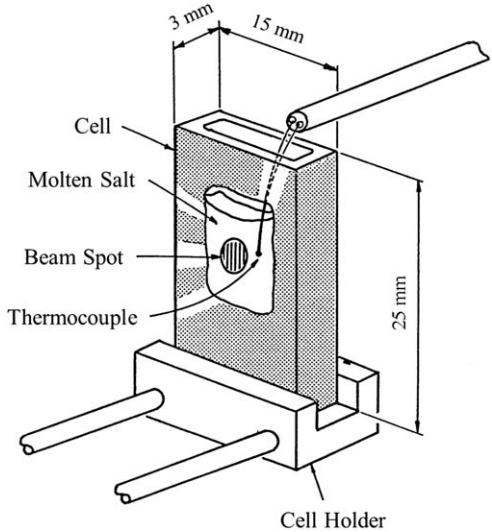

Figure 6.7 Sample cell used for molten salts with forced Rayleigh scattering.

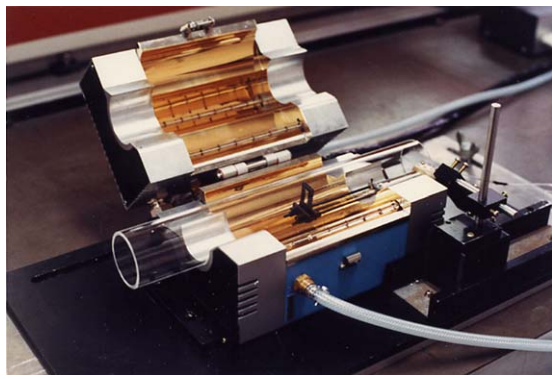

Figure 6.8 The forced Rayleigh scattering apparatus showing the sample cell including the infrared gold image furnace.

atmospheric pressure.[57–59] From the results it was found that the most of the previous experimental data for the thermal conductivity of molten alkali halides measured by conventional steady-state techniques contain significant systematic errors due to radiative and convective heat transfer in the sample salts which are inevitable at high temperatures.

As a typical example of these findings, Figure 6.9 shows the results for molten NaCl compared with those of previous works.[57] Since no previous experimental studies are available on the thermal diffusivity of molten alkali halides, we converted our thermal diffusivity data into thermal conductivity using carefully selected literature values of the density[66,67] and the specific heat capacity.[68] In these measurements, the grating period selected was

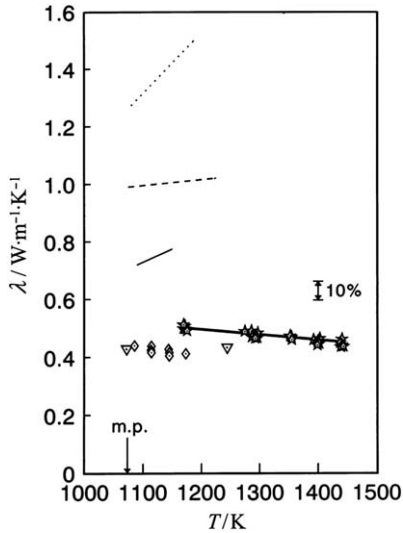

Figure 6.9 Thermal conductivity λ of molten NaCl as a function of temperature T. ☆, measured by forced Rayleigh scattering and reported in ref. 57, 58 and 59; - - -, ref. 60; · · · ·, ref. 61; ▽, ref. 62; ——, ref. 63; and ◇, ref. 64 and 65.

about 80 μm and the heating pulse duration time of the argon-ion laser was 1.2 ms. To colour the transparent molten alkali halides, we found through many trial-and-error experiments that $K_2Cr_2O_7$ is the most appropriate dye substance in terms of coloring ability and chemical stability at high temperatures. The dye was used with a mass fraction of 0.01 [about (2 to 3) mg]. It was experimentally confirmed that the effect of dye concentration on the measured thermal diffusivity is insignificant.[57] The relative uncertainty of the thermal diffusivity measurement of molten NaCl is within ± 2.6 % and the uncertainty of the converted thermal conductivity is to be ± 8 %. As shown in Figure 6.9, the previous thermal conductivity values of molten NaCl scatter from about (0.4 to 1.5) $W \cdot m^{-1} \cdot K^{-1}$ and their temperature coefficients are positive values. In contrast, the results obtained by the forced Rayleigh scattering technique are some of the lowest of all and agree well with the data by Golyshev *et al.*[62] measured by the steady-state concentric cylinder method (molybdenum wall; gap, 1 mm) with the radiation error correction and with the data by Harada measured by the modified laser flash method.[64,65] Moreover the present temperature dependence of the thermal conductivity exhibits a weak negativity. The data of Bystrai *et al.*[61] measured by the necked down sample method are almost 300 % larger than ours. It is thus considered that all these data are influenced strongly by the convection and radiation heat losses, all of which increase the apparent thermal conductivity. This conclusion is appropriate for all other molten salts measured by the forced Rayleigh scattering technique.

6.3.4 Experimental Apparatus Using CO_2 Laser for Molten Carbonates

Another type of forced Rayleigh scattering apparatus to measure thermal diffusivity of molten salts is shown in Figure 6.10[69] which uses a carbon dioxide laser as the heating source. Because of the use of the infrared laser, it is less necessary to add dye substances to samples than the previously used argon-ion laser. Therefore, the apparatus is applicable to a wide range of substances and conditions. The heating laser is a CO_2 laser (wavelength, 10.6 μm; power, 10 W) and its continuous beam is chopped by a rotating mechanical chopper to generate a short pulse of (0.1 to 2) ms. The short pulse heating beam is turned vertically up by M1 and divided by the beam splitter (BS) into two beams of equal intensity. The beams are made to cross on the surface of the sample by means of M3 and M4. The He-Ne probing laser impinges vertically on the heating spot area. The first-order diffracted beam is detected by a photomultiplier tube (PMT).

6.3.5 Thermal Diffusivity Measurement of Molten Carbonates

Figure 6.11 shows the thermal conductivity results of molten Li_2CO_3 in the temperature range from (1070 to 1355) K measured by the forced Rayleigh scattering apparatus using a CO_2 laser.[69] In order to compare the new results with the previous thermal conductivity data for molten Li_2CO_3 by Egorov and Revyakin,[70] we converted our thermal diffusivity data into thermal conductivity using literature values of the density[71] and the specific heat capacity.[72] The uncertainty of the thermal diffusivity measurement of molten Li_2CO_3 is within ± 9 % while the uncertainty of the converted thermal conductivity is estimated to be ± 17 %. As can be seen from Figure 6.11, the

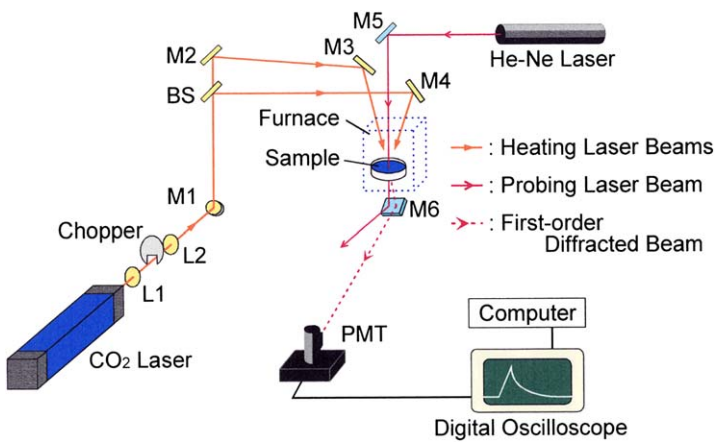

Figure 6.10 Experimental forced Rayleigh scattering apparatus with a CO_2 laser.

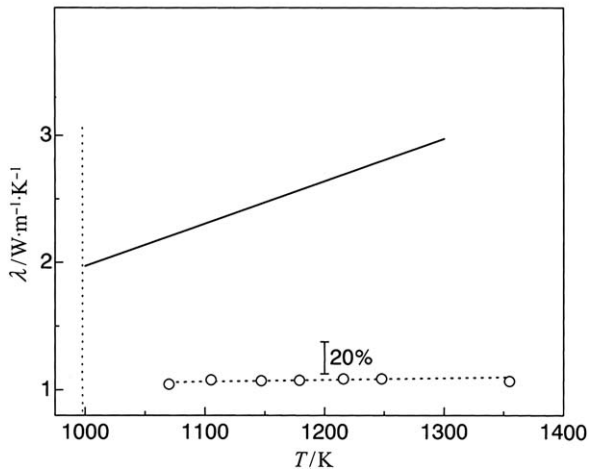

Figure 6.11 Thermal conductivity λ of molten Li_2CO_3 as a function of temperature T. ○, CO_2 forced Rayleigh scattering experiment, ref. 69; and ——, ref. 70.

results of Egorov and Revyakin[70] measured by the steady-state concentric cylinder method are between (200 to 300) % larger than the results obtained by the forced Rayleigh scattering apparatus using CO_2 laser and have a positive temperature dependence. This fact also supports the superiority of forced Rayleigh scattering technique for the measurement of thermal diffusivity of high temperature molten salts.

6.4 Surface Light Scattering Technique for Viscosity and Surface Tension of Molten Silicon and Molten $LiNbO_3$

YUJI NAGASAKA

6.4.1 Introduction

In the semiconductor and optoelectronic device manufacturing industries, there is a requirement to control and simulate the convection in the melts to obtain higher-quality and larger-size single crystals. The melt properties such as density, surface tension and viscosity are regarded as most important from the viewpoints of not only the proper control of the operation of crystal growth from the melt, but also the deeper understanding of the melt behaviour concerning particularly the defects and inhomogeneities which occur in the melt-grown crystals.[73] Although the thermophysical properties of the melts such as molten silicon and lithium niobate are needed, there have been a very limited number of experimental studies, with differences between the results often far beyond their claimed uncertainties. Single crystalline $LiNbO_3$ is one of the most important ferroelectric materials for optoelectronic devices, because of its excellent electro-optic, piezoelectric, and nonlinear characteristics,[74] so these differences are important. They arise because the measurement of the thermophysical properties of high temperature melts is extremely difficult to perform owing to their high melting temperatures and corrosiveness. In many cases, the conventional techniques may not be suitable.

It seems that in the case of the surface tension and viscosity, surface light scattering (SLS), described in section 2.1 is a technique with the potential to meet some of the above-mentioned demands. The advantages of the SLS technique for measurement of the surface tension and viscosity of high temperature melts such as molten Si and $LiNbO_3$ are as follows: (1), non-invasiveness of the technique does not cause any mechanical and thermal disturbances on the sample surface because it utilizes spontaneous thermal fluctuations; (2), the nano–micro scale wave requires only a small amount of a sample liquid, which is advantageous for high-temperature measurement; and (3), high frequency wave measurements can be performed rapidly and successively, and it is possible to detect the dynamic behavior of surface properties under high temperatures.

6.4.2 Principle of Surface Light Scattering Technique

The principle of surface light scattering (given the acronym SLS) for the measurement of surface tension and viscosity for liquids has been discussed in section 2.1.2.1 and the reader is referred there for detail. Here it is sufficient to recall that (assuming the density is known) we can simultaneously

determine the surface tension and viscosity of a liquid by measuring, in the frequency domain, the central frequency of the Brillouin laser light scattered from the liquids surface along with the width of the scattering peak at half of its height. Alternatively, as illustrated in section 2.1, equivalent measurements can be made in the time domain.

Since the first SLS experiment was performed by Katyl and Ingard,[75,76] the technique has been extensively utilized to study a wide variety of surface phenomena and to measure the surface tension and viscosity of a wide variety of substances and conditions because of its speed and non-invasive nature as a sensing technique for surface phenomena.

6.4.3 Experimental Apparatus

Figure 6.12 shows an example of experimental setup used for measurement of the surface tension and viscosity of molten $LiNbO_3$ under two different atmospheric conditions.[77] A He-Ne laser (for example that provided by NEC with model number GLG5740 operating at a wavelength of 632.8 nm and a maximum output power of 35 mW) is employed as a source of probe light, and the laser beam passes through a spatial filter (L1, pinhole, and L2) in order to reduce beam extension and to remove spatial noise. A transmission

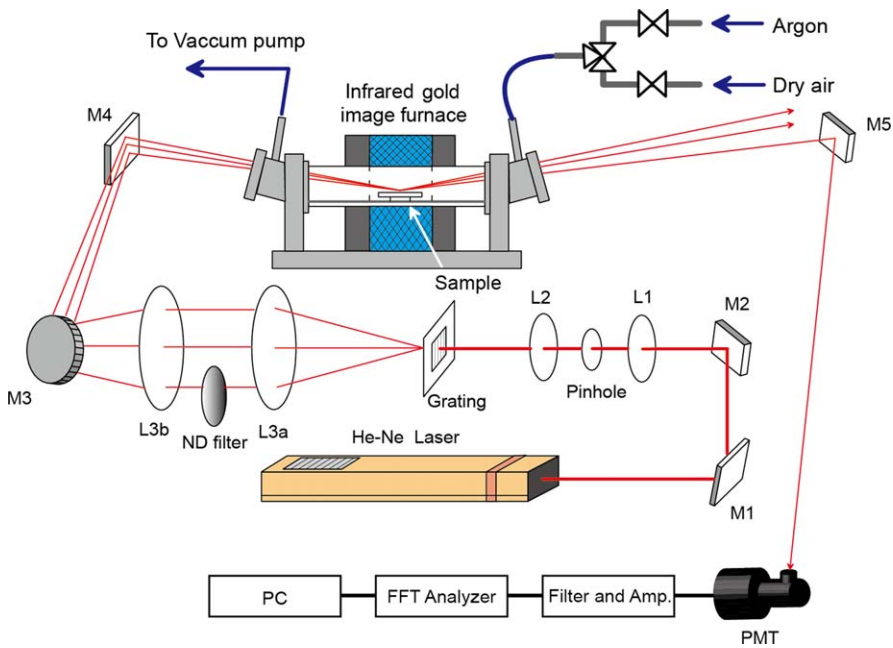

Figure 6.12 Experimental apparatus of surface laser-light scattering technique for molten $LiNbO_3$.

diffraction grating [grating period = (36.0 ± 0.2) μm] is employed to provide a well-controlled local oscillator laser beam (a first-order diffracted beam as a reference in this case) for heterodyne detection.[78] The main and reference laser beams are made parallel by lens L3a and are focused to one point on the surface of sample liquid by lens L3b (the beam diameter on the surface is about 800 μm). The intensity of the reference beam is controlled using a variable rotating ND filter. The main beam impinging on the liquid surface with an incident angle of 79° is scattered by ripplons around the reflection beam. A photo multiplier tube (PMT) (for example, that obtained from Hamamatsu, Japan, with model number R928) detects the scattered light mixed with the reference beam for heterodyne detection. The detected light signals are averaged over 256 times by a spectrum analyser (for example, that obtained from Ono, Japan, model number CF5210) and the averaged frequency-domain data are fitted to the Lorentzian profile. The entire optical system is fixed to an optical bench to minimize the effects of external vibrations.

The sample is heated by an infrared gold image furnace (Sinku-Riko, RHL-E64VHT). The main part of the furnace is constructed from a 330 mm long, 70 mm O.D. quartz tube. The ends of the quartz tube are each fitted with a flange on which a stainless-tube with an optical window and a pipe fitting is installed. The quartz tube is both pressure and vacuum tight and the atmosphere within the tube can be maintained with argon gas (with a mass fraction purity of 0.99999) or dry-air at a pressure of about 2.67 kPa by using two valves during an experiment. The sample is contained in an oval-shape shallow crucible made of platinum which shows no reaction against molten $LiNbO_3$. The temperature is monitored by two pairs of B-type thermocouples, which are attached at the wall of the crucible holders with the maximum relative uncertainty of ±4 K.

6.4.4 Interfacial Tension Measurement of Molten Silicon

Figure 6.13 shows measurement of the surface tension of molten Si obtained from the SLS along with values reported in the literature and obtained with different experimental methods.[79] In the analysis of the SLS measurements to determine surface tension, the recommended correlation for density reported by Lucas[80] was used. The surface tension obtained from the SLS at $T = 1685$ K was 801 $mN \cdot m^{-1}$ and the temperature coefficient of the surface tension. $d\gamma/dT$ was 0.24 $mN \cdot m^{-1} \cdot K^{-1}$. The relative uncertainty of the results was ± 7 % and the standard deviation was ± 2.3 %. The surface tension at temperatures near the melting temperature were close to those reported by Huang *et al.*[81] and Niu and Mukai.[82] The temperature coefficient was close to the value reported by Hardy[83] of 0.28 $mN \cdot m^{-1} \cdot K^{-1}$, however, the value obtained was larger than that reported by Huang *et al.*[81] of 0.093 $mN \cdot m^{-1} \cdot K^{-1}$ and smaller than the data of both Pryzborowski *et al.*[84] of 0.65 $mN \cdot m^{-1} \cdot K^{-1}$ and Niu and Mukai[82] of 0.43 $mN \cdot m^{-1} \cdot K^{-1}$.

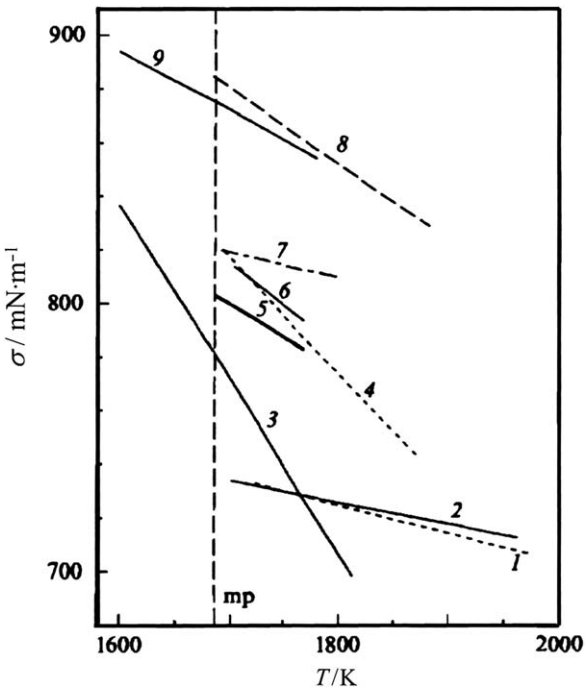

Figure 6.13 Measurements of the surface tension γ of molten silicon as a function of temperature T. 1, ref. 85; 2, ref. 86; 3, ref. 84; 4, ref. 82; 5, results obtained from the SLLS ref. 79; 6, ref. 87; 7, ref. 81; 8, ref. 83; 9, ref. 88. The vertical dashed line at a temperature of about 1687 K is the melting temperature of silicon.

6.4.5 Interfacial Tension and Viscosity Measurement of Molten $LiNbO_3$

The surface tension and viscosity of molten $LiNbO_3$ were determined with SLS at temperatures in the range (1537 to 1756) K with atmospheres above the molten $LiNbO_3$ of both argon and dry-air.[77] The $LiNbO_3$ sample was commercially available powder with the mole fraction congruent composition of $(0.485Li_2O + 0.515Nb_2O_5)$ and had a stated mole fraction purity of 0.99999. In these experiments, the wavelength of the ripplons was determined using the transmission diffraction grating and was about 190 μm. In order to determine the reliability of the experiment, the surface tension and viscosity of distilled water was determined at $T = 298$ K prior to the high temperature experiments with molten $LiNbO_3$. For the determination of surface tension and viscosity, the density of molten $LiNbO_3$ was calculated from the empirical equation reported by Hara *et al.*[89] with a claimed relative uncertainty of ± 0.19 %.

Figure 6.14 shows the results of measurement of the surface tension of molten $LiNbO_3$ in both an argon and dry-air atmosphere along with the

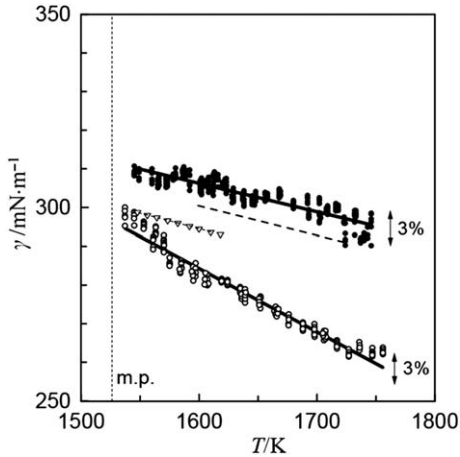

Figure 6.14 Surface tension γ of molten $LiNbO_3$ under atmospheres of both argon and dry-air as a function of temperature T. ○, obtained with the SLS and a dry-air atmosphere ref. 77; -----, results reported with a dry-air atmosphere by Tokizaki *et al.*;[90] ▽, results reported with a dry-air atmosphere by Anzai *et al.*;[73] ●, obtained with the SLS and a argon atmosphere ref. 77; — — —, results reported by Hara *et al.* in an argon atmosphere.[89] The vertical dashed line at a temperature of about 1525 K is the melting temperature of $LiNbO_3$. The solid lines are fits to the surface tension data obtained from the SLS with an argon and dry-air atmosphere.

values reported by other workers. The relative uncertainty of surface tension determined with SLS is estimated to be ± 2.6 % for the argon atmosphere and ± 1.9 % for the dry-air atmosphere. The surface tension of molten $LiNbO_3$ obtained with the SLS with a dry-air atmosphere lie about −5 % below those obtained with an argon atmosphere at temperatures near to the melting temperature. The temperature dependence of surface tension of molten $LiNbO_3$ under a dry-air atmosphere is twice that of the value obtained under an argon atmosphere. The surface tension of molten $LiNbO_3$ obtained in an argon atmosphere agree, within the combined uncertainty, with the values reported by Hara *et al.*[89] as determined with the maximum bubble pressure method. The surface tension of molten $LiNbO_3$ under a dry-air atmosphere coincide with the data reported by Tokizaki *et al.*[90] and Anzai *et al.*[73] at temperatures close to the melting temperature. The surface tension reported by both Tokizaki *et al.*[90] and Anzai *et al.*[73] was obtained with a ring method. The $d\gamma/dT$ for molten $LiNbO_3$ obtained with the SLS differs, as Figure 6.14 shows, from that determined from both Tokizaki *et al.*[90] and Anzai *et al.*[73] Based solely on these measurements we conclude the atmosphere above the molten $LiNbO_3$ gives rise to a variation in the measured surface tension.

The viscosity of molten $LiNbO_3$ obtained with the SLS under atmospheres of both argon and dry-air are shown in Figure 6.15 along with the results

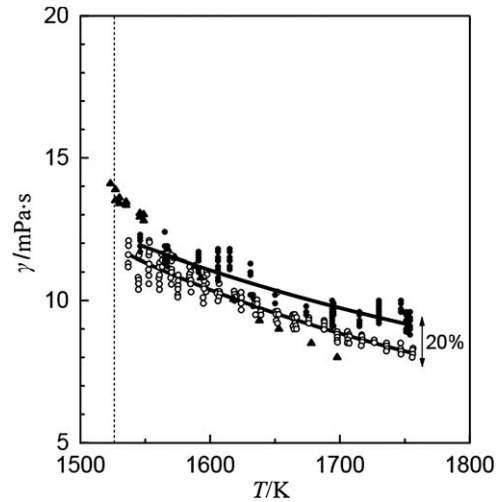

Figure 6.15 Viscosity η of molten $LiNbO_3$ under argon and dry-air atmospheres as a function of temperature T. ○, obtained with the SLS and a dry-air atmosphere Ref. 77; ●, obtained with the SLS and a argon atmosphere ref. 77; ▲, results reported with a non-oxygen atmosphere by Shigematsu *et al.*[91] The vertical dashed line at a temperature of about 1525 K is the melting temperature of $LiNbO_3$. The solid lines are an Arrhenius-type equation fit to the viscosity obtained from the SLS with an argon and dry-air atmosphere.

reported by Shigematsu *et al.*[91] The relative uncertainty of viscosity obtained from the SLS is estimated to be ± 11.1 % for the argon atmosphere and ± 14.3 % for the dry-air atmosphere.

It is clear from Figure 6.15 that the viscosity does not increase markedly as the temperature is reduced to the melting temperature as would be anticipated for pre-freezing. Figure 6.15 also shows the temperature dependence of viscosity is similar to that of a normal liquid over a wide range of temperature; this is supported by the fact the results can be correlated by an Arrhenius-type equation. The viscosity obtained with the SLS under the dry-air atmosphere was lower than those obtained with the argon atmosphere but were within the combined uncertainty of the SLS experiments. Shigematsu *et al.*[91] measured the viscosity of molten $LiNbO_3$ under a non-oxygen atmosphere with a oscillating cup viscometer employing appropriate working equations, and these results lie within ± 20 % of the values obtained with the SLS, albeit with a different temperature dependence $d\eta/dT$.

6.5 Application of the Transient Hot-Wire Technique to Melts

MARC J. ASSAEL AND WILLIAM A. WAKEHAM

6.5.1 Theoretical

The experimental method most recently employed to study molten materials is based on the transient hot-wire technique whose history is reviewed in section 5.1.[92,93] According to the simplest form of this method a vertical metallic wire is suspended in the test fluid and the temperature rise of the wire is measured as a function of time after initiation of a heat pulse within it. The temperature rise is followed by measuring the resistance change of a finite section of the wire.

In the case of measurements of electrically conducting materials, it is necessary to electrically isolate the wire from the test material.[94] For poor electrical conductors at modest temperatures it has been possible to achieve this isolation by means of a thin coating applied to the wire. Polymers and anodic oxide coating have both been employed.[95] However, for the aggressive conditions of molten metals and salts these approaches are inadequate. It has therefore been necessary to make significant adjustments to the simple technique while preserving most of its important features.

Figure 6.16 shows a cross section of a metallic wire embedded in an electrically insulating alumina substrate, with the whole immersed in the molten sample. An electrical current is initiated in the wire at time $t = 0$, and the resistive dissipation causes the temperature of the wire to rise in a manner determined by the thermal properties of the materials surrounding the wire. Therefore, unlike in the simple hot-wire case, the evolution of the temperature of the wire following the initiation of the heat pulse involves the properties of the alumina, its geometric shape as well as the properties of the wire and the fluid. Thus, while it is still possible to determine the temperature rise of the wire from transient measurements of its resistance, the relationship of that measurement to the thermal conductivity of the fluid

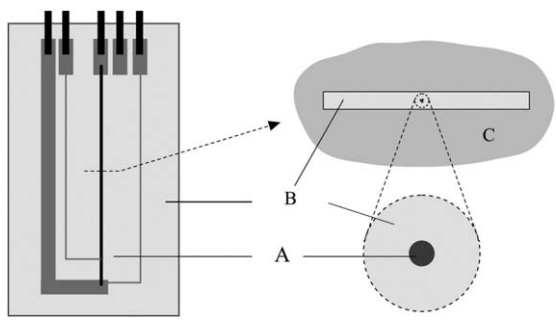

Figure 6.16 The metallic wire A in an insulating substrate B immersed in the melt C.

is considerably more complex than for the standard hot-wire system. For that reason there is no analytic solution to the governing equations of heat transport and so no simple analytical working equation. Neither, any longer, is such a working equation necessary. This is because the advent of sufficiently fast computing resources coupled with the development of accurate numerical solution methods mean that the working equations can be the full set of particle differential equations coupled with appropriate boundary conditions. This may be seen as a fundamental step beyond the approaches described in the first volume in this series twenty years ago.[93]

6.5.2 Working Equations

The working equations for the method are derived from the solution of the conservation of energy equation for a series of isotropic, and incompressible materials beginning with the wire, the solid substrate and the molten material which is itself supposed to be viscous. All materials have physical properties that are temperature independent. On the assumption that the perturbation of the temperature is small and that a local-equilibrium thermodynamic state exists, the governing equation for transient heat transfer in any material becomes[92]

$$\rho c_p \left(\frac{\partial T}{\partial t}\right) = \lambda \nabla^2 T. \tag{6.15}$$

In eqn (6.15), ρ is the density, c_p is the specific (massic) heat capacity at constant pressure, T is the thermodynamic temperature, t the time and λ the thermal conductivity.

The geometry of the thermal conductivity sensor comprising the wire in the alumina substrate surrounded by the fluid is defined by Figure 6.16. It is assumed, for the purpose of formulating the working equations, that the fluid is of infinite extent in the radial plane (x,y) perpendicular to the wire and that the sensor is sufficiently long that variations in the z-direction are negligible. It is then possible to treat the problem as one in two dimensions;[96] the experimental means to achieve this will be discussed later.

A constant heat flux per unit length q is generated within the wire from time $t = 0$. The wire is initially in equilibrium with the substrate and the melt at a temperature T_0 at time $t = 0$. The heating causes the temperature of the wire to increase so that applying eqn (6.15) for each of the three different regions in the present system gives the following set of coupled partial differential equations for the wire (denoted with subscript w):

$$\rho_{\mathrm{w}} c_{p,\mathrm{w}} \left(\frac{\partial T_{\mathrm{w}}}{\partial t}\right) = \lambda_{\mathrm{w}} \left[\frac{\partial^2 T_{\mathrm{w}}}{\partial x^2} + \frac{\partial^2 T_{\mathrm{w}}}{\partial y^2}\right] + \frac{q}{a^2}\ ; \tag{6.16}$$

for the substrate material (denoted with subscript s),

$$\rho_{\mathrm{s}} c_{p,\mathrm{s}} \frac{\partial T_{\mathrm{s}}}{\partial t} = \lambda_{\mathrm{s}} \left[\frac{\partial^2 T_{\mathrm{s}}}{\partial x^2} + \frac{\partial^2 T_{\mathrm{s}}}{\partial y^2}\right]\ ; \tag{6.17}$$

for the melt (denoted with subscript m),

$$\rho_{\mathrm{m}} c_{p,\mathrm{m}} \frac{\partial T_{\mathrm{m}}}{\partial t} = \lambda_{\mathrm{m}} \left[\frac{\partial^2 T_{\mathrm{m}}}{\partial x^2} + \frac{\partial^2 T_{\mathrm{m}}}{\partial y^2} \right]. \tag{6.18}$$

The solution of eqn (6.16), (6.17) and (6.18) is subject to the initial condition for $t = 0$ of

$$T_{\mathrm{w}} = T_{\mathrm{s}} = T_{\mathrm{m}} = T_{\mathrm{o}}, \tag{6.19}$$

for all x, y and the following boundary conditions in the ideal case for $t > 0$:

(a) for the wire-substrate interface,
when $y = \pm a$, x ranges from 0 to $\pm a$, and $x = \pm a$, y varies from 0 to $\pm a$,

then
$$T_{\mathrm{w}} = T_{\mathrm{s}}, \tag{6.20}$$

and
$$\lambda_{\mathrm{w}} \frac{\partial T_{\mathrm{w}}}{\partial x} = \lambda_{\mathrm{s}} \frac{\partial T_{\mathrm{s}}}{\partial x}, \tag{6.21}$$

$$\lambda_{\mathrm{w}} \frac{\partial T_{\mathrm{w}}}{\partial y} = \lambda_{\mathrm{s}} \frac{\partial T_{\mathrm{s}}}{\partial y}; \tag{6.22}$$

(b) for the substrate-melt interface,
when $y = -d$, x varies from 0 to $\pm w/2$, and $y = d$, x varies from 0 to $\pm w/2$,

then
$$T_{\mathrm{m}} = T_{\mathrm{s}} \tag{6.23}$$

and
$$\lambda_{\mathrm{m}} \frac{\partial T_{\mathrm{m}}}{\partial x} = \lambda_{\mathrm{s}} \frac{\partial T_{\mathrm{s}}}{\partial x}, \quad \text{and} \tag{6.24}$$

$$\lambda_{\mathrm{m}} \frac{\partial T_{\mathrm{m}}}{\partial y} = \lambda_{\mathrm{s}} \frac{\partial T_{\mathrm{s}}}{\partial y}; \tag{6.25}$$

(c) while for $x \to \infty$ or $y \to \infty$ $T_{\mathrm{m}} = T_{\mathrm{o}}$ $t > 0$. (6.26)

The system of equations can be solved using a finite-element method with an uncertainty better than or equal to that achieved in an experimental measurement for which an appropriate spatial grid is necessary. The grid system employed for the work of Bilek *et al.*[97] is shown in Figure 6.17. Evidently, the grid is finest in the regions of greatest gradients around the wire itself. The details of the numerical procedures themselves are standard and so are omitted here, but it is worth remarking that some experimentation

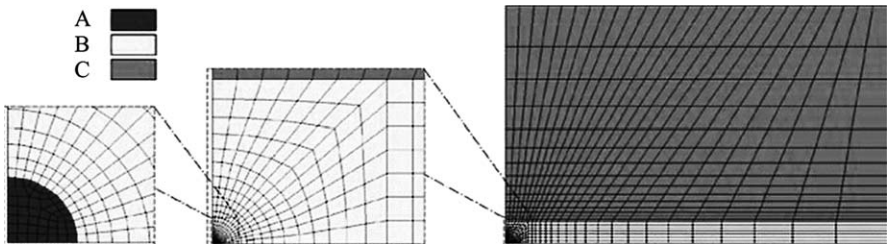

Figure 6.17 Mesh employed for 2D finite-element model of the cross section of the wire A, substrate B and melt C.

was required to find suitable spatial and temporal steps to secure the desired uncertainty of the computation.[97,98]

6.5.3 Practical Design

The first step in the development of this transient hot-wire technique for application to molten metals was reported by Peralta-Martinez, Wakeham and their collaborators.[96,98] In their application the metallic hot-wire of platinum was sandwiched between two thin (400 μm) rectangular substrates of alumina (see Figure 6.18a). For the substrate, pure green alumina tape of mass fraction purity 0.96 was employed, and the sensing element was made from a platinum wire of mass fraction purity 0.9999 and diameter 25 μm. The connections for the wire were printed directly on the top of one sheet of green alumina of dimensions 100 mm length, 58 mm width, using platinum ink and a screen printing technique. Platinum foils of mass fraction purity 0.9999 were attached at each end of the connections, and a second sheet of alumina was then placed on top of it. The sandwich was then hot pressed at a temperature of 353 K for a time of 1200 s with a force of 350 $kg \cdot cm^{-2}$ in order to guarantee the best contact between the substrate and the platinum wire. After pressing, the entire assembly was placed in a programmable high temperature furnace and baked with an appropriate temperature profile up to 1873 K. This process yields a rectangular, rigid sensor 85 mm long, 50 mm wide, and approximately 650 μm thick.

To facilitate connection of the sensor to the electrical measurement system, nickel wires of diameter 0.5 mm and mass fraction purity of 0.9998 (temper as hard), were spot-welded to each of the platinum leads of the active element.[4] To protect the connections, two pieces of fired alumina plates are glued to the sensor using a 2-part adhesive. Between the two pieces of alumina, two nickel wires were attached at each side for the sensing of the level of the molten metal in which the sensor is immersed.

The hot-wire shown in Figure 6.18 is in two parts and a connection to the hot-wire is located a short distance from one end. In part, this provides the means of making a four terminal measurement of the resistance of the longer part for the wire in a conventional sense. However, the same

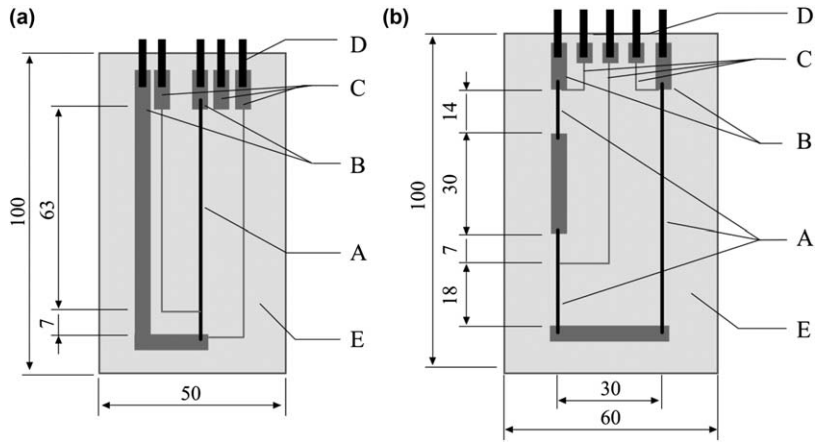

Figure 6.18 Plan view of the thermal conductivity instrument. (a), the instrument reported by Peralta *et al.*[98] (b), the instrument reported by Bilek *et al.*[99] In both (a) and (b) the letters define the following components: A, hot wire; B, input power terminals; C, resistance terminals; D, conductive coil; and E, alumina tape.

arrangement also creates a 'long' and a 'short' section of the hot-wire. The measurement of the resistance difference between the longer and shorter sections of the wire provides a means to eliminate the end effects of the wire so that the measurement yields the resistance of a finite section of an infinite wire. This technique is similar to that employed for the simple transient hot-wire technique employed earlier[93] and justifies the use of a two dimensional model of the heat transfer.

In 2007, Bilek *et al.*[99] introduced a new design, which uses the same materials and the same number of terminals and therefore does not require any further adjustments of the measuring devices. The new design, which is illustrated in Figure 6.18b, results in a sensor of similar dimensions but uses less platinum ink for the terminals. The most significant advantage of the new design is the creation of an increased length for the finite part of the infinitely long hot-wire. The end-effect correction is again automatically applied, but the length of the finite part of an infinitely long hot-wire is extended to 66 mm, (an increase of 18 % compared to the original design). This allows greater sensitivity in the measurement or a decrease in the perturbing heat flux for the same sensitivity. The latter point reduces the likelihood that the natural convection of the melt, which is driven by a buoyancy force, will perturb the measurement.

This new design has been tested in a number of experiments with molten indium, tin, and various lead-free solder alloys and the results compared to the values obtained from measurements of the thermal conductivity using the original design.[97,100] Both the designs shown in Figure 6.18 provided similar results with difference of no more than $\pm$ 2 %, which is less than the mutual relative uncertainty.

6.5.4 Instrument Assembly

In practice, the thermal conductivity transducer is mounted on a thin-walled metal tube which is itself mounted through the water-cooled, top sealing cap of a high-temperature furnace. The furnace is provided with a controlled atmosphere of argon with a mass fraction purity of 0.99999. The liquid metal is contained in an alumina crucible, placed inside the furnace on a platform mounted from the bottom of the furnace from where it can be pneumatically raised. The platform allows the crucible to be raised around the sensor for measurement, but to be withdrawn between measurements in order to limit any chemical reaction between the sensor and melt.

An extra heater is mounted on the tube that carries the sensor in order to ensure the temperature of the tube is ≈ 1 K above the melt temperature so that there is a stable density profile and convection currents are eliminated. The wires connecting to the sensor, the heater, and the thermocouples pass through the middle of the tube that suspends the sensor.

In order to perform measurements, the metal is melted from solid in the crucible and then the crucible is raised. The level of liquid in the crucible is detected using sensors on the substrate. If further metal is needed to increase the level, it can be added through the tube carrying the sensor. In use, the crucible is slightly above the middle of the furnace so that the best temperature distribution over the sensor is achieved. In this way, it is possible to achieve a uniform temperature environment around the sample of about ± 0.1 K.

6.5.5 Automatic Bridge

The basic measurements of the transient hot-wire method remain the same as before;[93] they consist of transient heating of the platinum wire by the application of a current through it and subsequent measurement of the resistance change of a part of the wire. To accomplish this, a Wheatstone electronic bridge circuit was developed,[98] in order to generate a constant heat flux within the wire and to monitor its change of resistance with a relative uncertainty of ± 0.1 % during 1 s. As has been explained, the technique is designed to eliminate, at the same time, the end effects. The temperature rise of the wire is calculated from temperature-resistance characteristics of the hot wire using a prior calibration. The principal difference between this bridge and earlier versions is that it allows much earlier and more rapid measurement for the temperature rise. It allows measurements of temperature rises at times as short as 20 μs after the application of the transient. This is essential in order that the entire history for the temperature rise of the wire is captured. In the first phase the rise of the temperature of the wire is dominated by its own thermal capacity and the properties of the substrate; later by the substrate in large measure and finally by the properties of the molten material. The acquisition of thousands of precise transient temperature rises in the first few microseconds ranging up

to 1 s is vital for the deduction of the thermal conductivity of the molten material from the observations.

6.5.6 Derivation of Thermal Conductivity

The derivation of the thermal conductivity of the molten material from the transient temperature response is carried out in an iterative fashion. First, using the known dimensions of the wire and substrate, a numerical (FEM) simulation of the transient temperature rise of the wire for the same heat input as applied in the experiment is conducted. For this simulation values are assumed for the thermal conductivity and the product (ρc_p) of platinum, the substrate, and the molten material The simulated temperature rise is compared over the entire range of five orders of magnitude in time from 10 μs to 1 s with the measured temperature rise. Adjustments are then made to the thermal properties of the substrate and melt so as to secure agreement between the simulated and experimental temperature rises over the entire period. Because the sensor is appropriately designed, the temperature rise of the wire is affected very differently by the properties of the substrate (ρc_p, λ) and those for the melt (ρc_p, λ) in different time zones so that each property can be determined more or less independently.

The typical experimental transient response is shown in Figure 6.19 which also identifies the different regimes of influence on the temperature rise. At each interface between the different materials, a small temperature discontinuity is always observed because of the mismatch at a molecular level between the materials. It is thus necessary to modify the boundary conditions for the differential equation at each interface to allow such a

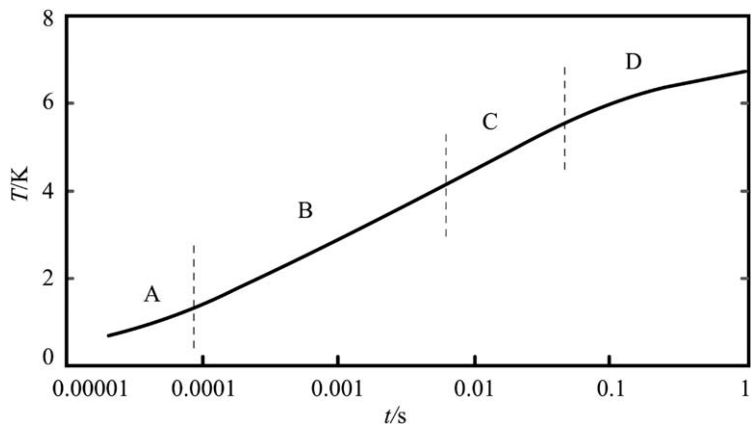

Figure 6.19 Typical measured transient temperature variation T (increase of the hot-wire temperature) from the thermal conductivity instrument as a function of time t over the main regions that are as follows: A, wire + interface; B, substrate; C, interface; and D, melt.

discontinuity and this is described elsewhere.[93,98] This has been achieved in practice by allowing a small interface heat transfer resistance at each interface; typically their thicknesses are about 5 nm for the wire–substrate interface and 0.5 μm for the substrate–melt interface. The thickness of the interfaces varies slightly for different sensors and also depends on the properties of the measured fluid. However, once the interface thickness is found to fit the model, it does not change relatively by more than ± 3 % for all measured temperatures with the same sensor and for all applied heat fluxes.

Figure 6.20 shows a typical comparison between experiment and modeled response after all material parameters in the model were set properly over four orders of magnitude in time. The difference is typically within ± 5 mK which equates relatively to about ± 0.07 % of the total temperature rise. This is very strong evidence that the theoretical and numerical model of the sensor provides a very good description of the practical instrument.

Bilek *et al.*[97] also investigated the effect of using different heat fluxes upon the thermophysical properties derived from the transient measurement. They have thus performed measurements in which the applied heat inputs varied from (70 to 140) $W \cdot m^{-1}$ and confirmed that the derived thermal conductivity for the fluid (and substrate) remains unchanged.

Finally, it is important to emphasize that the new technique can, in principle, be applied to the measurement of the thermal conductivity of any molten material: however, in this particular work, the sensor has been constructed and restricted for measurements on molten materials with a thermal conductivity above 8 $W \cdot m^{-1} \cdot K^{-1}$. This is mainly because of the properties and thickness of the substrate material employed. In this case the thickness of the alumina is relatively large (> 500 μm) with a relatively low

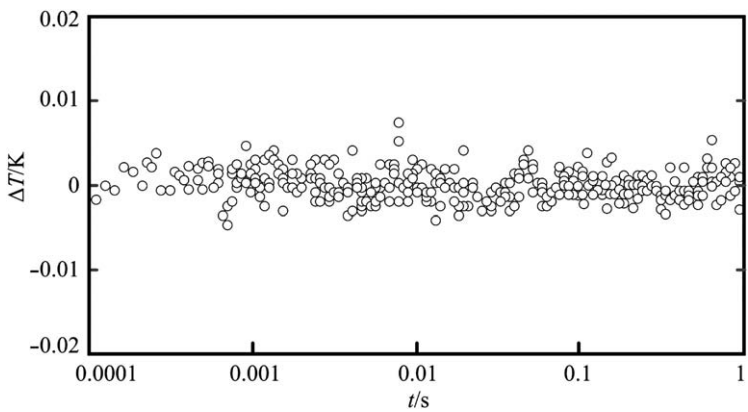

Figure 6.20 Example of the difference ΔT between measured temperature increase and that obtained from the working equation as a function of time for molten In at $T \approx 469$ K where the total temperature rise of the wire was 5.5 K.[100] ○, results from ref. 100.

thermal conductivity that tends to decrease when the temperature increases. Thus, if the test sample is a poorly conducting material, the substrate prevents heat transfer from the wire to the fluid and the latter barely affects the evolution of the temperature of the wire. Therefore, for measurements of low thermal conductivity materials, the sensor must be modified so that a thinner substrate material with higher thermal conductivity over the temperature range of interest is employed.

6.5.7 Uncertainty

It has been shown in a series of papers[98,100] that the heat transfer model developed for the description of the insulated hot-wire sensor is entirely consistent with the practical operation of the sensor over a time range of five orders of magnitude as the energy (heat) pulse transmits through three different materials. The analysis has also shown that with the temperature resolution available from the resistance bridge, ± 0.1 %, it is possible to distinguish the thermal conductivity of the melt to within an expanded relative uncertainty ± 1 %. Allowing for errors in the calibration of the resistance–temperature characteristics of the platinum wire, the effects of uncertainties in the dimensions of the sensor and in the remaining physical properties of the system, determined by simulation, it is possible to assert that the expanded relative uncertainty in the thermal conductivity of the molten metals determined by this technique is ± 2 %.

6.5.8 Selected Measurements

In Table 6.4, a selection of recent thermal conductivity measurements employing the hot-wire technique for substances with mass fraction purity w.

Table 6.4 Selected measurements.

Hg $w = 0.999994$[101]		Ga $w = 0.9999$[101]		In $w = 0.9999$[100]		Sn $w = 0.9999$[100]	
T/K	λ/W · m^{-1} · K^{-1}	T/K	λ/W · m^{-1} · K^{-1}	T/K	λ/W · m^{-1} · K^{-1}	T/K	λ/W · m^{-1} · K^{-1}
295.6	8.05	321.3	29.3	467.0	36.3	523.1	27.3
312.2	8.50	367.7	33.5	495.4	37.0	549.2	28.0
319.5	8.80	416.3	37.0	522.2	38.2	580.0	28.6
332.0	9.05	465.6	41.0	575.9	40.0	603.7	29.1
352.0	9.50	520.4	45.0	608.8	41.4	634.9	30.0
370.7	9.90	565.0	47.7	630.2	42.2	657.0	30.6
390.0	10.2	614.3	50.9	684.5	44.0	683.8	31.4
407.7	10.8			711.0	44.4	707.6	31.9
425.9	11.2			734.1	45.3	733.2	32.5
476.6	12.4						
515.2	13.0						

6.5.9 Conclusions

In this section, instruments for the measurement of the thermal conductivity of molten metals at high temperatures have been described. The two new instruments described are able to operate from ambient up to 1200 K. Problems of convection and thermal radiation are overcome, and the instruments operate in accord with a full theoretical model. The relative expanded uncertainty of the thermal conductivity results is estimated to be ± 2 % which is superior to that achieved in earlier work.

6.6 Ionic Liquids

JOAN F. BRENNECKE, MARJORIE MASSEL AND CHAOJUN SHI

6.6.1 Introduction

Ionic liquids (ILs) are salts with low melting points, usually defined as less than 373 K; many are liquids at room temperature. Most have exceedingly low vapor pressures so they do not evaporate. As a result, many can be used at temperatures well above 473 K, until they experience chemical or thermal degradation. The low volatility also reduces flammability concerns. ILs are being widely investigated for a myriad of applications, including as electrolytes, as solvents for separations and reactions, for dissolution and processing of biomass, in absorption and co-fluid vapour compression refrigeration systems, for materials synthesis and processing, as heat transfer fluids and as lubricants.

Owing to the Coulombic forces, ILs are inevitably more viscous than common organic solvents or water. This presents mass transfer challenges in almost every potential application. Thus, the viscosity of ILs and mixtures of ILs with other materials is extremely important. For heat transfer applications and for many applications where the IL will be heated and cooled in a process, the thermal conductivity is of primary importance. Finally, electrical conductivity is critically important for all types of electrochemical applications of ILs. Since they are salts, ILs conduct electricity, but many ILs also have wide electrochemical windows, which make them very attractive.

Thus, here we discuss the viscosity, thermal conductivity and electrical conductivity of ionic liquids.

6.6.2 Experimental Techniques for Viscosity, Thermal Conductivity and Electrical Conductivity

Standard experimental methods, including falling ball, rolling ball, cone-and-plate, parallel plate, and capillary viscometers, have been used to measure the viscosity of ILs. Thermal conductivities are typically measured with a transient hot-wire technique. The most common method for electrical conductivity of ILs is electrical impedance spectroscopy.

The most striking result presented below, especially for viscosities and electrical conductivities of ILs, is that there is much greater disagreement in the literature for the measured values than for other common substances. We attribute the greater uncertainty in the measurement of IL transport properties to impurities. Solid salts, which are typical difficult-to-remove by-products of the IL synthesis, can dramatically affect transport properties of ILs, as pointed out by Seddon and co-workers very early on.[102] All ILs (even ones that are labeled as 'hydrophobic' because they are not completely

miscible with water) are hygroscopic and can absorb substantial amounts of water (*e.g.*, mass fraction of 0.01) from the atmosphere in very short exposure times, even if they have been scrupulously dried prior to use. Water has a dramatic effect on IL transport properties.[103] If possible the entire transport property measurements should be done in a dry inert atmosphere (*e.g.*, a glove box). No transport properties of ILs should be reported without measurement and reporting of the water content, which can be easily done by Karl–Fisher coulometry. Preferably, the water content should be measured before and after the transport property measurements.

6.6.3 Viscosity

As mentioned above, a challenge that frequently arises when developing ILs for different applications is their relatively high viscosity in comparison to common molecular solvents. Common ILs that are considered fairly fluid can have viscosity values as low as 16.1 mPa · s for 1-ethyl-3-methyl-1*H*-imidazol-3-ium dicyanoazanide ([emim][DCA]) or as high as 734 mPa · s for 1-octyl-3-methyl-1*H*-imidazol-3-ium hexafluorophosphate ([omim][PF_6]),[104,105] in comparison to water, methylbenzene and methanol, which have viscosities less than 1 mPa · s at a temperature of 298.15 K and pressure of 0.1 MPa.

Viscosity is a measure of the resistance of a fluid to flow and electrostatic interactions between the two ions are important, as well as van der Waals interactions and the polarizability. In addition, shape, flexibility and the size of the ions play an important role in controlling the viscosity. Finally, hydrogen bonding, which is particularly prominent in ILs with hydrogen bond donor and acceptor groups (*e.g.*, hydroxyl or acetate groups)[106] significantly increases the viscosity.

The viscosity of ILs is strongly dependent on the temperature, thus all published viscosity data presented in this section were measured at a temperature of 298.15 K for accurate comparison (unless otherwise specified). The Vogel–Fulcher–Tammann, VFT, model is commonly used to describe the temperature dependence of IL viscosity and is given by

$$\eta = \eta_0 \exp\left(\frac{k}{T - T_0}\right). \tag{6.27}$$

In eqn (6.27), η is the viscosity, T is the temperature, η_0 and k are fitted parameters and T_0 can either be the IL glass transition temperature or a third fitted parameter.[107,108]

6.6.3.1 Effect of Anion on Viscosity

As has been seen with other physical properties (density, melting point, solubility), viscosity can be tuned by changing the cation or the anion of the IL. For example, the 1,1,1-trifluoro-*N*-[(trifluoromethyl)sulfonyl]methanesulfonamide [[Tf_2N]$^-$], and [DCA]$^-$ anions are particularly effective in reducing the viscosity.

Alternatively, the structure of the cation or anion can be adjusted (for instance, varying alkyl chain length or including flexible saturated rather than unsaturated alkyl chains) to achieve a desired viscosity.

For the same cation, the viscosity decreases, as Figure 6.22 shows, in the following order: $[DCA]^- < [Tf_2N]^- <$tetrafluoroborate $[BF_4]^- < [PF_6]^-$ < acetate $[OAc]^-$. The ability of the acetate ion to act as a hydrogen bond acceptor raises viscosity. The symmetry and rigidity of $[BF_4]^-$ and $[PF_6]^-$ anions contribute to their relatively high viscosities. The delocalization of the charge in $[DCA]^-$ and $[Tf_2N]^-$ ions weakens the ion–ion interactions and favors low viscosity.[109]

6.6.3.2 *Effect of Cation on Viscosity*

For a common anion the viscosity decreases in the following order: 1*H*-Imidazol-3-ium $[im]^+ <$ pyridinium $[py]^+ <$ pyrrolidinium $[pyr]^+ <$ piperidinium $[pip]^+$ (Figure 6.23). Phosphonium based ILs are generally less viscous than ammonium based ILs: hexyltrimethylphosphonium and triethyl(methoxymethyl)phosphonium $[Tf_2N]$) both have lower viscosities than the corresponding ammonium based ILs [of between (150 and 35) mPa · s versus (153 and 69) mPa · s, respectively].[116–118] The delocalization of the charge by aromatic rings leads to weaker electrostatic interactions; thus, ILs with aromatic cations have lower viscosities than their non-aromatic analogs.[108]

Elongating the alkyl chain substitutions on either the cation or the anion (thus increasing the van der Waals interactions) generally increases viscosity. This is illustrated in Figure 6.21 for a series of imidazolium ILs of the form $[C_n mim][Tf_2N]$, where n is the number of carbons of the alkyl chain in

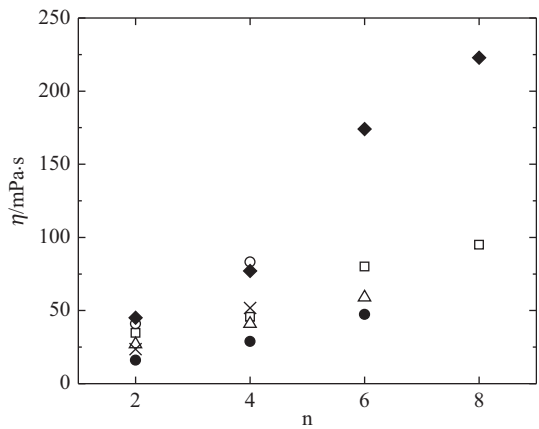

Figure 6.21 Viscosity, η, of n-alkyl-3-methylimidazolium based ionic liquids as a function of the number of carbon of the substituted alkyl chain, n, at $T = 298.15$ K and atmospheric pressure. □, $[Tf_2N]^-$ ($n = 2$),[110] ($n = 4$),[111] ($n = 6$ and 8);[112] ○, $[OTf]^-$ ($n = 2$),[107] ($n = 4$);[112] ◆, $[BF_4]^-$ ($n = 2$ and 4),[111] ($n = 6$ and 8);[113] △ $[C_2F_5BF_3]^-$ ($n = 2$, 4 and 6);[114] ×, $[SCN]^-$ ($n = 2$),[112] ($n = 4$);[115] ●, $[DCA]^-$ ($n = 2$, 4 and 6).[112]

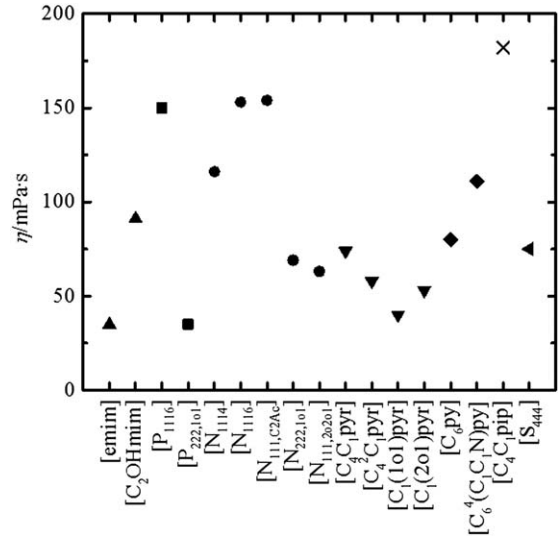

Figure 6.22 Viscosity, η, of a series of ionic liquids with the common $[Tf_2N]^-$ anion at $T = 298.15$ K and $p \approx 0.1$ MPa. Data taken from: ▲, ref. 110, 123; ■, ref. 116, 117; ●, ref. 116–118, 124; ▼, ref. 111, 120, 125; ◆, ref. 126; ×, ref. 120; ◀, ref. 127.

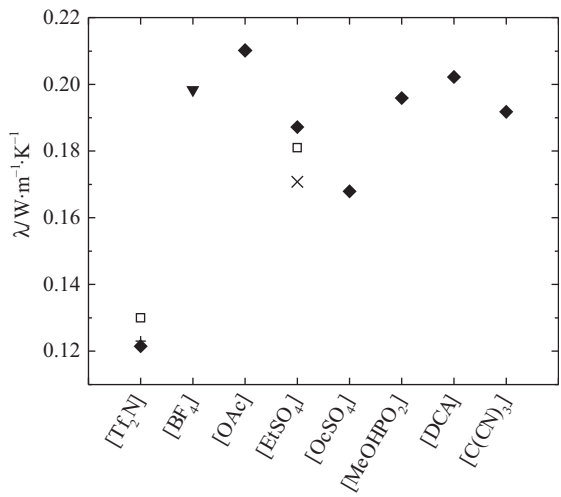

Figure 6.23 Experimental thermal conductivity, λ, for a series of ionic liquids with the common $[emim]^+$ cation at $T = 303$ K. Data taken from □, ref. 133; ◆, ref. 138; ▼, ref. 142; +, ref. 136; ×, ref. 135.

the C_1 position.[108] For $n = 2$, 4, 6 and 8, $[C_n mim][Tf_2N]$ viscosities are (34.7, 45.6, 80.1 and 95.0) mPa · s, respectively.[110–112] However, with very short alkyl chain substitutions (methyl and ethyl) the rigidity of the methyl group mitigates this effect.

Flexible ether or silyl groups are effective in reducing the viscosity.[106,119] However, indiscriminately adding multiple ether groups can be counter-productive, as it modifies the size and symmetry of the cation,[119] Moreover, it is preferable to have a methylene spacer between the oxygen ether and the cationic nitrogen to efficiently reduce the viscosity ($\eta = 40$ mPa·s for $[C_1(1o1)pyr][Tf_2N]$ and $\eta = 53$ mPa·s for $[C_1(2o1)pyr][Tf_2N]$), as seen in Figure 6.23.[106,120] The viscosities of 1*H*-Imidazol-3-ium based ILs with a (trimethylsilyl)methyl side chains are 1.6 and 7.4 times lower than the corresponding 1-methyl-3-(2,2-dimethylpropyl)-1*H*-imidazol-3-ium ILs with $[BF_4]^-$ and $[Tf_2N]^-$ anions, respectively,[121] but higher than the methyl analog ILs because of the increased bulk of the silyl substituents.[122]

6.6.3.3 *Effect of Impurities on Viscosity*

While the large number of experimental viscosity measurements of ionic liquids provides valuable information, there are still many inconsistencies in the published viscosity data. We mainly attribute these inconsistencies to the effect of water and halide impurities present in the IL samples.[128] Indeed viscosity appears to be one of the physical properties that are the most sensitive to impurities; even a small percentage of water in an IL significantly decreases its viscosity.[102,129] This effect is much larger than the typically reported relative uncertainty of ± (1 or 3) % for viscosity measurements. For instance, the viscosity of 'hydrophobic' $[Tf_2N]^-$ based ILs can be half of the corresponding dried IL viscosity values when they are saturated with water [for [bmim][Tf_2N] at $T = 293$ K the viscosity with water mass fraction of 0.02 is 59.8 mPa·s *versus* the viscosity of the dry [bmim][Tf_2N] of 32.0 mPa·s, while for $[N_{1114}][Tf_2N]$ at $T = 294$ K with water mass fraction of 0.014 the viscosity is 140.7 mPa·s *versus* the viscosity of the dry $[N_{1114}][Tf_2N]$ of 72.6 mPa·s]. By contrast, halide impurities increase the viscosity as Seddon *et al.*[102] demonstrated by adding [emim][Cl] to $[C_{4-6}mim][BF_4]$ and $[C_{4-6}mim][PF_6]$. Since contamination, especially with water, is likely to occur when ILs are used in industrial processes, understanding the effect of these contaminants on the viscosity is vital.

6.6.4 Thermal Conductivity

Currently, thermal conductivity data, λ, for ILs is underrepresented in the literature compared with other transport properties. However, the existing publications give indications of how ionic liquids compare with other fluids and how thermal conductivity varies depending on the ionic liquid structure.

The thermal conductivity of ILs is typically between (0.1 and 0.2) $W \cdot m^{-1} \cdot K^{-1}$ (at temperatures between (273.15 and 353.15) K at a pressure 0.1 MPa), corresponding to only (16 to 33) % of the thermal conductivity of water at a temperature of 300 K.[130] However, these values compare well with the heat transfer fluids currently used in chemical processes, such as

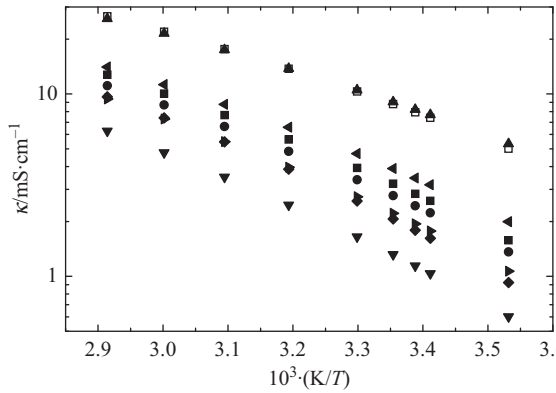

Figure 6.24 The influence of the cation structure on the electrical conductivity κ of $[Tf_2N]^-$ based ILs as a function of T^{-1}.[152] ▲, $[emim]^+$; □, $[mmim]^+$; ◀, $[bmim]^+$; ■, $[bpy]^+$; ●, $[bmpyr]^+$; ▶, $[C_6mim]^+$; ◆, $[N_{1114}]^+$; ▼, $[C_8mim]^+$.

Therminol VP-1 [$\lambda(333.15\ K) = 0.1323\ W \cdot m^{-1} \cdot K^{-1}$] (www.therminol.com) and Syltherm XLT [$\lambda(333.15\ K) = 0.1019\ W \cdot m^{-1} \cdot K^{-1}$] (Product Information Syltherm XLT).[131,132]

The transient hot-wire method[133–136] provides a direct measurement of thermal conductivity and is generally considered the most accurate method for liquids.[137] However, as seen in Figure 6.24, values obtained with a stationary guarded parallel-plate instrument agree well with the transient hot-wire technique.[138] In general the reported experimental relative uncertainty is between ± (2 and 5) %, although some discrepancies in the data are observed. Measurement and calibration errors may explain some of the discrepancies, but the purity of the ILs has also been proposed as a potential source of error.[135,136,138–140]

A number of studies have shown that there is a slight, linear decrease in the thermal conductivity values with an increase in temperature.[133,135,136,141,142] The alkyl chain length on the 1*H*-Imidazol-3-ium cation (in different substitution positions) has no effect on the thermal conductivity.[133,136] In fact, all of the ILs investigated with different cations but the same $[Tf_2N]^-$ anion exhibit thermal conductivities roughly between (0.12 and 0.13) $W \cdot m^{-1} \cdot K^{-1}$, except for the tetra-alkyl substituted phosphonium cation that has a somewhat higher value of 0.143 $W \cdot m^{-1} \cdot K^{-1}$.[133]

Variation of the anion has a greater effect on the thermal conductivity, as seen in Figure 6.24. ILs with bulkier anions seem to have lower thermal conductivity than ILs with smaller anions. For instance, $[Tf_2N]^-$, trifluorotris(1,1,2,2,2-pentafluoroethylphosphate and trifluoromethanesulfonate $[OTf]^-$ based ILs have thermal conductivities between (0.10 and 0.14) $W \cdot m^{-1} \cdot K^{-1}$,[133,134] whereas ILs with smaller anions, such as $[OAc]^-$ and $[DCA]^-$ have thermal conductivity values around 0.20 $W \cdot m^{-1} \cdot K^{-1}$.[138]

It appears that the effect of water and halide impurities on the thermal conductivity is much smaller than on viscosity. Van Valkenburg compared the thermal conductivity of three dried imidazolium ILs with their corresponding mixtures containing a water mass fraction of 0.25.[142] The difference in the two values was significant for the two $[BF_4]^-$ ILs (increases of 38 % and 50 %), whereas it was within the uncertainty for the $[Tf_2N]^-$ based IL. Measurements of aqueous solutions of [bmim][OTf] and [emim][$EtSO_4$] (ethyl sulfate) over the full composition range showed that the increase (the thermal conductivity of water is much greater than ILs) is minimal at water mass fractions up to 0.0001.[133] However, results recently published contradicted this trend.[135] For halides, Ge *et al*. found that a mass fraction of up to 0.05 % [hmim][Cl] in [hmim][Tf_2N] does not change the thermal conductivity significantly.[133]

The simple relationship suggested by Fröba *et al*.

$$\lambda M\rho = AM + B, \tag{6.28}$$

where ρ is the mass density, M the molar mass, and A and B two fitting parameters, is able to correlate the thermal conductivity of many different ILs with a relative standard deviation around ± 5.5 %.[138,139]

6.6.5 Electrical Conductivity

The intrinsic electrical conductivity of ILs is of vital significance for all electrochemical applications.[118,143] Since ILs are entirely composed of ions, they conduct charge but a major impediment of using ILs in electrochemical devices is their relatively high viscosities that result in lower conductivities (between 10^{-2} and 10^{-3} $S \cdot cm^{-1}$ at a temperature of 298 K) than current electrolytes.[144] Electrical conductivity (κ) is defined as the number of charged ions multiplied by the mobility of carrier ions.[145] The number of charged ions is associated with ionicity and the mobility of the carrier ions can be characterized by their diffusion coefficients.[146] The overall conductivity reflects both of these characteristics.

Ionicity is defined as the conductivity determined from electrical impedance measurements divided by the conductivity determined from ion diffusivities measured by NMR spectroscopy (and calculated using the Nernst–Einstein equation), $\Lambda_{imp}/\Lambda_{NMR}$.[147,148] Although a very simplistic viewpoint, this ratio is commonly interpreted as a measure of incomplete ion dissociation of ILs. High ionicity ILs can be envisioned as having a low degree of ionic association and/or aggregation.[149] Λ_{NMR} is always higher than Λ_{imp}, since ILs are highly concentrated electrolytes and it is impossible for a single ion to move without interacting with surrounding ion neighbours.

Numerous studies have shown that IL viscosity plays an important role in controlling the rate of ions transport. Anion and cation size and shape also appear to influence electrical conductivity. This section focuses on the effect of cation structure, anion structure, and alkyl chain substituents on the cation on electrical conductivity.

6.6.5.1 *Effect of Cation Structure on Electrical Conductivity*

The electrical conductivity of numerous combinations of organic cations with organic and inorganic anions has been investigated.[146,150,151] Figure 6.25 compares the electrical conductivities of $[Tf_2N]^-$ ILs with similar numbers of carbon atoms on the alkyl chains: 3-butyl-1-methyl-1*H*-imidazol-3-ium ($[bmim]^+$), 1-butylpyridinium ($[bpy]^+$), 1-butyl-1-methylpyrrolidinium ($[bmpyr]^+$) and *N*,*N*,*N*-trimethyl-1-butanaminium ($[N_{1114}]^+$). The conductivities are between (2 and 4) $mS \cdot cm^{-1}$ at ambient temperature, and they fall in the order: $[bmim][Tf_2N] > [bpy][Tf_2N] > [bmpyr][Tf_2N] > [N_{1114}][Tf_2N]$. Aromatic cations (imidazolium and pyridinium) have higher conductivity than non-aromatic cations (pyrrolidinium and quaternary ammonium). Interestingly, the ionicity (not shown) is $[bmpyr]^+ > [N_{1114}]^+ > [bpy]^+ > [bmim]^+$, which is not the same order as the electrical conductivities. The variations in the shapes of the cations (both the actual geometrical structure and steric hindrance that may result) influence the cation-anion interactions. Also shown in Figure 6.25 is the temperature dependence of the electrical conductivities of the four ILs which, like viscosity, can be fitted quite well with the VFT equation for electrical conductivity [see eqn (6.27) for the functional form].

6.6.5.2 *Effect of Alkyl Chain Length on Electrical Conductivity*

As shown in Figure 6.24 for imidazolium ILs with the $[Tf_2N]^-$ anion,[152] electrical conductivity decreases with increasing alkyl chain length, except for $[emim][Tf_2N]$, which has a conductivity very similar to $[mmim][Tf_2N]$. $[emim][Tf_2N]$ has a lower viscosity than $[mmim][Tf_2N]$. With increasing molecular weight, the molar concentration decreases, and the number of the

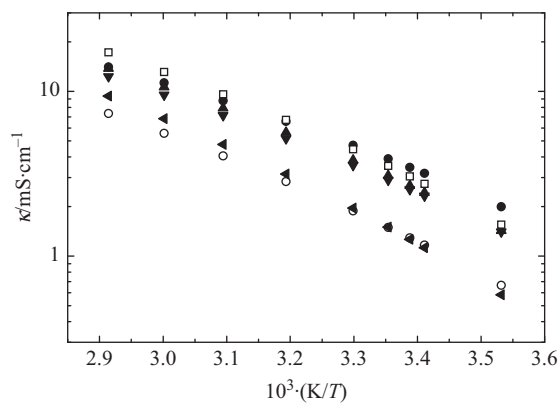

Figure 6.25 The influence of the choice of anion on the electrical conductivity κ of $[bmim]^+$ ILs as a function of T^{-1}.[156] ●, $[Tf_2N]^-$; □, $[BF_4]^-$; ▲, $[CF_3CO_2]^-$; ▼, $[CF_3SO_3]^-$; ◀, $[PF_6]^-$; ○, $[(C_2F_5SO_2)_2N]^-$.

cation–anion interactions and reduce viscosity. Meanwhile, increasing the number of hydrocarbon (–CH_2–) units on the alkyl chain of the cation should increase van der Waals interactions and increase viscosity. For chains greater than ethyl, it is clear the primary effect is the increased van der Waals interactions. Incorporation of functional groups that reduce viscosity, such as ethers, alkenyls and esters, tends to dramatically increase electrical conductivity.[153–155]

6.6.5.3 *Effect of Anion on Electrical Conductivity*

The anion has a large influence on the electrical conductivity of ILs.[156,157] Figure 6.25 compares ILs with the $[bmim]^+$ cation and $[BF_4]^-$, $[PF_6]^-$, $[Tf_2N]^-$, $[(C_2F_5SO_2)_2N]^-$, $[CF_3CO_2]^-$ and $[CF_3SO_3]^-$ anions. The electrical conductivity at room temperature decreases in the following order: $[Tf_2N]^- > [BF_4]^- > [CF_3CO_2]^- > [CF_3SO_3]^- > [(C_2F_5SO_2)_2N]^- > [PF_6]^-$. This cannot be explained just by viscosity (*i.e.*, ion mobility). Therefore, the number of charge carriers must be different for the different ILs. In fact, the ionicity follows the order: $[PF_6]^- > [BF_4]^- > [(C_2F_5SO_2)_2N]^- > [Tf_2N]^- > [CF_3SO_3]^- > [CF_3CO_2]^-$. The negative charge of imide anions is distributed among the nitrogen and the four oxygen atoms, weakening interactions with the cation. By contrast, one would expect the negative charge on $[CF_3SO_3]^-$ and $[CF_3CO_2]^-$ to be localized on the SO_3 and CO_2, which would increase interaction with the cation. For similar anions ($[Tf_2N]^-$ and $[(C_2F_5SO_2)_2N]^-$), lower molecular weight and smaller size results in higher conductivity.

6.6.5.4 *Effect of Impurities on Electrical Conductivity*

Residual water or water absorbed from the atmosphere has a tremendous effect on electrical conductivities of ILs,[158] so scrupulous removal and reporting of water content is absolutely critical. Inconsistent IL purity may be another reason for serious disagreement in published IL conductivity data. Reported electrical conductivity values for [emim][Tf_2N] around room temperature vary by as much as a factor of 2.[116,127,147,151,156,159–165]

6.6.6 Conclusions

Transport properties, including viscosity, thermal conductivity and electrical conductivity, are extremely important in designing, selecting and evaluating ionic liquids for many different applications. Viscosities of ILs are higher than most common organic solvents. High viscosities and strong cation/anion interactions that decrease the number of effective charge carriers limit electrical conductivities. Thermal conductivities of ILs, which are typically between (0.1 and 0.2) $W \cdot m^{-1} \cdot K^{-1}$, are lower than water but comparable to common industrial heat transfer fluids. The two most common impurities in ILs are halide salts and water. While thermal conductivities are not significantly affected by these impurities, they can have truly dramatic effects on

viscosity and electrical conductivity, which is a likely explanation for the large disagreement among various literature values.

References

1. A. Nagashima, J. V. Sengers and W. A. E. Wakeham, *Measurement of the Transport Properties of Fluids*, Blackwell Scientific, Oxford, 1991.
2. R. Tufeu, J. P. Petitet, L. Danielou and B. LeNeindre, *Int. J. Thermophys.*, 1985, **6**, 315.
3. Y. Nagasaka and A. Nagashima, *Int. J. Thermophys.*, 1991, **12**, 769.
4. E. P. Sakonidou, M. J. Assael, C. A. Nieto de Castro, H. R. van den Berg and W. A. Wakeham, *Thermal Conductivity*, 1999, **24**, 516.
5. D. Herlach, R. Cochrane, I. Egry, H. Fecht and L. Greer, *Int. Mat. Rev.*, 1993, **38**, 273.
6. J. Priede and G. Gerbeth, *IEEE Trans. Magn.*, 2000, **36**, 349.
7. J. Priede and G. Gerbeth, *IEEE Trans. Magn.*, 2000, **36**, 354.
8. T. Kordel, D. Holland-Moritz, F. Yang, J. Peters, T. Unruh, T. Hansen and A. Meyer, *Phys. Rev. B*, 2011, **83**, 104205.
9. G. Lohöfer, P. Neuhaus and I. Egry, *High Temp. – High Pressures*, 1991, **23**, 333.
10. J. Piller, A. Seidel, M. Stauber and W. Dreier, *Solidification*, TMS, Warrendale, 1999.
11. TEMPUS-Team, *Materials and Fluids Under Low Gravity*, Springer, Berlin, 1996.
12. *Solidification*, ed. W. Hofmeister, J. Rogers, N. Singh, S. Marsh and P. Vorhees, TMS, Warrendale, 1999.
13. E. E. Gorges, L. Racz, A. Schillings and I. Egry, *Int. J. Thermophysics*, 1996, **17**, 1163.
14. J. Brillo and I. Egry, *Int. J. Thermophysics*, 2003, **24**, 1155.
15. J. Brillo and I. Egry, *Jpn. J. Appl. Phys.*, 2011, **50**, 11RD02.
16. J. Brillo and I. Egry, *Z. Metallkd.*, 2004, **95**, 8.
17. Y. Sato, T. Nishizuka, T. Takamizawa, K. Sugisawa and T. Yamamura, *16th European Conference on Thermophysical Properties*, London, 2002.
18. B. Damaschke, K. Samwer and I. Egry, *Solidification*, ed. W. Hofmeister, J. Rogers, N. Singh, S. Marsh and P. Vorhees, TMS, Warrendale, 1999.
19. J. Brillo, A. I. Pommrich and A. Meyer, *Phys. Rev. Lett.*, 2011, **107**, 165902.
20. K. Ohsaka, S. K. Chung and W. K. Rhim, *Acta Mater.*, 1998, **46**, 4535.
21. S. Sauerland, K. Eckler and I. Egry, *J. Mater. Sci. Letters*, 1992, **11**, 330.
22. D. Cummings and D. Blackburn, *J. Fluid Mech.*, 1991, **224**, 395.
23. I. Egry, G. Lohöfer and G. Jacobs, *Phys. Rev. Lett.*, 1995, **75**, 4043.
24. J. Schmitz, J. Brillo, I. Egry and R. Schmid-Fetzer, *Int. J. Mater. Res.*, 2009, **100**, 11.
25. P. Laty, J. C. Joud and P. Desre, *Surf. Sci.*, 1977, **69**, 508.
26. R. Aune, L. Battezzati, R. Brooks, I. Egry, H. Fecht, J. Garandet, K. Mills, A. Passerone, P. Quested, E. Ricci, S. Schneider, S. Seetharaman, R. Wunderlich and B. Vinet, *Microgravity Sci. Technol.*, 2005, **XVI**, 11.

27. K. Higuchi, H.-J. Fecht and R. K. Wunderlich, *Adv. Eng. Mater.*, 2007, **9**, 349.
28. H. Fujii, T. Matsumoto, T. Ueda and K. Nogi, *J. Mater. Sci. Letters*, 2005, **40**, 2161.
29. T. Matsumoto, H. Fujii, T. Ueda, M. Kamai and K. Nogi, *Meas. Sci. Technol.*, 2005, **16**, 432.
30. H. Fujii, T. Matsumoto, S. Izutani, S. Kiguchi and K. Nogi, *Acta Mater.*, 2006, **54**, 1221.
31. I. Egry, G. Lohöfer, I. Seyhan, S. Schneider and B. Feuerbacher, *Appl. Phys. Lett.*, 1998, **73**, 462.
32. S. Lee, K. Tsang and H. Kai, *J. Appl. Phys.*, 1991, **70**, 4842.
33. W. K. Rhim, S. K. Chung, A. J. Rulison and R. E. Spjut, *Int. J. Thermophys.*, 1997, **18**, 459.
34. W. K. Rhim, K. Ohsaka and P. F. Paradis, *Rev. Sci. Instrum.*, 1999, **70**, 2796.
35. P. F. Paradis, T. Ishikawa, G. W. Lee, D. Holland-Moritz, J. Brillo, W. K. Rhim and J. T. Okada, *Mater. Sci. Eng. Res.*, 2014, **76**, 1.
36. E. Becker, W. J. Hiller and T. A. Kowalewski, *J. Fluid Mech.*, 1994, **258**, 191.
37. H. Fecht and W. Johnson, *Rev. Sci. Instr.*, 1991, **62**, 1299.
38. R. Wunderlich and H. Fecht, *Meas. Sci. Technol.*, 2005, **16**, 402.
39. R. Wunderlich, R. Sagel, C. Ettel, H.-J. Fecht, D. Lee, S. Glade and W. W. Johnson, in *Solidification*, ed. W. Hofmeister, J. Rogers, N. Singh, S. Marsh and P. Vorhees, TMS, Warrendale, 1999, p. 53.
40. H. Fukuyama, H. Kobatake, K. Takahashi, I. Minato, T. Tsukada and S. Awaji, *J. Cryst. Growth*, 2007, **260**, 2059.
41. T. Tsukada, H. Fukuyama and H. Kobatake, *Int. J. Heat Mass Transfer*, 2007, **50**, 3054.
42. H. Kobatake, H. Fukuyama, I. Minato, T. Tsukada and S. Awaji, *Appl. Phys. Lett.*, 2007, **90**, 094102.
43. H. Kobatake, H. Fukuyama, I. Minato, T. Tsukada and S. Awaji, *J. Appl. Phys.*, 2008, **104**, 054901.
44. H. Kobatake, H. Fukuyama, T. Tsukada and S. Awaji, *Meas. Sci. Technol.*, 2010, **21**, 025901.
45. H. Fukuyama, K. Takahashi, S. Sakashita and H. Kobatake, *ISIJ Int.*, 2009, **49**, 1436.
46. H. Sugie, H. Kobatake, M. Uckikoshi, M. Isshiki, K. Sugioka, T. Tsukada and H. Fukuyama, *Jpn. J. Appl. Phys.*, 2011, **50**, 11RD04.
47. G. Lohöfer and I. Egry, in *Solidification*, ed. W. Hofmeister, J. Rogers, N. Singh, S. Marsh and P. Vorhees, TMS, Warrendale, 1999.
48. T. Richardsen and G. Lohöfer, *Int. J. Thermophys.*, 1999, **20**, 1029.
49. D. Platzek, C. Notthoff, D. M. Herlach, G. Jacobs, D. Herlach and K. Maier, *Appl. Phys. Letts.*, 1994, **65**, 1723.
50. K. Mills, B. Monaghan and B. Keene, *Int. Mater. Rev.*, 1996, **41**, 209.
51. E. Sondermann, C. Neumann, F. Kargl and A. Meyer, *High Temp. – High Pressures*, 2013, **42**, 23.

52. F. Kargl, E. Sondermann, H. Weis and A. Meyer, *High Temp. – High Pressures*, 2013, **42**, 3.
53. H. Weis, T. Unruh and A. Meyer, *High Temp. – High Pressures*, 2013, **42**, 39.
54. S. Kitada, Y. Kobayashi, N. Y. and A. Nagashima, *High Temp. – High Pressures*, 1989, **21**, 219.
55. Y. Nagasaka, ed. W. A. Wakeham, A. Nagashima and J. V. Sengers, *Experimental Thermodynamics Vol. III: Measurement of the Transport Properties of Fluids*, Blackwell Scientific Publications, 1991, p. 213.
56. Y. Nagasaka, T. Hatakeyama, T. Okuda and A. Nagashima, *Rev. Sci. Instrum.*, 1988, **59**, 1156.
57. Y. Nagasaka, N. Nakazawa and A. Nagashima, *Int. J. Thermophys.*, 1992, **13**, 555.
58. N. Nakazawa, Y. Nagasaka and A. Nagashima, *Int. J. Thermophys.*, 1992, **13**, 753.
59. N. Nakazawa, Y. Nagasaka and A. Nagashima, *Int. J. Thermophys.*, 1992, **13**, 763.
60. V. I. Fedorov and V. I. Machuev, *Teplofiz. Vys. Temp.*, 1970, **8**, 912.
61. G. P. Bystrai, V. N. Desyatnik and V. A. Zlokazov, *Atom. Energ.*, 1974, **36**, 517.
62. V. D. Golyshev, M. A. Gonik, P. V. A. and Y. M. Putilin, *Teplfiz. Ves. Temp.*, 1983, **21**, 899.
63. M. V. Smirnov, V. A. Khokholov and E. S. Filatov, *Electrochim. Acta*, 1987, **32**, 1019.
64. Y. Tada, M. Harada, M. Tanigaki and W. Eguchi, *Rev. Sci. Instrum.*, 1978, **49**, 1305.
65. A. Shioi, T. Murata and M. Harada, *11th Jpn. Symp. Thermophys. Prop.*, 1990.
66. E. R. Van Artsdalen and I. S. Yaffe, *J. Phys. Chem.*, 1955, **59**, 118.
67. I. S. Yaffe and E. R. Artsdalen, *J. Phys. Chem.*, 1955, **60**, 1125.
68. I. G. Murgulescu and C. R. Telea, *Rev. Roum. Chim.*, 1977, **22**, 683.
69. S. Otsubo, Y. Nagasaka and A. Nagashima, *Trans. JSME*, 1998, **64**, 806.
70. B. N. Egorov and M. P. Revyakina, *High Temp. – High Pressures*, 1970, **8**, 1220.
71. N. Araki, M. Matsuura and A. Makino, *9th Jpn. Symp. Thermophys. Prop.*, 1988.
72. K. Kobayashi, N. Inoue and Y. Koyama, *9th Jpn. Symp. Thermophys. Prop.*, 1988.
73. Y. Anzai, S. Kimura, T. Sawada, T. Rudolph and K. Shigematsu, *J. Cryst. Growth*, 1993, **134**, 227.
74. A. M. Prokhorov and Y. S. Kuz'minov, *Physical and Chemistry of Crystalline Lithium Niobate*, Bristol and New York, 1990.
75. R. H. Katyl and U. Ingard, *Phys. Rev. Lett.*, 1967, **19**, 64.
76. R. H. Katyl and U. Ingard, *Phys. Rev. Lett.*, 1968, **20**, 248.
77. Y. Nagasaka and Y. Kobayashi, *J. Cryst. Growth 2007*, 2007, **307**, 51.
78. S. Hård, Y. Hamnerius and O. Nilsson, *J. Appl. Phys.*, 1976, **47**, 2433.

79. K. Kawasaki, K. Watanabe and Y. Nagasaka, *High Temp. – High Pressures*, 1998, **30**, 91.
80. L. D. Lucas, *Mem. Sci. Rev. Metal*, 1964, **61**, 1.
81. X. Huang, S. Togawa, S. Chung, T. K. and S. Kimura, *15th Jpn. Symp. Thermophysical Properties*, Tokyo, 1994.
82. Z. Niu and K. Mukai, 4th Asian Thermophysical Properties Conf., Tokyo, 1995.
83. S. C. Hardy, *J. Cryst. Growth*, 1984, **69**, 456.
84. M. Pryzborowski, T. Hibiya, M. Eguchi and I. Egry, *15th Jpn. Symp. Thermophysical Properties*, Tokyo, 1994.
85. E. S. Levin, P. V. Gel'd and B. A. Bum, *Russ. J. Phys. Chem.*, 1966, **40**, 77.
86. H. Sasaki, Y. Anzai, X. Huang, K. Terashima and S. Kimura, *15th Jpn Symp. Thermophysical Properties*, Tokyo, 1994.
87. A. Yokotani, S. Chung, K. Izunome and S. Kimura, *Jpn. J. Appl. Phys.*, 1955, **34**, L631.
88. W. Rhim, S. K. Chung, A. J. Rulison and R. E. Spjut, *4th Asian Thermophysical Properties Conf.*, Tokyo, 1995.
89. S. Hara, N. Ikemiya and K. Ogino, *J. Jp.n Inst. Metals*, 1989, **53**, 1148.
90. E. Tokizaki, K. Terashima and S. Kimura, *J. Cryst. Growth*, 1992, **123**, 121.
91. K. Shigematsu and S. Kimura, *Jpn. J. Appl. Phys.*, 1992, **31**, L582.
92. M. J. Assael, C. A. Nieto de Castro, H. M. Roder and W. A. Wakeham, in *Experimental Thermodynamics, Vol. III, Measurement of the Transport Properties of Fluids*, ed. A. Nagashima, J. V. Sengers and W. A. Wakeham, Blackwell Scientific, Oxford, 1991, pp. 161–195.
93. *Experimental Thermodynamics. Vol. III. Measurement of the Transport Properties of Fluids*, Blackwell Scientific Publications, London, 1991.
94. Y. Nagasaka and A. Nagashima, *J. Phys. E.*, 1981, **14**, 1435.
95. A. Alloush, W. B. Gosney and W. A. Wakeham, *Int. J. Thermophys.*, 1982, **3**, 225.
96. M. J. Dix, I. W. Drummond, M. Lesemann, V. M. Peralta-Martinez, W. A. Wakeham, M. J. Assael, L. Karagiannidis and H. R. van den Berg, *5th Asian Thermophys. Props. Conf. ATPC' 98*, Seoul, Korea, September 1988.
97. J. Bilek, J. Atkinson and W. A. Wakeham, *Int. J. Thermophys.*, 2006, **27**, 92.
98. M. V. Peralta-Martinez, M. J. Assael, M. J. Dix, L. Karagiannidis and W. A. Wakeham, *Int. J. Thermophys.*, 2006, **27**, 353.
99. J. Bilek, J. Atkinson and W. A. Wakeham, *Int. J. Thermophys.*, 2007, **28**, 496.
100. J. Bilek, J. Atkinson and W. A. Wakeham, *Int. J. Thermophys.*, 2006, **27**, 1626.
101. M. V. Peralta-Martinez, M. J. Assael, M. J. Dix, L. Karagiannidis and W. A. Wakeham, *Int. J. Thermophys.*, 2006, **27**, 681.
102. K. R. Seddon, A. Stark and M.-J. Torres, *Pure Appl. Chem.*, 2000, **72**, 2275.
103. J. A. Widegren and J. W. Magee, *J. Chem. Eng. Data*, 2007, **52**, 2331.

104. Y. Yoshida, O. Baba and G. Saito, *J. Phys. Chem. B*, 2007, **111**, 4742.
105. K. R. Harris, M. Kanakubo and L. A. Woolf, *J. Chem. Eng. Data*, 2006, **51**, 1161.
106. Z. J. Chen, T. Xue and J.-M. Lee, *RSC Adv.*, 2012, **2**, 10564.
107. H. Rodríguez and J. F. Brennecke, *J. Chem. Eng. Data*, 2006, **51**, 2145.
108. G. Yu, D. Zhao, L. Wen, S. Yang and X. Chen, *AIChE J.*, 2011, **58**, 2885.
109. D. R. MacFarlane, S. A. Forsyth, J. Golding and G. B. Deacon, *Green Chem.*, 2002, **4**, 444.
110. A. A. J. Torriero, A. I. Siriwardana, A. M. Bond, I. M. Burgar, N. F. Dunlop, G. B. Deacon and D. R. MacFarlane, *J. Phys. Chem. B*, 2009, **113**, 11222.
111. I. Stępniak and E. Andrzejewska, *Electrochim. Acta*, 2009, **54**, 5660.
112. G. McHale, C. Hardacre, R. Ge, N. Doy, R. W. K. Allen, J. M. MacInnes, M. R. Bown and M. I. Newton, *Anal. Chem.*, 2008, **80**, 5806.
113. Y. A. Sanmamed, D. González-Salgado, J. Troncoso, C. A. Cerdeiriña and L. Romaní, *Fluid Phase Equilib.*, 2007, **252**, 96.
114. Z.-B. Zhou, H. Matsumoto and K. Tatsumi, *Chem.–Eur. J.*, 2004, **10**, 6581.
115. U. Domańska and M. Laskowska, *J. Chem. Eng. Data*, 2009, **54**, 2113.
116. H. Matsumoto, H. Sakaebe and K. Tatsumi, *J. Power Sources*, 2005, **146**, 45.
117. K. Tsunashima and M. Sugiya, *Electrochem. Commun.*, 2007, **9**, 2353.
118. D. R. MacFarlane, J. Sun, J. Golding, P. Meakin and M. Forsyth, *Electrochim. Acta*, 2000, **45**, 1271.
119. S. Tang, G. A. Baker and H. Zhao, *Chem. Soc. Rev.*, 2012, **41**, 4030.
120. Z.-B. Zhou, H. Matsumoto and K. Tatsumi, *Chem.–Eur. J.*, 2006, **12**, 2196.
121. H. Shirota and E. W. Castner, *J. Phys. Chem. B*, 2005, **109**, 21576.
122. C. Liao, N. Shao, K. S. Han, X.-G. Sun, D.-E. Jiang, E. W. Hagaman and S. Dai, *Phys. Chem. Chem. Phys.*, 2011, **13**, 21503.
123. H. Jin, B. O'Hare, J. Dong, S. Arzhantsev, G. A. Baker, J. F. Wishart, A. J. Benesi and M. Maroncelli, *J. Phys. Chem. B*, 2008, **112**, 81.
124. O. O. Okoturo and T. J. VanderNoot, *J. Electroanal. Chem.*, 2004, **568**, 167.
125. J. Sun, D. R. MacFarlane and M. Forsyth, *Electrochim. Acta*, 2003, **48**, 1707.
126. J. M. Crosthwaite, M. J. Muldoon, J. K. Dixon, J. L. Anderson and J. F. Brennecke, *J. Chem. Thermodyn.*, 2005, **37**, 559.
127. H. Matsumoto, T. Matsuda and Y. Miyazaki, *Chem. Lett.*, 2000, 1430.
128. J. A. Widegren, A. Laesecke and J. W. Magee, *Chem. Commun.*, 2005, **1610**.
129. J. Jacquemin, P. Husson, A. A. H. Padua and V. Majer, *Green Chem.*, 2006, **8**, 172.
130. M. L. V. Ramires, C. A. Nieto de Castro, Y. Nagasaka, A. Nagashima, M. J. Assael and W. A. Wakeham, *J. Phys. Chem. Ref. Data*, 1995, **24**, 1377.
131. Solutia Inc., Therminol VP-1 technical bulletin 7239115C., http://www.therminol.com/pages/bulletins/therminol_vp1.pdf.

132. Dow Corning Corporation, Syltherm XLT product information, http://msdssearch.dow.com/PublishedLiteratureDOWCOM/dh_08a5/0901b803808a5a48.pdf?filepath=heattrans/pdfs/noreg/176-01468.pdf&fromPage=GetDoc.
133. R. Ge, C. Hardacre, P. Nancarrow and D. W. Rooney, *J. Chem. Eng. Data*, 2007, **52**, 1819.
134. C. A. Nieto de Castro, M. J. V. Lourenço, A. P. C. Ribeiro, E. Langa, S. I. C. Vieira, P. Goodrich and C. Hardacre, *J. Chem. Eng. Data*, 2010, **55**, 653.
135. J. M. P. França, S. I. C. Vieira, M. J. V. Lourenço, S. M. S. Murshed and C. A. Nieto de Castro, *J. Chem. Eng. Data*, 2013, **58**, 467.
136. A. P. C. Ribeiro, S. I. C. Vieira, P. Goodrich, C. Hardacre, M. J. V. Lourenço and C. A. Nieto de Castro, *J. Nanofluids*, 2013, **2**, 55.
137. J. Kestin and W. A. Wakeham, *Transport Properties of Fluids: Thermal Conductivity, Viscosity, and Diffusion Coefficient*, Hemisphere Publishing Corp., New York, 1988.
138. A. P. Fröba, M. H. Rausch, K. Krzeminski, D. Assenbaum, P. Wasserscheid and A. Leipertz, *Int. J. Thermophys.*, 2010, **31**, 2059.
139. D. Tomida, S. Kenmochi, T. Tsukada, K. Qiao, Q. Bao and C. Yokoyama, *Int. J. Thermophys.*, 2012, **33**, 959.
140. C. A. Nieto de Castro, *J. Mol. Liquids, 2010*, 2010, **156**, 10.
141. S. Y. Huang, Y. Y. Lin, N. Lisitza and W. S. Warren, *J.Chem.Phys.*, 2002, **116**, 10325.
142. M. E. Van Valkenburg, R. L. Vaughn, M. Williams and J. S. Wilkes, *Thermochim. Acta*, 2005, **425**, 181.
143. K. J. Fraser and D. R. MacFarlane, *Aust. J. Chem.*, 2009, **62**, 309.
144. D. R. MacFarlane, M. Forsyth, E. I. Izgorodina, A. P. Abbott, G. Annat and K. Fraser, *Phys. Chem. Chem. Phys.*, 2009, **11**, 4962.
145. K. Hayamizu, S. Tsuzuki, S. Seki, K. Fujii, M. Suenaga and Y. Umebayashi, *J. Chem. Phys.*, 2010, **133**, 194505.
146. M. Galinski, A. Lewandowski and I. Stepniak, *Electrochim. Acta*, 2006, **51**, 5567.
147. A. Noda, K. Hayamizu and M. Watanabe, *J. Phys. Chem. A*, 2001, **105**, 4603.
148. K. Hayamizu and W. S. Price, *J. Magn. Reson.*, 2004, **167**, 328.
149. S. Tsuzuki, H. Tokuda, K. Hayamizu and M. Watanabe, *J. Phys. Chem. B*, 2005, **109**, 16474.
150. K. Hayamizu, Y. Aihara, H. Nakagawa, T. Nukuda and W. Price, *J. Phys. Chem. B*, 2004, **108**, 19527.
151. B. Garcia, S. Lavallee, G. Perron, C. Michot and M. Armand, *Electrochim. Acta*, 2004, **49**, 4583.
152. H. Tokuda, K. Hayamizu, K. Ishii, M. Susan and M. Watanabe, *J. Phys. Chem. B*, 2005, **109**, 6103.
153. S. Fang, Z. Zhang, Y. Jin, L. Yang, S. Hirano, K. Tachibana and S. Katayama, *J. Power Sources*, 2011, **196**, 5637.

154. M. J. Monteiro, F. F. Camilo, M. C. C. Ribeiro and R. M. Torresi, *J. Phys. Chem. B*, 2010, **114**, 12488.
155. K. Tsunashima, Y. Ono and M. Sugiya, *Electrochim. Acta*, 2011, **56**, 4351.
156. H. Tokuda, K. Hayamizu, K. Ishii, S. M. Abu Bin Hasan and M. Watanabe, *J. Phys. Chem. B*, 2004, **108**, 16593.
157. S. Forsyth, J. Golding, D. MacFarlane and M. Forsyth, *Electrochim. Acta*, 2001, **46**, 1753.
158. J. Widegren, E. Saurer, K. Marsh and J. Magee, *J. Chem. Thermodyn.*, 2005, **37**, 569.
159. P. Bonhote, A. P. Dias, N. Papageorgiou, K. Kalyanasundaram and M. Gratzelm, *Inorg. Chem.*, 1996, **35**, 1168.
160. A. McEwen, H. Ngo, K. LeCompte and J. Goldman, *J. Electrochem. Soc.*, 1999, **146**, 1687.
161. R. Hagiwara, K. Matsumoto, Y. Nakamori, T. Tsuda, Y. Ito, H. Matsumoto and K. Momota, *J. Electrochem. Soc.*, 2003, **150**, D195.
162. C. Nanjundiah, S. McDevitt and V. Koch, *J. Electrochem. Soc.*, 1997, **144**, 3392.
163. H. Matsumoto, M. Yanagida, K. Tanimoto, M. Nomura, Y. Kitagawa and Y. Miyazaki, *Chem. Lett.*, 2000, 922.
164. J. Fuller, R. Carlin and R. Osteryoung, *J. Electrochem. Soc.*, 1997, **144**, 3881.
165. C. A. Angell, *Pure Appl. Chem.*, 1991, **63**, 1387.

CHAPTER 7

Dilute Gases

ECKARD BICH, JAMES B. MEHL, ROBERT HELLMANN AND VELISA VESOVIC

7.1 Monatomic Gases

ECKARD BICH, JAMES B. MEHL AND ROBERT HELLMANN

7.1.1 Introduction

The transport properties of dilute gases are a direct consequence of molecular motion and binary collisions between the molecules, which are governed by intermolecular forces. For monatomic gases, a kinetic theory approach relating the transport properties to the dynamics of the binary collisions was developed in the early 20th century. Chapman[1] in 1916 and Enskog[2] in 1917 independently found a solution of the Boltzmann equation for a dilute gas that is close to thermodynamic equilibrium and consists of particles interacting through a spherically-symmetric pair potential. The resulting expressions for the various transport coefficients can be found in many textbooks on kinetic theory.[3–6] The transport property values thus obtained are limiting values for zero density and are determined solely by binary collisions. Thermodynamically this corresponds to the ideal gas limit:

$$\lim_{\rho \to 0} X = X_0, \quad \lim_{\rho \to 0} \frac{p}{\rho RT} = 1, \tag{7.1}$$

where X is an arbitrary transport property (in the case of diffusion multiplied by the density).

A more modern approach for solving the Boltzmann equation is based on a perturbation-series expansion of the one-particle distribution function in

Experimental Thermodynamics Volume IX: Advances in Transport Properties of Fluids
Edited by M. J. Assael, A. R. H. Goodwin, V. Vesovic and W. A. Wakeham

Published by the Royal Society of Chemistry, www.rsc.org

terms of an orthonormal set of suitable velocity basis functions $\mathbf{\Phi}^{ps}$.[7] These basis functions are products of a normalization constant, a traceless p-fold tensor product of the reduced peculiar velocity vector $\mathbf{W}$ with itself and an associated Laguerre polynomial $L_s^{(p+1/2)}(W^2)$, where $W = |\mathbf{W}|$ (see ref. 7 for more details). For each transport property one obtains a system of linear equations, which for a pure monatomic gas can be symbolically written as

$$\sum_{s'=0}^{\infty} S\begin{pmatrix} ps \\ ps' \end{pmatrix} x_{s'} = c_s, \quad s = 0, 1, \ldots, \infty, \tag{7.2}$$

where $p = 1$ for thermal conductivity and diffusion and $p = 2$ for viscosity. The transport properties can be obtained from the solutions $x_{s'}$. The coefficients $S\begin{pmatrix} ps \\ ps' \end{pmatrix}$ are closely related to generalized cross sections $\mathfrak{S}\begin{pmatrix} ps \\ ps' \end{pmatrix}$, which in turn are linear combinations of traditional collision integrals $\Omega^{(l,m)}$.[3–7] Restricting s and s' yields solutions of different order. For $s,s' \leq n$ one obtains the $(n+1)$th-order approximations for viscosity and diffusion and the nth-order approximation for thermal conductivity. The shear viscosity η and the thermal conductivity λ of a pure monatomic gas can be expressed in terms of generalized cross sections as

$$\eta = \frac{k_B T}{\langle v \rangle_0} \frac{f_\eta^{(n)}}{\mathfrak{S}(20)}, \tag{7.3}$$

$$\lambda = \frac{5 C_V k_B T}{3 m \langle v \rangle_0} \frac{f_\lambda^{(n)}}{\mathfrak{S}(11)} = \frac{5 C_V k_B T}{2 m \langle v \rangle_0} \frac{f_\lambda^{(n)}}{\mathfrak{S}(20)}, \tag{7.4}$$

$$\mathfrak{S}(ps) \equiv \mathfrak{S}\begin{pmatrix} ps \\ ps \end{pmatrix}. \tag{7.5}$$

Here $\langle v \rangle_0 = 4(k_B T/\pi m)^{1/2}$ is the average relative thermal speed, m is the molecular mass, T is the temperature, C_V is the isochoric heat capacity and k_B is Boltzmann's constant. The quantities $f_\eta^{(n)}$ and $f_\lambda^{(n)}$ are higher-order correction factors. For $n = 2$ they are given by

$$f_\eta^{(2)} = \left[1 - \frac{\mathfrak{S}\begin{pmatrix} 20 \\ 21 \end{pmatrix}^2}{\mathfrak{S}(20)\mathfrak{S}(21)} \right]^{-1}, \quad f_\lambda^{(2)} = \left[1 - \frac{\mathfrak{S}\begin{pmatrix} 11 \\ 12 \end{pmatrix}^2}{\mathfrak{S}(11)\mathfrak{S}(12)} \right]^{-1}. \tag{7.6}$$

Explicit expressions for $f_\eta^{(n)}$ and $f_\lambda^{(n)}$ in terms of collision integrals $\Omega^{(l,m)}$ for pure monatomic gases have been derived up to $n = 5$ by Viehland *et al.*[8] However, in many cases the third-order approximations are sufficient for high-accuracy calculations.

This formalism can also be applied to mixtures.[7] However, the systems of linear equations that need to be solved to obtain the transport properties of

mixtures in higher-order approximations can become quite large. In such cases it is much more convenient to use a linear equation solver than to derive closed-form expressions for the transport coefficients. This approach is straightforward, but has seldom been applied (see, for example, ref. 9 and 10).

For heavy monatomic gases, such as the rare gases argon, krypton and xenon, the generalized cross sections or collision integrals can be accurately computed using classical mechanics. Most of the current software codes for such calculations are based on the code of O'Hara and Smith.[11–13] For gases such as helium and neon, the generalized cross sections or collision integrals should be computed quantum-mechanically.[14,15]

Precise knowledge of the interatomic pair potentials is a prerequisite for obtaining accurate transport property values. For many decades one had to rely on empirical potentials, where the parameters of the potential functions were fitted to experimental data for several properties simultaneously (see, for example, ref. 16–22). However, in recent years the tremendous advances in computational power make it possible to develop pair potentials of unprecedented accuracy for rare gases utilizing quantum-chemical *ab initio* methods. Highly accurate *ab initio* potentials are now available for the He–He,[23–25] Ne–Ne[26] and Ar–Ar[27,28] atom pairs in their electronic ground states. They are superior to the best empirical potentials. For the Kr–Kr and Xe–Xe atom pairs, the best available *ab initio* potentials[29–31] are still inferior to the best empirical ones, since relativistic effects, which are difficult to accurately account for in the quantum-chemical calculations, become more important in heavy atoms. High-quality *ab initio* potentials for pairs of unlike rare gas atoms have also been published,[29,32–38] although their accuracy is not on par with the above mentioned potentials for the He–He, Ne–Ne and Ar–Ar atom pairs.

The viscosity and the thermal conductivity in the limit of zero density have been calculated for helium,[15,25] neon[39] and argon[40,41] using the best available *ab initio* pair potentials. The results obtained for helium and argon will be presented below. In addition, we will discuss as yet unpublished results for the transport properties of helium–krypton mixtures.

7.1.2 Transport Properties of Pure Gases – Helium and Argon

Over the past two decades a series of increasingly accurate *ab initio* interaction potentials for helium has enabled the calculation of the thermophysical properties of dilute helium gas with greater accuracy than the corresponding measurements.[14,15,23–25,42–44] The most recent pair potential[24,25] systematically includes adiabatic, relativistic and quantum electrodynamic corrections to the potential; estimates of the potential uncertainty provide a method of estimating the uncertainty of derived properties. The calculated viscosity has recently been used as a standard,[45] as originally anticipated by Aziz *et al.*[42]

Figure 7.1 shows the calculated viscosity and thermal conductivity of helium-4. A full quantum-mechanical formulation, based on energy-dependent phase shifts, was used to calculate the collision integrals.[14] The

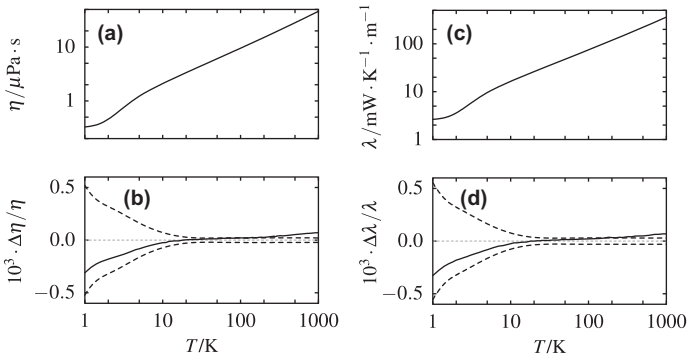

Figure 7.1 (a) Viscosity η of helium-4 in the limit of zero density as a function of temperature T. (b) Deviations, $\Delta\eta/\eta$, of other calculated viscosity values from the reference values of Cencek *et al.*[25] as a function of temperature T: ————, Bich *et al.*;[15] - - - - -, $\pm\sigma_{\mathrm{calc}}$. (c) Thermal conductivity λ of helium-4 in the limit of zero density as a function of temperature T. (d) Deviations $\Delta\lambda/\lambda$ of other calculated thermal conductivity values from the reference values of Cencek *et al.*[25] as a function of temperature T. Lines as in panel (b).

Table 7.1 Measured (M) and calculated (C) viscosity η of helium-4 in the zero-density limit at $T = 298.15$ K.

Date	Calc./Meas.	Source	$\eta/\mu\mathrm{Pa}\cdot\mathrm{s}$
1995	C	Aziz *et al.*[a]	19.800 ± 0.010
2000	C	Hurly and Moldover[b]	19.838 ± 0.012
2005	M	Berg[c]	19.842 ± 0.014
2007	C	Hurly and Mehl[d]	19.824 ± 0.004
2007	C	Bich *et al.*[e]	19.826 ± 0.004
2012	C	Cencek *et al.*[f]	19.8253 ± 0.0002

[a]Ref. 42. [b]Ref. 44. [c]Ref. 46. [d]Ref. 14. [e]Ref. 15. [f]Ref. 25.

higher-order correction factors $f_\eta^{(n)}$ and $f_\lambda^{(n)}$, see eqns (7.3) and (7.4), were evaluated up to fifth order. The viscosities calculated by Bich *et al.*[15] and by Cencek *et al.*[25] agree within ± 0.007 % for $T > 10$ K, and do not differ below 10 K by more than the estimated uncertainties reported in ref. 25. The two sets of thermal conductivity values agree within the same fractional limits.

Table 7.1 displays the systematic improvement of the theoretical viscosity values at $T = 298.15$ K, together with the comparison to the best recent measurement.[46]

Calculations of the interaction potential of two argon atoms have also improved significantly in recent years.[27,28,31,47] The most recent potentials have been used for classical calculations of the viscosity and thermal conductivity in the fifth-order approximations[40,41] including uncertainty

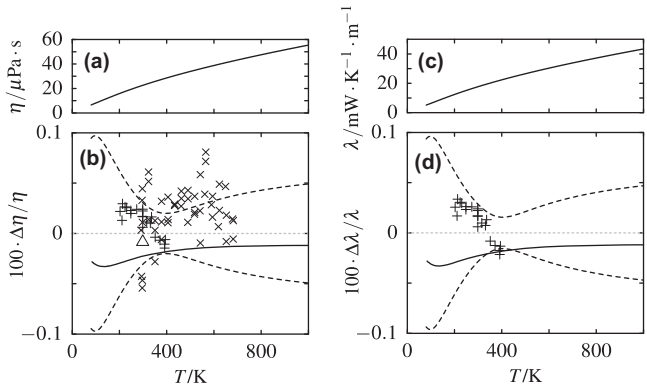

Figure 7.2 (a) Viscosity η of argon in the limit of zero density as a function of temperature T. (b) Deviations, $\Delta\eta/\eta$, of experimental and calculated values from viscosity values obtained with the potential of Patkowski and Szalewicz.[28] Selected experimental data: +, May *et al.*;[49] ×, Vogel;[50] △, Berg and Burton.[45] Calculated values: ————, Vogel *et al.*;[40] - - - - -, $\pm\sigma_{calc}$. (c) Thermal conductivity λ of argon in the limit of zero density as a function of temperature T. (d) Deviations, $\Delta\lambda/\lambda$, of experimentally based and calculated values from thermal conductivity values obtained with the potential of Patkowski and Szalewicz.[28] Selected experimentally based values: +, May *et al.*[49] Calculated values as in panel (b).

estimates based on the uncertainty of the potential.[28,48] The results are plotted in Figure 7.2 together with some selected experimental and experimentally-based data.[45,49,50] The fractional deviations in Figures 7.2b and 7.2d use calculations with the potential of ref. 28 as a baseline; the uncertainty estimates $\pm\sigma_{calc}$ are based on the uncertainty of this potential.[48] The calculated viscosities from ref. 40 and nearly all the measurements fall within $\pm\sigma_{calc}$. The reader is referred to ref. 40 for a comparison with a more extensive set of viscosity measurements.

Ref. 40 also includes deviation plots of a large set of measured thermal conductivity data. These generally have relative uncertainties of the order of ±1 % and agree with *ab initio* values at this level. An alternative to direct measurements of thermal conductivity is based on the use of theoretical Prandtl numbers and measured viscosities as was done by May *et al.*[49] Their thermal conductivities, shown in Figure 7.2d, were recalculated using the most recent helium viscosities[25] as standards. The use of these viscosity values reduces the overall relative uncertainty in their thermal conductivity values from ±0.08 % to ±0.02 % (see Table 1 of ref. 49 for more details).

7.1.3 Transport Properties of Gas Mixtures – Helium–Krypton Mixture

The viscosity, thermal conductivity and binary diffusion coefficient for mixtures of helium-4 and krypton were calculated in the fifth-order

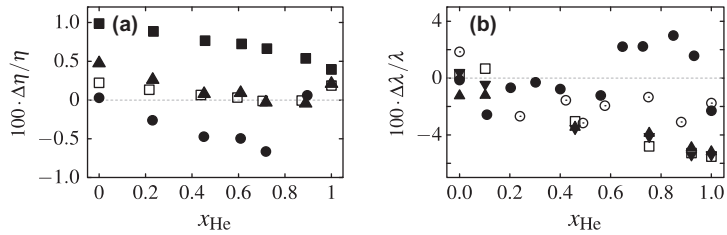

Figure 7.3 (a) Deviations, $\Delta\eta/\eta$, of experimental zero-density viscosities from theoretically calculated values for helium–krypton mixtures as a function of He mole fraction x_{He}. Experimental data of Kalelkar and Kestin:[52] □, 298.15 K; ■, 473.15 K; ▲, 675.16 K; ●, 873.15 K. (b) Deviations, $\Delta\lambda/\lambda$, of experimental zero-density thermal conductivities from theoretically calculated values for helium–krypton mixtures as a function of He mole fraction x_{He}. Experimental data: ○, von Ubisch[53] 302.15 K; ●, Thornton[54] 291.3 K; ▼, Gambhir and Saxena[55] 308.15 K; ▲, Gambhir and Saxena[55] 323.15 K; □, Gambhir and Saxena[55] 343.15 K.

approximations using *ab initio* potentials for the He–Kr and Kr–Kr atom pairs recently developed at the University of Rostock[51] and the best available He–He pair potential.[24,25] The generalized cross sections for collisions between two helium atoms (reduced mass $\mu = 2.00$ u)[†] and between a helium and a krypton atom ($\mu = 3.82$ u)[†] were computed quantum-mechanically. Collisions between two krypton atoms ($\mu = 41.90$ u)[†] were treated classically. The relative uncertainties of the computed transport property values are estimated to be smaller than 0.2 % for all temperatures and mixture compositions.

In Figure 7.3 calculated values for viscosity and thermal conductivity of helium-krypton mixtures (characterized by the mole fraction x_{He}) are compared with experimental data.[52–55] The viscosity data of Kalelkar and Kestin,[52] shown for four selected temperatures, differ relatively from the computed values by less than ±0.2 % at room temperature, but show less satisfactory agreement at higher temperatures. For the thermal conductivity, which is more difficult to measure accurately than viscosity, the experimental data show much larger deviations, which far exceed the estimated uncertainties of the theoretically calculated values. Figure 7.4 shows results for the helium–krypton binary diffusion coefficient. In Figure 7.4a the product of molar density and diffusion coefficient in the zero-density limit is shown at $T = 300$ K. In the first-order approximation the binary diffusion coefficient is determined solely by the He–Kr pair potential and is not a function of the mixture composition. A purely classical first-order calculation yields a slightly lower diffusion coefficient. In the higher-order approximations the binary diffusion coefficient is weakly composition-dependent. Arora *et al.*[20,56] obtained a very similar composition dependence

[†]u is the unified atomic mass unit, which is equivalent to $1.660538921(73) \cdot 10^{-27}$ kg.

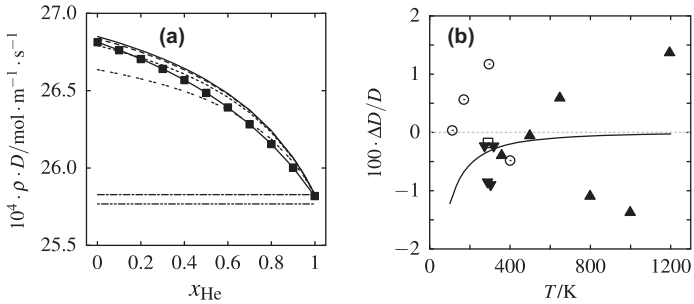

Figure 7.4 (a) Product of molar density and binary diffusion coefficient, $\rho \cdot D$, in the zero-density limit for helium–krypton mixtures at $T = 300$ K as a function of He mole fraction x_{He}. Experimentally based values: ———■———, Arora *et al.*[20,56] Calculated values: -••-••-••-, first order classical; -•-•-•-•-, first order; -- -- --, second order; - - - - -, third order; — — — —, fourth order; ——————, fifth order. (b) Deviations, $\Delta D/D$, of experimental data and classically calculated values from quantum-mechanically calculated values of the binary diffusion coefficient of a helium-krypton mixture with mole fraction $x_{\mathrm{He}} = 0.5$ in the zero-density limit as a function of temperature T. Experimental data: ▼, Srivastava and Barua;[57] □, Fedorov *et al.*;[58] ○, van Heijningen *et al.*;[59] ▲, Cain and Taylor.[60] Calculated values: ——————, classical.

when they fitted a smooth curve to their experimental data for different mole fractions. Figure 7.4a also illustrates that the higher-order approximations converge rapidly for helium-rich mixtures, but slowly for krypton-rich mixtures. This behaviour is caused by the extreme mass difference between the two atoms. In Figure 7.4b the calculated values of the binary diffusion coefficient for a mole fraction of 0.5 are compared with experimental data[57–60] and with the results of a purely classical calculation. The agreement with the experimental data is mostly within the estimated experimental uncertainties. As expected, the differences between the classical and quantum-mechanical results decrease with increasing temperature.

7.1.4 Summary and Outlook

The transport properties of dilute monatomic gases can currently be calculated with an accuracy that is often superior to that of the best available experimental data. The kinetic theory relating the transport properties to generalized cross sections can be evaluated up to arbitrary order for both pure gases and gas mixtures. The generalized cross sections, which are determined by the dynamics of the binary collisions and are therefore directly related to the interatomic pair potentials, can be computed either classically or, if necessary, fully quantum-mechanically. Thus, the uncertainties in the calculated transport property values are largely determined by the uncertainties in the pair potentials. In recent years, highly accurate *ab initio* potentials have become available for a number of rare gas atom pairs, most notably He–He, Ne–Ne and Ar–Ar. With the rapid developments in both

computational power and quantum-chemical *ab initio* methods, it will soon be possible to determine even the most challenging rare gas potentials, like those for the Kr–Xe or Xe–Xe atom pairs, with an accuracy similar to that of the Ne–Ne and Ar–Ar potentials today. Thus, we will be able to calculate reliable reference values for the transport properties of a wide range of pure rare gases and rare gas mixtures. This will be particularly helpful in assessing the accuracy of experimental data for transport properties of pure and mixed polyatomic gases, since many of the experimental setups used for measurements on polyatomic gases have also been used for measurements on rare gases.

7.2 Polyatomic Gases

ROBERT HELLMANN, JAMES B. MEHL AND VELISA VESOVIC

7.2.1 Introduction

For monatomic gases, as described in Section 7.1, the kinetic theory is well established and the calculation of transport properties can be performed accurately on a routine basis for any spherical pair potential. For polyatomic gases the situation is very different. The intermolecular forces are not only a function of separation, but also of the molecular orientation, and collisions between two molecules can result in the transfer of energy between translational and rotational/vibrational degrees of freedom. Hence, the complexity of the collision dynamics increases significantly. Initial attempts to include these effects focused on rather crude model molecules (rough spheres, loaded spheres, spherocylinders)[4] and it was not until the late 1950s that first attempts were made to establish the kinetic theory of dilute polyatomic gases. Subsequent years led to both classical and quantum mechanical formalisms[7,61–66] that not only provided expressions for transport properties of polyatomic gases, but also led to descriptions of new phenomena, not present in monatomic gases. It was recognized early on that it takes a finite time for the internal modes to relax through collisions, which at the observable level gives rise to volume viscosity (also known as bulk viscosity). Furthermore, molecular rotational angular momentum is coupled to velocity. This coupling can be altered by magnetic/electrical fields, resulting in changes in transport properties, the so called transport property field effects.[7] In this work we will focus only on reviewing the current status of traditional transport properties (shear viscosity, diffusion coefficient, thermal conductivity and volume viscosity).[67]

For a pure polyatomic gas in the limit of zero density and in the absence of external fields the shear viscosity η, the self-diffusion coefficient D, the thermal conductivity λ and the volume viscosity κ can be expressed as

$$\eta = \frac{k_B T}{\langle v \rangle_0} \frac{f_\eta^{(n)}}{\mathfrak{S}(2000)}, \tag{7.7}$$

$$D = \frac{k_B T}{nm\langle v \rangle_0} \frac{f_D^{(n)}}{\mathfrak{S}'(1000)}, \tag{7.8}$$

$$\lambda = \frac{5k_B^2 T}{2m\langle v \rangle_0} \frac{\mathfrak{S}(1001) - 2r\mathfrak{S}\begin{pmatrix}1001\\1010\end{pmatrix} + r^2\mathfrak{S}(1010)}{\mathfrak{S}(1010)\mathfrak{S}(1001) - \mathfrak{S}\begin{pmatrix}1001\\1010\end{pmatrix}^2} f_\lambda^{(n)}, \tag{7.9}$$

$$\kappa = \frac{k_B C_{int}}{C_V^2} \frac{k_B T}{\langle v \rangle_0} \frac{f_\kappa^{(n)}}{\mathfrak{S}(0001)}. \tag{7.10}$$

Here n is the number density, C_{int} is the contribution of internal degrees of freedom to C_V, and the other quantities have been defined in Section 7.1.1. The parameter r is given by

$$r = \left(\frac{2C_{int}}{5k_B} \right)^{1/2}. \tag{7.11}$$

The quantities $\mathfrak{S}(2000)$, $\mathfrak{S}'(1000)$, $\mathfrak{S}(1010)$, $\mathfrak{S}(1001)$, $\mathfrak{S}\begin{pmatrix} 1001 \\ 1010 \end{pmatrix}$ and $\mathfrak{S}(0001)$ are generalized cross sections and are an extension of the ones introduced in Section 7.1.1. They include all the details of the dynamics of the binary encounters in the pure polyatomic gas with appropriate statistical averaging over the internal states and translational energy. The notation and conventions employed in labelling the generalized cross sections are fully described elsewhere.[7,68] The higher-order correction factors, $f^{(n)}$, account for the effects of higher basis-function terms in the perturbation-series expansion of the solution of the Boltzmann equation and can be also expressed in terms of generalized cross sections.[7] Unlike the higher-order correction factors for monatomic gases, described in Section 7.1.1, for polyatomic molecules the higher-order correction factors contain contributions from both velocity and angular momentum coupling. They can be computed up to any desired order by simply considering more basis functions. In practice it has been found that for polyatomic gases the second-order corrections are usually sufficient to match experimental uncertainty.

Explicit closed-form expressions for the transport properties of gas mixtures involving polyatomic gases are also available.[7,69,70] As in the case of pure polyatomic gases, it is possible to derive higher-order correction factors up to any desired order by taking more basis functions into account. However, this leads to very complicated expressions. Since these expressions ultimately result from solving a large system of linear equations, it is now more convenient in practical applications to use a linear equation solver, thereby circumventing the need for a closed-form expression, as was described in Section 7.1.1.

Although the advent of the kinetic theory of polyatomic gases provided a general framework for linking the transport properties to intermolecular potentials, the calculations were initially too computationally expensive. Early attempts[71–74] relied on a number of approximations to both the collision dynamics and kinetic theory, with mixed results that were of lower accuracy than most of the available experimental data (see ref. 68 for a review of the field up to the 1990s). In the last two decades the situation has changed dramatically as developments in classical trajectory methods[75] have provided a fast and accurate way for calculating transport properties. The accuracy has been attested by detailed comparisons with quantum

calculations for atom–diatom systems[76,77] and with the most accurate experimental transport property data, making classical trajectories the method of choice at present time. The classical trajectory calculations are performed on the assumption that the colliding molecules behave as rigid rotors. This assumption is dictated by both the nature of the available *ab initio* intermolecular potentials and the lack of an accurate computational framework for inclusion of vibrational degrees of freedom, for which a quantum-mechanical treatment is essential, into the classical description. Although a number of theoretical approaches have been suggested,[78] the effects of vibrationally active modes are usually incorporated in transport property calculations through an approximation at the level of the generalized cross sections.[79,80] Once the molecular collisions are computed by means of classical trajectories, the full kinetic theory of polyatomic gases is employed to calculate the transport properties. A software code, TRAJECT, for calculating generalized cross sections using classical trajectories for a pair of like or unlike rigid linear molecules from their intermolecular potential energy surface is available.[81] The TRAJECT code has recently been extended to rigid molecules of arbitrary structure.[82]

Most of the advances in the last two decades in the field of transport properties of dilute molecular gases can be attributed to our ability to calculate the transport properties from *ab initio* intermolecular potentials. Thus, the focus of this review will be primarily on the results obtained and the insights gained from the recent computational studies. The transport properties have been evaluated using classical trajectory calculations and realistic intermolecular potentials for a number of molecular systems: diatoms (N_2, CO, O_2, HF, HCl),[83–93] linear triatoms (CO_2),[80,94,95] spherical tops (CH_4),[96,97] and polar asymmetric tops (H_2O, H_2S).[98,99] Although computations are currently limited to small molecules that do not readily exchange vibrational energy at temperatures of interest, there have been attempts to extend the calculations to larger molecules using model potentials. In particular, the transport properties have been calculated for a gas consisting of rigid chain-like molecules consisting of spherical segments that interact through a combination of site–site Lennard–Jones 12-6 potentials.[100,101] Calculations of transport properties were also performed[102,103] for H_2. However, in this case quantum approaches were used, as summarized in Section 7.2.2. For mixtures, accurate classical and quantum calculations of transport properties have been performed only for binary mixtures consisting of an atom and a linear molecule (He with H_2, HD, N_2, O_2, CO, CO_2; Ne with H_2, N_2, O_2; Ar with H_2, N_2; among others) and the reader is referred to ref. 7 and 68 for a more detailed discussion. Two of the present authors (RH and VV) are currently working on dissimilar molecule + molecule mixtures ($CH_4 + N_2$).

In the rest of Section 7.2 we will illustrate the advances made in computing the transport properties of dilute molecular gases by examples of calculations for H_2, CH_4 and H_2O. We then discuss the general trends

observed so far and their implications, finishing with a brief summary of the current status and future trends.

7.2.2 Transport Properties of Hydrogen

Owing to the low mass, hydrogen molecules require a quantum-mechanical treatment of transport properties. The interaction potential is nearly isotropic, and the effects of the anisotropy on generalized cross sections are small.[103] Hydrogen consists of a mixture of *para*- and *ortho*-hydrogen and, at low temperatures, both are in their ground states.[104] At temperatures above 100 K, excited rotational states are increasingly populated and the gas must be regarded as a multicomponent mixture of *para*- and *ortho*-hydrogen in different rotational states, with collisions between unlike species dominating. New calculations of transport properties[102,103] and extremely accurate experimental measurements of viscosity[49] have recently become available.

Recognising that the effect of modest anisotropy is small, Mehl *et al.*[102] performed a full quantum-mechanical calculation of the viscosity of hydrogen using only the spherical component of the interaction potential of Patkowski *et al.*[105] On the other hand, Schaefer used an older 6-term anisotropic rigid-rotor potential.[103] In contrast to Mehl *et al.*, Schaefer did not take higher-order correction factors for viscosity into account. Meanwhile, May *et al.*[49] determined the viscosity of hydrogen by measuring the ratio of hydrogen and helium viscosities with high precision over a wide range of temperature. We have recalculated the hydrogen viscosity using the viscosity ratios of May *et al.*[49] and the most recent *ab initio* helium viscosities.[25] The hydrogen viscosities obtained by this procedure have an estimated relative uncertainty of ± 0.05 %. Figure 7.5a compares these new experimental data with the quantum calculations of Mehl and co-workers,[102] and it is evident they lie 0.06 % to 0.09 % below them. This is a very convincing degree of agreement. In contrast, for the experimental temperature range, both classical calculations that were also performed by Mehl *et al.* as part of their investigation[102] and the quantum-mechanical calculations of Schaefer,[103] who used an older anisotropic potential, are much less consistent with the measurements, which is illustrated in Figure 7.5b, where relative deviations of more than 2 % can be seen at low temperatures for the classical calculation.

Figure 7.5c compares the thermal conductivity of hydrogen measured by a number of workers[106–110] to values calculated by Mehl *et al.*[102] The results were calculated[102] with the Maxwell–Boltzmann form of the collision cross sections that is appropriate for distinguishable particles. On the other hand, Cohen *et al.*[104] used a combination of symmetric and antisymmetric expressions for the cross sections, as required for a two-component mixture of indistinguishable *ortho*- and *para*-hydrogen molecules, as appropriate at low temperatures. The differences between the two approaches are small at low temperatures (less than 0.1 % for *para*-hydrogen below 42 K and *ortho*-hydrogen below 60 K). Measurements over a broader temperature range are, however, much closer to values calculated with the Maxwell–Boltzmann form.

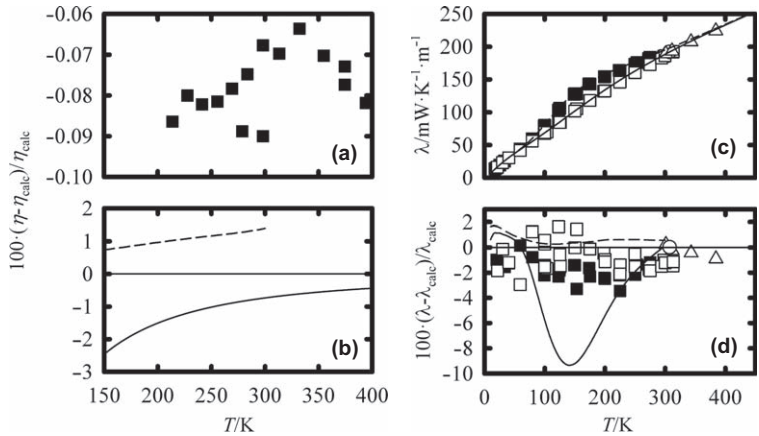

Figure 7.5 (a) Deviations, $(\eta - \eta_{calc})/\eta_{calc}$, between experimental[49] and computed[102] reference viscosities for hydrogen as a function of temperature T. (b) Deviations, $(\eta - \eta_{calc})/\eta_{calc}$, between other computed and the reference values[102] as a function of temperature T: ————————, Mehl *et al.* classical;[102] - - - - -, Schaefer.[103] (c) Thermal conductivity λ of hydrogen as a function of temperature T. Experimental data: ■, Roder and Diller[106] and Roder[109,110] *para*-H_2; □, Roder and Diller[106] and Roder[109,110] H_2; ○, Assael and Wakeham;[108] △, Clifford *et al.*[111] Calculated values: - - - - -, Mehl *et al. para*-H_2;[102] ————————, Mehl *et al.* H_2.[102] (d) Deviations, $(\lambda - \lambda_{calc})/\lambda_{calc}$, of experimental measurements and the calculations of Schaefer[103] from the reference values as a function of temperature T.[102] Symbols as in panel (c). Calculated values: - - - - -, Schaefer *para*-H_2;[103] ————————, Schaefer H_2.[103]

7.2.3 Transport Properties of Non-polar Gases – Methane

We illustrate the transport properties of non-polar gases with methane as an example. The transport and relaxation properties of methane were calculated in the limit of zero density for temperatures up to 1500 K[96,97] using the extended TRAJECT code.[81,82] These computations employed the best available intermolecular potential energy surface for methane,[112] which is based on supermolecular coupled-cluster computations and was fine-tuned to accurate experimental data for the second pressure virial coefficient of methane at room temperature.

In Figure 7.6 the calculated values for shear viscosity and thermal conductivity are compared with some selected experimental data.[49,108,113–118] The agreement is remarkable considering the complexity of the calculations and the *ab initio* nature of the potential. The deviations from the three viscosity data sets, which have relative uncertainties of less than ±0.2 %, indicate that the calculated viscosity values are relatively too high by about 0.5 % over a wide temperature range. Apart from this small systematic deviation, the calculated values reproduce accurately the temperature dependence of the viscosity. Because the uncertainty of the computed values is nearly temperature

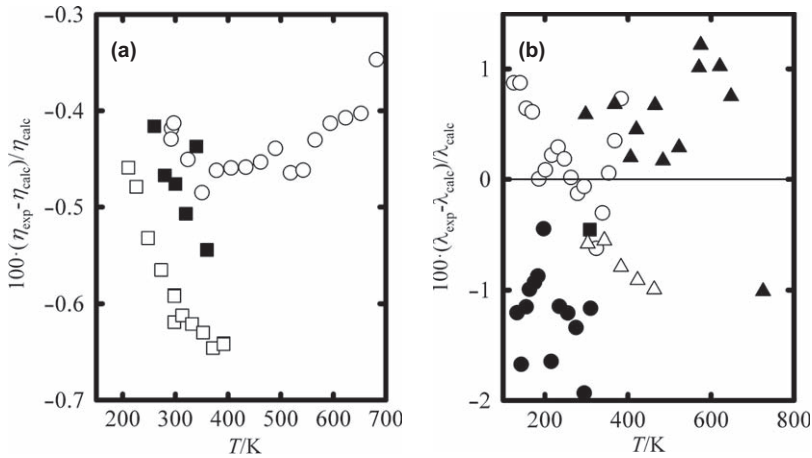

Figure 7.6 (a) Deviations, $(\eta - \eta_{calc})/\eta_{calc}$, of experimental zero-density viscosities from values theoretically calculated for methane as a function of temperature T: ■, Schley *et al.*;[113] □, May *et al.*;[49] ○, Vogel.[114] (b) Deviations, $(\lambda - \lambda_{calc})/\lambda_{calc}$, of experimental zero-density thermal conductivities from values theoretically calculated for methane as a function of temperature T: ○, Johnston and Grilly;[115] ▲, Tufeu *et al.*;[116] ■, Assael and Wakeham;[108] ●, Roder;[117] △, Hemminger.[118]

independent it is plausible to postulate that at temperatures above 700 K the calculated values still exhibit the proper temperature dependence. This has important consequences because at high temperatures the experimental data are either of low accuracy or non-existent and the computed values therefore provide the best available information on the viscosity.

The experimental data for the thermal conductivity have higher uncertainties and consequently show larger scatter. An exception for methane is the datum of Assael and Wakeham at a temperature of 308.15 K,[108] which has a relative uncertainty of ±0.2 % and deviates relatively from the theoretically calculated value at $T = 308.15$ K by −0.45 %. For methane, which has a weakly anisotropic intermolecular potential, it is not surprising that the calculated values for shear viscosity and thermal conductivity show a similar systematic shift, since for a spherically symmetric potential both properties are governed by the same generalized cross section in the first-order approximations. The results for other non-polar molecules studied (N_2, CO and CO_2) indicate that the computed values of viscosity and thermal conductivity differ relatively by ±1 % from the experimental data considered at this time to have the lowest uncertainty.

The computed values for the self-diffusion coefficient and the volume viscosity are compared with experimental data[119–124] in Figure 7.7. For the self-diffusion coefficient the experimental relative uncertainties are rather larger than for viscosity and thermal conductivity, ranging from ±2 % to ±8 % for the three data sets shown, while for the volume viscosity the experimental uncertainties are even higher, as shown by the error bars in Figure 7.7b.

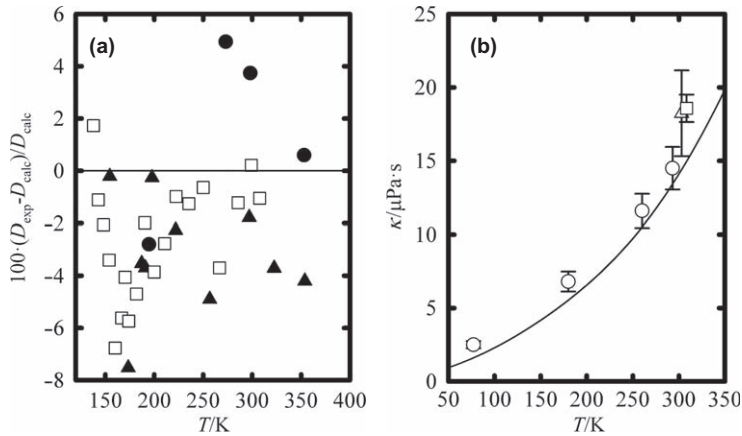

Figure 7.7 (a) Deviations, $(D_{exp} - D_{calc})/D_{calc}$, of experimental zero-density self-diffusion coefficients from values theoretically calculated for methane as a function of temperature T: ●, Winn;[119] ▲, Dawson *et al.*;[120] □, Oosting and Trappeniers.[121] (b) Comparison between experimental and theoretically calculated zero-density values for the volume viscosity κ of methane as a function of temperature T. Experimental data: △, Holmes *et al.*;[122] □, Kistemaker *et al.*;[123] ○, Prangsma *et al.*[124] Calculated values: ————————, Hellmann *et al.*[97]

Such high uncertainty precludes using these experimental data to validate the computed values. In general, both transport properties are more difficult to determine accurately than the viscosity or thermal conductivity. It is thus reasonable to assume, based on validation with shear viscosity and thermal conductivity, that the computed values will provide more accurate values of the self-diffusion coefficient and volume viscosity than are currently available. However, it is worth bearing in mind that the accuracy of the calculated volume viscosity is determined broadly by the uncertainty in the value of $\mathfrak{S}(0001)$, which is very sensitive to the anisotropy of the intermolecular potential (the cross section would be zero for a spherical potential) and at low temperatures to quantum effects.[77]

7.2.4 Transport Properties of Polar Gases – Water Vapour

For water vapour the transport and relaxation properties were calculated in the limit of zero density for temperatures as high as 2500 K[98] using again the extended TRAJECT code. Four different intermolecular potential energy surfaces for water were used. The two most accurate ones, CC-pol[125] and SDFT-5s,[126] are based on supermolecular coupled-cluster calculations and on the SAPT(DFT) variant of the symmetry-adapted perturbation theory (SAPT),[127,128] respectively. In the rest of the section, only the results for shear viscosity and thermal conductivity obtained with the CC-pol and SDFT-5s potentials will be discussed.

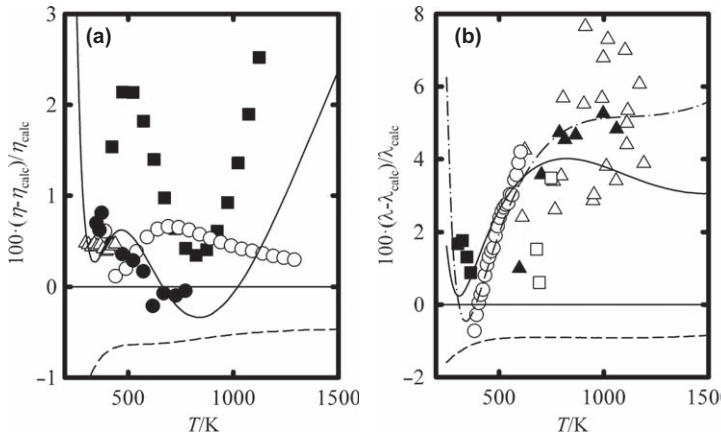

Figure 7.8 (a) Deviations, $(\eta - \eta_{calc})/\eta_{calc}$, of experimental data, of an experimentally based correlation and of values computed for the SDFT-5s potential from values calculated using the CC-pol potential[125] for the shear viscosity of dilute water vapour as a function of temperature T: ■, Shifrin;[129] ○, Latto;[130] ●, Timrot *et al.*;[131] △, Teske *et al.*;[132] ————————, IAPWS 2008;[138] - - - - -, SDFT-5s potential.[126] (b) Deviations, $(\lambda - \lambda_{calc})/\lambda_{calc}$, of experimental data, of experimentally based correlations and of values computed for the SDFT-5s potential from values calculated using the CC-pol potential[125] for the thermal conductivity of dilute water vapour as a function of temperature T: △, Vargaftik and Zimina;[133] ○, Le Neindre *et al.*;[134] ▲, Popov and Dulnev;[135] □, Tufeu and Le Neindre;[136] ■, Miroshnichenko and Makhrov;[137] -•-•-•-•-, IAPWS 2008;[139] ————————, IAPWS 2011;[140] - - - -, SDFT-5s potential.[126]

In Figure 7.8 the values for shear viscosity and thermal conductivity computed using the CC-pol potential model are compared with selected experimental data,[129–137] the correlations of the International Association for the Properties of Water and Steam (IAPWS)[138–140] as well as the values obtained for the SDFT-5s potential model.

For the shear viscosity the lowest-uncertainty experimental data are those of Teske *et al.*[132] with relative uncertainties of ±(0.2 to 0.3) %. They deviate relatively by about +0.5 % from the values obtained with the CC-pol potential. As was already observed for methane, the relative deviations are nearly independent of temperature. The computed values also show good agreement with the experimental values of Latto,[130] which cover a much larger temperature range. By contrast, the data of Shifrin[129] are reproduced within relative differences of +(0.4 to 2.6) % and the deviations are strongly temperature-dependent. In this case the computed values act as an additional tool in differentiating between sets of incompatible data and can guide the development of correlations. The experimentally based IAPWS 2008 viscosity correlation[138] also exhibits increasingly larger deviations from the calculated values with increasing temperature. This is not surprising as the IAPWS 2008 correlation was, at high temperatures, weighted towards the data of Shifrin.

Finally, we examine in Figure 7.8a the viscosity values obtained with the SDFT-5s potential. Although they underestimate the experimental data of Teske *et al.* and Latto relatively by about 1 %, the predicted temperature dependence above $T = 400$ K is consistent with that obtained for the CC-pol potential, indicating that the repulsive parts of both potentials are realistic and accurate.

As in the case of methane, experimental uncertainties for thermal conductivity are much higher than for shear viscosity. The values calculated with the CC-pol potential are for the most part consistent with the experimental data up to temperatures of about 500 K. However, Figure 7.8b clearly illustrates that there is a systematic trend with the calculated values progressively underestimating the experimental data and the corresponding IAWPS 2008 correlation[139] with increasing temperature. The strong experimental basis of the correlation, confirmed by most of the available experimental data, indicates that the computed values of the thermal conductivity for strongly polar molecules have, at high temperatures, higher uncertainties than those for non-polar molecules. It is not at present clear why this is the case, but a possible explanation is that the strong dipole–dipole and hydrogen-bonding interactions can induce a change of vibrational states during a collision (see, for example, ref. 141 and references therein). This invalidates the 'frozen vibrational states' assumption invoked in the calculation, as discussed in more detail in Section 7.2.5. Nevertheless, it should also be recognized that performing measurements of the thermal conductivity at such high temperatures is not straightforward and the accuracy might be worse than claimed. In order to reconcile some of the differences observed, a new correlation for the thermal conductivity of water (IAPWS 2011) has been proposed.[140] In its development the calculated values obtained with the CC-pol potential were used to supplement the experimental datasets at both very low and very high temperatures.[142]

7.2.5 General Observations

We are now in a position to calculate the viscosity of simple dilute gases with a relative uncertainty of ± 1 % over a large temperature range.[91,93,94,96,98,99] The good agreement with the temperature dependence of some of the most accurate experimental data indicates that the computed values can and do provide accurate estimates of viscosity at low and high temperatures, where experimental data are either of higher uncertainty or non-existent. For the molecules studied, the collisions involving an exchange of vibrational energy have a negligible effect on the viscosity. The work on rigid chains indicates that at high temperatures the viscosity is governed by an effective repulsive potential, whereby the hardness, measured by a repulsive exponent, increases with the size of the molecule.[100] The higher-order viscosity correction factors $f_\eta^{(n)}$ show a similar behaviour to that observed for monatomic systems, increasing with increasing temperature before reaching a plateau at high temperature. The magnitude of the corrections does increase with the

anisotropy of the intermolecular potential, but its relative contribution is at most +1 % for CO_2[94] and +3 % for a model gas made of rigid chain-like molecules, consisting of 16 spheres interacting through a combination of site–site Lennard–Jones 12-6 potentials.[100]

The self-diffusion coefficient can be computed to the same accuracy as viscosity,[91,94,96,98] thus providing very reliable estimates for this transport property, which is notoriously difficult to measure with high accuracy. It is customary in kinetic theory[7] to consider the ratio of the self-diffusion coefficient to viscosity by defining the dimensionless parameter A^* as

$$A^* = \frac{5}{6}\frac{\mathfrak{S}(2000)}{\mathfrak{S}'(1000)} \cong \frac{5}{6}\frac{nmD}{\eta}. \tag{7.12}$$

Figure 7.9a illustrates the temperature dependence of A^*. Although the temperature dependence confirms the trends established so far for monatomic species, the magnitude of A^* is generally relatively larger, of between (5 to 6) % for CO_2.[94] This supports the conclusion of Mason and Monchick, based on their approximate calculations, that inelastic collisions have a marginally larger effect on the transfer of mass than on the transfer of momentum.[71,72] The difference in magnitude also indicates that the traditional way of estimating the self-diffusion coefficient, by multiplying the experimental viscosity by a value of A^* obtained from a spherical potential, has a higher uncertainty than previously thought. However, as a tool for making estimates of self-diffusion coefficients, it retains its importance as long as it is refined by using A^* values based on non-spherical potentials.

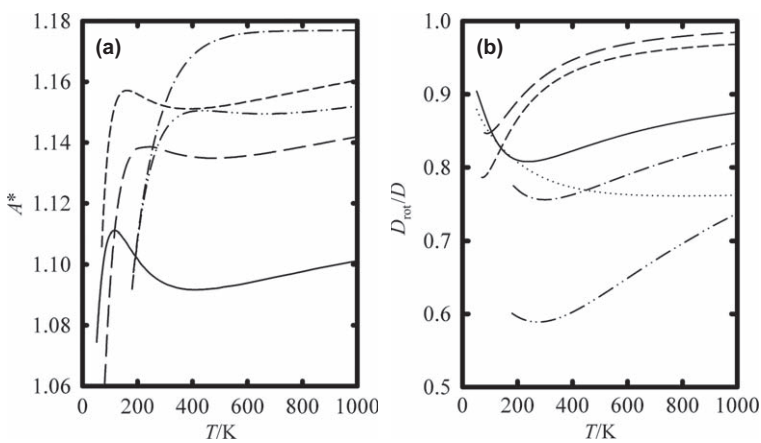

Figure 7.9 (a) Comparison of the temperature behaviour of A^* for different molecules as a function of temperature T: ————————, Lennard-Jones; —— —— ——, CH_4; - - - - -, N_2; -•-•-•-•-, CO_2; -••-••-••-, H_2S. (b) Comparison of the temperature behaviour of D_{rot}/D for different molecules as a function of temperature T: ————————, 2-segment LJ chain; •••••••••, 6-segment LJ chain; other lines as in panel (a).

Thermal conductivity measures the transport of energy through a gas and at the molecular level it is important to take into account that some of the energy can be stored in the vibrational degrees of freedom. At the temperatures of interest, even for simple gases, higher vibrational levels are often significantly populated. However, the collisions involving changes in the vibrational energies are rare, unless we are dealing with molecules that have low-lying vibrational states or possess strong dipoles. It is thus common practice[79,80,93,97–99] to incorporate the presence of vibrational energy in the current calculations by invoking the assumption of 'frozen vibrational states', that neglects collisions where the vibrational state of the molecule has changed. For thermal conductivity this results in two major corrections. First, the parameter r in eqn (7.11) is now calculated using C_{int}, the contribution of both the rotational and vibrational degrees of freedom to the isochoric heat capacity. Second, the generalized cross sections that arise from the coupling of non-zero terms in the internal energy need to be corrected. Specifically, for the cross section $\mathfrak{S}(1001)$, that enters the expression for thermal conductivity, eqn (7.9), the correction is of the form

$$\mathfrak{S}(1001) = \left(\frac{C_{\mathrm{rot}}}{C_{\mathrm{int}}}\right)\mathfrak{S}(1001)_{\mathrm{rr00}} + \left(\frac{C_{\mathrm{vib}}}{C_{\mathrm{int}}}\right)\mathfrak{S}'(1000)_{\mathrm{rr00}}, \qquad (7.13)$$

as first shown by Bich.[79] Here the subscript rr00 indicates that the generalized cross section was evaluated by means of classical trajectory calculations (rigid rotor) from the ground vibrational state potential. By means of the procedure outlined above, it is possible to calculate the thermal conductivity of simple gases[80,91,93,97–99] with a relative uncertainty of $\pm$(1 to 1.5) % over a large temperature range. The good agreement with experimental data supports the assumption that, at least for N_2, CO, CO_2, CH_4 and H_2S, the collisions involving exchange of vibrational energy have a negligible effect on thermal conductivity. For water vapour, as discussed in Section 7.2.4, this is probably not the case, and at high temperatures the contribution of such collisions to the thermal conductivity could be of the order of a few percent.[98]

The higher-order thermal conductivity correction factors $f_\lambda^{(n)}$ show similar behaviour to those for viscosity. The magnitude increases with the size of the molecule, but its relative contribution is at most $+$(1 to 2) % for the simple molecules studied so far.[80,91,93,97–99] However, for a model system made of chain-like molecules the relative contribution can be as large as $+7$ % at the highest temperatures.[100] Such large values could be an artefact of treating the chains as rigid rotors and not invoking the 'frozen vibrational energy' assumption in evaluating the thermal conductivity. It remains to be seen if real gases made of long chain molecules (*e.g.* alkanes) display large second-order correction factors.

Early investigations of the thermal conductivity of polyatomic gases found it useful to define a self-diffusion coefficient for the rotational energy, D_{rot}, which measures the rate at which rotational energy is transported through

the gas by the molecules.[71,72] The concept was found particularly useful in analysing thermal conductivity measurements and developing correlations when combined with the self-diffusion coefficient to form a ratio D_{rot}/D. Up to now it has been assumed, based on the work on model and real systems,[72,143–145] that at high enough temperatures the ratio D_{rot}/D tends to unity and this was used to differentiate between the thermal conductivity data at high temperatures and/or extrapolate correlations to temperatures at which no data were available. The current evidence based on computational studies and illustrated in Figure 7.9b no longer supports this assumption, apart from the molecules with the least anisotropic pair potentials (N_2 and CH_4).

Traditionally, kinetic theory equations are solved by a double perturbation-series expansion in terms of translational and internal energy. Thijsse and co-workers[146] proposed that a more natural choice, at least for thermal conductivity, would be to perform the expansion in terms of total energy. The resulting first-order expression for the thermal conductivity is much simpler, requiring knowledge of only a single cross section. All the results on simple non-polar and weakly polar molecules (N_2, CO, CO_2, CH_4 and H_2S)[80,97,147] and model chain-like molecules[100] indicate that the two approaches give nearly identical values of thermal conductivity, the largest relative deviations being 0.6 %. This provides further evidence that a single cross section is sufficient to describe closely the behaviour of the thermal conductivity, even for highly eccentric chain-like molecules, and can be used for correlating the thermal conductivity of real fluids.

Out of the four traditional transport properties considered, the volume viscosity is the most difficult to accurately determine experimentally. The currently computed values for simple gases are thus among the best estimates available.[91,95,97–99] However, it should be borne in mind that all the calculations have been performed by neglecting the molecular collisions that involve the exchange of vibrational energy, which could reduce the accuracy of the computed values at high temperatures. At low temperatures quantum effects can be important, as discussed in Section 7.2.3. Hence, the relative uncertainty of the volume viscosity for the non-polar and weakly polar gases considered so far is estimated to be ± 5 % at best.

The higher-order volume viscosity correction factors $f_\kappa^{(n)}$ show similar behaviour to those for shear viscosity in so far as they increase with increasing temperature before reaching a plateau at high temperature. However, the magnitude decreases with an increase in moment of inertia (or molecular size) and anisotropy. Small molecules interacting through weakly anisotropic intermolecular potentials have large second-order correction factors reaching values, at a temperature of 1000 K, of the order of 1.19 for CH_4[97] and 1.27 for N_2 (using the potential of ref. 93). However, for CO_2 the second-order correction factor is only 1.03 at a temperature of 1000 K.[95] Hence, taking the second-order correction factor, as first reported by Turfa *et al.*,[83] into account is only important for molecules with weakly anisotropic intermolecular potentials like N_2 and CH_4.

7.2.6 Summary and Outlook

This review has attempted to illustrate the developments over the last decade in our ability to calculate the traditional transport properties of dilute gases directly from accurate *ab initio* potentials. The classical trajectory method combined with the kinetic theory of polyatomic gases provides a reliable and accurate way of carrying out such calculations, except for molecules with very small masses and moments of inertia like H_2, for which a quantum-mechanical treatment is needed. As a result of these developments we can calculate the shear viscosity, self-diffusion coefficient, thermal conductivity and volume viscosity to an accuracy that is commensurate with the best experimental data. The present calculations not only improve our understanding of the transport properties at the molecular level and provide for an additional validation of *ab initio* potentials, but also allow us to supplement the available experimental data. This is especially useful because the volume of experimental work in this area has declined dramatically and all the indications are that in the future we will have to rely much more on computational efforts. There are a number of areas where the calculation of transport properties can address an immediate need for data: (i) at very low and high temperatures where accurate experimental measurements require substantial effort and investment; (ii) for gases that cannot be easily handled in normal laboratories (*e.g.* toxic, highly corrosive or explosive gases); (iii) for diffusion coefficients and volume viscosity where it can provide substantial improvements in accuracy; (iv) for selected mixtures that are either of industrial importance or of theoretical interest.

The obvious next step is to extend the calculations to a number of selected binary mixtures consisting of simple molecules. Such calculations are at present technically feasible and just require a major computational effort. Not only will this yield the necessary data, but also the quantities that describe unlike interactions (interaction viscosity, interaction thermal conductivity and binary diffusion coefficient) will become available. While the usefulness of the binary diffusion coefficient is self-evident, the interaction viscosity and interaction thermal conductivity are equally valuable. Accurate knowledge of the latter two will provide for a more secure characterization of both the viscosity and thermal conductivity of mixtures. This is especially important as the viscosity and thermal conductivity of multicomponent dilute-gas mixtures are only functions of binary encounters and hence the computational study of binary mixtures furnishes us with all the prerequisites to predict the transport properties of multicomponent mixtures. Furthermore, the kinetic theory of dense fluids relies on knowledge of dilute-gas behaviour. Thus, extending the current calculations to mixtures will provide the necessary building blocks for improving the accuracy of the prediction methods in a dense fluid.

The current trends in computational power indicate that extending the calculations to heavier molecules will be within our capabilities in the very near future. However, an increase in computational power alone will not be

sufficient and the issue of how to include the vibrational degrees of freedom into classical trajectory calculations needs to be resolved. For heavier molecules the collisions involving exchange of vibrational energy will become more common and they will manifest themselves at the level of transport properties, not only affecting thermal conductivity, but also viscosity and diffusion. Furthermore, *ab initio* potentials that take the intramolecular degrees of freedom into account will need to be used, increasing not only the complexity of the collisional dynamics calculation, but making serious demands on the required computational power.

The present computational work has provided a wealth of data not only on traditional transport properties, but also on generalized cross sections that govern many other physical phenomena, such as rotational relaxation, depolarized Rayleigh scattering and field effects on transport properties. Although great progress has been made in the last decade, the elucidation of the molecular processes that determine transport properties still remains an area where further work would be very beneficial. In particular, additional angular momentum polarizations present in symmetric and asymmetric tops (see ref. 82), vibrational contributions within the 'frozen vibrational states' approximation to higher-order thermal conductivity corrections, and the influence of vibrationally inelastic and resonant collisions on transport properties of polar gases all offer a rich research seam.

References

1. S. Chapman, *Proc. R. Soc. London A*, 1916, **93**, 1.
2. D. Enskog, *Inaugural Dissertation*, Almqvist & Wiksell, 1917.
3. J. O. Hirschfelder, C. F. Curtiss and R. B. Bird, *Molecular Theory of Gases and Liquids*, Wiley, New York, 1964.
4. S. Chapman and T. G. Cowling, *The Mathematical Theory of Non-Uniform Gases*, Cambridge University Press, New York, 1970.
5. J. H. Ferziger and H. G. Kaper, *The Mathematical Theory of Transport Processes in Gases*, North-Holland, Amsterdam, 1972.
6. G. C. Maitland, M. Rigby, E. B. Smith and W. A. Wakeham, *Intermolecular Forces: Their Origin and Determination*, Clarendon Press, Oxford, 1981.
7. F. R. W. McCourt, J. J. M. Beenakker, W. E. Köhler and I. Kuščer, *Nonequilibrium Phenomena in Polyatomic Gases*, *Vol. 1*, Clarendon Press, Oxford, 1990.
8. L. A. Viehland, A. R. Janzen and R. A. Aziz, *J. Chem. Phys.*, 1995, **102**, 5444.
9. R. M. Thomson, *Comput. Phys. Commun.*, 1979, **18**, 123.
10. S. K. Loyalka, E. L. Tipton and R. V. Tompson, *Physica A*, 2007, **379**, 417.
11. H. O'Hara and F. J. Smith, *J. Comput. Phys.*, 1970, **5**, 328.
12. H. O'Hara and F. J. Smith, *Comput. Phys. Commun.*, 1971, **2**, 47.
13. P. D. Neufeld and R. A. Aziz, *Comput. Phys. Commun.*, 1972, **3**, 269.
14. J. J. Hurly and J. B. Mehl, *J. Res. Natl. Inst. Stand. Technol.*, 2007, **112**, 75.

15. E. Bich, R. Hellmann and E. Vogel, *Mol. Phys.*, 2007, **105**, 3035.
16. R. A. Aziz, F. R. W. McCourt and C. C. K. Wong, *Mol. Phys.*, 1987, **61**, 1487.
17. R. A. Aziz and M. J. Slaman, *Chem. Phys.*, 1989, **130**, 187.
18. A. K. Dham, A. R. Allnatt, W. J. Meath and R. A. Aziz, *Mol. Phys.*, 1989, **67**, 1291.
19. A. K. Dham, W. J. Meath, A. R. Allnatt, R. A. Aziz and M. J. Slaman, *Chem. Phys.*, 1990, **142**, 173.
20. M. Keil, L. J. Danielson and P. J. Dunlop, *J. Chem. Phys.*, 1991, **94**, 296.
21. R. A. Aziz, *J. Chem. Phys.*, 1993, **99**, 4518.
22. S. J. Boyes, *Chem. Phys. Lett.*, 1994, **221**, 467.
23. R. Hellmann, E. Bich and E. Vogel, *Mol. Phys.*, 2007, **105**, 3013.
24. M. Przybytek, W. Cencek, J. Komasa, B. Jeziorski and K. Szalewicz, *Phys. Rev. Lett.*, 2010, **104**, 183003.
25. W. Cencek, M. Przybytek, J. Komasa, J. B. Mehl, B. Jeziorski and K. Szalewicz, *J. Chem. Phys.*, 2012, **136**, 224303.
26. R. Hellmann, E. Bich and E. Vogel, *Mol. Phys.*, 2008, **106**, 133.
27. B. Jäger, R. Hellmann, E. Bich and E. Vogel, *Mol. Phys.*, 2009, **107**, 2181; corrigendum: 2010, **108**, 105.
28. K. Patkowski and K. Szalewicz, *J. Chem. Phys.*, 2010, **133**, 094304.
29. T. P. Haley and S. M. Cybulski, *J. Chem. Phys.*, 2003, **119**, 5487.
30. A. E. Nasrabad and U. K. Deiters, *J. Chem. Phys.*, 2003, **119**, 947.
31. P. Slavíček, R. Kalus, P. Paška, I. Odvárková, P. Hobza and A. Malijevský, *J. Chem. Phys.*, 2003, **119**, 2102.
32. J. van de Bovenkamp, T. van Mourik and F. B. van Duijneveldt, *Mol. Phys.*, 1999, **97**, 487.
33. S. M. Cybulski and R. R. Toczyłowski, *J. Chem. Phys.*, 1999, **111**, 10520.
34. H. Partridge, J. R. Stallcop and E. Levin, *J. Chem. Phys.*, 2001, **115**, 6471.
35. T. J. Giese, V. M. Audette and D. M. York, *J. Chem. Phys.*, 2003, **119**, 2618.
36. J. L. Cacheiro, B. Fernández, D. Marchesan, S. Coriani, C. Hättig and A. Rizzo, *Mol. Phys.*, 2004, **102**, 101.
37. A. E. Nasrabad, R. Laghaei and U. K. Deiters, *J. Chem. Phys.*, 2004, **121**, 6423.
38. A. Baranowska, S. B. Capelo and B. Fernández, *Phys. Chem. Chem. Phys.*, 2010, **12**, 13586.
39. E. Bich, R. Hellmann and E. Vogel, *Mol. Phys.*, 2008, **106**, 1107.
40. E. Vogel, B. Jäger, R. Hellmann and E. Bich, *Mol. Phys.*, 2010, **108**, 3335.
41. J. B. Mehl, unpublished work.
42. R. A. Aziz, A. R. Janzen and M. R. Moldover, *Phys. Rev. Lett.*, 1995, **74**, 1586.
43. A. R. Janzen and R. A. Aziz, *J. Chem. Phys.*, 1997, **107**, 914.
44. J. J. Hurly and M. R. Moldover, *J. Res. Natl. Inst. Stand. Technol.*, 2000, **105**, 667.
45. R. F. Berg and W. C. Burton, *Mol. Phys.*, 2013, **111**, 193.
46. R. F. Berg, *Metrologia*, 2005, **42**, 11; erratum: 2006, **43**, 183.

47. K. Patkowski, G. Murdachaew, C.-M. Fou and K. Szalewicz, *Mol. Phys.*, 2005, **103**, 2031.
48. K. Patkowski, private communication, 2012.
49. E. F. May, R. F. Berg and M. R. Moldover, *Int. J. Thermophys.*, 2007, **28**, 1085.
50. E. Vogel, *Int. J. Thermophys.*, 2010, **31**, 447.
51. B. Jäger *et al.*, unpublished potentials for He–Kr and Kr–Kr atom pairs.
52. A. S. Kalelkar and J. Kestin, *J. Chem. Phys.*, 1970, **52**, 4248.
53. H. von Ubisch, *Arkiv Fysik*, 1959, **16**, 93.
54. E. Thornton, *Proc. Phys. Soc.*, 1961, **77**, 1166.
55. R. S. Gambhir and S. C. Saxena, *Mol. Phys.*, 1966, **11**, 233.
56. P. S. Arora, H. L. Robjohns and P. J. Dunlop, *Physica A*, 1979, **95**, 561.
57. K. P. Srivastava and A. P. Barua, *Ind. J. Phys.*, 1959, **33**, 229.
58. E. B. Fedorov, B. A. Ivakin and P. E. Suetin, *Sov. Phys. Tech. Phys.*, 1966, **11**, 424.
59. R. J. J. van Heijningen, J. P. Harpe and J. J. M. Beenakker, *Physica*, 1968, **38**, 1.
60. D. Cain and W. L. Taylor, *J. Chem. Phys.*, 1979, **71**, 3601.
61. L. Waldmann, *Z. Naturf. A*, 1957, **12**, 660.
62. L. Waldmann, in *Handbuch der Physik*, *Vol. 12*, ed. S. Flügge, Springer-Verlag, Berlin, 1958, pp. 295–514.
63. R. F. Snider, *J. Chem. Phys.*, 1960, **32**, 1051.
64. R. F. Snider, *Physica*, 1974, **78**, 387.
65. C. F. Curtiss, *J. Chem. Phys.*, 1981, **74**, 6718.
66. C. F. Curtiss and M. W. Tonsager, *J. Chem. Phys.*, 1985, **82**, 3795.
67. W. A. Wakeham and V. Vesovic, *Status and Future Developments in the Study of Transport Properties*, Dordrecht, Kluwer, 1992.
68. V. Vesovic and W. A. Wakeham, *Int. Rev. Phys. Chem.*, 1992, **11**, 161.
69. M. Mustafa, PhD Thesis, Imperial College London, 1987.
70. J. Millat, V. Vesovic and W. A. Wakeham, in *Transport Properties of Fluids: Their Correlation, Prediction and Estimation*, eds. J. Millat, J. H. Dymond and C. A. Nieto de Castro, Cambridge University Press, 1996, pp. 29–65.
71. L. Monchick and E. A. Mason, *J. Chem. Phys.*, 1961, **35**, 1676.
72. E. A. Mason and L. Monchick, *J. Chem. Phys.*, 1962, **36**, 1622.
73. G. A. Parker and R. T. Pack, *J. Chem. Phys.*, 1978, **68**, 1585.
74. F. A. Gianturco, S. Serna and N. Sanna, *Mol. Phys.*, 1991, **74**, 1071.
75. A. S. Dickinson, in *Handbook of Molecular Physics and Quantum Chemistry*, *Vol. 3*, ed. S. Wilson, Wiley, Chichester, 2003, pp. 547–573.
76. F. R. W. McCourt, V. Vesovic, W. A. Wakeham, A. S. Dickinson and M. Mustafa, *Mol. Phys.*, 1991, **72**, 1347.
77. V. Vesovic, W. A. Wakeham, A. S. Dickinson, F. R. W. McCourt and M. Thachuk, *Mol. Phys.*, 1995, **84**, 553.
78. G. D. Billing, *The Quantum-Classical Theory*, Oxford University Press, New York, 2002.
79. E. Bich, S. Bock and E. Vogel, *Physica A*, 2002, **311**, 59.

80. S. Bock, E. Bich, E. Vogel, A. S. Dickinson and V. Vesovic, *J. Chem. Phys.*, 2004, **120**, 7987.
81. E. L. Heck and A. S. Dickinson, *Comp. Phys. Commun.*, 1996, **95**, 190.
82. A. S. Dickinson, R. Hellmann, E. Bich and E. Vogel, *Phys. Chem. Chem. Phys.*, 2007, **9**, 2836.
83. A. F. Turfa, H. F. P. Knaap, B. J. Thijsse and J. J. M. Beenakker, *Physica A*, 1982, **112**, 18.
84. C. Nyeland, L. L. Poulsen and G. D. Billing, *J. Phys. Chem.*, 1984, **88**, 1216.
85. C. Nyeland, L. L. Poulsen and G. D. Billing, *J. Phys. Chem.*, 1984, **88**, 5858.
86. A. F. Turfa, J. N. L. Connor, B. J. Thijsse and J. J. M. Beenakker, *Physica A*, 1985, **129**, 439.
87. G. D. Billing and L. Wang, *J. Phys. Chem.*, 1992, **96**, 2572.
88. L. Wang and G. D. Billing, *J. Chem. Soc., Faraday Trans.*, 1992, **88**, 163.
89. L. Wang and G. D. Billing, *J. Phys. Chem.*, 1993, **97**, 2523.
90. E. L. Heck and A. S. Dickinson, *Mol. Phys.*, 1994, **81**, 1325.
91. E. L. Heck and A. S. Dickinson, *Physica A*, 1995, **217**, 107.
92. E. L. Heck and A. S. Dickinson, *Physica A*, 1995, **218**, 305.
93. R. Hellmann, *Mol. Phys.*, 2013, **111**, 387.
94. S. Bock, E. Bich, E. Vogel, A. S. Dickinson and V. Vesovic, *J. Chem. Phys.*, 2002, **117**, 2151.
95. S. Bock, E. Bich, E. Vogel, A. S. Dickinson and V. Vesovic, *J. Chem. Phys.*, 2004, **121**, 4117.
96. R. Hellmann, E. Bich, E. Vogel, A. S. Dickinson and V. Vesovic, *J. Chem. Phys.*, 2008, **129**, 064302.
97. R. Hellmann, E. Bich, E. Vogel, A. S. Dickinson and V. Vesovic, *J. Chem. Phys.*, 2009, **130**, 124309.
98. R. Hellmann, E. Bich, E. Vogel, A. S. Dickinson and V. Vesovic, *J. Chem. Phys.*, 2009, **131**, 014303.
99. R. Hellmann, E. Bich, E. Vogel and V. Vesovic, *Phys. Chem. Chem. Phys.*, 2011, **13**, 13749.
100. R. Hellmann, N. Riesco and V. Vesovic, *J. Chem. Phys.*, 2013, **138**, 084309.
101. R. Hellmann, N. Riesco and V. Vesovic, *Chem. Phys. Lett.*, 2013, **574**, 37.
102. J. B. Mehl, M. L. Huber and A. H. Harvey, *Int. J. Thermophys.*, 2010, **31**, 740.
103. J. Schaefer, *Chem. Phys.*, 2010, **368**, 38.
104. E. G. D. Cohen, M. J. Offerhaus, J. M. J. Van Leeuwen, B. W. Roos and J. De Boer, *Physica*, 1956, **22**, 791.
105. K. Patkowski, W. Cencek, P. Jankowski, K. Szalewicz, J. B. Mehl, G. Garberoglio and A. H. Harvey, *J. Chem. Phys.*, 2008, **129**, 094304.
106. H. M. Roder and D. E. Diller, *J. Chem. Phys.*, 1970, **52**, 5928.
107. A. A. Clifford, J. Kestin and W. A. Wakeham, *Ber. Bunsenges. Phys. Chem.*, 1980, **84**, 9.
108. M. J. Assael and W. A. Wakeham, *J. Chem. Soc., Faraday Trans. 1*, 1981, **77**, 697.

109. H. M. Roder, Natl. Bur. Stand. (U.S.), Interagency Report 84-3006, 1984.
110. H. M. Roder, *Int. J. Thermophys.*, 1984, **5**, 323.
111. A. A. Clifford, P. Gray, A. I. Johns, A. C. Scott and J. T. R. Watson, *J. Chem. Soc. Faraday Trans. 1*, 1981, **77**, 2679.
112. R. Hellmann, E. Bich and E. Vogel, *J. Chem. Phys.*, 2008, **128**, 214303.
113. P. Schley, M. Jaeschke, C. Küchenmeister and E. Vogel, *Int. J. Thermophys.*, 2004, **25**, 1623.
114. E. Vogel, *J. Chem. Eng. Data*, 2011, **56**, 3265.
115. H. L. Johnston and E. R. Grilly, *J. Chem. Phys.*, 1946, **14**, 233.
116. R. Tufeu, B. Le Neindre and P. Bury, *Physica*, 1969, **44**, 81.
117. H. M. Roder, *Int. J. Thermophys.*, 1985, **6**, 119.
118. W. Hemminger, *Int. J. Thermophys.*, 1987, **8**, 317.
119. E. B. Winn, *Phys. Rev.*, 1950, **80**, 1024.
120. R. Dawson, F. Khoury and R. Kobayashi, *AIChE J.*, 1970, **16**, 725.
121. P. H. Oosting and N. J. Trappeniers, *Physica*, 1971, **51**, 418.
122. R. Holmes, G. R. Jones and N. Pusat, *Trans. Faraday Soc.*, 1964, **60**, 1220.
123. P. G. Kistemaker, M. M. Hanna, A. Tom and A. E. de Vries, *Physica*, 1972, **60**, 459.
124. G. J. Prangsma, A. H. Alberga and J. J. M. Beenakker, *Physica*, 1973, **64**, 278.
125. R. Bukowski, K. Szalewicz, G. C. Groenenboom and A. van der Avoird, *Science*, 2007, **315**, 1249.
126. R. Bukowski, K. Szalewicz, G. C. Groenenboom and A. van der Avoird, *J. Chem. Phys.*, 2006, **125**, 044301.
127. B. Jeziorski, R. Moszynski and K. Szalewicz, *Chem. Rev.*, 1994, **94**, 1887.
128. A. J. Misquitta, R. Podeszwa, B. Jeziorski and K. Szalewicz, *J. Chem. Phys.*, 2005, **123**, 214103.
129. A. S. Shifrin, *Teploenergetika*, 1959, **6**(9), 22.
130. B. Latto, *Int. J. Heat Mass Transfer*, 1965, **8**, 689.
131. D. L. Timrot, M. A. Serednitskaya and M. S. Bespalov, *Teploenergetika*, 1973, **20**(8), 11.
132. V. Teske, E. Vogel and E. Bich, *J. Chem. Eng. Data*, 2005, **50**, 2082.
133. N. B. Vargaftik and N. Kh. Zimina, *Teploenergetika*, 1964, **11**(12), 84.
134. B. Le Neindre, P. Bury, R. Tufeu, P. Johannin and B. Vodar, Proc. 7th International Conference on the Properties of Steam (Tokyo, 1968), ASME, New York, 1970, Paper No. C-2, p. 231.
135. V. N. Popov and S. G. Dulnev, *Trudy Moskovskogo Energeticheskogo Instituta*, 1977, **336**, 57.
136. R. Tufeu and B. Le Neindre, *Inzh.-Fiz. Zh.*, 1979, **36**, 472.
137. V. I. Miroshnichenko and V. V. Makhrov, *Teploenergetika*, 1984, **31**(1), 64.
138. IAPWS, *Release on the IAPWS Formulation 2008 for the Viscosity of Ordinary Water Substance*, International Association for the Properties of Water and Steam, 2008.
139. IAPWS, *Revised Release on the IAPS Formulation 1985 for the Thermal Conductivity of Ordinary Water Substance*, International Association for the Properties of Water and Steam, 2008.

140. IAPWS, *Release on the IAPWS Formulation 2011 for the Thermal Conductivity of Ordinary Water Substance*, International Association for the Properties of Water and Steam, 2011.
141. H. K. Shin, *Chem. Phys. Lett.*, 1993, **202**, 260.
142. M. L. Huber, R. A. Perkins, D. G. Friend, J. V. Sengers, M. J. Assael, I. N. Metaxa, K. Miyagawa, R. Hellmann and E. Vogel, *J. Phys. Chem. Ref. Data*, 2012, **41**, 033102.
143. M. J. Assael, J. Millat, V. Vesovic and W. A. Wakeham, *J. Phys. Chem. Ref. Data*, 1990, **19**, 1137.
144. J. Millat and W. A. Wakeham, *J. Phys. Chem. Ref. Data*, 1989, **18**, 565.
145. S. I. Sandler, *Phys. Fluids*, 1968, **11**, 2549.
146. B. J. Thijsse, G. W. 'T Hooft, D. A. Coombe, H. F. P. Knaap and J. J. M. Beenakker, *Physica A*, 1979, **98**, 307.
147. R. Hellmann and V. Vesovic, unpublished results for N_2, CO and H_2S.

CHAPTER 8

Dense Fluids: Viscosity

VELISA VESOVIC, J. P. MARTIN TRUSLER, MARC J. ASSAEL, NICOLAS RIESCO AND SERGIO E. QUIÑONES-CISNEROS

8.1 Introduction

VELISA VESOVIC

The present chapter is devoted to the most recent developments in our ability to model and calculate the viscosity of dense fluids. Statistical thermodynamics and kinetic theory provide the formal basis for developing models based upon a rigorous theory of fluid behaviour and, at least in principle, allow a link to be established between the macroscopic properties of a fluid and interactions among individual molecules. We have seen in Chapter 7 that in the zero-density limit, where only the binary interactions are present, it is possible not only to establish a rigorous molecular description of transport properties, but also to make use of it to compute the properties from precise *ab initio* intermolecular potentials. For dilute gases one can thus argue that the goal of kinetic theory has been achieved, as we are now in a position to calculate the transport properties with an uncertainty commensurate with the best experimental measurements over a wide temperature range, albeit only for simple molecules.

The situation for dense fluids is markedly different. On purely physical grounds the collisional transfer of momentum and energy begins to dominate the transport processes as the density increases. At low densities the collision frequency rises linearly with the density, but as the mean free path of the molecules become smaller the molecular size becomes significant relative to it and the collisional rate increases more rapidly. It is therefore no longer possible to represent the behaviour of the fluid by means of the isolated interactions of two molecules whose initial velocities are

Experimental Thermodynamics Volume IX: Advances in Transport Properties of Fluids
Edited by M. J. Assael, A. R. H. Goodwin, V. Vesovic and W. A. Wakeham

Published by the Royal Society of Chemistry, www.rsc.org

uncorrelated as was possible in the kinetic theory of the dilute gas. These two factors lie behind the fact that the fundamental unresolved problem is that we lack a general solution of the Boltzmann integral-differential equation for the dense molecular system, as it has been impossible up to now to formulate a proper generalization of the Boltzmann equation for dense fluids.

Because no rigorous and complete molecular theory exists for dense fluids a number of different approximate approaches have been taken to model viscosity and in general transport properties. They range from the semi-theoretical, where approximations made allow for sufficient simplification, to purely empirical and correlative where the experimental data used govern both the form and predictive power of the model. In the present chapter we shall focus primarily on the former. There are a number of distinct routes that people have followed, depending on the theoretical framework used in developing the model. The first group of models have their basis in kinetic theory. The second group can be classified as those that are based on the corresponding-states principle. The third group broadly exploits the link with thermodynamics. Although conceptually different all these models share a number of characteristics. They all require experimental data, in one form or another, to determine a number of effective parameters of the model. Their predictive power is fluid-dependent, unless the effective parameters, sometimes expressed as a function of thermodynamic state, are also linked to molecular properties by a further correlation. Most importantly all such methods require mixing rules, for application to mixtures. It is at this level that further empiricism is introduced. Even for the simplest molecular models the mixing rules for dense fluids have no rigorous theoretical basis. Finally, some models exhibit extreme sensitivity to the value of one or more of the effective parameters, thus limiting their uncertainty.

One of the difficulties that all the models face, when applied to viscosity, is that viscosity exhibits a strong dependence on temperature and/or density even outside the critical region. This is not surprising since it measures the ease with which a fluid can flow. As we approach the solidification line, either by decreasing the temperature or increasing the density, the viscosity can change significantly. If we take a fluid composed of large and complex molecules, such as heavy oil, one can observe a reduction in viscosity of 2 to 3 orders of magnitude simply by increasing the temperature by ten degrees. Even for liquids that have a viscosity similar to that of water one can observe large changes. For instance at $T = 273$ K, the hexane viscosity increases from 0.981 mPa $\cdot$ s at $p = 90$ MPa to 1.057 mPa $\cdot$ s at $p = 100$ MPa, an increase of 7.7 %, whilst the density changes only by 0.6 %. Therefore, precise knowledge of the thermodynamic state variables is sometimes required, perhaps beyond what can realistically be achieved, in order to predict the value of viscosity with a useful uncertainty. This high sensitivity makes accurate estimation essentially impossible, irrespective of the complexity and sophistication of a given model.

In this chapter we concentrate on three approaches in modelling viscosity that have seen significant advances, since the publication of the most recent IUPAC volume on transport properties.[1] Sections 8.2 and 8.3 review the recent developments of two approaches that are based on the kinetic theory. They both take advantage of the Enskog formulation that takes the hard-sphere fluid as its starting point. Although this renders it unsuitable for *a priori* predictions, it provides a useful theoretical basis for both understanding and predicting the transport properties of dense fluids. The two approaches differ in the way they use effective parameters to address the limitations of the Enskog approximation. In both sections we focus on establishing models for predicting the viscosity of fluids. The application of the two models is illustrated by the prediction of the viscosity of alkanes and alkane mixtures at temperatures and pressures of interest to the oil industry. Knowledge of viscosity, is essential in that industry, for reliable flow characterisation through both porous media and transport pipelines and hence for optimal exploitation.

Section 8.4 also describes a model that is used to predict the viscosity of oil. However, the approach is very different. In this case the residual viscosity is related to friction concepts of classical mechanics. It is further postulated, that the pressure can be written, in the simplest form, as a sum of the attractive and repulsive contributions. This allows for the development of an expression for viscosity, which by the judicious choice of temperature and pressure dependence of different terms, is rather simple. The resulting Friction Theory model has been successfully used for predicting the viscosity of fluids of different complexity, as aptly summarized and illustrated in Section 8.4.

8.2 The V_0 Scheme

J. P. MARTIN TRUSLER AND MARC J. ASSAEL

In this section we describe modifications to the hard-spheres scheme initially proposed by Assael and Dymond for the transport properties of dense fluids. These modifications relate specifically to the viscosity, and extend the method to densities both above and below the range of applicability of the original method.

8.2.1 The Assael and Dymond Scheme

The scheme developed originally by Assael and Dymond,[2–8] is based on the Enskog hard-spheres theory, as corrected by Alder *et al.*,[9] for the coefficients of self diffusion, viscosity and thermal conductivity. Alder *et al.*[9] performed molecular-dynamics simulations of systems containing 108 or 500 molecules, and showed that these corrections were functions only of the ratio (V_m/V_0), where V_m is the molar volume, and V_0 is the molar volume for close packed spheres of diameter σ $(V_0 = N_A\sigma^3/2^{1/2})$. Erpenbeck and Wood[10] confirmed the diffusion results obtained by Alder and extrapolated them to a system of infinite size. However, in the case of the viscosity and thermal conductivity, the correction factors turn out to be associated with a rather large uncertainty and this limits somewhat their usefulness. Nevertheless, these results indicate that the dimensionless transport property X^*, defined by

$$X^* = \left(\frac{X}{X_E}\right)_{MD}\left(\frac{X_E}{X_0}\right)\left(\frac{V_m}{V_0}\right)^{2/3}, \tag{8.1}$$

is a universal function of (V_m/V_0), independent of the temperature T. In eqn (8.1), the factor $(X/X_E)_{MD}$ represents the correction to the Enskog theory computed from molecular dynamics simulations, X_E is the property according to the Enskog theory, and X_0 is the dilute-gas property.

In order to apply these results to real molecules without prior knowledge of V_0, Dymond[11] proposed a modified scheme in which the dimensionless transport property is defined simply as

$$X^* = \left(\frac{X}{X_0}\right)\left(\frac{V_m}{V_0}\right)^{2/3}. \tag{8.2}$$

Here, X_0 is the dilute-gas transport property for the hard-sphere model with $\sigma = (2^{1/2}V_0/N_A)^{1/3}$ and V_0 is permitted to be a function of temperature. We can thus employ the dilute-gas relations for the viscosity η_0 and thermal conductivity λ_0 of hard sphere which, in lowest order, are as follows:[12]

$$\eta_0 = \frac{5}{16}\left[\frac{m\,k_B T}{\pi}\right]^{1/2}\frac{1}{\sigma^2} \tag{8.3}$$

and

$$\lambda_0 = \frac{75}{64}\left[\frac{k_B^3 T}{m\pi}\right]^{1/2}\frac{1}{\sigma^2}. \tag{8.4}$$

The following expressions are then obtained for the dimensionless viscosity and dimensionless thermal conductivity:

$$\eta^* = \frac{16}{5}(2N_A)^{1/3}\left(\frac{\pi}{MRT}\right)^{1/2} V_m^{2/3}\frac{\eta}{R_\eta} = F_\eta(V_r) \tag{8.5}$$

and

$$\lambda^* = \frac{64}{75R}(2N_A)^{1/3}\left(\frac{\pi M}{RT}\right)^{1/2} V_m^{2/3}\frac{\lambda}{R_\lambda} = F_\lambda(V_r), \tag{8.6}$$

where M is the molar mass, and F_η and F_λ denote universal reference functions of $V_r = (V_m/V_0)$. The universal reference functions were established by considering a large amount of experimental data for dense monatomic gases, and the following universal curves were proposed:[12]

$$\log_{10}(\eta^*) = 1.0945 - 9.26324\cdot V_r^{-1} + 71.0385\cdot V_r^{-2} - 301.9012 V_r^{-3} + 797.69\cdot V_r^{-4} - 1221.977\cdot V_r^{-5} + 987.5574\cdot V_r^{-6} - 319.4636\cdot V_r^{-7}, \tag{8.7}$$

and

$$\log_{10}(\lambda^*) = 1.0655 - 3.538\cdot V_r^{-1} + 12.120\cdot V_r^{-2} - 12.469\cdot V_r^{-3} + 4.562\cdot V_r^{-4}. \tag{8.8}$$

Figure 8.1 illustrates the results for the viscosity reference function. In order to apply the method, with the same reference functions, to polyatomic

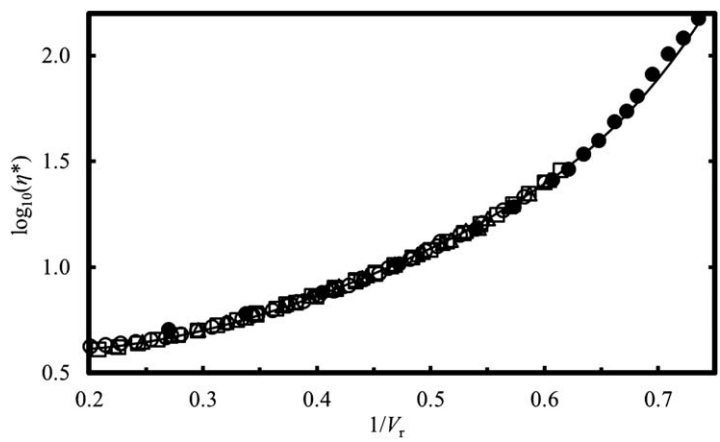

Figure 8.1 Reduced viscosity η^* as a function of $(1/V_r)$: ——, eqn (8.7); ●, computed values for hard spheres.[15] Also shown are smoothed experimental data at $T = 300$ K and along the saturated liquid curve for: ○, Ar; □, Kr; △, Xe.[16]

molecules, temperature independent roughness factors, R_η and R_λ, were introduced.

Experimental results over a range of temperatures at atmospheric pressure are sufficient to obtain both the characteristic volume and the roughness factors: V_0 is obtained from the horizontal translation and R_η or R_λ is obtained from the vertical translation needed to superimpose the experimental curves on the universal reference curves for η^* and λ^*. Better results were obtained when V_0 was optimized by simultaneous consideration of the three properties: self-diffusion, viscosity and thermal conductivity.[13]

This powerful scheme allowed the correlation and prediction of the thermal conductivity and viscosity of a wide range of simple molecules,[3] alkanes,[2] aromatic hydrocarbons,[6] alcohols,[7] and refrigerants,[8] as well as mixtures of liquids in a homologous series, *e.g.* alkane mixtures,[4] over a wide range of temperatures and pressures with a relative uncertainty of about ± 5 %. It permits the prediction of the transport properties of compressed liquids at very high pressures (it has been tested up to $p = 500$ MPa) based on experimental results for a single isobar at atmospheric pressure plus knowledge of the liquid density. The main drawback of the method is that the predictions are very sensitive to the values of (V_m/V_0) and an accurate equation of state for the liquid is therefore required. Furthermore, it has so far been unable to correlate or predict the thermal conductivity or viscosity of mixtures of liquids that do not belong to the same homologous series.[14]

8.2.2 The Extended Assael and Dymond Scheme

The hard-sphere scheme described in the previous section, was developed for dense fluids and does not approach the known dilute-gas limits as $V_r \rightarrow \infty$. Furthermore, the data from which the universal curves were initially obtained did not extend to reduced volume below 1.5. Accordingly the original scheme was limited to the range $1.5 \leq V_r \leq 5$.[1] In the case of the viscosity, both the upper and the lower bounds on reduced volume have been extended by means of two modifications: one proposed by Caudwell[17] and the other by Ciotta.[18] It seems likely that similar modifications could be developed for other transport properties but this has not yet been demonstrated.

8.2.2.1 The Caudwell Extension

Caudwell[17] compared the predictions of the original Assael and Dymond scheme with the experimental viscosity data for the light alkanes and found deviations of increasing magnitude, spanning -70 % to $+30$ %, as the reduced volume was increased above the upper limit of $V_r = 5$. To overcome this, Caudwell proposed a modification of the original scheme based on the residual viscosity $(\eta - \eta_0)$ as follows:[17]

$$\Delta\eta* = \frac{16}{5}\,(2N_A)^{1/3}\left(\frac{\pi}{MRT}\right)^{1/2} V_m^{2/3}\,\frac{\eta - \eta_0}{R_\eta}, \tag{8.9}$$

where $\Delta\eta^*$ is the reduced residual viscosity. Caudwell correlated $\log_{10}(\Delta\eta^* + 1)$ as a polynomial function of $1/V_r$ with powers ranging from 1 to 7:

$$\log_{10}(\Delta\eta* + 1) = \sum_{i=1}^{7} a_i (1 / V_r)^i \,. \tag{8.10}$$

In this way, $\log_{10}(\Delta\eta^* + 1) \to 0$ and $\eta \to \eta_0$ as $V_r \to \infty$, so that the method formally has the correct zero-density limit. The correlation of $\log_{10}(\Delta\eta^* + 1)$ was constructed by fitting to the original Assael-Dymond[2] scheme in order to reproduce the original viscosity predictions over the range $1.5 < V_r < 2.5$. This was done so as to retain the V_0 correlations of the original scheme in this region where it was known to perform with good accuracy. The coefficients so determined are given in Table 8.1.

As the method requires knowledge of the dilute gas viscosity η_0, the scheme is accompanied by correlative methods, such as the Lucas method or the approximation of Chung, which are used to estimate dilute gas viscosity values.[19] To test the modified scheme, a consistent set of experimental data from methane to *n*-butane was employed to correlate V_0 with temperature, using the roughness factor expression of Assael *et al.*[2] The light alkanes were chosen as they were part of the original scheme and there are data extending from the dilute gas through to the dense gas, super-critical and liquid regimes. Although the modification of Caudwell is not intended as the preferred method for predicting gas viscosities, it was shown to agree with experimental data in this region to within approximately ± 5 %.

8.2.2.2 *The Ciotta Extension*

Following the work of Caudwell, Ciotta[18] extended the scheme to better represent the viscosity of high-density and high-viscosity fluids. To achieve this, the experimental data for a number of alkanes were considered in the high-density region where the dilute gas viscosity can be neglected. Since R_η is a function only of the carbon number, and V_0 of the carbon number and temperature, fixing a component and an isotherm implies unique values for V_0 and R_η, independent of the reduced volume V_r. Hence the procedure involved, first, determining $V_0(T)$ and R_η for components not included the original scheme for alkanes by matching the reduced viscosity data to the

Table 8.1 Coefficients in eqn (8.10) for correlation of the reduced residual viscosity.

Coefficient	Caudwell[17]	Ciotta[18]	Ciotta *et al.*[20]
a_1	5.14034	5.14262	6.27593
a_2	−35.4051	−35.5878	−48.5343
a_3	189.206	192.050	243.272
a_4	−555.836	−573.372	−652.150
a_5	907.176	957.420	972.838
a_6	−766.625	−833.368	−763.260
a_7	266.267	299.409	251.454

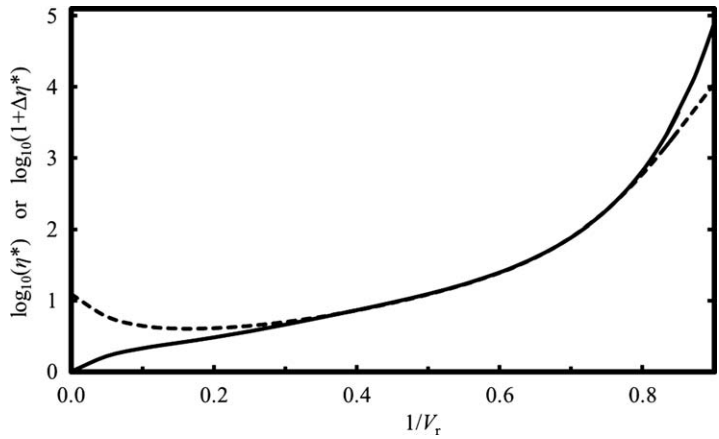

Figure 8.2 Universal curves for reduced viscosity η^* as a function of $1/V_r$ in the whole fluid domain, where V_r is reduced molar volume: dotted line, eqn (8.7); solid line, eqn (8.10) with the coefficients reported by Ciotta.[18]

universal curve of Assael and Dymond in the region $V_r > 1.5$. For components that were part of the original scheme, $V_0(T)$ and R_η were obtained from the existing correlation.[2] The reduced viscosity data that extended into the high-density region $V_r < 1.5$ were then used to construct an extension to the universal curve. Since the scheme is very sensitive to errors in the density, Ciotta used a restricted set of critically-evaluated experimental data for hexane, octane, decane, dodecane, hexadecane, and octadecane.[18] Ciotta also incorporated the extension of Caudwell and hence developed a correlation for $\log_{10}(\Delta\eta^* + 1)$ in the form of eqn (8.10), such that $\Delta\eta^*(V_r)$ follows Caudwell's correlation in the dilute region, the original scheme in the range $1.5 \leq V_r \leq 5$, and the new results extending down to reduced volumes of approximately $V_r = 1.2$. The coefficients of Ciotta's correlation are given in Table 8.1.

The universal curve of Ciotta is compared with the original correlation for η^*, eqn (8.7), in Figure 8.2. Although the differences at high densities appear quite small in the figure, the scale is logarithmic and the viscosities predicted by the two curves at $V_r < 1.5$ are actually very different. For example, at $1/V_r = 0.85$, $\Delta\eta^*$ from Ciotta's universal curve is about 85 % higher than the value of η^* given by eqn (8.7).

8.2.2.3 Optimized Reference Function

The universal curve emerging from the work of Caudwell[17] and Ciotta[18] allows the viscosity to be correlated over essentially the entire fluid range. The development of the extended universal curves described by Caudwell and Ciotta involved a certain amount of matching of one function to another and the problem has recently been revisited by Ciotta *et al.*[20] In this analysis, a large set of critically-evaluated viscosity and density data were assembled for alkanes ranging from methane to octadecane at temperatures in the range $110 \leq T/\mathrm{K} \leq 400$. Gaseous, liquid and supercritical states were

Table 8.2 Average absolute relative deviation Δ_{AAD}, maximum absolute relative deviation Δ_{MAD} and mean relative deviation Δ_{bias} for experimental viscosity data from the extended hard-sphere model of Ciotta *et al.*[20]

Substance	$10^2\Delta_{AAD}$	$10^2\Delta_{MAD}$	$10^2\Delta_{bias}$
Methane	2.8	11.8	−1.8
Ethane	2.3	9.6	1.8
Propane	1.4	6.4	0.4
Butane	1.7	7.6	1.1
Pentane	1.9	7.7	0.6
Hexane	2.5	5.3	1.0
Heptane	0.9	2.9	0.3
Octane	2.1	8.0	−1.6
Nonane	1.4	2.5	−1.4
Decane	1.7	4.5	−0.5
Undecane	0.6	1.8	−0.2
Dodecane	2.6	8.5	1.1
Hexadecane	1.2	3.9	0.0
Heptamethylnonane	2.4	9.6	0.1
Octadecane	1.1	3.8	0.0

included. The analysis was based on the reduced residual viscosity defined by eqn (8.9). For the alkanes up to decane, the dilute-gas viscosity was obtained from the correlations available in the REFPROP database,[16] while in other cases this term was estimated from the Lucas method. The correlations for $V_0(T)$ and R_η proposed by Assael *et al.*[2] were retained for the components up to dodecane. In the case of the other components considered (hexadecane, heptamethylnonane and octadecane), the values of R_η and the parameters of quadratic polynomials for $V_0(T)$ were optimized as a part of the analysis. The reduced residual viscosity was correlated with eqn (8.10), leading to the coefficients given in Table 8.1.

The data used in the determination of the new reference function covered the range $V_r \geq 1.19$, corresponding to $1/V_r \leq 0.84$ and $\Delta\eta^* \leq 2300$. Figure 8.3 compares the experimental reduced viscosities with the universal curve over the full range of the analysis. The relative deviations of $\Delta\eta^*$ seen at low densities appear large but, owing to effect of the term $(V_m)^{2/3}$ in eqn (8.9), they in fact correspond to small deviations of viscosity. The method was successfully applied to correlate viscosity data, not used in the development of the new reference function, extending up to $1/V_r = 0.9$ and $\Delta\eta^* \approx 80\,000$.

The ability of the extended hard-sphere model to represent the experimental data was quantified in terms of the average absolute relative deviation, Δ_{AAD}, the maximum absolute relative deviation, Δ_{MAD}, and the mean relative deviation, or bias, Δ_{bias}. These statistics are presented in Table 8.2 and show that the method provides a reliable correlation of the data.

8.2.3 Summary and Outlook

In conclusion, the extended hard sphere model, as refined by Ciotta *et al.*[20] is a useful tool for correlating the viscosity of complex fluids, irrespective of

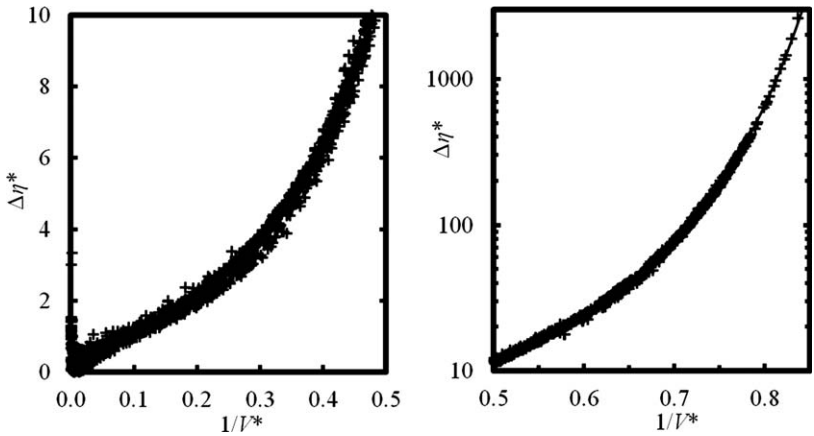

Figure 8.3 Comparison of experimental and correlated reduced resdiual viscosities $\Delta\eta^*$ as a function of $1/V_r$, where V_r is reduced molar volume, for C_1 to C_{18} alkanes in the temperature range $110 \leq T/K \leq 400$: +, experimental $\Delta\eta^*$; solid line, eqn (8.10) with parameters from Ciotta *et al.*[20]

molecular shape, over wide ranges of temperature, density and viscosity. Although, compared with the original scheme, the density range over which the reference function was fitted was extended by only 25 %, the viscosity range was increased by nearly a factor of 50. For the 16 alkanes considered in the determination of the universal curve,[20] 97 % of the data were fitted with relative deviations within ± 5 %, which is considered satisfactory for many industrial applications. The model was tested by correlating viscosity data not used in the development of the new reference function and was found to be successful at reduced densities up to 0.9, corresponding to a reduced residual viscosity of approximately 80 000. The simplicity and immediate applicability render the method a viable approach to describe highly viscous fluids.

It seems likely that the methodology described in this chapter could be applied to the thermal conductivity and self-diffusion coefficients, thereby extending the range of densities over which these properties may be correlated with the hard-sphere scheme. A considerable amount of new high-quality transport-property data has become available since the correlations for $V_0(T)$ and the roughness factors were developed in the early 1990s. For alkanes, these new data extend to higher temperatures and higher carbon numbers, and it would therefore be appropriate to revisit the correlations of $V_0(T)$ and roughness factors for this homologous series.

The hard-sphere scheme has been successfully applied to predict the transport properties of mixtures comprising molecules from the same homologous series.[4] This was accomplished by means of simple mixing rules for V_0 and the roughness factor. A remaining challenge is to develop generalized mixing rules that can be applied to more complex mixtures.

8.3 The Viscosity of Dense Mixtures: The Vesovic–Wakeham Method

NICOLAS RIESCO

8.3.1 Introduction

As discussed in Section 8.1, there is no molecular description of the viscosity of dense fluids that has reached the level of accuracy attained for dilute gases. The first attempt at such a description for a dense fluid of hard spheres and one of the most influential is due to Enskog.[21] The Enskog theory and its generalisation by Thorne[22] to model the viscosity of mixtures form the basis of the Vesovic–Wakeham (VW) method discussed in this section. The section starts with a presentation of the theoretical foundations of the VW method. This includes the original Enskog theory for pure fluids and two modifications known as Enskog-2σ and Enskog-chain that originated within the development of the VW method. It continues with a description of the VW method and its application to mixtures of spherical molecules (VW-sphere) and to mixtures of chain molecules (VW-chain). It finishes with a discussion on the future developments of the VW method.

8.3.1.1 The Enskog Theory

In the Enskog theory, molecules are represented as hard spheres that interact by means of elastic collisions. In principle, the viscosity of such a fluid can be determined by solving the Boltzmann equation. However, the complexity is such that only approximate solutions are known. The first approximate solution for a dilute fluid of hard-spheres was derived independently by Chapman and Enskog[23] in 1916 and 1917, respectively, and today is known as the Chapman–Enskog theory. The Enskog theory that extends the previous solution to dense conditions was derived in 1922 and it expresses the viscosity of a dense hard-sphere fluid as:

$$\eta = \eta^{(0)}\left[\frac{1}{\chi} + \alpha\rho_m + \frac{1}{\beta}\alpha^2\rho_m^2\chi\right], \tag{8.11}$$

where $\eta^{(0)}$ is the viscosity in the zero-density limit, ρ_{m} is the molar density, β is a constant equal to $(\mathbf{1}/\mathbf{4} + \mathbf{3}/\pi)^{-1}$, and parameters α and χ account for the two corrections originally introduced by Enskog: the excluded volume of a hard sphere and the increased collision frequency observed in dense fluids, respectively. The parameter α of a hard-sphere fluid is given by:

$$\alpha = \frac{8}{15}N_A\pi\sigma^3, \tag{8.12}$$

where N_A is the Avogadro number and σ is the hard-sphere diameter.

Using the Clausius virial expression for pressure, it is possible to prove that in the thermodynamic limit the parameter χ converges to the radial distribution function at contact.[23] For a hard-sphere fluid the radial distribution function at contact χ is often estimated using the following expression by Carnahan and Starling:[24]

$$\chi = \frac{1 - \frac{1}{2}y}{(1-y)^3}, \tag{8.13}$$

which is written in terms of the packing fraction $y = (\pi/6)\sigma^3\rho_m N_A$. The Enskog theory provides a good representation of the viscosity of a hard-sphere fluid up to moderate densities. For real fluids, however, a number of modifications have been proposed with varying degrees of success. Enskog himself[23] was first to propose that an effective hard-sphere diameter could be estimated by using the equation of state of a real fluid. Hanley *et al.*[25] showed that this approach, known as the *modified Enskog theory*, could reproduce the viscosity and thermal conductivity of simple gases up to twice the critical density within $\pm$(10 to 15)% as long as the hard-sphere diameter σ is allowed to vary with temperature. The current consensus is that the effective hard-sphere diameter is not only temperature dependent but also specific to a property.

Subsequently, di Pippo *et al.*[26] showed that a relative uncertainty of about $\pm$ 5 % for densities up to 1.8 times the critical density, could be achieved by using viscosity data to estimate the effective function χ. To ensure that the effective function χ determined from viscosity at a given temperature yields a realistic physical dependence on density, Sandler and Fiszdon[27] proved that it is essential that the effective parameter α is determined at the so-called *switch-over point* by solving the following equations:

$$\left(\frac{\partial\eta(T,\rho_m^*)}{\partial\rho_m}\right)_T = \frac{\eta^*}{\rho_m^*}, \tag{8.14}$$

and

$$\alpha = \frac{\eta^*}{\rho_m^*\eta^{(0)}\left(1 + \frac{2}{\sqrt{\beta}}\right)}, \tag{8.15}$$

where ρ_m^* and η^* are the molar density and viscosity at the switch-over point.

8.3.1.2 The Enskog-2σ Theory

The previous section presented the use of an effective hard-sphere diameter to model the viscosity of real fluids up to moderate densities. This limitation in density can be addressed with the Enskog-2σ theory.[28] It is based on a postulate that two effective hard-sphere diameters are required to account for the two assumptions originally made by Enskog, because there is no reason to believe that the effective size of a molecule contributing to the

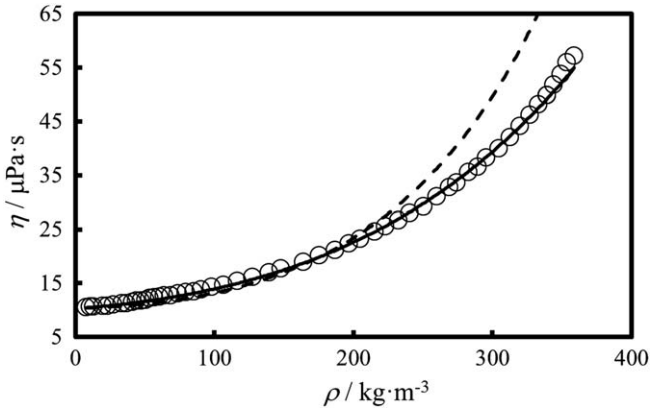

Figure 8.4 Viscosity of methane η at a temperature of 270.10 K and pressures up to 100 MPa as a function of mass density ρ. ○, measurements reported by van der Gulik *et al.*;[29] – –, Enskog; and —, Enskog-2σ.

dynamics of collision and to the excluded volume are the same. Thus, the Enskog-2σ theory proposes the use of two effective hard-sphere diameters: σ_α defined by eqn (8.12) (*i.e.* $\sigma_a = [15\alpha/(8\pi N_A)]^{1/3}$) that accounts for the excluded volume, and σ_χ defined by eqn (8.13) that accounts for the increased collision rate observed in dense fluids in comparison to the dilute gas.

The ability of the Enskog and the Enskog-2σ theories to reproduce the viscosity of methane at $T = 273.10$ K and pressures up to 100 MPa are compared in Figure 8.4. In the case of the Enskog theory, the effective hard-sphere diameter, σ, has been calculated from the value of parameter α by means of eqn (8.12). The parameter α was estimated at 273.10 K from the switch-over point by means of eqn (8.14) and (8.15). In the case of the Enskog-2σ theory, although the effective diameter σ_α has also been calculated at the switch-over point, the diameter σ_χ has been used as a fitting parameter to reproduce the viscosity of methane along the given isotherm. By introducing a pair of effective diameters, the Enskog-2σ theory is able to reproduce the viscosity of methane up to $p = 100$ MPa to within a relative difference of ± 3.3 %, as illustrated in Figure 8.4.

8.3.1.3 The Enskog-chain Theory

The Enskog theory is built on the assumptions that molecules can be represented as hard spheres and that only collisions between pairs of spheres contribute significantly to the transport properties of a fluid. For linear molecules at dense conditions it is not possible to ignore that, compared with spheres, they are more likely to collide with multiple molecules as they expose a larger surface. To overcome this difficulty, de Wijn *et al.*[30] proposed that linear molecules, such as *n*-alkanes, could be modelled as chains of hard spheres, and that collisions between those chains were so frequent

that they could be approximated by collisions between the segments making up the chains. To this end, the Enskog theory was modified by assuming that the viscosity of a dense fluid made up of N chain molecules with m spheres per chain could be approximated by that of the so-called *segment fluid*, made up of mN spheres. de Wijn *et al.*[30] also noted that the excluded volume and the radial distribution function of such spheres in the segment fluid must be corrected to account for the spheres belonging to a chain. Under these assumptions, the Enskog equation for chain molecules is written as:

$$\eta = \tilde{\eta}^{(0)}\left[\frac{1}{\tilde{\chi}} + \tilde{\alpha}\tilde{\rho} + \frac{1}{\beta}\tilde{\alpha}^2\tilde{\rho}^2\tilde{\chi}\right], \tag{8.16}$$

where all the physical quantities marked with a tilde refer to a segment belonging to a chain molecule. For instance, $\tilde{\rho}$ is the segment density and is given by $\tilde{\rho} = \rho m$. We follow this notation here, unlike in ref. 30, to avoid confusion between the usual symbol for viscosity in the zero-density limit $\eta^{(0)}$ and the corresponding parameter in the segment fluid, $\tilde{\eta}^{(0)}$. The excluded volume of a chain molecule was approximated by that of a spherocylinder, which resulted in the following expression for parameter α:

$$\tilde{\alpha} = \frac{8\pi}{15}N_A\sigma_\alpha^3\left(1 + \frac{3}{2}(m_\alpha - 1) + \frac{3}{8}(m_\alpha - 1)^2\right). \tag{8.17}$$

In the same work, de Wijn *et al.*[30] also proposed that the radial distribution function at contact $\tilde{\chi}$ of a hard sphere belonging to a chain could be determined using the Wertheim first-order perturbation theory (TPT1):[31]

$$\tilde{\chi} = \frac{1 - \frac{1}{2}y_\chi}{(1 - y_\chi)^3} - \frac{5}{8}\left(\frac{m_\chi - 1}{m_\chi}\right)\frac{1 - \frac{2}{5}y_\chi}{\left(1 - \frac{1}{2}y_\chi\right)(1 - y_\chi)}. \tag{8.18}$$

Lastly, $\tilde{\eta}^{(0)}$ is defined so that in the zero-density limit eqn (8.16) converges to $\eta^{(0)}$:

$$\tilde{\eta}^{(0)} = \eta^{(0)}\tilde{\chi}^{(0)} = \eta^{(0)}\left\{1 - \frac{5}{8}\left(\frac{m_\alpha - 1}{m_\alpha}\right)\right\}, \tag{8.19}$$

where $\tilde{\chi}^{(0)}$ is the radial distribution function at contact in the zero-density limit.

By using methane to define a fluid made of hard spheres and by analysing the viscosity of alkanes up to hexadecane in terms of eqn (8.14), (8.15) and (8.17) only, de Wijn *et al.*[30] found that m_α, the effective number of segments of the hard-sphere chain representing an alkane molecule, is independent of temperature and it is linked to C, the number of carbon atoms, by a simple linear relationship:

$$m_\alpha = 1 + (C - 1)/3. \tag{8.20}$$

It is remarkable that by using the same relationship, SAFT-HS EOS[32,33] is also able to predict the critical properties, vapour pressure and saturated

densities of alkanes. This relationship is usually[32] interpreted as a result of the carbon–carbon bond length for alkanes, 0.15 nm, being about one-third of the effective diameter of methane (*i.e.* the molecular simulation of thermodynamic properties by means of Lennard–Jones potential give a value of 0.38 nm).

8.3.2 Mixture Viscosities

Section 8.3.1 has introduced the theoretical foundations of the VW method. This section will present the VW method, a self-consistent procedure to interpolate mixture viscosities from the viscosity of each component. It starts with a review of its historical development and it concludes with a description of its latest formulation: VW-chain.

8.3.2.1 The VW Method for Spherical Molecules

The VW method is a predictive procedure to estimate mixture viscosities. It is based on the Enskog–Thorne theory[22] and therefore it models each component in the mixture by means of the effective parameters α and χ introduced in the preceding sections. The function χ is obtained by solving eqn (8.11), while the effective parameter α is determined following the switch-over procedure described by Sandler and Fiszdon,[27] eqn (8.14) and (8.15). This procedure not only ensures a realistic dependence of χ on density, but also that in the limit of composition of a mixture tending to one of its components viscosity tends to the viscosity of that component.

Vesovic and Wakeham[34,35] applied their formulation to both supercritical and liquid mixtures. The best results were observed for mixtures of supercritical gases, such as mixtures of (hydrogen + methane) with a maximum relative deviation of $\pm 2.7\,\%$ from experimental data and air with a maximum relative deviation of $\pm 1.7\,\%$. The uncertainty of the predictions increased when any of the components were below their critical temperature. For example, a maximum relative deviation of $\pm 5\,\%$ was reported for mixtures of (carbon dioxide + methane). The largest deviations were observed for liquid mixtures of propane and methane ranging from relative differences of $\pm$(5 to 7) %.

The deterioration observed for mixtures at temperatures where one of the components is in the sub-critical state can be ascribed to the difficulty in determining the switch-over point for that component. It has been observed for all the fluids studied to this date that if one could define the switch-over density below the critical temperature, this density would be located in the two-phase region. In other words, the switch-over density would be larger than the vapour density and smaller than the liquid density at the same temperature. The VW formulation proposed in 1989[35] addressed this difficulty by using the residual viscosity at supercritical temperatures to estimate the viscosity in the two phase region.

In a later attempt to extend the application of the 1989 formulation of the VW method to liquid mixtures, Assael *et al.*[36] proposed the use of their correlations for hard-sphere core volumes V^0 (see Section 8.2) to estimate the effective parameter α. The authors concluded[37–40] that the viscosities predicted in this manner were limited both in density and to molecules of similar viscosity at the same molar density.

In 2003, it became apparent[41,42] that the previously reported limitations in density were actually due to limitations in the mixing rule for χ. The mixing rule proposed in the 1989 formulation of the VW method and used by Assael *et al.*[37–40] was a truncated expression[43] that is only accurate up to moderate densities. Royal *et al.*[42] examined the use of two alternative expressions: the Lebowitz solution of the Percus–Yevick equation[44] and the empirical Carnahan–Starling equation,[45,46] and found both led to similar results. The use of the Carnahan–Starling equation extended significantly the density range of validity of the VW method, as Royal *et al.*[42] demonstrated with the prediction of the viscosities of liquid mixtures of (hexane + heptane) within relative differences of ± 2.3 %.

Royal *et al.*[42,47] also attempted to address the limitations observed in mixtures of molecules of different size and polarity. They argued that for these mixtures the hard-sphere diameters σ_i in the Lebowitz–Percus–Yevick mixing rule have to be replaced by the effective values resulting from a compositional average: $\bar{\sigma}_i = \sum_j x_j(\sigma_i + \sigma_j)/2$. We refer to the VW method using the modified Lebowitz–Percus–Yevick mixing rule as *the RVW method* and the VW method using the Carnahan–Starling equation as *VW-sphere*.

The RVW method has been used to predict the viscosity of liquid linear, cyclic and aromatic alkane mixtures,[42] and also of refrigerant blends.[47] In all cases, a significant improvement was observed. In the case of liquid alkane mixtures, all the viscosities were predicted within relative differences of ± 8.8 % and in the case of refrigerant blends it was estimated that, although there was a slight bias towards under prediction, the relative differences of the RVW method is about ± 7 %. Despite this significant improvement, it has to be noted that both the RVW method and VW-sphere work best for mixtures of similarly-sized molecules.

One of the applications of the VW method is for the prediction of natural gas viscosity. The early works[48,49] using the 1989 formulation of the VW method already reported predictions with relative differences within ± 5 %. More recent work[50] using the RVW method estimated that the relative uncertainty of the viscosity predictions for natural gas at temperatures between (260 and 400) K and pressures up to 20 MPa is within ± 2 %, and at lower temperatures and higher pressures is in the order of between ± (3 and 4) %. Figure 8.5 illustrates that this remarkably small uncertainty can also be achieved using VW-sphere to predict the experimental data for natural gas measured by Schley *et al.*,[51] which has a relative experimental uncertainty of ± 0.5 %.

As discussed above, the VW-sphere works best for mixtures of similarly-sized molecules. For this reason, it is important that natural gas mixtures

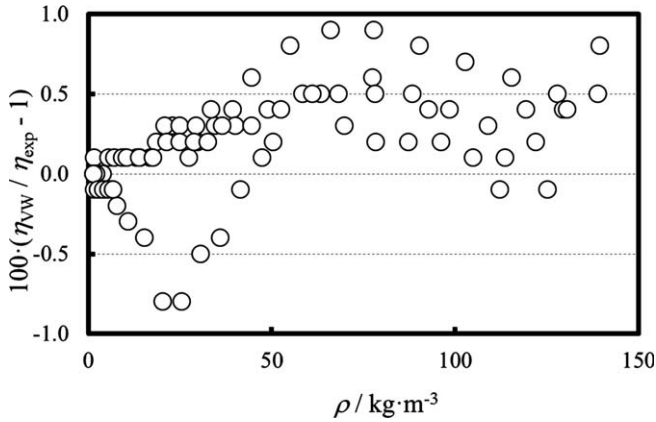

Figure 8.5 Fractional differences ($\eta_{VW}/\eta_{exp} - 1$) of the viscosity obtained using VW-sphere η_{VW} from the experimental data for natural gas of Schley *et al.*[51] η_{exp} as a function of mass density ρ.

modelled using VW-sphere exclude any trace amounts of long chain alkanes, hexane and longer. Although their presence does not contribute significantly to the mixture viscosity,[52] modelling them as effective spheres leads to a deterioration of the predictions obtained using the VW method for spheres.

8.3.2.2 The VW Method for Chain Molecules

This section presents the latest formulation of the VW method: *VW-chain*.[53] VW-chain extends the VW method so that the viscosity of mixtures of linear molecules of different size can be predicted accurately. To do so, the components of the mixture are now modelled using the Enskog-chain theory described in Section 8.3.1.3. The Enskog-chain theory represents molecules as chains of m tangentially-joined hard spheres, each sphere of diameter σ. VW-chain also follows the principles of the Enskog-2σ theory and for each component it defines four effective parameters: σ_α, m_α, σ_χ and m_χ. One set of effective parameters is designated by subscript α and is computed at the switch-over point using eqn (8.14) and (8.15). The other set of parameters is designated by subscript χ and is computed using the values of χ that reproduce the experimental viscosity of each component.

The VW-sphere method states that the effective function χ of each component is to be calculated at the same temperature and molar density as that of the mixture. This is a reasonable choice when all the components in the mixture are similarly sized. However, this choice becomes unsuitable for mixtures of molecules of different size, because it leads to very different packing fractions. For this reason, the VW-chain method recommends the effective parameter χ of a pure species is calculated at a reduced density that provides a good representation of the conditions found in the mixture. In the case of alkane mixtures, this reduced density was defined in terms of the critical density.[53]

Once the parameters for each component are known, the viscosity of their mixtures can be predicted using the following equations:

$$\eta = \tilde{K}_{\mathrm{mix}} - \frac{\begin{vmatrix} \tilde{H}_{11} & \dots & \tilde{H}_{1N} & \tilde{Y}_1 \\ \vdots & \ddots & \vdots & \vdots \\ \tilde{H}_{N1} & \dots & \tilde{H}_{NN} & \tilde{Y}_N \\ \tilde{Y}_1 & \dots & \tilde{Y}_N & 0 \end{vmatrix}}{\begin{vmatrix} \tilde{H}_{11} & \dots & \tilde{H}_{1N} \\ \vdots & \ddots & \vdots \\ \tilde{H}_{N1} & \dots & \tilde{H}_{NN} \end{vmatrix}}, \tag{8.21}$$

$$\tilde{K}_{\mathrm{mix}} = \frac{3\tilde{\rho}^2}{\pi} \sum_{\mathrm{i,j}} \tilde{x}_{\mathrm{i}} \tilde{x}_{\mathrm{j}} \tilde{\chi}_{\mathrm{ij}} \tilde{\alpha}_{\mathrm{ij}}^2 \tilde{\eta}_{\mathrm{ij}}^{(0)}, \tag{8.22}$$

$$\tilde{Y}_{\mathrm{i}} = \tilde{x}_{\mathrm{i}} \left[1 + \tilde{\rho} \sum_{\mathrm{j}} \frac{\tilde{M}_{\mathrm{j}}}{\tilde{M}_{\mathrm{i}} + \tilde{M}_{\mathrm{j}}} \tilde{x}_{\mathrm{j}} \tilde{\alpha}_{\mathrm{ij}} \tilde{\chi}_{\mathrm{ij}} \right], \tag{8.23}$$

$$\tilde{H}_{\mathrm{ij}} = \frac{-\tilde{x}_{\mathrm{i}} \tilde{x}_{\mathrm{j}} \tilde{\chi}_{\mathrm{ij}}}{2A_{\mathrm{ij}}^{*} \tilde{\eta}_{\mathrm{ij}}^{(0)}} \frac{\tilde{M}_{\mathrm{i}} \tilde{M}_{\mathrm{j}}}{\left(\tilde{M}_{\mathrm{i}} + \tilde{M}_{\mathrm{j}}\right)^2} \left[\frac{20}{3} - 4A_{\mathrm{ij}}^{*} \right], \tag{8.24}$$

and

$$\tilde{H}_{\mathrm{ii}} = \tilde{x}_{\mathrm{i}}^2 \frac{\tilde{\chi}_{\mathrm{ii}}}{\tilde{\eta}_{\mathrm{i}}^{(0)}} + \sum_{j \neq i} \frac{\tilde{x}_i \tilde{x}_j \tilde{\chi}_{\mathrm{ij}}}{2A_{\mathrm{ij}}^{*} \tilde{\eta}_{\mathrm{ij}}^{(0)}} \frac{\tilde{M}_{\mathrm{i}} \tilde{M}_{\mathrm{j}}}{\left(\tilde{M}_{\mathrm{i}} + \tilde{M}_{\mathrm{j}}\right)^2} \left[\frac{20}{3} + 4 \frac{\tilde{M}_{\mathrm{j}}}{\tilde{M}_{\mathrm{i}}} A_{\mathrm{ij}}^{*} \right], \tag{8.25}$$

where now the segment density $\tilde{\rho}$ is computed as $\tilde{\rho} = \left(\sum_{\mathrm{i}} x_{\mathrm{i}} m_{\mathrm{i}}\right)\rho$, x_{i} is the mole fraction of component i and $\tilde{x}_{\mathrm{i}} = x_{\mathrm{i}} m_{\mathrm{i}} / \left(\sum_{\mathrm{j}} x_{\mathrm{j}} m_{\mathrm{j}}\right)$ is the segment fraction. $\tilde{M}_{\mathrm{i}}$ equals $M_{\mathrm{i}}/m_{\mathrm{i}}$, where M_{i} and $\tilde{M}_{\mathrm{i}}$ are the molecular and segment masses, respectively. A_{ij}^{*} is the ratio of collision integrals[54] and the interaction parameters $\tilde{\eta}_{\mathrm{ij}}^{(0)}$, $\tilde{\alpha}_{\mathrm{ij}}$ and $\tilde{\chi}_{\mathrm{ij}}$ are estimated using the following series of mixing rules:

$$\tilde{\eta}_{\mathrm{ij}}^{(0)} = \eta_{\mathrm{ij}}^{(0)} \tilde{\chi}_{\alpha,\mathrm{ij}}^{(0)}. \tag{8.26}$$

The mixing rule for $\tilde{\alpha}_{\mathrm{ij}}$ was derived using only geometric arguments:[30]

$$\frac{\tilde{\alpha}_{\mathrm{ij}}}{\tilde{\alpha}_{\mathrm{segment,\,ij}}} = 1 + \frac{3}{2} \left(\frac{\left(\frac{\tilde{\alpha}_{\mathrm{segment,\,i}}}{\tilde{\alpha}_{\mathrm{segment,\,ij}}}\right)^{1/3} \left(m_{\alpha,\mathrm{i}} - 1\right) + \left(\frac{\tilde{\alpha}_{\mathrm{segment,\,j}}}{\tilde{\alpha}_{\mathrm{segment,\,ij}}}\right)^{1/3} \left(m_{\alpha,\mathrm{j}} - 1\right)}{2} \right)$$

$$+ \frac{3}{8} \left(\frac{\tilde{\alpha}_{\mathrm{segment,\,i}}}{\tilde{\alpha}_{\mathrm{segment,\,ij}}}\right)^{1/3} \left(m_{\alpha,\mathrm{i}} - 1\right) \left(\frac{\tilde{\alpha}_{\mathrm{segment,\,j}}}{\tilde{\alpha}_{\mathrm{segment,\,ij}}}\right)^{1/3} \left(m_{\alpha,\mathrm{j}} - 1\right), \tag{8.27}$$

$$\tilde{\alpha}^{1/3}_{\text{segment, ij}} = \frac{1}{2}\left(\tilde{\alpha}^{1/3}_{\text{segment, i}} + \tilde{\alpha}^{1/3}_{\text{segment, j}}\right) \propto \tilde{\sigma}_{\alpha,\text{ij}} = \frac{1}{2}\left(\tilde{\sigma}_{\alpha,\text{i}} + \tilde{\sigma}_{\alpha,\text{j}}\right), \tag{8.28}$$

and the mixing rule for $\tilde{\chi}_{\text{ij}}$ was derived[53] following the approach described in SAFT-HS-EOS:[32]

$$\tilde{\chi}_{\text{ij}} = \tilde{\chi}_{\text{CS,ij}}\left(\tilde{\chi}^{(0)}_{\text{ij}} + F(\tilde{\rho})\right), \tag{8.29}$$

$$\tilde{\chi}_{\text{CS,ij}} = \frac{1}{1-\tilde{\xi}_3} + 3\left(\frac{\tilde{\sigma}_{\chi,\text{i}}\tilde{\sigma}_{\chi,\text{j}}}{\tilde{\sigma}_{\chi,\text{i}} + \tilde{\sigma}_{\chi,\text{j}}}\right)\frac{\tilde{\xi}_2}{\left(1-\tilde{\xi}_3\right)^2} + 2\left(\frac{\tilde{\sigma}_{\chi,\text{i}}\tilde{\sigma}_{\chi,\text{j}}}{\tilde{\sigma}_{\chi,\text{i}} + \tilde{\sigma}_{\chi,\text{j}}}\right)^2\frac{\tilde{\xi}_2^2}{\left(1-\tilde{\xi}_3\right)^3}, \tag{8.30}$$

$$\tilde{\chi}^{(0)}_{\text{ij}} = 1 - \frac{1}{8}\left[\left(\frac{m_{\chi,\text{i}}-1}{m_{\chi,\text{i}}}\right)\left(\frac{\tilde{\sigma}^3_{\chi,\text{j}} + \frac{3}{2}\tilde{\sigma}_{\chi,\text{i}}\tilde{\sigma}^2_{\chi,\text{j}}}{\left(\frac{\tilde{\sigma}_{\chi,\text{i}} + \tilde{\sigma}_{\chi,\text{j}}}{2}\right)^3}\right) + \left(\frac{m_{\chi,\text{j}}-1}{m_{\chi,\text{j}}}\right)\left(\frac{\tilde{\sigma}^3_{\chi,\text{i}} + \frac{3}{2}\tilde{\sigma}_{\chi,\text{j}}\tilde{\sigma}^2_{\chi,\text{i}}}{\left(\frac{\tilde{\sigma}_{\chi,\text{i}} + \tilde{\sigma}_{\chi,\text{j}}}{2}\right)^3}\right)\right], \tag{8.31}$$

$$F(\tilde{\rho}) = \frac{\sum_{\text{i,j}}\tilde{x}_\text{i}\tilde{x}_\text{j}\left(\frac{\pi}{6}\left(\frac{\tilde{\sigma}_{\chi,\text{i}} + \tilde{\sigma}_{\chi,\text{j}}}{2}\right)^3\right)\tilde{\chi}_{\text{CS,ij}}\left(1-\tilde{\chi}^{(0)}_{\text{ij}}\right) + \frac{\tilde{Z}_{\text{chain}}}{4\tilde{\rho}}}{\sum_{\text{i,j}}\tilde{x}_\text{i}\tilde{x}_\text{j}\left(\frac{\pi}{6}\left(\frac{\tilde{\sigma}_{\chi,\text{i}} + \tilde{\sigma}_{\chi,\text{j}}}{2}\right)^3\right)\tilde{\chi}_{\text{CS,ij}}}, \tag{8.32}$$

and

$$\tilde{Z}_{\text{chain}} = -\sum_\text{i}\tilde{x}_\text{i}\left(\frac{m_{\chi,\text{i}}-1}{m_{\chi,\text{i}}}\right)\left(\frac{\tilde{\xi}_3\left(1-\tilde{\xi}_3\right) + \frac{3}{2}\tilde{\sigma}_{\chi,\text{i}}\tilde{\xi}_2\left(1+\tilde{\xi}_3\right) + \frac{1}{2}\tilde{\sigma}^2_{\chi,\text{i}}\tilde{\xi}^2_2\left(\frac{2+\tilde{\xi}_3}{1-\tilde{\xi}_3}\right)}{\left(1-\tilde{\xi}_3\right)^2 + \frac{3}{2}\tilde{\sigma}_{\chi,\text{i}}\tilde{\xi}_2\left(1-\tilde{\xi}_3\right) + \frac{1}{2}\tilde{\sigma}^2_{\chi,\text{i}}\tilde{\xi}^2_2}\right). \tag{8.33}$$

The VW-chain method has been successfully used to estimate the viscosity of liquid alkane mixtures. Figure 8.6 illustrates the remarkable accuracy achieved using the VW-chain method to predict the viscosity of octane and dodecane mixtures over a wide range of temperatures from 298 K up to 473 K and at pressures up to 200 MPa. All the predictions are within ± 4 % and the overall average absolute relative deviation is ± 1.5 %.

The VW-chain method has also been applied to predict the viscosity of very asymmetric mixtures, *i.e.* mixtures that contain molecules with large size differences. This kind of mixtures is characterised by a significant variation

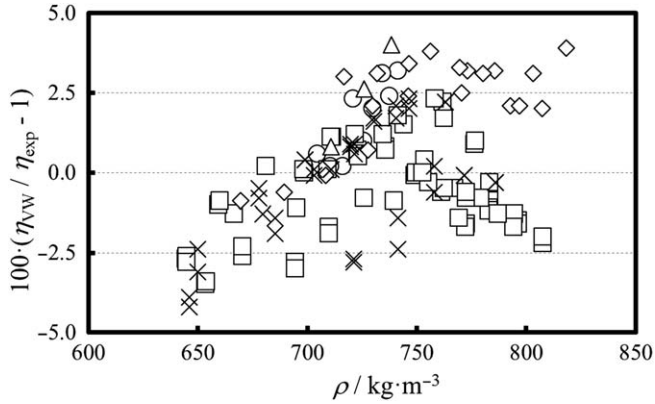

Figure 8.6 Viscosity η_{VW} estimated using VW-chain as deviations from η_{exp} the experimentally determined viscosity for (octane + dodecane) as a function of mass density ρ at temperatures between (298 and 473) K and pressures up to 200 MPa. ◇, Dymond *et al.*;[56] △, Chevalier *et al.*;[57] ○, Aucejo *et al.*;[58] □, Caudwell;[17] and ×, Peleties.[59]

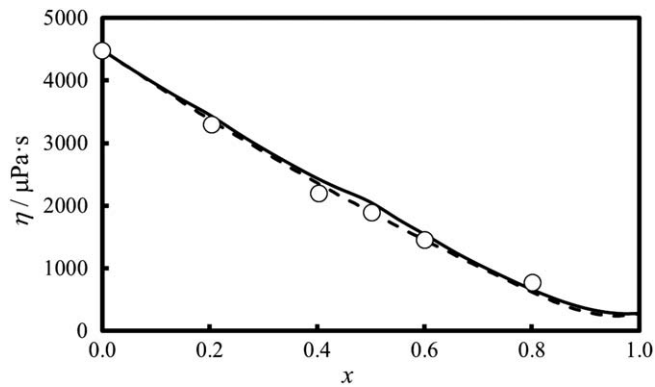

Figure 8.7 Viscosity η of [x heptane + (1 − x) tetracosane] mixtures at a temperature of 333.15 K and pressure of 0.1 MPa. ○, measurements reported by Queimada *et al.*;[60] —, VW method and experimental mixture densities; – –, VW method and ideal mixture densities.

of viscosity and density with composition. The estimation of their thermophysical properties is known to be a challenging problem,[55] and especially for viscosity it is also very sensitive to density. This sensitivity is illustrated in Figure 8.7, where small changes in density ranging from (0.2 to 0.7) % translate into viscosity changes from (2 to 8) %.

8.3.3 Summary and Outlook

The preceding sections have illustrated the ability of the VW method to interpolate mixture viscosities with no adjustable parameters in a manner

that is both accurate and consistent with the viscosity of each component. A number of different formulations of the VW method have been presented, each with varying ranges of application, and the results reported in the literature have been reviewed. Based on these results, we recommend the use of VW-chain to estimate mixture viscosities at dense conditions, and VW-sphere to estimate mixture viscosities of similarly-sized molecules, from dense conditions to the dilute limit. We can reasonably expect further developments in the VW method and in this final section we will outline some of them.

We start the discussion with the limitations ascribed to the underlying theories behind the VW-sphere and VW-chain methods. Whereas VW-sphere is based on the Enskog theory for hard spheres and has been found to be limited to mixtures of similarly-sized molecules, VW-chain is based on the Enskog-chain theory and has been found to be limited to dense mixtures. These limitations in density can be understood by considering the collision dynamics between a pair of chain molecules in the dilute limit and at dense conditions. In the dilute limit, the collision frequency is low enough that collisions other than binary can be neglected. At dense conditions, as described in Section 8.3.1.3, it is not possible to ignore that the segment of a chain molecule undergoes collisions with segments of other chain molecules. A focus of current research is a modification of VW-chain that defines an effective number of segments that in the dilute limit converges to one and at dense conditions to the value predicted using VW-chain.

As discussed in Section 8.3.2.1, both VW-sphere and VW-chain require a choice of reference density at which the effective parameter χ of each component is calculated. Although the theory behind VW-sphere suggests the use of molar density, this choice is not suitable for VW-chain and a number of alternatives have been explored.[53] At this time it is not possible to determine what the optimum choice is and further research with molecules of different nature is required.

Soon after the 1989 formulation was proposed, it became clear the switch-over density at subcritical temperatures was located in the two-phase region, *i.e.* between the vapour and liquid densities. To this date, five approaches have been proposed to extend the definition of the switch-over point into the two-phase region: (i) the use of the residual viscosity at supercritical temperatures as an estimation of its value at subcritical temperatures,[35] (ii) the use of the V^0 correlations from the Dymond–Assael scheme,[36] (iii) the use of the switch-over point of methane to estimate the switch-over point for other alkanes,[53] (iv) the use of viscosity correlations that interpolate smoothly between the vapour and liquid phases, (v) the extrapolation of the switch-over point correlated at supercritical temperatures into the subcritical region. At Imperial College, we are currently developing an alternative approach that takes advantage of the ability of the Enskog-2σ theory to interpolate the viscosity of a fluid between the vapour and liquid phases.

Another area where further progress is expected is in the extension of the mixing rule for $\tilde{\chi}_{ij}$ to highly asymmetric mixtures, especially at compositions rich in the component of the smallest molar mass. As discussed in the

previous section, this is a problem compounded not only by the choice of density reference at which the parameters characterising each component are calculated, but also by the accuracy with which mixture densities are known.

We finish this section by mentioning the latest development in the family of VW methods: *VW-pseudo*. VW-pseudo is a novel approach that aims at predicting the viscosity of mixtures for which the components are not fully known in nature or composition, such as petroleum fluids. It is not possible, or desirable, to describe every component present in this kind of mixture. Rather, VW-pseudo introduces an alternative description where the original components are lumped into pseudo-components defined by their molecular mass and it applies the mixing rules in the VW method to predict the viscosity of the resulting mixture. Preliminary results for alkane mixtures are promising and are precise for mixtures containing components consisting of up to 30 carbon atoms.

Acknowledgements

The author would like to acknowledge that this work was supported by Qatar Carbonates and Carbon Storage Research Centre. QCCSRC is funded jointly by Qatar Petroleum, Shell, and the Qatar Science & Technology Park.

8.4 The Friction Theory for Viscosity Modelling

SERGIO E. QUIÑONES-CISNEROS

8.4.1 Basic Concepts

In the Friction Theory (FT) for viscosity modelling, the total shear viscosity η is separated into a dilute gas viscosity, η_0 and a residual friction viscosity, η_f

$$\eta = \eta_0 + \eta_f. \tag{8.34}$$

The dilute gas viscosity is theoretically well understood and is defined as the viscosity in the zero-density limit arising from the motion and interactions between particles of a finite mass (see Chapter 7), whereas the residual viscosity term, in the FT perspective, is related to friction concepts of classical mechanics.

The fundamental mechanical concept of friction is well known and can be found in almost all elementary engineering textbooks on statics and dynamics.[61] Mechanical friction deals with the macroscopic description of the forces that oppose the sliding of two bodies against each other. In the case of dense fluids, if a shear stress is applied to any portion of a confined fluid, the fluid will move (or deform as in the case of viscoelastic fluids). For instance, considering a fluid placed between two close but large parallel plates of area A, if an appropriate shearing force F is applied to the upper plate in order to achieve a constant velocity u_0, while keeping the lower plate fixed, a shear stress $\tau = F/A$ will be exerted on the fluid between the plates. Experiments show that the fluid in immediate contact with the solid boundaries has the same velocity as the boundaries (the no-slip boundary condition), and that F is, for many fluids, directly proportional to A as well as u_0, and inversely proportional to the thickness z. That is, by considering the fluid to be made up of many layers of differential thickness parallel to the flat surface, the flow may be described in terms of the rate of shear (du/dz), *i.e.* the change of rate at which one layer moves relative to an adjacent layer. Thus, the Newton's law of viscosity properly describes the flow:

$$\tau = \eta \frac{du}{dz}. \tag{8.35}$$

In general, η is not a constant, and fluids are classified as *Newtonian* or *non-Newtonian* depending on whether or not η is, for practical purposes, found to be independent of the shear rate (du/dz). Furthermore, there are fluids that under some conditions behave like an elastic solid body instead of flowing spontaneously. All these concepts, definitions and derivations can be found elsewhere within the extensively available rheology literature.[62,63]

In the case of a fluid at rest, for the sake of generality, let us assume that the normal stress, *i.e.* the isotropic total pressure p, is given by some contributions that may be of different physicochemical nature, *i.e.*

$$p = p_{\mathrm{I}} + p_{\mathrm{II}} + p_{\mathrm{III}} + \cdots \tag{8.36}$$

These contributions can be due to a repulsive pressure term p_{r}, an attractive pressure term, p_{a}, or even a renormalization scaling term, p_{sc}, according to the detailed physicochemical concepts that may be built into the specific equation of state (EoS). For instance we could consider the crossover model proposed by Kiselev and Ely,[64,65] which is based on the cubic Patel–Teja[66] EoS, from which the p_{r}, p_{a} and crossover p_{sc} terms can be separated.[67] As the fluid is subjected to an external shear force, we assume that each one of the physicochemical interactions also give rise to shear stress (friction force) contributions of a related nature, *i.e.*

$$\tau = \tau_{\mathrm{I}} + \tau_{\mathrm{II}} + \tau_{\mathrm{III}} + \cdots \tag{8.37}$$

Then, by analogy with the general derivation of the Amontons–Coulomb law of friction, we further assume that each one of the contributions to the shear stress follows from a series expansion of its corresponding normal stress. That is,

$$\tau = \left(\sum_{i=1}^{n_{\mathrm{I}}} \mu_{\mathrm{I},i} p_{\mathrm{I}}^{i}\right) + \left(\sum_{i=1}^{n_{\mathrm{II}}} \mu_{\mathrm{II},i} p_{\mathrm{II}}^{i}\right) + \left(\sum_{i=1}^{n_{\mathrm{III}}} \mu_{\mathrm{III},i} p_{\mathrm{III}}^{i}\right) + \cdots . \tag{8.38}$$

In eqn (8.38) $\mu_{\mathrm{I},i}$, $\mu_{\mathrm{II},i}$, $\mu_{\mathrm{III},i}$,... are the kinematic friction coefficients associated with the possible contributions contemplated on the right hand side of eqn (8.37). Consequently, substituting eqn (8.38) into the Newton's law of viscosity, eqn (8.35), yields

$$\eta_{\mathrm{f}} = \left(\sum_{i=1}^{n_{\mathrm{I}}} \kappa_{\mathrm{I},i} p_{\mathrm{I}}^{i}\right) + \left(\sum_{i=1}^{n_{\mathrm{II}}} \kappa_{\mathrm{II},i} p_{\mathrm{II}}^{i}\right) + \left(\sum_{i=1}^{n_{\mathrm{III}}} \kappa_{\mathrm{III},i} p_{\mathrm{III}}^{i}\right) + \cdots \tag{8.39}$$

where the different $\kappa_{\mathrm{I},i}$, $\kappa_{\mathrm{II},i}$, $\kappa_{\mathrm{III},i}$, ... are friction coefficients given by

$$\kappa_{\mathrm{I},i} = \frac{\mu_{\mathrm{I},i}}{\mathrm{d}u/\mathrm{d}z}, \quad \kappa_{\mathrm{II},i} = \frac{\mu_{\mathrm{II},i}}{\mathrm{d}u/\mathrm{d}z}, \quad \kappa_{\mathrm{III},i} = \frac{\mu_{\mathrm{III},i}}{\mathrm{d}u/\mathrm{d}z}, \ldots , \tag{8.40}$$

and which in the case of Newtonian fluids must be independent of the rate of shear ($\mathrm{d}u/\mathrm{d}z$); it should be observed that the relaxation of this condition leads to a general model for non-Newtonian fluids.

8.4.2 Applications of the Friction Theory

8.4.2.1 Cubic EoS

The FT approach has been successfully applied to many different fluids, from simple fluids to even complex heavy oils.[68] Necessarily, the application of the FT requires an equation of state (EoS) that will allow the derivation of

the different terms described in eqn (8.36). One of the simplest and most successful applications has been the extension of the FT to the viscosity modelling of industrial fluids, such as reservoir fluids, in wide ranges of conditions (temperature, pressure and composition) based on the popular cubic EoS[69,70] of the van der Waals type. Following the van der Waals separation of the total pressure into a repulsive, p_r, and an attractive contribution, p_a,

$$p = p_r + p_a, \tag{8.41}$$

from eqn (8.37) the shear stress is also separated into a repulsive (τ_r) and an attractive contribution (τ_a),

$$\tau = \tau_r + \tau_a. \tag{8.42}$$

According to eqn (8.38), the contributions to τ are given by

$$\tau_r = \sum_{i=1}^{n_r} \mu_{r,i} p_r^i, \tag{8.43}$$

and

$$\tau_a = \sum_{i=1}^{n_a} \mu_{a,i} p_a^i. \tag{8.44}$$

Thus, from eqn (8.39) and (8.40) the friction contribution to the viscosity may be represented by the following series,

$$\eta_f = \sum_{i=1}^{n_a} \kappa_{a,i} p_a^i + \sum_{i=1}^{n_r} \kappa_{r,i} p_r^i, \tag{8.45}$$

where, assuming Newtonian behaviour, the $\kappa_{r/a,i}$ are temperature-dependent friction parameters related to friction coefficients between sliding surfaces subject to the p_a and p_r normal stresses and independent of the rate of shear. For applications involving a cubic EoS, owing to the strong high-pressure dominance of the repulsive term given by the hard-core excluded volume, a linear model for the attractive contribution together with a quadratic model for the repulsive contribution ($n_a = 1$, $n_r = 2$) have been found to be sufficient for many engineering applications.[68,71–76]

The direct application of this approach to normal alkanes has resulted in the development of a pragmatic one-parameter FT model[77]

$$\eta_f = \eta_c \left(\widehat{\kappa}_a \left(\frac{p_a}{p_c} \right) + \widehat{\kappa}_r \left(\frac{p_r}{p_c} \right) + \widehat{\kappa}_r \left(\frac{p_r}{p_c} \right)^2 \right), \tag{8.46}$$

where the $\widehat{\kappa}_{a/r}$ are universal functions of temperature for a given EoS and η_c is a scaling parameter for a particular fluid. The one-parameter model is capable of accurately describing several fluids of industrial relevance. Figure 8.8 illustrates its application to propane.[78]

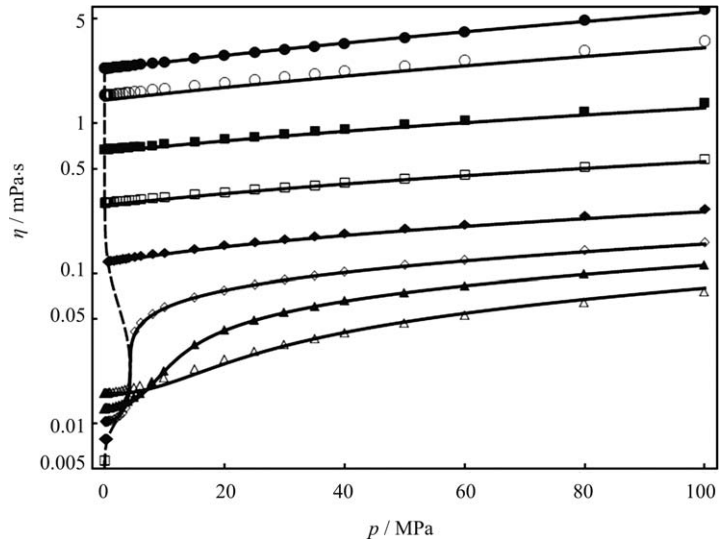

Figure 8.8 Comparison of the viscosity η obtained from one parameter FT model results for propane along with the recommended values reported by Vogel *et al.*[78] as a function of pressure p. ———, FT model isotherms; – – – –, FT model phase boundary; recommended data reported by Vogel *et al.*[78]: ●, $T = 110$ K; ○, $T = 120$ K; ■, $T = 150$ K; □, $T = 200$ K; ◆, $T = 280$ K; ◇, $T = 370$ K; ▲, $T = 460$ K; △, $T = 600$ K.

By taking advantage of an additional compressibility correction parameter,[68] as well as related mixing rules,[77] the one-parameter model approach has been further developed for the accurate description of such complex systems as reservoir fluids at the high pressure and high temperature conditions normally found in deep water reservoirs, shown in Figure 8.9, as well as for heavy oils shown in Figure 8.10.

8.4.2.2 *Generalized Friction Theory*

The previous results were achieved using cubic EoS, which exhibit explicit separation into repulsive and attractive terms. However, for general applications a suitable EoS may not be explicitly defined in terms of "attractive" and "repulsive" contributions. For such cases it has been proposed to use the internal pressure (π_T),[67]

$$\pi_T = \left(\frac{\partial U}{\partial V_m}\right)_T = T\left(\frac{\partial p}{\partial T}\right)_{V_m} - p, \tag{8.47}$$

where U is the internal energy. Although, as pointed out by van Uden *et al.*,[79] the literature concerning the internal pressure is confusing, it is a useful thermodynamic property. Indeed, it is of relevance to point out that for the van der Waals EoS,[80]

$$p = \frac{RT}{V_m - b} - \frac{a}{V_m^2}, \tag{8.48}$$

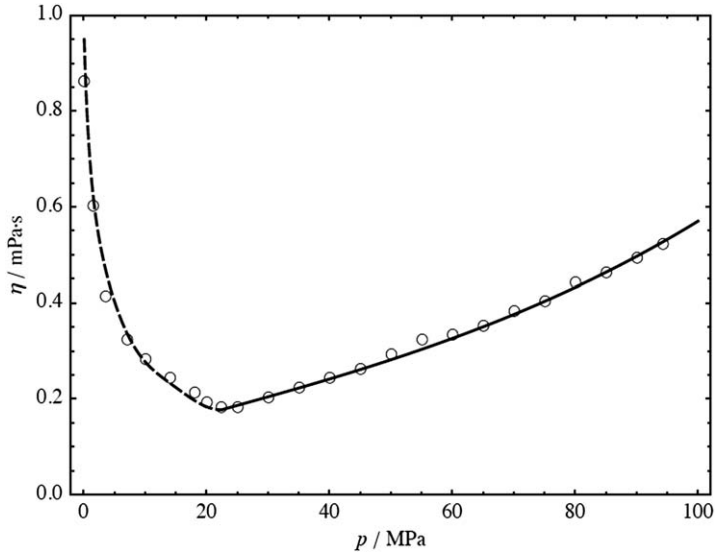

Figure 8.9 FT model predicted viscosity η for a light North Sea oil with molar mass of 80.9 $g \cdot mol^{-1}$ at $T = 418$ K as a function of pressure p. ———, FT model results for the high pressure one-phase region; – – – – –, FT model results for the oil phase after differential separation; ○, experimental results.

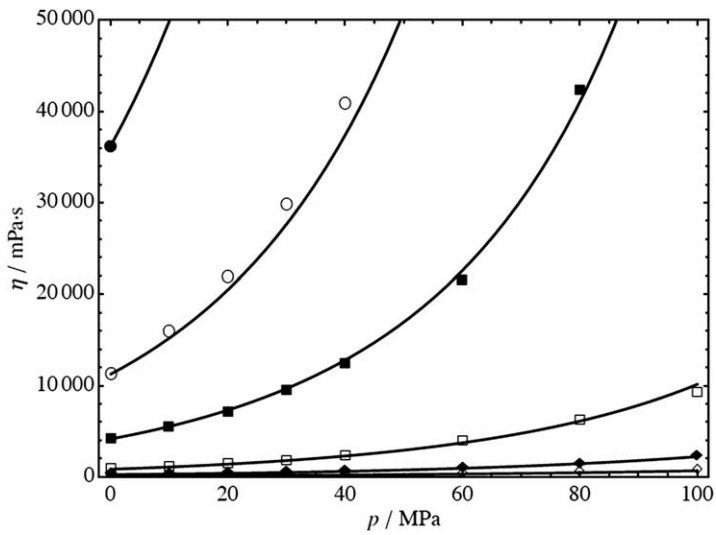

Figure 8.10 FT model predicted viscosity η for a stabilized heavy Mexican oil with molar mass of 418 $g \cdot mol^{-1}$ as a function of pressure p. ———, FT model isotherms; ●, $T = 293.15$ K; ○, $T = 303.15$ K; ■, $T = 313.15$ K; □, $T = 333.15$ K; ◆, $T = 353.15$ K; ◇, $T = 373.15$ K.

the internal pressure is given by,

$$\pi_T = \frac{a}{V_m^2}. \tag{8.49}$$

This leads to the interpretation of π_T as a property related to intermolecular cohesion. Furthermore, the substitution of the classical van der Waals repulsive term by the hard-spheres term of Carnahan–Starling[24] naturally leads to similar results. In fact, eqn (8.49) holds for all EoS that consists of a van der Waals attractive term and a repulsive term that is linear in T. Thus, for the purposes of the FT approach, the following pragmatic definitions, for the attractive and the repulsive part of the EoS, were proposed,[67]

$$p_a = -\pi_T \tag{8.50}$$

and

$$p_r = p - p_a = T\left(\frac{\partial p}{\partial T}\right)_{V_m}. \tag{8.51}$$

Two relevant examples are shown in Figures 8.11 and 8.12, where this definition has been applied to the Span and Wagner[81] reference EoS for

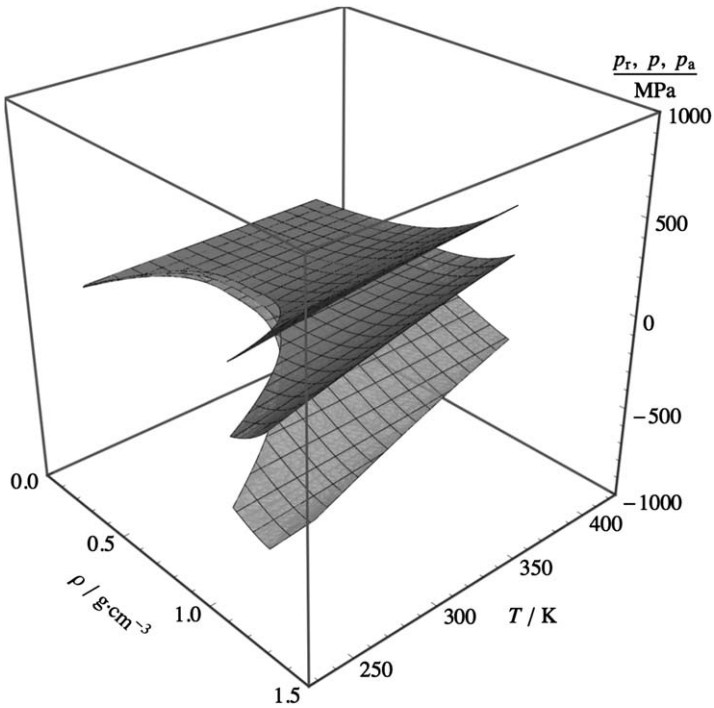

Figure 8.11 Internal pressure p separated into repulsive p_r and attractive terms p_a using the Span and Wagner[81] reference EoS for CO_2 as a function of density ρ and temperature T. Upper surface is the repulsive term p_r, the middle surface is the EoS pressure p and the lower surface the attractive term p_a.

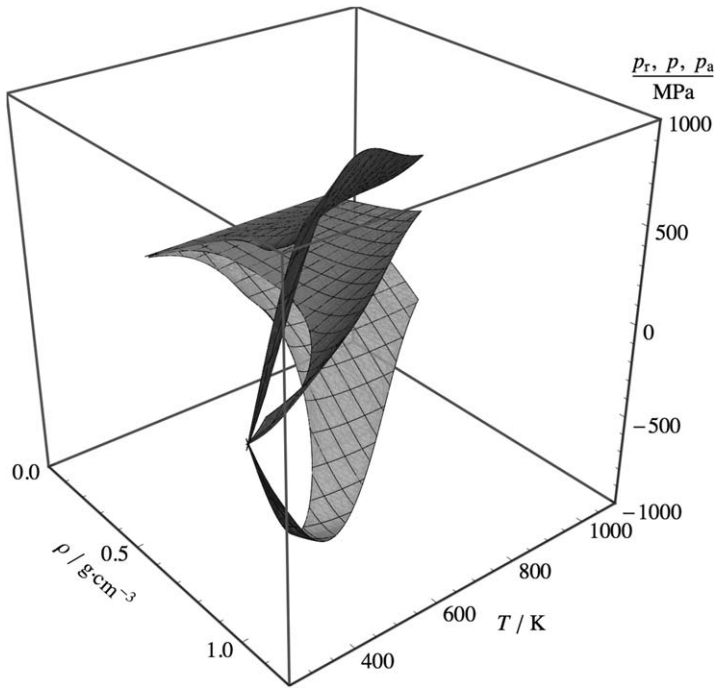

Figure 8.12 Internal pressure p separated into repulsive p_r and attractive terms p_a using the Wagner and Pruß[82] reference EoS for water as a function of density ρ and temperature T. In the case of water, the separation shows the anomalous inversion of the internal pressure of water at low-temperature. Upper surface is the repulsive term p_r, the middle surface is the EoS pressure p and the lower surface the attractive term p_a.

CO_2 and the Wagner and Pruß[82] reference EoS for water. While Figure 8.11 shows a clean separation of the CO_2 thermodynamic pressure into predominately repulsive and attractive terms, one can observe in Figure 8.12 the anomalous behaviour that water exhibits related to a low-temperature internal pressure inversion. The FT viscosity modelling results then reflect this behaviour as we compare Figure 8.13, where the FT model results are shown along with the recommended viscosity data by Fenghour *et al.*,[83] with Figure 8.14, where the FT model results are shown along with the recommended data by the International Association for the Properties of Water and Steam[84] (IAPWS). In the case of CO_2, Figure 8.13 shows the expected low-temperature viscosity increase with pressure. However, in the case of water an anomalous low-temperature viscosity decrease with pressure is evident in Figure 8.14.

Other results, such as the prediction of the viscosity critical exponent, when applied to a renormalized EoS, are also reported.[67] As pointed out before, this approach has been applied to the renormalized cross-over Patel–Teja[66] EoS model proposed by Kiselev and Ely.[64,65] The procedure results in the derivation of a singular term that, as the critical point is approached, will

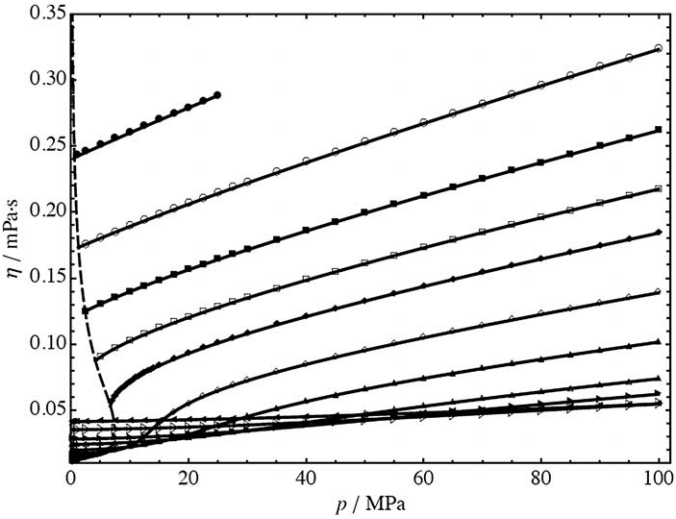

Figure 8.13 Comparison of the viscosity η obtained from the generalized FT viscosity model based on the Span and Wagner[81] reference EoS for CO_2 along with the recommended η reported by Fenghour *et al.*[83] as a function of pressure p. ———, FT model isotherms; - - - - -, FT model phase boundary; recommended data reported by Fenghour *et al.*[83]: ●, T = 220 K; ○, 240 K; ■, 260 K; □, 280 K; ◆, 300 K; ◇, 340 K; ▲, 400 K; △, 500 K; ▶, 600 K; ▷, 800 K; ◀, 1000 K.

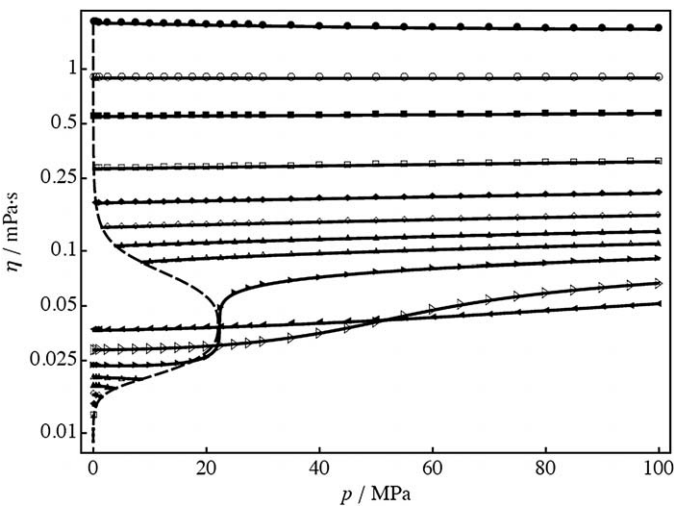

Figure 8.14 Comparison of the generalized FT viscosity model based on the Wagner and Pruß[82] reference EoS for water with the IAPWS recommended viscosity data.[84] Solid lines FT model isotherms; dashed lines FT model phase boundary; recommended data: ●, 273.15 K; ○, 298.15 K; ■, 323.15 K; □, 373.15 K; ◆, 423.15 K; ◇, 473.15 K; ▲, 523.15 K; △, 573.15 K; ▶, 648.15 K; ▷, 773.15 K; ◀, 973.15 K.

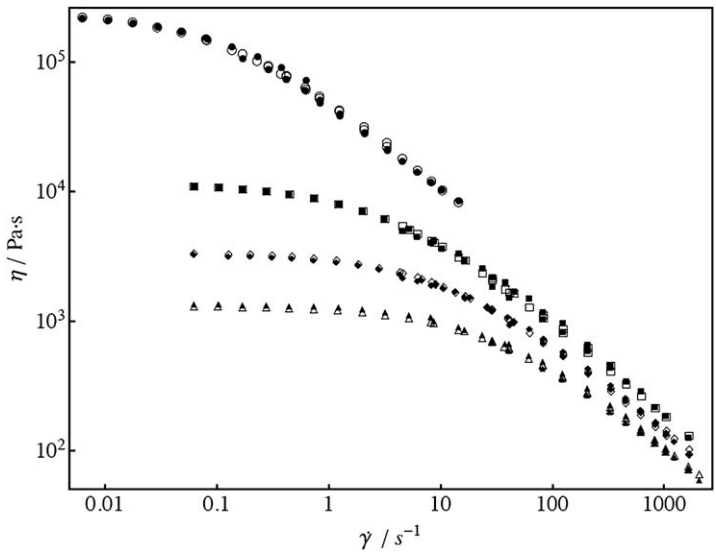

Figure 8.15 PC-SAFT based FT rheological modeling results for viscosity η as a function of the rate of shearing $\dot{\gamma}$ for polystyrene melts of average molar mass $\langle M \rangle = 13\ 2000\ g \cdot mol^{-1}$ along with the measurements reported by Kwang.[85] Experimental results reported by Kwang[85]: ●, $T = 423.15$ K; ■, $T = 448.15$ K; ◆, $T = 461.15$ K; ▲, $T = 423.15$ K. FT model: ○, $T = 423.15$ K; □, $T = 448.15$ K; ◇, $T = 461.15$ K; △, $T = 423.15$ K.

weakly diverge at a rate of one half of the critical exponent α,[67] which is remarkably close to what is believed to correspond to the weak divergence of viscosity.[86] The main point to be stressed here is the fact that the FT has been shown capable of mapping onto the viscosity surface the physics that may already be built into the core EoS model, incorporating into the viscosity model the substantial amount of experience and effort already been invested in the development of the EoS.

8.4.3 Summary and Outlook

As illustrated in this chapter, the FT can be summarized as a pragmatic approach that is based on the large amount of work, started over a century ago by van der Waals,[80] dealing with the development of accurate and physically realistic EoS. Much of the physics that now is found in modern EoS, going from highly accurate engineering reference EoS to highly theoretical ones, is reflected in the viscosity models that may be derived with the FT approach.

Although most of the current FT applications have been to Newtonian shear viscosity, it is possible to further extend the FT to non-Newtonian fluids[87] by introducing in the friction coefficients κ's a dependency on the rate of shear ($\dot{\gamma} = du/dz$). For example, by choosing the PC-SAFT EoS version

that was developed for the optimal description of polymer blends,[88] highly non-Newtonian behaviour, as for instance exhibited by the polystyrene (PS) melts studied by Kwang,[85] can be modelled with low uncertainty[89] (see Figure 8.15). The area of rheology is a current focus of the FT approach where the FT models are based on modelling of the shear stress, as indicated in eqn (8.38). Newtonian fluid models can then be derived under the assumption that the friction coefficients defined in eqn (8.40) are independent of rate of shearing. The relaxation of this condition opens new challenges, beyond just viscosity, into the full modelling of mechanical properties of complex fluids.

Nevertheless, the fundamental molecular understanding of the physics that governs the rheology of complex fluids and how this can be related to pragmatic approaches, such as the FT, remains a challenge for the future.

References

1. J. Millat, J. H. Dymond and C. A. Nieto de Castro, *Transport Properties of Fluids: Their Correlation, Prediction and Estimation*, Cambridge University Press, Cambridge, U.K., 1996.
2. M. J. Assael, J. H. Dymond, M. Papadaki and P. M. Patterson, *Int. J. Thermophys.*, 1992, **13**, 269.
3. M. J. Assael, J. H. Dymond, M. Papadaki and P. M. Patterson, *Fluid Phase Equilib.*, 1992, **75**, 245.
4. M. J. Assael, J. H. Dymond, M. Papadaki and P. M. Patterson, *Int. J. Thermophys.*, 1992, **13**, 659.
5. M. J. Assael, J. H. Dymond and P. M. Patterson, *Int. J. Thermophys.*, 1992, **13**, 729.
6. M. J. Assael, J. H. Dymond and P. M. Patterson, *Int. J. Thermophys.*, 1992, **13**, 895.
7. M. J. Assael, J. H. Dymond and S. K. Polimatidou, *Int. J. Thermophys.*, 1994, **15**, 189.
8. M. J. Assael, J. H. Dymond and S. K. Polimatidou, *Int. J. Thermophys.*, 1995, **16**, 761.
9. B. J. Alder, D. M. Gass and T. E. Wainwright, *J. Chem. Phys.*, 1970, **53**, 3813.
10. J. J. Erpenbeck and W. W. Wood, *Phys. Rev. A*, 1991, **43**, 4254.
11. J. H. Dymond, in *Proc. 6th Symp. Thermophys. Prop.*, ASME, New York, 1973, p. 143.
12. M. J. Assael, J. P. M. Trusler and T. T. F., *Thermophysical Properties of Fluids. An Introduction to their Prediction*, Imperial College Press, London, U.K., 1996.
13. M. J. Assael, J. H. Dymond and V. Tselekidou, *Int. J. Thermophys.*, 1990, **11**, 863.
14. M. J. Assael, A. Kalyva, K. E. Kakosimos and K. Antoniadis, *Int. J. Thermophys.*, 2009, **30**, 1733.
15. H. Sigurgeirsson and D. M. Heyes, *Mol. Phys.*, 2003, **101**, 469.

16. E. W. Lemmon, M. L. Huber and M. O. McLinden, *NIST Standard Reference Database 23: Reference Fluid Thermodynamic and Transport Properties-REFPROP*, National Institute of Standards and Technology, Gaitherburg, 2013.
17. D. Caudwell, PhD Thesis, University of London, 2004.
18. F. Ciotta, PhD Thesis, University of London, 2010.
19. R. C. Reid, J. M. Prausnitz and B. E. Poling, *The Properties of Gases and Liquids*, 4th edn, McGraw-Hill, London, U.K., 1987.
20. F. Ciotta, J. P. M. Trusler and V. Vesovic, *Fluid Phase Equilib.,* 2014, **363**, 239.
21. D. Enskog, *K. Sven. Vetenskapsakad. Handl.*, 1922, **63**, 4.
22. H. H. Thorne, quoted in ref. 23, Section 16.6.
23. S. Chapman and T. Cowling, *The Mathematical Theory of Non-uniform Gases*, Cambridge University Press, 1970.
24. N. F. Carnahan and K. E. Starling, *J. Chem. Phys.*, 1969, **51**, 635.
25. H. J. M. Hanley, R. D. McCarty and E. G. D. Cohen, *Physica*, 1972, **60**, 322.
26. R. DiPippo, J. R. Dorfman, J. Kestin, H. E. Khalifa and E. A. Mason, *Physica A*, 1977, **86**, 205.
27. S. I. Sandler and J. K. Fiszdon, *Physica A*, 1979, **95**, 602.
28. R. Umla, N. Riesco and V. Vesovic, *Fluid Phase Equilib.*, 2012, **334**, 89.
29. P. S. van der Gulik, R. Mostert and H. R. van den Berg, *Fluid Phase Equilib.*, 1992, **79**, 301.
30. A. S. de Wijn, V. Vesovic, G. Jackson and J. P. M. Trusler, *J. Chem. Phys.*, 2008, **128**, 204901.
31. M. S. Wertheim, *J. Stat. Phys.*, 1986, **42**, 459; M. S. Wertheim, *J. Stat. Phys.*, 1986, **42**, 477.
32. G. Jackson and K. E. Gubbins, *Pure Appl. Chem.*, 1989, **61**, 1021.
33. A. Gil-Villegas, A. Galindo, P. J. Whitehead, S. J. Mills, G. Jackson and A. N. Burgess, *J. Chem. Phys.*, 1997, **106**, 4168.
34. V. Vesovic and W. A. Wakeham, *Int. J. Thermophys.*, 1989, **10**, 125.
35. V. Vesovic and W. A. Wakeham, *Chem. Eng. Sci.*, 1989, **44**, 2181.
36. M. J. Assael, N. K. Dalaouti, J. H. Dymond, E. Perperi and W. A. Wakeham, *Int. J. Thermophys.*, 2000, **21**, 357.
37. M. J. Assael, N. K. Dalaouti and J. H. Dymond, *Int. J. Thermophys.*, 2000, **21**, 621.
38. M. J. Assael and N. K. Dalaouti, *Int. J. Thermophys.*, 2001, **22**, 659.
39. M. J. Assael, N. K. Dalaouti and W. A. Wakeham, *Int. J. Thermophys.*, 2001, **22**, 1727.
40. M. J. Assael, N. K. Dalaouti and I. Metaxa, *Fluid Phase Equilib.*, 2002, **199**, 237.
41. M. J. Assael, C. M. B. P. Oliveira and W. A. Wakeham, *Fluid Phase Equilib.*, 2003, **210**, 5.
42. D. D. Royal, V. Vesovic, J. P. M. Trusler and W. A. Wakeham, *Mol. Phys.*, 2003, **101**, 339.
43. J. Kestin and W. A. Wakeham, *Ber. Bunsen. Phys. Chem.*, 1980, **84**, 762.
44. J. L. Lebowitz, *Phys. Rev. A*, 1964, **133**, 895.

45. T. Boublik, *J. Chem. Phys.*, 1970, **53**, 471.
46. G. A. Mansoori, N. F. Carnahan, K. E. Starling and T. W. Leland, *J. Chem. Phys.*, 1971, **54**, 1523.
47. D. D. Royal, V. Vesovic, J. P. M. Trusler and W. A. Wakeham, *Int. J. Refrig.*, 2005, **28**, 311.
48. V. Vesovic, *Int. J. Thermophys.*, 2001, **22**, 415.
49. M. J. Assael, N. K. Dalaouti and V. Vesovic, *Int. J. Thermophys.*, 2001, **22**, 61.
50. V. Vesovic, *Flow Assurance: Reliable and Accurate Prediction of the Viscosity of Natural Gas*, Society of Petroleum Engineers, 2007, 107154, DOI: 10.2118/107154-MS.
51. P. Schley, M. Jaeschke, C. Kuchenmeister and E. Vogel, *Int. J. Thermophys.*, 2004, **25**, 1623.
52. L. I. Langelandsvik, S. Solvang, M. Rousselet, I. N. Metaxa and M. J. Assael, *Int. J. Thermophys.*, 2007, **28**, 1120.
53. A. S. de Wijn, N. Riesco, G. Jackson, J. P. M. Trusler and V. Vesovic, *J. Chem. Phys.*, 2012, **136**, 74514.
54. G. C. Maitland, M. Rigby, E. B. Smith and W. A. Wakeham, *Intermolecular Forces – Their Origin and Determination*, Clarendon, Oxford, 1981.
55. M. L. Huber and J. F. Ely, *Fluid Phase Equilib.*, 1987, **37**, 105.
56. J. H. Dymond, J. Robertson and J. D. Isdale, *Int. J. Thermophys.*, 1981, **2**, 133.
57. J. L. E. Chevalier and P. J. Petrino, *J. Chem. Eng. Data*, 1990, **35**, 206.
58. A. Aucejo, M. C. Burguet, R. Munoz and J. L. Marques, *J. Chem. Eng. Data*, 1995, **40**, 141.
59. F. Peleties, *PhD Thesis*, University of London, 2007.
60. A. J. Queimada, S. E. Quinones-Cisneros, I. M. Marrucho, J. A. P. Coutinho and E. H. Stenby, *Int. J. Thermophys.*, 2003, **23**, 1221.
61. L. E. Goodman and W. H. Warner, *Statics and Dynamics*, Wadsworth Publishing Company, Inc., Belmont, California, U.S.A., 1964.
62. A. Y. Malkin and A. I. Isayev, *Rheology. Concepts, Methods, and Applications*, 2nd edn, ChemTec Publishing, Toronto, Canada, 2011.
63. C. W. Macosko, *Rheology: Principles, Measurements, and Applications*, Wiley-VCH, New York, 1994.
64. S. B. Kiselev and J. F. Ely, *Fluid Phase Equilib.*, 2004, **222–223**, 149.
65. S. B. Kiselev and J. F. Ely, *Fluid Phase Equilib.*, 2007, **252**, 57.
66. N. C. Patel and A. S. Teja, *Chem. Eng. Sci.*, 1982, **37**, 463.
67. S. E. Quiñones-Cisneros and U. K. Deiters, *J. Phys. Chem. B*, 2006, **110**, 12820.
68. S. E. Quiñones-Cisneros, C. K. Zéberg-Mikkelsen, A. Baylaucq and C. Boned, *Int. J. Thermophys.*, 2004, **25**, 1353.
69. G. S. Soave, *Chem. Eng. Sci.*, 1972, **27**, 1197.
70. D.-Y. Peng and D. B. Robinson, *Ind. Eng. Chem. Fundam.*, 1976, **15**, 59.
71. C. K. Zéberg-Mikkelsen, S. E. Quiñones-Cisneros and E. H. Stenby, *Fluid Phase Equilib.*, 2002, **194–197**, 1191.

72. C. K. Zéberg-Mikkelsen, S. E. Quiñones-Cisneros and E. H. Stenby, *Pet. Sci. Technol.*, 2002, **20**, 27.
73. C. K. Zéberg-Mikkelsen, S. E. Quiñones-Cisneros and E. H. Stenby, *Int. J. Thermophys.*, 2002, **23**, 437.
74. C. K. Zéberg-Mikkelsen, S. E. Quiñones-Cisneros and E. H. Stenby, *Ind. Eng. Chem. Res.*, 2001, **40**, 2966.
75. C. K. Zéberg-Mikkelsen, S. E. Quiñones-Cisneros and E. H. Stenby, *Ind. Eng. Chem. Res.*, 2001, **40**, 3848.
76. S. E. Quiñones-Cisneros, J. García, J. Fernández and M. A. Monsalvo, *Int. J. Refrig.*, 2005, **28**, 714.
77. S. E. Quiñones-Cisneros, C. K. Zéberg-Mikkelsen and E. H. Stenby, *Fluid Phase Equilib.*, 2001, **178**, 1.
78. E. Vogel, C. Küchenmeister, E. Bich and A. Laesecke, *J. Phys. Chem. Ref. Data*, 1998, **27**, 947.
79. N. W. A. van Uden, H. Hubel, D. A. Faux, A. C. Tanczos, B. Howlin and D. J. Dunstan, *J. Phys.: Condens. Matter*, 2003, **15**, 1577.
80. J. D. van der Waals, *Doctoral Dissertation*, Leyden University, 1873.
81. R. Span and W. Wagner, *J. Phys. Chem. Ref. Data*, 1996, **25**, 1509.
82. W. Wagner and A. Pruß, *J. Phys. Chem. Ref. Data*, 2002, **31**, 387.
83. A. Fenghour, W. A. Wakeham and V. Vesovic, *J. Phys. Chem. Ref. Data*, 1998, **27**, 31.
84. K. Watanabe and R. B. Dooley, *Revised Release on the IAPS Formulation 1985 for the Viscosity of Ordinary Water Substance*, The International Association for the Properties of Water and Steam, Vejle, Denmark, 2003.
85. C. Kwang, *PhD Thesis*, Wayne State University, 1998.
86. R. F. Berg and M. R. Moldover, *Physics Review E*, 1999, **60**, 4076.
87. P. V. Ramírez-González, J. P. Aguayo, S. E. Quiñones-Cisneros and U. K. Deiters, *Int. J. Thermophys.*, 2009, **30**, 1089.
88. F. Tumakaka, J. Gross and G. Sadowski, *Fluid Phase Equilib.*, 2002, **194–197**, 541.
89. S. E. Quiñones-Cisneros and U. K. Deiters, in VDI ''*Thermodynamik-Kolloquium'', Dortmund*, Germany, 2006.

CHAPTER 9

Dense Fluids: Other Developments

HORACIO R. CORTI, M. PAULA LONGINOTTI, JOSEFA FERNÁNDEZ, ENRIQUETA R. LÓPEZ AND ALOIS WÜRGER

9.1 Introduction

In Chapter 8 we focussed on recent advances in modelling and predicting the viscosity of dense fluids based on kinetic theory and on macroscopic considerations. In the present chapter we review other recent developments for dense fluids. We start with a fluid state that is at one extreme of molecular mobility and thus of considerable interest. Section 9.2 is focussed on recent developments in the theory and modelling of supercooled liquids with special emphasis on water and aqueous binary solutions. Particular attention is paid to the importance of structural relaxation within the supercooled fluid. Understanding those relaxation processes is vital and leads to a number of different theoretical models including those proposed to explain the diffusion-viscosity decoupling, or put more simply the breakdown of the Stokes–Einstein relation. This is an interesting phenomenon, which indicates that in supercooled liquids, near the glass transition, the cooling process changes the nature of diffusional transport at the molecular scale.

The developments described in the subsequent section, Section 9.3, take as their starting point the studies of the effect of pressure on the vitrification process. The observed density–temperature scaling of transport and relaxation properties is extended to other thermodynamic regions and the relationships that describe transport properties in terms of residual entropy are discussed. The recent extensive testing of the proposed scaling

Experimental Thermodynamics Volume IX: Advances in Transport Properties of Fluids
Edited by M. J. Assael, A. R. H. Goodwin, V. Vesovic and W. A. Wakeham

Published by the Royal Society of Chemistry, www.rsc.org

laws is illustrated and their applicability to correlating the viscosity and self-diffusion of a large number of complex fluids is demonstrated.

Section 9.4 is dedicated to a review of recent developments in the fundamental understanding and modelling of thermal diffusion; the Onsager phenomenon that leads to non-convective, compositional separation generated by thermal gradients. Recent work has led to elucidation of the processes that take place in various applications, ranging from isotope separation to estimating the connectivity of petroleum reservoirs and tracking seasonal changes in the historical, climatic records.

9.2 Transport in Supercooled Liquids

HORACIO R. CORTI AND M. PAULA LONGINOTTI

9.2.1 Supercooled Liquids: Crystallization *vs.* Vitrification

A supercooled liquid, that is a liquid below its normal melting temperature (T_m), is metastable with respect to the crystalline state. The crystallization of a certain volume of supercooled liquid takes place with a characteristic time, τ_c, which goes through a minimum as the supercooling extension, $(T_m - T)$, increases. This behavior is a result of two opposite effects: the decrease in the time required to reach the critical nucleus size, and the reduction in the molecular mobility owing to the viscosity increment upon increasing supercooling.[1]

A second characteristic time of the dynamics of supercooled liquids is the structural relaxation time, τ_α, which represents an internal molecular relaxation time that increases very sharply from the high temperature ($T > T_m$) value corresponding to the quasi-lattice vibration time ($\approx 10^{-13}$ s) to a value where it becomes comparable to a typical laboratory experiment time scale ($\approx$100 s). At this point, which defines the glass transition temperature, T_g, the liquid molecular movements become arrested and the liquid converts into a glass.[2]

While certain liquids such as propane-1,2,3-triol (glycerol) or 1,1′:2′,1″-terphenyl (OTP) can vitrify upon normal cooling, others require very high cooling rates in order to overcome the rate of nucleus formation that leads to crystallization. Thus, for water, the critical cooling rate needed to prevent crystallization, $(T_m - T)/\tau_c$, is close to 10^7 K·s^{-1},[1] which can be achieved by rapid cooling of aqueous aerosol droplets on a solid cryoplate,[3] a method known as ''hyper-quenching''. Additionally, glassy water can also be obtained by rapid quenching of emulsified water in a liquid cryomedia such as liquid propane or ethane or by pressurizing ice Ih at pressures higher than 1 GPa. These methods lead directly to the glassy state, but water can resist crystallization and remain supercooled when it is cooled down in capillaries or emulsified in organic liquids above the homogeneous nucleation temperature (T_h), which is close to 235 K at 0.1 MPa. The application of pressure expands the supercooled region, as can be observed in the p,T diagram of Figure 9.1. The region between T_h and T_g is what Stanley and coworkers[4] called the ''no-man's land'' zone, meaning that this region cannot be reached experimentally owing to water crystallization.

The existence of a second critical point of water has been suggested by computer simulation studies and some indirect evidence has been reported from experimental studies in nanoconfined water, where deeper supercooled conditions can be achieved.[4] The liquid–liquid equilibrium (or Widom line) in Figure 9.1 is a hypothetical transition between low-density and high-density liquid water (LDL and HDL, respectively), extrapolated

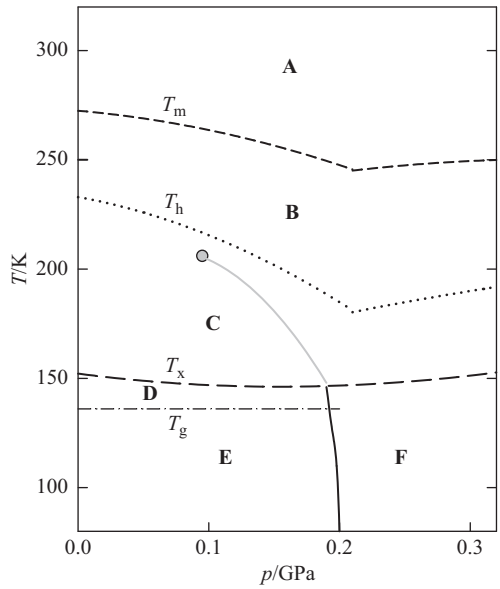

Figure 9.1 Temperature T as function of pressure p phase diagram for water showing the stable (A), supercooled (B), ''no man's land'' (C), ultra viscous (D), LDA glassy (E), and HDA glassy regions (F). A hypothetical second critical point (gray circle) and the low-density/high-density liquid phase transition (gray line), which is a continuation of the LDA to HDA coexistence curve, shown with a solid black line, are also indicated in the diagram. Adapted from ref. 4.

from the experimentally observed low-density/high-density amorphous solid water transition. As we will discuss later, the existence of this liquid–liquid transition could explain anomalous behavior in some thermodynamic and dynamic properties of supercooled aqueous solutions.

Fortunately, supercooling of aqueous solutions containing electrolytes and polyols can be performed much more easily than for pure water. For instance, LiCl concentrated solutions with mole fractions in the range $0.12 < x < 0.25$ can be vitrified at cooling rates less than $0.1\ \mathrm{K \cdot s^{-1}}$ and the supercooled solutions remain metastable for a long time.

9.2.2 Relaxation Dynamics of Glass Forming Liquids: α- and β-Relaxations

A microscopic insight into the relaxation dynamics of glass forming systems can be obtained from the scattering functions derived from light or neutron scattering experiments. At short times (few fs), the molecules of a stable liquid move as in a system of non-interacting particles, and this time window is known as ''ballistic regime''. At longer times the molecules in the dense

fluid feel the presence of other molecules and their trajectories become erratic because of the collisions among them, and the correlation function decays exponentially.[5]

At low temperatures, deep in the supercooled regime, the time correlation function becomes more complex. After the ballistic regime, the correlation function shows a plateau where the particles oscillate around their equilibrium positions, without relaxing, because each molecule is trapped in a ''cage'' formed by the neighboring molecules that prevent it to move along large distances. In this time window the relaxation dynamics of the liquid is similar to that of the glass. Finally, at longer times, the molecules can escape their cages and the correlation function decays to zero, not in a single exponential manner but following the Kohlrausch–Williams–Watts (KWW) or stretched exponential function:

$$\phi(t) = \exp\left(-\frac{t}{\tau}\right)^{\beta}, \tag{9.1}$$

where the value of the β coefficient indicates the degree of non-exponentiality of the response function ($\beta = 1$ corresponds to a single exponential function). The existence of a ''stretched'' relaxation has been associated to ''dynamical heterogeneities'', meaning that in the supercooled liquid a heterogeneous set of environments exist where each molecule has a different relaxation time in every different environment. The mean relaxation function can be represented by an average of exponential functions having different time scales, described by a stretched exponential function. Although experimental and computer simulation studies confirm that the relaxation dynamics are not homogeneous, the nature of the heterogeneities and the reasons of their origin are not well understood yet.[5,6]

The α-relaxation for non-polymeric liquids is the result of cooperative molecular rotations,[7,8] involving large angle orientations, necessary for the molecules to escape out of the cages. As mentioned above, τ_α increases dramatically when a supercooled liquid is cooled down to T_g and, due to a very non-exponential relaxation function ($\beta \ll 1$), its temperature dependence exhibits large deviations from the Arrhenius equation,

$$\tau = \tau_0 \exp\left(\frac{E_a}{RT}\right), \tag{9.2}$$

where τ_0 is the relaxation time at infinite temperature, E_a is the activation energy and R is the gas constant.

The faster secondary or β-relaxation is only detectable near T_g, and extends down to the glassy state, being an Arrhenius-like process. Johari and Goldstein[9] proposed that this process is due to the existence of ''islands of mobility'', that is, regions of lower local density as compared to the macroscopic density where molecular movements are possible.

Owing to the different temperature dependence of the α- and β-relaxations both processes merge at a given temperature $T_{crossover} > T_g$, that for different

glass forming liquids was found in the interval $1.11 < T_{crossover}/T_g < 1.46$.[10] It should be stressed that the crossover temperature observed for the primary and secondary processes is related to the critical temperature observed for the diffusion–viscosity decoupling which will be discussed below.[11]

9.2.3 Structural Relaxation and Viscosity: Strong and Fragile Liquids

The α-relaxation time, τ_α, is proportional to the viscosity and its change with temperature depends notably on the nature of the glass forming system. Angell[12] classified glass forming liquids into "strong" and "fragile" depending on their primary relaxation time temperature dependence. For strong liquids τ_α temperature dependence is given by the Arrehnius eqn (9.2), while fragile systems deviate from this expression. Angell defined the fragility degree of a given liquid, m, as:

$$m = \left[\frac{\mathrm{d}\log x}{\mathrm{d}\log(T_g/T)}\right]_{T=T_g}, \tag{9.3}$$

with $x = \tau_\alpha$ or η, which increases with increasing fragility.

Figure 9.2 shows the variation of the viscosity of different glass forming liquids as a function of the reduced inverse temperature (T_g/T). It can be

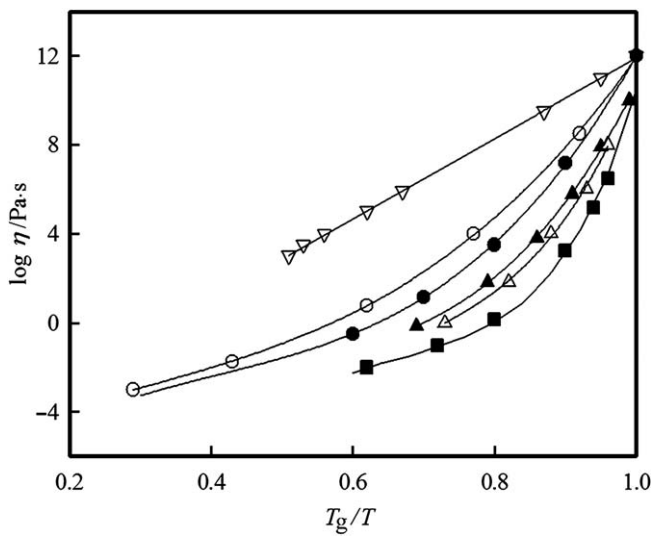

Figure 9.2 Viscosity η of pure liquids and aqueous solutions as a function of T_g/T. ▽, SiO_2; ○, propanol; ●, glycerol; ▲, sucrose aqueous solution mass fraction $w = 0.64$; △, sucrose aqueous solution with $w = 0.8$; ■, $CaNO_3 \cdot 8H_2O$.

observed that SiO_2 behaves as a strong liquid while propanol, glycerol[†] and aqueous sucrose[‡] and ionic mixtures behave as fragile systems.

The fragility of a liquid can be determined, as proposed by Angell and coworkers,[13] from a plot of $\Delta S/\Delta S_m$ as a function of T/T_m, where $\Delta S/\Delta S_m$ is the entropy difference between the liquid and the crystal normalized by the entropy difference at the melting point (ΔS_m). Liquids with higher fragility approach the Kauzmann temperature (the temperature at which $\Delta S/\Delta S_m = 0$) more rapidly.

Water presents a different behavior from that observed for other liquids. The thermodynamic method indicates that near T_m water is the most fragile of all liquids studied, while the kinetic approach indicates that close to the glass transition it behaves as a strong liquid. This behavior suggests the hypothesis that water experiences a fragile-to-strong transition at a temperature of around 228 K, as seems to be confirmed by experiments on confined water.[14]

Chen *et al.*[15] have shown that the dynamic crossover observed in confined water coincides with a maximum heat capacity value. This maximum was also observed in molecular dynamics simulation experiments in bulk water and is believed to be related to the liquid–liquid coexistence line shown in Figure 9.1.

9.2.4 Theories for the Behavior of the Viscosity of Supercooled Liquids

Near T_g fragile liquids (such as OTP) may have apparent activation energies of 500 $kJ \cdot mol^{-1}$ or higher. Such a value is unlikely to be associated with the motion of one molecule in a field of fixed neighbors, but it is most probably associated to a group of molecules that are rearranging in a cooperative manner.[16]

The Adam–Gibbs theory[17] is one explanation built on cooperative dynamics. The most important result of the Adam–Gibbs theory is the relationship found between the structural relaxation time and the configurational entropy, S_{conf}, of the supercooled liquid, approximated to the entropy difference between the supercooled liquid and the crystal, ΔS,[1]

$$\tau \propto \exp\left(\frac{C}{T\Delta S}\right). \tag{9.4}$$

Eqn (9.4) relates the increment of the molecular relaxation time with the growth of cooperatively rearranging regions. Considering that the difference between the supercooled liquid and crystal heat capacities is inversely

[†]IUPAC name propane-1,2,3-triol.
[‡]IUPAC name (2*R*,3*R*,4*S*,5*S*,6*R*)-2-[(2*S*,3*S*,4*S*,5*R*)-3,4-dihydroxy-2,5-bis(hydroxymethyl)oxolan-2-yl]oxy-6-(hydroxymethyl)oxane-3,4,5-triol.

proportional to the temperature, eqn (9.4) is of similar form to an expression for the viscosity proposed by Vogel, Fulcher and Tammann (VFT):[18–20]

$$\eta = \eta^0 \exp\left(\frac{C'T_0}{T - T_0}\right), \tag{9.5}$$

where η^0, C', and T_0 are constants. In the Adam–Gibbs theory T_0 is the Kauzmann temperature, while in the VFT equation T_0 is the temperature where the viscosity becomes infinite, and C' is a parameter related to Angell's fragility ($m = 16 + 590/C'$).[21] Eqn (9.5), commonly used to correlate the temperature dependence of the viscosity of supercooled liquids, is known to fail close to T_g.

An expression for the viscosity of supercooled liquids can be also derived from a dynamic model of the glass transition, the mode-coupling theory (MCT).[22] Debenedetti has reviewed the main features of the MCT and remarked that they lead to a viscosity feedback mechanism because it considers that the shear stress relaxation take places mainly through diffusive motions. However, the self-diffusion coefficient is inversely related to the viscosity, which in turn, is proportional to the shear stress relaxation time. Finally, the MCT prediction for the viscosity takes the form of a power-law equation:

$$\eta = \eta^0 (T - T_c)^{-\gamma}. \tag{9.6}$$

Typically, the coefficient γ varies between 1.5 and 2.3,[23] and the range of validity of the power law, given by eqn (9.6), extends from high temperatures down to $T_{crossover}$, which is the crossover temperature of the MCT. Below $T_{crossover}$ a low-temperature regime emerges that follows either VFT or Arrhenius viscosity behaviour.

Tarjus and Kivelson[24] proposed a frustration-limited continuous cluster model of supercooled liquids, where the clusters are formed through a process similar to the formation of crystal embryos, but they could not grow and extend over the entire system. The main parameter of the model is the cluster size, L, and the activation energy for the viscosity of the liquid is given by:

$$E_\eta(T) - E_\eta(\infty) = BT^* \left(\frac{T - T^*}{T^*}\right)^3, \tag{9.7}$$

where $E_\eta(\infty)$, B, and T^* depend on the liquid, and T^* is identified with a critical temperature below which structured domains are formed. A relationship between $E_\eta(\infty)$ and the fragility has been observed, while the degree of clustering is given by the ratio $BT^*/E_\eta(\infty)$. Eqn (9.7) describes the viscosity of fragile and strong glass forming liquids quite well over a wide range of temperatures.

More recently, Avramov and Milchev[25,26] developed a theory to describe the temperature dependence of the viscosity of fragile liquids. The Avramov–Milchev (AM) model is based on the assumptions that: (i) the viscosity is

inversely proportional to the average jump frequency of the molecules; and (ii) the molecules jump with frequencies given by an exponential relation with activation energy, E_i.

The spatial disorder of glass forming systems leads to some unknown probability distribution of the activation energies for the elementary jumps of the molecules. It was found that, assuming uniform distributions with an activation energy dispersion of width σ; and independently of the type of distribution (truncated Poisson or Gaussian), the entropy (S) is related to the dispersion by,

$$S - S_0 = \frac{RZ}{2} \ln\left(\frac{\sigma}{\sigma_0}\right), \tag{9.8}$$

where S_0 is the entropy for some reference state corresponding to dispersion σ_0, R is the gas constant, and $Z/2$ is the number of escape channels available for the molecule; that is, the number of directions along which the particle can move out of the cell considering that each channel can be used in two directions. Thus, Z is related to the coordination of the network.

In the AM model the viscosity is a function of σ, and therefore of the entropy. The viscosity at T_g is fixed to $\eta_g = 10^{12.5}$ Pa · s,[25,26] and the following expression for the viscosity is obtained

$$\eta = \eta_0 \cdot \exp\left[\left(\ln \eta_g - \ln \eta_0\right) \cdot \left(\frac{T_g}{T}\right)^{\alpha}\right], \tag{9.9}$$

with $\alpha = 2\langle C_p \rangle / ZR$, where $\langle C_p \rangle$ is the average heat capacity for a range of temperatures between T and T_g. Thus, α increases with the heat capacity, which is proportional to the number of vibrational degrees of freedom, and decreases with the coordination of the network, proportional to Z. The fragility parameter α is related to Angell's fragility by $m = \alpha(\ln \eta_g - \ln \eta_0)$, with $\alpha = 1$ corresponding to a strong liquid, while higher values imply more fragile behavior.

If we use the experimental T_g of the liquid in eqn (9.9), the AM model becomes a two parameter model, which can fit experimental data of glass-forming liquids over an impressive range of temperatures. For instance, the AM model can describe the viscosity of glycerol and glycerol–water mixtures over a viscosity range of more than 12 decades.[27]

9.2.5 Mass and Charge Transport in Supercooled Liquids

The structural relaxation time of a liquid changes by up to 14 orders of magnitude as it is cooled down towards its glass transition. This dramatic change affects the transport properties, such as the translational and rotational diffusion or the ionic conductivity, in different ways depending on the nature of the liquid and the size of the probe species used to test the transport coefficients.

The molecular mobility in liquids is usually compared to the predictions of the Stokes–Einstein and Stokes–Einstein–Debye relationships, which describe the translational and rotational motion of a particle of radius a in a hydrodynamic continuum with viscosity η and temperature T. The Stokes–Einstein relation (SER) predicts the translational tracer diffusion coefficient of traces of a probe species (solute),

$$D_t = \frac{k_B T}{6\pi\eta a}, \tag{9.10}$$

where k_B is the Boltzmann constant, and the coefficient 6π accounts for slip boundary conditions (for stick boundary conditions this coefficient should be replaced by 4π). Here the term 'tracer diffusion' is used to indicate diffusion of a solute at infinite dilution. Eqn (9.10) gives a good estimation of the tracer diffusion coefficient for solutes with sizes larger than that of the solvent molecules. The SER fails when the size of the solute molecule is lower than the size of the solvent, although it can be used to describe the self-diffusion in pure liquids (see Chapter 3).

The Stokes–Einstein–Debye relation (SEDR) predicts the rotational tracer diffusion coefficient,

$$D_r = \frac{k_B T}{8\pi\eta a^3}, \tag{9.11}$$

which is related to the rotational correlation time by $\tau_c = (6D_r)^{-1}$. Combining the SER and SEDR it is found that the ratio D_t/D_r should be a constant independent of the viscosity and the temperature, with a value that only depends on the size of the probe molecule.

Sillescu and coworkers[28] reported for the first time the different temperature (viscosity) dependence of translational and rotational tracer diffusion coefficients in supercooled OTP. Rotational tracer diffusion coefficient of OTP followed the predictions of SEDR, eqn (9.11), as the viscosity was varied by 12 orders of magnitude, while close to T_g the translational diffusion of a probe of similar size to OTP molecule exhibited an enhancement of more than two orders of magnitude with respect to the predictions of the SER, eqn (9.10). A number of studies in different glass-forming systems confirm the decoupling of viscosity from translational diffusion and, to a lesser extent, from rotational diffusion at temperatures below $(1.2 \text{ to } 1.3) \cdot T_g$. In line with the current literature we use the term 'decoupling' to indicate the failure of SER to describe the relationship between the translational tracer diffusion coefficient and viscosity. Larger decouplings were also reported for probes of smaller sizes.[29]

In the case of an ionic solute of charge z_i, its tracer diffusion coefficient is related to its ionic molar electrical conductivity, λ_i, through the Nernst–Einstein equation,

$$\lambda_i = \frac{z_i^2 F^2 D_i}{RT}, \tag{9.12}$$

where F is Faraday's constant. This equation is strictly valid at infinite dilution and using the SER for D_i, the ionic conductivity λ_i of an ion of radius a_i can be expressed in the form

$$\lambda_i \eta = \frac{z_i^2 eF}{6\pi a_i}. \tag{9.13}$$

The product $\lambda_i \eta$ is known as the Walden product and it should be constant if the size of the ionic particle does not change with temperature. This relationship is known as the Walden law (WL). The WL can be considered as the equivalent to the SER in ionic systems where the ionic conductivity is the most easily measurable transport coefficient. Thus, it is not surprising to observe a viscosity–conductivity decoupling in supercooled pure and mixed ionic melts or aqueous and non-aqueous salt solutions when the glass transition is approached.[30,31]

9.2.6 Diffusion–Viscosity Decoupling

Since Goldstein[32] postulated, more than 40 years ago, that the diffusion in liquids upon cooling changes from free diffusion at high temperatures to an activated or hopping diffusion at low temperatures, several models have been proposed to explain the diffusion–viscosity decoupling observed experimentally. Most of them assume the existence of dynamical spatial heterogeneities or mesoscopic domains with different mobility.

Analyzing experimental results, Rössler[11] concluded that there is a temperature, $T_{decoupling} > T_g$, at which the decoupling between viscosity and any translational diffusion process takes place. That temperature corresponds approximately to the interval $1.18 < T_{decoupling}/T_g < 1.28$ (viscosities between 10 Pa · s and 100 Pa · s) and is related to the crossover temperature where the viscosity changes from power-law to Arrhenius or VFT behavior. Below $T_{decoupling}$ the relation between either the self-diffusion coefficient or tracer diffusion coefficient and the viscosity follows a fractional Stokes–Einstein relation (FSER)

$$\frac{D}{T} \propto \left(\frac{1}{\eta}\right)^{\delta}, \tag{9.14}$$

where δ is a temperature independent constant ($0 \leq \delta \leq 1$), also used for describing tracer diffusion in a range of solvents and polymeric systems.

Stillinger and Hodgdon[33] proposed that thermal fluctuations lead to domains in the liquid, as in the Adam and Gibbs theory, that become temporarily more fluidized, where molecules can diffuse, but this is inhibited in the unfluidized regions. They assume that approaching T_g the supercooled liquid exhibits structural excitations leading to the formation of fluidized domains, with average volume $\langle v_i \rangle$, rate of appearance per unit of volume r_i, and lifetimes t_i. The formation of these domains does not affect the rotational and translational relaxation in the same way. Only the first part of

the domain lifetime contributes to the rotation relaxation if t_i is large (because the rotation is fast). But, at the same time, if $\langle \nu_i \rangle$ is large, the translational relaxation extends over the whole lifetime of the domain.

Another basic assumption is that the viscosity also depends on the appearance of fluidized domains and it is proportional to $(r_i \nu_i)^{-1}$. Therefore, using the SEDR they concluded that $\eta D_r/T \approx$ *constant*, while for the translational diffusion $\eta D_t/T \propto t_i/\eta_i$, that is, it could deviate significantly from the SER if t_i/η_i were to exhibit a strong temperature dependence.

Chang and Sillescu[34] adopted a model where the supercooled liquid is formed by fast (f) and slow (s) regions with translational or rotational diffusion coefficients D^f and D^s, respectively. The residence times, τ_i, of the molecules in each region are given by $\tau_f = \tau_s \phi_f/(1-\phi_f)$, where ϕ_I is the volume fraction of each region.

Assuming $\phi_f = \phi_s = 0.5$ (that is, $\tau_f = \tau_s$) near T_g: $\tau_f = \tau_s \gg (D_r^s)^{-1} \gg (D_r^f)^{-1}$, and if the SEDR is valid in the fast and slow regions: $\langle D_r{}^{-1} \rangle = \frac{1}{2}(D_r^f)^{-1} + \frac{1}{2}(D_r^s)^{-1} \approx \frac{1}{2}(D_r^s)^{-1}$, that is, the rotational diffusion coefficient is dominated by the slow regions. The translational diffusion coefficient averaged on times longer than $\tau_f = \tau_s$ leads to: $\langle D_t \rangle = \frac{1}{2}(D_r^f) + \frac{1}{2}(D_r^s) \approx \frac{1}{2}(D_r^f)$, that is, the translational diffusion coefficient is dominated by the fast regions. It is also concluded that the ratio D_r^f/D_r^s is a measure of the enhancement of the translational diffusion near T_g.

Ediger and co-workers[35] analysed the deviation from the SER by performing translational diffusion simulations in a supercooled liquid represented by a heterogeneous lattice divided into different cubic blocks representing domains with different relaxation times. Their goal was to find an explanation for the experimental fact that the lower is the coefficient β of the KWW distribution [eqn (9.1)] for a given rotational time, the larger is the deviation to the SER. The model assumes a characteristic time, τ_{ex}, for the blocks to exchange relaxation times (static heterogeneities correspond to $\tau_{ex} = \infty$), and β is related to the rotational correlation time, τ_r, obtained from the simulations.

It was found that, for a constant β value, the decoupling was smaller when the heterogeneities were static. For instance the deviations from SER were one order of magnitude for $\beta = 0.43$, and rise to three orders of magnitude for $\beta = 0.26$ in the static case. However, when $\tau_{ex} = \tau_r$ the deviation is one order of magnitude for $\beta = 0.80$. Ediger also analysed density and entropy fluctuations as the cause of slow and fast mobility observed in supercooled liquids, concluding that entropy fluctuations correctly predict the translational decoupling of probe molecules in OTP and polystyrene.[36]

Xia and Wolynes[37–39] considered a model based on the random theory of first order transition, where the distribution of activation energies is the cause of the non-exponential relaxation function, eqn (9.1), and yields a scale of sizes for spatial heterogeneities. The main conclusions of the Xia–Wolynes model are: (i) the deviations from the SER depend on the ratio between the radius of the probe molecule and the radius of the solvent molecule ($a_{solute}/a_{solvent}$). The decoupling, measured as the ratio between the

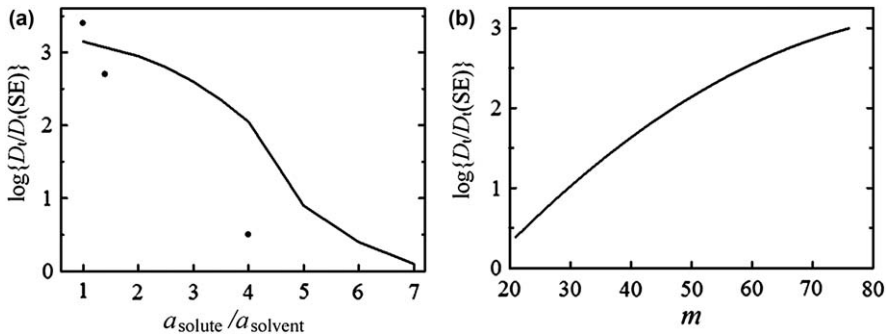

Figure 9.3 SER deviations as a function of the relation of solute/solvent radius (a) and the liquid fragility (b). The points correspond to experimental data.[35]
Adapted from ref. 39 with permission.

calculated translational diffusion coefficient and that obtained from the SER, $D_t/D_t(SE)$, diminishes from a factor 1000 for similar sizes down to 1 for a ratio of diameters probe/solvent higher than 6 to 7, as shown in Figure 9.3(a); (ii) the temperature dependence of the decoupling is very strong near T_g; (iii) the decoupling depends on the liquid fragility. Thus, as observed in Figure 9.3(b), at $T \approx T_g$, the decoupling $D_t/D_t(SE) \approx 1000$ for OTP ($m = 76$), but $D_t/D_t(SE) = 3$ for SiO_2 ($m = 21$).

Chandler and co-workers[40,41] formulated a model of the dynamics of deep supercooled liquids based on the idea that molecular movements are scarce and they arise when the molecule is adjacent to other molecules that can move. Dynamic heterogeneity is a manifestation of excitation lines in space-time formed by these mobile molecules. The dynamical facilitation model states that the molecules occupy a site i of the lattice that corresponds to a mobile (unjammed) region ($n_i = 1$), or a site corresponding to an non-mobile (jammed) region ($n_i = 0$). The dynamics of the model is determined by the rate constants for site i, k_i^+ and k_i^-,

$$n_i = 0 \underset{k_i^-}{\overset{k_i^+}{\rightleftharpoons}} n_i = 1,$$

which depend on the configuration of nearest neighbours. For instance in one dimensional systems the rate constants depend on temperature and a function $f(n_{i-1}, n_{i+1})$ that indicates the type of dynamical facilitation. Thus, in the Fredrickson–Andersen model,[42] where a state change is allowed when it is next to at least one defect, the tracer diffusion coefficient of a probe molecule has an Arrhenius behaviour at low temperature, and corresponds to a strong liquid. In the case of the East model,[43–45] dynamical facilitation has directional persistence and the diffusion coefficient of the probe exhibits a super-Arrhenius behaviour, like a fragile liquid, owing to the hierarchical nature of dynamics.

In order to test the violation of the SER in the one dimensional case ($d = 1$), Jung *et al.*[41] compared the diffusion of the probe, D_t, with the relaxation time, τ_α, of the matrix liquid, and utilized the scale law $D_t \propto \tau_\alpha^{-\delta}$, which is similar to the FSER [eqn (9.14)] to describe the magnitude of the deviations. The product $D_t\tau_\alpha \approx$ constant at high temperatures, but for both models $D\tau_\alpha$ increases by 2 or 3 orders of magnitude in the low temperature region. A detailed analysis of the $d = 1$ case shows that for the Fredrickson–Andersen model,[42] $\delta \approx 2/3$, while for $d = 3$, $\delta \approx 0.95$, that is, there is only a weak breakdown of the SER for strong liquids in the three dimensional case.

For the East model[43–45] (fragile liquids), both the tracer diffusion coefficient and the relaxation time show super-Arrhenius behaviour, and $D_t \approx \tau_\alpha^{-0.73}$ for $d = 1$. The exponent $\delta = 0.73$ is similar to that found experimentally for several fragile glass forming liquids. The good agreement of the exponent δ for $d = 1$ with those reported experimentally[35,46,47] for real systems seems to be related with persistence in the directionality in the facilitation observed for fragile liquids.

9.2.7 Diffusivity and Viscosity of Supercooled Water

Harris[48] analyzed the behavior of liquid water regarding the validity of the SER and found slight deviations that can be accounted by using the FSER (eqn (9.14)). It was observed that $\delta = 0.94$ at temperatures above T_m, which is a value close to that found for molecular and ionic liquids and also to the results obtained by molecular dynamics for a hard sphere ($\delta = 0.97$) and a Lennard–Jones ($\delta = 0.92$) fluid.[49,50] When the temperature dependence of the viscosity,[51] and the diffusion coefficient[52] of water in the supercooled regime down to temperatures of 235 K are included in the analysis, a transition temperature of about 258 K is observed. Below that temperature the fractional coefficient decreases to $\delta = 0.67 \pm 0.01$, which is smaller than that observed for glass forming liquids close to T_g.

Since $T_h = 235$ K is 100 K above T_g of water, the possibility of testing the SER in the no-man's land is discarded in bulk water. Smith *et al.*[53] measured the self-diffusion coefficient of amorphous solid water (ASW) thin films in the temperature range (150 to 157) K and found a very sharp temperature dependence, with D decreasing from 10^{-12} cm$^2 \cdot$ s^{-1} to 10^{-15} cm$^2 \cdot$ s^{-1} with decreasing temperature. They proposed the continuity between the ASW and liquid water but the lack of diffusion and viscosity coefficients in the intermediate region makes this hypothesis highly speculative.

By confining water in mesoporous silica (MCM-41-S) with pore diameters of 1.4 nm and 1.8 nm, Chen *et al.*[54] were able to explore the self-diffusion and translational relaxation time (proportional to the viscosity) of supercooled water down to 200 K, using NMR and QENS spectroscopy. The measured self-diffusion coefficient, D, and the translational relaxation time, τ, show a VFT behavior at temperatures above $\approx$225 K, while an Arrhenius-like behavior is observed below that crossover temperature. The product $D\tau/T$, which is analogous to the SE ratio, remains almost constant down to

a temperature of 250 K and then increases steeply as T goes below what they call the fragile-to-strong dynamic crossover temperature ($T_{crossover} \approx 225$ K), and at $T = 200$ K reaches a value 40 times larger than the high temperature value, indicating a similar behavior in comparison with glass forming liquids as T_g is approached.

More interestingly, Chen *et al.*[54] found that the decoupling can be described by the scale law $D \propto \tau^{-\delta}$, which is similar to the FSER (eqn (9.14)). The results show that, in the fragile side ($T > 225$ K), δ is 0.74, while it switches to $\delta \approx 2/3$ in the strong side ($T < 225$ K). These results are in excellent agreement with the predictions of the dynamical facilitation model,[41] considering that nano-confined water in pores with diameters < 2 nm behaves as a one-dimension fluid, and also supports the hypothesis of two different liquid structures in supercooled nano-confined water.

More evidence on the violation of the SER in deeply supercooled water is provided by the work by Banerjee *et al.*,[55] using electron spin resonance spectroscopy to study the dynamical properties of the spin probe TEMPOL dissolved in the water film coexisting with cubic ice in the temperature range (140 to 210) K. The rotational mobility of the probe exhibits deviations from the SEDR [eqn (9.11)], which increase sharply below a temperature of 225 K, while two coexisting fractions of the probe were observed, having different mobility and fragility. The slower fraction is strong and predominates at low temperatures, below the fragile-to-strong dynamic crossover, while the fragile (non-Arrhenius) behavior predominates at high temperatures.

The relationship between the Widom line, as shown in Figure 9.1, and the breakdown of the SER was discussed by Kumar *et al.*,[56] who performed molecular dynamics simulations using TIP5P and ST2 water models. They calculated the diffusion coefficients and the α-relaxation times between 0 and 200 MPa, and observed that the product $D\tau_\alpha/T$ is constant for both models at high temperatures, and increases with decreasing temperature. Interestingly, the curves at different pressures collapse onto a single master curve as plotted as a function of $T - T_w(p)$, where $T_w(p)$ defines the Widom line. The authors concluded that the crossover to a more structured low density liquid (LDL) when approaching $T_w(p)$ appears to be correlated with the breakdown of the SER and with the growth of dynamic heterogeneities.

Recently, Bagchi and coworkers[57] have performed molecular dynamics simulations with the TIP5P water model, focusing on the mechanism of interconversion between 5 and 4 coordinated molecules and the propagation of such events in bulk, by analyzing the molecular trajectories. They found that at low temperatures, large amplitude (≈ 333 K) rotational jumps propagate like strings, with a characteristic propagation length which increases with decreasing temperature. The strings are formed by mobile 5-coordinated water molecules which move causing water molecules in the path to switch from 4 to 5-coordination and then back to 4-coordination, as shown in Figure 9.4(a), following essentially the mechanism proposed by Laage and Hynes.[58]

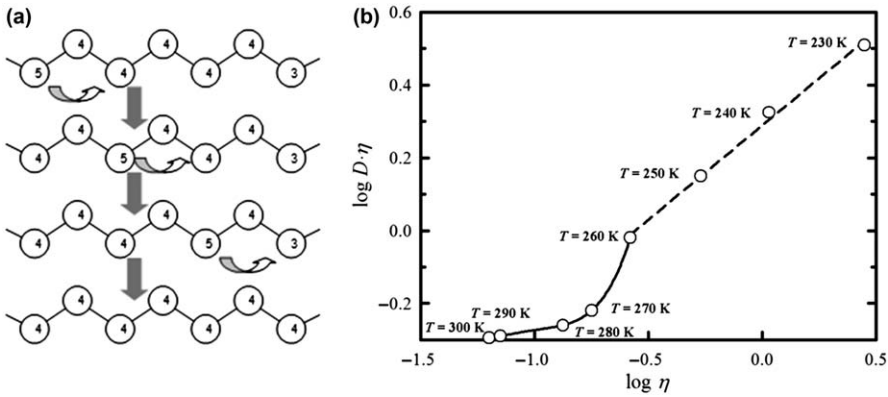

Figure 9.4 (a), Schematic of the string-like propagation mechanisms. (b), SE plot for supercooled water calculated using the TIP5P water model. The temperatures (in K) are indicated in the plot and the dotted line corresponds to data fit with $\delta = 0.5$.
Reproduced from ref. 57 with permission.

Bagchi[57] assumed that the self-diffusion coefficient is an average over the 4- and 5-coordinated water molecules that are the predominant species, while the viscosity is an average over the corresponding lifetimes, related to the distribution of correlation lengths, P_i, that is:

$$D = C_1\left(\frac{P_4}{\tau_4} + \frac{P_5}{\tau_5}\right) \tag{9.15}$$

and

$$\eta = C_2(P_4\tau_4 + P_5\tau_5). \tag{9.16}$$

From the values of P_i and τ_i obtained from the simulation, they derived the SE plot shown in Figure 9.4(b), where it can be observed that SER is valid at temperatures above 270 K, but large deviations occur at temperatures below 260 K where the diffusion-viscosity relation can be described with the FSER with scaling factor $\delta = 0.5$. The origin of the dynamical heterogeneities is attributed to the fact that water molecules visited by defects exhibit a rather large diffusivity (3×10^{-5} cm$^2\cdot$s^{-1}), while those not visited show negligible diffusivity.

9.2.8 Mobility–Viscosity Decoupling in Water Solutions

The first experimental evidence of conductivity–viscosity decoupling in aqueous solutions was reported by Moynihan *et al.*[59] for the LiCl–H_2O system. Concentrated LiCl solutions ($0.12 < x_{LiCl} < 0.25$) can be easily supercooled at moderate cooling rates, and the ratio τ_α/τ_σ between the structural and the conductivity relaxation times, proportional to the Walden product, becomes higher than unity as T_g is approached.[59]

A crossover of the water diffusion dynamics was observed by QENS for a supercooled LiCl solution ($x_{LiCl} = 0.12$) around 225 K, which suggests a breakdown of the SER occurring at the same temperature as in supercooled water.[60] Suzuki and Mishima[57] proposed that hydration water in supercooled LiCl solutions corresponds to HDL, which is the predominant phase of liquid water at pressures above the liquid–liquid transition line. Thus, the effect of the electric field near the ions will be equivalent to the pressure effect in promoting the HDL phase of water.[61] A similar conclusion has been derived from experimental and MD simulation results on supercooled H_3PO_4 and NaCl aqueous solutions, respectively.[62,63]

The conductivity–viscosity decoupling for ionic solutes in supercooled aqueous solutions is present even well above the glass transition temperature of the aqueous mixtures, as recognized since many years ago. Thus, Stokes and Stokes[64] proposed a fractional WL (FWL), $\Lambda \propto \eta^{-\alpha}$, which is the ionic equivalent to the FSER, Λ being the molar conductivity of the salt.

By studying the conductivity of NaCl in supercooled trehalose[§] aqueous solutions, Miller *et al.*[65] found that $\alpha = 0.64$, a value much lower than that found for smaller polyols as D-glucose and glycerol.[¶] Thus, the deviations to the WL seem to increase with the size of the polyol. MD simulations for the tracer diffusion of ions in trehalose–water mixtures indicate the presence of slower domains, consisting mostly of trehalose, and faster domains that include the ions and their accompanying hydration shells.[65]

The conductivity–viscosity relationship was further studied for electrolytes with different ionic sizes (LiCl, NaCl, KCl, CsCl, $(C_4H_9)_4NBr$, and $(C_4H_9)_4NI$) in supercooled aqueous sucrose[‖] and trehalose solutions.[66] The α coefficient decreases, that is the magnitude of the deviations to the WL [eqn (9.13)] increase, with decreasing ionic size. This effect is explained taking into account that the WL is deduced considering only the viscous friction of ions in the solvent, while the dielectric friction due to the electrostatic ion–dipole interactions is more important in the case of small ions.[67] Figure 9.5 shows the ratio D/D_{SE} for different solutes in aqueous trehalose and sucrose solutions. It is interesting to note that for ionic solutes in supercooled sucrose and trehalose aqueous solutions the decoupling increases monotonically, following the behaviour observed for the diffusion of water,[68] and supporting the MD results showing that ions would move in water rich environments of local reduced viscosity.[65]

The most studied supercooled non-ionic aqueous solutions, are those containing polyols, such as glycerol, sucrose, and trehalose[68–70] because of their application in the criopreservation of biomolecules, tissues and organs.

[§]IUPAC name (2*R*,3*R*,4*S*,5*S*,6*R*,2′*R*,3′*R*,4′*S*,5′*S*,6′*R*)-2,2′-Oxybis[6-(hydroxymethyl)tetrahydro-2*H*-pyran-3,4,5-triol].
[¶]IUPAC name propane-1,2,3-triol.
[‖]IUPAC name (2*R*,3*R*,4*S*,5*S*,6*R*)-2-[(2*S*,3*S*,4*S*,5*R*)-3,4-dihydroxy-2,5-bis(hydroxymethyl)oxolan-2-yl]oxy-6-(hydroxymethyl)oxane-3,4,5-triol

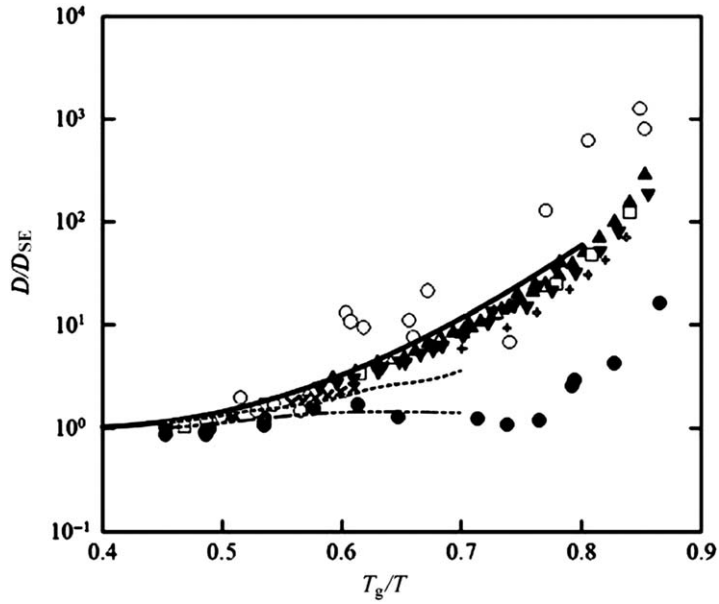

Figure 9.5 Stokes–Einstein plot for the ratio of tracer diffusion coefficients of different solutes as a function of T_g/T. ●, Ferrocene methanol; ▲, NaCl; △, KCl; ▼, CsCl; and +, Bu_4NBr in aqueous sucrose solutions; ○, fluorescein disodium anion; □, NaCl; and ×, Bu_4NI in aqueous trehalose solutions. —·— —, diffusion of trehalose in trehalose aqueous solutions) taken from Ref. 68; - - - -, sucrose in sucrose aqueous solutions taken from ref. 68; and ——, water in disaccharides aqueous solutions taken from ref. 68.

The diffusion of fluorescein and ferrocene methanol was measured in aqueous sucrose and trehalose solutions, and deviations from SER were observed at $T_g/T \approx 0.6$ for fluorescein disodium anion, and $T_g/T = 0.75$ for ferrocene methanol,[70] as shown in Figure 9.5. Thus, for these solutes the SER is valid over a narrow T_g/T range, with a similar decoupling to that of ionic solutes when the temperature is reduced.

The self-diffusion of water in a methanol aqueous solution ($x_{CH3OH} = 0.22$) was studied using NMR by Mallamace *et al.*[71] A cross-over temperature at 223 K was detected where the diffusion is super-Arrhenius at higher temperatures and Arrhenius at lower temperatures, suggesting a fragile-to-strong transition at that temperature. Moreover, $\delta = 0.9$ on the strong (low temperature) side in good agreement with the predictions of the dynamical facilitation model.[41]

9.2.9 Summary and Outlook

In spite of the several models and molecular simulation studies reported, our understanding of the heterogeneous dynamics in supercooled

glass-forming liquids and the associated breakdown of the SER, SEDR and WL is still incomplete and constitutes one of the strong challenges of the physics of condensed matter.

In the case of water the transport properties were explored in the supercooled region close to the melting point at temperatures between (235 to 273) K, but the analysis in the no-man's land region is, and will be, elusive. However the transport behavior in water is expected to be influenced by the existence of a low-density/high-density liquid–liquid transition, or strong to fragile transition, which is responsible for the diffusion–viscosity decoupling. Indirect information on the dynamics behavior of water in that region could be inferred from the properties of nanoconfined water, although the nature of water under these conditions could be strongly perturbed by the confinement surfaces.

The study of the transport properties of supercooled aqueous solutions is incomplete and the theoretical approach in terms of theories for pure glass forming liquids is a simplification. New models taking into account the effect of the second component on the heterogenous dynamics of water are needed to advance in our understanding of these systems of extreme practical relevance.

9.3 Density Scaling Approach

JOSEFA FERNÁNDEZ AND ENRIQUETA R. LÓPEZ

9.3.1 Introduction

Recent advances in the study of the effect of pressure on the vitrification process of van der Waals liquids, hydrogen-bonded systems, polymers, polymer blends, and biopolymers have led to extensive use of the approach named variously, density scaling, thermodynamic scaling or power-law density scaling.[72,73] This approach postulates that for a given liquid, properties such as viscosity, diffusion coefficient, electrical conductivity or structural relaxation time can be expressed solely as a function of the variable (Tv^{γ}),

$$X(T,v) = f(Tv^{\gamma}) = f(T\rho^{-\gamma}), \tag{9.17}$$

where X is a given liquid dynamic property, T the temperature, v the specific volume and ρ the mass density. The parameter γ is the scaling coefficient and quantifies for each liquid the dependency of dynamic property on volume, in comparison to that on temperature. An example showing how the experimental viscosities at different pressures and temperatures collapse onto a single master curve (with deviations comparable with an experimental uncertainty of a few percent) is presented in Figure 9.6 for the ionic liquid 1-butyl-3-methyl-1*H*-imidazol-3-ium tetrafluoroborate ($[C_4C_1Im][BF_4]$).

When the scaling coefficient is large ($\gamma > 20$), as for the viscosity of 2,3-dimethylpentane,[75] the transport property X does not depend explicitly on temperature, *i.e.*, $X(\rho)$. This is equivalent to assuming that the value of the transport property is only determined by the free volume (the volume of the liquid which is not occupied by its molecules), and the latter is only dependent on the density of the liquid. Thus, for this kind of materials at the

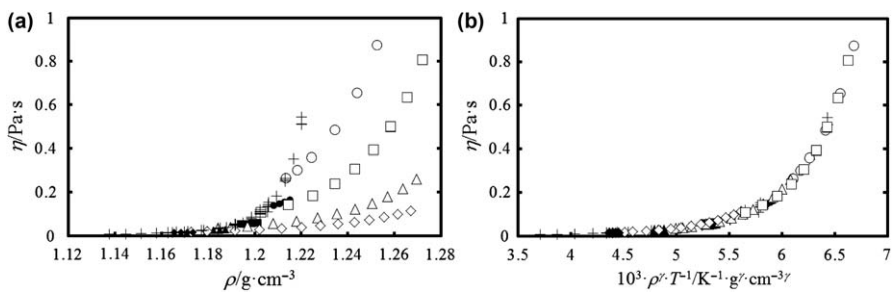

Figure 9.6 Viscosity, η, of $[C_4C_1Im][BF_4]$ at pressures up to 300 MPa as a function of (a) density, ρ, and (b) the group ρ^{γ}/T with $\gamma = 2.83$.[74] +, $p = 0.1$ MPa; ○, $T = 283.15$; ●, $T = 293.15$ K; □, $T = 298.15$ K; ■, $T = 313.15$ K; △, $T = 323.15$ K; ▲, $T = 333.15$ K; ◇, $T = 348.15$ K; ◆, $T = 353.15$ K.

glass transition the jamming of molecular motions occurs because of the reduction in the volume available for the molecules to rearrange.[76–78] By contrast, when γ is close to 0 [0.13 was found for relaxation times of (2S,3R,4R,5R)-hexane-1,2,3,4,5,6-hexol (sorbitol)[79]], it is assumed[75,79,80] that the dynamics is controlled by the temperature, *i.e.* it is driven near the glass transition temperature by thermally activated processes with a barrier energy, which is density independent. Thus, at the glass transition the jamming of the molecular motions is caused by a decrease in the energy available to each molecule, reducing the rate at which local potential barriers to positional changes are overcome, as described by energy landscape models.[73,81,82] For most fluids the scaling coefficient γ takes intermediate values, *i.e.* the molecular transport is driven by thermally activated processes with potential energy barriers that depend on local density. Thus, the γ values reflect the intensity of the intermolecular and intramolecular interactions. Focusing on viscosity,[74,75,83–88] γ values lower than 3.5 are mainly found for associated compounds; γ values between 3.5 and 7 correspond to several polar compounds; while higher γ values are obtained for compounds with saturated or aromatic rings and alkanes up to decane.

The quality of the description of the dynamic properties using the power-law density scaling depends on: (i) the shape and the number of parameters of function f; (ii) the quality, range and coherence of the experimental values of the dynamic property and the density. It was successfully applied over many decades of viscosity (*e.g.* for 2,6,10,15,19,23-hexamethyltetracosane[87] from 10^{-1} to 10^{7} mPa·s) and regression coefficients better than 0.9906 were found for the viscosity of 46 compounds by López *et al.*[74] Power-law density scaling fails badly only for very few H-bonding compounds,[75,83] such as water, whose viscosity presents an anomalous behaviour [*i.e.*, viscosity decreases with increasing pressure in the temperature range $T = (254 \text{ to } 303)$ K[89,90]] and for some van der Waals liquids over a very broad density range.[91]

In this section we focus the attention on the studies performed to determine the scaling coefficients for viscosity, diffusion, and relaxation times for non-polar, polar and ionic liquids and polymers as well as fluid models based on the Lennard–Jones interaction potential. Power-law scaling for the electrical conductivity of ionic liquids is also reviewed. We start by briefly reviewing the physics underlying the thermodynamic scaling.

9.3.2 Thermodynamic Scaling and Models

The origins of the density scaling can be traced back to molecular dynamics (MD) results on very simple fluids such as soft spheres.[92–97] Such fluids interact according to the inverse power law (IPL) potential of the form,

$$\Phi = \varepsilon_{\mathrm{IPL}} \left(\frac{\sigma_{\mathrm{IPL}}}{r} \right)^{n}, \tag{9.18}$$

where n is the repulsive power law exponent and $\varepsilon_{\mathrm{IPL}}$ and σ_{IPL} are the characteristic energy and distance parameters, respectively.

Ashurst and Hoover[95] observed for soft spheres, superposition of the reduced residual viscosities, expressed as a function of $\{\rho^*/(T^*)^{n/3}\}$ where ρ^* $(=\rho_n\sigma_{IPL}^3$, where ρ_n is the number density) and T^* $(=k_BT/\varepsilon_{IPL})$ are the reduced density and temperature, respectively. It is important to note that the reduced thermodynamic properties of soft-spheres are also only dependent on the same variable $\{\rho^*/(T^*)^{n/3}\}$.[97]

In 2001, Tölle[98] deduced from inelastic neutron scattering at high pressure that the relaxation times of 1,4-diphenylbenzene can be rescaled onto a master curve when plotted against $T^{-1}v^{-4}$. In 2004, Casalini and Roland showed[79] that the relaxation times over many decades of frequency and a wide range of temperatures and specific volumes of ten glass-forming liquids, encompassing van der Waals molecules, associated liquids, and polymers, obey eqn (9.17) (more information on glass-forming liquids is given in Section 9.2). As far as we are aware, they were also the first to introduce the concept of the scaling coefficient γ.

In 2006, Casalini *et al.*[99] deduced a form for the function f [as given by eqn (9.17)], based on a modification of the Avramov entropic model[100] for the viscosity of the glass-forming melts. This model is based on the notion that molecular motions are thermally activated, with a jump frequency, as in the solid state. In the Avramov model, an average jump frequency,

$$\langle\nu\rangle \cong \nu_0 \exp\left(-\frac{E_{\max}}{\sigma}\right), \tag{9.19}$$

depends on some distribution $w(E,\sigma)$ of the energy barrier heights E, which are characterized by a maximum energy barrier $E_{\max}$ and the system energy dispersion σ, which is related to the entropy (more information about the Avramov model is given in Section 9.2).

The relaxation time τ (or the viscosity η) and the entropy S are related through the expression:[99,100]

$$\tau = \tau_0 \exp\left\{\frac{E_{\max}}{\sigma_r} \exp\left[\frac{2(S-S_r)}{ZR}\right]\right\}, \tag{9.20}$$

where the parameter Z is the system degeneracy, *i.e.* the number of available pathways for local motion of a molecule (or macromolecular segment) and R is the gas constant. The parameter τ_0 represents the limiting value of τ at extremely high temperatures and subscript r stands for reference state. Casalini *et al.*[99] assumed that the molar heat capacity at constant volume, C_V, is temperature independent and that the difference between the heat capacities at constant pressure (C_p) and at constant volume does not vary with volume. Under these conditions, the relaxation times, τ, (or the viscosities η) can be written as

$$\tau(T,v) = \tau_0 \exp\left(\frac{A}{Tv^{\gamma_G}}\right)^{\phi}, \tag{9.21}$$

where A is given by

$$A = \left(\frac{E_{\max}}{\sigma_r}\right)^{\frac{1}{\phi}} T_r v_r^{\gamma_G}, \tag{9.22}$$

with $\phi = (2C_V/ZR)$ and γ_G the Grüneisen parameter given by

$$\gamma_G = \frac{C_p/C_V - 1}{\alpha T}. \tag{9.23}$$

α is the cubic expansion coefficient, also known as the thermal expansion coefficient. A very similar equation can be also obtained[99] using the fluctuation theory of Landau and Lifshitz.[101]

Lately, Casalini and Roland[102] and subsequently Pensado *et al.*[75] proposed to use the same form of eqn (9.21) to analyze the relaxation times and the viscosity of liquids

$$X(T, v) = X_0 \exp\left[\left(\frac{A_X}{Tv^{\gamma_X}}\right)^{\phi_X}\right], \tag{9.24}$$

while a similar equation

$$X(T,\ v)\ =\ X_0\ \exp\left[-\left(\frac{A_X}{Tv^{\gamma_X}}\right)^{\phi_X}\right], \tag{9.25}$$

was proposed by López *et al.*[74] for the analysis of the self-diffusion coefficient, D, the ratio (D/T), the electrical conductivity, κ, and the molar conductivity, Λ. The parameters X_0, A_X, γ_X and ϕ_X entering eqn (9.24) and (9.25) are material constants for each dynamic property X. When the scaling laws based on eqn (9.24) and (9.25) were applied to the analysis of data to perform the density scaling, the parameters γ_X and ϕ_X did not coincide with the values of the Grüneisen parameter γ_G and $\phi = (2C_V/ZR)$.[74,99,102,103] Thus, Casalini *et al.*[99] found that γ_G obtained from literature data is about 30 % lower than the γ values obtained by superpositioning the relaxation times. According to the authors,[99] this fact is due to the following: (i) some of the contributions to the heat capacity may not affect τ; and (ii) the non-ideal behavior of the thermal pressure coefficient $(\partial p/\partial T)_V$.

Unlike the Avramov approach, other well-known models such as the extensions to high pressure of Adam–Gibbs[17,104,105] (see Section 9.2.4) and VFT[20,84,88] [see eqn (9.5)] cannot be used to obtain functional forms f for the thermodynamic scaling [eqn (9.17)] because both models are characterized by the presence of divergences at specified temperatures.[99]

Grzybowski *et al.*[106] analyzed relaxation times and postulated that the maximum energy barrier $E_{\max}$ should increase with the density, proposing the following expression

$$E_{\max} = A_E \left(\frac{\rho}{\rho_r}\right)^{\gamma_E} = A_E \left(\frac{v_r}{v}\right)^{\gamma_E}, \tag{9.26}$$

where A_E and γ_E are material constants. Using this relation in eqn (9.22) and substituting in eqn (9.21), it can be shown that:

$$\ln\left(\frac{\tau(T,v)}{\tau_0}\right) = \frac{E_{\max}}{\sigma_r}\left(\frac{T_r}{T}\left(\frac{v_r}{v}\right)^{\gamma_G}\right)^{\phi} = \left(\frac{A_E}{\sigma_r}\right)\left(\frac{T_r}{T}\left(\frac{v_r}{v}\right)^{\gamma_G+\gamma_E/\phi}\right)^{\phi}. \quad (9.27)$$

Under these conditions the new parameter A [see eqn (9.21)] is given by

$$A = \left(\frac{A_E}{\sigma_r}\right)^{\frac{1}{\phi}} T_r v_r^{\gamma_G+\gamma_E/\phi}. \quad (9.28)$$

Taking into account that when eqn (9.24) and (9.25) are used to fit the data the scaling coefficient should not be identified with the Grüneisen parameter γ_G and comparing eqn (9.22) and (9.28), the following relation is obtained[106]

$$\gamma = \frac{\gamma_E}{\phi} + \gamma_G, \quad (9.29)$$

where γ and ϕ are obtained by using eqn (9.24) for relaxation times (γ_τ and ϕ_τ) or for viscosities (γ_η and ϕ_η). This equation combined with eqn (9.25) could be also applied to the analysis of the self-diffusion coefficient, D, the ratio (D/T) or the electrical conductivity, κ.

Grzybowski *et al.*[106] postulated that the exponent γ_E which enables the scaling of the maximum energy barrier according to eqn (9.26), is approximately equal to the exponent γ_{EOS} determined by fitting pVT experimental data with equations such as:

$$p = \frac{RT\rho}{M} + p_r + B(T)\left[\left(\frac{\rho}{\rho_r}\right)^{\gamma_{EOS}} - 1\right], \quad (9.30)$$

where $B(T)$ is some temperature dependent parameter, M is the molar mass, and ρ_r and p_r denote density and a configurational pressure in a chosen reference state, respectively. The configurational pressure is defined within the framework of thermodynamic perturbation theory as $p_r = \langle W \rangle / V_r$ where the virial W is given by $W = pV - Nk_BT$.

In 2009, an important insight into the density scaling was provided by Dyre and collaborators[107] who introduced the concept of "isomorphous" thermodynamic states. Two state points with particle density and temperature (ρ_1, T_1) and (ρ_2, T_2) are isomorphic if all pairs of physically relevant micro-configurations of the state points that trivially scale into one another (*i.e.*, $\rho_1^{1/3}\mathbf{r}_i^{(1)} = \rho_2^{1/3}\mathbf{r}_i^{(2)}$ for all particles i) have proportional configurational Boltzmann factors:

$$\exp(-U(\mathbf{r}_1^{(1)} + \ldots + \mathbf{r}_N^{(1)})/(k_BT_1)) = C_{12}\exp(-U(\mathbf{r}_1^{(2)} + \ldots + \mathbf{r}_N^{(2)})/(k_BT_2)). \quad (9.31)$$

The constant C_{12} depends only on the two state points, not on the microscopic configurations. For an IPL liquid, the constant C_{12} is unity for states which obey $\rho_1^{n/3}T_1 = \rho_2^{n/3}T_2$. Assuming that power-law density scaling[107] reflects an underlying effective power-law potential, the scaling exponent

can be found from the *NVT* equilibrium fluctuations of the potential energy U and the virial W as follows:

$$\gamma = \frac{\langle \Delta W \Delta U \rangle}{\langle (\Delta U)^2 \rangle}. \tag{9.32}$$

Gnan *et al.*[107] introduced the label ''strongly correlating liquids'' for those liquids for which the virial and potential energy correlate to better than 90 % in their thermal equilibrium fluctuations in the *NVT* ensemble (*e.g.* $\langle \Delta W \Delta U \rangle / (\langle (\Delta W)^2 \rangle \langle (\Delta U)^2 \rangle)^{0.5} > 0.9$).[107] This type of liquids has isomorphs, *i.e.*, continuous curves of state points that are all pair wise isomorphic [*i.e.*, they obey eqn (9.31)]. Along such curves in the phase diagram, the structure and dynamics are, to a good approximation, invariant, in the reduced units. Thus, isomorphic state points have the same excess entropy, the same reduced average relaxation time, the same dynamics, and the same scaled radial distribution functions. Isomorph invariance is not limited to static quantities; the mean-square displacement, time auto-correlation functions, and higher-order correlation functions are also invariant in reduced units along an isomorph.[108] Recently, Dyre and collaborators[109,110] decided to rename these liquids as ''Roskilde simple liquids'' or ''Roskilde groups'' because of the similarly named strongly correlated quantum systems. Based on computer simulations and known properties of liquids, Ingebrigtsen *et al.*[111] postulated that van der Waals and metallic liquids are simple whereas the hydrogen, ionically, and covalently bonding liquids are not, as they are not strongly correlated. However, Dyre[110] has recently indicated that van der Waals liquids of highly elongated molecules may not be Roskilde liquids, whereas room temperature ionic liquids could be strongly correlated.

It has been recently shown[112] that for strong correlated liquids, the temperature is a product of a function of excess entropy per particle, s, and a function of density, *i.e.* $T = f(s)h(\rho)$. Since the excess entropy is an isomorph invariant, the isomorphs also obey the rule that $h(\rho)/T$ is constant. This implies that any reduced dynamic property X^*, which is also an isomorph invariant, can be described by

$$X^* = G\left\{\frac{h(\rho)}{T}\right\}. \tag{9.33}$$

In addition, Gnan *et al.*[107] defined the state-point dependent density-scaling exponent,[112] γ, as

$$\gamma = \left(\frac{\partial \ln T}{\partial \ln \rho}\right)_{S_{ex}} = \left(\frac{\mathrm{d} \ln h}{\mathrm{d} \ln \rho}\right), \tag{9.34}$$

where S_{ex} is the excess entropy over that of the ideal gas. The exponent γ is a function of density only, *i.e.* $\gamma = \gamma(\rho)$ since h depends only on ρ. When the density function is of the form $h(\rho) = \rho^{\gamma}$, eqn (9.33) reduces to the ''classical'' scaling equation [*i.e.* eqn (9.17)] for reduced properties. It is important to point out that the form of the eqn (9.33) was already proposed for

non-reduced relaxation times by Alba-Simionesco *et al.*[113] in 2004. Bøhling *et al.*[91] found that the scaling using eqn (9.17) breaks down for the reduced structural relaxation times over a broad density range of two real liquids and three fluid models, whereas with the new formulation, given by eqn (9.33), the data collapse onto a master curve.

9.3.3 Scaling of Different Transport Properties

Most of the calculations of the scaling coefficient, γ, were performed for relaxation times of glass-forming liquids at high-pressures – with the objective to further our understanding of the dynamics in the liquid close to vitrification. In 2005, Roland *et al.*[72] reported γ values determined from relaxation times of an important number of glass-forming liquids and polymers. These authors found that both the γ values and the ratio of the isochoric activation energy E_V to the isobaric activation energy E_p quantify the roles of the temperature and the volume in the relaxation dynamics. Nowadays super-positioning of relaxation data as a function of the variable Tv^{γ} has been confirmed by an analysis of experimental data for hundreds of liquids.[73]

Pensado *et al.*[75] and López *et al.*[74] have calculated γ values using high viscosity pressure data for around fifty molecular or ionic liquids, proposing a modified method[75] to quantity the temperature and volume dependency through two contributions to the pressure–viscosity derivative. These authors have found that: (i) the highest γ values corresponds to relatively short alkanes and cycloalkanes; (ii) for these compounds γ decreases with the number of methylene groups; (iii) addition of methyl groups or non-aromatic cycles to the aromatic rings increases the value of γ; (iv) the polar compounds 2,2-bis(hydroxymethyl)propane-1,3-diol (pentaerythritol) esters, polyethers, alkyl carbonates and acetonitrile have lower γ than the hydrocarbons of the same size; and (v) γ decreases with the polarity and in the presence of hydrogen-type bonds.

López *et al.*[74] observed the existence of a relationship between the values of γ_η and ϕ_η which can be correlated to give $\phi_\eta(\gamma_\eta) = 7.1/(1+\gamma_\eta)$. A similar relationship has been already established by Casalini and Roland[102] who found that the analysis of relaxation times, τ, yields values of ϕ_τ and γ_τ that are not independent, but can be correlated with $\phi_\tau(\gamma_\tau) = 20.8/(1+\gamma_\tau)$. Although, the shape of $\phi_\tau(\gamma_\tau)$ and $\phi_\eta(\gamma_\eta)$ curves is similar, the values of ϕ_η are lower than those of ϕ_τ for a given scaling coefficient. Furthermore, López *et al.*[74] have applied eqn (9.25) to the ratio of self-diffusion coefficients and temperature, D/T, for ionic liquids and molecular fluids finding the relationship $\phi_{D/T} = 6.1/(1+\gamma_{D/T})$. This correlation and the $\gamma_{D/T}$ values are quite close to those obtained for viscosities. The scaling law given by eqn (9.25) was also used to analyze the electrical and molar conductivities for six ionic liquids, finding that the scaling coefficients and the ϕ values are very close to those obtained for the viscosity. This indicates that the temperature and density dependency is similar for the three properties (η, κ, D/T).

Bair *et al.*[114,115] have analyzed the effect of the value of ϕ_η on the Stickel function, defined as $S(Y) = (\mathrm{d}\ln\eta/\mathrm{d}Y)^{(-1/2)}$ where $Y = 1/Tv^{\gamma}$. The slope of the Stickel plots [$S(Y)$ against Y] is positive when $\phi < 1$ and negative when $\phi > 1$. Bair[115] found that for 1,1,1,3,3,5,5,7,7,7-decamethyl-tetrasiloxane (decamethyltetrasiloxane) the $S(Y)$ curve has a maximum. This indicates that eqn (9.24) should be modified to correctly describe the dynamics in broad ranges of temperature and pressures especially near the glass transition. New functional forms were proposed to address this issue.[115,116]

A number of workers have analyzed the relationship given by eqn (9.29), which relates γ, ϕ, γ_E and γ_G, assuming $\gamma_E = \gamma_{EOS}$. Grzybowski and his collaborators[106,117–120] have found that it holds true near the glass transition temperature for seven molecular liquids, including glass-forming ones, and a single ionic liquid. López *et al.*[103] have analyzed viscosities at broad temperature and pressure ranges for 48 liquids and found that the ratio (γ_{EOS}/ϕ) is generally higher than γ_η, the only exceptions being 4-methyl-1,3-dioxolan-2-one and 1-methylnaphthalene. Similar results were found for self-diffusion coefficients or electrical conductivities.[103] Therefore, it seems that eqn (9.29) is not generally applicable to viscosities, self-diffusion coefficients or electrical conductivities over broad ranges of temperature and pressure, especially far from the glass transition. The fact that the experimental data on relaxation times are observed to obey different relationships than the viscosity, self-diffusion coefficients or electrical conductivities can be rationalized by taking into account that the measurements of the former are performed nearer to the glass transition temperature in the third dynamic region (the highly supercooled regime).[103]

Another interesting issue is that the scaling of data from MD simulations[121,122] [eqn (9.17)] is carried out using the reduced transport properties whereas the scaling of experimental values[72,74,75,83] is performed using absolute quantities. The use of absolute values is justified by the Avramov model, for example, whereas the use of reduced quantities is based on the analysis of the intermolecular forces. If the intermolecular potential varies with distance as r^{-n}, the reduced configurational Helmholtz energy F^* may be written as $F^* = f(\rho^{\gamma}/T)$ where $\gamma = n/3$. Hence the residual thermodynamic properties and the residual viscosities[95] of the soft-spheres fluid obey the scaling only in reduced forms. The generalized form of the density scaling through eqn (9.33) is also expressed in reduced form. Molecular simulations of IPL fluids, Lennard–Jones fluids, Lennard–Jones mixtures, Lennard–Jones dumbbell fluids and Lennard–Jones chain fluids have shown that reduced transport properties obey the density scaling.[121–125] This finding also indicates that the dynamic properties of viscous liquids are governed primarily by the repulsive component of the intermolecular potential, with the long-range attractive part exerting a negligible effect.

The density scaling applied to reduced forms of the viscosity,[87] η^*, and the self-diffusion coefficient, D^*, can be expressed by:

$$\eta^* = \left(\frac{V}{N}\right)^{2/3} (mk_BT)^{-1/2}\eta = f\left(Tv^{\gamma^*_\eta}\right) \tag{9.35}$$

and

$$D^* = \left(\frac{V}{N}\right)^{-1/3} (mk_B T)^{-1/2} D = f\left(T v^{\gamma^*_D}\right). \tag{9.36}$$

These expressions for both reduced transport properties are based on a time scale defined by $(k_B T/m)^{1/2}$ where m is the mass of the molecule and on a length scale defined by $(v/N)^{1/3}$, where N is the number of molecules in a volume v.

Fragiadakis and Roland[87] and López *et al.*[74] have analyzed the differences between the values of the scaling coefficient γ [corresponding to eqn (9.17)] and those of the scaling coefficient γ^*, obtained by the analysis of the reduced properties [eqn (9.35) or (9.36)]. From now on, for brevity we refer to the scaling coefficients γ^* as the reduced scaling coefficients. The density scaling for the viscosity and self-diffusion coefficients in reduced and non-reduced forms for octane and 1-butyl-3-methyl-1*H*-imidazol-3-ium bis[(trifluoromethyl)sulfonyl]-azanide ([C_4C_1Im][NTf_2]) are illustrated in Figure 9.7 and Figure 9.8, as a way of example. For viscosity, the values of the reduced scaling exponent, γ^*_η, are in general lower than γ_η.[74,87,88,126,127] The differences are almost negligible for the liquids with the lowest scaling coefficients such as short alcohols and some ionic liquids. For the self-diffusion coefficient of molecular liquids and anion and cation diffusion in ionic liquids the following trend[74] is generally observed: $\gamma_D < \gamma^*_D < \gamma_{D/T}$. The effect of the volume is small in comparison with the effect of the temperature in performing the reduction by means of eqn (9.35) and (9.36).[74] The trends $\gamma^*_\eta < \gamma_\eta$ and $\gamma_D < \gamma^*_D$ are opposite because the viscosity decreases with the temperature whereas diffusion coefficients increase. Thus, the product $\eta T^{-1/2}$ decreases more strongly with temperature than the viscosity, whereas the product $DT^{-1/2}$ decreases less strongly. For both transport properties, the differences among the scaling coefficients for the reduced and non-reduced forms decrease as the magnitude of the coefficients decreases. It is important to remark that the reduced scaling coefficients, γ^*_η and γ^*_D, are much closer together than the scaling coefficients, γ_η and γ_D, especially when γ is high.

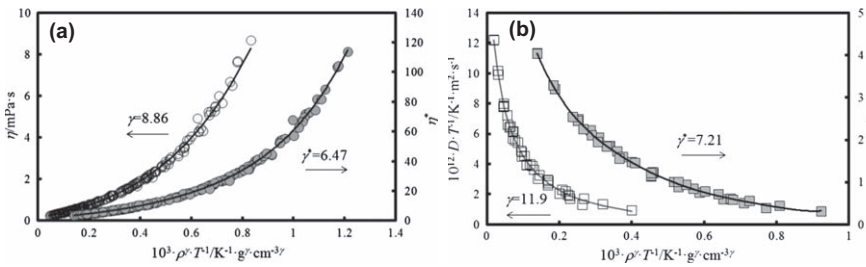

Figure 9.7 Density scaling for octane: (a) ○, viscosity, η, and ●, reduced viscosity, η^*, and (b) □, ratio D/T and ■, reduced self-diffusion coefficient, D^* as function of the group ρ^γ/T. The arrows indicate the corresponding axis. The original sources of experimental results are given in ref. 74. ———, verification of eqn (9.17) with the indicated scaling coefficients.[74]

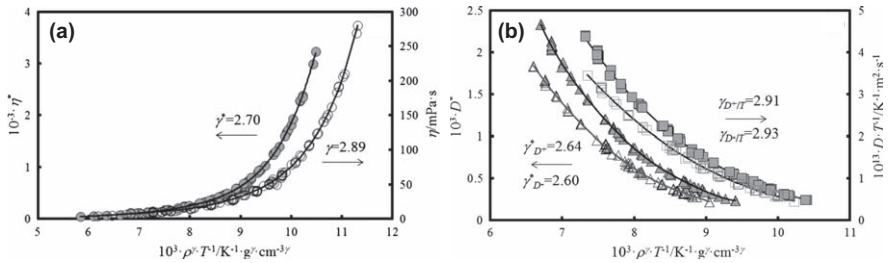

Figure 9.8 Density scaling for $[C_4C_1Im][NTf_2]$ of (a) ○, viscosity, η, and ●, reduced viscosity, η^*, and (b) □, ■, ratio D/T and △, ▲, reduced self-diffusion coefficients, D^*, of anion (unfilled symbols) and cation (filled symbols). The arrows indicate the corresponding axis. The original sources of experimental points are given in ref. 74. ———, verification of eqn (9.17) with the indicated scaling coefficients.[74]

With the above procedures the liquid state, including also the supercooled conditions, is modeled. To enlarge the range of scaling to gas and supercritical conditions, Galliero *et al.*[122] have proposed a new procedure for the thermodynamic scaling of viscosities for supercritical, liquid and gas states with one curve. The procedure has been applied to the flexible Lennard–Jones chain fluid (from monomer to hexadecamer) and to real non-polar fluids, such as argon and the normal alkanes (up to decane), considerably expanding the range of thermodynamic conditions to low densities for the scaling methods using eqn (9.17) and (9.35). γ^* values obtained from residual reduced viscosities increase with the number of the freely-jointed tangent spheres of the LJ chain model. This trend is just the same as that found for γ^* (up to decane), but it is opposite to that obtained from the absolute viscosity.[74,75] Boned *et al.*[128] have also used this procedure to describe dynamic viscosity of sulphur hexafluoride (SF_6) in a very broad range of thermodynamic conditions (of temperatures from 225.18 K to 473.15 K and pressures between 0.0264 MPa to 51.21 MPa) with a modified Avramov function with six adjustable parameters, obtaining an absolute relative average deviation (AAD) of ± 1.5 %. With the same primary set of experimental data, the authors obtained an AAD of ± 1.7 % with the free volume model (three parameters) and of ± 3.8 % (one parameter). The friction theory (see Section 8.3) provides a better fit, but with 21 parameters.[129]

9.3.4 Summary and Outlook

Since the reappearance of the density scaling in 2004, the conformance to eqn (9.17) for relaxation times has been demonstrated for hundreds of materials, limited only by the availability of the density and relaxation measurements.[73,130,131] As regards to viscosity, scaling was applied to around eighty liquids,[74,75,83] whereas for diffusion coefficients[74] it was applied to roughly 30 molecular and ionic liquids. The work performed with electrical conductivities (10 ionic liquids) and thermal conductivity[132,133]

(some lubricants) is relatively limited. The different forms of the functions proposed by several authors,[114–116,128] and the different expressions [eqn (9.17), (9.33), (9.35) and (9.36)] for the density scaling have shown great flexibility to correlate the different dynamic properties in very broad ranges (several decades, eight orders of magnitude in viscosity[114]) for supercooled, liquid, supercritical and gas conditions.

Deviations from density scaling were reported for some liquids that exhibit hydrogen-bonding[73,75,134] mainly water, which can form up to four hydrogen bonds per molecule. The breakdown of the thermodynamic scaling can be explained[83] by the fact that the number of hydrogen bonds changes with temperature[135,136] and pressure.[137]

Fluid models were extensively used to analyze the physics underlying density scaling,[121–125] especially the relationship between the scaling coefficient and the form of the intermolecular potential. These studies led to several important conclusions. In particular it was shown that the scaling law should be applied to the reduced properties. Thus, the scaling coefficients of the reduced viscosity and diffusion coefficient are closer than those obtained from scaling the actual properties.[87] Furthermore, when using the residual reduced viscosities, the density scaling can be applied to a wide range of thermodynamic conditions covering not only the liquid but also the gas and supercritical states.[122,128]

Dyre and collaborators[91,107,108,112] have recently concluded that the power-law density scaling is an approximation to a more general form of scaling, which is derived from the theory of isomorphs. A statistical mechanics derivation of this scaling was recently provided, and its prediction agrees very well with simulations over large density changes. With the new formulation of the density scaling [eqn (9.33) and (9.34)] superposition curves are obtained for some liquids for which there is a breakdown of the classical formulation [eqn (9.17)] because of their scaling coefficients are density-dependent. This is a very promising and interesting result for the liquids for which there are dynamic data over a very broad density range.

In our opinion, since the reappearance of the density scaling, there was an increasing evolution from a fundamental point of view, *e.g.* the new concept of an isomorph in statistical mechanics. The scaling concept led to correlations of the transport properties of fluids in very broad ranges from gas to supercooled states near glass transition over very broad pressures ranges. A big challenge would be to extend the current models to encompass all the thermodynamic and transport properties.

Acknowledgements

The authors are indebted to Dr Kristine Niss and Arno Veldhorst (Roskilde University) for providing constructive critiques of an early version of this section. Support from the Spanish Ministry of Economy and Competitiveness and FEDER Programme through CTQ2011-23925 project is acknowledged.

9.4 Thermal Diffusion in Binary Mixtures

ALOIS WÜRGER

9.4.1 Introduction

Thermal diffusion, or the Soret effect, describes the thermally driven non-convective separation of the components of molecular gas or liquid phases.[138–142] For the gas phase, Enskog[143] and Chapman[144] derived, independently of each other, the existence of a steady-state concentration gradient in a gas mixture with non-uniform temperature. They found in particular that the component with the larger molecular mass diffuses to the cold side.

For liquid mixtures, however, things turned out to be more complex.[145] In his 1926 paper, Eastman related thermal diffusion of salt ions to the ''entropy of transfer'' exchanged with the environment upon temperature variation; identifying this quantity with the canonical entropy, he obtained a description in terms of equilibrium properties.[146] In his 1945 thesis,[147] de Groot discussed this picture in view of Onsager's phenomenological theory of irreversible processes.

Thermal diffusive transport operates in various natural and technological systems. In liquids, thermal flow field fractionation has proven an efficient means for colloidal separation and analysis,[148] and quite generally a strong isotope effect is observed.[149–151] The isotope concentration in permafrost provides a signature for seasonal changes of the Palaeolithic climate.[152] A similar effect occurs during rock formation from cooling magma and silica melts.[153] In petroleum reservoirs, thermal diffusion results in separation of light and heavy oil components.[154] In recent years thermal diffusion has been used for separating molecules by size,[155] DNA translocation through nanopores,[156] and moving Janus particles along a given trajectory.[157]

The Soret and Dufour effects provide a classical example for Onsager's reciprocal relations for heat and mass flow. The formal theory was developed by de Groot and Mazur in their textbook on non-equilibrium thermodynamics.[158] As an important result they separate the non-equilibrium transport factors from the thermodynamic equilibrium properties. Regarding the latter, they find that enthalpy is the relevant thermodynamic property, thus confirming earlier work by Haase[159] and Derjaguin.[160,161]

With the development of specific non-equilibrium schemes for systems with non-uniform temperature,[162,163] molecular dynamics simulations have become a valuable tool for studies of thermal diffusion, providing information on issues such as the effect of molecular mass and size[164] and the origin of the composition dependence.[164–166]

9.4.2 Non-equilibrium Thermodynamics

In this review we focus on a binary mixture, with volume fractions c_1 and $c_2 = 1 - c_1$. The volume flow of component 1 reads

$$J_1 = -D\nabla c_1 - c_1 c_2 D_T \nabla T, \tag{9.37}$$

where D and D_T** are the mutual diffusion and thermal diffusion coefficients. In an incompressible liquid the flows of the two components cancel each other, $J_1 + J_2 = 0$.

The stationary state in a non-uniform temperature $T(x)$ is characterized by vanishing currents, $J_i = 0$, and a non-uniform composition. If both D and D_T are constant, the steady-state equation is readily integrated,

$$c_1(x) = (1 - \exp\{-S_T[T(x) - T_0]\})^{-1}, \tag{9.38}$$

where the reference temperature T_0 is determined by the global composition and where the Soret parameter is defined as

$$S_T = \frac{D_T}{D}. \tag{9.39}$$

Thermal diffusion arises from a non-uniform temperature and thus is a truly non-equilibrium effect. De Groot and Mazur[158] worked out a detailed description in terms of Onsager's phenomenological equations. Since their results have perhaps not been given full attention, we find it useful to repeat their key findings. We mainly deal with the case where viscous effects are absent, which applies to molecular mixtures where all components have comparable mass and size.

In the framework of non-equilibrium thermodynamics, diffusion and thermal diffusion fluxes are driven by generalized forces $-\nabla(\mu_i/T)$, which are given by the gradient of the Planck potential, which is the ratio of the chemical potential μ_i per mole of substance i and temperature T. It turns out to be convenient to use thermodynamic quantities per volume rather than per mole. Such quantities are indicated by a hat, for example the chemical potential

$$\hat{\mu}_i = \frac{\mu_i}{V_{m,i}}, \tag{9.40}$$

where $V_{m,i}$ is the molar volume of substance i.

In most cases the chemical potential depends on the position only through the non-uniform temperature $T(x)$ and composition $c_i(x)$. Thus, taking the gradient of the Planck potential leads to two terms,

$$\nabla \frac{\hat{\mu}_i}{T} = -\frac{\hat{h}_i}{T^2}\nabla T + \frac{1}{T}\sum_j \frac{d\hat{\mu}_i}{dc_j}\nabla c_j, \tag{9.41}$$

**The IUPAC *Green Book* recommends the symbol D^T for the thermal diffusion coefficient, however, for the sake of consistency with Chapter 2 D_T will also be used in this chapter.

where we have used the Gibbs–Helmholtz relation for the enthalpy. The first term on the right hand side of eqn (9.41), that is proportional to the temperature gradient, gives rise to a thermal diffusion current, whereas the second one depends on the concentration gradients and thus leads to Fick diffusion.

9.4.3 Thermal Diffusion Coefficient in the Absence of Viscous Effects

In terms of the thermodynamic forces, the current of component 1 reads

$$J_1 = -B_1 \nabla \frac{\hat{\mu}_1}{T} - B_2 \nabla \frac{\hat{\mu}_2}{T}. \tag{9.42}$$

The two terms are products of the generalized forces, eqn (9.41), and mobility factors B_i; the latter are linear volume-fraction weighted superpositions of the coefficients a_{ij} used by de Groot and Mazur, for example, $B_2 = (c_1 a_{22} - c_2 a_{21})/c_1 c_2$.[167] In physical terms, the first term is due to the generalized force exerted on component 1. The second one arises from the force on component 2; the resulting current J_2, in turn, drives the molecules of species 1 in the opposite direction.

Inserting the generalized forces in the currents, using the Gibbs–Duhem relation, and comparing with the defining eqn (9.37), results in the Einstein coefficient

$$D = (c_1 B_2 + c_2 B_1) \frac{c_1 \mathrm{d}\hat{\mu}_1 / \mathrm{d}c_1}{k_\mathrm{B} T}. \tag{9.43}$$

where k_B is the Boltzmann constant. The expression in parentheses may be viewed as a volume fraction-weighted mean mobility. By the same token, identifying the prefactor of the temperature gradient results in the thermal diffusion coefficient

$$D_\mathrm{T} = \frac{B_2 \hat{h}_2 - B_1 \hat{h}_1}{k_\mathrm{B} T^2}. \tag{9.44}$$

which is given by the product of a thermodynamic factor (the enthalpy per volume $\hat{h}_\mathrm{i}$) and a transport quantity B_i.

The enthalpies can be calculated in the framework of equilibrium statistical mechanics. This is not the case, however, for the mobilities that describe the dynamical properties of the system which can be determined only by taking into account the molecular motion; possible approaches are based on kinetic theory models or hydrodynamics.

For notational convenience we express the derivative of the chemical potential in eqn (9.43) as

$$c_1 \frac{\mathrm{d}\hat{\mu}_1}{\mathrm{d}c_1} = \frac{k_B T}{c_2 V_{\mathrm{m}1} + c_1 V_{\mathrm{m}2}} Q, \tag{9.45}$$

where the first factor describes a thermodynamically ideal mixture,[158] V_m is the molar volume and the correction factor Q accounts for non-ideal behaviour. The latter is closely related to the activity coefficient γ.

Then the Soret coefficient reads

$$S_T = \frac{B_2\hat{h}_2 - B_1\hat{h}_1}{Qk_BT^2}\frac{c_1V_{m2} + c_2V_{m1}}{c_1B_2 + c_2B_1}. \tag{9.46}$$

The enthalpies and molar volumes are equilibrium quantities, and their experimental values are known for various systems. In practice we tend to use experimentally easily available vaporization enthalpy, as it provides a very good approximation. Little is known, on the contrary, about the mobility factors $B_i(T,c)$.[158] In the following we discuss a few simple cases and relate them to previously developed models.

A particularly simple situation arises if the molecular components have identical shape, volume, and diffusion properties, as illustrated in the left panel of Figure 9.9. Then the mobility factors satisfy $B_1 = B = B_2$, and the mutual diffusion coefficients D and D_T carry the same mobility factor which is independent of composition. In this case the Soret parameter is no longer dependent either on the mobility or on volume,

$$S_T = \frac{H_2 - H_1}{Qk_BT^2}, \tag{9.47}$$

but is entirely determined by the molar-enthalpy difference and the thermodynamic factor Q. The component with the lower enthalpy flows to the cold side.

In an early attempt to include the effect of unlike molecular masses, Haase[159] introduced the specific enthalpy difference. Later on, Kempers[168] proposed a similar expression, albeit with the molar volume instead of the

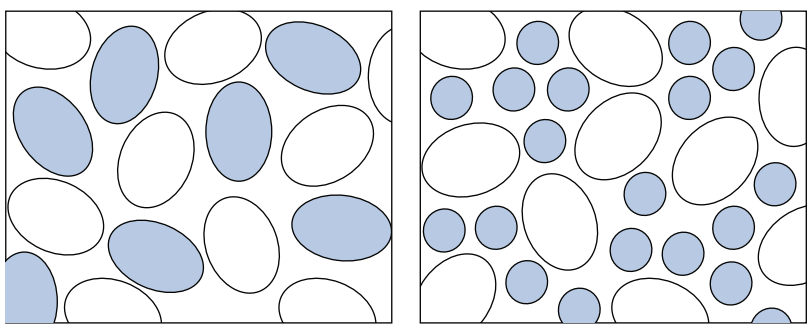

Figure 9.9 The left panel shows a binary mixture where the components have the same shape and size. Then the transport coefficients may be replaced by a single constant, $B = B_i$, and the Soret coefficient is given by the molar-enthalpy difference $H_2 - H_1$. The right panel shows the general case, where the molecular species differ in the transport coefficients B_i. Then one expects a rather complex variation of the Soret coefficient with composition.

mass. These models are obtained from eqn (9.46) by keeping identical mobility factors, yet allowing for different molecular masses or volumes. Then the Soret coefficient reads

$$S_T = \frac{\hat{h}_2 - \hat{h}_1}{Qk_BT^2}(c_1V_{m2} + c_2V_{m1}) \quad (B_1 = B_2). \tag{9.48}$$

Its sign and magnitude are determined by the difference in enthalpy per volume of the two components; the species with the lower value flows to the cold side.

Clearly the above assumption of identical mobility factors is hard to justify for real systems; as illustrated in the right panel of Figure 9.9, molecules of unlike shape and size will in general differ in mobility. In order to account for this difference, Shukla and Firoozabadi[169] proposed weight factors related to the parameters of Eyring's viscosity model. When comparing their non-equilibrium molecular dynamics data for Lennard–Jones liquids to these models, Artola and Rousseau[166] found a qualitative agreement, suggesting that the weight factors account at least partly for the underlying physics.

We briefly compare eqn (9.47) with early approaches to thermal diffusion that were developed prior to Onsager's theory. Thus Eastman[146] related the Soret coefficient to the "entropy of transfer"; identifying the latter with the canonical entropy $-\mathrm{d}\mu/\mathrm{d}T$ results in the Soret coefficient $S_T = (\mathrm{d}\mu/\mathrm{d}T)/k_BT$, which, however, is not compatible with the enthalpy in eqn (9.47). Still, for small molecules in aqueous solution, H and $-\mathrm{d}\mu/\mathrm{d}T$ often take similar values because of the "enthalpy–entropy compensation" of the structuration of water.[170]

9.4.4 Mixtures of Alkanes

There has been a long-standing debate whether the Soret effect can be described in terms of equilibrium properties, or whether it necessarily reflects the irreversible nature of the underlying diffusion processes.[171] Haase's formula, eqn (9.48), which depends on thermodynamic state functions only, is an example of the "equilibrium" picture, whereas the Onsager mobility factors B_i appearing in eqn (9.45) provide a signature of irreversibility.

In the following we discuss Soret data of binary mixtures in terms of physical insight gained by eqn (9.45) and (9.48). As a first example, Figure 9.10 shows room temperature Soret data for mixtures of decane C_{10} with a second component C_n where n varies from 5 to 20.[172,173]

This system is particularly attractive because of its simple thermodynamic behaviour. Alkanes form almost ideal mixtures. (For example, for hexane and hexadecane one has $H_6 = 31\ \mathrm{kJ \cdot mol^{-1}}$ and $H_{16} = 77\ \mathrm{kJ \cdot mol^{-1}}$, whereas the excess enthalpy (at a temperature of 303 K) takes the value of $0.26\ \mathrm{kJ \cdot mol^{-1}}$.) Hence, the ideal mixture enthalpy $H_m = c_1H_1^0 + c_2H_2^0$ varies linearly with volume fraction. Thus we identify the partial enthalpy of each component with the enthalpy of vaporization of the pure species, which is

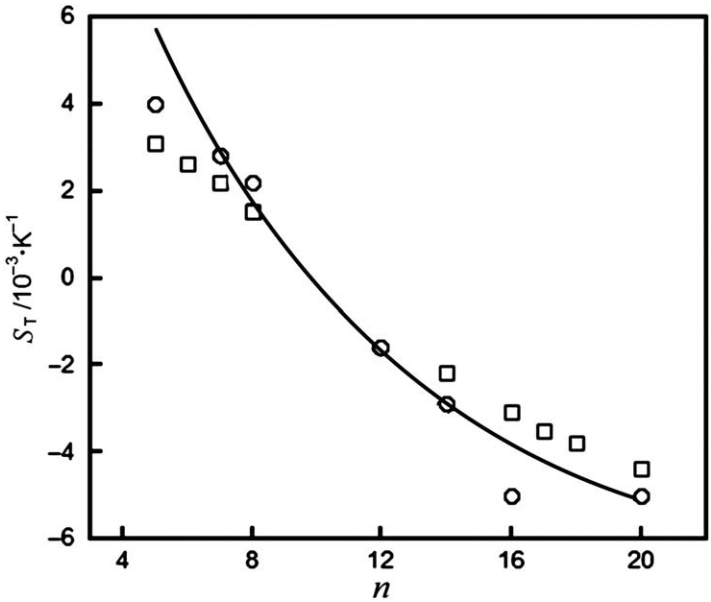

Figure 9.10 Soret coefficient S_T of decane in alkane mixtures $[C_{10}H_{22} + C_nH_{(2n+2)}]$ as a function of the number n of carbon atoms of the second component. □, Blanco *et al.*;[172] and ○, Leahy-Dios *et al.*;[173] ———, calculated from eqn (9.48) with measured enthalpies and volumes.

very well described by the empirical relationship $H_n^0 = (2.9 + 4.64n)$ kJ · mol^{-1}.[172]

The theoretical curve in Figure 9.10 is calculated from eqn (9.48) with equal volume fractions and known enthalpies and volumes. The thermodynamic factor Q is set to unity, in good agreement with available data.[174] Eqn (9.48) provides an overall good fit to the data and in particular accounts well for the variation as a function of the number of carbon atoms n. Thus the equimolar alkane mixtures considered here are well described by Haase's equilibrium expression, indicating that irreversibility plays a minor role.

This latter statement is not generally valid, and for most liquid mixtures Haase's expression eqn (9.48) fails even on the qualitative level. A striking example is provided by the Soret data for benzene-cyclohexane mixtures discussed in the next section.

9.4.5 Composition Dependence

A host of experimental data indicate that the Soret coefficient significantly varies with the composition and in many instances even changes sign. This is illustrated in Figure 9.11 by data on benzene–cyclohexane mixtures: the sign of S^T implies that benzene diffuses to the hot side at low mole fractions of benzene and to the cold side at mole fractions above 0.8.

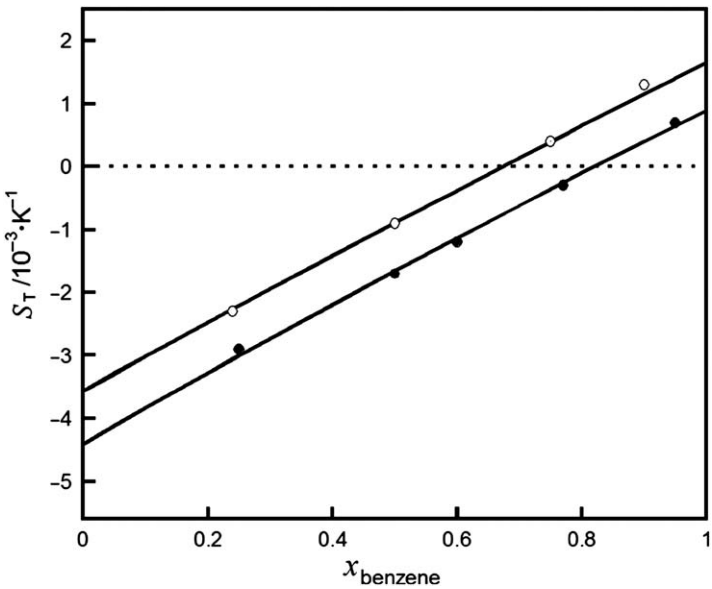

Figure 9.11 Composition dependence of the Soret coefficient S_T of {x benzene + $(1-x)$ cyclohexane) mixtures as a function of mole fraction x. Data from Debuschewitz and Köhler.[150] Open symbols give values for deuterated benzene C_6D_6 in cyclohexane C_6H_{12}, and full symbols for protonated benzene C_6H_6 in cyclohexane. The theoretical curves are calculated from eqn (9.49) with measured values of molecular enthalpies and volumes, and irreversibility parameter $B_1/B_2 = 0.785$ for C_6D_6 and 0.765 for C_6H_6.

For discussing these data it is convenient to rewrite eqn (9.46) in terms of mole fractions $x_i = n_i/(n_1 + n_2)$ instead of the volume fractions $c_i = n_i V_{m,i}$ used so far. Changing variables one finds

$$S_T = \frac{\hat{h}_2 B_2 - \hat{h}_1 B_1}{Q k_B T^2} \frac{1}{x_1 B_2 / V_{m2} + x_2 B_1 / V_{m1}}. \qquad (9.49)$$

Besides the explicit appearance of x_i in the denominator, both the mobility factors and enthalpies depend on composition; note that a change of sign of S_T can only arise from the numerator. The molar enthalpy of "regular mixtures" is a parabolic function of the mole fractions, $H = x_1 H_1^0 + x_2 H_2^0 + x_1 x_2 \omega$, where H_i^0 describe the pure species and the parameter ω the excess enthalpy. Thus, parameter ω accounts for the deviation from the ideal behaviour.

The pure species vaporization enthalpies of benzene and cyclohexane are (33.9 and 33.3) kJ · mol^{-1}, respectively; the excess enthalpy at a temperature of 298.15 K is $\omega = 3.2$ kJ mol^{-1}. The molar volumes of benzene and cyclohexane are (89 and 109) cm^3 mol^{-1}, respectively, and the excess volume, $V_m^E = 0.65$ cm^3 · mol^{-1}, is negligible. With these values one finds a very large positive Soret coefficient of about 1 K^{-1}, whereas the data shown in

Figure 9.11 are mostly negative and of the order of 10^{-3} K^{-1}. In other words, Haase's expression completely fails to describe these data.

A satisfactory description requires us to take into account different mobility factors B_i.[167] The solid curves in Figure 9.11 are calculated from eqn (9.49) with $B_1/B_2 = 0.765$ for protonated benzene C_6H_6 and $B_1/B_2 = 0.785$ for the deuterated isotope C_6D_6. The change of sign of the Soret coefficient is entirely due to the composition dependence of the excess enthalpy in the numerator of eqn (9.49). The mole fraction dependence in the denominator and the excess enthalpy contribute equally to the linear variation with composition.

9.4.6 Isotope Effect

Thermal diffusion shows a strong isotope effect. Upon substituting an atom or molecular group by its isotope, the Soret coefficient may significantly change in magnitude and even take the opposite sign. As an example we plot in Figure 9.11 Soret coefficient data for protonated and deuterated benzene in cyclohexane mixtures as a function of composition. The Soret coefficient of the C_6D_6 is by about 10^{-3} K^{-1} larger than that of C_6H_6. In other words, the heavier isotope has a stronger tendency towards diffusing to the cold side. This is most obvious at $x_1 = 0.8$ where the deuterated species diffuses to the cold side while the protonated one diffuses towards the hot side. This agrees with the well-known rule of thumb that the Soret coefficient increases for heavier molecules, which has been observed in many experiments on gaseous[175,176] and liquid mixtures,[149–151] and is confirmed by molecular simulations.[163–165,177]

Debuschewitz and Köhler measured the isotope effect for various partly deuterated equimolar benzene–cyclohexane mixtures and found that besides the mass, the molecular moment of inertia plays an important role.[150] In Figure 9.12 we plot the Soret coefficient of eight isotopes at molar fraction $x_{\text{benzene}} = 0.5$ as a function of the dimensionless quantity[178]

$$\Psi = \frac{m_1^{-1} - m_2^{-1} + b^2(I_1^{-1} - I_2^{-1})}{m_1^{-1} + m_2^{-1} + b^2(I_1^{-1} + I_2^{-1})}, \tag{9.50}$$

that expresses the difference in molecular mass m_i and moment of inertia I_i. The parameter b is a length of the order of the molecular radius. Since Ψ is linear in the relative change of mass and moment of inertia, the linear behaviour of the data confirms that the isotope effect is proportional to these changes.

A hard-bead model with collisions that conserve both linear and angular momentum, gives the Soret coefficient[178]

$$S_T = S_{T0} + \frac{R}{\ell}\frac{\Psi}{T}, \tag{9.51}$$

where S_{T0} is a mass-independent constant, R the particle size, and ℓ the mean-free path. The role of the moment of inertia is highlighted by

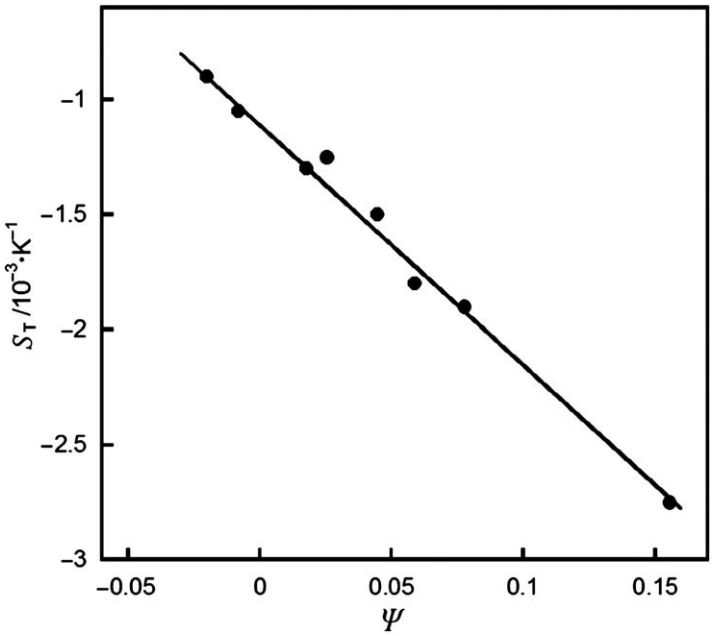

Figure 9.12 Soret coefficient S_T for equimolar mixtures of various benzene and cyclohexane isotopes as a function of Ψ. Experimental data from Debuschewitz and Köhler.[150] From left to right the data points are (C_6D_6 + C_6H_{12}), (C_6HD_5 + C_6H_{12}), ($C_6H_3D_3$ + C_6H_{12}), ($^{13}C_6H_6$ + C_6H_{12}), (C_6H_5D + C_6H_{12}), (C_6H_6 + C_6H_{12}), (C_6D_6 + C_6D_{12}), (C_6H_6 + C_6D_{12}). The solid line is given by eqn (9.51).

comparing fully deuterated benzene C_6D_6 with $^{13}C_6H_6$ containing the carbon isotope ^{13}C. These molecules have the same mass but different moment of inertia. Their Soret coefficients differ by about $0.4 \cdot 10^{-3}$ K^{-1}.

Simple kinetic models for the mass effect of thermal diffusion rely on the collision rate in a hard-bead system or on activated jump diffusion. The hard-bead model describes the thermal velocity fluctuations of a molecule in the cage formed by its neighbours.[178] The collision rate ω is proportional to the thermal velocity $v_T = \sqrt{k_B T / m}$, and thus varies with the inverse square of the molecular mass. Because of its higher thermal velocity, a light particle (L) undergoes more frequent collisions that a heavy one (H),

$$\frac{\omega_L}{\omega_H} = \sqrt{\frac{m_H}{m_L}}. \tag{9.52}$$

In the framework of kinetics of hard-beads, this ratio implies that, because of their stronger velocity fluctuations, the lighter molecules diffuse to higher temperatures, in agreement with experiment.

Activated jump diffusion relies on the potential barrier for molecular hops between nearby stable positions. In analogy to Eyring's model for chemical kinetics, the jump rate is given by $\omega = \Omega e^{-\phi / k_B T}$, where ϕ is the barrier height

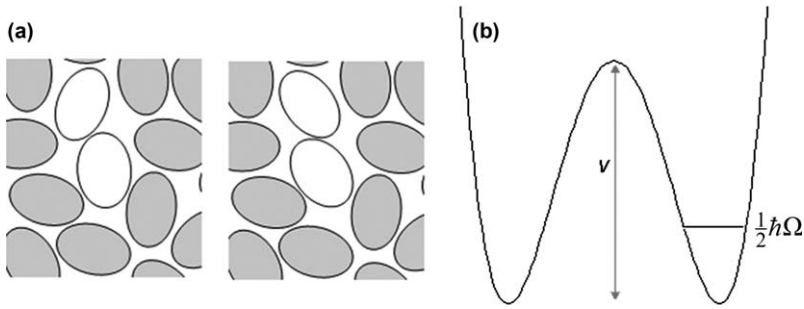

Figure 9.13 Schematic view of the activated jump model and the corresponding potential barrier.

as illustrated in Figure 9.13b. The attempt frequency $\Omega = \sqrt{K/m}$ depends on the potential curvature K and the molecular mass m. This activated jump model shows well-known classical and quantum isotope effects. The classical effect arises from the attempt frequency Ω. Light molecules vibrate more rapidly in each well; the higher attempt frequency results in a ratio of jump rates ω_L/ω_H of light and heavy particles that is identical to eqn (9.52) above.

In a quantum mechanical model, the effective barrier height $\phi_{eff} = \phi - \hbar\Omega/2$ is reduced by the ground-state energy which reflects the zero-point fluctuations in the well. One readily obtains the ratio of jump rates as,

$$\frac{\omega_L}{\omega_H} = \sqrt{\frac{m_H}{m_L}} e^{\frac{\hbar\Omega_L - \hbar\Omega_H}{2k_B T}}, \tag{9.53}$$

where the first factor is the classical effect and the exponential accounts for the quantum effect. Note that both enhance the jump frequency of the lighter molecule. The quantum mechanical factor $\omega_L/\omega_H = e^{\hbar\Omega_L - \hbar\Omega_H/2k_B T}$ has recently been proposed as the origin of the isotope separation in rocks, which is a signature for mass-dependent thermal diffusion in the melt.[179] With typical vibrational frequencies in the liquid state, $\Omega \approx 10^{12}$ s^{-1}, one finds, however, that the exponential factor is less important than the classical prefactor in eqn (9.53).

At present it is not clear how this mass effect affects the Onsager mobilities B_i. Intuitively one would expect that B_1 is smaller for heavier molecules, whereas the experimental data, shown in Figure 9.11 for example, suggest that the ratio B_1/B_2 becomes larger upon increasing the molecular mass of the first component. One may suspect that the jump model is too simplistic since it considers the mass of the first component only.

9.4.7 Viscous Effects

So far we have discussed thermal diffusion in terms of molecular mobilities that describe local motion. It is well known, however, that the diffusion of large solutes or polymers induces long-range flow patterns in the

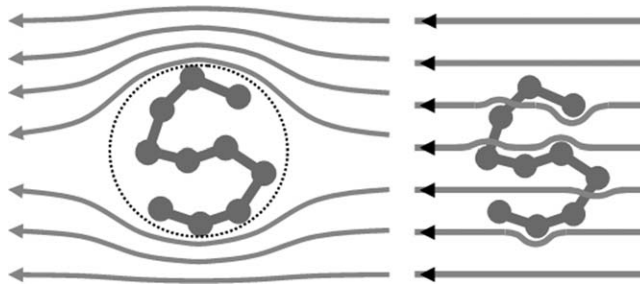

Figure 9.14 Schematic view of the flow pattern induced by a polymer in the surrounding liquid. The left panel shows the velocity field related to the diffusive motion in the frame attached at the solute molecule; because of hydrodynamic interactions, the polymer retains a volume of the size of the gyration radius R, which leads to an Einstein coefficient similar to that of a solid particle of radius R. The right panel shows the flow pattern due to thermal diffusion; due to the short-range velocity field, there are no hydrodynamic interactions between monomers, and the surrounding liquid is hardly affected by the moving polymer.

surrounding liquid. The resulting viscous shear stress slows down the diffusive motion and strongly affects the Soret coefficient. The essential arguments were developed by Brochard and de Gennes,[180] following experimental work of Giddings.[181]

Diffusion of a polymer is accompanied by a long-range velocity field in the surrounding fluid, which is the origin of hydrodynamic interactions between monomers. This flow results in the characteristic dependence of the Stokes–Einstein diffusion coefficient, $(D = k_B T/6\pi\eta R)$ on the gyration radius R. This slow diffusion arises from hydrodynamic interactions, as illustrated in Figure 9.14a. Thermal diffusion, on the other hand, leads to a rather short-range flow pattern that hardly affects the coefficient D_T, as shown in Figure 9.14b. Thus the Soret coefficient $S_T = D_T/D$ is proportional to the gyration radius and increases with the molecular weight of the chain according to $S_T \propto N^{\nu}$ where N is the number of Kuhn segments[182] and ν varies between 0.5 and 0.6 depending on the solvent.[181]

Recent experiments found, however, that the thermal diffusion coefficient of short polymers varies with the molecular weight.[183] For chains of less than ten building units, D_T is significantly reduced and even changes sign for monomers and dimers. Whereas high polymers mostly migrate toward the cold side $(D_T > 0)$, the opposite behaviour occurs for short molecules. Thus there is a crossover from thermal diffusion of small molecules, where macroscopic viscosity is irrelevant, to thermophoresis of high polymers where viscous effects play a major role.

9.4.8 Thermal Diffusion in Electrolyte Solutions

More than 150 years ago, the Soret effect was discovered in salt solutions,[138] and for a long time theory and experimental efforts focussed on thermal

diffusion of small ions.[147] In view of the mechanisms of thermohaline circulation, the thermal diffusion in salt solutions was studied depending on salinity, temperature, and pressure.[184]

The Soret coefficient of salt is given by the mean molar enthalpy $H_\pm$ of positive and negative ions,

$$S_T = -\frac{H_+ + H_-}{2k_B T^2}, \tag{9.54}$$

which is often written in terms of the "heat of transfer" $Q_\pm = -H_\pm$.[158] This solvation enthalpy consists of electrostatic, van der Waals, and hydration contributions; the electric self-energy contribution of an ion of charge q reads $-q^2/4\pi\varepsilon\lambda$, with the absolute permittivity ε and the Debye screening length λ. Measured values for various single-atom and molecular ions range from 0 to 20 kJ · mol^{-1};[185] this strong dispersion indicates the importance of specific-ion effects.

Since the molar enthalpies $H_\pm$ of a given salt are not identical, the positive and negative ions diffuse at a different pace in a themal gradient ∇T, thus resulting in a macroscopic thermoelectric field $E = S\nabla T$, where the Seebeck coefficient is given by the enthalpy difference

$$S = \frac{k_B}{e}\frac{H_- - H_+}{2k_B T}. \tag{9.55}$$

In recent years it was realized that salt thermal diffusion and the Seebeck effect, provide a dominant mechanism for colloidal thermophoresis.[141,186,187]

9.4.9 Outlook and Open Problems

In this chapter we showed that the Soret coefficient is essentially determined by molecular enthalpy and mobility factors. The former are thermodynamic equilibrium properties, whereas the latter account for the irreversible nature of thermal diffusion and in particular for the isotope effect.

At present little is known about the dependence of the mobility factors B_i on molecular parameters. In the absence of viscous effects, the B_i determine both mutual diffusion and thermal diffusion coefficients D and D_T, respectively, and thus can in principle be obtained from diffusion and Soret data through eqn (9.43) and (9.44). In the simplest approach, the functions $B_i(c_1,T)$ are reduced to two or three constants.[187] Because of their close-to-ideal mixing behaviour, normal alkanes constitute a particularly promising system.[188]

With increasing size of one of the components, viscous effects come into play. Thermal diffusion of polymers shows a cross-over as a function of the molecular weight, which so far is not well understood.

We conclude with a few remarks on ions in an electrolyte solution. As a striking feature, the Soret coefficient of salt strongly increases with temperature and in most cases changes sign well below room temperature.[184] This temperature variation is strongly correlated with the thermal expansivity of water. A similar behaviour has been observed for colloidal

suspensions of nanoparticles and macromolecules; so far there is no satisfactory explanation for this rather universal temperature dependence.[189] Moreover, thermal diffusion shows strong specific-ion effects, which determine the thermophoresis of charged colloids.[186,187] On the other hand, these specific-ion effects indicate large non-electrostatic contributions to the salvation enthalpies and thus could be closely related to the Hofmeister effect of protein interactions.[190]

Acknowledgements

A.W. acknowledges generous support through the Leibniz program of Universität Leipzigduring the summer term of 2013, and thanks the groups of Frank Cichos and Klaus Kroy for their kind hospitality.

References

1. P. Debenedetti, *Metastable Liquids. Concepts and Principles*, Princeton University Press, 1996, ch. 4, pp. 235–344.
2. M. D. Ediger, C. A. Angell and S. R. Nagel, *J. Phys Chem.*, 1996, **100**, 13200.
3. E. Mayer, *J. Appl. Phys.*, 1985, **58**, 663.
4. H. E. Stanley, S. V. Buldyrev, M. Campolat, O. Mishima, M. R. Sadr-Lahijany, A. Scala and F. W. Starr, *Phys. Chem. Chem. Phys.*, 2000, **2**, 1551.
5. K. Binder and W. Kob, *Glassy Materials and Disordered Solids.*, World Scientific, 2005, ch 5, pp. 311–429.
6. R. Richert, *J. Non-Cryst. Solids*, 1994, **172–174**, 209.
7. S. S. N. Murthy, *J. Mol. Liquids*, 1992, **44**, 119.
8. G. P. Johari and C. P. Smyth, *J. Chem. Phys.*, 1972, **56**, 4411.
9. G. P. Johari and M. Goldstein, *J. Chem. Phys.*, 1970, **53**, 2372.
10. M. Beiner, H. Huth and K. Schöter, *J. Non-Cryst. Solids*, 2001, **279**, 126.
11. E. Rösler, *Phys. Rev. Lett.*, 1990, **65**, 1595.
12. C. A. Angell, *J. Phys. Chem. Solids*, 1988, **49**, 863.
13. K. Ito, C. T. Moynuhan and C. A. Angell, *Nature*, 1990, **398**, 492.
14. J. Swenson, *J. Phys. Condens. Matter*, 2004, **16**, S5317.
15. S. H. Chen, Y. Zhang, M. Lagi, S. H. Chong, P. Baglioni and F. Mallamace, *J. Phys. Condens. Matter*, 2009, **21**, 504102.
16. M. D. Ediger, *Annu. Rev. Phys. Chem.*, 2000, **51**, 99.
17. G. Adam and J. H. Gibbs, *J. Chem. Phys.*, 1965, **43**, 139.
18. H. Vogel, *J. Phys. Z*, 1921, **22**, 645.
19. G. S. Fulcher, *J. Am. Ceram. Soc.*, 1925, **8**, 339.
20. G. Tammann and W. Hesse, *Z. Anorg. Allg. Chem.*, 1926, **156**, 245.
21. M. E. Elias and A. M. Elias, *J. Mol. Liquids*, 2011, **357**, 3841.
22. W. Götze and L. Sjörgen, *Rep. Prog. Phys.*, 1992, **55**, 241.
23. P. Taborek, R. N. Kleiman and D. J. Bishop, *Phys. Rev. B*, 1986, **34**, 1835.
24. G. Tarjus and D. Kivelson, *J. Chem. Phys.*, 1995, **103**, 3071.

25. I. Avramov and A. Milchev, *J. Non-Cryst. Sol.*, 1988, **104**, 253.
26. I. Avramov, *J. Non-Cryst. Sol.*, 2005, **351**, 3163.
27. J. A. Trejo Gonazalez, M. P. Longinotti and H. R. Corti, *Cryobiology*, 2012, **65**, 159.
28. F. Fujara, B. Geil, H. Sillescu and G. Z. Fleisher, *Z. Phys. B*, 1992, **88**, 195.
29. F. R. Blackburn, C.-Y. Wang and M. D. Ediger, *J. Phys. Chem.*, 1996, **100**, 18249.
30. C. A. Angell, *Chem. Rev.*, 1990, **90**, 523.
31. A. Voronel, E. Veliyulin and V. S. Machavariani, *Phys. Rev. Lett.*, 1998, **80**, 2630.
32. M. Goldstein, *J. Chem. Phys.*, 1969, **51**, 3728.
33. F. H. Stillinger and J. A. Hodgdon, *Phys. Rev. E*, 1994, **50**, 2064.
34. I. Chang and H. Sillescu, *J. Phys. Chem. B*, 1997, **101**, 8794.
35. M. T. Cicerone, P. A. Wagner and M. D. Ediger, *J. Phys. Chem. B*, 1997, **101**, 8727.
36. M. D. Ediger, *J. Non-Cryst. Solids*, 1998, **10**, 235–237.
37. X. Xia and P. G. Wolynes, *Proc. Natl. Acad. Sci. U. S. A.*, 2000, **97**, 2990.
38. X. Xia and P. G. Wolynes, *Phys. Rev. Lett.*, 2001, **86**, 5526.
39. X. Xia and P. G. Wolynes, *J. Phys. Chem. B*, 2001, **105**, 6570.
40. J. P. Garrahan and D. Chandler, *Proc. Natl. Acad. Sci. U. S. A.*, 2003, **100**, 9710.
41. Y. Jung, J. P. Garrahan and D. Chandler, *Phys. Rev. E*, 2004, **69**, 061205.
42. G. H. Fredrickson and H. C. Andersen, *Phys. Rev. Lett.*, 1984, **53**, 1244.
43. F. Ritort and P. Sollich, *Adv. Phys.*, 2003, **52**, 219.
44. J. Jackle and S. Eisinger, *Z. Phys. B: Condens. Matter*, 1991, **84**, 115.
45. P. Sollich and M. R. Evans, *Phys. Rev. Lett.*, 1999, **83**, 3238.
46. R. Yamamoto and A. Onuki, *Phys. Rev. Lett.*, 1998, **81**, 4915.
47. L. Berthier, *Phys. Rev. E*, 2004, **69**, 020201.
48. K. R. Harris, *J. Chem. Phys.*, 2009, **131**, 054503; K. R. Harris, *J. Chem. Phys.*, 2010, **132**, 231103.
49. D. M. Heyes, M. J. Cass, J. G. Powles and W. A. B. Evans, *J. Phys. Chem. B*, 2007, **111**, 1455.
50. K. Meier, A. Laesecke and S. Kabelec, *J. Chem. Phys.*, 2004, **121**, 3671.
51. A. Yu, B. Ossipov, B. V. Zheleznyi and N. F. Bondarenko, *Russ. J. Phys. Chem.*, 1977, **51**, 748.
52. W. S. Price, H. Ide and Y. Arata, *J. Phys. Chem. A*, 1999, **103**, 448.
53. R. S. Smith, Z. Dohnálek, G. A. Kimmel, K. P. Stevenson and B. D. Kay, *Liquid Dynamics. Experiment, Simulation and Theory,* ACS Symposium Series 820, 2002, 198–211.
54. S. H. Chen, F. Mallamace, C. Y. Mou, M. Broccio, C. Corsaro, A. Faraone and L. Liu, *Proc. Natl. Acad. Sci. U.S. A.*, 2006, **103**, 12974.
55. D. Banerjee, S. N. Bhat, S. V. Bhat and D. Leporini, *Proc. Natl. Acad. Sci. U. S. A.*, 2009, **106**, 11448.
56. P. Kumar, S. V. Buldyrev, S. R. Becker, P. H. Poole, F. W. Starr and H. E. Stanley, *Proc. Nat. Acad. Sci. U. S. A.*, 2007, **104**, 9575.

57. B. Jana, R. S. Singh and B. Bagchi, *Phys. Chem. Chem. Phys.*, 2011, **13**, 16220.
58. D. Laage and J. T. Hynes, *Science*, 2006, **311**, 832.
59. C. T. Moynihan, N. Balitactac, L. Boone and T. A. Litovitz, *J. Chem. Phys.*, 1971, **55**, 3013.
60. E. Mamontov, *J. Phys. Chem. B*, 2009, **113**, 14073.
61. Y. Suzuki and O. Mishima, *J. Chem. Phys.*, 2013, **138**, 084507.
62. H. R. Corti, F. J. Nores-Pondal and C. A. Angell, *Phys. Chem. Chem. Phys.*, 2011, **13**, 19741.
63. M. P. Longinotti, M. A. Carignano, I. Szleifer and H. R. Corti, *J. Chem. Phys.*, 2011, **134**, 244510.
64. J. M. Stokes and R. H. Stokes, *J. Phys. Chem.*, 1958, **62**, 497.
65. D. P. Miller, P. B. Conrad, S. Fucito, H. R. Corti and J. J. de Pablo, *J. Phys. Chem. B*, 2000, **104**, 10419.
66. M. P. Longinotti and H. R. Corti, *J. Phys. Chem. B*, 2009, **113**, 5500.
67. P. G. Wolynes, *Annu. Rev. Phys. Chem.*, 1980, **31**, 345.
68. M. Rampp, C. Buttersack and H. D. Ludemman, *Carb. Res.*, 2000, **328**, 561.
69. H. R. Corti, G. A. Frank and M. C. Marconi, *J. Phys. Chem. B*, 2008, **112**, 12899.
70. M. P. Longinotti and H. R. Corti, *Electrochem. Commun.*, 2007, **9**, 1444.
71. F. Mallamace, C. Branca, C. Corsaro, N. Leone, J. Spooren, H. E. Stanley and S. H. Chen, *J. Phys. Chem. B*, 2010, **114**, 1870.
72. C. M. Roland, S. Hensel-Bielowka, M. Paluch and R. Casalini, *Rep. Prog. Phys.*, 2005, **68**, 1405.
73. C. M. Roland, *Rubber Chem. Technol.*, 2012, **85**, 313.
74. E. R. López, A. S. Pensado, M. J. P. Comuñas, A. A. H. Pádua, J. Fernández and K. R. Harris, *J. Chem. Phys.*, 2011, **134**, 144507.
75. A. S. Pensado, A. A. H. Pádua, M. J. P. Comuñas and J. Fernández, *J. Phys. Chem. B*, 2008, **112**, 5563.
76. G. S. Grest and M. H. Cohen, *Adv. Chem. Phys.*, 1981, **48**, 455.
77. T. Pakula, *J. Mol. Liq.*, 2000, **86**, 109.
78. J. T. Bendler, J. J. Fontanella and M. Schlesinger, *Phys. Rev. Lett.*, 2001, **87**, 195503.
79. R. Casalini and C. M. Roland, *Phys. Rev. E*, 2004, **69**, 062501.
80. G. Tarjus, D. Kivelson, S. Mossa and C. Alba-Simionesco, *J. Chem. Phys.*, 2004, **120**, 6135.
81. C. A. Angell, *Science*, 1995, **267**, 1924.
82. S. Sastry, *Nature*, 2001, **409**, 164.
83. C. M. Roland, S. Bair and R. Casalini, *J. Chem. Phys.*, 2006, **125**, 124508.
84. K. R. Harris, *J. Chem. Eng. Data*, 2009, **54**, 2729.
85. X. Paredes, A. S. Pensado, M. J. P. Comuñas and J. Fernández, *J. Chem. Eng. Data*, 2010, **55**, 3216.
86. X. Paredes, A. S. Pensado, M. J. P. Comuñas and J. Fernández, *J. Chem. Eng. Data*, 2010, **55**, 4088.

87. D. Fragiadakis and C. M. Roland, *J. Chem. Phys.*, 2011, **134**, 044504.
88. F. M. Gaciño, X. Paredes, M. J. P. Comuñas and J. Fernández, *J. Chem. Thermodyn.*, 2013, **62**, 162.
89. E. W. Lemmon, M. L. Huber and M. O. McLinden, NIST Standard Reference Database 23: Reference Fluid Thermodynamic and Transport Properties-REFPROP, Version 9.0, National Institute of Standards and Technology, Standard Reference Data Program, Gaithersburg, 2010.
90. M. L. Huber, R. A. Perkins, A. Laesecke, D. G. Friend, J. V. Sengers, M. J. Assael, I. M. Metaxa, E. Vogel, R. Mares and K. Miyagawa, *J. Phys. Chem. Ref. Data*, 2009, **38**, 101.
91. L. Bøhling, T. S. Ingebrigtsen, A. Grzybowski, M. Paluch, J. C. Dyre and T. B. Schrøder, *New J. Phys.*, 2012, **14**, 113035.
92. J. P. Hansen, *Phys. Rev. A*, 1970, **2**, 221.
93. W. G. Hoover and M. Ross, *Contemp. Phys.*, 1971, **12**, 339.
94. W. T. Ashurst and W. G. Hoover, *AIChE J.*, 1975, **21**, 410.
95. W. T. Ashurst and W. G. Hoover, *Phys. Rev. A*, 1975, **11**, 658.
96. R. Agrawal and D. A. Kofke, *Phys. Rev. Lett.*, 1995, **74**, 122.
97. N. H. March and M. P. Tosi, *Introduction to the Liquid State Physics*, World Scientific Publishing Company, 2002.
98. A. Tólle, *Rep. Prog. Phys.*, 2001, **64**, 1473.
99. R. Casalini, U. Mohanty and C. M. Roland, *J. Chem. Phys.*, 2006, **125**, 014505.
100. I. Avramov, *J. Non-Cryst. Solids*, 2000, **262**, 258.
101. L. D. Landau and E. M. Lifshitz, *Statistical Physics*, Pergamon, New York, 1977.
102. R. Casalini and C. M. Roland, *J. Non-Cryst. Solids*, 2007, **353**, 3936.
103. E. R. López, A. S. Pensado, J. Fernández and K. R. Harris, *J. Chem. Phys.*, 2012, **136**, 214502.
104. J. P. Johari, *J. Chem. Phys.*, 2003, **119**, 635.
105. D. Prevosto, M. Lucchesi, S. Capaccioli, R. Casalini and P. A. Rolla, *Phys. Rev. B*, 2003, **67**, 174202.
106. A. Grzybowski, M. Paluch, K. Grzybowska and S. Haracz, *J. Chem. Phys.*, 2010, **133**, 161101.
107. N. Gnan, T. Schrøder, U. R. Pedersen, N. P. Bailey and J. C. Dyre, *J. Chem. Phys.*, 2009, **131**, 234504.
108. T. S. Ingebrigtsen, T. B. Schrøder and J. C. Dyre, *J. Phys. Chem. B*, 2012, **116**, 1018.
109. L. Separdar, N. P. Bailey, T. B. Schrøder, S. Davatolhagh and J. C. Dyre, *J. Chem. Phys.*, 2013, **138**, 154505.
110. J. C. Dyre, *Phys. Rev. E,* 2013, **88**, 042139.
111. T. S. Ingebrigtsen, T. B. Schrøder and J. C. Dyre, *Phys. Rev. X*, 2012, **2**, 011011.
112. T. S. Ingebrigtsen, L. Bøhling, T. B. Schrøder and J. C. Dyre, *J. Chem. Phys.*, 2012, **136**, 061102.
113. C. Alba-Simionesco, A. Cailliaux, A. Alegria and G. Tarjus, *Europhys. Lett.*, 2004, **68**, 58.

114. S. Bair and R. Casalini, *J. Tribol.*, 2008, **130**, 041802.
115. S. Bair, *Proc. IMechE, Part C: J. Mech. Eng. Sci.*, 2010, **224**, 2568.
116. A. Laesecke and S. Bair, *J. Tribol.*, 2012, **134**, 021801.
117. A. Grzybowski, S. Haracz, M. Paluch and K. Grzybowska, *J. Phys. Chem. B*, 2010, **114**, 11544.
118. A. Grzybowski, K. Grzybowska, M. Paluch, A. Swiety and K. Koperwas, *Phys. Rev. E*, 2011, **83**, 041505.
119. M. Paluch, S. Haracz, A. Grzybowski, M. Mierzwa, J. Pionteck, A. Rivera-Calzada and C. Leon, *J. Phys. Chem. Lett.*, 2010, **1**, 987.
120. A. Grzybowski, M. Paluch and K. Grzybowska, *Phys. Rev. E*, 2010, **82**, 013501.
121. D. Coslovich and C. M. Roland, *J. Phys. Chem. B*, 2008, **112**, 1329.
122. G. Galliero, C. Boned and J. Fernández, *J. Chem. Phys.*, 2011, **134**, 064505.
123. U. R. Pedersen, N. P. Bailey, T. B. Schrøder and J. C. Dyre, *Phys. Rev. Lett.*, 2008, **100**, 015701.
124. D. Coslovich and C. M. Roland, *J. Chem. Phys.*, 2009, **130**, 014508.
125. T. B. Schrøder, U. R. Pedersen, N. P. Bailey, S. Toxvaerd and N. P. Dyre, *Phys. Rev. E*, 2009, **80**, 0414502.
126. D. Fragiadakis and C. M. Roland, *Phys. Rev. E*, 2011, **83**, 031504.
127. K. R. Harris, L. A. Woolf, M. Kanakubo and T. Rüther, *J. Chem. Eng. Data*, 2011, **56**, 4672.
128. C. Boned, G. Galliero, J. P. Bazile and W. Magrini, *Chem. Phys.*, 2013, **423**, 105.
129. S. E. Quiñones-Cisneros, M. L. Huber and U. K. Deiters, *J. Phys. Chem. Ref. Data*, 2012, **41**, 023102.
130. C. M. Roland, *Viscoelastic Behavior of Rubbery Materials*, Oxford University Press, 2011.
131. C. M. Roland, *Macromolecules*, 2010, **43**, 7875.
132. S. Bair, *Proc. Inst. Mech. Eng., Part J*, 2009, **223**, 617.
133. W. Habchi, P. Vergne, S. Bair, O. Andersson, D. Eyheramendy and G. E. Morales-Espejel, *Tribol. Int.*, 2010, **43**, 1842.
134. C. M. Roland, R. Casalini, R. Bergman and J. Mattsson, *Phys. Rev. B*, 2008, **77**, 012201.
135. W. L. Jorgensen and J. D. Madura, *Mol. Phys.*, 1985, **56**, 1381.
136. J. Zielkiewicz, *J. Chem. Phys.*, 2005, **123**, 104501.
137. D. J. Wilbur, T. DeFries and J. Jonas, *J. Chem. Phys.*, 1976, **65**, 1783.
138. W. Köhler and S. Wiegand, *Thermal Nonequilibrium Phenomena in Fluid Mixtures, Lecture Notes in Phys.*, Springer, Berlin, Heidelberg, New York, vol. 584, 2002.
139. S. Wiegand, *J. Phys. Condens. Matter*, 2004, **16**, R357.
140. J. K. Platten, *J. Appl. Mech.*, 2006, **73**, 5.
141. A. Würger, *Rep. Prog. Phys.*, 2010, **73**, 126601.
142. S. Srinivasan and M. Z. Saghir, *Thermodiffusion in Multicomponent Mixtures*, Springer, Berlin, Heidelberg, New York, 2013.
143. D. Enskog, *Phys. Z.*, 1911, **12**, 56 and 533.

144. S. Chapman, *Philos. Trans. A*, 1917, **217**, 184.
145. S. Chapman, *Philos. Mag.*, 1929, **7**, 1.
146. E. D. Eastman, *J. Am. Chem. Soc.*, 1926, **48**, 1482.
147. S. R. de Groot, *L'effet Soret*, Nord-hollandsche Uitgevers Maatschappij, Amsterdam, 1945.
148. J. C. Giddings, *Science*, 1993, **260**, 1456.
149. W. M. Rutherford, *J. Chem. Phys.*, 1984, **81**, 6136.
150. C. Debuschewitz and W. Köhler, *Phys. Rev. Lett.*, 2001, **87**, 055901.
151. G. Wittko and W. Köhler, *J. Chem. Phys.*, 2005, **123**, 014506.
152. J. P. Severinghaus, A. Grachev and M. Battle, *Geochem. Geophys. Geosyst.*, 2001, **2**, 1048.
153. F. Huang, P. Chakraborty, C. C. Lundstrom, C. Holmden, J. J. G. Glessner, S. W. Kieffer and C. E. Lesher, *Nature*, 2012, **464**, 396.
154. M. Touzet, G. Galliero, V. Lazzeri, M. ZiadSaghir, F. Montel and J. C. Legros, *CRAS Mécanique*, 2011, **339**, 318.
155. Y. T. Maeda, A. Buguin and A. Libchaber, *Phys. Rev. Lett.*, 2011, **107**, 038301.
156. Y. He, M. Tsutsui, R. H. Scheicher, F. Bai, M. Taniguchi and T. Kawai, *ACS Nano*, 2013, **7**, 538.
157. B. Qian, D. Montiel, A. Bregulla, F. Cichos and H. Yang, *Chem. Sci.*, 2013, **4**, 1420.
158. S. R. de Groot and P. Mazur, *Non-equilibrium Thermodynamics*, Dover, New York, 1984.
159. R. Haase, *Z. Phys.*, 1949, **127**, 1.
160. B. Derjaguin and G. Sidorenkov, *Dokl. Acad. Nauk SSSR*, 1941, **32**, 622.
161. B. Derjaguin, N. Churaev and V. Muller, *Surface Forces*, Plenum, New York, 1987.
162. B. Hafskjold, T. Ikeshoji and S. Ratkje, *Mol. Phys.*, 1993, **80**, 1389.
163. F. Müller-Plathe and D. Reith, *Comp. Theor. Polym. Sci.*, 1999, **9**, 203.
164. G. Galliero, B. Duguay, J.-P. Caltagirone and F. Montel, *Fluid Phase Equilib.*, 2003, **208**, 171.
165. S. Yeganegi and M. Zolfaghari, *Fluid Phase Equilib.*, 2006, **243**, 161.
166. P.-A. Artola and B. Rousseau, *Phys. Rev. Lett.*, 2007, **98**, 12590.
167. A. Würger, *J. Phys. Cond. Matt.*, 2014, **26**, 034105.
168. L. J. T. M. Kempers, *J. Chem. Phys.*, 1989, **90**, 6541.
169. K. Shukla and A. Firoozabadi, *Ind. Eng. Chem. Res.*, 1998, **37**, 3331.
170. R. Schmid, *Monatsh. Chem.*, 2001, **132**, 1295.
171. A. Würger, *CRAS Mécanique*, 2013, **341**, 438.
172. P. Blanco, P. Polyakov, M. M. Bou-Ali and S. Wiegand, *J. Phys. Chem. B*, 2008, **112**, 8340.
173. A. Leahy-Dios, M. M. Bou-Ali, J. K. Platten and A. Firoozabadi, *J. Chem. Phys.*, 2005, **122**, 234502.
174. Dortmund Data Base, http://www.ddbst.com.
175. S. Chapman and F. W. Dootson, *Philos. Mag.*, 1917, **33**, 248.
176. L. Waldmann, *Z. Naturforsch. A*, 1949, **4**, 105.
177. G. Galliero and S. Volz, *J. Chem. Phys.*, 2008, **128**, 064505.

178. S. Villain-Guillot and A. Würger, *Phys. Rev. E*, 2011, **83**, 030501.
179. G. Dominguez, G. Wilkins and M. H. Thiemens, *Nature*, 2011, **473**, 70.
180. F. Brochard and P.-G. de Gennes, *C. R. Acad. Sci. Paris Série II*, 1981, **293**, 1025.
181. J. Giddings, K. Caldwell and M. N. Myers, *Macromolecules*, 1976, **9**, 106.
182. P.-G. de Gennes, *Scaling Concepts in Polymer Physics*, Cornell University Press, Ithaca, USA, 1979.
183. D. Stadelmaier and W. Köhler, *Macromolecules*, 2008, **41**, 6205.
184. D. R. Caldwell and S. A. Eide, *Deep-Sea Res.*, 1981, **28a**, 1605.
185. J. N. Agar, C. Y. Mou and J.-I. Lin, *J. Phys. Chem.*, 1989, **93**, 2079.
186. S. A. Putnam and D. G. Cahill, *Langmuir*, 2005, **21**, 5317.
187. A. K. Eslahian, M. Maskos, A. Majee and A. Würger, *Soft Matter*, 2014, **10**, 1931.
188. D. Alonso De Mezquia, M. M. Bou-Ali, M. Larranaga, J. A. Madariaga and C. Santamaría, *J. Phys. Chem. B*, 2012, **116**, 2814.
189. S. Iacopini, R. Rusconi and R. Piazza, *Eur. Phys. J. E: Soft Matter Biol. Phys.*, 2006, **19**, 59.
190. Y. Zhang and P. S. Cremer, *Curr. Opin. Chem. Biol.*, 2006, **10**, 658.

CHAPTER 10

Fluids near Critical Points†

JAN V. SENGERS AND RICHARD A. PERKINS

10.1 Introduction

The purpose of this chapter is to present a status report on the effect of critical fluctuations on the transport properties of fluids. In particular we shall elucidate our current understanding of the critical enhancement of thermal conductivity and viscosity. To account for the critical enhancement of the thermal conductivity λ and the shear viscosity η, one considers these transport coefficients as the sum of critical enhancement contributions, $\Delta_c\lambda$ and $\Delta_c\eta$, and non-critical background contributions, λ_b and η_b:[1]

$$\lambda = \Delta_c\lambda + \lambda_b, \tag{10.1}$$

$$\eta = \Delta_c\eta + \eta_b. \tag{10.2}$$

The critical enhancements of these transport properties are related to the critical slowing down of the fluctuations of the order parameter, which near the vapor–liquid critical point of one-component fluids is governed by the thermal diffusivity $a = \lambda/\rho C_P$, such that

$$a = \Delta_c a + a_b, \tag{10.3}$$

with $\Delta_c a = \Delta_c\lambda/\rho C_P$ and $a_b = \lambda_b/\rho C_P$. Here ρ is the molar density and C_P the molar isobaric heat capacity. Asymptotically close to the critical point, $\Delta_c a$ approaches a Stokes–Einstein relation of the form[2]

$$\Delta_c a \approx \frac{R_D k_B T}{6\pi\eta\xi}, \tag{10.4}$$

†Contribution of the National Institute of Standards and Technology. The US Government is authorized to reproduce and distribute reprints for Governmental purpose notwithstanding any copyright notation thereon.

Experimental Thermodynamics Volume IX: Advances in Transport Properties of Fluids
Edited by M. J. Assael, A. R. H. Goodwin, V. Vesovic and W. A. Wakeham

Published by the Royal Society of Chemistry, www.rsc.org

where k_B is Boltzmann's constant, T the temperature, ξ the correlation length, and R_D a universal dynamic amplitude with a value close to unity. Hence, the thermal conductivity will diverge asymptotically as

$$\Delta_c\lambda \approx \frac{\rho C_p R_D k_B T}{6\pi\eta\xi}. \tag{10.5}$$

The viscosity diverges asymptotically as[2,3]

$$\eta \approx \eta_b (Q\xi)^{z_\eta}, \tag{10.6}$$

where Q is a fluid-specific coefficient and $z_\eta \simeq 0.068$ a universal dynamic critical exponent.[4,5] From eqn (10.5) and (10.6) it follows that the thermal conductivity asymptotically diverges as

$$\Delta_c\lambda \approx \Lambda\xi^{z_\lambda}, \tag{10.7}$$

with $z_\lambda = (\gamma/\nu) - 1 - z_\eta \simeq 0.899$, where γ and ν are static critical exponents defined in Appendix 10.A. In addition to two universal static critical exponents, there is only one universal dynamic critical exponent, z_η.[2] The coefficient Λ in eqn (10.7) is a fluid-specific amplitude.

The asymptotic power laws {eqns (10.6) and (10.7)} for these transport coefficients are valid only very close to the critical point. In particular, the critical enhancement of the thermal conductivity is significant over a substantial range of temperatures, densities or pressures, as illustrated in Figure 10.1 for H_2O as an example.[6,7] Hence, to represent the actually observed critical thermal–conductivity enhancement, one needs a theory for the non-asymptotic critical behavior of the thermal conductivity. To elucidate the nature of such a non-asymptotic theory, we need first to review the behavior of the transport properties asymptotically close to the critical point in some more detail.

10.2 Wave-number Dependence of Diffusivity near the Critical Point

In addressing the dynamic behavior of fluids one distinguishes between non-conserved quantities that decay rapidly as a result of molecular collisions, and conserved quantities, such as mass, momentum, and energy, which decay slowly in accordance with the hydrodynamic equations. Near the critical point a clear separation between fast and slow variables is no longer adequate. Specifically, the product of momentum and energy, although not a conserved quantity, cannot be treated as a fast variable in the critical region. As a consequence, a coupling between heat and viscous modes needs to be accounted for, yielding a set of coupled integral equations for the critical contributions to the thermal diffusivity and the viscosity.[8–10]

$$\Delta_c a(q) = \frac{k_B T}{(2\pi)^3 \rho} \int d\boldsymbol{k} \left[\frac{C_p(|\boldsymbol{q}-\boldsymbol{k}|)}{C_P(q)}\right] \frac{\sin^2\theta}{k^2\eta(k)/\rho + |\boldsymbol{q}-\boldsymbol{k}|^2 a(|\boldsymbol{q}-\boldsymbol{k}|)}, \tag{10.8}$$

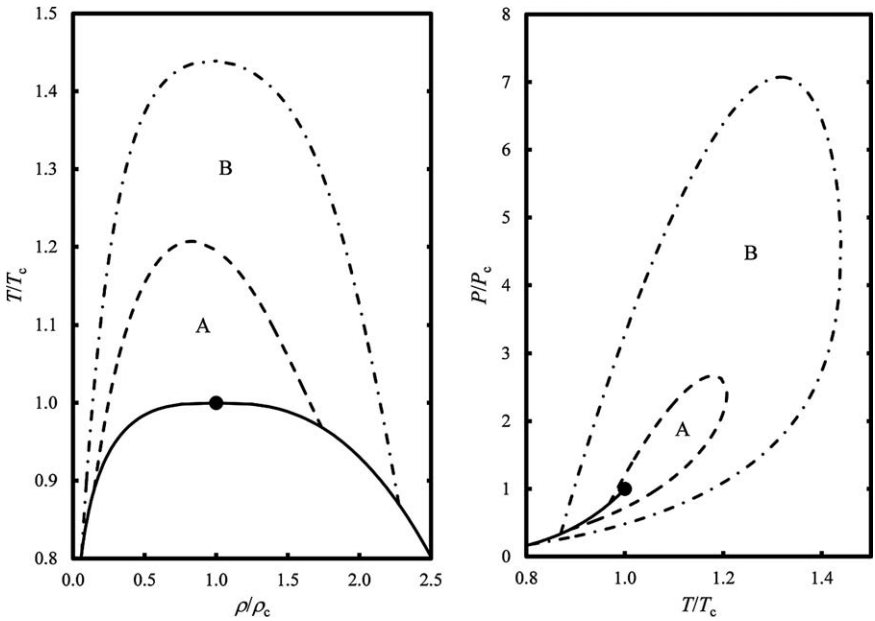

Figure 10.1 Reduced ranges of density (ρ), temperature (T), and pressure (P), relative to their values ρ_c, T_c, P_c at the critical point, ●, where the critical enhancement contribution to the thermal conductivity is larger than 1 % for H_2O. The critical enhancement exceeds 5 % in the region A between the dashed curve and the saturation curve (solid), while it ranges from 1 % to 5 % in the region B between the dot-dashed curve and the dashed curve. Reprinted with permission from *Int. J. Thermophys.*[7]

$$\Delta_c\eta(q) = \frac{1}{2q^2}\frac{k_B T}{(2\pi)^3}\int d\boldsymbol{k} C_P(k) C_P(|\boldsymbol{q}-\boldsymbol{k}|)\left[\frac{1}{C_P(k)} - \frac{1}{C_P(|\boldsymbol{q}-\boldsymbol{k}|)}\right]^2 \times \frac{k^2 \sin^2\theta \sin^2\phi}{k^2 a(k) + |\boldsymbol{q}-\boldsymbol{k}|^2 a(|\boldsymbol{q}-\boldsymbol{k}|)}, \tag{10.9}$$

where θ and ϕ are the polar and azimuthal angles of the wave vector $\boldsymbol{k}$ with respect to the wave vector $\boldsymbol{q}$.[8–10] Note that $\Delta_c a(q)$ and $\Delta_c\eta(q)$ only depend on the wave-number q of the critical order-parameter fluctuations.

The critical viscosity enhancement is very weak, so to evaluate eqn (10.8) for $\Delta_c a(q)$ one may neglect in first approximation its wave-number dependence and approximate the viscosity in the integrand of eqn (10.8) by $\eta(k) \simeq \eta$, where η is independent of the wave-number k. The wave-number dependence of the isobaric heat capacity C_P can be related to that of the susceptibility $\chi = \rho(\partial\rho/\partial P)_T$ by

$$C_P(k) \simeq C_V + \frac{T}{\rho^3}\left(\frac{\partial P}{\partial T}\right)_\rho^2 \chi(k) \simeq C_V + \frac{T}{\rho^3}\left(\frac{\partial P}{\partial T}\right)_\rho^2 \frac{\chi(0)}{(1+k^2\xi^2)}. \tag{10.10}$$

The molar isochoric heat capacity C_V diverges only weakly so that, just as for the viscosity, its wave-number dependence can be neglected, while $\chi(k)$ in eqn (10.10) is given by the Ornstein–Zernike approximation.[11] The thermal diffusivity in the integrand of eqn (10.8) becomes small near the critical point, and asymptotically close to the critical point the wave-number dependence of $\Delta_c a(q)$ is given by

$$\Delta_c a(q) = \frac{k_B T}{(2\pi)^3 \eta} \int d\boldsymbol{k} \left[\frac{C_P(|\boldsymbol{q}-\boldsymbol{k}|)}{C_P(q)}\right] \frac{\sin^2\theta}{k^2}. \tag{10.11}$$

Near the critical point $C_V \ll C_P$ in eqn (10.10) and one obtains from eqn (10.11)

$$\Delta_c a(q) = \frac{k_B T}{6\pi\eta\xi} \Omega(q\xi) \tag{10.12}$$

with

$$\Omega(z) \simeq \Omega_K(z) = \frac{3}{4z^2}\left\{1 + z^2 + \left[z^3 - z^{-1}\right] \arctan(z)\right\}, \tag{10.13}$$

such that

$$\lim_{z\to 0} \Omega_K(z) = 1, \quad \text{and} \quad \Omega_K(z) = \frac{3\pi}{8} z \quad \textit{for} \quad z \gg 1. \tag{10.14}$$

The function $\Omega_K(z)$ is known as the Kawasaki function.[8,9] Near the critical mixing point in nearly incompressible liquid mixtures the anomalous dynamical behavior originates from the slowing down of the concentration fluctuations, whose decay rate is determined by the mass diffusivity (binary diffusion coefficient) $D = \Delta_c D + D_b$. The critical contribution $\Delta_c D(q)$ also satisfies the mode-coupling eqn (10.8) provided that the heat capacity C_P is replaced with the osmotic compressibility, which near a critical mixing point diverges with the same asymptotic power law as the one for C_P near the vapor–liquid critical point. Hence, $\Delta_c a(q)$ in one-component fluids near the vapor–liquid critical point and $\Delta_c D(q)$ in liquid mixtures near a critical mixing point exhibit the same asymptotic critical behavior.[1] This is also the case for the asymptotic critical behavior of the viscosity. However, because the background viscosity, η_b in eqn (10.6), is much larger in liquid mixtures than in fluids near a vapor-liquid critical point, the critical behavior of the viscosity is more significant in liquid mixtures near a critical mixing point.[1] In the hydrodynamic limit $q \to 0$, one recovers from eqn (10.12) the Stokes–Einstein relation given by eqn (10.4) for $\Delta_c a(q)$ and $\Delta_c D(q)$ with $R_D = 1$. When higher-order effects are included in the mode-coupling theory one finds $R_D = 1.03$.[12] Values reported for R_D have varied appreciably, as reviewed by Sengers,[1] Privman *et al.*,[13] Folk and Moser,[14] and most recently by Sengers *et al.*[15] The more reliable experimental determinations have yielded a value for R_D close to unity.[16–20]

Eqn (10.13) neglects any effect of the singular behavior of the viscosity on the diffusivity. This minor deficiency can be remedied by generalizing eqn (10.13) to[12]

$$\Omega(z) = \frac{3}{4z^2}\left\{1 + z^2 + \left[z^3 - z^{-1}\right]\arctan(z)\right\}\left[1 + b^2 z^2\right]^{z_\eta/2}, \tag{10.15}$$

with $b \simeq 0.5$. A slightly different expression has been proposed by Paladin and Peliti.[21] The validity of a wave-number dependence of the form of eqn (10.15) has been confirmed experimentally for binary liquid mixtures.[12,22–24] However, the difference between eqn (10.13) and eqn (10.15) is small[19,25–27] and is expected to be negligible for fluids near the vapor–liquid critical point.

10.3 Non-asymptotic Critical Behavior of Thermal Conductivity of One-component Fluids

The asymptotic behavior of the enhancement of the thermal conductivity, $\Delta_c\lambda = \rho C_P \Delta_c a(0)$, is obtained from eqn (10.8) by taking the hydrodynamic limit $q \to 0$. Near the critical point the correlation length is very large, and in first approximation one may extend the integration over all wave-numbers. However, to obtain a non-asymptotic description one needs to limit the integration to wave-numbers smaller than a maximum Debye-like cutoff wave-number q_D which corresponds to a microscopic distance where a hydrodynamic mode-coupling description is no longer applicable. Hence, for a non-asymptotic theoretical description of the critical thermal conductivity enhancement one considers

$$\Delta_c\lambda = \frac{\rho C_P R_D k_B T q_D}{6\pi\eta} Z(q_D\xi), \tag{10.16}$$

with

$$Z(q_D\xi) = \frac{3}{(2\pi)^2 q_D}\int_0^{q_D} d\boldsymbol{k}\left[\frac{C_p(k)}{C_P(0)}\right]\frac{k^{-2}\sin^2\theta}{1 + \rho a(k)/\eta}. \tag{10.17}$$

In eqn (10.16) we have entered a factor R_D so as to reproduce the asymptotic limit (10.5) near the critical point. Mode coupling yields not only a critical thermal conductivity enhancement $\Delta_c\lambda$, but also a contribution to the background thermal conductivity λ_b resulting from so-called long-time tails in the dynamic correlation functions.[28,29] To ensure that eqn (10.17) represents only the critical thermal conductivity enhancement, the dynamic crossover function $Z(y)$ should satisfy the condition $\lim_{y\to 0} Z(y) = 0$ far away from the critical point.

10.3.1 Olchowy–Sengers Approximation

Near the critical point the thermal diffusivity $a(k)$ in the integrand of eqn (10.17) becomes small. Hence, the leading non-asymptotic contributions to the critical thermal conductivity enhancement can be obtained as

$$Z_1(y) = \frac{3}{(2\pi)^2 q_D} \int_0^{q_D} d\boldsymbol{k} \left[\frac{C_p(k)}{C_P(0)}\right] \frac{\sin^2\theta}{k^2} = \frac{2}{\pi y}\left[\left(1-\kappa^{-1}\right)\arctan(y) + \kappa^{-1} y\right], \tag{10.18}$$

where $\kappa = C_P/C_V$.[‡] Eqn (10.18) yields only the leading non-asymptotic corrections, but does not vanish as $y \to 0$, since $\lim_{y\to 0} Z_1(y) = 2/\pi$. This deficiency can be remedied by generalizing eqn (10.18) for the dynamic crossover function to

$$Z(y) = Z_1(y) - \frac{2}{\pi y}\left[1 - \exp\left(\frac{-1}{y^{-1} + cy^2}\right)\right]. \tag{10.19}$$

Taking $c = \rho_c^2 / 3\rho^2$, where ρ_c is the critical density, one obtains the Olchowy–Sengers approximation[30]

$$Z_{OS}(y) = \frac{2}{\pi y}\left\{\left[\left(1-\kappa^{-1}\right)\arctan(y) + \kappa^{-1} y\right] - \left[1 - \exp\left(\frac{-1}{y^{-1} + y^2\rho_c^2/3\rho^2}\right)\right]\right\}, \tag{10.20}$$

to be substituted into eqn (10.16). In order to evaluate eqn (10.16) for $\Delta_c\lambda$, one needs an estimate for the correlation length ξ as a function of temperature and density. In practice one uses a procedure also proposed by Olchowy and Sengers:[30,31]

$$\xi = \xi_0\left\{\overline{\Gamma}_0^{-1}\left[\overline{\chi}(T,\rho) - \overline{\chi}(T_R,\rho)\frac{T_R}{T}\right]\right\}^{\nu/\gamma}, \tag{10.21}$$

where T_R is a reference temperature well above the critical temperature T_c, and where the critical thermal conductivity enhancement is assumed to be negligibly small. In eqn (10.21), ξ_0 and $\overline{\Gamma}_0$ are critical amplitudes, and $\overline{\chi}$ is a dimensionless susceptibility, all defined in Appendix 10.A. The correlation length ξ should be set equal to zero when $\left[\overline{\chi}(T,\rho) - \overline{\chi}(T_R,\rho)\frac{T_R}{T}\right] \le 0$ in eqn (10.21). The correlation length ξ in the mode-coupling integral is to be interpreted as the correlation length associated with the long-range critical fluctuations so that the critical thermal conductivity enhancement $\Delta_c\lambda$ vanishes as $\xi \to 0$ far away from the critical point.

The Olchowy–Sengers approximation, given by eqn (10.16) and (10.20), together with eqn (10.21), has been used to represent the critical thermal

[‡]In this chapter the symbol κ is used to indicate the heat-capacity ratio, since in the theory of critical phenomena the symbol γ is used to designate a critical exponent.

conductivity enhancement for a large number of fluids.[6,30,32–46] As reviewed by Perkins *et al.*,[7] it can be concluded that the Olchowy–Sengers approximation yields a universal representation for the critical thermal-conductivity enhancement with[7]

$$R_D = 1.02, \quad T_R / T_c = 1.5, \quad \nu = 0.630, \quad \gamma = 1.239. \tag{10.22}$$

For atomic and molecular fluids, except for helium, the critical amplitudes ξ_0 and $\overline{\Gamma}_0$ in eqn (10.21) can be estimated from the acentric factor ω and the critical molecular volume ν_c as given by eqn (10.A.6) and (10.A.7) in Appendix 10.A. The cutoff wave number q_D, the only adjustable parameter, can in practice be estimated from $q_D^{-1} / \text{nm} = -0.0240 + 0.863\, \nu_c^{1/3} / \text{nm}$.[7] As an example, we show in Figure 10.2 the thermal conductivity of H_2O in the critical region with $\Delta_c\lambda$ represented by the universal Olchowy–Sengers approximation as described above.[7]

As alternatives to eqn (10.21), other procedures for estimating the correlation length ξ in the expression for the critical thermal conductivity

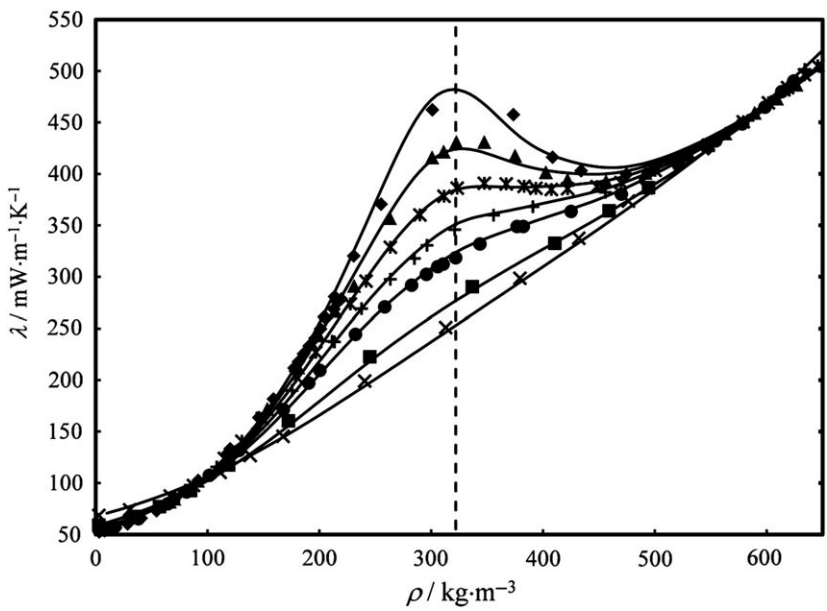

Figure 10.2 Thermal conductivity λ of H_2O in the critical region as a function of density ρ. The symbols indicate experimental thermal conductivity data reported by Tufeu and Le Neindre.[47] The solid curves represent values of $\Delta_c\lambda$ calculated with the universal Olchowy–Sengers representation[7] and with an equation for the background thermal conductivity λ_b developed by Huber *et al.*[6] The dashed line represents the critical density, $\rho_c = 322\ \text{kg} \cdot \text{m}^{-3}$. The isotherms are indicated as: ◆, 652 K; ▲, 655 K; ✱, 659 K; +, 665 K; ●, 673 K; ■, 706 K; and ×, 784 K. Reprinted with permission from *Int. J. Thermophys.*[7]

enhancement have also been proposed in the literature. A simple representation adopted by Luettmer-Strathmann and Sengers[48] reads

$$\xi = \xi_0 \left[\left(\overline{\Gamma}_0^{-1} \overline{\chi} \right)^{\nu/\gamma} - 1 \right]. \tag{10.23}$$

Kiselev and coworkers first adopted eqn (10.21),[49] but then replaced it with[50]

$$\xi = \xi_0 \left(\overline{\Gamma}_0^{-1} \overline{\chi} \right)^{\nu/\gamma} \left[1 - \left(\frac{r_0}{\xi_0 \left(\overline{\Gamma}_0^{-1} \overline{\chi} \right)^{\nu/\gamma}} \right)^2 \right], \tag{10.24}$$

with $r_0 \simeq \xi_0$, and subsequently with[51–54]

$$\xi = \xi_0 \left(\overline{\Gamma}_0^{-1} \overline{\chi} \right)^{\nu/\gamma} \exp \left(- \frac{1}{q_D \xi_0 \left(\overline{\Gamma}_0^{-1} \overline{\chi} \right)^{\nu/\gamma}} \right). \tag{10.25}$$

Just like eqn (10.21), the correlation length ξ should be set equal to zero, when the right-hand-sides of eqn (10.23) and (10.24) become negative. Eqn (10.21), (10.23), (10.24) and (10.25) all reproduce the same asymptotic values close to the critical point, while ξ vanishes far away from the critical point. An advantage of eqn (10.23) to (10.25) is that one no longer needs to select a reference temperature T_R where the critical thermal conductivity enhancement is assumed to be negligibly small. Theoretically, the correlation length should exhibit a crossover from $\xi \propto \chi^{\nu/\gamma}$ asymptotically close to the critical point to $\xi \propto \chi^{1/2}$ far away from the critical point.[55] Since a reliable estimate for the correlation length in the expression for the critical thermal conductivity enhancement is most important close to the critical point, we do not see a pressing need for adopting the Ornstein–Zernike approximation $\gamma = 2\nu$ in eqn (10.23) to (10.25), as was done by previous investigators.[48,50–54] After reviewing the various options, we recommend that the correlation length be calculated from[56]

$$\xi = \xi_0 \left(\Gamma_0^{-1} \overline{\chi} \right)^{\nu/\gamma} \exp \left(\frac{-1}{\overline{\Gamma}_0^{-1} \chi} \right), \tag{10.26}$$

which is essentially the exponential version of eqn (10.24).

It is possible to consider some additional approximations. Within the available uncertainty, the dynamic amplitude ratio R_D in eqn (10.16) may be taken to be unity. Second, in the critical region $C_P \gg C_V$, so that, following Kiselev and Kulikov,[49,50] one may consider neglecting the inverse heat capacity ratio $\kappa^{-1} = C_V/C_P$ in eqn (10.20). Then one obtains as a simplified Olchowy–Sengers approximation,

$$Z^*_{OS}(y) = \frac{2}{\pi y} \left\{ \arctan(y) - 1 + \exp \left(\frac{-1}{y^{-1} + y^2 \rho_c^2 / 3\rho^2} \right) \right\}. \tag{10.27}$$

In order to obtain alternative representations for the critical thermal conductivity enhancement, we return to eqn (10.17), in which $a(k) = \Delta_c a(k) + a_b(k)$. In the hydrodynamic limit $k \to 0$, $\Delta_c a$ vanishes approximately as ξ^{-1}, while the background thermal diffusivity a_b represents the classical slowing down of the fluctuations, which vanishes approximately as ξ^{-2}. Hence, as a next step beyond the Olchowy–Sengers approximation, given by eqn (10.11), we consider

$$Z(q_D\xi) = \frac{3}{(2\pi)^2 q_D} \int_0^{q_D} \mathrm{d}\boldsymbol{k} \left[\frac{C_p(k)}{C_P(0)}\right] \frac{k^{-2}\sin^2\theta}{1 + \rho\Delta_c a(k)/\eta}. \tag{10.28}$$

10.3.2 Kiselev–Kulikov Approximation

In order to evaluate eqn (10.28) one needs to substitute into the integrand an estimate for $\Delta_c a(k)$, for which eqn (10.12) with eqn (10.13) is a natural choice. The resulting integration cannot be performed analytically. To obtain an analytical expression, Kiselev and Kulikov (KK) replaced the dynamical scaling function $\Omega(z)$ in eqn (10.12) by an approximant of the form[49]

$$\Omega_{KK}(z) = \sigma_{KK}(z)\left(1 + z^2\right) \simeq \sigma_0\left(1 + z^2\right), \tag{10.29}$$

with a constant coefficient σ_0. One then obtains from eqn (10.28)

$$\begin{aligned} Z_{KK}(y) = \frac{2}{\pi y}\Bigg[&\left(1 - \kappa^{-1}\right)\arctan(y) \\ &+ \left\{\kappa^{-1}\sqrt{1 + y_D y} - \frac{1}{\sqrt{1 + y_D y}}\right\}\arctan\left(\frac{y}{\sqrt{1 + y_D y}}\right)\Bigg] \end{aligned} \tag{10.30}$$

with

$$y_D = \frac{6\pi\eta^2}{k_B T \rho q_D \sigma_0}. \tag{10.31}$$

For the coefficient σ_0 in the expression (10.31) for y_D, Kiselev and Kulikov[49] have recommended $\sigma_0 = \Omega_K(0.1y)/(1 + 0.01y^2)$, where Ω_K is again the Kawasaki function, eqn (10.13), although the simple choice $\sigma_0 \simeq 1$ may already be adequate. The Olchowy–Sengers approximation corresponds to $\sigma_0 \simeq 0$, so that eqn (10.30) reduces to eqn (10.18) in the limit that y_D approaches infinity. However, unlike eqn (10.18), $\lim_{y\to 0} Z_{KK}(y) = (2/\pi)y_D y \to 0$, so that there is no need for an additional empirical subtraction to be added to eqn (10.30). The present KK approximation, eqn (10.30), differs from the original KK approximation, since Kiselev and Kulikov[49,50] have used the approximation $\kappa^{-1} \simeq 0$:

$$Z^*_{KK}(y) = \frac{2}{\pi y}\left[\arctan(y) - \frac{1}{\sqrt{1 + y_D y}}\arctan\left(\frac{y}{\sqrt{1 + y_D y}}\right)\right]. \tag{10.32}$$

As a next step, we consider eqn (10.28) again, but now with $\Delta_c a(k)$ replaced by $a(k) = \Delta_c a(k) + a_b(k)$ including the background contribution $a_b(k)$. In the KK approximation, one then obtains again eqn (10.30) or eqn (10.32), but with the coefficient y_D to be replaced by

$$y_{1D}^{-1} = y_D^{-1} + \frac{q_D \xi \lambda_b}{\eta C_P}. \tag{10.33}$$

The Kiselev–Kulikov approximation, eqn (10.32) with $R_D = 1$ in eqn (10.16), has been used to represent the critical thermal conductivity enhancement in carbon dioxide, ethane, and methane[49–53] and also in some refrigerants.[54]

10.3.3 Ferrell Approximation

The dynamical scaling function eqn (10.13) becomes proportional to z for large values of z, while the approximant $\Omega_{KK}(z)$, defined by eqn (10.29), diverges as z^2. Another approximant has been proposed by Ferrell[57]

$$\Omega_F(z) = \sigma_F(z)\sqrt{(1+z^2)} \simeq \sigma_0\sqrt{(1+z^2)}. \tag{10.34}$$

On comparing eqn (10.34) with eqn (10.13), we note that $\sigma_F(z)$ varies from 1 to $3\pi/8 \simeq 1.18$. Thus replacing $\sigma_F(z)$ in eqn (10.34) by a constant σ_0 of order unity is a more realistic approximation than in eqn (10.29). We then obtain from eqn (10.28)

$$\begin{aligned} Z_F(y) = \frac{2}{\pi y}\Bigg[& \left(1-\kappa^{-1}\right)\arctan(y) + \kappa^{-1} y_D y \,\mathrm{arcsin\,h}(y) \\ & + \frac{1-\kappa^{-1}\left(1-y_D^2 y^2\right)}{\left(1-y_D^2 y^2\right)^{1/2}}\left\{\arctan\left(\frac{y_D y^2}{\left(1-y_D^2 y^2\right)^{1/2}\left(1+y^2\right)^{1/2}}\right)\right. \\ & \left. - \arctan\left(\frac{y}{\left(1-y_D^2 y^2\right)^{1/2}}\right)\right\}\Bigg], \end{aligned} \tag{10.35}$$

or, if we again use the Kiselev–Kulikov approximation $\kappa^{-1} = 0$,

$$\begin{aligned} Z_F^*(y) = \frac{2}{\pi y}\Bigg[& \arctan(y) + \frac{1}{\left(1-y_D^2 y^2\right)^{1/2}} \\ & \times\left\{\arctan\left(\frac{y_D y^2}{\left(1-y_D^2 y^2\right)^{1/2}\left(1+y^2\right)^{1/2}}\right)\right. \\ & \left. - \arctan\left(\frac{y}{\left(1-y_D^2 y^2\right)^{1/2}}\right)\right\}\Bigg]. \end{aligned} \tag{10.36}$$

A complication of the Ferrell approximation is that a numerical evaluation requires use of complex variables for $y \geq y_D^{-1}$. Following Kiselev and Kulikov,

the effect of adding the background contribution $a_b(k)$ to the integrand in eqn (10.28) may be approximately accounted for by replacing y_D in eqn (10.35) or eqn (10.36) with y_{1D}, given by eqn (10.33).

We have found that the crossover functions in the KK approximation and in the Ferrell approximation approach zero at larger densities more slowly than the crossover function in the OS approximation. Hence, it should be noted that use of any of the crossover functions $Z_{OS}(y)$, $Z^*_{OS}(y)$, $Z_{KK}(y)$, $Z^*_{KK}(y)$, $Z_F(y)$, or $Z^*_F(y)$ will require not only slightly different values for the cutoff wave number q_D, but also different decompositions of the thermal conductivity λ into critical enhancement, $\Delta_c\lambda$, and background, λ_b, contributions.

Olchowy and Sengers[31] and Luettmer-Strathmann *et al.*[10] have developed a more comprehensive expression for the crossover function $Z(y)$ in eqn (10.16). The wave-number dependence eqn (10.12) for $\Delta_c a(q)$ is obtained by taking $q_D \to 0$ before evaluating the limiting critical behavior from eqn (10.11). For the wave-number dependence of $\Delta_c a(q)$, Luettmer-Strathmann *et al.*[10] considered the limiting critical behavior of eqn (10.17) at a constant finite value for q_D and, instead of the Kawasaki function, $\Omega_K(q\xi)$, they obtained

$$\Omega_L(z) = \frac{3}{4}\left(1+z^2\right)^{1/2}\left\{\arctan(y) + \frac{(1+z^2)^{1/2}}{(1+y^2)^{1/2}} \times \left[-\arctan(y) + \arctan\left(\frac{y}{(1+y^2)^{1/2}}\right)\right]\right\}, \tag{10.37}$$

for use in eqn (10.28). Unlike eqn (10.13) for $\Omega(z)$, eqn (10.37) for $\Omega(z)$ depends not only on $z = q\xi$, but also on $y = q_D\xi$. The crossover equation obtained by Luettmer-Strathmann *et al.*[10] has been used to describe the critical thermal conductivity enhancement in carbon dioxide,[10,33] in nitrogen,[58] in argon,[59,60] in some hydrocarbons,[36–38,61–63] and in some refrigerants.[64–66] However, this representation is rather complex. While there is experimental confirmation for the wave-number dependence of the critical diffusivity in agreement with eqn (10.13) or (10.15), there is not yet convincing experimental evidence that requires the more complex wave-number dependence of the critical diffusivity in accordance with eqn (10.37). Moreover, use of eqn (10.37) in the integrand of equation (10.28) still appears to require an empirical subtraction to satisfy the requirement $\lim_{y\to 0} Z(y) = 0$, as was needed in the Olchowy–Sengers approximation. Hence, we recommend the Olchowy–Sengers approximation, the Kiselev–Kulikov approximation, or the Ferrell approximation for practical use.

10.4 Non-asymptotic Critical Behavior of Viscosity of One-component Fluids

Just as in the transition from eqn (10.8) to eqn (10.17), one should restrict the integration in the mode-coupling integral, eqn (10.9), for the critical

viscosity enhancement to an upper cutoff wave-number q_D. If one then neglects the molar isochoric heat capacity C_V in eqn (10.10), one obtains in the limit $q \to 0$:[3]

$$\Delta_c\eta = \frac{k_B T}{(2\pi)^3}\int_0^{q_D} dk \sin^2\theta \cos^2\theta \sin^2\phi \left(\frac{k^2\xi^2}{1+k^2\xi^2}\right)^2 \frac{1}{k^2 a(k)}. \tag{10.38}$$

Since the critical enhancement of the viscosity is present only very close to the critical temperature, the assumption $C_V \ll C_P$ is an excellent approximation in this case. Eqn (10.38) has been evaluated by Bhattacharjee *et al.*[3] For this purpose they substituted into eqn (10.38) $a(k) = \Delta_c a(k) + a_b(k)$ and adopted the Ferrell approximant, eqn (10.34), for $\Omega(z)$ with $\sigma_0 = 3\pi/8$ to best estimate the contributions to the integral for large values of z. They thus obtained

$$\eta = \eta_b\left(1 + z_\eta H\right). \tag{10.39}$$

In order to make this result consistent with the asymptotic critical behavior of the viscosity in accordance with eqn (10.6), eqn (10.39) is considered as representing the first two terms of the expansion of an exponential function, so that[3,10]

$$\eta = \eta_b \exp\left(z_\eta H\right), \tag{10.40}$$

where H is a crossover function defined by

$$\begin{aligned} H = {} & \frac{1}{12}\sin(3\psi_D) - \frac{1}{4q_C\xi}\sin(2\psi_D) + \frac{1}{(q_C\xi)^2}\left[1 - \frac{5}{4}(q_C\xi)^2\right]\sin(\psi_D) \\ & - \frac{1}{(q_C\xi)^3}\left\{\left[1 - \frac{3}{2}(q_C\xi)^2\right]\psi_D - |(q_C\xi)^2 - 1|^{3/2} L(w)\right\}, \end{aligned} \tag{10.41}$$

with $\psi_D = \arccos\left(1/\sqrt{1+q_D^2\xi^2}\right)$. The function $L(w)$ is given by

$$L(w) = \left\{ \begin{array}{ll} \ln\left(\dfrac{1+w}{1-w}\right), & \text{for } q_c\xi > 1 \\ 2\arctan|w|, & \text{for } q_c\xi \le 1 \end{array} \right\}. \tag{10.42}$$

The variable w is given by

$$w = \left|\frac{q_C\xi - 1}{q_C\xi + 1}\right|^{1/2} \tan\left(\frac{\psi_D}{2}\right). \tag{10.43}$$

The function H contains two system-dependent constants, namely the wave numbers q_C and q_D Asymptotically close to the critical point, eqn (10.38) reproduces eqn (10.6) with an amplitude Q that is related to q_C

and q_D such that $Q^{-1} = (q_C^{-1} + q_D^{-1})e^{4/3} / 2$.[3,12] The wave-number q_C is given by[3]

$$q_C = \frac{\nu_c T_c}{16\eta_b^c \lambda_b^c} \frac{\overline{\Gamma}_0}{\xi_0^2} \left(\frac{\partial P}{\partial T}\right)^2_{\rho=\rho_c}, \tag{10.44}$$

where η_b^c and λ_b^c are the values of the background viscosity and background thermal conductivity, respectively, at the critical point, while $(\partial P/\partial T)\rho = \rho_c$ is the slope of the critical isochore at the critical temperature.[§] Just as in the theory for the non-asymptotic critical behavior of the thermal conductivity, the cutoff wave number q_D is again the only adjustable parameter. Because of some approximations in the theory, the actual value for q_D will be similar, but not identical, to its value in the representation for the critical thermal conductivity enhancement.

Eqn (10.40) has been used to represent the critical viscosity enhancement in nitrogen,[3,67] in ethane,[67] in carbon dioxide,[68] in xenon,[5,68] and in H_2O.[69,70] As an example, we show in Figure 10.3 the viscosity of H_2O in the critical region.

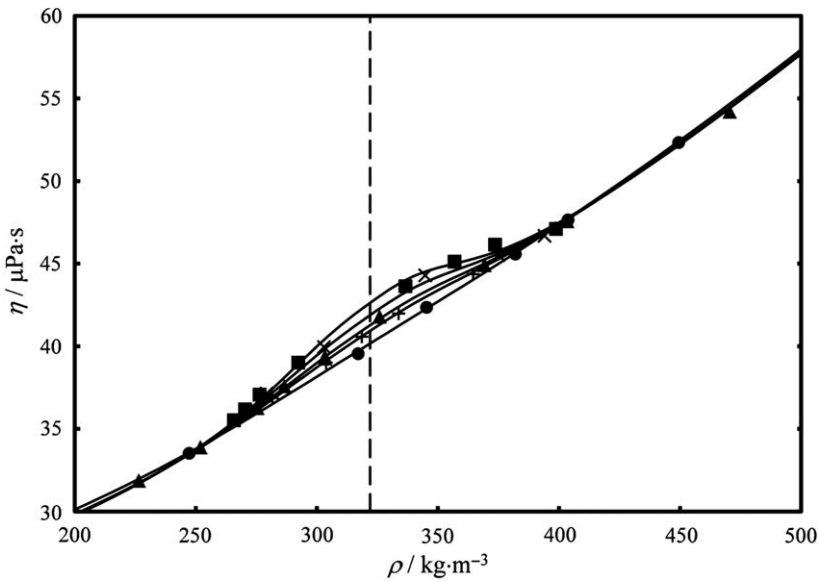

Figure 10.3 Viscosity η of H_2O in the critical region as a function of density ρ. The symbols represent data deduced from the experimental literature, and the solid curves represent eqn (10.38) with $q_D^{-1} = 1.1$ nm and $q_C^{-1} = 1.9$ nm. The dashed line represents the critical density, $\rho_c = 322$ kg · m^{-3}. The isotherms are indicated as: ■, 647.434 K; ×, 647.734 K; ▲, 648.234 K; +, 648.734 K; and ●, 653.234 K. Reprinted with permission from *J. Phys. Chem. Ref. Data*.[70]

[§]In an alternative expression for q_C a factor P_c is missing in ref. 3, 69 and 70.

Eqn (10.40) supersedes an earlier more simplified approach for representing the critical viscosity enhancement of fluids near the critical point.[71–73]

There are some important conceptual differences between the critical enhancement of the thermal conductivity and the critical enhancement of the viscosity. First, theory[8,9,74] and experiments[75] have indicated that the critical viscosity enhancement is a multiplicative enhancement, *i.e.*, $\Delta_c\eta$ in eqn (10.39) is proportional to the background viscosity η_b. On the other hand, the critical thermal conductivity enhancement is an additive enhancement in accordance with eqn (10.1) and (10.16). Second, the viscosity diverges weakly with a critical exponent $z_\eta \simeq 0.068$ in eqn (10.6), while the thermal conductivity diverges strongly with a critical exponent $z_\lambda \simeq 0.899$ in eqn (10.7). Third, because of the strong critical anomalous behavior of the thermal diffusivity and thermal conductivity, the integration over the wave-numbers in the corresponding mode-coupling integral, eqn (10.8), can indeed be taken asymptotically over all wave-numbers, while the cutoff wave-number q_D appears only in the corrections to the asymptotic critical behavior of the thermal conductivity. However, the cutoff q_D of the wave-number integration in eqn (10.38) does contribute to the amplitude Q of the symptotic critical behavior, eqn (10.6).[76] Fourth, the background contribution $a_b(k)$ to the wave-number dependent thermal diffusivity $a(k)$ in the mode-coupling integral, eqn (10.38), also contributes to the amplitude Q of the asymptotic critical behavior of the viscosity through the wave number q_C in addition to q_D.[77]

As was done for the thermal conductivity, Olchowy and coworkers[10,31,33,78] have also formulated a more complete (but more complex) crossover formulation for the critical enhancement of the viscosity. However, eqn (10.40) appears to be adequate in practice. The critical viscosity enhancement near the vapor–liquid critical point is very weak, and corrections to the asymptotic critical behavior already appear very close to the critical temperature.[5] Near the critical mixing point in liquid mixtures, however, the critical viscosity enhancement is much more pronounced and the asymptotic behavior in accordance with eqn (10.6) is observed in a substantial temperature range (after suitable corrections for shear-gradient and frequency effects have been made).[79,80]

10.5 Asymptotic Critical Behavior of Transport Properties of Binary Fluid Mixtures

In fluid mixtures one encounters a variety of vapor–liquid, gas–gas, and liquid–liquid critical phenomena.[81] In this section we shall specifically be concerned with the critical behavior of the thermal conductivity in binary fluid mixtures near vapor–liquid critical points. For binary fluids one starts from the relations between the diffusion current $\boldsymbol{J}_d$ and the heat current $\boldsymbol{J}_q$ associated with the chemical-potential gradient $\nabla\mu_{21}$ and the temperature gradient ∇T:

$$\boldsymbol{J}_d = -\widetilde{\alpha}\nabla\mu_{21} - \widetilde{\beta}\nabla T, \quad \boldsymbol{J}_q - \mu_{21}\boldsymbol{J}_d = -T\widetilde{\beta}\,\nabla\mu_{21} - \widetilde{\gamma}\,\nabla T, \tag{10.45}$$

where $\widetilde{\alpha}$, $\widetilde{\beta}$, and $\widetilde{\gamma}$ are Onsager kinetic coefficients, while $\mu_{21} = \mu_2 - \mu_1$ is the chemical-potential difference between the two components.[48,82] The thermal conductivity λ of the mixture is defined by $\boldsymbol{J}_q = -\lambda \nabla T, \boldsymbol{J}_d = 0$, so that

$$\lambda = \widetilde{\gamma} - \frac{T\widetilde{\beta}^2}{\widetilde{\alpha}}. \tag{10.46}$$

Just as in eqn (10.1) for the thermal conductivity of a one-component fluid, the kinetic coefficients are separated into critical enhancement contributions and non-critical background contributions, such that

$$\widetilde{\alpha} = \Delta_c\widetilde{\alpha} + \widetilde{\alpha}_b,\ \widetilde{\beta} = \Delta_c\widetilde{\beta} + \widetilde{\beta}_b, \quad \text{and} \quad \widetilde{\gamma} = \Delta_c\widetilde{\gamma} + \widetilde{\gamma}_b. \tag{10.47}$$

As originally pointed out by Mistura,[83,84] $\Delta_c\widetilde{\alpha}$, $\Delta_c\widetilde{\beta}$, and $\Delta_c\widetilde{\gamma}$ satisfy Stokes–Einstein relations similar to eqn (10.5):

$$\Delta_c\widetilde{\alpha} = \frac{k_B T\rho}{6\pi\eta\xi}\left(\frac{\partial x}{\partial \mu_{21}}\right)_{T,P},\ \Delta_c\widetilde{\beta} = \frac{k_B T\rho}{6\pi\eta\xi}\left(\frac{\partial x}{\partial T}\right)_{P,\mu_{21}}, \quad \text{and} \quad \Delta_c\widetilde{\gamma} = \frac{k_B T\rho}{6\pi\eta\xi} C_{P,\mu_{21}}, \tag{10.48}$$

where $C_{P,\mu_{21}}$ is the molar isobaric heat capacity at constant field μ_{21}, and where we have approximated the amplitude R_D in eqn (10.5) by unity. The asymptotic expressions for $\Delta_c\widetilde{\alpha}$ and $\Delta_c\widetilde{\beta}$ are not independent but are related by[48]

$$\Delta_c\widetilde{\beta} = -\left(\partial\mu_{21} / \partial T\right)_{P,x}\Delta_c\widetilde{\alpha}. \tag{10.49}$$

Substituting the equations for the kinetic coefficients into eqn (10.46) and using some thermodynamic relations, one obtains for the thermal conductivity[85,86]

$$\lambda = \frac{k_B T\rho}{6\pi\eta\xi}\left(\frac{\Delta_c\widetilde{\alpha}}{\widetilde{\alpha}} C_{P,x} + \frac{\widetilde{\alpha}_b}{\widetilde{\alpha}} C_{P,\mu}\right) - \frac{T\widetilde{\beta}_b}{\widetilde{\alpha}}\left(2\Delta_c\widetilde{\beta} + \widetilde{\beta}_b\right) + \widetilde{\gamma}_b. \tag{10.50}$$

For the physical interpretation of eqn (10.50) one may distinguish two regimes. Somewhat away from the critical point ($\Delta_c\widetilde{\alpha} \ll \widetilde{\alpha}_b,\ \Delta_c\widetilde{\beta} \ll \widetilde{\beta}_b$) the expression for the thermal conductivity reduces to

$$\lambda = \frac{k_B T\rho}{6\pi\eta\xi} C_{P,\mu} - \frac{T\widetilde{\beta}^2}{\widetilde{\alpha}} + \widetilde{\gamma}_b. \tag{10.51}$$

Eqn (10.51) shows a divergent critical behavior of the thermal conductivity of the mixture, since according to the principle of isomorphic critical behavior, $C_{P,\mu}$ diverges like C_P of a one-component fluid.[87,88] Very close to the critical point ($\Delta_c\widetilde{\alpha} \gg \widetilde{\alpha}_b,\ \Delta_c\widetilde{\beta} \gg \widetilde{\beta}_b$) one obtains

$$\lambda = \frac{k_B T\rho}{6\pi\eta\xi} C_{P,x} + \frac{1}{\widetilde{\alpha}}\left(\frac{k_B T\rho}{6\pi\eta\xi}\widetilde{\alpha}_b C_{P,\mu} - 2T\widetilde{\beta}_b\Delta_c\widetilde{\beta}\right) + \widetilde{\gamma}_b. \tag{10.52}$$

The first contribution in eqn (10.52) vanishes at the critical point, since $C_{P,x}$ diverges only weakly except in the case of an azeotropic critical mixture, while the second contribution goes asymptotically to a finite value. The third term represents a background contribution like in a one-component fluid. Hence, the thermal conductivity will exhibit a crossover from a one-component-like critical behavior away from the critical point to a finite limiting value at the critical point. Such a crossover critical behavior of the thermal conductivity has indeed been observed experimentally, as shown in Figure 10.4.[89,90] However, the finite limiting behavior of the thermal conductivity in simple fluid mixtures is seen only extremely close to the critical point.[48,91] In an azeotropic critical mixture the thermal conductivity will continue to diverge at the critical point, as it does in a one-component fluid.[86]

The viscosity near the vapor–liquid critical point in binary fluids diverges asymptotically in accordance with eqn (10.6).[48] For a discussion of the

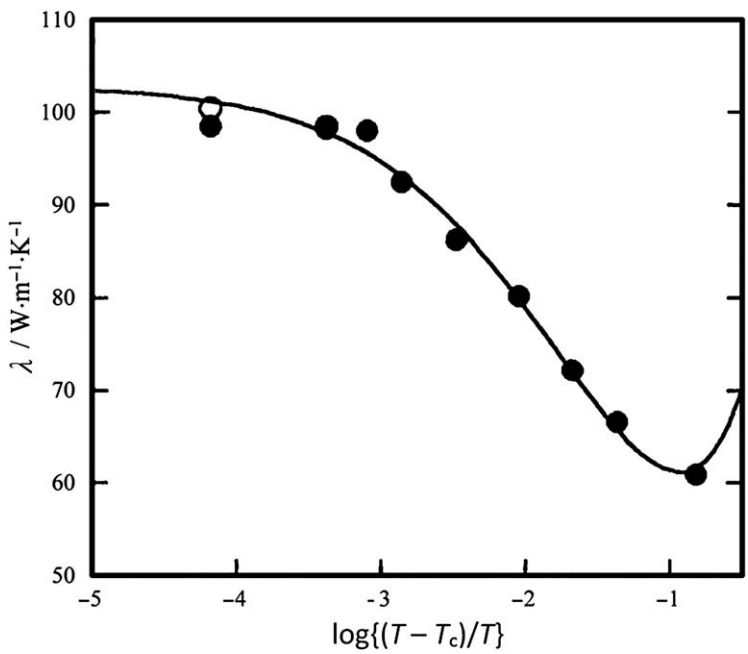

Figure 10.4 Thermal conductivity λ of the equimolar mixture of $(0.5CH_4 + 0.5C_2H_6)$ along the critical isochore ($\rho = 8.527$ mol·L^{-1}) as a function of $(T - T_c)/T$. The filled symbols, ●, represent experimental data, while the open symbol, ○, represents the result of a small gravity correction to the experimental value closest to the critical temperature. The curve represents a theoretical calculation that includes the crossover from a divergent behavior of the thermal conductivity away from the critical temperature to a finite limiting value at the critical temperature.
Reprinted with permission from *J. Chem. Phys.*[90]

asymptotic critical behavior in mixtures of some other transport properties, such as mass diffusion coefficient, thermal diffusion coefficient, thermal diffusion ratio, and Soret coefficient, implied by eqn (10.47) and (10.48), the reader is referred to work of Luettmer-Strathmann.[48,92,93]

While we focus here our attention on transport properties, especially on the thermal conductivity, of mixtures near vapor–liquid critical points, eqn (10.47) and (10.48) can also be used to deal with the critical behavior of transport properties in mixtures that exhibit crossover from vapor–liquid to liquid–liquid critical phenomena.[94,95] Anisimov and Kiselev[96] have elucidated the consequences of eqn (10.47) and (10.48) for the behavior of transport properties in critical dilute solutions.

We conclude this discussion with some remarks about the description of the critical behavior of transport properties in mixtures. In the application of theoretical expressions, such as eqn (10.48), the kinetic coefficients $\widetilde{\alpha}$, $\widetilde{\beta}$ and $\widetilde{\gamma}$ will need to be related to experimentally accessible transport properties, as has been discussed in detail elsewhere.[48,97] In addition, the critical thermodynamic behavior of mixtures is isomorphic with that of one-component fluids, provided that the thermodynamic properties are considered at constant chemical potential μ_{21}.[88] However, the actual value of this chemical potential depends on the zero-points of energy and entropy for the two components. Hence, thermodynamic properties like $C_{P,\mu_{21}}$ are not experimentally accessible and appear as intermediate properties in the calculations. While this issue has been mentioned by some authors,[97–103] the topic could benefit from a more systematic analysis not yet available in the literature.

10.6 Non-asymptotic Critical Behavior of Thermal Conductivity of Binary Fluid Mixtures

Just as in the case of a one-component fluid, for a comprehensive description of the effects of critical fluctuations on the thermal conductivity of fluid mixtures, one needs a proper representation that includes the non-asymptotic critical behavior of the thermal conductivity. Such a non-asymptotic description has been developed by Kiselev and Kulikov[49,50] and by Luettmer-Strathmann and Sengers.[48] In a one-component fluid the critical behavior of the transport properties is caused by a coupling between the heat mode associated with entropy fluctuations and the viscous mode associated with the transverse-momentum fluctuations. In a binary fluid mixture one needs to consider a coupling of both the entropy fluctuations and the concentration fluctuations and the viscous fluctuations. Using this idea, Kiselev and Kulikov[49] were the first authors who derived crossover equations for the critical enhancements $\Delta_c\widetilde{\alpha}$, $\Delta_c\widetilde{\beta}$ and $\Delta_c\widetilde{\gamma}$ of the kinetic coefficients $\widetilde{\alpha}$, $\widetilde{\beta}$ and $\widetilde{\gamma}$. The crossover formulation of Kiselev and Kulikov has been used to represent the critical thermal conductivity enhancement in mixtures of (methane + ethane) and (carbon

dioxide + ethane)[49–53] and in some refrigerant mixtures.[54] The problem has subsequently been considered by Luettmer-Strathmann and Sengers,[48] who included a more detailed account of the mutual coupling between entropy and concentration fluctuations. Their crossover formulation has been used to represent the critical enhancement in (methane + ethane)[90] and (carbon dioxide + ethane).[48,86] All formulations account for a crossover of a divergent behavior of the thermal conductivity away from the critical point to a finite limiting value at the vapor–liquid critical point of mixtures.

In Section 10.3, we have derived crossover functions $Z^*_{\mathrm{KK}}(y)$, given by eqn (10.32), and $Z^*_{\mathrm{F}}(y)$, given by eqn (10.36), in which we have neglected the background thermal conductivity contribution λ_{b}, and hence, a_{b} in the mode-coupling integral of eqn (10.17). If we apply the same principle, neglecting the background contributions $\widetilde{\alpha}_{\mathrm{b}}$, $\widetilde{\beta}_{\mathrm{b}}$ and $\widetilde{\gamma}_{\mathrm{b}}$ in the expressions for the critical enhancements $\Delta_{\mathrm{c}}\widetilde{\alpha}$, $\Delta_{\mathrm{c}}\widetilde{\beta}$ and $\Delta_{\mathrm{c}}\widetilde{\gamma}$, we find that the representation proposed by Kiselev and Kulikov[49,50] reduces to

$$\widetilde{\alpha} = \frac{k_{\mathrm{B}}T\rho q_{\mathrm{D}}}{6\pi\eta}\left(\frac{\partial x}{\partial \mu_{21}}\right)_{T,P} Z^*(q_{\mathrm{D}}\xi) + \widetilde{\alpha}_{\mathrm{b}}, \tag{10.53}$$

$$\widetilde{\beta} = \frac{k_{\mathrm{B}}T\rho q_{\mathrm{D}}}{6\pi\eta}\left(\frac{\partial x}{\partial T}\right)_{P,\mu_{21}} Z^*(q_{\mathrm{D}}\xi) + \widetilde{\beta}_{\mathrm{b}}, \tag{10.54}$$

and

$$\widetilde{\gamma} = \frac{k_{\mathrm{B}}T\rho q_{\mathrm{D}}}{6\pi\eta} C_{P,\mu_{21}} Z^*(q_{\mathrm{D}}\xi) + \widetilde{\gamma}_{\mathrm{b}}, \tag{10.55}$$

where the crossover function $Z^*(y)$ is now identical with the crossover function, eqn (10.32), for the critical thermal conductivity enhancement of a one-component fluid in the Kiselev–Kulikov approximation or with the crossover function, eqn (10.36), in the Ferrell approximation. We note that $C_{P,\mu_{21}}$ in eqn (10.55) can be related to $C_{P,x}$ by[50]

$$C_{P,\mu_{21}} = C_{P,x} + T\left(\frac{\partial \mu_{21}}{\partial T}\right)^2_{P,x}\left(\frac{\partial x}{\partial \mu_{21}}\right)_{P,T}. \tag{10.56}$$

The resulting expression for the thermal conductivity is then obtained by substituting eqn (10.53) to (10.56) into eqn (10.46). One then obtains

$$\begin{aligned}\lambda = {} & \frac{k_{\mathrm{B}}T\rho q_{\mathrm{D}} C_{P,x}}{6\pi\eta} Z^*(q_{\mathrm{D}}\xi) - \frac{T}{\Delta_{\mathrm{c}}\widetilde{\alpha} + \widetilde{\alpha}_{\mathrm{b}}}\left[\widetilde{\beta}_{\mathrm{b}} + \left(\frac{\partial \mu_{21}}{\partial T}\right)_{P,x}\widetilde{\alpha}_{\mathrm{b}}\right]^2 \\ & + T\left(\frac{\partial \mu_{21}}{\partial T}\right)^2_{P,x}\widetilde{\alpha}_{\mathrm{b}} + 2T\left(\frac{\partial \mu_{21}}{\partial T}\right)_{P,x}\widetilde{\beta}_{\mathrm{b}} + \widetilde{\gamma}_{\mathrm{b}}\end{aligned} \tag{10.57}$$

with

$$\Delta_c\tilde{\alpha} = \frac{k_B T \rho q_D}{6\pi\eta}\left(\frac{\partial x}{\partial \mu_{21}}\right)_{T,P} Z^*(q_D\xi). \tag{10.58}$$

Eqn (10.57) is the non-asymptotic generalization of an asymptotic equation in the form earlier presented by Anisimov and Kiselev.[96] We note that eqn (10.57) remains valid, even if one does not neglect the background contributions $\tilde{\alpha}_b$ and $\tilde{\gamma}_b$ in the mode-coupling integrals for $\Delta_c\tilde{\alpha}$ and $\Delta_c\tilde{\gamma}$, provided one imposes the approximation $\tilde{\alpha}_b = \tilde{\gamma}_b$, so that y_D in eqn (10.32) or eqn (10.36) can be replaced by y_{1D}, given by eqn (10.33) with λ_b replaced with $\tilde{\alpha}_b$ or equivalently $\tilde{\gamma}_b$. The equations need to be supplemented with a procedure for estimating the correlation length ξ. For this purpose we recommend use of eqn (10.26), where the susceptibility χ is now to be identified with the appropriate isomorphic susceptibility $\chi_{T,\mu_{21}}$ for mixtures:

$$\chi_{T,\mu_{21}} = \rho\left(\frac{\partial \rho}{\partial P}\right)_{T,\mu_{21}}. \tag{10.59}$$

The more detailed crossover formulation of Luettmer-Strathmann and Sengers[48] is considerably more complex. One complication is that their crossover functions do not vanish far away from the critical point. The simple representation for the critical thermal conductivity enhancement in mixtures, given by eqn (10.57), seems to be the more practical one for future applications.

10.7 Discussion

In this chapter we have reviewed the information available for the critical behavior of the transport properties of fluids and fluid mixtures. Special attention has been devoted to the critical thermal conductivity enhancement. For the critical enhancement of the thermal conductivity in one-component fluids, either the Olchowy–Sengers approximation discussed in Section 10.3.1, the Kiselev–Kulikov approximation discussed in Section 10.3.2, or the Ferrell approximation discussed in Section 10.3.3, is recommended for practical use. For the critical enhancement of the thermal conductivity in fluid mixtures, eqn (10.57), obtained by substituting eqn (10.53) to (10.55) into eqn (10.46), would appear to provide the simplest approach in practice.

The equations for the critical behavior of the thermal conductivity presented in this chapter have been obtained on the basis of the mode-coupling theory of critical dynamics.[8,9] An alternative approach, based on a renormalization-group theory of critical dynamics,[2] has been explored by Folk and Moser.[14,104–108] The relationship between the mode-coupling theory and dynamic renormalization-group theory has been discussed by Hohenberg and Halperin.[2] Equations provided by the mode-coupling theory for critical dynamics seem to us more useful for practical applications.

10.A Appendix: Critical Exponents and Critical Amplitudes

In this Appendix we briefly summarize the critical exponents and critical amplitudes associated with the asymptotic critical power-law behavior of some thermodynamic properties. In the theory of critical phenomena, it is convenient to express all thermodynamic properties in dimensionless form. The procedure adopted here is to express the temperature T in terms of the critical temperature T_c, the density ρ in terms of the critical density ρ_c, and the chemical potential μ per mole in terms of RT_c, where R is the gas constant. One thus defines[55]

$$\overline{T}=\frac{T}{T_c},\quad \overline{\rho}=\frac{\rho}{\rho_c},\quad \overline{P}=\frac{P}{\rho_c RT_c},\quad \overline{\mu}=\frac{\mu}{RT_c},\quad \overline{C}_V=\frac{\rho C_V}{\rho_c R},\ \text{and}\ \overline{\chi}=\frac{RT_c}{\rho_c}\chi, \tag{10.A.1}$$

where $\chi=(\partial\rho/\partial\mu)_T=\rho(\partial\rho/\partial P)_T$ is the susceptibility. In addition, one defines the difference functions

$$\Delta\overline{T}=\frac{T-T_c}{T_c}\quad\text{and}\quad \Delta\overline{\rho}=\frac{\rho-\rho_c}{\rho_c}. \tag{10.A.2}$$

Asymptotically close to the critical point, the isochoric heat capacity, the susceptibility, and the correlation length diverge as a function of temperature in the one-phase region ($\Delta\overline{T}\geq 0$) along the critical isochore $\rho=\rho_c$ as

$$\overline{C}_V\approx\overline{A}_0(\Delta\overline{T})^{-\alpha},\quad \overline{\chi}\approx\overline{\Gamma}_0(\Delta\overline{T})^{-\gamma},\quad\text{and}\quad \xi\approx\xi_0(\Delta\overline{T})^{-\nu}. \tag{10.A.3}$$

The density $\rho=\rho_{\text{cxc}}$ on either side of the phase boundary below the critical temperature($\Delta\overline{T}\leq 0$) depends on the temperature asymptotically close to the critical point as

$$\Delta\overline{\rho}_{\text{cxc}}\approx\pm\overline{B}_0|\Delta\overline{T}|^{\beta}. \tag{10.A.4}$$

In these power laws α, β, γ, and ν are universal critical exponents such that $\gamma=2-\alpha-2\beta$ and $\nu=(2-\alpha)/3$. Currently accepted values are:[109,110]

$$\alpha\approx 0.110,\ \beta\approx 0.326,\ \gamma\approx 1.239,\ \nu\approx 0.630. \tag{10.A.5}$$

The critical amplitudes $\overline{A}_0$, $\overline{B}_0$, $\overline{\Gamma}_0$ and ξ_0 satisfy universal relations[109,111]

$$\frac{\alpha\overline{A}_0\overline{\Gamma}_0}{\overline{B}_0^2}\simeq 0.058\quad\text{and}\quad \xi_0\left(\alpha\overline{A}_0N_A\rho_c\right)^{1/3}\simeq 0.266\,, \tag{10.A.6}$$

where N_A is Avogadro's constant, so that $N_A\rho_c$ is the inverse of the molecular volume, ν_c, at the critical point. The fluid-specific critical amplitudes are to

be obtained from a properly scaled equation of state for fluids near the critical point. In the absence of such information, the critical amplitudes $\overline{A}_0$ and $\overline{B}_0$ for many molecular fluids may be estimated as[7]

$$\overline{A}_0 \simeq 5.58 + 7.94\,\omega \quad \text{and} \quad \overline{B}_0 \simeq 1.45 + 1.21\,\omega, \tag{10.A.7}$$

where ω is the acentric factor. The amplitudes $\overline{\Gamma}_0$ and ξ_0 are then obtained by substituting eqn (10.A.7) into eqn (10.A.6).

An alternative procedure for dealing with the thermodynamic behavior of fluids near the critical point uses, instead of RT_c, the critical pressure P_c as a reduction parameter. One then defines[112]

$$T^* = \frac{T}{T_c}, \quad \rho^* = \frac{\rho}{\rho_c}, \quad P^* = \frac{P}{P_c}, \quad \mu^* = \mu\frac{\rho_c}{P_c}, \quad C_V^* = \rho C_V \frac{T_c}{P_c}, \quad \text{and } \chi^* = \chi\frac{P_c}{\rho_c^2}. \tag{10.A.8}$$

Although the option defined by eqn (10.A.8) appears to be the one most frequently adopted in the literature, we prefer to adopt the option defined by eqn (10.A.1). The reason is that in the theory of critical phenomena, the ordering field is μ/RT and not $\mu\rho/P$, so that the first option has a better physical foundation. The relationship between these two options has been elucidated elsewhere.[7]

Acknowledgement

The authors are indebted to Marcia L. Huber of NIST for valuable discussions.

References

1. J. V. Sengers, *Int. J. Thermophys.*, 1985, **6**, 203.
2. P. C. Hohenberg and B. I. Halperin, *Rev. Mod. Phys.*, 1977, **49**, 435.
3. J. K. Bhattacharjee, R. A. Ferrell, R. S. Basu and J. V. Sengers, *Phys. Rev. A*, 1981, **24**, 1469.
4. H. Hao, R. A. Ferrell and J. K. Bhattacharjee, *Phys. Rev. E*, 2005, **71**, 021201.
5. R. F. Berg, M. R. Moldover and G. A. Zimmerli, *Phys. Rev. Lett.*, 1999, **82**, 920.
6. M. L. Huber, R. A. Perkins, D. G. Friend, J. V. Sengers, M. J. Assael, I. N. Metaxa, K. Miyagawa, R. Hellmann and E. Vogel, *J. Phys. Chem. Ref. Data*, 2012, **41**, 033102.
7. R. A. Perkins, J. V. Sengers, I. M. Abdulagatov and J. V. Sengers, *Int. J. Thermophys.*, 2013, **34**, 191.
8. K. Kawasaki, *Ann. Phys.*, 1970, **61**, 1.

9. K. Kawasaki, in *Phase Transitions and Critical Phenomena*, ed. C. Domb and M. S. Green, Academic Press, New York, 1976, ch. 5a, pp. 162–403.
10. J. Luettmer-Strathmann, J. V. Sengers and G. A. Olchowy, *J. Chem. Phys.*, 1995, **103**, 7482.
11. M. E. Fisher, *J. Math. Phys.*, 1964, **5**, 944.
12. H. C. Burstyn, J. V. Sengers, J. K. Bhattacharjee and R. A. Ferrell, *Phys. Rev. A*, 1983, **28**, 1567.
13. V. Privman, P. C. Hohenberg, and A. Aharony, in *Phase Transitions and Critical Phenomena*, ed. C. Domb and J. L. Lebowitz, Academic Press, New York, 1999, ch. 14, pp. 1–134.
14. R. Folk and G. Moser, *Phys. Rev. Lett.*, 1995, **75**, 2706.
15. J. V. Sengers, R. A. Perkins, M. L. Huber and B. Le Neindre, *Int. J. Thermophys.*, 2009, **30**, 1453; J. V. Sengers, R. A. Perkins, M. L. Huber and B. Le Neindre, *Int. J. Thermophys.*, 2011, **32**, 704.
16. H. C. Burstyn, J. V. Sengers and P. Esfandiari, *Phys. Rev. A*, 1980, **22**, 282.
17. H. Güttinger and D. S. Cannell, *Phys. Rev. A*, 1980, **22**, 285.
18. K. Hamano, T. Nomura, T. Kawazura and N. Kuwahara, *Phys. Rev. A*, 1982, **26**, 1153.
19. S.-H. Chen, C.-C. Lai, J. Rouch and P. Tartaglia, *Phys. Rev. A*, 1983, **27**, 1086.
20. R. A. Wilkinson, G. A. Zimmerli, H. Hao, M. R. Moldover, R. F. Berg, W. L. Johnson, R. A. Ferrell and R. W. Gammon, *Phys. Rev. E*, 1998, **57**, 436.
21. G. Paladin and L. Peliti, *J. Phys. Lett.*, 1982, **43**, 15; G. Paladin and L. Peliti, *J. Phys. Lett.*, 1984, **45**, 289(E).
22. A. Zielesny, J. Schmitz, S. Limberg, A. G. Alzpiri, S. Fusenig and D. Woermann, *Int. J. Thermophys.*, 1994, **15**, 67.
23. K. Hamano, T. Kawazura, T. Koyama and N. Kuwahara, *J. Chem. Phys.*, 1985, **82**, 2718.
24. K. Hamano, S. Teshigawara, T. Koyama and N. Kuwahara, *Phys. Rev. A*, 1986, **33**, 485.
25. H. L. Swinney and D. L. Henry, *Phys. Rev. A*, 1973, **8**, 2586.
26. B. Kalbskof, D. Woermann, B. Chu and E. Gulari, *J. Chem. Phys.*, 1981, **74**, 5842.
27. J. Rouch, P. Tartaglia and S. H. Chen, *Phys. Rev. A*, 1988, **37**, 3046.
28. M. H. Ernst, E. H. Hauge and J. M. J. van Leeuwen, *Phys. Lett. A*, 1971, **34**, 419.
29. T. R. Kirkpatrick, D. Belitz and J. V. Sengers, *J. Stat. Phys.*, 2002, **109**, 373.
30. G. A. Olchowy and J. V. Sengers, *Int. J. Thermophys.*, 1989, **10**, 417.
31. G. A. Olchowy and J. V. Sengers, *Phys. Rev. Lett.*, 1988, **61**, 15.
32. E. W. Lemmon and R. T. Jacobsen, *Int. J. Thermophys.*, 2004, **25**, 21.
33. V. Vesovic, W. A. Wakeham, G. A. Olchowy, J. V. Sengers, J. T. R. Watson and J. Millat, *J. Phys. Chem. Ref. Data*, 1990, **19**, 763.
34. M. J. Assael, J.-A. M. Assael, M. L. Huber, R. A. Perkins and Y. Takata, *J. Phys. Chem. Ref. Data*, 2011, **40**, 033101.

35. D. G. Friend, H. Ingham and J. F. Ely, *J. Phys. Chem. Ref. Data*, 1991, **20**, 275.
36. K. N. Marsh, R. A. Perkins and M. L. V. Ramires, *J. Chem. Eng. Data*, 2002, **47**, 932.
37. R. A. Perkins, M. L. V. Ramires, C. A. Nieto de Castro and L. Cusco, *J. Chem. Eng. Data*, 2002, **47**, 1263.
38. R. A. Perkins, *J. Chem. Eng. Data*, 2002, **47**, 1272.
39. M. L. Huber and R. A. Perkins, *Fluid Phase Equilib.*, 2005, **227**, 47.
40. R. A. Perkins and M. L. Huber, *J. Chem. Eng. Data*, 2006, **51**, 898.
41. R. A. Perkins, A. Laesecke, M. L. V. Ramires, A. Gurova and L. Cusco, *Experimental Thermal Conductivity Values for the IUPAC Round Robin Sample of 1,1,1,2-Tetrafluoroethane (R134a)*, National Institute of Standards and Technology, Gaithersburg, MD, 2000.
42. M. L. Huber, A. Laesecke and R. A. Perkins, *Ind. Eng. Chem. Res.*, 2003, **42**, 3163.
43. R. A. Perkins, U. Hammerschmidt and M. L. Huber, *J. Chem. Eng. Data*, 2008, **53**, 2120.
44. M. J. Assael, I. A. Koini, K. D. Antoniadis, M. L. Huber, I. M. Abdulagatov and R. A. Perkins, *J. Phys. Chem. Ref. Data*, 2012, **41**, 023104.
45. M. J. Assael, S. K. Mylona, M. L. Huber and R. A. Perkins, *J. Phys. Chem. Ref. Data*, 2012, **41**, 023101.
46. M. J. Assael, E. K. Mihailidou, M. L. Huber and R. A. Perkins, *J. Phys. Chem. Ref. Data*, 2012, **41**, 043102.
47. R. Tufeu and B. Le Neindre, *Int. J. Thermophys.*, 1987, **8**, 283.
48. J. Luettmer-Strathmann and J. V. Sengers, *J. Chem. Phys.*, 1996, **104**, 3026; J. Luettmer-Strathmann and J. V. Sengers, *J. Chem. Phys.*, 1997, **106**, 438.
49. S. B. Kiselev and V. D. Kulikov, *Int. J. Thermophys.*, 1994, **15**, 283.
50. S. B. Kiselev and V. D. Kulikov, *Int. J. Thermophys.*, 1997, **18**, 1143.
51. S. B. Kiselev and M. L. Huber, *Fluid Phase Equilib.*, 1998, **142**, 253.
52. S. B. Kiselev and J. F. Ely, *Fluid Phase Equilib.*, 2004, **222**, 149.
53. S. B. Kiselev and J. F. Ely, *Fluid Phase Equilib.*, 2007, **252**, 57.
54. S. B. Kiselev, R. A Perkins and M. L. Huber, *Int. J. Refrig.*, 1999, **22**, 509.
55. M. A. Anisimov, S. B. Kiselev, J. V. Sengers and S. Tang, *Physica A*, 1992, **188**, 487.
56. R. A. Perkins and J. V. Sengers, *Int. J. Thermophys.*, 2013, **34**, 2046.
57. R. A. Ferrell, *Phys. Rev. Lett.*, 1970, **24**, 1169.
58. R. A. Perkins, H. M. Roder, D. G. Friend and C. A. Nieto de Castro, *Physica A*, 1991, **173**, 332.
59. R. A. Perkins, D. G. Friend, H. M. Roder and C. A. Nieto de Castro, *Int. J. Thermophys.*, 1991, **12**, 965.
60. B. W. Tiesinga, E. P. Sakonidou, H. R. van den Berg, J. Luettmer-Strathmann and J. V. Sengers, *J. Chem. Phys.*, 1994, **101**, 6944.
61. R. Mostert, H. R. van den Berg, P. S. van der Gulik and J. V. Sengers, *J. Chem. Phys.*, 1990, **92**, 5454.
62. V. Vesovic, W. A. Wakeham, J. Luettmer-Strathmann, J. V. Sengers, J. Millat, E. Vogel and M. J. Assael, *Int. J. Thermophys.*, 1994, **15**, 33.

63. E. P. Sakonidou, H. R. van den Berg, C. A. ten Seldam and J. V. Sengers, *J. Chem. Phys.*, 1996, **105**, 10535.
64. A. Laesecke, R. A. Perkins and C. A. Nieto de Castro, *Fluid Phase Equilib.*, 1992, **80**, 263.
65. R. Krauss, J. Luettmer-Strathmann, J. V. Sengers and K. Stephan, *Int. J. Thermophys.*, 1993, **14**, 951.
66. R. Krauss, V. C. Weiss, T. A. Edison, J. V. Sengers and K. Stephan, *Int. J. Thermophys.*, 1996, **17**, 731.
67. R. S. Basu and J. V. Sengers, in *Proceedings of the 8th Symposium on Thermophysical Properties*, ed. J. V. Sengers, American Society of Mechanical Engineers, 1982, pp. 434–439.
68. R. F. Berg and M. R. Moldover, *J. Chem. Phys.*, 1990, **93**, 1926.
69. J. V. Sengers, R. A. Perkins, M. L. Huber and D. G. Friend, *Int. J. Thermophys.*, 2009, **30**, 374.
70. M. L. Huber, R. A. Perkins, A. Laesecke, D. G. Friend, J. V. Sengers, M. J. Assael, I. N. Metaxa, E. Vogel, R. Mareš and K. Miyagawa, *J. Phys. Chem. Ref. Data*, 2009, **38**, 101.
71. R. S. Basu, J. V. Sengers and J. T. R. Watson, *Int. J. Thermophys.*, 1980, **1**, 33.
72. J. T. R. Watson, R. S. Basu and J. V. Sengers, *J. Phys. Chem. Ref Data*, 1980, **9**, 1255.
73. C. Yokoyama, M. Takahashi and S. Takhashi, *Int. J. Thermophys.*, 1994, **15**, 603.
74. T. Ohta, *J. Phys. C: Solid State Phys.*, 1972, **10**, 791.
75. J. V. Sengers, in *Critical Phenomena, Proceedings of the International School of Physics "Enroci Fermi", Course LI*, ed. M. S. Green, Academic Press, New York, 1971, pp. 445–507.
76. R. Perl and R. A. Ferrell, *Phys. Rev. A*, 1972, **6**, 2358.
77. D. W. Oxtoby and W. M. Gelbart, *J. Chem. Phys.*, 1974, **61**, 2957.
78. S. Hendl, J. Millat, E. Vogel, V. Vesovic, W. A. Wakeham, J. Luettmer-Strathmann, J. V. Sengers and M. J. Assael, *Int. J. Thermophys.*, 1994, **15**, 1.
79. R. F. Berg and M. R. Moldover, *J. Chem. Phys.*, 1988, **89**, 3694.
80. J. C. Nieuwoudt and J. V. Sengers, *J. Chem. Phys.*, 1989, **90**, 457.
81. A. Boltz, U. Deiters, C. J. Peters and Th. W. de Loos, *Pure Appl. Chem.*, 1998, **70**, 2233.
82. S. R. de Groot and P. Mazur, *Non-Equilibrium Thermodynamics*, Dover, New York, 1984.
83. L. Mistura, *Nuovo Cimento B*, 1972, **12**, 35.
84. L. Mistura, *J. Chem. Phys.*, 1975, **62**, 4571.
85. R. Mostert and J. V. Sengers, *Fluid Phase Equilib.*, 1992, **75**, 235; R. Mostert and J. V. Sengers, *Fluid Phase Equilib.*, 1993, **85**, 347.
86. R. Mostert and J. V. Sengers, *Int. J. Thermophys.*, 2008, **29**, 1205.
87. R. B. Griffiths and J. C. Wheeler, *Phys. Rev. A*, 1970, **2**, 1047.
88. M. A. Anisimov, E. E. Gorodetskii, V. D. Kulikov and J. V. Sengers, *Phys. Rev. E*, 1995, **51**, 1199.
89. E. P. Sakonidou, H. R. van den Berg, C. A. ten Seldam and J. V. Sengers, *Phys. Rev. E*, 1997, **56**, R4943.

90. E. P. Sakonidou, H. R. van den Berg, C. A. ten Seldam and J. V. Sengers, *J. Chem. Phys.*, 1998, **109**, 717.
91. D. G. Friend and H. M. Roder, *Phys. Rev. A*, 1985, **32**, 1941.
92. J. Luettmer-Strathmann and J. V. Sengers, *Int. J. Thermophys.*, 1994, **15**, 1241.
93. J. Luettmer-Strathmann, in *Thermal Nonequilibrium Phenomena in Fluid Mixtures*, ed. W. Köhler and S. Wiegand, Springer, Berlin, 2002, pp. 24–37.
94. H. Cheng, M. A. Anisimov and J. V. Sengers, *Fluid Phase Equilib.*, 1997, **128**, 67.
95. M. A. Anisimov, V. A. Agayan, A. A. Povodyrev and J. V. Sengers, *Phys. Rev. E*, 1998, **57**, 1946.
96. M. A. Anisimov and S. B. Kiselev, *Int. J. Thermophys.*, 1992, **13**, 873.
97. M. A. Anisimov, E. E. Gorodetskii, V. D. Kulikov, A. A. Povodyrev and J. V. Sengers, *Physica A*, 1995, **220**, 277; M. A. Anisimov, E. E. Gorodetskii, V. D. Kulikov, A. A. Povodyrev and J. V. Sengers, 1996, **223**, 272.
98. S. S. Leung and R. B. Griffiths, *Phys. Rev. A*, 1973, **8**, 2670.
99. M. R. Moldover and J. S. Gallagher, *AIChE J.*, 1978, **24**, 267.
100. J. C. Rainwater, in *Supercritical Fluid Technology: Reviews in Modern Theory and Applications*, ed. T. J. Bruno and J. F. Ely, CRC Press, Boca Raton, FL, 1991, pp. 57–162.
101. M. A. Anisimov and J. V. Sengers, *Phys. Lett. A*, 1992, **172**, 114.
102. G. X. Jin, S. Tang and J. V. Sengers, *Phys. Rev. E*, 1993, **47**, 388.
103. J. C. Rainwater and D. G. Friend, *Phys. Lett. A*, 1994, **191**, 431.
104. R. Folk and G. Moser, *Int. J. Thermophys.*, 1995, **16**, 1363.
105. R. Folk and G. Moser, *Condensed Matter Phys.*, 1996, **7**, 27.
106. R. Folk and G. Moser, *Int. J. Thermophys.*, 1998, **19**, 1003.
107. R. Folk and G. Moser, *Phys. Rev. E*, 1998, **57**, 683.
108. R. Folk and G. Moser, *Phys. Rev. E*, 1998, **57**, 705.
109. A. Pelisseto and E. Vicari, *Physics Reports*, 2002, **368**, 549.
110. J. V. Sengers and J. G. Shanks, *J. Stat. Phys.*, 2009, **137**, 857.
111. M. E. Fisher and S. Y. Zinn, *J. Phys. A*, 1998, **31**, L629.
112. J. V. Sengers and J. M. H. Levelt Sengers, *Ann. Rev. Phys. Chem.*, 1986, **37**, 189.

CHAPTER 11

Computer Simulations

GUILLAUME GALLIERO

11.1 Introduction

The accurate modelling and prediction of transport properties of fluids still remains a quite challenging task. This is indeed an open problem with the exception of systems composed of simple molecules in the dilute gas limit (see Chapter 7). Furthermore, in spite of recent progress, some transport properties are still difficult to measure experimentally. As a consequence, Molecular Simulations (MS) methods,[1–8] a complementary *in silico* approach based on a set of numerical tools, has emerged during the last sixty years taking advantage of the constantly increasing computer performance.

At the microscopic scale, the classical Molecular Dynamics (MD) method is probably the most well suited approach to deal with transport properties of bulk fluids and has been widely used since the 1990s,[8] in particular to study close to equilibrium properties.[6] The most interesting aspect of MD is that, in almost all thermodynamics states, it yields the ''exact'' transport properties (within the statistical uncertainties) for a given molecular model. The few exceptions deal with a small region close to the critical point where the correlation length is larger than the simulated system (see Chapter 10). As a result MD has proved useful in assisting theoretical developments of modelling transport properties and in providing pseudo-experimental data in situations where experiments are difficult to perform.

The current chapter aims at providing an overview of various MD methods applied to transport properties of pure fluids and mixtures. In Section 11.2 the general features of classical MD simulations are briefly presented. Section 11.3 reviews the various approaches that are used to compute the transport properties during MD simulations. Finally, Sections 11.4 and 11.5

Experimental Thermodynamics Volume IX: Advances in Transport Properties of Fluids
Edited by M. J. Assael, A. R. H. Goodwin, V. Vesovic and W. A. Wakeham

Published by the Royal Society of Chemistry, www.rsc.org

summarize some important results, and present new ones, on the transport properties of both simple and realistic molecular models.

11.2 Classical Molecular Dynamics

Classical Molecular Dynamics consist of a set of computational deterministic techniques aiming at describing the evolution over time of a set of interacting particles which are moving according to the laws of classical mechanics. In other words, MD simulations allow for exploring numerically the possible configurations of a set of interacting particles. The main underlying assumption of MD is that particles can be treated as classical objects, *i.e.* the de Broglie thermal wavelength is small compared to the inter-particle distance.[3] It is a particularly simple and straightforward method in which the results that emerge from collective effects rely mostly on the way molecules are described and interact together (the molecular model).

11.2.1 Molecular Models

Choosing an appropriate molecular model is the most important step when performing MD simulations. The molecular representation and the associated effective force field are chosen regarding the desired accuracy, transferability and efficiency. This in turn depends on whether one is willing to test a theory based on a simple representation of the simulated molecules (*e.g.* hard-sphere, corresponding to one molecular parameter) or is expecting accurate properties estimations (*e.g.* a model derived from quantum computations,[3,5] which may lead to dozen of parameters). A simple model will lead to computations that may last a few minutes on a standard desktop machine to several days on supercomputers for the most realistic molecular models.

Among simple molecular models (*i.e.* containing only 1 or 2 molecular parameters), the most popular ones are those that describe the molecules as simple spheres such as the hard-sphere (HS), the soft-sphere (SS) and the Lennard–Jones (LJ) models.[1] The corresponding interaction potentials, ϕ, between two particles i and j separated by a distance r_{ij} can be written, respectively as,

$$\phi_{\mathrm{HS}} = \begin{cases} \infty & (\sigma_{ij} > r_{ij}) \\ 0 & (r_{ij} \geq \sigma_{ij}) \end{cases}, \tag{11.1}$$

$$\phi_{\mathrm{SS}} = \varepsilon_{ij}\left(\frac{\sigma_{ij}}{r_{ij}}\right)^{n}, \tag{11.2}$$

and,

$$\phi_{\mathrm{LJ}} = 4\varepsilon_{ij}\left[\left(\frac{\sigma_{ij}}{r_{ij}}\right)^{12} - \left(\frac{\sigma_{ij}}{r_{ij}}\right)^{6}\right], \tag{11.3}$$

where ε_{ij} represents the energy well depth and σ_{ij} is a characteristic length (the atomic ''diameter'').

A more realistic representation of the system can be achieved by taking into account the molecular internal degrees of freedom. In such a case, the following effective pair-wise force field is used in most classical MD simulations by also invoking the Born–Oppenheimer assumption:

$$\phi_{\text{tot}} = \sum \phi_{\text{non-bonded}} + \sum \phi_{\text{bonded}}, \tag{11.4}$$

where ϕ_{tot} is the total potential energy acting on a given particle, $\phi_{\text{non-bonded}}$ describes non-bonded interactions (inter- and intra-molecular) and ϕ_{bonded} corresponds to the interactions due to a presence of atomic bonds.

The non-bonded interactions between two particles i and j separated by a distance r_{ij} are often described using the 12-6 Lennard–Jones potential, eqn (11.3), combined with partial charges, q_i, mimicking electrostatic contributions:

$$\phi_{\text{non-bonded}} = \phi_{\text{LJ}} + \frac{q_i q_j}{4\pi\varepsilon_0 r_{ij}}. \tag{11.5}$$

The LJ potential, which is convenient from a numerical point of view but lacks physical justification concerning the exponent of the repulsive part,[1] is sometimes replaced by Mie or Buckingham potentials even if the results are not always significantly improved.[9]

It is worth noting that, most of the time, the non-bonded interactions are truncated at a given cut-off radius, typically 2.5σ for the LJ interactions and half of the simulation box for electrostatic ones. The effect of this truncation of interactions may be accounted for using long-range corrections[1,10] as it has a large impact on thermodynamic properties. Concerning transport properties, this truncation has a rather limited effect[10–12] except in the noticeable case of thermodiffusion.[13]

Bonded interactions are commonly described by:

$$\phi_{\text{bonded}} = \frac{k_l}{2}(l - l_0)^2 + \frac{k_\theta}{2}(\theta - \theta_0)^2 + \sum_n \frac{k_\varphi}{2}\{1 + \cos(n\varphi - \delta)\}, \tag{11.6}$$

in which l, θ, φ are bond length, bond angle, and dihedral angle, respectively. In eqn (11.5) and (11.6), the parameters (k_l, k_s, k_φ) and the values of the intermolecular parameters (ε,σ) and intra-molecular coordinates (l_0,θ_0,δ) are typically fitted to experimental data (often only to equilibrium properties) and/or adjusted to reproduce geometries and energy profiles obtained from *ab initio* computations.[5,14]

When dealing with a mixture, a set of empirical combining rules is used to describe cross-interactions such as the widely used Lorentz–Berthelot rules which are potential independent:

$$\sigma_{ij} = \frac{\sigma_{ii} + \sigma_{jj}}{2} \quad \text{and} \quad \varepsilon_{ij} = \sqrt{\varepsilon_i \varepsilon_j}. \tag{11.7}$$

There exists a broad variety of other combining rules, some being potential dependent but none of them is perfect nor do any of them have solid theoretical basis. They have usually a smaller impact on transport properties than on static ones,[15,16] except on mutual[15] and thermal diffusion[17] coefficients which are highly sensitive to the definition of the cross-interactions.

11.2.2 Main Principles

As mentioned previously, MD simulations consist of following the time evolution of a set of N interacting particles simply by integrating Newton's equations of motion. Thus, the description of the dynamics is deduced from the Hamiltonian of the system:

$$H(\mathbf{r}^N, \mathbf{p}^N) = \phi(\mathbf{r}^N) + K(\mathbf{p}^N), \tag{11.8}$$

where $\mathbf{r}^N$ and $\mathbf{p}^N$ represent the set of particle positions and momenta, ϕ the potential energy function as defined in Section 11.2.1 and K the kinetic energy. Hence, the Hamiltonian equations of motion of a particle i are given by:

$$\frac{\partial H}{\partial \mathbf{p}_i} = \frac{\mathbf{p}_i}{m_i} = \dot{\mathbf{r}}_i \quad \text{and} \quad \frac{\partial H}{\partial \mathbf{r}_i} = \nabla_{\mathbf{r}_i}\phi = -\dot{\mathbf{p}}_i, \tag{11.9}$$

where m_i is the mass of the considered particle. This particular Hamiltonian allows MD simulations to be performed in the microcanonical ensemble. Modified Hamiltonians are used to sample different ensembles (canonical, isothermal–isobaric *etc.*)[1,6] which allow a more straightforward comparison with experiments. In addition, to limit the finite size effects while doing simulations on a finite number of particles, the number of particles N is chosen usually between 10^3 and 10^7, and periodic boundary conditions in all directions are employed,[1] as shown in Figure 11.1.

When the interaction potential ϕ is continuous, the equations of motion of the N particles are integrated forward in time, t, using simple finite-difference techniques. The time-step, δt, is of the order of 10^{-15} s and the integration is performed during millions of time-steps to accurately compute transport properties. To integrate the equations of motion, the "velocity Verlet" algorithm[1] is probably the most commonly used:

$$\mathbf{r}_i(t+\delta t) = \mathbf{r}_i(t) + \mathbf{v}_i(t)\delta t + \frac{1}{2}\mathbf{a}_i(t)\delta t^2 \tag{11.10}$$

and

$$\mathbf{v}_i(t+\delta t) = \mathbf{v}_i(t) + \frac{1}{2}[\mathbf{a}_i(t) + \mathbf{a}_i(t+\delta t)]\delta t, \tag{11.11}$$

where $\mathbf{a}_i$ is the acceleration of particle i. For polyatomic molecules, the fastest modes (often vibration) are sometimes frozen by using a constraint

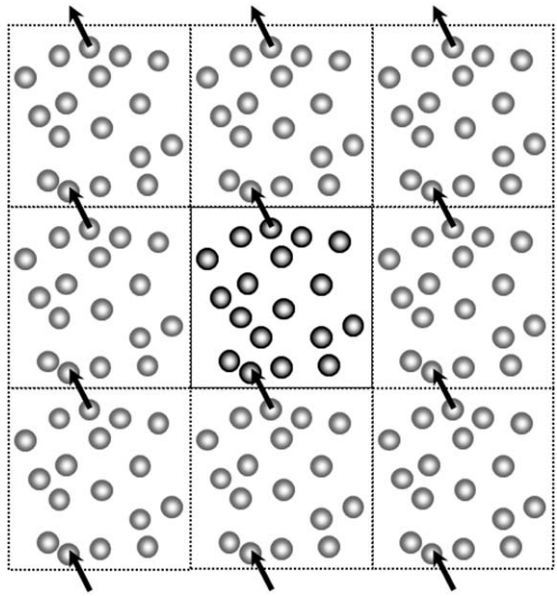

Figure 11.1 Periodic boundary conditions: the simulation box is replicated in all directions to mimic an infinite system.

algorithm that maintains bond lengths or angles constant. When dealing with discontinuous potentials (HS) the algorithms are somewhat different.[1,8]

Without optimisation, the computational time to perform the simulations is proportional to N^2 which is problematic when trying to simulate transport properties of complex fluids. However one can take advantage of the cut-off radius that is used in MD simulations, as discussed in Section 11.2.1. This localisation of the information allows the noticeable reduction of the computational time (roughly $\propto N \log N$) by using a neighbour list and cell decomposition methods.[1]

Thus, starting from an initial configuration it is possible to follow, over time, the positions and the velocities of all particles composing the system. From these sets of configurations, that sample the phase space of a given system in a given ensemble, it is possible to compute time-averaged physical "macroscopic" quantities $\langle X \rangle$ using:

$$\langle X \rangle = \frac{1}{t} \int_0^t X(t) \mathrm{d}t. \tag{11.12}$$

11.3 Computing Transport Properties

There are basically three main approaches[6] to compute transport properties during MD simulations. The first one takes advantage of the inherent

equilibrium fluctuations by monitoring how they dissipate over time. The two other methods consist in establishing a non-equilibrium state. In one, a homogeneous external perturbation to the equation of motion is introduced, while in the other an external constraint (often boundary driven) is applied to mimic an experimental situation.

11.3.1 Equilibrium Approach

In principle, all transport properties in the linear response regime can be deduced from a single Equilibrium Molecular Dynamics (EMD) simulation by looking at the relaxation of the spontaneous fluctuations of the simulated fluid. To do so the Green–Kubo (GK) relations,[4,11] or the equivalent Einstein relations, are employed. They relate Onsager transport coefficients L_{ij} to the Time Correlation Functions (TCF) of the corresponding fluxes, J_i, at equilibrium:

$$L_{ij} = \frac{V_{\text{box}}}{k_{\text{B}}} \int_0^\infty \langle J_i(0) J_j(t) \rangle \mathrm{d}t, \tag{11.13}$$

where V_{box} is the volume of the simulation box and k_{B} the Boltzmann constant.

Knowing the microscopic expression of the various fluxes (mass, heat, momentum),[6,11,15] it is then possible to compute all Onsager transport coefficients from a single EMD simulations. Consequently, the self-diffusion coefficient, D, shear viscosity η, bulk viscosity κ and thermal conductivity, λ, of a pure fluid are given by:

$$D = \frac{1}{3N} \sum_{i=1}^{N} \int_0^\infty \langle \mathbf{v}_i(0).\mathbf{v}_i(t) \rangle \mathrm{d}t, \tag{11.14}$$

$$\eta = \frac{V_{\text{box}}}{k_{\text{B}}T} \int_0^\infty \langle \sigma_{\alpha\beta}(0) \sigma_{\alpha\beta}(t) \rangle \mathrm{d}t, \tag{11.15}$$

$$\kappa = \frac{V_{\text{box}}}{k_{\text{B}}T} \int_0^\infty \langle \delta p(0) \delta p(t) \rangle \mathrm{d}t, \tag{11.16}$$

and

$$\lambda = \frac{V_{\text{box}}}{3k_{\text{B}}T^2} \int_0^\infty \langle \mathbf{J}_q(0).\mathbf{J}_q(t) \rangle \mathrm{d}t, \tag{11.17}$$

where $\mathbf{v}_i$ is the particle velocity δp is the deviation of the instantaneous pressure from its average value. In eqn (11.15) and (11.17), $\sigma_{\alpha\beta}$ and $\mathbf{J}_q$ are,

respectively, off diagonal component (α,β are two distinct Cartesian coordinates) of the pressure tensor, *i.e.* shear stress, and the heat flux which for a pure molecular fluid[12] are given by:

$$\sigma_{\alpha\beta} = \frac{1}{V_{\text{box}}} \sum_a \frac{1}{m_a} p_{a,\alpha} p_{a,\beta} + \frac{1}{2V_{box}} \sum_a \sum_{b \neq a} \left(r_{a,\alpha} - r_{b,\alpha}\right) \sum_{i \in a} \sum_{j \in b} F_{ij,\beta} \qquad (11.18)$$

and

$$\mathbf{J}_q = \frac{1}{V_{\text{box}}} \left\{ e_a \mathbf{v}_a - \frac{1}{2} \sum_{i \in a} \sum_{b \neq a} \sum_{j \in b} \mathbf{r}_{ab} \times \left[\mathbf{F}_{ij} \cdot \mathbf{v}_i\right] \right\}, \qquad (11.19)$$

where a, b are molecular indices and i, j are atomic indices. $\mathbf{F}_{ij}$ is the force acting on i because of j and e_a is the internal energy of molecule a. It is interesting to note that these two microscopic expressions of momentum and heat flux, eqn (11.18) and (11.19), are composed of contributions from both translational and kinetic energy, the first term on the right hand side, and contributions from both the collisional and configurational integrals, the second term on the right hand side.[11] This decomposition can be used to quantify the translational and collisional contributions to the corresponding transport property.[18,19]

When dealing with mixtures, it is possible to compute the Onsager transport coefficients corresponding to mass[20] and thermal diffusion[21] using TCF. However, to deduce quantities comparable to experiments from these EMD simulations, *i.e.* Fick diffusivities and thermal diffusion coefficients, one needs to compute additional thermodynamic quantities such as the thermodynamic factor[20] or partial enthalpies[21] which is not always straightforward.

11.3.2 Non-equilibrium Approaches

Equilibrium Molecular Dynamics (EMD) schemes are usually not very efficient in computing accurate transport properties, owing to a relatively poor signal to noise ratio, especially in complex fluids. Hence, two types of Non-Equilibrium Molecular Dynamics (NEMD) schemes have been developed for a given transport property to overcome this problem.

The first type of NEMD approaches, called synthetic or homogeneous NEMD, is based on the introduction of an external perturbation in the equation of motions as proposed by Evans and Morriss.[6] This induces a non-equilibrium flux that allows computing one type of Onsager transport coefficients for a given perturbation amplitude. Such an approach yields a high signal to noise ratio and can be used to study far from equilibrium transport properties, such as non-Newtonian behavior[22] for a wide range of shear rates.[23] However, several simulations are necessary to deduce the Onsager transport coefficient L_{ij} for zero-limit perturbation. In addition, as when using GK relations, one has to convert the Onsager transport coefficient, L_{ij},

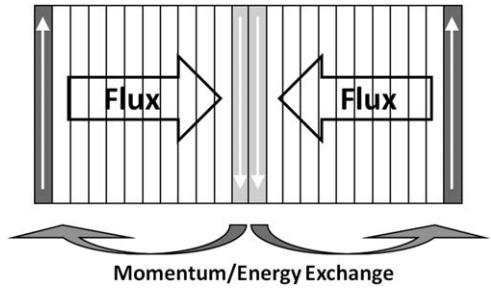

Figure 11.2 Schematic description of the principle of a boundary-driven Non-Equilibrium Molecular Dynamics scheme. Momentum (to induce shear and compute shear viscosity) or kinetic energy (to induce heat flow and to compute thermal conductivity) is exchanged between the central part and the boundaries of the simulation box.

to measurable transport properties which may need additional MD simulations to compute thermodynamic quantities.

The second type of NEMD, called direct or boundary driven NEMD, consist of driving the system out of equilibrium *via* the boundaries or *via* an external force. The experimentally accessible transport properties, and not the L_{ij}, are then directly deduced from the constitutive relations at the stationary state (*e.g.* Fourier's law for thermal conductivity)[24,25] or from analytical solutions of the conservation equations during the transient state (*e.g.* Navier–Stokes equations for shear viscosity).[26,27] Among these direct NEMD approaches the most popular ones are those based on a modification of the boundaries to induce a heat, mass or momentum flow in pure fluids and in mixtures.[28] This approach was first proposed by Tenenbaum *et al.*[24] to study heat transport and further refined by Hafskjold *et al.*[28] to keep periodic boundary conditions, see Figure 11.2. Then, Müller-Plathe[25,29] proposed an elegant direct NEMD algorithm based on the swapping of particles between boundary regions that is compliant with periodic boundary conditions and keeping constant the total energy and the total momentum.

These direct NEMD methods are usually rather efficient compared to EMD and synthetic NEMD approaches, in particular when dealing with complex molecules[27] and/or complex properties such as evaluation of the Soret coefficient.[21,28] However they require usually huge fluxes which can be experimentally inaccessible.[23] Thus, care should be taken when employing these methods since strong gradients may lead to the breakdown of the constitutive equation used to deduce the transport property.

11.4 Transport Properties of Model Fluids

While considerable progress has been made on the modelling of the structural and static properties of dense fluids,[30] an accurate molecular-based theory on transport properties is still lacking despite recent progress (see Chapter 8). Thus, since the very beginning of its use, MD simulations have

been applied to compute transport properties of model fluids.[30–32] These results have then been employed to improve the modelling of such properties, *e.g.* correlated molecular motions in hard-sphere systems[30] and the associated corrections to the Enskog theory.[31] Nowadays, MD is still commonly used to check and enrich theories of transport properties (in the linear response regime) in moderate to dense bulk fluids, especially of simple dense fluids for which significant progress has recently been made.[33]

As a result of MD simulations, noticeable progress has also been achieved in the non-linear response regime[6,22] and for the transport properties of strongly confined fluids.[34,35] However, the following sections will be restricted to transport properties of bulk fluids in the linear response regime.

11.4.1 Pure Fluids Composed of Spheres

The simplest fluid models are those based on a spherical representation of the molecules of the fluids interacting through the potentials described by eqn (11.1) to (11.3). A large number of MD simulations have been performed on these simple fluids. However, until the last ten years, non-negligible differences between the MD values of the transport properties for these simple fluid models provided by different authors[11,36,37] were encountered. This was mostly owing to the lack of important computational resources required for MD simulations which led to problems arising from finite size effects and run duration. Nowadays, it is possible to get agreement of a few percent.

11.4.1.1 Hard-spheres Fluid

The main advance in understanding the hard-spheres fluid, since the seminal work of Alder and Wainwright[31] and the MD based corrections to the Enskog approach proposed by Dymond,[40] is due to Heyes and co-workers.[37,38] They have shown that the self-diffusion coefficient of the HS fluid, D_{HS}, is the single transport property that is especially sensitive to the number of particles simulated.[37] More precisely D_{HS} increases with N, especially at intermediate reduced density, $\rho^* = N\sigma^3/V_{box}$, (*e.g.* D_{HS} for $N \to \infty$ is roughly 9 % higher than when $N = 500$ at $\rho^* \approx 0.6$).

These accurate MD results[36,37] have also confirmed that D, η and κ were not well described by the Enskog model (noted in the following with a subscript E) especially at high density.[36,37] In addition, the discrepancies between Enskog and MD results are transport property dependent:[37]

- D_E underestimates D_{HS} (up to 25 %) at intermediate density ($\rho^* \approx 0.6$) and overestimate D_{HS} when the density is higher than ≈ 0.85, shown in Figure 11.3a.
- η_E yields a reasonable estimation of η_{HS} up to $\rho^* \approx 0.75$, above it leads to an increasing underestimation, shown in Figure 11.3b.
- κ_{HS} is correctly estimated by κ_E up to $\rho^* \approx 0.85$. For higher density κ_E is underestimating κ_{HS}.

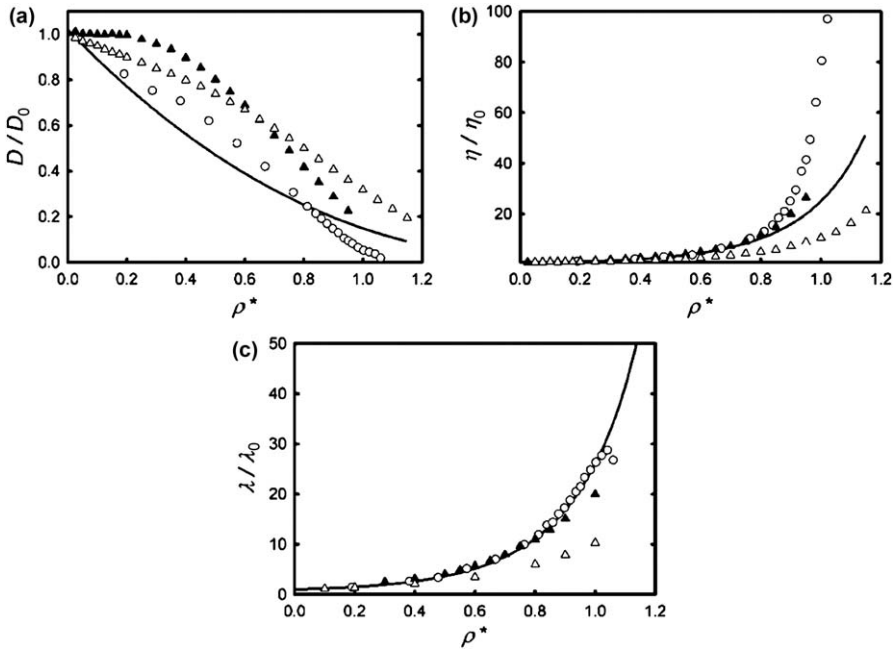

Figure 11.3 Transport properties, relative to their zero-density values indicated by the subscript 0 as a function of reduced density $\rho^* \approx N\sigma^3/V_{box}$: Enskog approximation (full line) and MD simulations on the HS fluid[37] (open circles) and the LJ fluid[19,45–48] for two temperatures ($T^* = 1.5$, filled triangle, $T^* = 4$, open triangles). (a), Ratio D/D_0 where D is the self-diffusion coefficient and D_0 the zero-density value; (b), Ratio η/η_0 where η is the shear viscosity and η_0 the zero density value; (c), Ratio λ/λ_0 where λ is the thermal conductivity and λ_0 is the zero density value.

Rather surprisingly, the thermal conductivity provided by the Enskog approximation is very close to that of the MD simulations except at extremely high densities, see Figure 11.3c.

Because of the weakness of the Enskog approach at high density for D and η, numerous authors have proposed alternative relations to describe more accurately the transport properties of the HS fluid. The main idea of these approaches consists of adjusting the transport properties by providing a correction term that is a polynomial function of density. For further information, the reader is referred to the corresponding literature.[36–41]

11.4.1.2 Soft-spheres Fluid

One of the main applications of the soft-sphere fluid, eqn (11.2), is that it can be used to test perturbation approaches[30] for dynamic properties using the HS fluid as the reference.[41] Furthermore, it has been shown recently that in

dense states, the SS fluid is mimicking the behaviour of more complex fluids, if an appropriate scaling is applied.[33]

One recent interesting MD result is that when the steepness of the potential (n in eqn 11.2) exceeds 72, the SS fluid transport properties are hardly distinguishable from those of a HS fluid.[41] In addition, it has been found that D_{SS}^{-1}, η_{SS}, κ_{SS} and λ_{SS} increase when n decreases for a given density.[41] Such behaviour is consistent with the fact that increasing the steepness of the repulsion wall induces a decrease of the maximum packing fraction. In other words, the effective hard-sphere diameter decreases with n, as expected.

Furthermore, a simple Batschinski–Hildebrand scheme (*i.e.* D_{SS}^{-1}, η_{SS}, κ_{SS} and λ_{SS} have a linear dependence on the inverse of the molar volume)[41] or even Dymond's approach,[39] are able to represent the data reasonably well. It has been also shown that in dense states some SS fluid transport properties (diffusion and shear viscosity) are very well described by scaling approaches, namely the thermodynamic scaling[33,42] and the excess entropy scaling[43,44] (see Section 9.2). However, these approaches are not yet applicable to the full range of fluid states.[38]

11.4.1.3 Lennard–Jones Fluid

Contrary to the previous purely repulsive fluid models, the Lennard–Jones fluid possesses an attractive contribution, see eqn (11.3). Hence, it can mimic gas and liquid phases, as well as a critical point (located at $\rho_c^* \approx 0.3$ and $T_c^* = k_B T/\varepsilon \approx 1.3$). It is therefore a more realistic fluid model than the previous ones, while still remaining relatively simple. The LJ fluid model is characterised by only two molecular parameters ε and σ and so follows corresponding states behaviour.

A large number of MD studies have focused on the LJ model. Hence, reliable and accurate databases of the LJ fluid transport properties are available in the literature.[11,18,19,45–50] In the case of not too strongly polar fluids, this model represents well the self-diffusion[36,51,52] and the shear viscosity[47,53] for a large range of thermodynamic conditions.

Interestingly, it has been reported that only the self-diffusion coefficient is noticeably affected by system size.[19,54] This is consistent with what was found for the HS fluid.[37] In addition, when MD simulations are performed carefully, there is excellent agreement between the LJ collective transport properties (viscosity, thermal conductivity and bulk viscosity) provided by EMD and NEMD approaches.[19,21,27] The LJ transport properties have been also computed at very low density, to check the initial density dependence,[55] as well as in the metastable fluid region[56,57] or even close to the critical point[11,19] where an expected enhancement of the thermal conductivity is observed (see Chapter 10).

As can be seen in Figure 11.3, the transport properties of the LJ fluid exhibit some similarities with those of the HS fluid. The main difference is that the LJ transport properties are temperature dependent, and this dependence

is not always simple, as illustrated in Figure 11.3 for two supercritical reduced temperatures. More precisely, if a temperature-dependent hard-sphere diameter is employed, the LJ shear viscosity and the thermal conductivity can be reasonably well estimated from the HS values.[58] However such an approach is not easily applicable to self-diffusion.[36,58,59]

As initially proposed by Ashurst and Hoover[42] using a very limited amount of data, the transport properties of the LJ fluid exhibit scaling laws similar to those based on the excess entropy scaling.[19,43,60,61] This indicates that, despite its attractive contribution, the dense LJ fluid can probably be mapped by an ''equivalent'' purely repulsive fluid with an effective softness.[33,62] The validity of mapping is not strongly temperature dependent, as long as the fluid is sufficiently dense.

It is worth noting that the most available relationships to estimate the transport properties of the LJ fluid over the full range of thermodynamic states are still largely empirical[19,47,52] and do not yet take advantage of the recent developments, described in the previous paragraph.

11.4.2 Mixtures Composed of Spheres

The modelling of transport properties of dense fluid mixtures is even more challenging than that of pure fluids. There are two main reasons for this:

- to apply the schemes that have been developed for pure fluids to mixtures, one often needs mixing rules for the ''molecular'' parameters (aiming at representing a mixture by an ''equivalent'' pure pseudo-component). However, for dense fluids, even for spheres, these mixing rules are not easy to define and are often empirical.
- additional transport mechanisms emerge in mixtures such as thermo-diffusion or mutual diffusion which are sensitive to cross interactions between the species. Unfortunately, despite recent progress, these properties are known to be difficult to measure, especially in more than two-component mixtures (see Section 2.4 and 5.2 to 5.4).

MD is a well suited numerical tool to tackle these problems, in mixtures composed of spheres, and has already provided some interesting results.

11.4.2.1 Viscosity and Thermal Conductivity

When dealing with a mixture of spheres, one option is to approximate the mixture by an ''equivalent'' fluid composed of only one type of spheres (the so-called 1-fluid approximation)[63] using mixing rules for the molecular parameters. It is then possible to treat the mixture as a simple pure fluid.[63,64] However, even if there are efficient mixing rules at low density, this is not the case in dense fluids, especially when dealing with asymmetric mixtures.[63–68]

To illuminate this problem, the behaviour of the shear viscosity and the thermal conductivity of a LJ binary mixture is chosen as an example. More

precisely the mixture is chosen so that only the mass differs between the components ($m_2/m_1 = 10$, $\sigma_2 = \sigma_1$ and $\varepsilon_2 = \varepsilon_1$). Then, the shear viscosity and thermal conductivity are computed for different mole fractions and for two states, one supercritical at $T^* = 2.5$ and $\rho^* = 0.3$ and one liquid at $T^* = 1$ and $\rho^* = 0.8$. Here, we only examine the contribution to the thermal conductivity that neglects the contribution owing to diffusional fluxes, referred in literature as the Dufour contribution.[69] Finally these transport properties are compared with those of the equivalent 1-fluid, *i.e.* a pure fluid with a mass $m_{1-fluid} = x_1 m_1 + x_2 m_2$. Results are shown in Figure 11.4.

The most striking feature illustrated in Figure 11.4, is that the 1-fluid approximation (assuming the simple linear approximation for the ''equivalent'' mass) is inadequate whatever the property and the conditions. In the liquid state the deviations between the mixture and the 1-fluid transport properties reach 30 %! Furthermore these deviations are state and property dependent.

This result is consistent with what has been reported in the literature,[63,64,66] *i.e.* the ''static'' mass is not a good approximation for the ''dynamic'' mass, and there does not yet exist any simple efficient mixing rule on mass apart from in the low density regime.[66] This further indicates that any scheme aiming at predicting transport property in fluid mixtures and relying on a 1-fluid approximation will suffer from the same problem. This might partly explain the weakness of most predictive models when dealing with mixtures asymmetric in mass.

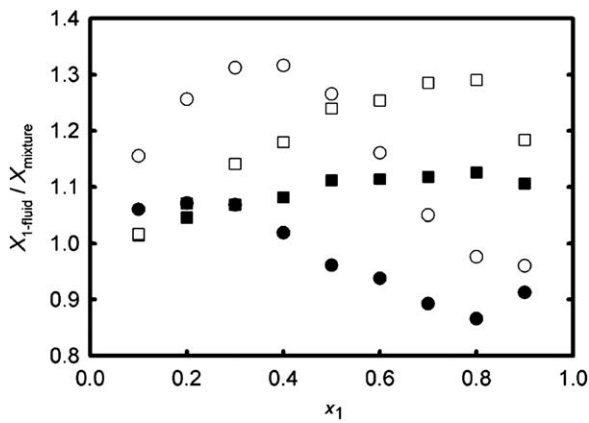

Figure 11.4 Ratios between the shear viscosity (squares) and the thermal conductivity (circles) of 1-fluid model (noted $X_{1\text{-fluid}}$) and the corresponding mixture (noted X_{mixture}) for different mole fractions, x_1. MD simulations have been performed on LJ fluids for two states: one supercritical at $T^* = 2.5$ and $\rho^* = 0.3$ (full symbols) and one liquid at $T^* = 1$ and $\rho^* = 0.8$ (open symbols). In the mixtures, $m_2/m_1 = 10$, $\sigma_2 = \sigma_1$ and $\varepsilon_2 = \varepsilon_1$.

11.4.2.2 Thermal Diffusion

In mixtures, coupling between heat and mass flux may occur.[69] This gives rise to cross transport properties (*e.g.* thermal diffusion coefficients) which quantify the amplitude of that coupling.[70] This is an intriguing phenomenon, as discussed in Section 9.3, and its modelling is very much less satisfactory than that of viscosity, and thermal conductivity.[70,71]

Thermal diffusion in mixtures composed of spheres has been relatively well studied by MD simulations in moderate to dense fluid states.[13,22,28,70,72–77] More specifically, in binary LJ mixtures, it has been shown that the species with the largest mass, the largest potential well-depth and the smallest volume tend to migrate towards the cold area relatively to the other species.[13,70,72] Furthermore, it has been confirmed that in dense LJ fluids, this phenomena is highly sensitive to the cross interactions (described by combining rules, eqn 11.7) between particles of different species.[13,73]

From the modelling point of view, MD simulations have shown that the thermal diffusion in isotopic binary mixtures of HS is correctly described by the revised Enskog theory,[74] whereas this is not the case for a LJ binary mixture.[75] MD simulations of binary mixtures have confirmed that thermal diffusion can be described by one contribution due to mass difference and a second one due to thermodynamical differences.[73] In addition, it has been found that ternary LJ mixtures are reasonably well approximated by binary ones using a simple van der Waals one fluid approximation.[76,77]

11.4.3 Polyatomic Fluids

Transport properties, mainly those related to thermal transport, are often sensitive to the internal degrees of freedom of a given molecule. Molecular models based on a representation by a sphere are therefore likely to be insufficient to tackle all the phenomena that may govern transport properties of real polyatomic fluids. Thus, albeit being more complex to simulate and interpret, MD computations have been performed recently on flexible chains of tangent spheres.[13,17–19,78–82] This choice has proved to be valuable when dealing with thermodynamic properties.[83,84] Such a molecular representation adds one parameter, the chain length, N_c, to those that describe each sphere. As an illustration, the discussion will be restricted here to short (*i.e.* composed of 16 spheres or less) flexible chains of tangent spheres.

Among the interesting results provided by MD simulations, it has been found that the zero density viscosity of systems of LJ chains decreases when the chain length increases.[18,82] Such a result is consistent with what was found recently using a Classical Trajectory approach for the same system (see Section 7.2).[85] Furthermore, for a given reduced dense state the self-diffusion and the thermal conductivity of systems of LJ chains decrease with the chain length, whereas the shear viscosity increases,[18,19,79] as is illustrated in Figure 11.5. In addition, consistent with the assumption of a dynamic behaviour of the Rouse type, η and D^{-1} increase roughly linearly with

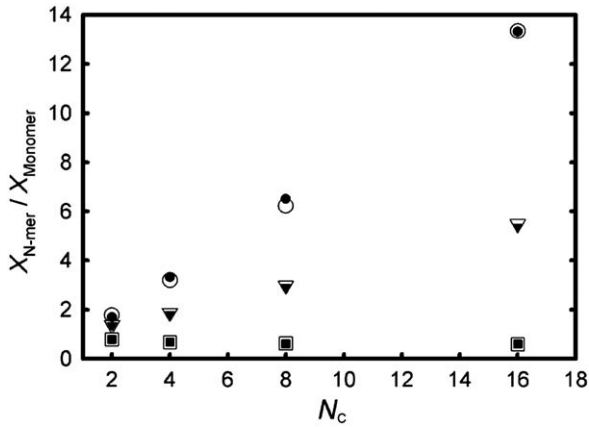

Figure 11.5 Transport properties (noted X) of the LJ chain[18,19] *versus* the chain length N_c for two different dense states at $\rho^* = 0.8$ ($T^* = 1.5$: open symbols and $T^* = 4$: full symbols). Circles: D^{-1}, down triangles: η and squares: λ.

the chain length. Moreover, this increase is weakly dependent on the temperature when η and D^{-1} are expressed relative to the monomer (LJ) values, see Figure 11.5.

From the modelling point of view, it has been shown that the excess entropy scaling (see Section 9.2) is able to correctly describe the self-diffusion of the HS and LJ chains fluid[61,80] and the shear viscosity of the LJ chain fluid.[18,80] There exist several approaches that are extensions of the Enskog relation to polyatomic fluids.[60,79] However, the most accurate (compared to MD results) relations to estimate the transport properties of these model fluids are still mostly empirical.[18,19,61]

11.5 Transport Properties of Realistic Fluids

Nowadays, MD simulations are more and more often used to estimate bulk transport properties of fluid systems for which experiments are difficult and/or too expensive to carry out. Such an alternative to experiments is employed either because of:

- the features of the fluid (*e.g.* toxicity,[16] costs[86]),
- the peculiar thermodynamic conditions (*e.g.* metastable states,[56] high pressures[87])
- the nature of the investigated property (*e.g.* mass diffusion[20] or thermal diffusion[76,88] in multicomponent mixtures).

To obtain quantitative results on transport properties of realistic systems, one needs efficient and transferable force fields. There exist several sets of

classical non-reactive force fields such as OPLS,[89] TraPPE,[90] AUA[91] or even CHARMM.[92] However, these force fields are often adjusted using thermodynamic equilibrium data which in some cases is insufficient to accurately predict transport properties without further refinement.[93–95]

This section is intended to briefly illustrate the possibilities and the limitations when using classical MD simulations to predict transport properties of various types of fluids.

11.5.1 Simple Fluids

Noble gases are probably the simplest fluids to model, as their atoms interact through perfectly spherical potentials and there are no internal degrees of freedom to consider. As a consequence, MD results for spheres were compared with the experiments on noble gases (mainly Argon) since the very first simulations.[1] Fairly good agreement was observed when using the simple LJ fluid model, although more accurate potentials are available.[96] As an illustration, the LJ molecular parameters of Rowley *et al.*[97] (*i.e.* $\sigma = 0.3405$ nm, $\varepsilon/k_B = 119.8$ K), that have been fitted to equilibrium data, were used in accurate MD simulations to obtain transport properties.[11,19,47,48] Results are shown in Figure 11.6 and compared to a reference correlation for shear viscosity and thermal conductivity[98] and experimental data for the bulk viscosity.[99]

It is interesting to note that the LJ fluid model, despite its simplicity, is able to yield a very good prediction of shear viscosity and thermal conductivity over a wide range of thermodynamics conditions, especially in subcritical conditions. This is somewhat surprising as the repulsive part of the LJ potential has no theoretical justification.[1] Nevertheless, this result is consistent with previous work[100–102] which has shown that the repulsive term of the LJ potential leads generally to good results compared to more complex forms.[100] Concerning the bulk viscosity there is only a qualitative agreement between simulations and experiments as already noted.[102] Assuming that the experiments are accurate and there is some doubt expressed in literature,[102] this indicates that care should be taken concerning the MD predictions of bulk viscosity. However, it should be also noted that if three-body interactions are included a better agreement is apparently achieved for bulk viscosity, without deteriorating the predictions for shear viscosity.[103]

When dealing with simple molecular non-polar fluids, such as CH_4, N_2, and O_2, it has been shown that a good estimation of self-diffusion coefficient and shear viscosity is achievable using a simple LJ fluid model.[36,47] Reasonable results can also be obtained when dealing with the viscosity of mixtures of these species.[47,102] However, a more complex molecular model should be used to describe thermal conductivity.[104] This is understandable as thermal conductivity (mainly the zero density contribution) is strongly dependent on the number of degrees of freedom included in the model, as discussed in Section 7.2.

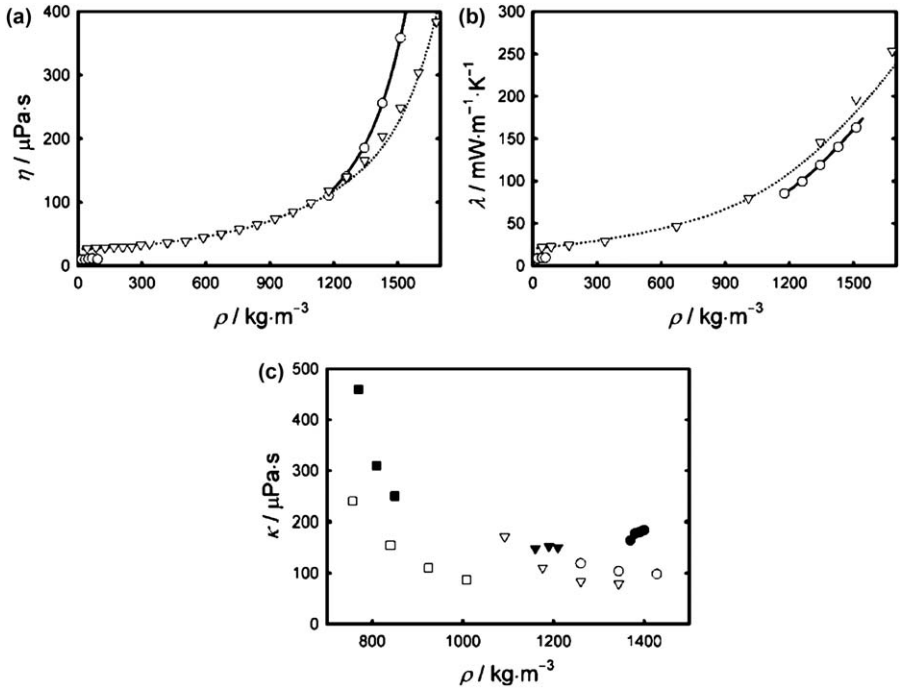

Figure 11.6 Comparisons between MD simulations on a LJ fluid[11,19,47,48] and experimental data on transport properties of Ar at two temperatures and for pressures up to 1000 MPa. (a) Shear viscosity η, (b) thermal conductivity λ and (c) bulk viscosity κ. Lines in (a) and (b): experimental data[98] (full: $T = 119.8$ K and dotted: $T = 359.4$ K). Symbols in (a) and (b): MD simulations[11,19,47,48] (circles: $T = 119.8$ K and squares: $T = 359.4$ K). Full symbols in (c): experimental data[99] (diamonds: $T = 90$ K, down triangles: $T = 120$ K and squares: $T = 150$ K). Open symbols in (c): MD simulations[11] (diamonds: $T = 95.8$ K, down triangles: $T = 119.8$ K and squares: $T = 149.8$ K).

The situation is slightly more complex for small weakly polar molecules without hydrogen bonding, such as H_2S. To introduce the polar contribution one can add to the non-polar interactions an effective isotropic term,[105] a point-dipole/quadrupole[106] or even point charges,[16] the latter being the most computationally demanding. Rather surprisingly it has been found, albeit on a limited number of systems, that such an approach is able to yield reasonable results for the shear viscosity of small weakly polar molecules.[16,106]

A recent study focusing on the shear viscosity of H_2S exemplifies how MD simulations can replace actual experiments, especially when the latter are too difficult to perform. In 2007 a simple isotropic multipolar model[105] was proposed to deal with H_2S with parameters adjusted to thermodynamic equilibrium data.[16] It was shown that this model gives a good estimate of the

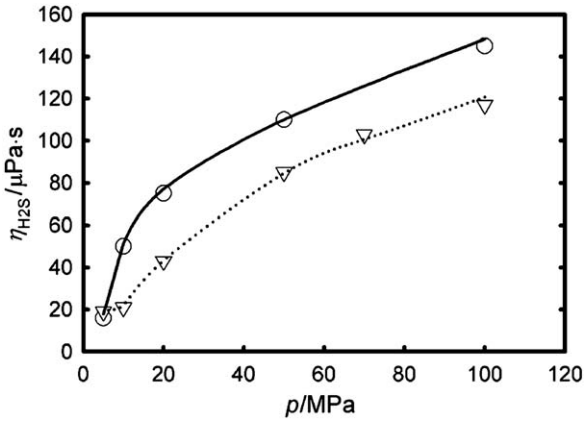

Figure 11.7 Shear viscosity of H_2S η_{H_2S} along two isotherms as a function of pressure p; comparison between MD predictions (full line: $T = 373$ K and dotted line: $T = 423$ K)[16] and experiments (circles: $T = 373$ K and down triangles: $T = 423$ K).[108]

shear viscosity along the vapour–liquid co-existence line.[16,107] Sometime later, experiments on shear viscosity of H_2S under high pressure were performed[108] at thermodynamic conditions for which no data were previously available.

Results shown in Figure 11.7 clearly indicate that the *a priori* predictions of the MD simulations using the isotropic multipolar model[16] are in very good agreement with the experiments.[108] Thus, for this simple polar molecule, the shear viscosity predictions of the MD simulations have been validated *a posteriori*. MD can therefore, in some cases, stand as a cheap and efficient alternative to the actual experiments.

11.5.2 Molecular Fluids

For non-spherical molecules, accounting for internal degrees of freedom (see eqn 11.6) is crucial when dealing with transport properties over a wide range of thermodynamic conditions. This refinement is also critical in the case of transport properties strongly affected by internal degrees of freedom, such as thermal conductivity.

For instance, there are several papers dealing with pure alkanes[4,18,109–114] which illustrate the interest of using either All-Atoms or United Atoms (methyl group ($-CH_3$) and methene group ($=CH_2$) are described as a single interaction centre) force fields. By doing so, the transport properties computed by MD simulations are usually in qualitative, and sometimes quantitative, agreement with the experiments. The deviations (of about 20 % to 30 %) are mostly due to the force fields fitting procedure. Indeed, the force field parameters are frequently adjusted to match equilibrium properties

which are quantities usually less sensitive to internal degrees of freedom (such as the global rigidity of the molecule) than transport properties. It is possible to slightly modify the force field parameters, like the torsion constant, to improve the results on transport properties without deteriorating the prediction of equilibrium quantities.[112,115,116]

There are, as well, some studies on alkane mixtures[17,21,88,117–120] dealing with viscosity, mass diffusion, thermal conductivity and even thermal diffusion. When experimental data are available, results indicate that MD simulations are able to estimate the transport properties in mixtures with the accuracy similar to that obtained for pure fluids. However, deviations from experimental data tend to increase when dealing with more complex compounds such as aromatics,[121] especially concerning thermal diffusion.[122]

11.5.3 Hydrogen Bonding and Ionic Fluids

Among small molecules, the most difficult to model, using classical force fields, are probably those that can form hydrogen bonding; above all water for which there exists a huge number of molecular models,[123] from a simple coarse grained model[124] to complex polarisable models.[125,126] However, most of these models only reproduce qualitatively the transport properties of water,[27,110,127] apart from the TIP4P/2005[128] model which seems to be reasonably accurate.[127] The results are somewhat better for other hydrogen bonding pure fluids, such as alcohols for which a reasonable agreement between the MD simulations and experiments is usually obtained with deviations around 20 %.[111,127,129] When dealing with water–alcohol mixtures, the results are usually poorer than for pure fluids, while remaining qualitatively correct[127,130] even for thermal diffusion.[73,131]

From the MD point of view ionic liquids are another type of complex fluid on which a lot of effort has been spent over the last ten years.[132–136] However, it is still difficult to draw any conclusions about the predictive capabilities of MD simulations for such fluids. Although the experimental transport property data are becoming more readily available (see Section 6.6), the simulations are still very computationally demanding.[137]

11.6 Summary and Outlook

As emphasized in this chapter, Classical Molecular Dynamics is a complementary tool to both theory and experiments. It has already led to valuable improvement on the modelling of the transport properties of pure fluids and mixtures and is able to provide pseudo-experimental data in some specific cases.

One of the drivers behind the recent rise of MD is the availability of efficient and free software for academic research, such as DLPOLY,[138] GROMACS[139] and LAMMPS.[140] In addition, the computing capabilities of standard hardware are such that a transport property for a given molecular

model can be obtained within a day or less with an accuracy of a few percent. These two reasons largely explain the explosion, during the last fifteen years, of the number of research papers employing MD simulations to compute the transport properties of fluids (over 300 articles a year in the 2010s). However, the exploitation of such techniques in the industry is still at its infancy, compared to more conventional approaches. This is probably due to the fact that there are no general rules on what is an adequate molecular model and the associated force field, because it is always a compromise between the degree of complexity chosen and the targeted accuracy.

In the future, the MD algorithms will progress in line with the evolution of the computer architecture. However, the development of novel MD approaches will probably slow down, as the already available techniques are efficient.

Concerning the modelling of transport properties, with the help of MD simulations, one may expect noticeable advances within ten years mainly because accurate transport properties of model fluids are now easily accessible. First, recent results[33,62] indicate that we are probably not far from an efficient theory of dynamic properties in dense fluids composed of spheres, even if the extension to mixtures may not be straightforward. Second, for more complex fluids, one can expect developments similar to what has been acheived for ''molecular based'' equations of state (like those based on perturbation theory)[30] for transport properties, directly,[18,19,59,141] or by using molecular based thermodynamic quantities.[60,61,142]

Regarding the force fields, enormous progress has been made during the last 15 years, even if most applications were geared towards the equilibrium properties. In the near future, one can expect a refinement of the existing force fields and an enhancement of their transferability by including transport properties in the fitting database.[112,115,116] In the more distant future, the development of force fields will probably mostly rely on systematic quantum mechanics computation, implying less and less approximation over time.[5,143]

Acknowledgments

The author expresses his warm thanks to Dr S. Delage-Santacreu who significantly contributed to this work, to Dr A.R.H Goodwin, Dr R. Vermorel and Prof. V. Vesovic for the help in preparing this chapter and to Prof. C. Boned and Dr F. Montel for the continuous stimulating discussions on this topic. It is a pleasure to acknowledge the continued support of TOTAL EP and the ''Failflow'' project (advanced grant from the European Research Council). The author gratefully acknowledges computational facilities (in link with a ''Conseil Regional d'Aquitaine'' project) provided by Pau University, by the I2M and the MCIA in Bordeaux University.

References

1. M. P. Allen and D. J. Tildesley, *Computer simulations of Liquids*, Oxford University Press, New York, 1st edn, 1987.
2. D. C. Rapaport, *The Art of Molecular Dynamics Simulation*, Cambridge University Press, Cambridge, 2nd edn, 2004.
3. H. J. C. Berendsen, *Simulation the Physical World: Hierarchical Modeling from Quantum Mechanics to Fluid Dynamics*, Cambridge University Press, Cambridge, 1st edn, 2007.
4. P. Ungerer, C. Nieto-Draghi, B. Rousseau, G. Ahunbay and V. Lachet, *J. Mol. Liquids*, 2007, **134**, 71–89.
5. A. Hinchliffe, *Molecular Modelling for Beginners*, John Wiley & Sons, UK, 1st edn, 2008.
6. D. J. Evans and G. Morriss, *Statistical of Nonequilibrium Liquids*, Cambridge University Press, Cambridge, 2nd edn, 2008.
7. A. Satoh, *Introduction to Practice of Molecular Simulation: Molecular Dynamics, Monte Carlo, Brownian Dynamics, Lattice Boltzmann and Dissipative Particle Dynamics*, Elsevier, New York, 1st edn, 2010.
8. E. J. Maginn and J. R. Elliott, *Ind. Eng. Chem. Res.*, 2010, **49**, 3059–3078.
9. G. Galliero, C. Boned, A. Baylaucq and F. Montel, *Phys.Rev. E*, 2006, **73**, 061201.
10. K. Takahashi, K. Yasuoka and T. Narumi, *J. Chem. Phys.*, 2007, **127**, 114511.
11. K. Meier, *Computer Simulation and Interpretation of the Transport Coefficients of the Lennard–Jones Model Fluid*, Shaker Verlag GmBH, Germany, 1st edn, 2002.
12. D. K. Dysthe, A. H. Fuchs and B. Rousseau, *J. Chem. Phys.*, 1999, **110**, 4047–4059.
13. G. Galliero, B. Duguay, J. P. Caltagirone and F. Montel, *Fluid Phase Equilib.*, 2003, **208**, 171.
14. K. E. Gubbins and J. D. Moore, *Ind. Eng. Chem. Res.*, 2010, **49**, 3026–3046.
15. D. K. Dysthe, A. H. Fuchs and B. Rousseau, *Int. J. Thermophys.*, 1998, **19**, 437–448.
16. G. Galliero, C. Nieto-Draghi, C. Boned, J. B. Avalos, A. D. Mackie, A. Baylaucq and F. Montel, *Ind. Eng. Chem. Res.*, 2007, **46**, 5238–5244.
17. G. Galliero, S. Srinivasan and M. Z. Saghir, *High Temp.– High Pressures*, 2009, **38**, 315–328.
18. G. Galliero and C. Boned, *Phys. Rev. E*, 2009, **79**, 021201.
19. G. Galliero and C. Boned, *Phys. Rev. E*, 2009, **80**, 061202.
20. X. Liu, S. K. Schnell, J. M. Simon, D. Bedeaux, S. Kjelstrup, A. Barlow and T. J. H. Vlugt, *J. Phys. Chem. B*, 2011, **115**, 12921–12929.
21. A. Perronace, C. Leppla, F. Leroy, B. Rousseau and S. Wiegand, *J. Chem. Phys.*, 2002, **116**, 3718–3729.
22. S. S. Sarman, D. J. Evans and P. T. Cummings, *Phys. Rep.*, 1998, **305**, 1–92.
23. G. Pan and C. McCabe, *J. Chem. Phys.*, 2006, **125**, 194527.
24. A. Tenenbaum, G. Ciccotti and R. Gallico, *Phys. Rev. A*, 1982, **25**, 2778–2787.

25. F. Müller-Plathe, *J. Chem. Phys.*, 1997, **106**, 6082–6085.
26. G. Arya, E. J. Maginn and H. C. Chang, *J. Chem. Phys.*, 2000, **113**, 2079–2087.
27. B. Hess, *J. Chem. Phys.*, 2002, **116**, 209–217.
28. B. Hafskjold, T. Ikeshoji and S. Ratkje, *Molec. Phys.*, 1993, **80**, 1389.
29. F. Müller-Plathe, *Phys. Rev. E*, 1999, **59**, 4894–4898.
30. J. P. Hansen and I. R. McDonald, *Theory of Simple Liquids*, Academic Press, 3rd edn, 2006.
31. B. J. Alder and T. E. Wainwright, *Phys. Rev. Lett.*, 1963, **18**, 988–990.
32. B. J. Alder, D. M. Glass and T. E. Wainwright, *J. Chem. Phys.*, 1970, **53**, 3813–3826.
33. J. C. Dyre, *Phys. Rev. E*, 2013, **87**, 022106.
34. H. Bock, K. E. Gubbins and M. Schoen, *J. Phys. Chem C*, 2007, **111**, 15493–15504.
35. H. Hoang and G. Galliero, *Phys. Rev. E*, 2012, **86**, 021202.
36. H. Liu, C. M. Silva and E. Macedo, *Chem. Eng. Science*, 1998, **53**, 2403–2422.
37. H. Sigurgeirsson and D. M. Heyes, *Mol. Phys.*, 2003, **101**, 469–482.
38. D. M. Heyes and A. C. Branka, *Phys. Chem. Chem. Phys.*, 2008, **10**, 4036–4044.
39. J. H. Dymond, *J. Chem. Phys.*, 1974, **60**, 969–973.
40. R. J. Speedy, *Mol. Phys.*, 1987, **62**, 509.
41. D. M. Heyes and A. C. Branka, *J. Chem. Phys.*, 2005, **122**, 234504.
42. W. T. Ashurst and W. G. Hoover, *Phys. Rev. A*, 1975, **11**, 658–678.
43. Y. Rosenfeld, *J. Phys.: Condens. Matter*, 1999, **11**, 5415.
44. Y. D. Fomin, V. V. Brazhkin and V. N. Ryzhov, *JETP Letters*, 2012, **95**, 320–325.
45. K. Meier, A. Laesecke and S. Kabelac, *J. Chem. Phys.*, 2004, **121**, 9526–9535.
46. K. Meier, A. Laesecke and S. Kabelac, *J. Chem. Phys.*, 2004, **121**, 3671–3687.
47. G. Galliero, C. Boned and A. Baylaucq, *Ind. Eng. Chem. Res.*, 2005, **44**, 6963–6972.
48. A. E. Nasrabad, R. Laghaei and B. C. Eu, *J. Chem. Phys.*, 2006, **124**, 084506.
49. K. Meier, A. Laesecke and S. Kabelac, *J. Chem. Phys.*, 2005, **122**, 014513.
50. R. L. Rowley and M. M. Painter, *Int. J. Thermophys.*, 1997, **18**, 1109–1121.
51. Y. Zhu, J. Zhou, Y. Wang and J. Shi, *Fluid Phase Equilib.*, 2002, **194–197**, 1141–1159.
52. M. S. Zabaloy, V. R. Vasquez and E. A. Macedo, *Fluid Phase Equilib.*, 2006, **242**, 43–56.
53. M. S. Zabaloy, V. R. Vasquez and E. A. Macedo, *J. Supercrit. Fluids*, 2005, **36**, 106.
54. I. C. Yeh and G. hummer, *J. Phys. Chem. B*, 2004, **108**, 15873–15879.
55. H. Y. Oderji, H. Ding and H. Behnejad, *Phys. Rev. E*, 2011, **83**, 061202.
56. V. G. Baidakov, S. P Protsenko and Z. R. Kozlova, *J. Chem. Phys.*, 2012, **137**, 164507.

57. V. G. Baidakov, S. P. Protsenko and Z. R. Kozlova, *Fluid Phase Equilib.*, 2011, **305**, 106–113.
58. D. M. Heyes, *Phys. Rev. B*, 1988, **37**, 5677–5696.
59. O. Suarez-Iglesias, I. Medina, C. Pizarro and J. L. Bueno, *Chem. Eng. Sci.*, 2007, **62**, 6499–6515.
60. G. Galliero, C. Boned and J. Fernandez, *J. Chem. Phys.*, 2011, **134**, 064505.
61. R. V. Vaz, A. L. Magalhaes, D. L. A. Fernandez and C. M. Silva, *Chem. Eng. Sci.*, 2012, **79**, 153–162.
62. M. S. Shell, *J. Chem. Phys.*, 2012, **137**, 084503.
63. D. J. Evans and H. J. M Hanley, *Phys. Rev. A*, 1979, **20**, 1648–1654.
64. S. Murad, *AIChE J.*, 1990, **36**, 948–950.
65. R. Castillo, A. Villaverde and J. Orozco, *Fluid Phase Equilib.*, 1992, **79**, 277–288.
66. G. Galliero, C. Boned, A. Baylaucq and F. Montel, *Fluid Phase Equilib.*, 2005, **234**, 56–63.
67. G. Galliero, C. Boned, A. Baylaucq and F. Montel, *Fluid Phase Equilib.*, 2006, **245**, 20–25.
68. M. N. Bannerman and L. Lue, *J. Chem. Phys.*, 2009, **130**, 164507.
69. S. R. De Groot and P. Mazur, *Non-Equilibrium Thermodynamics*, Dover, New York, 1st edn, 1984.
70. S. Wiegand, *J. Phys. Condensed Matter*, 2004, **16**, R357–R379.
71. A. Würger, *C. R. Mecanique*, 2013, **341**, 438–448.
72. D. Reith and F. Müller-Plathe, *J. Chem. Phys.*, 2000, **112**, 2436–2443.
73. P. A. Artola, G. Galliero and B. Rousseau, *J. Am. Chem. Soc.*, 2008, **130**, 10963–10969.
74. S. Yeganegi and M. Zolfaghari, *Fluid Phase Equilib.*, 2006, **243**, 161–165.
75. J. M. Kincaid and B. Hafskjold, *Mol. Phys.*, 1994, **82**, 1099–1114.
76. G. Galliero, B. Duguay, J. P. Caltagirone and F. Montel, *Philos. Mag.*, 2003, **83**, 2097–2108.
77. G. Galliero and F. Montel, *Phys. Rev. E*, 2008, **78**, 041203.
78. S. W. Smith, C. K. Hall and B. D. Freeman, *J. Chem. Phys.*, 1995, **102**, 1057–1073.
79. R. A. Reis, F. C. Silva, R. Nobrega, J. V. Oliveira and F. W. Tavares, *Fluid Phase Equilib.*, 2004, **221**, 25–33.
80. T. Goel, C. N. Patra, T. Mukherjee and C. Chakravarty, *J. Chem. Phys.*, 2008, **129**, 164904.
81. T. A. Hunt and B. D. Todd, *Mol. Sim.*, 2009, **35**, 1153–1167.
82. S. Delage Santacreu, G. Galliero, M. Odunlami and C. Boned, *J. Chem. Phys.*, 2012, **137**, 204306.
83. A. GilVillegas, A. Galindo, P. J. Whitehead, S. J. Mills, G. Jackson and A. N. Burgess, *J. Chem. Phys.*, 1997, **106**, 4168–4186.
84. E. Müller and K. Gubbins, *Ind. Eng. Chem. Res.*, 2001, **40**, 2193–2211.
85. R. Hellmann, N. Riesco and V. Vesovic, *J. Chem. Phys.*, 2013, **138**, 084309.
86. Z. Liu, S. Huang and W. Wang, *J. Phys. Chem. B*, 2004, **108**, 12978–12989.

87. M. Aquing, F. Ciotta, B. Creton, C. Fejean, A. Pina, C. Datiguelongue, J. P. M. Trusler, R. Vignais, R. Lugo, P. Ungerer and C. Nieto-Draghi, *Energy Fuels*, 2012, **26**, 2220–2230.
88. M. Touzet, G. Galliero, V. Lazzeri, M. Z. Saghir, F. Montel and J. C. Legros, *C. R. Mecanique*, 2011, **339**, 318–323.
89. W. L. Jorgensen, D. S. Maxwell and J. Tirado-Rives, *J. Am. Chem. Soc.*, 1996, **118**, 11225–11236.
90. M. G. Martin and J. I. Siepmann, *J. Phys. Chem. B*, 1998, **102**, 2569–2577.
91. S. Toxvaerd, *J. Chem. Phys.*, 1990, **93**, 4290–4295.
92. B. R. Brooks, R. E. Bruccoleri, B. D. Olafson, D. J. States, S. Swaminathan and M. Karplus, *J. Comp. Chem.*, 1983, **4**, 187–217.
93. M. G. Martin and A. P. Thompson, *Fluid Phase Equilib.*, 2004, **217**, 105–110.
94. C. Nieto-Drgahi, P. Ungerer and B. Rousseau, *J. Chem. Phys.*, 2006, **125**, 044517.
95. M. S. Kelkar, J. L. Rafferty, E. J. Maginn and J. I. Siepmann, *Fluid Phase Equilib.*, 2007, **260**, 218–231.
96. R. A. Aziz, *J. Chem. Phys.*, 1993, **99**, 4518–4525.
97. L. A. Rowley, D. Nicholson and N. G. Parsonage, *J. Comp. Phys.*, 1975, **17**, 401–414.
98. E. W. Lemmon and R. T. Jacobsen, *Int. J. Thermophys.*, 2004, **25**, 21–69.
99. J. A. Cowan and R. N. Ball, *Can. J. Phys.*, 1972, **50**, 1881–1886.
100. G. Galliero, C. Boned, A. Baylaucq and F. Montel, *Phys. Rev. E*, 2006, **73**, 061201.
101. S. H. Lee and P. T. Cummings, *J. Chem. Phys.*, 1993, **99**, 3919–3925.
102. G. A. Fernandez, J. Vrabec and H. Hasse, *Fluid Phase Equilib.*, 2004, **221**, 157–163.
103. S. V. Lishchuk, *J. Chem. Phys.*, 2012, **136**, 164501.
104. M. Bugel and G. Galliero, *Chem. Phys.*, 2008, **352**, 249–257.
105. E. A. Müller and L. D. Gelb, *Ind. Eng. Chem. Res.*, 2003, **42**, 4123–4131.
106. G. A. Fernandez, J. Vrabec and H. Hasse, *Mol. Sim.*, 2005, **31**, 787–793.
107. G. Galliero and C. Boned, *Fluid Phase Equilib.*, 2008, **269**, 19–24.
108. B. R. Giri, P. Blais and R. A. Marriot, *Carbon Dioxide Sequestration and Relative Technologies*, ed. Y. Wu, J.J Caroll and Z. Du, Wiley-Scrivener, Salem, Massachusetts, USA, 1st edn, 2011, ch. 3, pp. 23–40.
109. D. K. Dysthe, A. H. Fuchs and B. Rousseau, *J. Chem. Phys.*, 2000, **112**, 7581–7590.
110. D. Bedrov and G. D. Smith, *J. Chem. Phys.*, 2000, **113**, 8080–8084.
111. H. Zhang and J. F. Ely, *Fluid Phase Equilib.*, 2004, **217**, 111–118.
112. S. W. I. Siu, K. Pluhakova and R. A. Böckmann, *J. Chem. Theory Comput.*, 2012, **8**, 2012.
113. R. S. Payal, S. Balasubramanian, I. Rudra, K. Tandon, I. Mahlke, D. Doyle and R. Cracknell, *Mol. Sim.*, 2012, **38**, 1234–1341.
114. H. Feng, W. Gao, J. Nie, J. Wang, X. Chen, L. Chen, X. Liu, H. D. Lüdemann and Z. Sun, *J. Mol. Mod.*, 2013, **19**, 73–82.
115. C. Nieto-Draghi, P. Ungerer and B. Rousseau, *J. Chem. Phys.*, 2006, **125**, 044517.

116. C. Nieto-Draghi, A. Bocahut, B. Creton, P. Have, A. Ghoufi, A. Wender, A. Boutin, B. Rousseau and L. Normand, *Mol. Sim.*, 2008, **34**, 211–230.
117. D. K. Dysthe, A. H. Fuchs, B. Rousseau and M. Durandeau, *J. Chem. Phys.*, 1999, **110**, 4060–4067.
118. J. M. Van Baten and R. Krishna, *Ind. Eng. Chem. Res.*, 2005, **44**, 6939–6947.
119. H. A. Patel, S. Garde and E. B. Nauman, *AIChE J.*, 2006, **52**, 1304–1307.
120. J. M. Simon, D. K. Dysthe, A. H. Fuchs and B. Rousseau, *Fluid Phase Equilib.*, 1998, **150**, 151–159.
121. H. M. Schaink, H. Luo and C. Hoheisel, *J. Chem. Phys.*, 1993, **99**, 9912–9916.
122. P. Polyakov, F. Mülelr-Plathe and S. Wiegand, *J. Phys. Chem. B*, 2008, **112**, 14999–15004.
123. B. Guillot, *J. Mol. Liquid*, 2002, **101**, 219–260.
124. L. Gao and W. Fang, *J. Chem. Phys.*, 2011, **135**, 184101.
125. G. Lamoureux, A. D. MacKerell and B. Roux, *J. Chem. Phys.*, 2003, **119**, 5185–5197.
126. P. Ren and J. W. Ponder, *J. Phys. Chem. B*, 2003, **107**, 5933–5947.
127. G. Guevara-Carrion, J. Vrabec and H. Hasse, *J. Chem. Phys.*, 2011, **134**, 074508.
128. J. L. Abascal and C. Vega, *J. Chem. Phys.*, 2005, **123**, 234505.
129. M. S. Kelkar, J. L. Rafferty, E. J. Maginn and J. I. Siepmann, *Fluid Phase Equilib.*, 2007, **260**, 218–231.
130. E. J. W. Wensink, A. C. Hoffman, P. J. Van Maaren and D. Van Der Spoel, *J. Chem. Phys.*, 2003, **119**, 7308–7317.
131. C. Nieto-Draghi, J. B. Avalos and B. Rousseau, *J. Chem. Phys*, 2005, **122**, 114503.
132. C. Cadena, Q. Zhao, R. Q. Snurr and E. J. Maginn, *J. Phys. Chem. B*, 2006, **110**, 2821–2832.
133. T. Köddermann, D. Paschek and R. Ludwig, *ChemPhysChem*, 2007, **8**, 2464–2470.
134. O. Borodin, *J. Phys. Chem. B*, 2009, **113**, 11463–11478.
135. M. H. Kowsari, S. Alavi, M. Ashrafizaadeh and B. Najafi, *J. Chem. Phys.*, 2009, **130**, 014703.
136. O. Andreussi and N. Mazari, *J. Chem. Phys.*, 2012, **137**, 044508.
137. S. Gabz, C. Schröder and O. Steinhauser, *J. Chem. Phys.*, 2012, **137**, 094501.
138. http://www.stfc.ac.uk/cse/default.aspx.
139. http://www.gromacs.org/.
140. http://lammps.sandia.gov/.
141. A. S. De Wijn, V. Vesovic, G. Jackson and J. P. M. Trusler, *J. Chem. Phys.*, 2008, **128**, 204901.
142. F. Llovell, R. M. Marcos and L. F. Vega, *J. Phys. Chem. B*, 2013, **117**, 5195–5205.
143. W. Xie and J. Gao, *J. Chem. Theory Comput.*, 2007, **3**, 1890–1900.

Subject Index